IAHR 2017

Supported by Spain Water and IWHR, China

37th IAHR WORLD CONGRESS

13-18 August, 2017

Kuala Lumpur, Malaysia

DYNAMICS AND EXCHANGES IN ESTUARY-COASTAL ZONE

PRELIMINARY ANALYSIS ON EVOLUTION OF PEARL RIVER ESTUARY

JIAQUAN DENG[(1)] & HUI DENG[(2)]

[(1,2)]Key Laboratory of the Pearl River Estuarine Dynamics and Associated Process Regulation;
Pearl River Hydraulic Research Institute, Ministry of Water Resources, Guangzhou, China
jiaquandeng@163.com

ABSTRACT

The Pearl River consists of the West, North and East Rivers and the river Delta consists of more than 200 waterways which form a complex network-river estuary. The Pearl River discharges into the South China Sea through eight outlets. Both the upstream fresh water and the downstream tide are mixed and form back and forth flows in the estuary. Under the dual roles of both nature and human activities, the evolution of the rivers at the estuary is of complex. Based on analysis of the variations in water-sediment processes both in the network-rivers and the river-outlets, this paper explores the responses of the hydrodynamics, including the flow-diversion ratios at the first- and second-level flow-diversion nodes in the network rivers, and the flow-diversion ratios at outlets. The results show that in the recent three decades: (1) the water-sediment amount diverting towards south-east has increased in the network-rivers and hence, resulted in an increase of the flow distribution of the Lingdingyang Bay, and (2) the extensive human activities have dramatically changed the topographic and hydrodynamic features of the estuary, especially, the uncontrolled sediment mining from the network-rivers has caused a large amount of river-bed-sediment being excavated, and the large-scale reclamation of beaches or shoals along coastal areas outside the outlets has caused a significant influence on the evolution of the estuary.

Keywords: Pearl River Estuary; sediment transport; estuary evolution; human activities; network-rivers.

1 INTRODUCTION

The Pearl River consists of the West River, the North River and the East River. It is the largest river in south China, with the basin area 453,700 km^2. The lengths of the West, the North and the East Rivers are 2075km, 468km and 520km, respectively. The West River and the North River converge to the Pearl River Delta at the Shixianjiao, and the East River flows to the Delta at the Shilong, The three rivers form complicated network rivers at the Delta and discharge into the South China Sea through eight outlets named the Humen, Jiaomen, Hongqimen, Hengmen, Modaomen, Jitimen, Hutiaomen and Yamen (Fig. 1). The first four east outlets discharge into the Lingdingyang Bay. Different outlets have different characters of the water flow and sediment transport. The Modaomen is the largest runoff outlet and the Humen is the largest tidal outlet. Although the sediment concentration is relatively lower in the estuary, the sediment amount transported is very large due to the huge upstream runoff.

Under the dual roles of both natural changes and strong human activities, the evolution of the rivers at the estuary has become extremely complex. Naturally, the network-rivers and the outlets have been in the sediment deposition over a long period of time which has caused various problems. Firstly, due to the sedimentation in the network-rivers, the water level in the Delta center has been getting higher in recent years, which has caused the flood problem. And due to the sedimentation in the outlets, the bars and shoals have been growing and the outlets extend to the sea further. Secondly, the sediment depositions in the harbors or navigational channels have been bothering the navigation development in the estuary, and the sediment deposition is always a key problem for the constructions of the new harbors or navigational channels.

On the other hand, the extensive human activities have showed an obvious influence on the river water-sediment transport in the estuary. In recent three decades, with the rapid economic development in the Estuary area, a lot of infrastructures, such as harbors, navigational channels, bridges, bases for building or repairing ships, and etc. have been built along or in the rivers or outlets. In addition, a large-scale reclamation of the beaches or shoals along coastal areas outside the outlets has been continuously carried out. The uncontrolled sediment manning from the river-bed for the building construction has caused a large amount of river-bed-sediment being excavated. A large-scale levees or dikes have been constructed along rivers or outlets. Furthermore, the navigational channels have been dredging deeper and deeper. Many new and large harbors and navigational channels are under construction. These extensive human activities have changed the topographic and hydrodynamic features of the rivers at the Estuary and resulted in many problems including the flood-protection, sea-water intrusion, fresh-water supply, waterlogged-land drainage, and etc.

Based on analysis of the variations in water-sediment processes, this paper explores the responses of the hydrodynamics, including upstream runoff and tidal currents, and the sediment transport at the Estuary under extensive human activities. On these grounds, a river-bed evolution is analyzed. These results provide a basis for the governing, developing and protecting of the estuary.

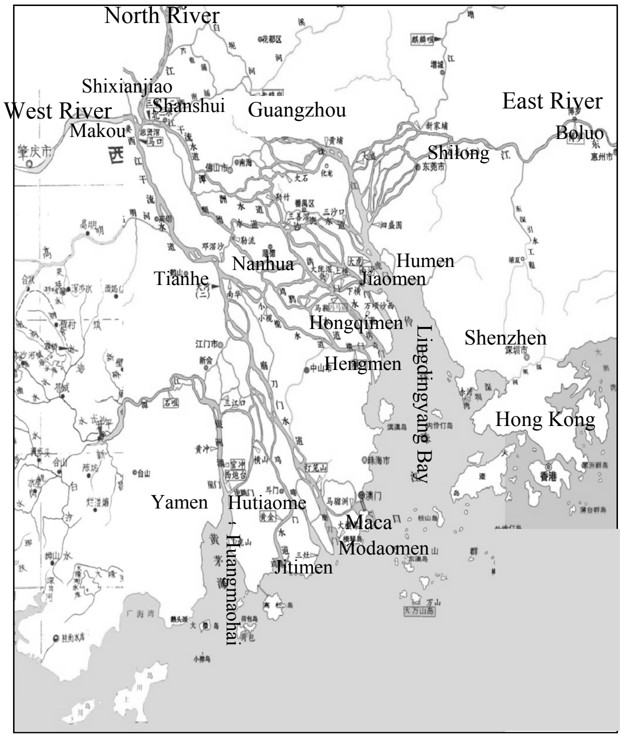

Figure 1. Pearl River Estuary

2 WATER- SEDIMENT AT PEARL RIVER ESTUARY

Naturally, the water flow and sediment transport in the Estuary are influenced not only by the upstream runoff and sediment, but also by the tidal current from the South China Sea. In addition, the wind wave and the salinity also have influence on the sediment movement in the estuary.

2.1 Upstream water-sediment

(1) The upstream runoff is mainly from the West, North and East Rivers; accounting for 70.6%, 14.63% and 7.32%, respectively, and other is from local rivers accounting for 6.45%.

The temporal distribution of the runoff is extremely uneven. In flood seasons from April to September, the runoffs of the West, North and East Rivers account for 71.55%, 83.41%, and 71.32%, respectively.
Figure 2 shows annual runoffs from the West (at Makou station), North (at Shanshui station) and East (at Boluo station) rivers, indicating a large inter-annual variation and a large difference between the low and high runoff. The ratios of the runoffs in flood seasons to those in dry seasons for the West, North and East rivers are 2.62, 9.86 and 4.62, respectively.

(2) The runoff variations of the West and North rivers during dry seasons

By comparing the average runoffs between the West and North rivers in dry seasons, it shows that the average runoff in dry seasons at Shanshui after 1990 doubly increases than that before 1990, while the corresponding runoff at Makou decreases by 8.5%.

(3)Inter-annual sediment variation

Since 1990, the upstream sediment concentration has gradually reduced, especially, after 2000, the average annual sediment concentrations at the Makou and Shanshui stations have reduced by 61.6% and 66.1%, respectively, comparing with 1980s. The average concentration at the Boluo station has reduced by 80% comparing with 1990s.

2.2 Water-sediment in outlets

The annual average runoff of the Pearl River is about 326 billion m^3, 53.4% of which going through the east four outlets, and 46.6% of which going through the west four outlets into the sea. The Modaomen has the largest runoff, through which 28.3% fresh water of the Pearl River discharges into the sea.

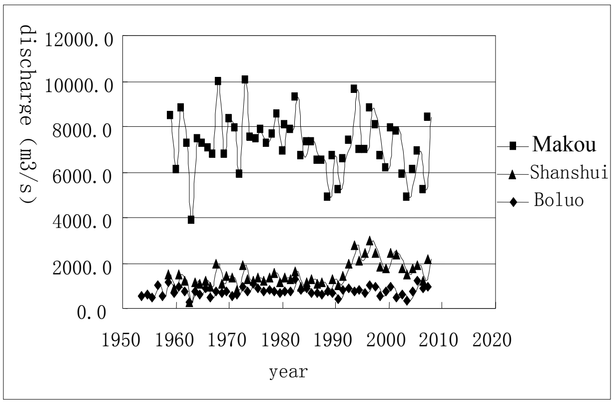

Figure 2. Runoffs at Makou, Sanshui and Boluo in dry seasons

The average sediment amount of the Pearl River is about 71 million t, 47.7% of which transported through the east four outlets, and 52.3% of which transports through the west four outlets into the sea. Through the Modaomen, 33% sediment of the Pearl River transports into the sea. Table 1 shows the details of the sediment distribution among the eight outlets.

Table 1. Sediment distribution among eight outlets

	Humen	Jiaomen	Hongqi	Hengmen	Modaomen	Jitimen	Hutiaomen	Yamen
Annual amount (10^5 t)	65.8	128.9	51.7	92.5	234.1	49.6	50.9	36.3
percentage	9.3	18.1	7.3	13	33	7	7.2	5.1

The average sediment concentration in the network rivers of the estuary ranges from 0.19kg/m^3 to 0.25kg/m^3. In the coastal area near the outlets or the Bay, the sediment concentration is between 0.02kg/m^3 and 0.33kg/m^3. The sediment concentration is closely related with the current velocity. When the tide is larger, the sediment concentration is higher. In addition, the sediment concentration during flood seasons is higher than that in dry seasons; the concentrations during ebb tidal periods are higher than flood tidal periods. The high concentration occurs near the bars or shoals.

2.3 The variations of flow-diversion ratios in network rivers

(1) Variations of the flow-diversion ratios at the Makou and Shanshui stations

The West River links the North River at the Sixianjiao which is the first-level flow-diversion node. After the flow re-distribution, the water flows through the Makou (representing the entrance of the West River) and the Shanshui (representing the entrance of the North River). Table 2 and Figure 3 show the variations of flow-diversion ratios with the average discharges at the Makou and the Shanshui after the first level diversion node.

Table 2. Variations of flow-diversion ratios at Makou and Sanshui stations

period	Makou		Sanshui	
	average discharge (m^3/s)	account for(%)	average discharge (m^3/s)	account for(%)
1959~1989	7179.0	86.03	1166.0	13.97
1990~1999	7264	79.18	1910	20.82
2000~2009	6232	77.51	1808	22.49

It shows that the diversion ratio at the Shanshui increases with the flow discharges. During 1960s-1980s, the diversion ratios at the Shanshui and Makou kept stable and the diversion ratio at Shanshui varied between 7.2~16.5%. During 1990~1999, the diversion ratio at Shanshui increased to 15.6~25.5% and reached the maximum in 1996. After 2000, the ratio at Shanshui varied from 21.5~24%.

(2)Variations of flow-diversion ratios at the Tianhe and Nanhua stations (the second-level diversion nodes).

After the Shixianjiao (the first-level flow-diversion node), the Tianhe and Nanhua stations are of the second-level diversions (Fig. 1). Study shows that the flow-diversion ratios at the Nanhua increased with the discharges at Makou, ranged from 38.1~46% before 1990. Since then, the diversion ratios have increased to 44.5~48%.

(3) Variations of flow-diversion ratios at outlets

From above analysis on the variations of the flow-diversion ratios at two nodes, it is known that since 1990, the eastward flow-diversions in the network rivers have increased, resulting in an increase of the runoff discharging into the Lingdingyang Bay from the eastern four outlets. Table 3 shows the variations of the diversion ratios at eight outlets, indicating that the diversion ratios from the eastern four outlets in 2000s have increased by approximately 12%, comparing with the case in 1980s.

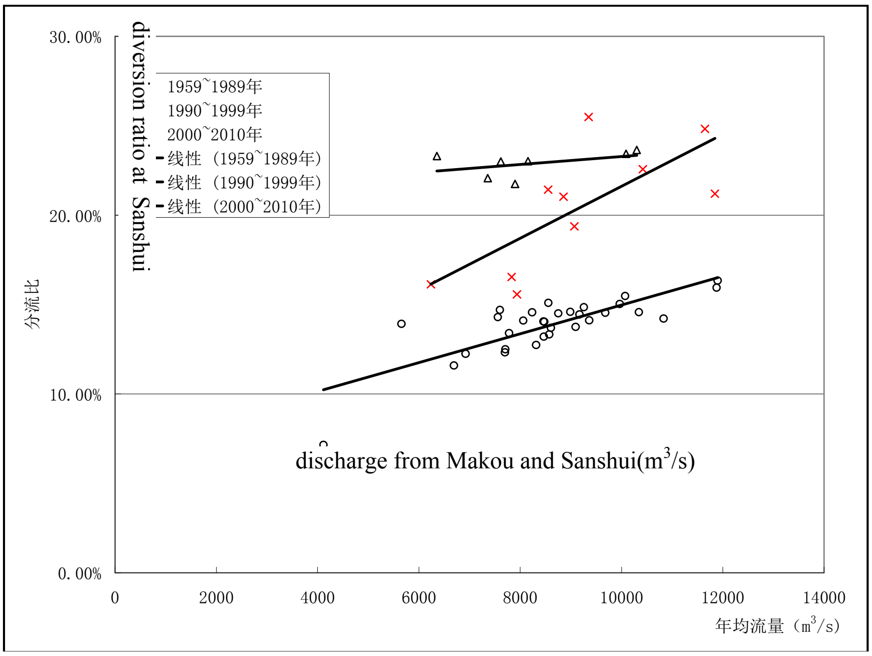

Figure 3. Relations of flow-diversion ratio at Shanshui with the discharge from Makou & Shanshui

2.4 Characteristics of sediment transport in network rivers

The sediment in the estuary comes mainly from the flood season. Since 1990, the upstream sediment amount has reduced about 52%, resulting in the unsaturated sediment transport in network rivers during flood seasons. Figure 4 shows the variations of the bed load and suspended load sizes along the main stream of the West River.

Table 3. Variations of flow-diversion ratios at eight outlets (%)

period	East four outlets					West four outlets				
	Humen	Jiaomen	Hongqimen	Hengmen	Mini-total	Modaomen	Jitimen	Hutiaomen	Yamen	Mini-total
1980s	18.5	17.3	6.4	11.2	53.4	28.3	6.1	6.2	6	46.6
1990s	23.05	18.79	10.95	11.14	63.94	24.48	3.86	3.85	3.88	36.06
2000s	27.85	18.49	9.05	10.41	65.79	23.26	3.19	3.31	4.45	34.21

Figure 5 shows the variations of the sediment concentration along the West River. It shows that sediment concentration in flood seasons increases along the river. This indicates that the sediment is not only from the upstream but also from the local erosion. This further explains that since 1990s, the river erosion strengthens the network rivers cutting down.

According to the analysis of the suspended sediment size distribution in the network rivers in recent years, it is found that the median particle size decreases and the sediments are refined along the rivers. With the refinement, the sediment in the network rivers can be transported farther towards outlets.

2.5 Characteristics of sediment transport in the outlets

Characteristics of sediment transport in the outlets are different in different seasons. During flood period, the sediment is mainly transported by the runoff in the estuary. The runoff carries a large amount of sediment to the shallow water areas. In the Lingdingyang Bay, under the influence of the strong tidal flow on the east-side, the sediment is transported southward along the west-side, and spread to the east-side. The sediment concentration distribution takes on higher on the west-side and lower on the east-side, and higher on the north-side and lower on the south-side.

In the Modaomen, the sediment is transported towards the southwest and the shallow water areas of the Jitimen and Huangmaohai Bay under the influence of the runoff from Lingdingyang Bay.

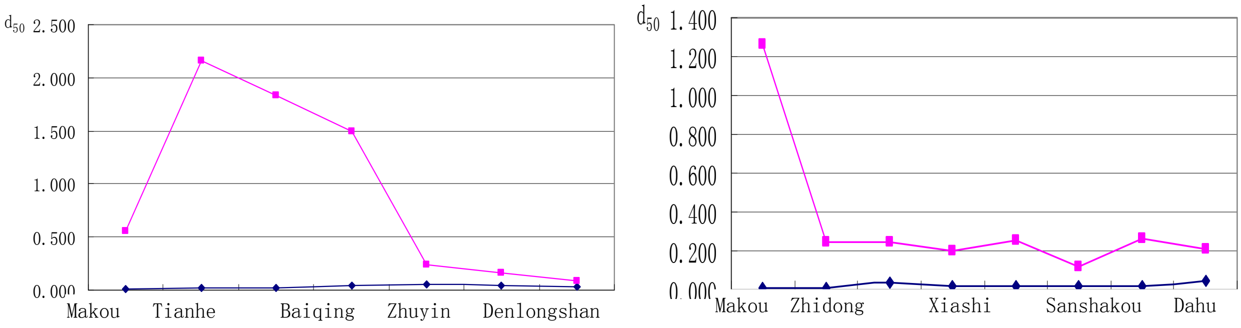

（a）Along main stream of West River （b）Along main stream of North River

Figure 4. Variation of bed load and suspended load sizes along main streams

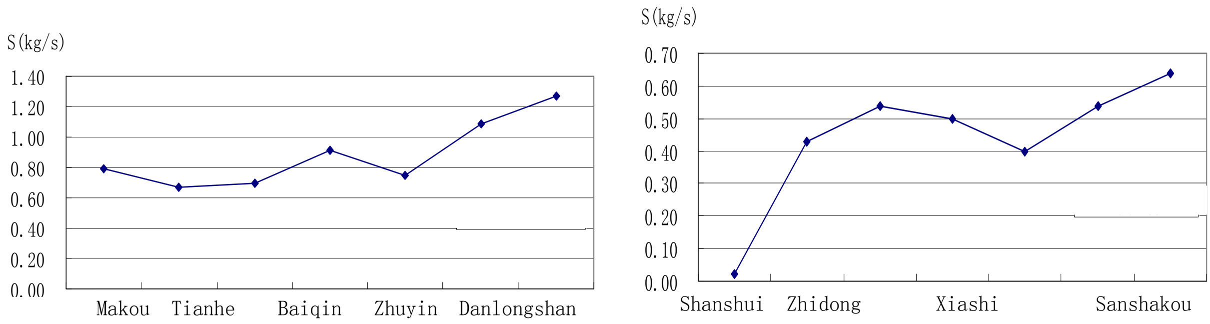

(a) Along main stream of West River (b) Along main stream of North River

Figure 5. Variation of suspended concentration along main streams

In the Huangmaohai Bay, under the influence of the tidal flow on the east- channel, the sediment is transported southward and spread to the east-side.

During the dry season, the runoff dynamic and the sediment carried from upstream sharply reduce, while offshore tidal dynamic strengthens. The characteristics of the sediment transport take on “the waves lift the sediment from river-beds and the tides transport the sediment”. And there obviously are phenomena of the secondary sediment transport from shoals. The suspended sediment distribution takes on the features "shoals higher and channels lower”.

In Lingdingyang Bay and Huangmaohai Bay, under influences of the tidal flow on their east- channels, the sediments are transported towards southwest along the west shores.

3 SEDIMENT FLOCCULATING SETTLING AND SEDIMENT-LADEN CAPACITY AT THE PEARL RIVER ESTUARY

3.1 Sediment flocculating settling velocity

Sediment flocculating settling velocity is one of important parameters of sediment transport in estuaries.

(1)Relationship between the flocculation settling velocity, sediment piratical size and deposition distance.

Study shows that there is the following relationship between the flocculation settling velocity ω_f, the sediment practical size and the deposition distance:

$$\omega_f = 0.00177 \mathrm{d}_{50}{}^{-1.82} \omega_0 \left[1 - (1 - 0.056 S^{0.5}) \cdot 10^{-0.5 H^{0.7} S^{0.1}} \right]^2 \qquad [1]$$

where ω_0 is the settling velocity without flocculation; S is the deposition distance; d_{50} is the mean particle size. H is the water depth.

(2) Effects of salinity on sediment flocculation settling

The salinity and sediment grain size have a direct impact on sediment flocculation and settling. Through the experiments of the cohesive sediment flocculation in a salt water environment, it shows that the sediment with median sizes ranging from 0.003~0.011mm is easy to flocculate, while the sediment with median sizes greater than 0.034mm and less than 0.003mm is basically not of flocculation.

The experiments give the typical relationships between the sediment flocculation settling velocities and the salinities in the Pearl River Estuary (Figure 6). It shows that the salinities between 18~20‰ benefit the sediment to settle down.

Through the analysis of the sediment settling velocity in different salinity in estuary, the following relationships between the flocculation velocity ω_{fc}, and the salt content *C* are obtained (Figure 7):

$$\omega_{fc} = (125 + 10.1C) d_{50}^{0.89} \omega_f \quad C \leq 20‰; \tag{2}$$

$$\omega_{fc} = (630 - 15.1C) d_{50}^{0.89} \omega_f \quad C > 20‰; \tag{3}$$

(3) Effects of water flow velocity on sediment flocculation settling

Through the experiments and analysis, the effect of the water flow velocity *v* on the sediment flocculation settling velocity ω_{fv}, is obtained as follows (Figure 8):

$$\omega_{fv} = (1 - 1.4189v)\omega_{fc} \tag{4}$$

It shows that when the water flow velocity is 0.705, the flocculation settling velocity is zero, indicating no sediment flocculation occurring.

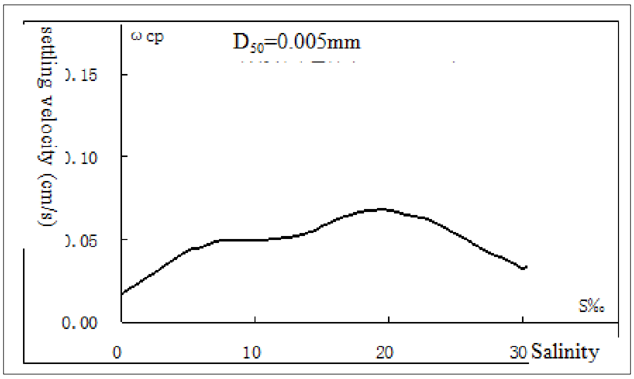

Figure 6. Relationship between salinity and flocculation settling velocity at Lingdingyang Bay

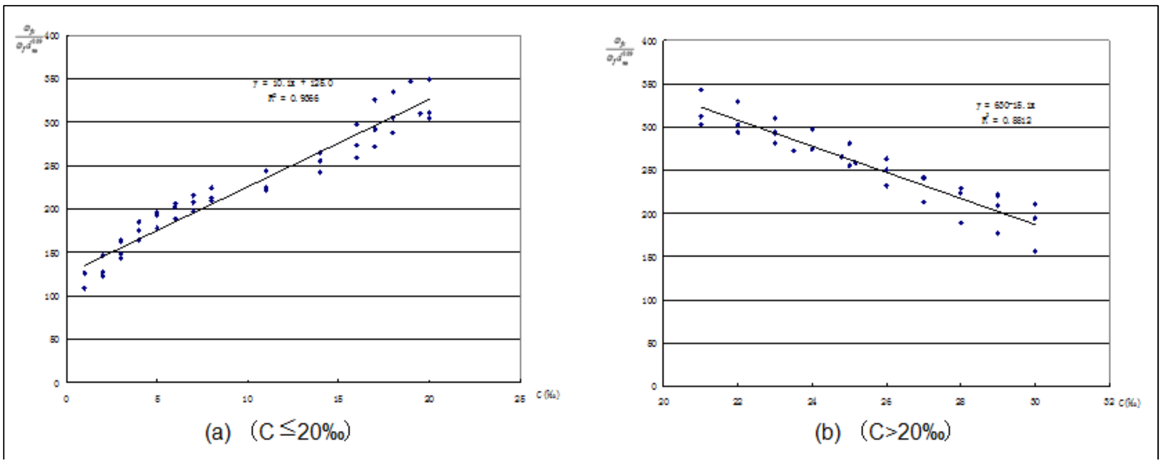

Figure 7. Relationship between salinity and flocculation settling velocity

By taking multi-factors into account, the following flocculation settling velocity formulas are obtained:

When C=0,

$$\omega_{fv} = \max\{0.00177\,(1-1.4189\,v)\mathrm{d}_{50}{}^{-1.82}\,\omega_0 \left[1-(1-0.056\,S^{0.5})\cdot 10^{-0.5H^{0.7}S^{0.1}}\right]^2, \omega_0\} \quad [5]$$

When 0<C ≤20‰,

$$\omega_{fv} = \max\{0.00177(1-1.4189v)(125+10.1C)\,\mathrm{d}_{50}{}^{-0.93}\omega_0\left[1-(1-0.056S^{0.5})\cdot 10^{-0.5H^{0.7}S^{0.1}}\right]^2, \omega_0\} \quad [6]$$

When C >20‰,

$$\omega_{fv} = \max\{0.00177(1-1.4189v)(630-15.1C)\,\mathrm{d}_{50}{}^{-0.93}\omega_0\left[1-(1-0.056S^{0.5})\cdot 10^{-0.5H^{0.7}S^{0.1}}\right]^2, \omega_0\} \quad [7]$$

3.2 Tidal sediment-laden capacity

Based on analysis of the measured data in the network rivers of the estuary, the sediment-laden capacity is proportional to the third power of the water flow velocity, and is inversely proportional to the settling velocity and hydraulic radius. The sediment-laden capacity in network rivers is as follows (Figure 9):

$$S_* = 312.85 d_{50}^{2.11}\frac{U^3}{R\omega} \quad [8]$$

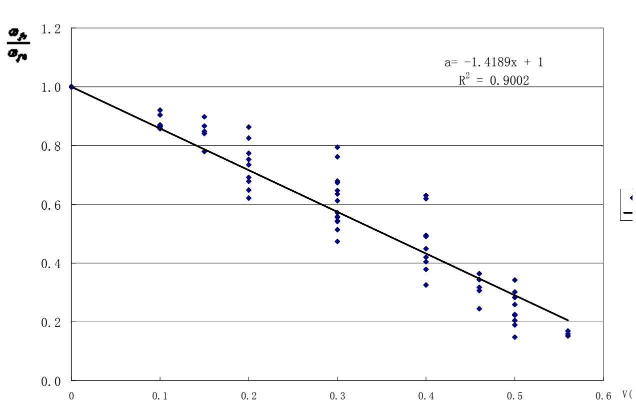

Figure 8. Flow velocity and settling velocity

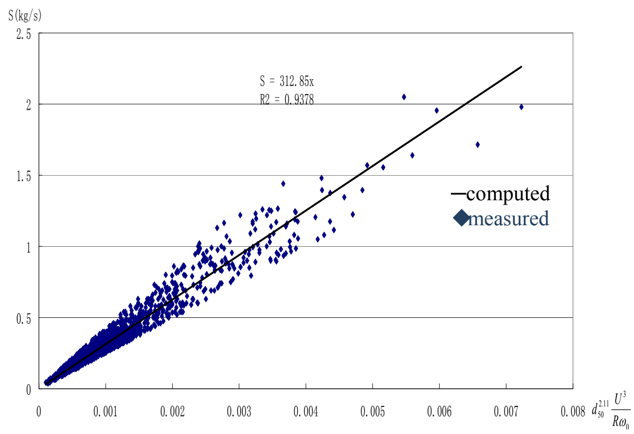

Figure 9. Tidal sediment-laden capacity

4 ANALYSIS OF THE EVOLUTION OF THE PEARL RIVER ESTUARY

4.1 Influence of the human activities on the evolution of the estuary

As mentioned in the Introduction, in recent three decades, with the rapid economic development, a lot of infrastructures have been built along or in the rivers or outlets of the Estuary. These extensive human activities have changed the topographic and hydrodynamic features of the rivers at the Estuary. Especially, the uncontrolled sediment manning from the river-bed for the building construction has caused a large amount of river-bed-sediment being excavated, and the constructions of harbors and navigational channels have enhanced the river-bed cutting down. Furthermore, the navigational channels have been dredging deeper and deeper, and many new and large harbors and navigational channels are under construction. In addition, a large-scale reclamation of the beaches or shoals along coastal areas outside the outlets has been continuously carried out, which has a significant influence on the evolution of the estuary.

4.1.1 Influence of the sand manning on the evolution of the estuary

(1) Changes of river topographies

Since 1980s, a large-scale sand manning from the rivers have caused obvious topographic changes of the rivers in the estuary. According to statistics, the gross sand manning amount from the network rivers in the Delta has reached 1.1 billion m^3. By comparing with the annual sediment yield of the Pearl River Basin of 71 million t, this means that it will take more than 100 years to fill up the sand manning space in the network rivers.

In the last twenty years, the average depths of network rivers have increased. The river-beds have been cut down averagely by 0.5-3.0m, and in some places it reached 6.0m. Figure 10 demonstrates the changes of typical cross-sections of the network rivers. And Figure 11 shows the longitudinal depth changes of the mainstream from Makou-Tianhe to the outlet.

(2)Analysis of variations of diversion ratios at network rivers

The uneven river-bed cutting down in the mainstreams of the network rivers is the main factor influencing the changes of the diversion ratios in the network rivers. Since 1980s, the sand mining from rivers, the harbor and navigational engineering have caused the uneven cutting on river beds (see Figure 10 and Figure 11). Due to the changes in the river topography, the water surface slopes of the rivers have correspondently been re-adjusted, as mentioned before. This has, in turn, resulted in the changes of the flow-diversion ratios at network nodes and the re-adjustment of the runoff and tidal dynamic distribution in network rivers. It shows that at the same discharge, the water level at the Shanshui dropped by 1.9m~2.3m, while the water level at the Makou dropped by 1.0m~1.2m by comparing the cases before and after 1980. The biggest decline of water levels occurs near the Makou and Sanshui stations.

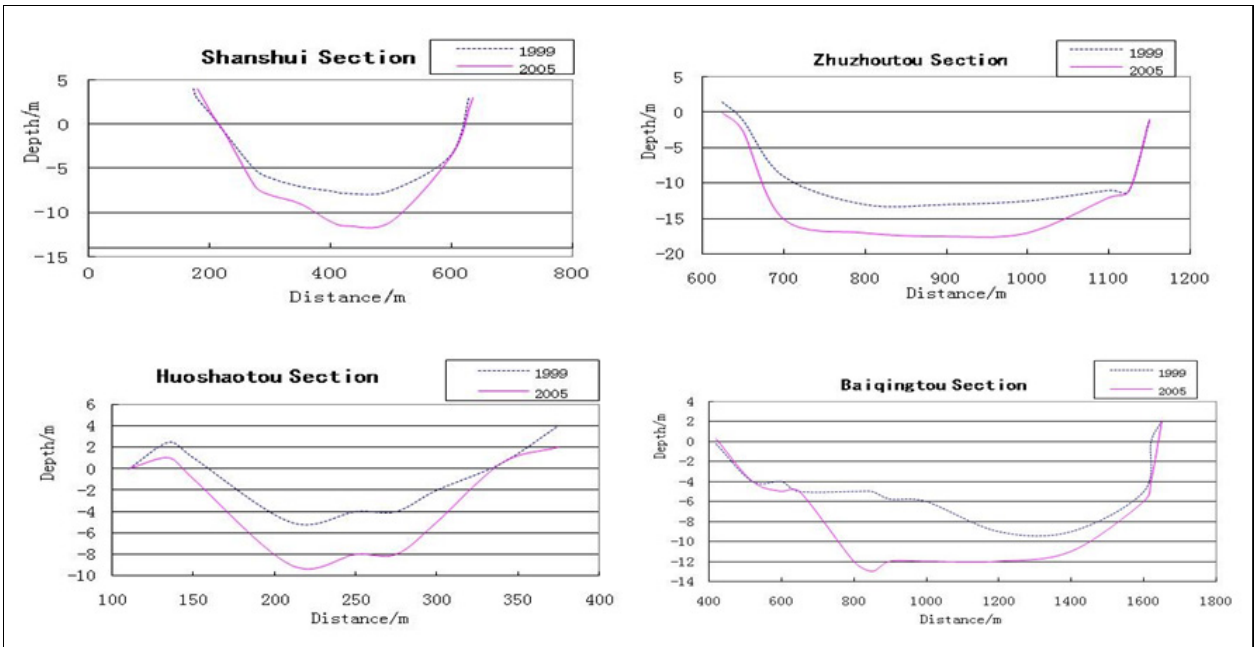

Figure 10. Changes of cross-sections of network rivers

(3) Analysis of variations in flow-diversion ratios at outlets

From above analysis on the variations of the flow-diversion ratios at two nodes, it is known that with the uneven river bed cutting down, the eastward flow-diversion has increased, resulting in an increase of the runoff discharging into the Lingdingyang Bay from the eastern four outlets. As shown in Table 3, the variations of the diversion ratios at the eight outlets indicate that the diversion ratios from the eastern four outlets in 2000s have increased by approximately 12%, comparing with the case in 1980s (Table 3).

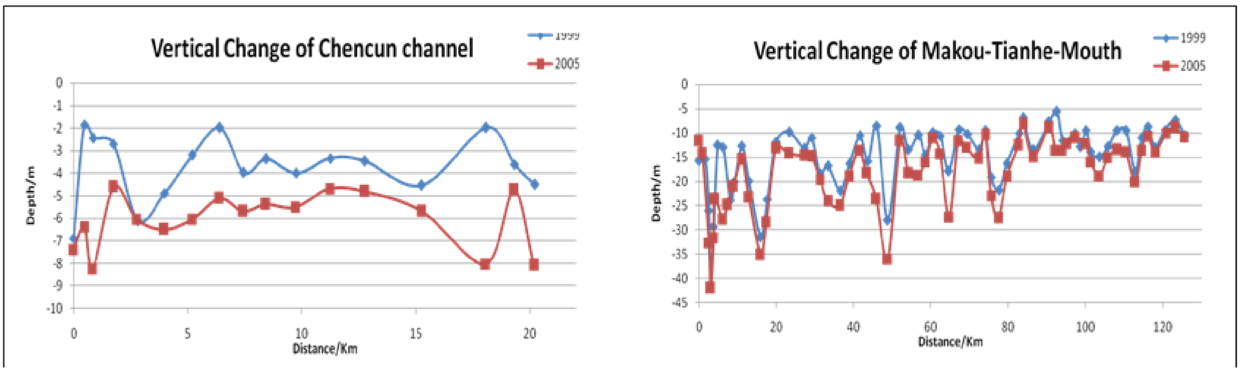

Figure 11. Longitudinal changes of water depths in network rivers

  / ISSN 1562-6865 (Online) - ISSN 1063-7710 (Print)

(4) Influence on tidal flows

With the river-bed cutting down, the tidal dynamics at the 8 outlets have increased. The spring tidal amount has increased by 2.03% and the ebb tidal amount has increased by 1.73%. At the eastern four outlets, the spring tidal amount has increased by 1.63% and the ebb tidal amount has increased by 1.54%, while at the west four outlets, the spring tidal amount increases by 3.16% and the ebb tidal amount increases by 2.14%.

4.1.2 Influence of the reclamation on the evolution of the estuary

(1) Reclamation in the estuary

In recent 30 years, a large-scale reclamation in the Pearl River estuary has been carried out. The shoreline changes of the estuary reflect how enormous and extensive the impact of human activities on the evolution of the estuary. From 1980s to 2010s, the reclamation area in the Lingdingyang Bay has reached 250.0km^2. The maximum length of the coastline extending outwards has reached 12.81km. The reclamation area in the Modaomen outlet has reached 134.91km^2, and the maximum length of the coastline extending outwards has reached 16.0km. The reclamation area in the Huangmaohai Bay and the Jitimen outlet has reached 154.15km^2. A large proportion of water areas have become lands. The morphologies of the outlets have been considerably changed. Figure 12 and Figure 13 show the reclamations in the Lingdingyang Bay and the Huangmaohai Bay.

(2) Influence of the reclamation on the estuarine dynamic process

The large-scale reclamation has changed the natural estuary evolution. The extension of the river outlets has been speeded up. The reclamation has reduced the tide-hold area, weakened the tidal dynamic, and caused sediment deposition outside the outlets. It shows that the tide-hold area of the Lingdingyang Bay and the four east outlets has reduced by 117.82km^2 due to the reclamation. And the volume under the zero-elevation has reduced by 131 million m^3. The reclamation has extended the waterways near the outlets. With the flow width reduction, the tidal dynamics in the main channel have relatively strengthened. Additionally, the navigational channels in the estuary have continuously dredged and widened. The depth of the Lingdingyang western navigational channel has increased from 8m to 17m since 1980s. The expansion of the main channels has increased the tidal dynamic and resulted in channel erosion and sediment transported further towards the sea.

4.2 Characteristics of the evolution of the estuary

(1)The evolution of network rivers can be characterized as "horizontal erosion and longitudinal deposition"

The Pearl River is rich of water and less of sediment, and the mean sediment concentration at the estuary is about 0.25kg during flood seasons. The network rivers take obviously on non-saturated sediment transport characteristics in flood seasons. The network rivers are characterized as "horizontal erosion and longitudinal deposition", namely rivers along the east-west direction (horizontal) are undergoing erosion and rivers along the north-south direction (longitudinal) are undergoing deposition. In addition, the network rivers are characterized as "erosions in flood seasons and depositions in dry seasons".

(2) In the Lingdingyang Bay, there exists a pattern of "three shoals and two channels" over the past century.

The three shoals are the West, Middle and East shoals and the two channels are the West and East channels. This pattern has basically not been changed. But the bay is increasingly becoming shallow and narrow. The area of the west shoals has decreased gradually on north-side but on south-side it has increased. The Middle shoals has been depositing and growing, and extending eastwards. The area of the east shoals has continuously decreased. The West channel has basically been stable. The East Channel has slightly narrowed. The mean deposition rate of the Bay is about 2.4cm/a.

A stable dynamic balance line between the West Shoals and the Middle Shoals in the Lingdingyang Bay has been formed. Due to the rich sediment and shallow water on the West Shoals, there is a stable separated boundary between clear and turbid waters, which is also called the dynamic balance line between the West Shoals and the Middle Shoals. The West Shoals is the main sediment transport corridor.

(3) In the Huangmaohai Bay, with the reclamation on both sides, the cross-sections are getting narrow and the hydrodynamic is enhanced, which causes the river-bed erosion. The irregular shoreline reclamation along the west coast causes the hydrodynamic to be weakened, resulting in the West shoals being deposited. The reclamation along the east coast makes the shoreline straight, which enhances the tide dynamic and reduces sedimentation on the East shoals. The Nanshui-Gaolan levee built in 1990 cuts off the water and sediment entering the Huangmaohai Bay, which increases the hydrodynamic of the east channel. And the channel is extending towards the north-south. The channels on the west shoals are of shrinkage.

(4) In the Jitimen outlet, the evolution trend is generally of deposition. The deposition on the west-side shallow is larger and the sedimentation in the downstream of the island is also apparent. The position of the sand bar shoals has not changed but it is slowly under deposition.

(5) The unbalance of the water and sediment results in the imbalance of the geomorphologic pattern in the estuary. As shown before, the water and sediment in the estuary are mainly from the West and North

Rivers, while the water and sediment from the East River and the Tanjiang River on both sides of the Delta are relatively smaller. This has caused the unbalanced development of the Delta. In the middle, the deposition and extension of the Delta have been fast, forming the river-dominated delta. While on both sides of the Delta, the tide-dominated delta has formed, and thereby two large tidal channels, i.e. the Lingdingyang Bay and the Huangmaohai Bay have formed.

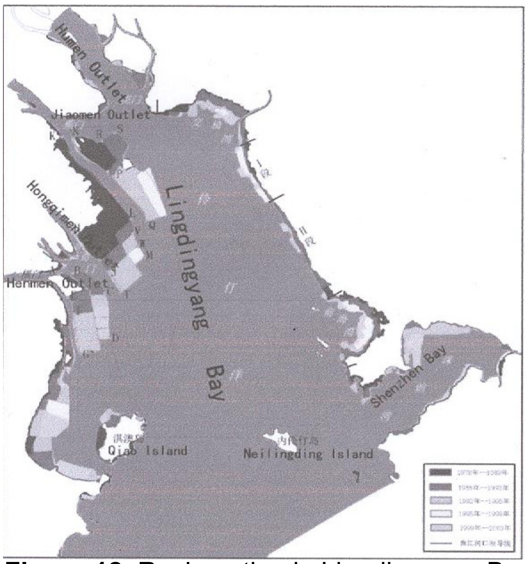

Figure 12. Reclamation in Lingdingyang Bay

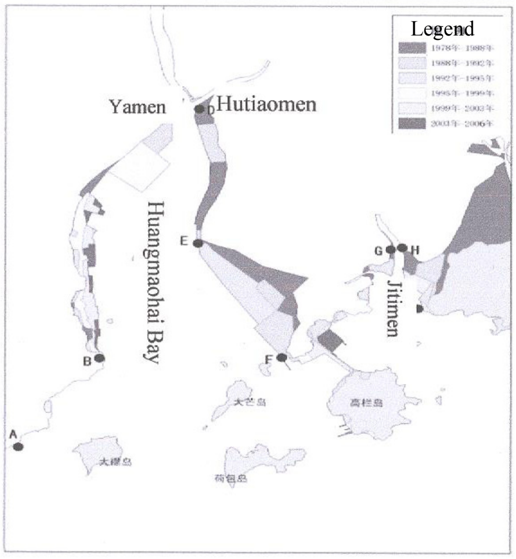

Figure 13. Reclamation in Huangmaohai Bay

5 CONCLUSIONS

Based on analysis of the variations in water-sediment processes both in the network-rivers and the river-outlets, this paper explores the responses of the hydrodynamics, including the flow-diversion ratios at the first- and second-level flow-diversion nodes in the network rivers, and the flow-diversion ratios at outlets. The characteristics of sediment transport and the sediment-laden capacity, together with the sediment flocculating settling, in the estuary are studied. On these grounds, the evolution of the estuary under extensive human activities is analyzed and the characteristics of the evolution of the estuary are summarized. The results show that in recent three decades: (1) the water-sediment amount diverting towards south-east has increased in the network-rivers and hence, resulted in an increase of the flow distribution of the Lingdingyang Bay, and (2) the extensive human activities have dramatically changed the topographic and hydrodynamic features of the estuary, especially, the uncontrolled sediment mining from the network-rivers has caused a large amount of river-bed-sediment being excavated, and the large-scale reclamation of beaches or shoals along coastal areas outside the outlets has caused a significant influence on the evolution of the estuary.

ACKNOWLEDGEMENTS

The study is supported by the project " working with water: land and water management in the Pearl River Delta under climate change and sea level rise" funded by the Chinese Academy of Science (project No. GJHZ1019).

REFERENCES

Deng, J. & Ding, X. (2012). An Analysis on the Movement of the Tide, Sediment and Salinity at the Pearl River Estuary. *Proc. Of 4th Int. Conf. On Estuaries and Coasts (ICEC-2012)*. Vietnam, Science and Technics Publishing House. 21-28.

Deng, J., Liu C. & Yu Z. (2013). Analysis on Salinity Intrusion in Pearl River Estuary. *Proc. of 35th IAHR World Congress*, China, Tsinhua University Press. 102-108.

Deng, J. (1989). Sediment-Laden Capacity of Tidal River. *Journal of Tropical Oceanology,* 8(2) 5-12. (In Chinese).

Deng, J. (1987). Evolution analysis on the East and West navigational channels in the Lingdingyang Bay. *Journal of Pearl River* (In Chinese). 2, 24-31.

Chen, W., Deng, J. & Xu X. (1999). Study on the governance of the Lingdingyang Bay at the Pearl River Estuary. *Journal of Shuilixuebao* (in Chinese). 3, 35-42.

Dou, G., Dong, F., and Dou, X. (1995). Sediment-Laden Capacity of Tide and Wave, *Journal of since Report* (In Chinese), 1, 15-22.

Jia, L., Luo, Z., Yang, Q., OU, S., & LEI, Y. (2006). Impacts of Huge Amount of Sand Dredging on Riverbed Morphology and Tidal Dynamics of the Lower Reaches of the Dongjiang River and the Dongjiang River Delta. *Acta Geographica Sinica-Chinese Edition*, 61(9), 985-994.

WATER EXCHANGE PHYSICAL MODEL TEST IN MONSOON AND OCEAN CURRENTS EFFECT

MENWU WU(1), LI YAN(2), GUOZHEN LIU(3), XIAOLEI TONG(4) & XIAOMING WU(5)

(1, 2, 3, 4, 5) Key Laboratory of the Pearl River Estuarine Dynamics and Associated Process Regulation, Guangzhou, China
wumw@163.com; yanlijane@163.com; 153341027@qq.com; 136975391@qq.com; 179941009@qq.com

ABSTRACT

The model of gravity and viscous force is simulated by physical model. There are very useful methods. However, the inertia force is the main criteria of water simulation, which needs to be further studied. The water in Sri Lanka West Coast has more influences by the Indian Ocean monsoon season; meanwhile ocean currents and West Indian coastal current are less affected by the tide. So, monsoon season and ocean currents must be considered especially when physical model test are being used. The Sri Lankan authorities intend to build a Colombo Port City infrastructure project on the south side of the south bank of Colombo. After the implementation of the project, the water exchange within the project is a major problem. In this paper, the hydraulic engineering method is used to convert the kinetic energy into potential energy, and the tide level in the north and south of the engineering waters is fitted to meet the requirements of model control in the physical model test. The fitting results show that the design boundary condition is better at reflecting the characteristics of water flow in this region. The physical model test results also show that the fitting model test can be carried out by fitting the hydrological conditions and the test precision and result can meet the relevant requirements. The method can be used for hydrodynamic simulation based on inertial force in the case of insufficient data.

Keywords: Colombo; ocean currents; water exchange; physical model; experiment.

1 INTRODUCTION

The construction of breakwater, semi-enclosed port can achieve anti-wave, reduce sediment siltation, and increase the wharf shoreline, providing berthing conditions and other functions. Such is the existence of pollution sources in the harbor which is mixed with offshore water bodies, the exchange capacity of weak waters will face accumulation of pollutants and water environment deterioration risk (Zhang et al., 2013). The water exchange capacity of engineering waters is of great significance to the demonstration of water environment, breakwaters and land area schemes. It is controlled by a variety of factors such as monsoon current, tidal power, Gulf terrain, tidal volume, artificial river and engineering scheme. The mathematical model such as box model (Lv, 2009), Lagrange particle model (Wang et al., 2011), random walk model (Wang et al., 2014) and convection diffusion model (Qin et al., 2012; Yuan et al., 2015) is used to study the water exchange capacity in this aspect. In general river and estuarine area, the physical model is mainly considered when the gravity is similar and the resistance is similar (viscous resistance and turbulence mixed resistance) (Hui and Wang, 1999). The monsoon, ocean current greater impact of the marine area, inertia force also cannot be ignored of a force because velocity distribution is a combination of various forces of the embodiment. However, the physical model of water flow is mainly affected by gravity, and subject to various factors and it is more difficult to achieve. In this paper, at the west coast of Sri Lanka, Colombo port at the south port area; the use of hydraulics method, the kinetic energy into potential energy to meet the physical model test requirements are studied.

The harbor area is located on the west coast of Sri Lanka, east of the Arabian Sea, on the north side of the narrow south of the Gulf of Mannar, south of the Indian Ocean waters. The water movement in this area is influenced by the Indian Ocean monsoon current and the west coast of India, which is less affected by the tide. The tidal range is small in the area, and there is a long-term unidirectional flow in the water flow, and the water flow is smooth in the winter and summer. Therefore, the model test simulation should focus on the impact of the flow field.

2 PROJECT PROFILE

2.1 Project Profile

The proposed port city of Colombo is located on the north side of the existing south slope of Colombo, with a reclamation area of about 2.52km^2. The north side of the entire land area is the existing breakwater at the south port of Colombo, the east side is the existing road, the west and the south sides are surrounded by a ring breakwater. The west side of the breakwater is arranged at the contour line about -20m and the south side of the breakwater basically is perpendicular to the isometric arrangement. In order to prevent the loss of sand on the beach, two sand bar in the north and south mouth of breakwater were arranged. The north side of the sand embankment was at elevation of -8m, width of 392m and the south side elevation was at -5m with width of 324m. At the same time, in the direction perpendicular to the Gore Road, the top elevation of -1.0m of the dyke with a length of 420m was arranged to reduce coastal sediment transport and works as a cover for the south side of the yacht area revetment. The main body of the land area planning has a width of 110m with the end of the elevation of -3m for artificial canal, as shown in Figure 1. The change of shoreline boundary had little effect on the overall hydrodynamics of the west coast, but it will have a significant effect on the hydrodynamic environment of the local waters, especially the artificial river.

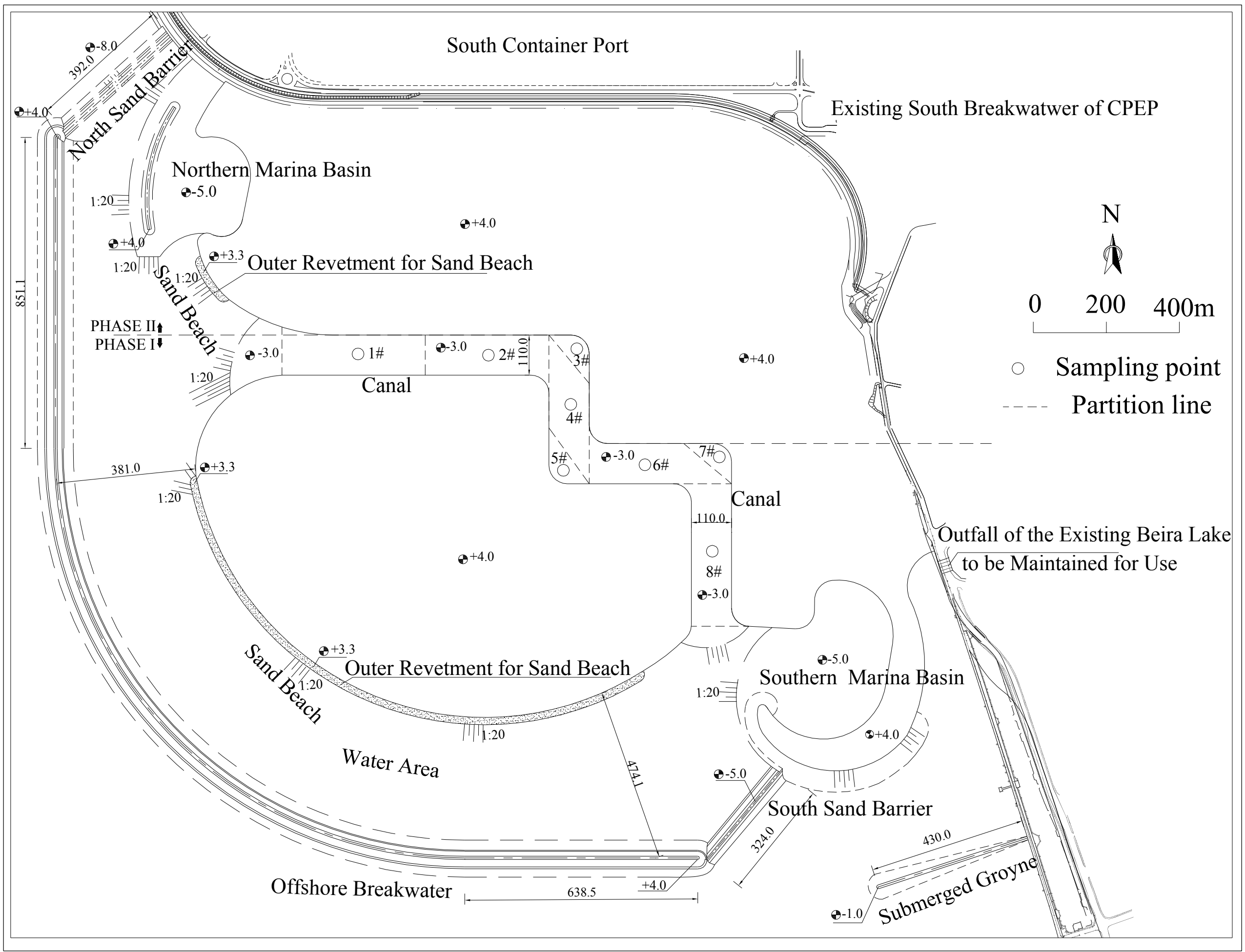

Figure 1. The schematic of engineering design and water sample zoning.

2.2 Hydrological Situation

(1) Relationship between flow velocity and tidal level

The field data shows that there was no direct relationship between the water flow and tide of the two stations (see Figure 2). The tide had obvious daily change of rule which presented a southward flowing trend every day. During southwest monsoon period, flowing southward prevails when the spring tides transformed to neap tides and during northeast monsoon period, flowing northward prevails when spring tides transformed to neap tides. The water level of the two tide level station differs relatively during daily fluctuation process as well. However, unidirectional flow exists for a long time, which indicates that water was flowing upwards at this place and that the water flow was strongly influenced by monsoon currents.

At the same time, both in the southwest monsoon or the northeast monsoon period, in the tide, the low tide velocity was higher than the high tide. In the small tide, the flow rate changes and tide level fluctuations did not significantly related to each other. From the relationship between the rising tide and the flow, the fluctuating tide of the region is not necessarily related to the flow of water.

(2) Remote Sensing Analysis on Local Flow Pattern of the Project

The south coast of Sri Lanka's Colombo harbor is affected by ocean currents, coastal currents, tides, waves and other factors, as well as the terrain border of Colombo harbor. The hydrodynamic environment is relatively complex. In the summer, due to the influence of the southwest monsoon ocean currents, the southwestern coast of Sri Lanka was mainly affected by ocean currents. In the winter, influenced by the northeastern monsoon current and the west coast of India, the flow currents in the adjacent waters show different characteristics at different stages. These were the following characteristics of water flow near Colombo:

(a) The water movement in the west coast of Sri Lanka is influenced by the lateral ocean currents, and the tidal effect is relatively small. The change of the rising and falling tides is not obvious.
(b) By the boundary of the Cape Point slope, the local flow of the project is deflected, forming weak flow and slow flow in the south and north sides of the port area respectively; port area and the artificial headland pick flow effect is obvious.

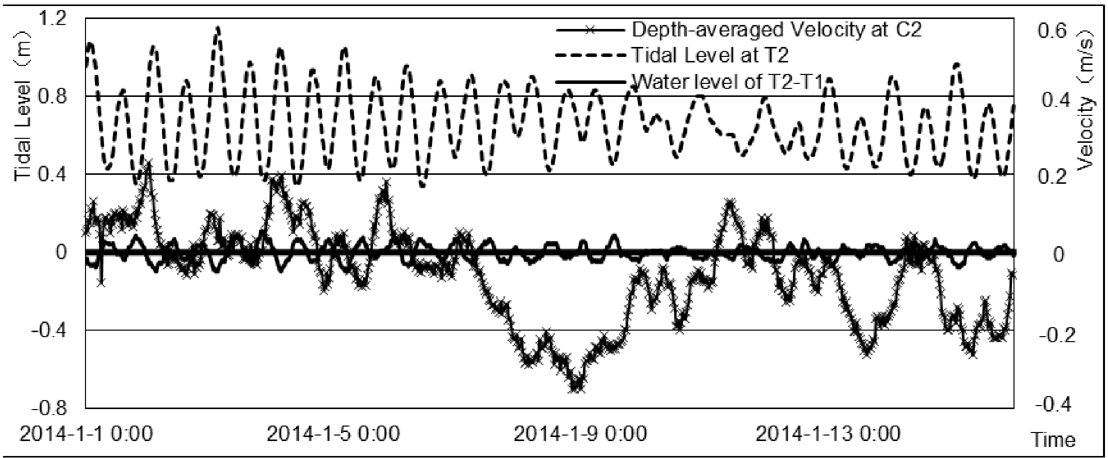

Figure 2. Relationship among Velocity at C2 and Tide Level at T2 and Water Level of T2-T1 during Northeast Monsoon.

3 DESIGN BOUNDARIES

The physical model test can only reflect the gravity flow but cannot reflect the monsoon, ocean current. The measured flow velocity data is the result of the combined effect of various factors such as gravity, viscous force and inertia force. To this end, we need to measure the flow rate data, feedback to the model boundary water level difference, and then according to the water level difference, the study must be carried out via the model test. Based on the measured tide level and velocity data, this paper uses the flow tube analysis method in fluid mechanics to convert the kinetic energy into potential energy, and the process of the north and south tide of the model was fitted to it. Assuming that the water flow in the project area was a uniform flow then there is a single width flow of 1m, according to the uniform flow formula:

$$v = C\sqrt{Ri} = \frac{1}{n}R^{1/6}\sqrt{Ri} = \frac{1}{n}R^{2/3}i^{1/2} = \frac{1}{n}\left(\frac{A}{x}\right)^{2/3} i^{1/2} \qquad [1]$$

It can be derived that: $i = \left(\frac{vn}{(A/x)^{2/3}}\right)^2$

The distance between the north and south of the prototype is about 2600m. According to the measured flow rate and water depth, the water level difference between the north and the south can be calculated.

The distance between the two tide points is about 14.5km and the south side is about 5.5km from the T2 point. According to the two stations, measured tide process, you can interpolate the south side of the import tide process. According to the same time the north and south imports of the water level differences, can be calculated according to the north side of the import tide process. The water level difference at the same time is shown in Figure 3.

During southwest monsoon period, the maximum water level difference at the south and north entrance was about 5.1mm at spring tides, 3.6mm at middle tides and 1.1mm at neap tides. While the maximum value of actually measured spring tides with vertical average velocity was 0.18m/s, the max value of middle tides was 0.15m/s and the max value of neap tides was 0.08m/s. During northeast monsoon period, the max water level difference at the south and north entrance was about 1.0mm at spring tides, 0.5mm at middle tides and 7.1mm at neap tides. While the max value of actually measured spring tides vertical average velocity was 0.10m/s, the max value of middle tides was 0.07m/s and the max value of neap tides was 0.25m/s. It can be seen that the fitted curve of maximum water level differences matches the measured maximum vertical average velocity.

It can be seen from Fig. 3 that in the southwest monsoon period, the water level difference between the selected tidal tide of north and south ports was not the maximum water level difference. At the beginning of the half tide, there was long time one-way water level difference, and this difference was larger. At the end of the half-moon, there is a long time one-way water level difference as well. In the northeastern monsoon period, the water level difference between the north and south tide was not the largest water level difference. In the front and back period, there was a long time one-way water level difference, and the difference was larger as well.

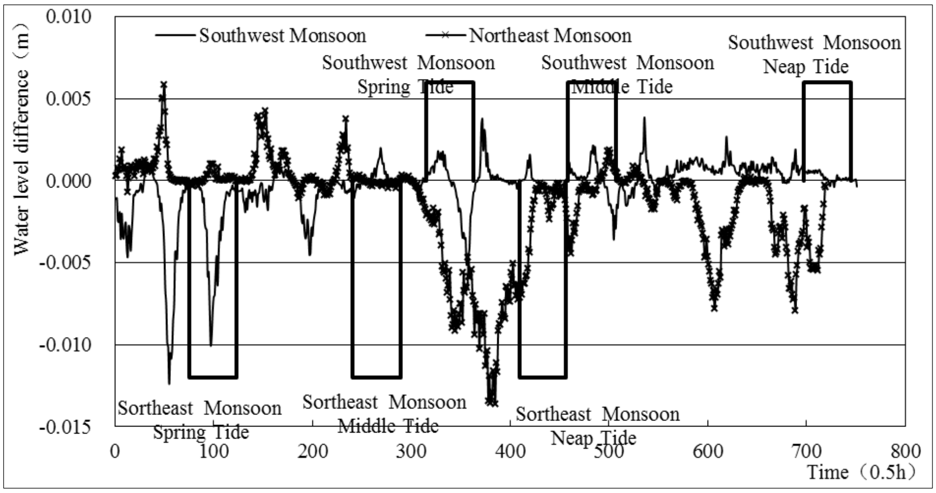

Figure 3. Calculated Water Level Difference at the Same Time between South and North Entrances.

4 PHYSICAL MODEL DESIGN AND VERIFICATION

4.1 Model Design

According to the similar research experience of domestic and foreign models (Yao et al., 1999; Dou et al., 2007), the hydrodynamic simulation of corners and braided river channels is greatly influenced by the model variability, which usually requires small model variability. The pilot study focuses on the artificial canal waters; the northern bar sand embankment. South bar sand between the waters is the proposed artificial water area. Taking into account the purpose and task requirements of the model test, the model includes the whole artificial water system and part of the sea area, northwest out of the mouth -8m bar sand embankment and at an extension of 220m, southeast out of -1m submerged southward extension of about 220m. This was the simulated prototype from south to north for about 3.64km and from east to west for about 2.0km. According to the characteristics of the research problem, the model was determined as the metamorphic model. The model horizontal scale was 60, the vertical scale was 10, the variance was 6 (Wu et al., 2015).

4.2 Measurement and Control Equipment

The model control system adopts the distributing industry control system developed by our institute. The central monitor is mainly to store various parameters of the model test, to release commands, to display real time monitoring charts, process curves, historical test data and to print relevant parameters and to alarm etc. This was done to connect with the field machine through RS232 serial communication wire. The field machine shall complete data acquisition, tidal equipment control and other tasks automatically according to the commands from the central monitor.

The tidal physical model consists of two borders, one of which was controlled by flow control and the other boundary control gate was controlled by water level. The flow control door was equipped with an electromagnetic flow meter. Both sides of the model were equipped with a water level gauge and a stylus (the measurement accuracy is 0.1 mm). The model uses a frequency converter to adjust the water supply quantity provided by the pump directly to the model. The system regulates the output frequency of each inverter according to a given tide control curve to meet the needs of boundary segment tide control. During the test, the measurement data of the electromagnetic flow meter were collected through the measurement and control system, and the two models of water exchange can be measured accurately.

At the time of experiment, the concentration of the tracer was measured by using a fluorescence indexer with rhodamine as a tracer. Rhodamine is a reddish stable substance that does not degrade during the test. During the test, the changes of the tracer concentration in the artificial canal with different hydrological combinations were observed to reflect the effect of water exchange on the water quality of different waters in the area.

4.3 Model Verification

Due to the lack of measured data and limitation of the scope of the physical model, this model used mathematical modeling to verify the results. Mathematical model was used to verify the two water levels and two velocity measurement points in the southeast monsoon and the northwest monsoon. The results show that the simulation results were in good agreement with the measured values during the hydrological period. The trend of velocity and flow is in good agreement with the measured data. The flow rate and flow velocity test are shown in Fig. 4. The physical model shows that the maximum difference between the water level and the numerical model is ±0.002m. The average flow velocity of the model was slightly larger than that of the numerical model, which indicates that the model was similar to the prototype. Figure 5 shows the water flow from north to south for comparison of the physical model test and mathematical model calculated flow rate .

It can be considered that the design and production of the model were rough and the test method was correct. The model test adopts the computer to control, collect and process the data accurately and reliably, and can be used in a scheme test.

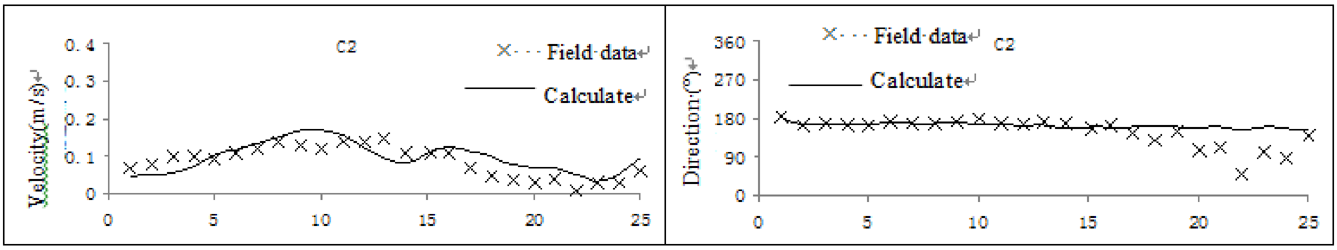

Figure 4. (a) The velocity verification when Southwest Monsoon Spring Tide.

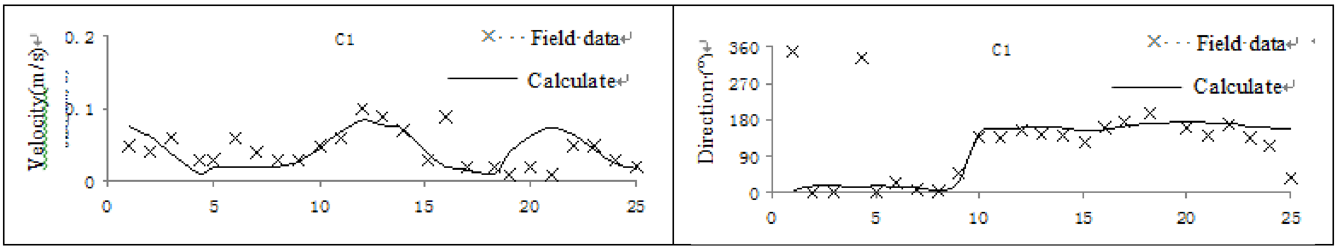

Figure 4. (b) The velocity verification when Northeast Monsoon Neap Tide.

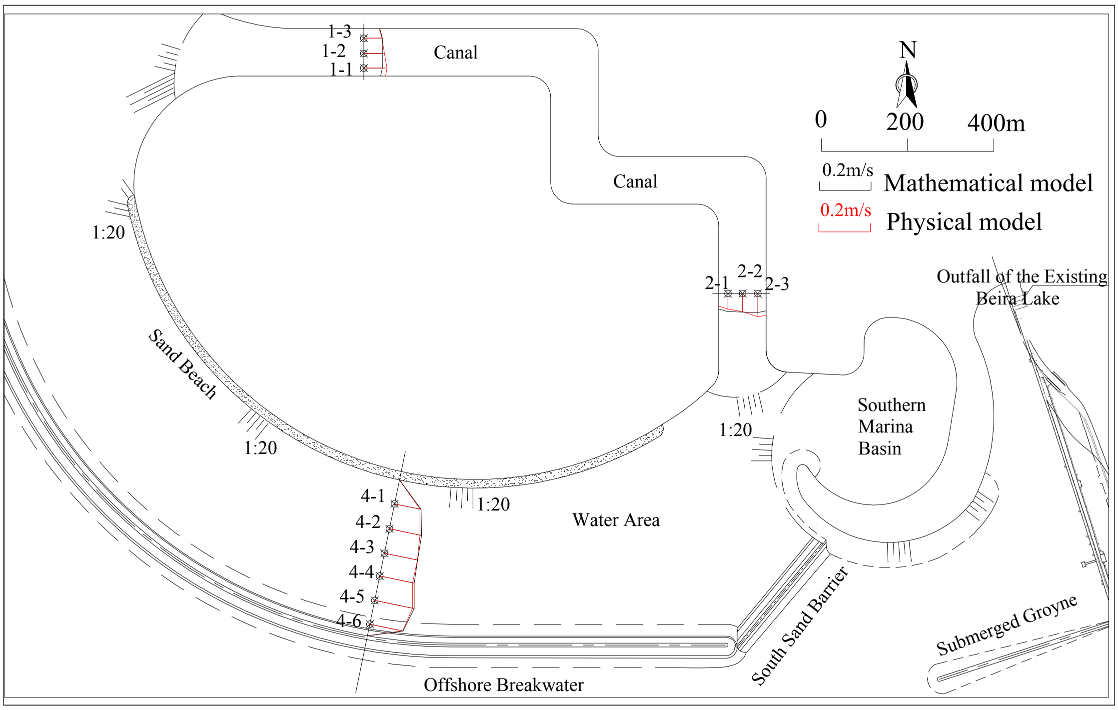

Figure 5. The velocity contrasts about physical model test and mathematical calculate.

5 THE MODEL TEST AND RESULT ANALYSIS

(1) Test conditions

In this study, the experimental boundary conditions were fitted according to the measured data and controlled by the model test. The water exchange test was carried out only on the two tidal conditions of the southwest monsoon tide and the northeastern monsoon tide. As the monsoon, the influence of ocean currents has been fed back to the flow conditions; this test no longer considers the effects of wind alone.

(2) Sampling points arrangement

According to the hydrodynamic characteristics of the test results, the man-made canal is divided into eight different regions (Figure 1), respectively. Each of the eight regions will be the sampling points for sampling analysis. Different water volume of the partition was used to calculate the water depth by considering the most adverse effects. For example select the highest tide level of simulated tide.

(3) Test method

At the time of experiment, the concentration of the tracer was measured by using a fluorescence indexer with rhodamine as a tracer. Rhodamine is a reddish conserved substance that does not degrade during the test. During the test, the changes of the tracer concentration in the artificial canal with different hydrological combinations were observed to reflect the effect of water exchange on the water quality of different waters in the area.

During the test, when the tides go to the high tidal level, blocks both ends of the Canal and add Rhodamine to the water of the Canal. The water storage of the Canal is the biggest at this moment and was the most unfavorable condition for the water exchange. Water area generates tides in accordance with the normal control conditions. When the dyed water was even and the tides of the water area go to the high tidal level again, open the baffle of the Canal to make the internal and external region to be connected. The Rhodamine tracer water will begin to transmit and spread. Take water samples after each tide fluctuation, using as fluorescent dividing meter to measure the collected water samples. Monitor the tracer concentration change, and analyze water exchange capacity. According to the changes of tracer concentration from the sampling point, get the water exchange ratio of the Canal.

(4) Results analysis of the test

The results of the water exchange rate test of the artificial canal in the southwest monsoon tide and the northeastern monsoon tide are shown in Table 1. The Table indicates that:

Southwest monsoon spring tide boundary: at the initial time, water flows from north to south. Because the water level difference was small relatively, the flow velocity of canal is not big. The water in the canal exchange was poor in the first 12 hours of the first day. The water exchange ratio of the canal accounted for only 5.3%. In the last 12 hours where water flows from south to north, the water level different was relatively bigger, and flow velocity of canal also increase. Thus the water exchange ratio of the canal also increased to 41.8%. After movement for 2 days, the water exchange ratio in the Canal reaches 57.8% and water exchange rate can reach 69.9% in 3 days.

Northeast monsoon neap tidal boundary is the condition where water flows from south to north all the time. At the initial time, the water level difference was relatively bigger, and flow velocity of canal was big also. Thus the water exchange ratio in the canal was good. In the first 12 hours of the first day, the water exchange ratio in the canal reached 65.1%. In the last 12 hours, the water level difference decreases thus the flow velocity of the canal decreases either. But the water still flow from south to north. The water exchange ratio in the canal also increases to 80.1% during this period. After movement for 2 days, the water exchange rate in the Canal reaches 91.8%, and water exchange rate can reach 95.3% in 3 days.

Different boundary conditions of testing results also showed that the one-way flow velocity magnitude and duration of water exchange outcomes have a greater impact. When unidirectional flow velocity was greater, the faster the water exchange takes place with longer duration of the one-way flow. Due to this, the water exchange capacity is also possible.

In the corners of artificial canal, water near the hydrodynamic axis can get effective exchange, but t in the three stagnant area at the top of the corners, the capacity of water exchange was poor. However, for specific performance, the exchange period in this area was greater than the whole artificial canal.

South yacht pier was almost closed, only about 210m narrow mouth facing east which was connected to the water in the dike. The water in south yacht pier flow in and out of the port area as the tide fluctuates, but due to the tidal range it was limited and the amount of exchange water was small. The water in the whole basin was spinning and stagnating and exchange capacity was poor. In the condition of southward flow, the water from artificial canal that flow into the south yacht pier is limited. Thus, water quality in south yacht pier were least influenced no matter how the artificial canal water quality was.

Table 1. Water Exchange in the Canal (%).

Time(h)	6	12	18	24	36	48	60	72
Southwest Monsoon Spring Tide	1.7	5.3	10.2	41.8	45.9	57.8	61.3	69.9
Northeast Monsoon Neap Tide	49.7	65.1	72.7	80.1	88.8	91.8	93.7	95.3

6 DISCUSSION

Water exchange capacity evaluation indicators are mainly water exchange rate, semi-exchange cycle, replacement cycle, etc. In this case it is: (1) the rate of water exchange, the ratio of the pollutants flowing out of the study area to the total amount of the initial pollutants; (2) the time required for the average concentration of contaminants to be 50% of the initial concentration after convection-diffusion dilution; (3) update cycle according to International Shipping Association (RecCom Working Group, 2008) Guidelines for Marine Environmental Protection where the concentration of the initial tracer shall not be greater than 37% after the intermittent land area and the enclosed or partially enclosed sea area of exchange after 8 tidal cycles. The US Environmental Protection Agency (Agency, 1985) proposed that the study of water replacement cycles less than 4 days can be considered "excellent"; 4-10 days can be considered "better", more than 10 days is unacceptable.

The results of the experimental study show that the man-made canal water exchange is generally better; basically it met the 10-day exchange requirements. The existence of the recirculation zone in the bend of the artificial canal has some influence on the water exchange rate, but also basically meets the requirement of water exchange. As the depth of the southern yacht dock concave, awakening the weakest hydrodynamic, is not up to the requirements of water exchange. The measured hydrological data indicated that the long-term unidirectional flow characteristics of the sea area will be beneficial to the water exchange of artificial water system.

7 CONCLUSIONS

1) The unidirectional flow in the engineering waters has a longer duration. The tidal current is affected by monsoon currents, tides and winds, which are dominated by monsoon currents.
2) The hydrodynamic method is used to convert the potential energy into kinetic energy. The boundary condition of the design reflects the flow velocity characteristics of the region, and the design boundary can meet the requirements of the physical model test.
3) The results show that the water exchange of man-made canal can meet the requirement of changing water. The existence of the recirculation area of the artificial canal bend has some influence on the water exchange rate, but also basically meets the requirements of water exchange. As the depth of the south yacht dock is deep, the hydrodynamic force is the weakest, and the requirement of water exchange is not reached.
4) Water exchange test results show that: water exchange capacity depends mainly on the size of one-way flow rate and its duration. It is suggested that the artificial water system has a long term unidirectional flow characteristic, which will be beneficial to the water exchange of artificial water system.

REFERENCES

Agency, U. S. E. P. (1985). *Coastal Marinas Assessment Handbook*. U.S.Environmental Protection Agency.

Dou, X.P., Wang, X.M. & Zhao, X.D. (2007). Advances in Study of Physical Model Distortion Ratio. *Advances in Water Science*, (11), 907-914.

Hui, Y.J. & Wang, G.X. (1999). *River Model Experiment*, *Beijing*: *China Water.* Conservancy and Hydropower Press*,* BOOK, Chapter C4.

Lv, Y.X. (2009). Numerical Method on Water Exchange and Its Application, *MSc Thesis*, Tianjin University.

Qin, Y.W., Zhang, L., Zheng, B.H., Cao, W., Liu, X.B. & Jia, J. (2012). Impact of Shoreline Changes on the Costal Water Quality of Bohai Bay (2003-2011), *Acta Scientiae Circumstantiate*, 32(9), 2149-2159.

RecCom Working Group. (2008). *Protecting Water Quality in Marinas*, PIANC Report.

Wang, J.H., Shen, Y.M., Shi, F. & Chen, X.L. (2011). Study of Bohai Sea Circulation and its Influencing Factors During Winter and Summer Based on Lagrangian Particle Tracing Method. *SHUILIXUEBAO*, 42(5), 544-553.

Wang, L.N., Pan, W.R., Luo, Z.B., Zhang, G.R., Tao, X.Q. & Zheng, Y.F. (2014). Numerical Simulation on Water Exchange in Tieshan Bay Based on a Random Walk Model. *Journal of Xiamen University (Natural Science)*, 53(6), 840-847.

Wu, M.W., Zhang, J., Ma, M.S., Liu G.Z. & Yan, L. (2015). Water Exchange Physical Model Test on Colombo Port City Development Project. *Port & Waterway Engineering,* (1), 86-92.

Yao, S.M., Zhang, Y.Q. & Li, H.Y. (1999). Study on Distortion Ratio of Physical Model. *Journal of Yangtze River Scientific Research Institute*, (5), 1-4.

Yuan, D.K., Li, G., Wang, D.S. & Yang, Z.B. (2015). Numerical Simulation of Effects of Land Reclamation on Water Exchange Capability of Bohai Bay. *Journal of Tianjin University (Science and Technology)*, 48(7), 605-613.

Zhang, W., Wang, G.C., Liu, R., Chen, Z. & Tang, L. (2013). Water Exchange and Improvement Measures for Encircled Basin. *Port & Waterway Engineering*, (4), 37-41.

CHARACTERISTICS OF DUAL JETS UNDER THE EFFECT OF A WAVY CROSSFLOW

ZHENSHAN XU[1] & YONGPING CHEN[2]

[1,2] College of Harbor, Coastal and Offshore Engineering, Hohai University, Nanjing, China
zsxu2006@hhu.edu.cn; ypchen@hhu.edu.cn

ABSTRACT

The discharge of wastewater into coastal waters, which forms the single jet or multiple jets, is subjected to the coastal dynamics (i.e., crossflow and waves). The characteristics of dual jets vertically discharged into a wavy crossflow are investigated in this study, by use of the particle image velocimetry (PIV) technique as well as a large eddy simulation (LES) model. The results show that, (i) the wavy crossflow leads to the deflection and swaying of the dual jets, (ii) the leading jet has a shielding effect on the rear one, (iii) the wave effect leads to further deflection of the jet body, (iv) the counter-rotating vortex pair (CVP) structure is a significant feature of dual jets in the wavy crossflow environment.

Keywords: Dual jets; wavy crossflow; particle image velocimetry; large eddy simulation.

1 INTRODUCTION

Nowadays, the wastewater is being frequently discharged into surrounding ambiences, such as rivers or coastal waters, which has a significant effect on the local environment. Hence, the effective dilution of wastewater is expected by the engineers. The discharged wastewater can be considered as a jet. Compared with a single jet, the multiple jets (two or more jets) could improve the dilution through the mixing between the adjacent jets as well as between jets and surrounding waters. Multiple jets are easily found in the applications of wastewater discharge projects. Apart from the parameters of the jet itself, the movement and dilution are extremely subjected to the surrounding dynamics, such as a crossflow in rivers and a wavy crossflow in coastal areas.

Over the past decades, the multiple jets in crossflow has been investigated both experimentally (Toshiaki and Yoshihiro, 1978; Yu et al., 2006; Gutmark et al., 2011; Li et al., 2012) and numerically (Xiao et al., 2011; Yao and Maidi, 2011). Numerous valuable results were obtained from previous studies. The flow field of multiple jets can be identified as the pre-merging region and the post-merging region. It was found that the leading jet has a shielding effect on the rear jets and the trajectory of rear jets is less deflected in the pre-merging region. Based on the experimental data of PIV and PLIF system, Ali (2003) found that the trajectory of the combined jet in the post-merging region is slightly higher than that of the single jet injected from a nozzle having the same equivalent initial volume and momentum flux. Similar with the single jet in crossflow, four types of large-scale vortices, including shear-layer vortices, horseshoe vortices, counter-rotating vortex pair and wake vortices, are investigated in the flow of the multiple jets in crossflow.

In recent years, many researchers started to investigate the behaviours of jet under the combined effects of crossflow and waves. Xia and Lam (2004) studied a vertical round jet into an unsteady crossflow that consists of a mean flow and a sinusoidally oscillating component and found that the unsteadiness in the oscillating crossflow leads to an increase in the time-averaged jet width. Hsu et al. (2014) identified four characteristic flow modes (downwash, crossflow-dominated, jet-dominated, and transitional) within one cycle of an oscillating jet in crossflow. Wang et al. (2015) conducted a series of experiments on the vertical round jet in the wavy crossflow environment and it was found that the waves impose a positive effect on the enhancement of jet initial dilution. Xu et al. (2016) reproduced the three-dimensional flow structures of the vertical round jet under the combined effects of wave and current using the LES method.

The above studies mainly focused either on the multiple jets in crossflow or on the single jets in the flow of combined wave and crossflow, while there is lack of investigations on the multiple jets in a wavy crossflow environment. In this paper, the aim is to understand the characteristic behaviours of dual jets under the combined effects of crossflow and regular wave, by use of the particle image velocimetry (PIV) technique as well as a large eddy simulation (LES) model.

2 EXPERIMENTAL STUDY

2.1 Experimental Setup

The experiments were conducted in a 46.0 m long, 0.5 m wide and 1.0 m deep wave flume. Two round acrylic pipes, with the diameter (d) of 1.0 cm, were installed at the mid-section of the flume. The dual jets were discharged vertically through the pipes at the centerline of the flume, with the jet orifices 10.0 cm above the bottom. The spacing (S) between the orifices was 5.0 cm (namely 5d). The jet water was supplied from a constant tank above the wave flume, using an adjustable valve to control the volume flow rate. Regular waves were generated by a piston-type paddle movement, controlled by the computer. After propagating through the test section, the waves were dissipated by a wave absorber installed at the tail of the flume. The currents were generated via a flow control valve at one end and a V-notch weir at the other end. The static water depth in the flume was kept at 0.5 m throughout the experiments. The free surface elevation was measured using two resistance wave gauges located at the upstream and downstream sides 1.0 m away from the centerline of the first jet.

In this study, the three dimensional Cartesian-coordinate system (x, y, z) is defined such that x is the horizontal coordinate that follows the wave direction, y is the transverse coordinate, and z is the vertical coordinate. The origin of the coordinate system is located at the center of the first jet orifice. The sketch of experimental setup is illustrated in Figure 1.

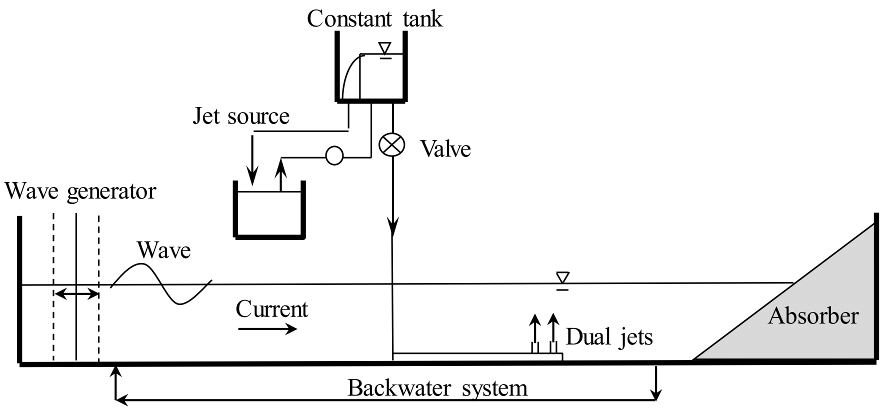

Figure 1. Sketch of experimental setup.

The particle image velocimetry (PIV) technique was used to measure 2D flow velocities of jet on the symmetrical plane (y/d = 0). The PIV system used in the present study includes a dual-head pulsed laser, laser light sheet optics, a CCD camera, and a synchronizer. The dual-head pulsed laser is a Nd:YAG laser that has a 15 Hz repetition rate and 380mJ pulse maximum energy output. It was used as the laser light sheet optics illumination source. Images were recorded using a 14-bit CCD camera with a 2048 × 2048 pixel resolution and 15 frames per second (fps) maximum framing rate. The sampling frequency was 7.25 Hz, and the sampling time was about 20 times of the wave periods. The PIV measurements were taken at a certain fields of view (FOV). The size of the FOV was 0.36 m× 0.36 m. The experimental cases are shown in Table 1, including one case of dual jets in the crossflow environment and one case of dual jets in the wavy crossflow environment.

Table 1. Experimental cases.

Cases	Jet Initial Velocity w_0 (m/s)	Crossflow Velocity u_0 (m/s)	Wave Height H (m)	Wave Period T (s)
CJ2	0.42	0.07	/	/
WCJ2	0.42	0.07	0.05	1.0

2.2 Experimental Results

2.2.1 Instantaneous images

Figure 2 shows the snapshots of the dual jets in the crossflow environment and the dual jets in the wavy crossflow environment, respectively. It can be clearly seen that the jet body is deflected along the current in both environments. Under the effect of the crossflow, the leading jet has a larger deflection than the rear one. A clear entrainment between the jet and surrounding water can be identified at the shear layer of the leading jet. Under the combined effects of the crossflow and the wave, the dual jets is not only deflected along the current direction, but also sways back and forth.

The distinctive 'large-scale effluent clouds' appeared at the upper part of the jet body in the wavy crossflow environment, which has been observed from the single jet in the wave and current coexisting environment by Xu et al. (2016). However, the large-scale effluent clouds of dual jets are more complicated. The effluent clouds formed from one single jet had a fixed distance with each other and the effluent clouds from the leading jet were adjacent to the ones from the rear jet. As a result, the adjacent effluent clouds of dual jets had a smaller distance. They merged with each other and it became more difficult to distinguish the effluent clouds after a downstream distance.

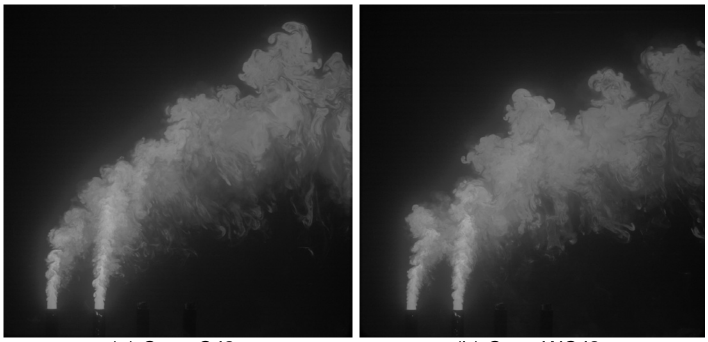

(a) Case CJ2 (b) Case WCJ2

Figure 2. Photo of the dual jets.

2.2.2 Flow field

Figure 3 shows the phase-averaged flow field of dual jets under the effect of crossflow and regular wave, when the orifice of the leading jet is at four typical wave phases, namely up-zero crossing, wave crest, down-zero crossing and wave trough. The formation of the large-scale effluent clouds is clearly observed in Figure 3. It is attributed to the overlapping of the current flow and the wave-induced oscillating flow. The wave-current flow has a sinusoidal motion, which is in a periodic accelerating or decelerating state. For a jet in crossflow, the jet-to-crossflow velocity ratio primarily determines the jet characteristics (Kelso et al., 1996). In the wavy crossflow, this ratio is not a constant value, resulting in the periodic deflections and penetrations of the jet within one wave period. When the wave crest passed through the leading-jet orifice, the jet suffered a maximum deflection and penetrated the lowest height, with the vertical momentum waning rapidly. When the wave trough passed through the leading-jet orifice, the jet suffered a minimum deflection and maintained the vertical momentum at the most.

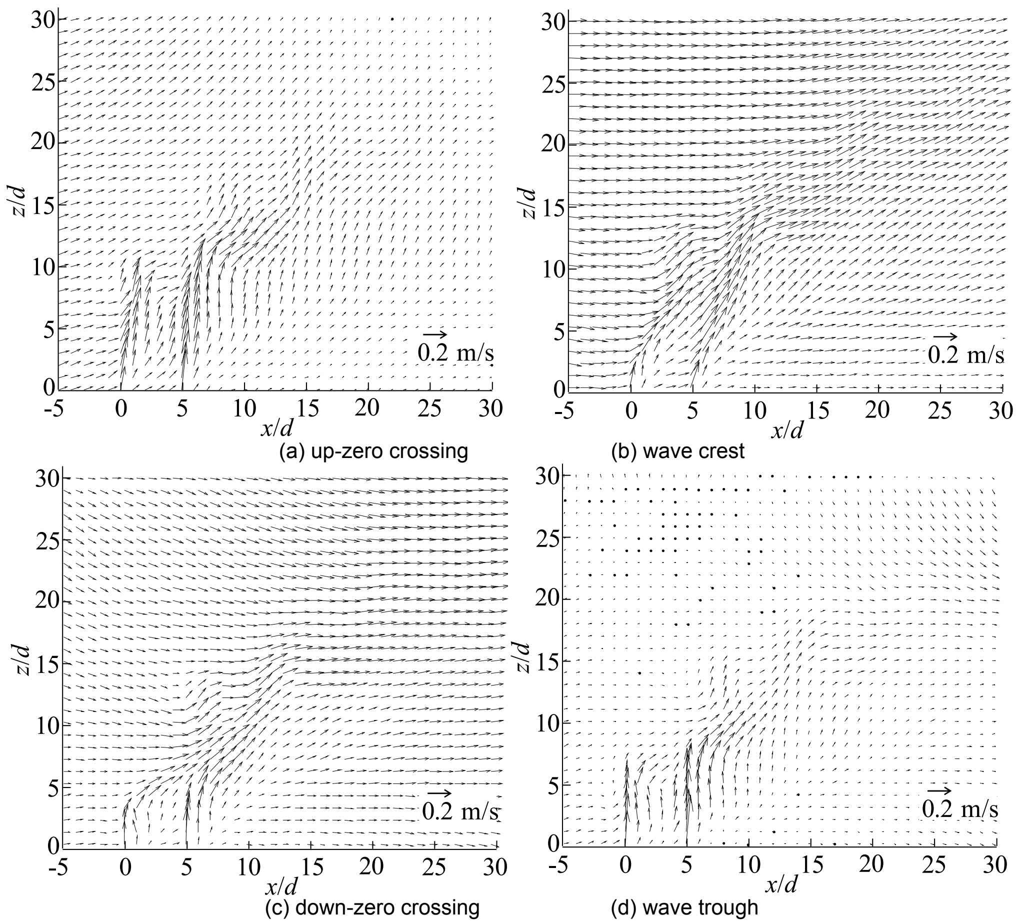

Figure 3. Phase-averaged flow field of dual jets under the effect of crossflow and regular wave (Case WCJ2).

As illustrated in Figure 3, the fluid discharged from the rear-jet orifice at each wave phase has a higher penetration than that from the leading-jet orifice. It indicates that the leading jet does have a shielding effect on the rear jet, which is similar with the dual jets in the crossflow environment.

Figure 4 shows the mean vertical velocity distribution on several downstream locations for Case CJ2 and Case WCJ2. Due to the effect of regular wave, the vertical velocity has a faster decay. The velocity distribution for the dual jets in the wavy crossflow environment gets more flat than that in the crossflow environment. Moreover, the position of the maximum velocity is lower in the wavy crossflow environment, which implies that the wave effect leads to a further deflection of the dual jets.

The experimental study only shows the characteristics of dual jets on the symmetrical plane. In the following section, a three dimensional LES model will be established and validated to present the three dimensional flow structures of the dual jets in the wave and current environment.

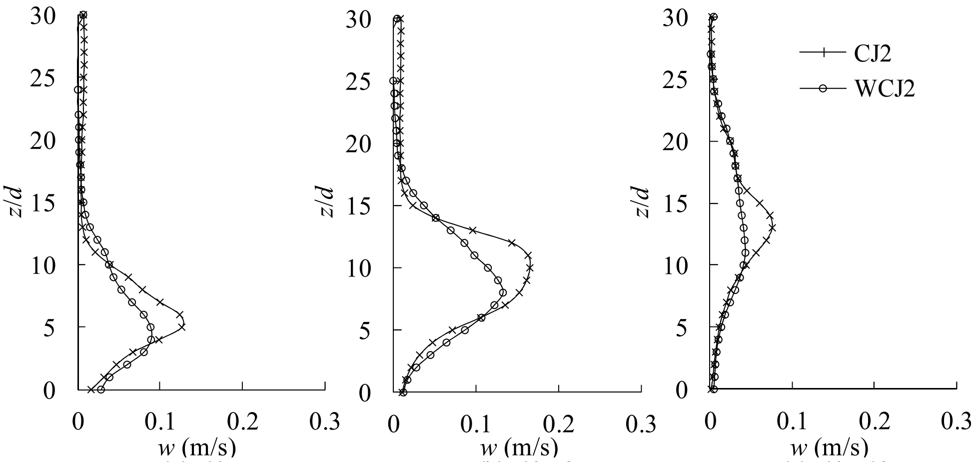

(a) x/d = 4 (b) x/d = 8 (c) x/d = 18

Figure 4. Mean vertical velocity distribution on several downstream locations.

3 NUMERICAL STUDY

3.1 Model Description

The governing equations of LES model, which is the spatially filtered Navier-Stokes equations (Chen et al., 2008), can be written as:

$$\frac{\partial \overline{u_i}}{\partial x_i} = 0 \tag{1}$$

$$\frac{\partial \overline{u_i}}{\partial t} + \overline{u_j}\frac{\partial \overline{u_i}}{\partial x_j} = -\frac{1}{\rho}\frac{\partial \overline{p}}{\partial x_i} + \left(\nu + \nu_t\right)\frac{\partial^2 \overline{u_i}}{\partial x_j \partial x_i} \tag{2}$$

where x_i (i=1, 2, 3) are the spatial coordinates in horizontal, transverse and vertical directions, respectively; u_i (i=1, 2, 3) are the corresponding velocity components; p is the pressure; ρ is the water density; t is the time; v is the kinematic viscosity, v_T is the eddy viscosity and is expressed as:

$$\nu_T = \left(C_s \Delta\right)^2 \sqrt{2\overline{S_{ij}}\,\overline{S_{ij}}} \tag{3}$$

$$\overline{S_{ij}} = \frac{1}{2}\left(\frac{\partial \overline{u_i}}{\partial x_j} + \frac{\partial \overline{u_j}}{\partial x_i}\right) \tag{4}$$

where C_s is a Smagorinsky constant equal to 0.21; Δ is a representative grid spacing which is defined as:

$$\Delta = \left(\Delta x_1 \Delta x_2 \Delta x_3\right)^{1/3} \tag{5}$$

where Δx_1, Δx_2, Δx_3 are the grid sizes in x_1, x_2 and x_3 directions, respectively.

The σ-coordinate transformation (Lin and Li, 2002) was introduced to solve the problem of changing computational domain. The operator splitting method (Lin and Li, 2002), which splits the solution procedure into advection, diffusion and pressure propagation steps, was adopted to solve the various physical processes by use of different numerical schemes.

The surface elevation at the inflow boundary can be given by:

$$\eta = \frac{H}{2}\cos\left(kx_0 - \omega t\right) \quad [6]$$

where H and k are the wave height and wave number; ω is the wave frequency; x_0 is the x coordinate of inflow boundary.

The vertical velocity at the inflow boundary is given by:

$$w = \frac{\pi H}{T}\frac{\sinh\left[k\left(z+h\right)\right]}{\sinh\left(kh\right)}\sin\left(kx_0 - \omega t\right) \quad [7]$$

where T is the wave period related to current and h is the static water depth.

The transverse velocity is set to 0.

The horizontal velocity at the inflow boundary is given by:

$$u = \frac{\pi H}{T}\frac{\cosh\left[k\left(z+h\right)\right]}{\sinh\left(kh\right)}\cos\left(kx_0 - \omega t\right) + u_0 \quad [8]$$

where u_0 is the time-averaged velocity of crossflow.

To prevent initial numerical oscillations, a ramp function is multiplied to the inflow boundary function f:

$$f_R = f\tanh\left(t/2\pi T\right) \quad [9]$$

where t is the computational time; T is the wave period; f denotes the water elevation or velocity and f_R is the resulting boundary function. At the outflow boundary, the radiation condition combined with a sponger layer (Park et al., 2001) is specified.

At the jet inlet boundary, the jet mean velocity plus the 'artificial turbulence' is specified. The no-slip and zero-gradient boundary conditions were imposed at the bottom and two lateral boundaries, respectively. The dynamic and kinematic conditions are applied at the free surface. A so-called Lagrange-Euler Method (Chen et al., 2006) was applied to update the free surface elevation at every new time step.

The wave, crossflow and jet parameters for the numerical model were identical to those of Case WCJ2 in the experiments. As shown in Figure 5, a cubic region of 15.0 m long, 0.50 m wide and 0.50 m deep is selected as the computational domain, which is discretized into a convergent non-uniform grid system of 275×73×51 nodes in x, y and z directions, with gradual grid refinement near the jet center on the x-y plane as well as near the jet exit and the free surface on the x-z plane. A total of 9×9 nodes were used to discretized the cross-section of jet nozzle with the uniform spacing of 1.11mm. The time step was 0.002s.

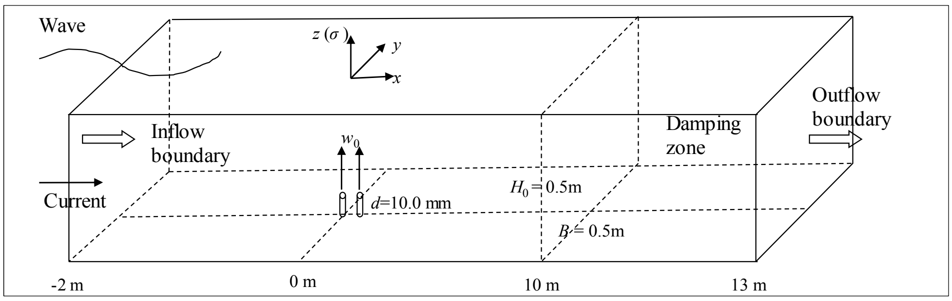

Figure 5. Computational domain of LES model.

3.2 Model Results

3.2.1 Model validation

Figure 6 shows the comparison between the experimental and numerical results of the mean vertical velocity distribution on different downstream locations. It was found that the agreement between the numerical results and the experimental data is acceptable. The numerical model can reproduce the velocity distribution on each downstream location of the dual jets in the wavy crossflow environment. At the upwards of the rear jet, the value of maximum velocity on each downstream location decays with the distance away from the lead-jet orifice. At the downwards of the rear jet, the value of maximum velocity decays with the distance away from the rear-jet orifice. The model catches the value and the position of the maximum velocity on each downstream.

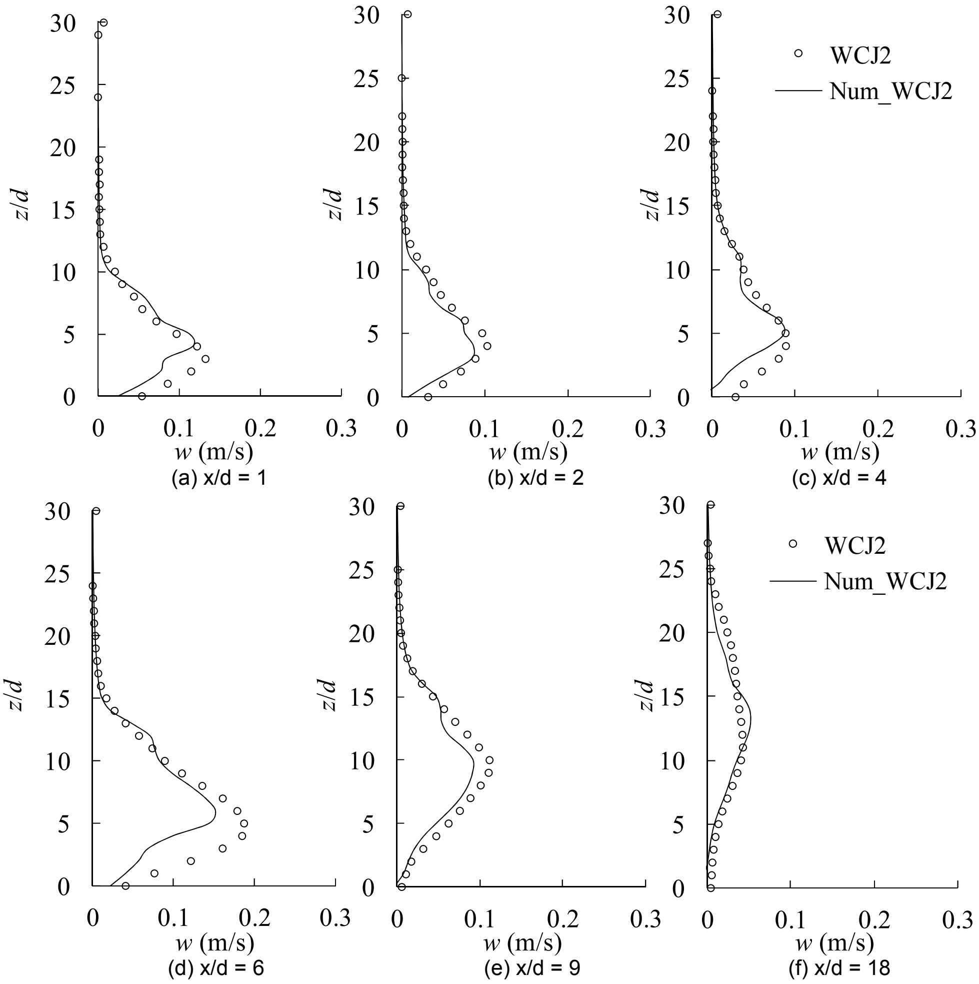

Figure 6. Comparison between the experimental and numerical results of the mean vertical velocity distribution on different downstream locations.

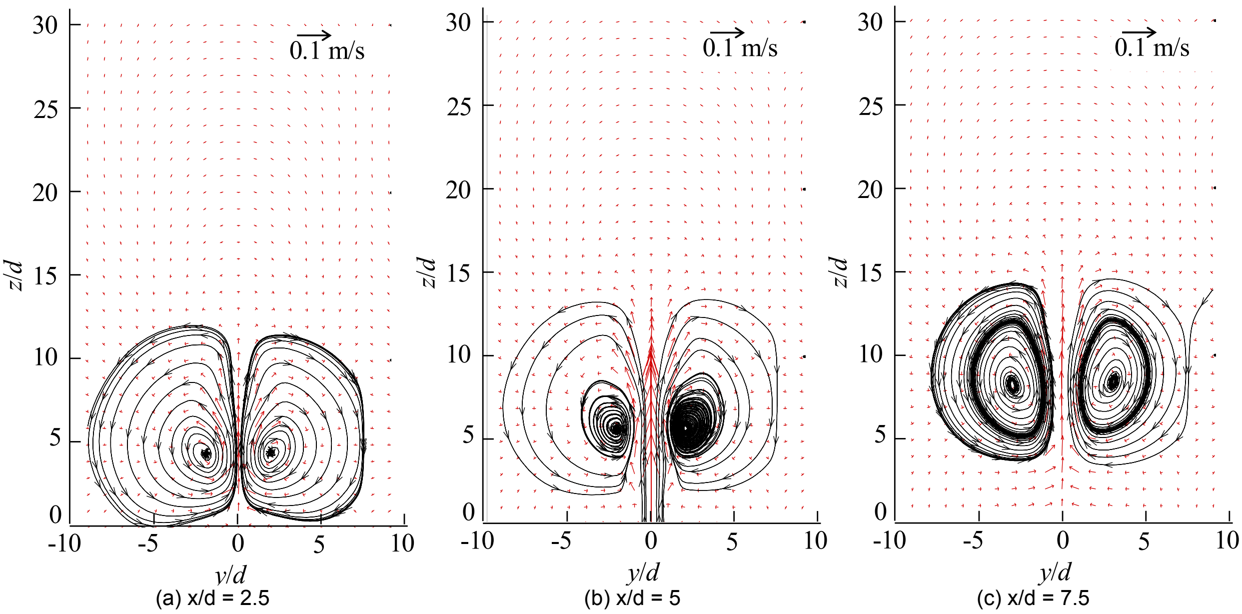

Figure 7. Mean flow field of dual jets in the wavy crossflow environment on the downstream cross-sections.

3.2.2 Mean flow field on downstream cross-sections

Figure 7 shows the mean flow field of dual jets in the wavy crossflow environment on the downstream cross-sections (x/d = 2.5, x/d = 5, and x/d = 10). Similar with those of dual jets in crossflow, the structure of the counter-rotating vortex pair (CVP) exists on each downstream cross-section. It is a significant feature of dual jets in the wavy crossflow environment as well as in the crossflow environment. Despite of the junction of the rear jet, the position of the vertex center increases gradually with the increasing of the distance away from the leading-jet orifice. It indicated that the leading jet is the dominant one when moving downwards and the rear jet has an effect that enhances the vertical momentum of the whole jet body.

4 CONCLUSIONS

The PIV technique is used to measure the 2D flow field on the symmetric plane of dual jets in the wavy crossflow environment. Under the combined effects of the crossflow and the wave, the dual jets is not only deflected along the current direction, but also sways back and forth. As a result, the distinctive 'large-scale effluent clouds' appear at the upper part of the jet body. The vertical momentum has a faster decay in the wavy crossflow environment compared with that in crossflow. The wave effect leads to a further deflection of the dual jets. A three dimensional LES model was established and used to present the three-dimensional structure of dual jets. It was found that, the numerical results are consistent with the experimental data. The CVP structure, which is a significant feature of dual jets in the wavy crossflow environment, was observed on each downstream cross-section. It should be noted that, only one case of dual jets in the wavy crossflow environment was discussed in this study. Further studies will be conducted to obtain more quantitative results, such as the effects of the jet spacing, the wave and crossflow parameters, etc.

ACKNOWLEDGEMENTS

This work was partly supported by the National Natural Science Foundation of China (Grant No. 51379072) and the Fundamental Research Funds for the Central Universities (Grant No. 2016B13214).

REFERENCES

Ali, M.S. (2003). Mixing of a Non-buoyant Multiple Jet Group in Crossflow, *MSc Thesis*. The University of Hong Kong.
Chen, Y.P., Li, C.W. & Zhang, C.K. (2006). Large Eddy Simulation of Vertical Jet Impingement with a Free Surface. *Journal of Hydrodynamics*, 18(2), 148-155.
Chen, Y.P., Li, C.W. & Zhang, C.K. (2008). Numerical Modeling of a Round Jet Discharged Into Random Waves. *Ocean Engineering*, 35(1), 77-89.
Gutmark, E.J., Ibrahim, I.M. & Murugappan, S. (2011). Dynamics of Single and Twin Circular Jets in Cross Flow. *Experiments in Fluids*, 50, 653-663.
Hsu, C.M., Huang, R.F. & Loretero, M.E. (2014). Unsteady Flow Motions of an Oscillating Jet in Crossflow. *Experimental Thermal and Fluid Science*, 55, 77-85.
Kelso, R.M., Lim, T.T. & Perry, A.E. (1996). An Experimental Study of Round Jets in Crossflow. *Journal of Fluid Mechanics*, 306, 111–144.
Li, Z.W., Huai, W.X. & Qian, Z.D. (2012). Study on the Flow Field and Concentration Characteristics of the Multiple Tandem Jets in Crossflow. *Science China Technological Sciences*, 55(10), 2778-2788.
Lin, P.Z. & Li, C.W. (2002). A σ-coordinate Three-Dimensional Numerical Model for Surface Wave Propagation. *International Journal for Numerical Methods in Fluids*, 38(11), 1045-1068.
Park, J.K., Kim, M.H. & Miyata, H. (2001). Three-dimensional Numerical Wave Tank Simulations on Fully Nonlinear Wave-Current-Body Interactions. *Journal of Marine Science and Technology*, 6(2), 70-82.
Toshiaki, M. & Yoshihiro, M. (1978). Experiments on the Characteristics of Multiple Jets in a Crossflow. *Bulletin of University of Osaka Prefecture. Series A, Engineering and Natural Sciences*, 26(2), 15-36.
Wang, Y.N., Chen, Y.P., Xu, Z.S., Pan, Y., Zhang, C.K. & Li, C.W. (2015). Initial Dilution of a Vertical Round Non-Buoyant Jet in Wavy Cross-Flow Environment. *China Ocean Engineering*, 29(6), 847-858.
Xia, L.P. & Lam, K.M. (2004). Unsteady Effluent Dispersion in a Round Jet Interacting with an Oscillating Cross-flow. *Journal of Hydraulic Engineering*, 130 (7), 667-677.
Xiao, Y., Tang, H.W., Liang, D.F. & Zhang, J.D. (2011). Numerical Study of Hydrodynamics of Multiple Tandem Jets in Cross Flow. *Journal of Hydrodynamics*, 23(6), 806-813.
Xu, Z.S., Chen, Y.P., Tao, J.F., Pan, Y., Sowa, D.M.A. & Li, C.W. (2016). Three-dimensional Flow Structure of a Non-buoyant Jet in a Wave-current Coexisting Environment. *Ocean Engineering*, 116, 42-54.
Yao, Y.F. & Maidi, M. (2011). Direct Numerical Simulation of Single and Multiple Square Jets in Cross-Flow. *Journal of Fluids Engineering*, 133(3), 1-10.
Yu, D., Ali, M.S. & Lee, J.H.W. (2006) Multiple Tandem Jets in Cross-flow. *Journal of Hydraulic Engineering*, 132(9), 971-982.

Proceedings of the 37th IAHR World Congress
August 13 – 18, 2017, Kuala Lumpur, Malaysia

VARIABILITY OF PHYTOPLANKTON IN ESTUARIES, A CASE STUDY IN THE NETHERLANDS

LIXIA NIU[(1)]

[(1)]Sun Yat-sen University, Guangzhou, China
xiaoxia3623@outlook.com

ABSTRACT

The present study develops a vertical phytoplankton model to investigate the phytoplankton variability coupled with the analysis of the Delft3D model. A case study of the Frisian Inlet (the Netherlands) is performed, determined by the dataset of 2009. The graphical comparisons between the model output and the monitored phytoplankton biomass demonstrated that the vertical phytoplankton model can reproduce reliable predictions in this case. Significant correlations (0.71-0.84) between phytoplankton biomass and chlorophyll a are established. Higher values of the phytoplankton biomass appear in spring and autumn (March, April, July, and September), accompanied by a rapid reduction of the nutrients. The variables of light intensity, salinity, and phosphorus are distinguished as the driving forces. The findings are expected to characterize the applicability of the phytoplankton model in coastal waters.

Keywords: Phytoplankton biomass; vertical phytoplankton model; Delft3D model; frisian inlet.

1 INTRODUCTION

The role of phytoplankton to a coastal ecosystem is significant, and more attention has been paid to the interactions (Boyer et al., 2009; Godrijan et al., 2013). The development of phytoplankton dynamics (i.e. growth, loss, grazing, biomass, bloom) has become an influential issue as is consequence of many environmental factors, like vertical mixing rate, nutrients, light intensity, temperature, salinity, and water turbidity. Among all the factors, phytoplankton dynamics is mainly refined by the limitations of light and nutrient availability (Boyer et al., 2009).

In the context of the limited observations, mathematical models are convenient and flexible to perform the investigation of the phytoplankton. The case study, Frisian Inlet, is a part of the Wadden Sea, located in the north of the Netherlands as shown in Figure 1. The Frisian Islands separate the Wadden Sea from the North Sea. The water environment in this area is favorable for phytoplankton (van Beusekom et al., 2012; Niu et al., 2015a; 2015b; 2015c). Two barrier islands of Ameland (the left one) and Schiermonikoog (the right one) are included. Huibertgat (53.56°N, 6.40°E) and Lauwersoog (53.41°N, 6.20°E) are selected as proxies to conduct the analysis. Niu et al. (2015a; 2015b) have introduced an ecological model of BLOOM II (one module of the Delft3D suit) to investigate the phytoplankton (in terms of chlorophyll a) in this area, but no discussion of the phytoplankton biomass is given due to the unknown properties of the species. Although many studies have accepted that chlorophyll a is a reliable measure of the phytoplankton biomass, the relationship (linear or non-linear) between them is not fixed but site-specific (Felip and Catalan, 2007; Huot et al., 2007). It is not acceptable to give a full view in the coastal ecosystem only through the study of chlorophyll a but also phytoplankton. Thus, a mathematical phytoplankton model is developed to investigate the phytoplankton variability in this study, determined by the dataset over the year of 2009.

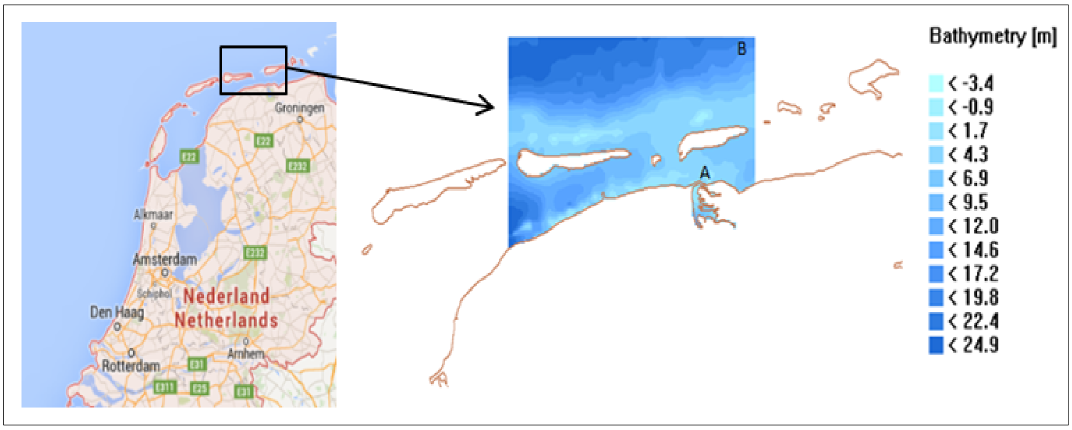

Figure 1. Case area of Frisian Inlet and surrounding water zones. A: Lauwersoog; B: Huibertgat.

2 MATERIALS AND METHODS

2.1 Data information

The observation programme in this area had been carried out by Rijkswaterstaat (the Netherlands). Seven variables (chlorophyll a, Chla, nitrate, NO_3, ammonium, NH_4, phosphorus, PO_4, silicate, Si, suspended mater, SPM, and salinity), were measured biweekly or monthly and were collected from the main database of DONAR, accessible through http://www.eea.europa.eu/data-and-maps/data/external/donar-historical-water-measurement-data. Another three variables which is light intensity (I), ambient water temperature (T) and wind profile (speed and direction)were measured daily and were collected from the database of KNMI, accessible through www.knmi.nl. Note that the variables of light intensity, temperature and wind profile were set as domain parameters, while the others were station-specific. In addition, the monitored phytoplankton biomass and euphotic depth are extracted from the NASA (the Ocean Colour web, accessible through http://oceancolor.gsfc.nasa.gov/cms/) and processed with the SeaDAS 7.0.

2.2 Phytoplankton model

In the general form, the characteristics of phytoplankton dynamics are coupled with a physical model, written as:

$$\frac{\partial C}{\partial t}+u_x\frac{\partial C}{\partial x}+u_y\frac{\partial C}{\partial y}+(u_z+u_s)\frac{\partial C}{\partial z}=E_h(\frac{\partial^2 C}{\partial x^2}+\frac{\partial^2 C}{\partial y^2})+E_z\frac{\partial^2 C}{\partial z^2} + \text{Phytoplankton dynamics} \quad [1]$$

In which, C denotes the concentration of the state variable; u_x, u_y, u_z denote the velocity in the x-, y- and z-direction, respectively; u_s denotes the sinking velocity; E_h, E_z denote the horizontal and vertical eddy diffusivity. Phytoplankton dynamics has been discussed by the researchers (Steele and Henderson, 1992; Henderson and Steele, 1995; Edwards, 2001) and described as the form of

$$\begin{aligned}\frac{dP}{dt}&=\mu P-gZ-lP\\ \frac{dZ}{dt}&=\gamma gZ-l'Z\end{aligned} \quad [2]$$

In which, P denotes the phytoplankton biomass, Z denotes the zooplankton biomass; μ denotes the specific growth rate of phytoplankton; g denotes the grazing rate by zooplankton; l denotes the loss terms of phytoplankton; γ denotes the assimilation coefficient; l' denotes the loss terms of zooplankton.

Stressing the significance of the phytoplankton in this study, the solution of the vertical phytoplankton model ($z-$) has been described after Niu et al. (2016). To explore the solution of the vertical phytoplankton model, five transfer functions need to be investigated: E_z, u_s, u_z, μ and l. In which, u_s and l are referred as constants. Our concern was on the descriptions of the vertical mixing rate and the growth rate. The vertical mixing process can be explained by the Delft3D model which has been well validated in this area or the neighbouring zones (Los, 2009; Blauw et al., 2009; Niu et al., 2015a; 2015b). The commonly used estimation of the specific growth rate is as the functions of temperature, light intensity, and nutrients (Eppley, 1972; Bissinger and Montagnes, 2008). In this study, we integrate the growth-temperature function into the photosynthetic light curve, $\mu(I,T)$, according to the view of Smith (1980).

3 RESULTS

3.1 Observational analysis

The statistics of the observed variables at the Frisian Inlet in 2009 is shown in Table 1, including the minimum value (Min), the maximum value (Max), the mean value and the standard deviation (SD). At Lauwersoog station, chlorophyll a fluctuates around a big interval, 0.64-87.89 mg m^{-3}, with the mean value of 26.92 mg m^{-3} and the standard deviation of 25.1 mg m^{-3}. The minimum chlorophyll a appears on 18th May and the maximum appears on 17th April. The dissolved nitrate ranges from 0.01 mg l^{-1} to 0.53 mg l^{-1}, while 0.005-0.520 mg l^{-1} for ammonium, 0.013-0.14 mg l^{-1} for phosphorus and 0.03-1.42 mg l^{-1} for silicate. Most of the ratios of N/P are lower than the optimal condition of 16:1 (Brzezinski, 1985), which indicates a nitrogen deficiency relative to phosphorus. The nutrients show a similar pattern at two stations, increasing in winter but decreasing quickly in spring.

Table 1. Statistical analysis of the observed variables over the year of 2009 at the Frisian Inlet.

	Lauwersoog station				Huibertgat station			
Variables	Min	Max	Mean	SD	Min	Max	Mean	SD
$Chla$ (mg m^{-3})	0.64	87.89	26.92	25.1	1.11	124	12.07	25.67
NO_3 (mg l^{-1})	0.01	0.53	0.15	0.16	0.01	0.72	0.19	0.2
NH_4 (mg l^{-1})	0.005	0.52	0.147	0.16	0.005	0.3	0.08	0.08
PO_4 (mg l^{-1})	0.013	0.14	0.051	0.03	0.008	0.043	0.021	0.01
Si (mg l^{-1})	0.03	1.42	0.47	0.4	0.01	0.9	0.28	0.27
N/P [-]	0.22	21.6	7.41	6.8	1.35	51.43	14.1	14.28
SPM (mg l^{-1})	27	390	105	77.3	3.6	37	17.6	8.79
Salinity (PSU)	25.9	31.7	29.56	1.81	27.4	31.9	30.2	1.35
I (W m^{-2})	4.51	354.63	123.5	97.3				
T (^{0}C)	2.1	19.8	11.27	5.59				

At Huibertgat station, chlorophyll a varies from 1.11 mg m^{-3} to 124 mg m^{-3}, with the mean value of 12.07 mg m^{-3} and the standard deviation of 25.67 mg m^{-3}. The minimum appears on 20th February and the maximum appears on 20th April. The concentrations of nutrients are lower than that at Lauwersoog station. It is to infer that phosphorus limits the phytoplankton growth from November to March because the ratios of N/P are larger than 16:1 during that time period.

3.2 Parameter estimation

The specific growth rate of the phytoplankton presents a seasonal variation over the year of 2009, increasing gradually since the winter time, reaching the peak values in the summer days and then decreasing till the winter. Normally, the maximum growth rate is around 2.0 day^{-1} in coastal waters (Bowie et al., 1985; Arhonditsis and Brett, 2005). In this case, the maximum growth rate was 1.87 day^{-1} which appeared on 18th August, and the minimum was 0.38 day^{-1} which appeared on 6th March. The net growth rate of the phytoplankton shows a completely different trend. The positive values of the net growth rate indicate an increase in phytoplankton biomass from the previous time interval. The specific growth rate has a big potential range, varying from 0.38 day^{-1} to 1.87 day^{-1}. The net growth rate varies from -0.25 day^{-1} to 0.25 day^{-1} at Lauwersoog station, while from -0.14 day^{-1} to 0.12 day^{-1} at Huibertgat station.

The Delft3D model can produce the observed levels of chlorophyll a, nutrients and salinity, displayed in Figure 2. Thus, the estimate of vertical turbulent diffusivity was derived from the Delft3D model, depicted in Figure 3. In view of the specific demand, the phytoplankton species can be distinguished by the classification of Margalef (1978): the order of vertical turbulent diffusivity and nutrient availability. The order of vertical turbulent diffusivity is 10^{-4} at Lauwersoog station, while 10^{-3} at Huibertgat station. Therefore, dinoflagellates and diatoms are equally significant at Lauwersoog station, while only diatoms are predominant at Huibertgat station.

3.3 Validation of the phytoplankton model

The graphical comparisons between the model outputs and the monitored phytoplankton biomass are displayed in Figure 4. All of the values were confined near the surface layer in the area-averaged scale. The Delft3D model can reproduce the observed levels of chlorophyll a and nutrients (Figure 2) but only 40% was in agreement with the phytoplankton biomass when the properties of the species are unknown, while the vertical phytoplankton model reproduces 70% agreement. Therefore, the vertical model is applicable in this case. The modelled phytoplankton biomass varies from 0.145 g m^{-3} to 1.105 g m^{-3}, with the mean value of 0.44 g m^{-3} and the standard deviation of 0.30 g m^{-3}. The monitored phytoplankton biomass varies from 0.17 g m^{-3} to 1.40 g m^{-3}, with the mean value of 0.57 g m^{-3} and the standard deviation of 0.26 g m^{-3}. The common disadvantage of chlorophyll a and phytoplankton here is that they both indicate the characteristics of all the species.

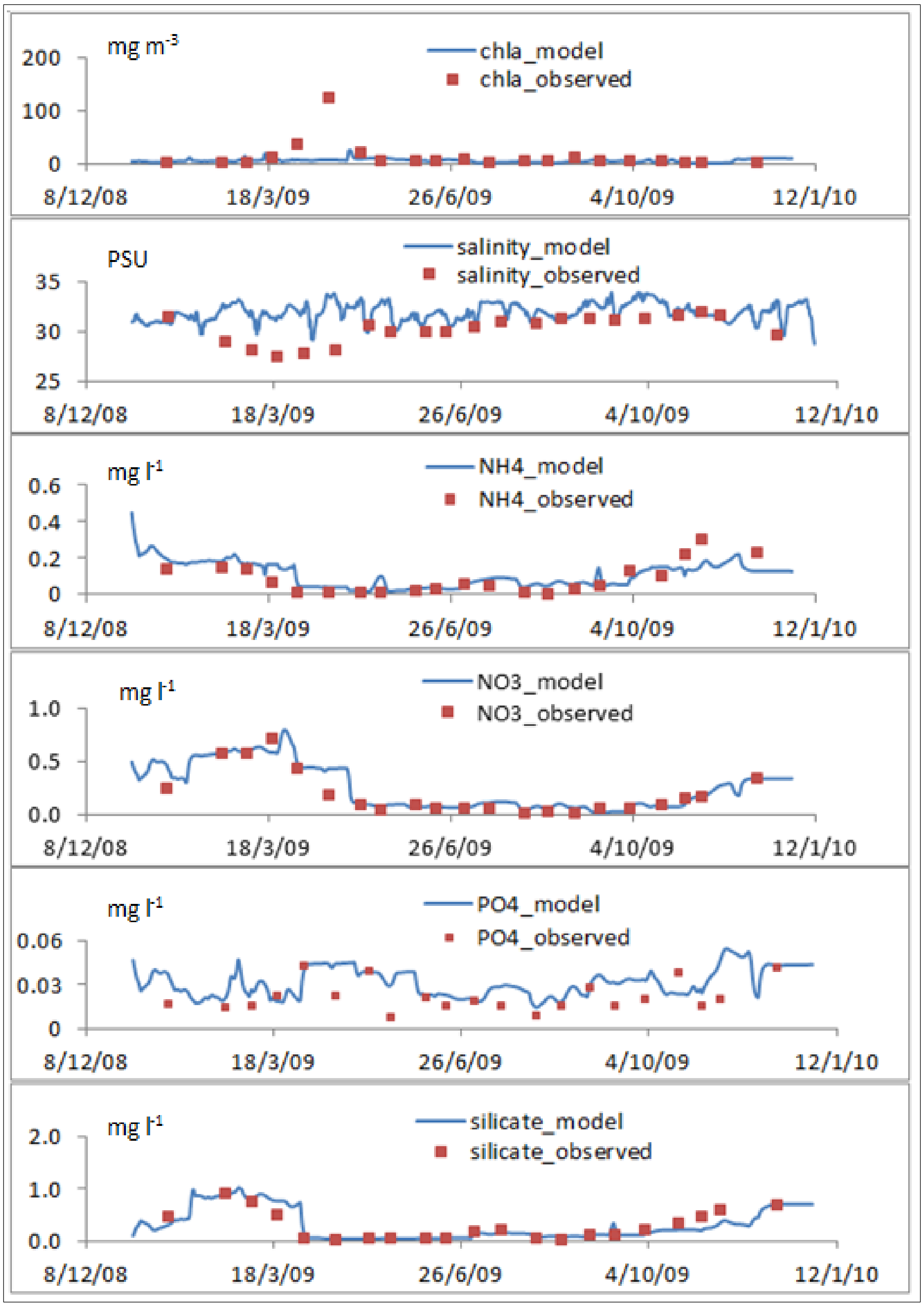

Figure 2. Graphical comparisons of chlorophyll *a*, salinity and nutrients between the Delft3D model output and the observations in 2009 at Huibertgat station (after Niu et al., 2015b).

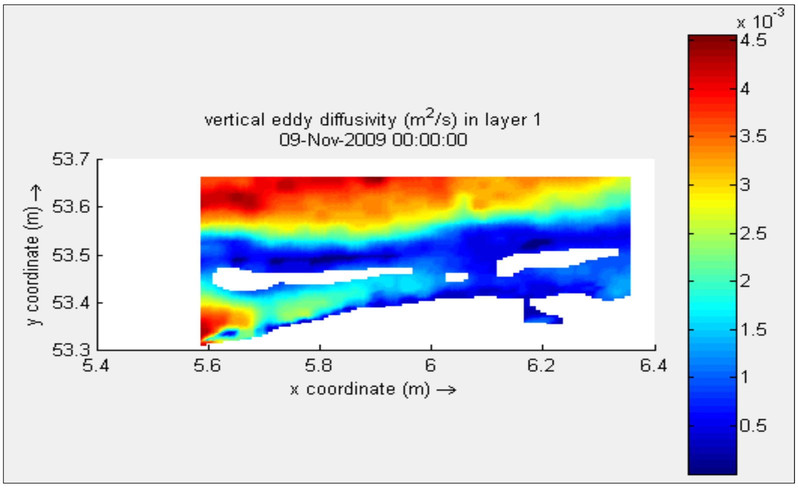

Figure 3. Estimation of vertical turbulent diffusivity (E_z) with the Delft3D model at the Frisian Inlet, driven by the physical-chemical condition and expressed in m^2 s^{-1}. This factor is influenced by the tidal currents and the wind profile, mixing with the mass transport. The appropriate range of the vertical turbulent diffusivity can promote the phytoplankton growth (Margalef, 1978).

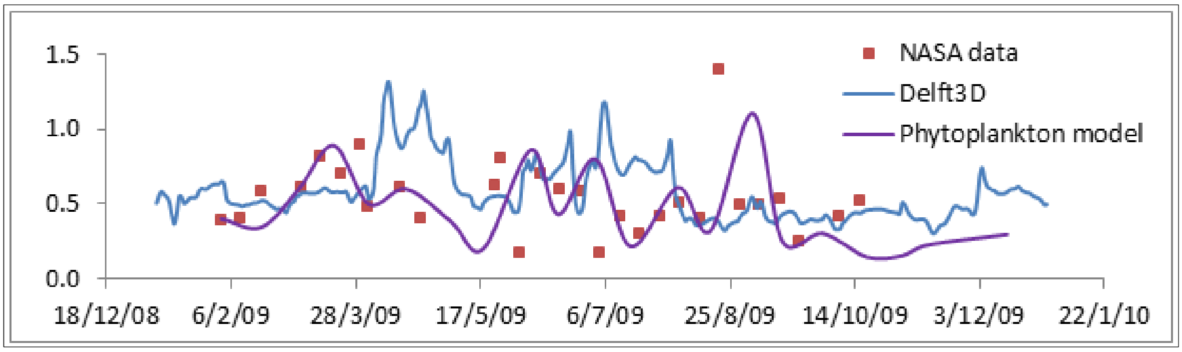

Figure 4. Graphical comparisons between the model outputs (Delft3D model and vertical phytoplankton model) and monitored phytoplankton biomass in 2009 at the Frisian Inlet, expressed in g m^{-3}.

3.4 Vertical distributions of the phytoplankton biomass

In this section, the general patterns of the phytoplankton biomass over water depth are illustrated. Table 2 reveals the statistical analysis of the model output for the different water depths (z=0m, 2m, 5m, 10m, and 20m) and gives insight in the prediction with uncertainty analysis using the Bootstrap method. At the surface layer, the phytoplankton biomass, varies from 0.014 g m^{-3} to 2.29 g m^{-3} which fits with chlorophyll a by a power function ($P = 31.43 \times Chla^{0.67}$, $R^2 = 0.50$). In the early June, chlorophyll a rises sharply from 0.64 mg m^{-3} to 80.27 mg m^{-3} in the course of weeks, so does the pattern of the phytoplankton biomass increasing from 0.01 g m^{-3} to 1.90 g m^{-3}. Higher values of the phytoplankton biomass appear in the months of March, April, July and September. Nutrients ($NO_3 + NH_4 + PO_4 + Si$), acts as another limiting factor of the phytoplankton growth and it showed specific properties over the year. The lower values of the nutrients are in the months of May and August, accompanied with the rapid growth of the phytoplankton. Light intensity becomes limited in winter, that constrains the phytoplankton growth regardless of sufficient nutrients. Normally, the sharp decreasing of nutrients happens during or before the bloom event and followed by increasing process which indicates the end of the bloom event.

Table 2. Statistical analysis of the model output for the different water depths (z=0m, 2m, 5m, 10m and 20m) over the year of 2009 at Lauwersoog station, expressed in g m^{-3}.

			Bootstrap			
					95% CI	
Lauwersoog		Statistic	Bias	Standard Error	Lower	Upper
	Mean	0.591	0.003	0.137	0.350	0.900
	SD	0.619	-0.033	0.153	0.174	0.835
P(0)	Skewness	1.922	-0.057	0.764	0.267	3.531
	Mean	0.291	0.003	0.066	0.179	0.438
	SD	0.294	-0.014	0.074	0.131	0.405
P(2)	Skewness	1.803	-0.315	0.709	-0.190	2.719
	Mean	0.452	0.006	0.130	0.240	0.729
	SD	0.573	-0.039	0.185	0.172	0.847
P(5)	Skewness	2.549	-0.497	0.771	0.571	3.675
	Mean	0.390	0.007	0.134	0.172	0.691
	SD	0.604	-0.036	0.178	0.190	0.871
P(10)	Skewness	2.405	-0.242	0.717	0.923	3.696
	Mean	0.569	0.009	0.128	0.348	0.851
	SD	0.578	-0.024	0.134	0.258	0.791
P(20)	Skewness	1.747	-0.216	0.555	0.550	2.831

*: unless otherwise noted, bootstrap results are based on 1000 bootstrap samples
*the object of the 95% confidence interval (95% CI) in the Bootstrap is the estimates of the mean value, the standard deviation and the skewness.

For the water depth of 2m at Lauwersoog station, the phytoplankton biomass shows a relatively small fluctuation, with the mean value of 0.291 g m^{-3} and the standard deviation of 0.294 g m^{-3}. The maximum value is 1.11 g m^{-3} which appeared on 2nd July. Higher values were concentrated in the months of March and July. Considering the uncertainty arising from the model, the mean value varies at a range of [0.178, 0.438] g m^{-3} within the 95% CI. The positive skewness (1.803) indicates a long right tail in the distribution. The values follow a Gamma distribution, with the shape parameter of 0.978 g m^{-3} and the scale parameter of 3.361 g m^{-3}.

For the water depth of 5m at Lauwersoog station, the phytoplankton biomass varies from 0.013 g m^{-3} to 2.406 g m^{-3}, with the mean value of 0.452 g m^{-3} and the standard deviation of 0.573 g m^{-3}. The maximum value occurs on the 19th March. Take the uncertainty into account, the mean value fluctuates at a range of [0.240, 0.729] g m^{-3} within the 95% CI. For the water depth of 10m, the maximum value is 2.331 g m^{-3} which appeared on the 19th March, the same day as the depth of 5m. The average phytoplankton biomass was 0.390 g m^{-3}, varying at a range of [0.172, 0.691] g m^{-3} within the 95% CI. For the water depth of 20m, the phytoplankton biomass varies from 0.007 g m^{-3} to 2.260 g m^{-3}, with the mean value of 0.569 g m^{-3}. 80% of the values were less than 1.0 g m^{-3}.

4 DISCUSSION AND CONCLUSIONS

As the most important indicator of the coastal ecosystem, the study of phytoplankton is proposed at the Frisian Inlet (the Netherlands). This study aims to investigate the phytoplankton variability over water depth, integrating the analyses of Delft3D model with the vertical phytoplankton model. With the course of year, phytoplankton dynamics will move forward to a steady state (Evans and Parslow, 1985; Steele and Henderson, 1992; Behrenfeld, 2010). The annual cycle of phytoplankton dynamics is driven by the cycle of physical-chemical characteristics, separately or comprehensively.

In this case, there is a low vertical mixing rate due to the semi-enclosed inlet position (Figure 1). The slow exchange between the tidal inlet and the North Sea also increases the water residence time, that promotes the phytoplankton growth. The vertical mixing process, affecting the vertical distribution of the phytoplankton, is performed with the Delft3D model which has been well validated in this area (Niu et al., 2015a; 2015b).

The findings of this research are expected to investigate the phytoplankton variability in the coastal waters and to provide valuable information for coastal management. Several assumptions are considered in order to get a practical solution of the phytoplankton model. The net growth rate is not derived from the function of the phytoplankton biomass but as a function of chlorophyll a where we assume the same property in the water layer. Here the components of the loss term are set as constants, but actually vary with the environmental factors. The biological properties are not considered in the current study, like cell size, species community and etc. More available data is still required to improve the model in future analysis.

ACKNOWLEDGEMENTS

The authors would like to thank the Rijkswaterstaat (http://www.eea.europa.eu/data-and-maps/data/external/donar-historical-water-measurement-data) and the NASA (the Ocean Colour web, accessible through http://oceancolor.gsfc.nasa.gov/cms/) for providing the data used in this study.

REFERENCES

Arhonditsis, G.B. & Brett, M.T. (2005). Eutrophication Model for Lake Washington (USA), Part I. Model Description and Sensitivity Analysis. *Ecological modelling*, 187, 140-178.

Behrenfeld, M.J. (2010). Abandoning Sverdrup's Critical Depth Hypothesis on Phytoplankton Blooms. *Ecology*, 91, 977-989.

Bissinger, J.E. & Montagnes, J.S. (2008). Predicting Marine Phytoplankton Maximum Growth Rates from Temperature: Improving on the Eppley Curve using Quantile Regression. *Limnology and Oceanogrphy*, 53, 487-493.

Blauw, A., Los, F.J., Bokhorst, M. & Erftemeijer, L.A. (2009). GEM: a Generic Ecological Model for Estuaries and Coastal Waters. *Hydrobiologia*, 618, 175-198.

Boyer, J.N., Kelble, C.R., Ortner, P.B. & Rudnick, D.T. (2009). Phytoplankton Bloom Status: Chlorophyll a Biomass as an Indicator of Water Quality Condition in the Southern Estuaries of Florida, USA. *Ecological Indicators*, 98, 856-867.

Bowie, G.L., Mills, W.B., Porcella, D.B., Campbell, C.L., Pagenkopf, J.R., Rupp, G.L., Johnson, K.M., Chan, P.W.H. & Gherini, S.A. (1985). *Rates Constants and Kinetics Formulations in Surface Water Quality modeling (second edition)*. US.EPA, Athens, Georgia, 455.

Brzezinski, M.A. (1985). The Si:C:N Ratio of Marine Diatoms: Interspecific Variability and the Effect of Some Environmental Variables. *Phycology*, 21, 347-357.

Edwards, A.M. (2001). Adding Detritus to a Nutrient-Phytoplankton-Zooplankton Model: a Dynamical-Systems Approach. *Journal of Plankton Research*, 23(4), 389-413.

Evans, G.T. & Parslow, J.S. (1985). A Model of Annual Plankton Cycles. *Biological Oceanography*, 3, 327-347.

Eppley, R.W. (1972). Temperature and Phytoplankton Growth in the Sea. *Fishery Bulletin*, 70, 1063-1085.

Felip, M. & Catalan, J. (2007). The Relationship between Phytoplankton Biovolume and Chlorophyll a in a Deep Oligotrophic Lake: Decoupling in their Spatial and Temporal Maxima. *Journal of Plankton Research*, 22, 91-105.

Godrijan, J., Daniela, M., Igor, T., Robert, P. & Martin, P. (2013). Seasonal Phytoplankton Dynamics in the Coastal Waters of North-Eastern Adriatic Sea. *Journal of Sea Research*, 77, 32-44.

Henderson, E.W. & Steele, J.H. (1995). Comparing Models and Observations of Shelf Plankton. *Journal of Plankton Research*, 17(8), 1679-1692.

Huot, Y., Babin, M., Bruyant, F., Grob, C. & Twardowski, M.S. (2007). Does Chlorophyll a Provide the Best Index of Phytoplankton Biomass for Primary Productivity Studies?. *Biogeoscience Discussions*, 4, 707-745.

Los, F.J. (2009). Eco-hydrodynamic Modeling of Primary Production in Coastal Waters and Lakes using BLOOM. *PhD Thesis*, Wageningen University.

Margalef, R. (1978). Life-Form of Phytoplankton as Survival Alternatives in an Unstable Environment *Oceanologica Acta*, 1, 493-509.

Niu, L., Van Gelder, P.H.A.J.M., Guan, Y., Zhang, C. & Vrijling, J.K. (2015a). Probabilistic Analysis of Phytoplankton Biomass at the Frisian Inlet (NL). *Estuarine, Coastal and Shelf Science*, 155, 29-37.

Niu, L., Van Gelder, P.H.A.J.M., Guan, Y. & Vrijling, J.K. (2015b). Uncertainty Analysis and modeling of Phytoplankton Dynamics in Coastal Waters. *Journal of Environment Protection and Sustainable Development*, 1(4), 193-202.

Niu, L., Van Gelder, P.H.A.J.M., Zhang, C., Guan, Y. & Vrijling, J.K. (2015c). Statistical Analysis of Phytoplankton Biomass in Coastal Waters: Case Study of the Wadden Sea Near Lauwersoog (The Netherlands) from 2000 through 2009. *Ecological Informatics*, 30, 12-19.

Niu, L., Van Gelder, P.H.A.J.M., Zhang, C., Guan, Y. & Vrijling, J.K. (2016). Physical Control of Phytoplankton Bloom Development in the Coastal Waters of Jiangsu (China). *Ecological Modeling* 321, 75-83.

Smith, R.A. (1980). The Theoretical Basis for Estimating Phytoplankton Production and Specific Growth Rate from Chlorophyll, Light and Temperature Data. *Ecological Modelling*, 10, 243-264.

Steele, J.H. & Henderson, E.W. (1992). The Role of Predation in Plankton Models. *Journal of Plankton Research*, 14, 157-172.

Van Beusekom, J.E.E., Buschbaum C. & Reise, K. (2012). Wadden Sea Tidal Basins and the Mediating Role of the North Sea in Ecological Processes: Scaling up of Management? *Ocean & Coastal Management*, 68, 69-78.

Proceedings of the 37th IAHR World Congress
August 13 – 18, 2017, Kuala Lumpur, Malaysia

APPLICATIONS OF NEAR- AND FAR-FIELD COUPLED MODELS FOR MARINE OUTFALLS

JING FEN CHUA(1), CHI WEI CHENG(2), AAROUN LEIKING(3), EDGAR PETER DABBI(4), JACOB HJELMAGER JENSEN(5) & JUAN CARLOS SAVIOLI(6)

(1,2,3,4,5,6) DHI Water & Environment (M) Sdn. Bhd., 3A01&02 Block G, Phileo Damansara 1,
Jalan 16/11 Off Jalan Damansara, 46350 Petaling Jaya, Selangor, Malaysia,
cjf@dhigroup.com; ccw@dhigroup.com; aal@dhigroup.com; edp@dhigroup.com; jhj@dhigroup.com; jcs@dhigroup.com

ABSTRACT

Predicting the dispersion of discharged contaminants is critical to support engineering design and the assessment of impacts on the ambient waters. Dispersion is crucial for the engineering design of marine outfalls as well as for the optimization of outfall configurations. The mixing of a discharged effluent with the receiving water can be described by its near-field and intermediate to far-field characteristics. CORMIX is capable of predicting the effluent dilution from the outfall in the near-field and far-field regions, however, the three-dimensional model of MIKE 3 FM is better at describing the natural-varying ambient current conditions that govern the intermediate and far-field dispersion. In order to provide a robust framework that encapsulates both regions, a dynamic coupling between the two models has been developed. This coupling ensures that the ambient conditions in the far-field modelling are imposed on the near-field simulation, and conversely, CORMIX predictions are influencing the far field. The latter by transferring the plume as discrete sources distributed in both vertical and horizontal layers of the MIKE 3 FM model. This paper presents the applications of various modelling approaches to predict the thermal effluent dispersion based on a synthetic case study in positive thermal release via two marine outfalls in the Malacca Straits, Malaysia. MIKE 21 FM and MIKE 3 FM modelling have been carried out to evaluate the two-dimensional and three-dimensional dispersal patterns and finally, coupling models between CORMIX and MIKE 3 FM have also been established for the case study.

Keywords: Effluents; near-field and far-field; CORMIX; MIKE 3 FM; dynamic coupling.

1 INTRODUCTION

The application of marine outfalls for the discharge of effluents into the marine environment is common in the recent years in Malaysia. The effluents being released through the outfalls may include wastewater effluents by industrial or domestic purposes, heated seawater from an energy plant for cooling water system, cooled seawater from a LNG plant to contribute thermal energy for a degasification process, used water for a desalination plant that may result in the release of more saline water than the ambient conditions.

The release may potentially bring adverse impacts to the receiving marine environment and in some cases, may affect other marine developments or its own system (such as once-through cooling water system) that are located nearby the outfalls. The assessment of impacts mainly relies on the prediction of the dispersion of contaminant release into the marine system. The prediction results are crucial for the engineering design of marine outfalls, particularly in optimizing the outfall configuration in order to promote better initial mixing with the ambient water, which in turns reduces the adverse impact to the marine environment. In Malaysia, some developments have to undergo impact assessment study and to obtain approval from the relevant authorities are a legal requirement prior to constructing and operating the developments.

The mixing of the effluent with the receiving waters can conceptually be described in two separate regions (Morelissen, 2011), i.e. the near-field (meters around the outfall where the geometry of the outfall diffuser and the characteristics of the effluent govern the initial jet trajectory) and the far-field region (away from the source and the conditions of the ambient waters dominate the mixing processes). In most cases, positive buoyant tends to disperse towards surface while the negative buoyant tends to sink to the bottom. This density function available in the 3D model is the key element that made it more practical than the 2D (depth-averaged) model.

1.1 Near-field and far-field regions

The dilution of chemical release in open waters occurs due to the mixing process induced by a number of parameters including the geometry of the diffuser, the location of the release, the characteristics of effluent and ambient waters and the flow conditions. An illustration of the release of a positive buoyant effluent is presented in Figure 1. As it can be observed that the mixing process varies in space, as follows:

- Jet Approach/Near-field. This is the first mixing phase (jet/plume phase) where the effluent discharge enters the marine environment in a jet or plume-like flow. In this area, the jet trajectory and mixing in the jet-like flow are determined by the momentum flux, buoyancy flux, and outfall geometry; it is during the rise of the plume that the most significant portion of the mixing process occurs and it is the only portion of the mixing area that is influenced by the geometry and location of diffuser;
- Transition Area. This is the area between the jet/plume phase and buoyant spreading and is called "layer boundary impingement/ upstream spreading". This transition phase is where the plume hits the water surface and is still considered in the near field mixing;
- Far-field. This is an area where the plume dynamics are governed by the conditions of the ambient water, here, predominantly currents and turbulence induced by the tides or the wind. As the turbulent plume travels further away from the released source, the source characteristics become less important and no longer influenced by the mixing behavior.

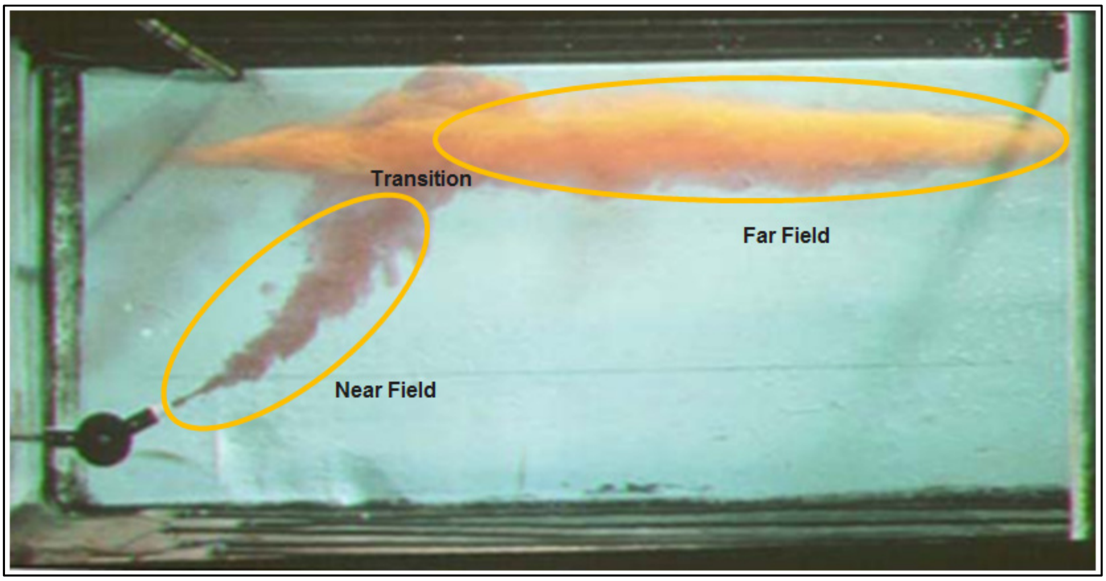

Figure 1. Illustration of the mixing of a positive buoyant effluent discharge in open waters (Hofer, 1978).

1.2 Model application

1.2.1 CORMIX

The CORMIX modelling system (Doneker, 2007) is a software system for the analysis, prediction, and design of aqueous toxic or conventional pollutant discharges into diverse water bodies. The effluent dispersion near the outfall was modelled using CORMIX that has become an industrial standard tool for the prediction of effluent plume behavior in the near-field region where the strong initial mixing of effluent with seawater occurs due to the momentum of the discharge jet.

It is a steady state three-dimensional model which was used to produce the dilution and trajectory of a submerged port discharge of arbitrary density (positive; neutral; negative) into a stratified or uniform density ambient environment with or without cross flow. The model describes the discharge dispersal based on the geometry of the release outfall, the height of the release point in the water column and the typical ambient current speeds. The near field region is the first mixing zone where the discharged effluent enters the marine environment in a jet or plume-like flow. The mixing process in this region is mainly determined by the momentum flux, buoyancy flux, and outfall geometry. The most significant portion of the mixing process occurs during the rise or descend of the plume.

Near field mixing processes are characterized by the geometry of diffuser configurations, effluent characteristics, ambient water and current conditions, as described below.

- Port diameter;
- Port orientation relative to ambient current;
- Port height above and orientation relative to seabed;
- Ambient current flow conditions;
- Discharge rate of the effluent;
- Exit velocity of the effluent;
- Temperature and salinity concentration of the effluent.

An illustration of a diffuser of a marine outfall is presented in Figure 2. The port height above the seabed and orientation relative to the seabed (or horizontal plan) may depend on the effluent plume buoyancy and the density stratification of the ambient water which affects the initial mixing. It should be noted that changes in the diffuser configuration will induce a significant variation of the concentration in the near field area where dilution values can vary significantly. Different port angle orientations are illustrated in Figure 3.

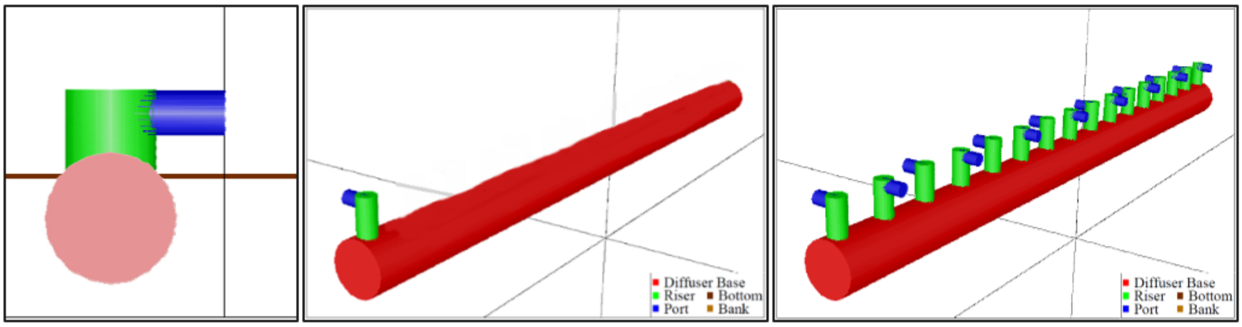

Figure 2. Examples of diffusers from a pipeline outfall.

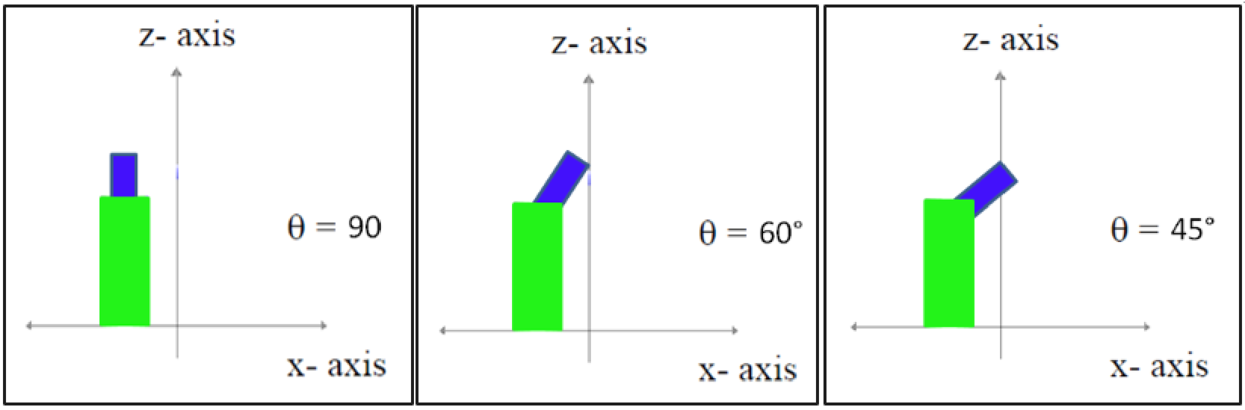

Figure 3. Examples of port orientation relative to the seabed.

1.2.2 MIKE

DHI's MIKE 21 and MIKE 3 Flow Model FM are modelling systems based on a flexible mesh approach, developed for the applications within coastal, estuary and oceanographic environments (DHI, 2016). Both models utilize unstructured Flexible Mesh (FM) and Hydrodynamic (HD) module. The HD module is the basic computational component to provide the necessary hydrodynamic basis for the subsequent modelling such as the Transport Module (advection-dispersal of particles), ECO Lab Module (water quality modelling), Oil Spill Module, Mud Transport Module, Sand Transport Module and Particle Tracking Module.

The MIKE 21 FM HD module is based on two-dimensional hydrostatic model depth-integrated incompressible Reynolds averaged Navier-Stokes equations invoking the Boussinesq assumptions. This means that the model contains the equations for continuity, momentum, temperature, salinity as well as density. Both Cartesian and spherical coordinates can be used in the horizontal domain. Cell-centered finite volume method was performed for the spatial discretization of the primitive equations. Discretization of the spatial domain was performed by subdivision of the continuum into non-overlapping element or cells. For the horizontal plane, unstructured triangles or quadrilateral element grid was used. For the computation of the convective fluxes, an approximate Riemann solution was used to handle discontinuous solutions. An explicit scheme was used for the time integration.

The MIKE 3 FM HD module is based on the numerical solution of the three-dimensional incompressible Reynolds averaged Navier-Stokes equations invoking the assumptions of Boussinesq and of hydrostatic pressure. Accordingly, the model contains equations of continuity, momentum, temperature, salinity as well as density and is closed by a turbulent closure scheme. Both Cartesian and spherical coordinates can be utilized in the horizontal domain. A sigma-coordinate transformation approach was used to take account of the free surface. Using a cell-centered finite volume method, the spatial discretization of the primitive equations was performed. Discretization of the spatial domain is accomplished by subdivision of the continuum into non-overlapping element or cells. An unstructured grid was used in the horizontal plane whilst a structured discretization was utilized in the vertical domain. The element comes in the form of prisms or bricks with corresponding horizontal faces in shapes of triangles and quadrilateral elements, respectively. For the computation of the convective fluxes, an approximate Riemann solver was used, which makes it possible to handle discontinuous solutions. A semi-explicit approach was used for the time integration in where the horizontal and vertical terms were treated explicitly and implicitly, respectively.

1.3 Objectives

This paper presents the applications of various modelling approaches to predict the dispersion of thermal effluents based on a synthetic case study in positive thermal release in the Malacca Straits, Malaysia. Three (3) modelling approaches have been identified, as follows:

- Two-dimensional (2D) far-field model, MIKE 21 FM;
- Three-dimensional (3D) far-field model, MIKE 3 FM;
- Coupling models between near-field model, CORMIX and 3D far-field model, MIKE 3 FM.

Based on the predictions of the various modelling approach, the objectives of the present study are set out in the following:

(a) To evaluate the dispersion prediction of MIKE 21 FM and MIKE 3 FM;
(b) To evaluate the dispersion prediction of coupling models between CORMIX and MIKE 3 FM.

2 BACKGROUND INFORMATION: A SYNTHETIC CASE STUDY

A synthetic case study was established in the southern part of the Malacca Straits, Malaysia and based on once-through cooling water system for power plants for which seawater was extracted from an offshore intake structure to travel through the power plant to absorb heat energy before it is released back into the sea through an offshore marine outfall. This case study assumed two (2) sets of the once-through system. For a typical ambient water temperature of 31°C and according to Malaysian DOE (2009) guideline for Standard B effluent, the maximum absolute effluent temperature must not be more than 40°C before discharging from the site. The difference of temperature increase between the intake and the outfall is assumed to be +8°C. This allows 1°C margin to account for recirculation and safety risk in order to be lower than the 40°C maximum limit by DOE. The specifications of the synthetic case study are set out in Table 1. It is assumed that the release does not involve any changes in the salinity conditions from the ambient.

Table 1. Design specifications for the synthetic case study.

	Seabed Level (m CD)	Structure Height (m)	Design Release (m^3/s)	Design Excess Temperature, ΔT (°C)	Design Excess Salinity (PSU)
Intake 1	-10.5	3 m above seabed	14	Modelled temperature at intake, T_{i1}	Salinity is not modified
Outfall 1	-5.5	1 m above seabed		T_{i1}+8°C	
Intake 2	-10.5	3 m above seabed	64	Modelled temperature at intake, T_{i2}	
Outfall 2	-14.5	1 m above seabed		T_{i2}+8°C	

3 RECIRCULATION STUDY: 2D AND 3D MODELLING

The hydrodynamic model was established to derive the hydrodynamic conditions within the Malacca Straits using MIKE 21 FM and MIKE 3 FM. The horizontal resolution of the model domain varies from 50 m around the marine outfalls area to 500 m near the open model boundaries. For MIKE 3 FM, the vertical resolution is defined in sigma layer type of distribution, for which the vertical water columns of every mesh element was distributed into 10 equidistant-layer for simulation. For MIKE 21 FM, the vertical resolution was preset at one (1) depth-average layer. The bathymetry information is based on DHI's in-house database from the past projects in the region, supplemented by C-Map data. Bed roughness across the model domain was assumed constant at 45 $m^{1/3}/s$ Manning number or 0.01 m roughness height. The boundary conditions are predicted water level, current flow conditions in u- and v-components extracted from DHI's in-house regional HD models in the format of time-varying profiles. The regional model covers the Andaman Sea, Malacca Straits, and the South China Sea and it is able to capture the seasonal variations of the hydrodynamic conditions induced by the wind forcing blowing over the large water surface. Both models have applied baroclinic conditions, which means that the calculation of the water density is dependent on the water temperature and salinity conditions. Ambient temperature and salinity reference values were modelled as some typical values of 31°C and 32 PSU. In the model setup, the synthetic intakes were extracting water at 14 m^3/s and 64 m^3/s respectively and releasing at the same flow rate with an excess temperature of +8°C to the receiving environment through the synthetic marine outfalls. Both models were carried out for 30 days (allowing 2 days warm-up period for the model to stabilize during start-up, 14 days for recirculation to warm-up, and final 14 days production period for statistical analysis).

The modelling results of the MIKE 21 FM and MIKE 3 FM model were used to compute statistical mean temperature over 14 days spring-neap cycle, as shown in Figure 4. The comparison between 2D and 3D are quite different, which demonstrates the complexity of the physics and the difficulty in intuitively predicting the results. It is observed that the excursion plume of the 3D model results is larger than those shown in the depth-averaged model. This is due to a better description of transport processes over vertical and horizontal dispersal pattern in the 3D modelling.

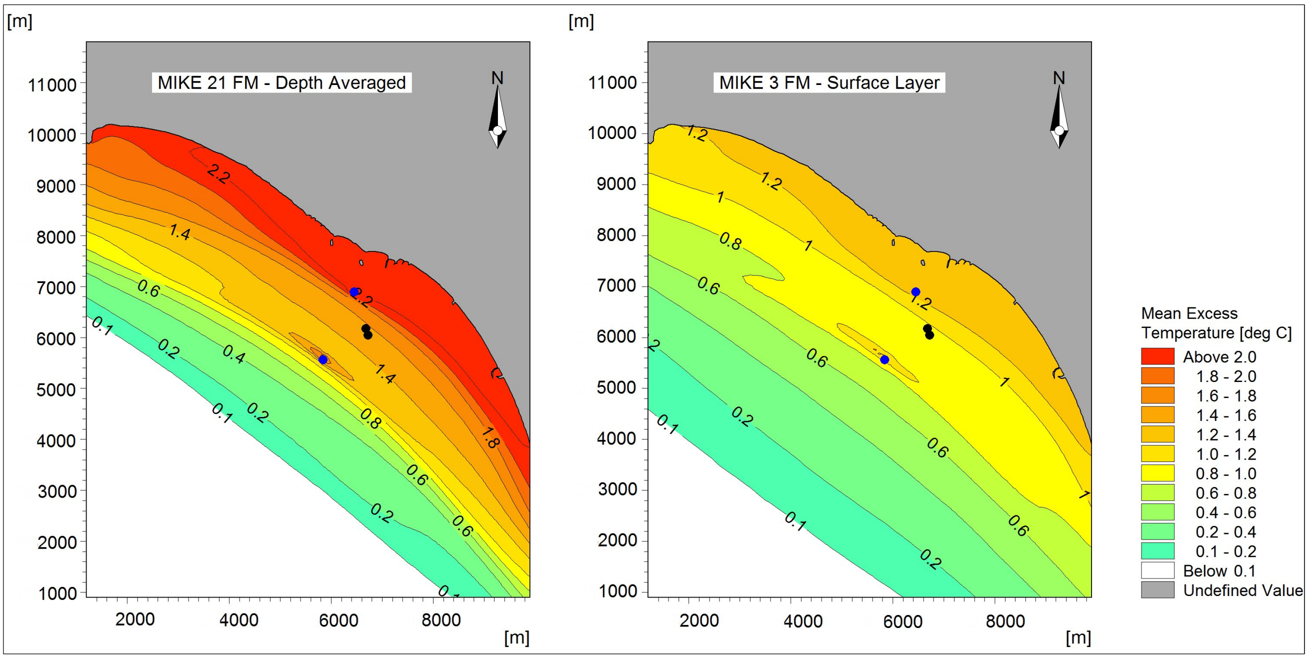

Figure 4. Predicted dispersion plume using (Left) MIKE 21 FM and (Right) MIKE 3 FM surface layer. Blue dots indicate outfalls and black dots indicate intakes.

4 RECIRCULATION STUDY: COUPLING MODELS (NEAR- AND FAR-FIELD)

The effluent dispersion in the near field region around the outfalls was simulated using CORMIX GT Advanced Tool. The CORMIX model was assumed an effluent density of 1015.75 kg/m^3 while the ambient density was 1020 kg/m^3. It was further assumed that Outfall 1 has 2 diffuser ports and Outfall 2 has 6 diffuser ports, see Figure 5. The port diameter was assumed to be 1.8m. The port's horizontal angle relative to true north is 235° and vertical angle to the seabed is 15°. Current flow velocity were extracted from the MIKE 3 FM HD and for the marine outfalls, some typical ambient velocities for low, medium and high speeds were selected as 0.3, 0.5 and 0.65 m/s for Outfall 1 and 0.4, 0.65 and 0.8 m/s for Outfall 2.

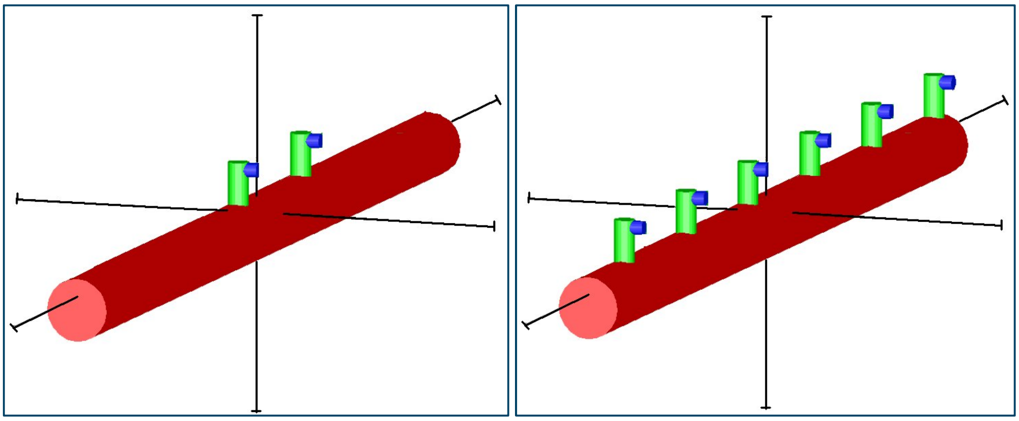

Figure 5. Illustrations of diffuser ports and discharge pipe.

The CORMIX results at the end of the near-field-zone were then incorporated into the MIKE 3 FM model setup as a number of discrete sources distributed in vertical and horizontal layers as well as in temporal resolution (different mixing process due to different current flow conditions within the near field zone). The MIKE 3 FM model (this time with CORMIX's inputs) was carried out for 30 days (allowing 2 days warm-up period for the model to stabilize during start-up, 14 days for recirculation to warm-up, and final 14 days production period for statistical analysis).

The modelling results of the coupled models (CORMIX-MIKE 3 FM) were used to compute statistical mean temperature over 14 days spring-neap cycle, as shown in Figure 6. The coupled modelling approach is able to promote better initial mixing around the near-field region and resulting in a generally lower mean temperature, as well as a smaller temperature excursion plume, as compared to the MIKE 3 FM model (without CORMIX inputs). Finally, a predicted temperature time series was extracted from the three (3) modelling approaches, as shown in Figure 7, to show that the temperature prediction at a proposed intake vary and thus, it is essential to select appropriate modelling approach for the design of cooling water system and/or other cases involving releases via marine outfalls.

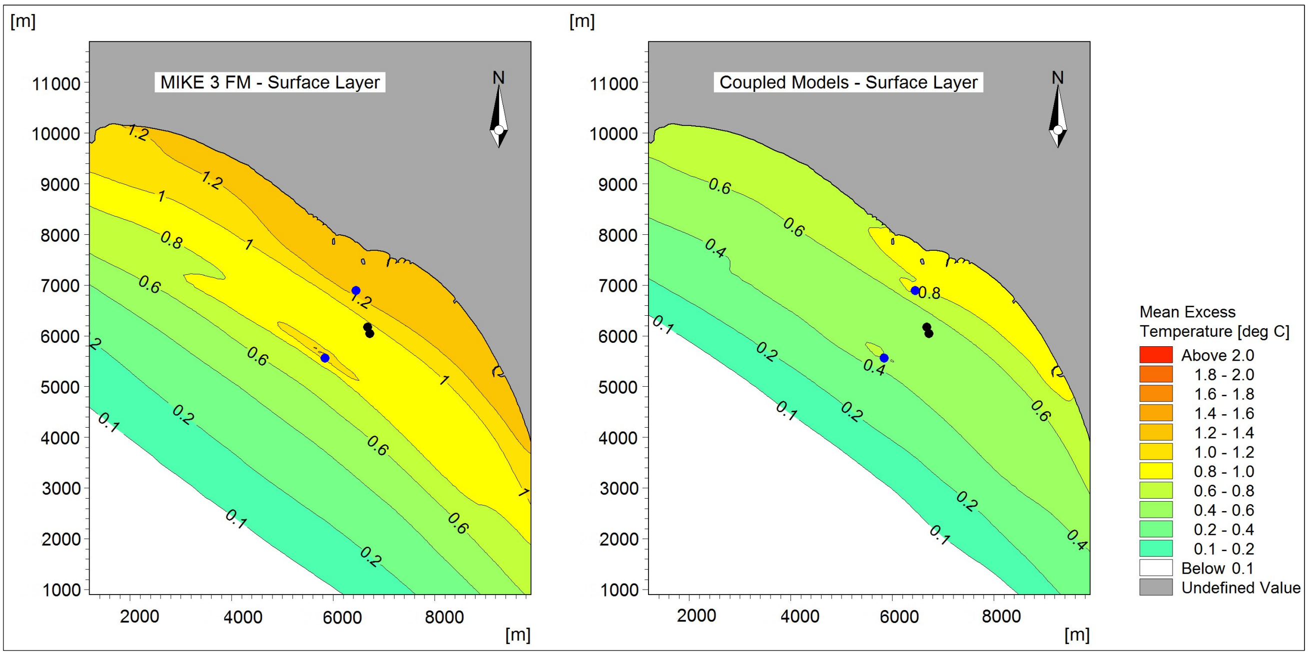

Figure 6. Predicted dispersion plume using (Left) MIKE 3 FM only, surface layer and (Right) Coupling models between CORMIX and MIKE 3 FM, surface layer. Blue dots indicate outfalls and black dots indicate intakes.

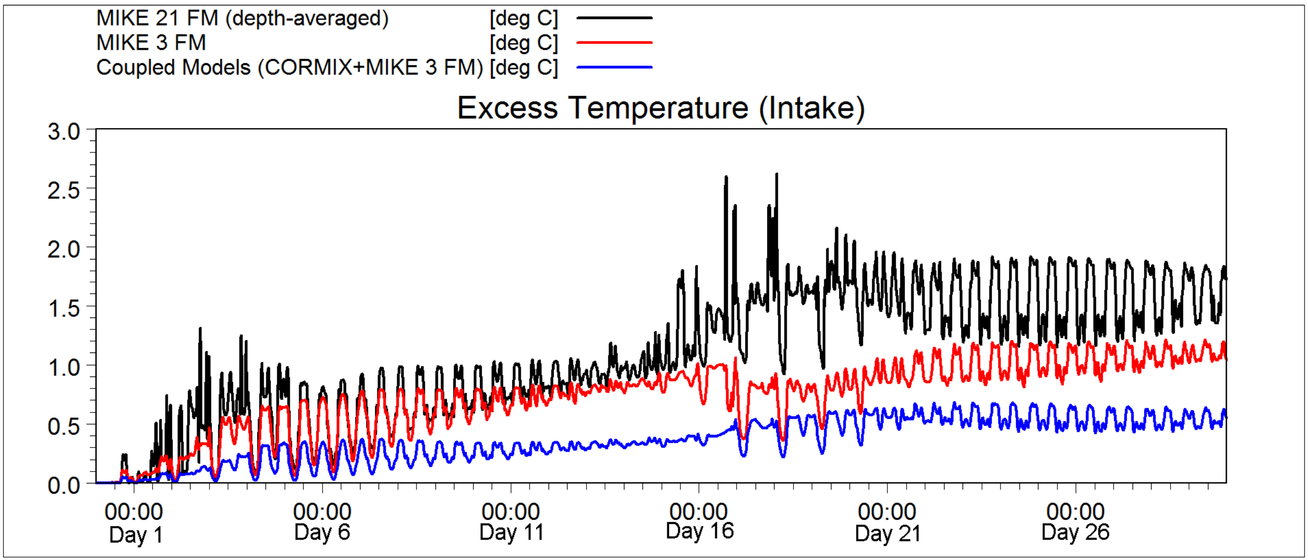

Figure 7. Predicted excess temperature at a location between the synthetic marine intakes using (black) MIKE 21 FM model, (red) MIKE 3 FM model and (blue) coupling models between CORMIX and MIKE 3 FM.

5 CONCLUSIONS

A number of modelling using MIKE 21 FM, MIKE 3 FM and coupled model between CORMIX and MIKE 3 FM has been carried out to predict the thermal recirculation pattern based on a synthetic case study in the Malacca Straits, Malaysia. A comparison between MIKE 21 FM and MIKE 3 FM modelling results showed that the depth-averaged 2D far-field model is insufficient to describe the vertical mixing process especially in a thermal release case where warm water tends to float to the surface within a short distance from the release point (near-field zone). While a 3D far-field model enhances the vertical and horizontal dispersion of the recirculation process, the near-field region could be better described by a near-field model such as CORMIX. The results around the end-of-near-field-region in the 3D far-field model should be cross-validated by a CORMIX prediction or using coupling method to incorporate the near-field process into the entire modelling system for dispersal prediction to support in detailed engineering design as well as impact assessments for the marine environment.

ACKNOWLEDGEMENTS

The authors would like to thank DHI Malaysia for the supports and resources allocated to the team to complete the paper.

REFERENCES

Doneker, R.L. & Jirka, G.H. (2007). *A Hydrodynamic Mixing Zone Model and Decision Support System for Pollutant Discharges into Surface Waters,* CORMIX User Manual.

DHI (2016). *MIKE 21 & MIKE 3 Flow Model FM. Hydrodynamic and Transport Module,* Scientific Documentations.

DOE (2009). Standard B of the Fifth Schedule, Environmental Quality (Industrial Effluents) Regulations, P.U. (A) 434/2009, Department of Environment Malaysia.

Hofer, K. (1978). *Eine Verbesserte Theorie Turbulenter Freistrahlen im stratifizierten Medium und ihr Vergleich mit dem Experiment,* Mitteilung VAW-ETH No. 31.

Morelissen, R., Kaaij, T.V.D. & Bleninger, T. (2011). Waste Water Discharge Modelling With Dynamically Coupled Near Field and Far Field Models. *International Symposium on Outfall Systems*, May 15-18, 2011, Mar del Plata, Argentina.

A GEOCHEMICAL APPROACH TO VALIDATE HYDRODYNAMIC MODEL IN BOHAI BAY

YUANYI LI[1], HUAN FENG[2], DEKUI YUAN[3], LEI GUO[4] & JIANHUA TAO[5]

[1,3,5] Tianjin University, Tianjin, 300350, PRC,
liyuanyi@tju.edu.cn; dkyuan@tju.edu.cn; jhtao@tju.edu.cn
[2] Montclair State University, Montclair NJ, 07003, USA,
fengh@mail.montclair.edu
[4] Guangdong Research Institute of water resources and Hydropower, Guangzhou, Guangdong, 510610, PRC,
gl_gdsky@126.com

ABSTRACT

Water circulation is one of the important driving forces in controlling the transport processes in the ocean. Trace metals originating from land sources and entering the ocean are controlled by multiple processes including water circulation in the ocean. Driven by hydrodynamics and sediment dynamics, the transport of trace metals associated with sediments often has longer temporal scales than the water flow. Considering this fact, we should realize that distributions of the trace metals on the sea bed record the information of long-term circulation. The region around the Bohai Bay is one of the key area of economic development in China, where trace metals such as Cr, Cu, Pb and Zn are discharged into the Bohai Bay through the outlets of waste water. In this study, water circulation and transport of the trace metals in the Bohai Bay were numerically simulated and the results of the hydrodynamic model and particle tracking model were validated by the distributions of trace metals in the sediments, with the several important characteristics of the distributions of trace metals and sediments being well accounted by the results of the numerical model. It means that the numerical model used in this research can well be used to study the water circulation and processes of transport in the Bohai Bay.

Keywords: Trace metal; sediment; residual flow; numerical model; model validation.

1 INTRODUCTION

Marine pollution caused by anthropogenic activities is a global environmental concern. Among the environmental contaminations, trace metals are of much concern due to their persistency in degradation. Transported through the food chains or food web, trace metals can cause a series of damage to human beings and organisms. The long-term environmental impact of the metals are the main concern to the environmentalists (Reddy et al., 2004; Gonzalez-Macias et al., 2006; Feng et al., 2011; Bazzi, 2014; Li et al., 2015) and have been extensively investigated around the world (Pempkowiak et al., 2000; Sweeney and Sanudo-Wilhelmy, 2004). It has been reported that most of trace metal contaminants in the ocean come from anthropogenic sources (Zhan et al., 2010; Zhang et al., 2011), entering the ocean with the runoff of polluted rivers, which are the important sources.

Dissolved trace metals in sea water can be adsorbed by the suspended particles in water. With the transport of water and sediments, the contaminants having entered the ocean can be transported farther, and the distributions of the trace metals are mainly determined by the transport processes of water and sediment. Xu et al. (2009) pointed out that the elevation of metal levels in the sea water often results in a high concentration in the bottom sediments. Therefore, the sediments become a sink of metals and can provide valuable information in resolving the source and sink of metal pollution, and the water flow direction. In this sense, the distribution of trace metals in the sediments can be used as evidence to validate the numerical hydrodynamic models.

However, the distributions of trace metals in the sediments are also related to the sedimentation condition which is closely related to the hydrodynamic condition. Radionuclides with different half-life time have proven to be useful to track the fate of sediments and estimate sediment deposition rates (Hirschberg et al., 1996; Feng et al., 1998; Sommerfield et al., 1999; Woodruff et al., 2001; Su and Huh, 2002; Feng et al., 2010). Therefore, the hydrodynamic condition can also be inferred from the distributions of radionuclides in the sediments.

The Bohai Sea is the largest inner sea in China. With the fast development in the regions around it, the Bohai Sea is facing lots of environmental problems, one of which is the contamination caused by the trace metals discharged from the rivers around it (Luo et al., 2010; Gao et al., 2014; Li et al., 2015). As a fast developing region, the trace metal contamination in the Bohai Bay is attracting more attention from the researchers. A number of field investigations on the sediments and their associated trace metals in this region were carried out recently (Feng et al., 2011; Lei et al., 2011; Zhang et al., 2011). Most of these researchers considered that the sediments in this region have been contaminated by the trace metals. These available data have provided us with a chance to validate the model that we have developed.

In this study, historic data on trace metal distributions in the Bohai Bay were collected from the publications and they are used to examine the distributions of trace metals in the Bohai Bay. The hydrodynamic model and particle-tracking model developed by us were set up and run for the Bohai Bay. Data analysis on the trace metal distributions and results of numerical models reveal a close relationship between the trace metal distribution patterns and ocean currents in the Bohai Bay. This result is also supported by the distributions of radionuclide ^{210}Pb in the sediment cores in the bay. These close relations among the trace metal distributions, radionuclide distribution and results of numerical models mean that the models we have set up have the ability to simulate the movement of water in the Bohai Bay.

2 BOHAI BAY AND BOHAI SEA

The Bohai Sea is the largest inner sea in China, surrounded by three provinces and a metropolis (Liaoning Province, Hebei Province, Shandong Province and the City of Tianjin, see Figure 1). As a semi-closed sea, it is connected to North of the Yellow Sea through the Bohai Strait in the east. The Bohai Sea consists of the central basin and three bays including the Liaodong Bay in the north, the Bohai Bay in the west and the Laizhou Bay in the south. The Bohai Sea also is a shallow margin sea with an average depth of about 18m. The deepest area is about 86m in the north of the Bohai Strait. The semi-diurnal tidal component, M_2, is the dominant tidal constituent in the Bohai Sea with an average height of about 2m. Therefore, the water exchange ability in the Bohai Sea is relatively weak.

The Bohai Bay is one of the three bays making up of the Bohai Sea. Since the bay is near Tianjin and Beijing, it is facing a series of environmental problems. For the region around it is the industrial area and populated towns, the rivers flowing into it are often polluted and bringing tons of polluted water into it as well as numerous nutrients which support the whole ecosystem of the Bohai Bay. Along with Economic Integration of Jing-Jin-Ji Area, which is an economic policy supported by China's central government, the economic bloom in the region is putting more threat on the environment in the Bohai Bay. Several past issues of Annual Report of Oceanic Environment in the Bohai Sea released by the State Oceanic Administration of China during past several years indicated that some of the outfalls around the Bohai Bay were still discharging the waste water exceeding the criteria implemented by the government (SOA, 2009; SOA, 2010). According to the Annual Report of Oceanic Environment in the Bohai Sea 2008 (SOA, 2009), the main outfalls around the Bohai Bay are Jian River, Yongding River, Ziya River and Dakou River shown in Figure 1.

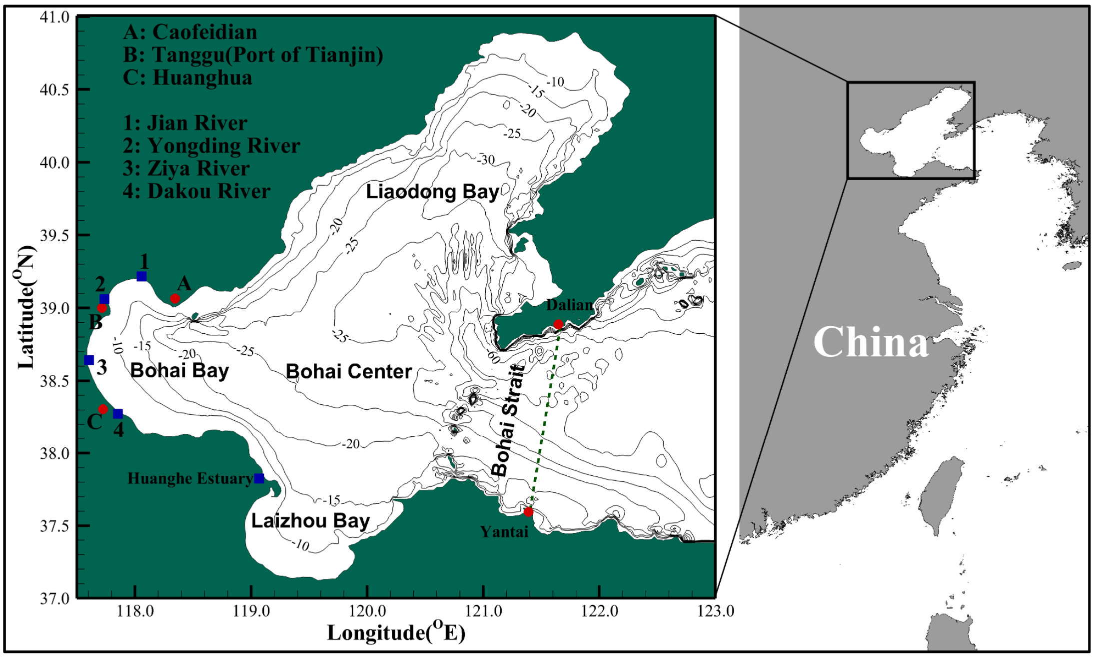

Figure 1. The concerned area and the bathymetry in the Bohai Sea.

3 MODEL DESCRIPTION

The Bohai Sea is a tidal-dominant coastal sea where the semi-diurnal tidal component M_2 is dominant. With relative shallow water, vertical movement of the sea water and contaminant are much weaker than that in the horizontal direction and can be neglected. Therefore, a two dimensions (2D) model is rational to predict the water flow in the bay. In this paper, a 2D hydrodynamic model is used to simulate the currents and a particle-tracking model is used to simulate the transport of the metal contaminants.

The governing equations of the hydrodynamic model that we have developed are the Reynolds-Averaged Naiver-Stokes (RANS) equations, which are integrated from the bottom to the free surface of the ocean and are expressed as:

$$\frac{\partial \zeta}{\partial t}+\frac{\partial p}{\partial x}+\frac{\partial q}{\partial y}=S \quad [1]$$

$$\frac{\partial p}{\partial t}+\frac{\partial(\beta pU)}{\partial x}+\frac{\partial(\beta pV)}{\partial y}=fq-gH\frac{\partial \zeta}{\partial x}-\frac{H}{\rho}\frac{\partial P_s}{\partial x}+\frac{\tau_{wx}}{\rho}-\frac{\tau_{bx}}{\rho}+\frac{\tau_{sx}}{\rho}+\varepsilon\left(\frac{\partial^2 p}{\partial x^2}+\frac{\partial^2 p}{\partial y^2}\right) \quad [2]$$

$$\frac{\partial q}{\partial t}+\frac{\partial(\beta qU)}{\partial x}+\frac{\partial(\beta qV)}{\partial y}=-fp-gH\frac{\partial \zeta}{\partial y}-\frac{H}{\rho}\frac{\partial P_s}{\partial y}+\frac{\tau_{wy}}{\rho}-\frac{\tau_{by}}{\rho}+\frac{\tau_{sy}}{\rho}+\varepsilon\left(\frac{\partial^2 q}{\partial x^2}+\frac{\partial^2 q}{\partial y^2}\right) \quad [3]$$

where Eq.[1] is the mass conservation equation and Eq.[2] and [3] are the momentum conservation equations, H is the local water depth, ζ is the water tidal level, p and q are the fluxes in the x and y direction respectively, U and V are the velocity components in the x and y direction respectively, ρ is the density of the sea water, g is the gravity acceleration, β is the momentum correction coefficient caused by the non-uniform distribution of the horizontal velocity along the vertical direction. P_s is the atmosphere pressure on the surface of the water, τ_s, τ_w and τ_b are the radiation stress, wind stress and bottom stress, respectively, and ε is the comprehensive diffusion coefficient including the effects of molecular viscous diffusion and eddy viscous diffusion in horizontal directions.

The Finite Difference Method (FDM) and Alternating Direction Implicit (ADI) scheme were used to solve the governing equations of hydrodynamic model (Li et al., 2016). The computational domain is discretized by staggered rectangle cells, with the free surface elevation and water depth defined at the cell centers and the velocity and the flux components defined at the middle points of the cell edges.

An open boundary connecting the computational domain and the sea out of it is defined by the water level along it. In order to eliminate the influence of the open boundary on the area concerned, the open boundary in this research is located between the Dalian in Liaoning Province and Yantai in Shandong Province (Figure 1). The water level on the nodes along the open boundary were calculated by the linear interpolation using the water levels in Dalian and Yantai calculated by the tidal constants of eight tidal constituents (K_1, O_1, P_1, Q_1, N_2, K_2, M_2, S_2) in the two locations, respectively.

The transport of trace metal contaminants was simulated by particle-tracking method which has already been described by Li et al. (2011) for the water exchange in the large-scale bay. This method is based on the Lagrange viewpoint which studies the fluid and the contaminant movement by tracing every particle representing a certain quantity of the water or the contaminant in the water. Using the method, the track of water and the contaminant can be directly studied because the position of every particle is calculated every time step of the hydrodynamic model. Therefore, it provides us with the detailed knowledge of transport of water and the contaminant discharged from river outfalls. Mathematically, it can prove that the equations used in particle-tracking model are equivalent to the convection-diffusion equations when proper methods are used to generate random number to control the random walk of the particles. The convection-diffusion can be written as:

$$\frac{\partial(Hc)}{\partial t}+\frac{\partial(pc)}{\partial x}+\frac{\partial(qc)}{\partial y}=\frac{\partial}{\partial x}\left(HD_{xx}\frac{\partial c}{\partial x}+HD_{xy}\frac{\partial c}{\partial y}\right)+\frac{\partial}{\partial y}\left(HD_{yx}\frac{\partial c}{\partial x}+HD_{yy}\frac{\partial c}{\partial y}\right)+S_c \quad [4]$$

where, c is the concentration of the trace metal in the sea water, D_{xx}, D_{xy}, D_{yx} and D_{yy} are the four components of tensor of comprehensive diffusion coefficient in horizontal plane. S_c is the source and sink term of the contaminant. Without the numerical dispersion in FDM, the particle-tracking model is able to simulate the cases with large gradient of concentration such as contaminant discharged from outfalls, which often has a large gradient near the outfalls and may not be well simulated by FDM using the convection-diffusion equations for the reason of numerical dispersion. Additionally, particle-tracking method does not require a mesh covering the whole computational domain and can show the pathway of the mass transport directly.

The hydrodynamic model and particle-tracking model were run simultaneously. The water levels and velocities which are the outputs of the hydrodynamic model were transferred to the particle-tracking model immediately after every time step of the hydrodynamic model. Hereafter, the position of every particle was calculated using the particle-tracking method.

4 RESULTS

1) Distribution of the trace metals

In this paper, we only focus on the distributions and the transport of several kinds of trace metals, including Chromium (Cr), Copper (Cu), Lead (Pb) and Zinc (Zn) (Li and Li, 2008; Peng et al., 2009; Zhang et al., 2011; Zhou et al., 2013), which are more stable and easily measured for reason of the reliability of the data.

Figure 2 shows the distribution of trace metals in the Bohai Bay. We observed that the four kinds of trace metals have similar distributions in the Bohai Bay. This founding indicates that the four kinds of trace metal may have common originations, as it has been confirmed by other researchers (Lei et al., 2011; Zhang et al., 2011). For the four kinds of trace metals, three regions with higher concentrations of them in the sediments can be found in the northwest, center and mouth of the bay. This means the trace metals entering the bay can get there and accumulate in the sediments at these regions. For the reason that the mouth of the bay may be affected by the contaminates from Liaodong Bay (Xing et al., 2013) and we have not collected enough data there, we shall not put much emphasis on the region with higher concentrations of trace metals on the north part of the bay mouth.

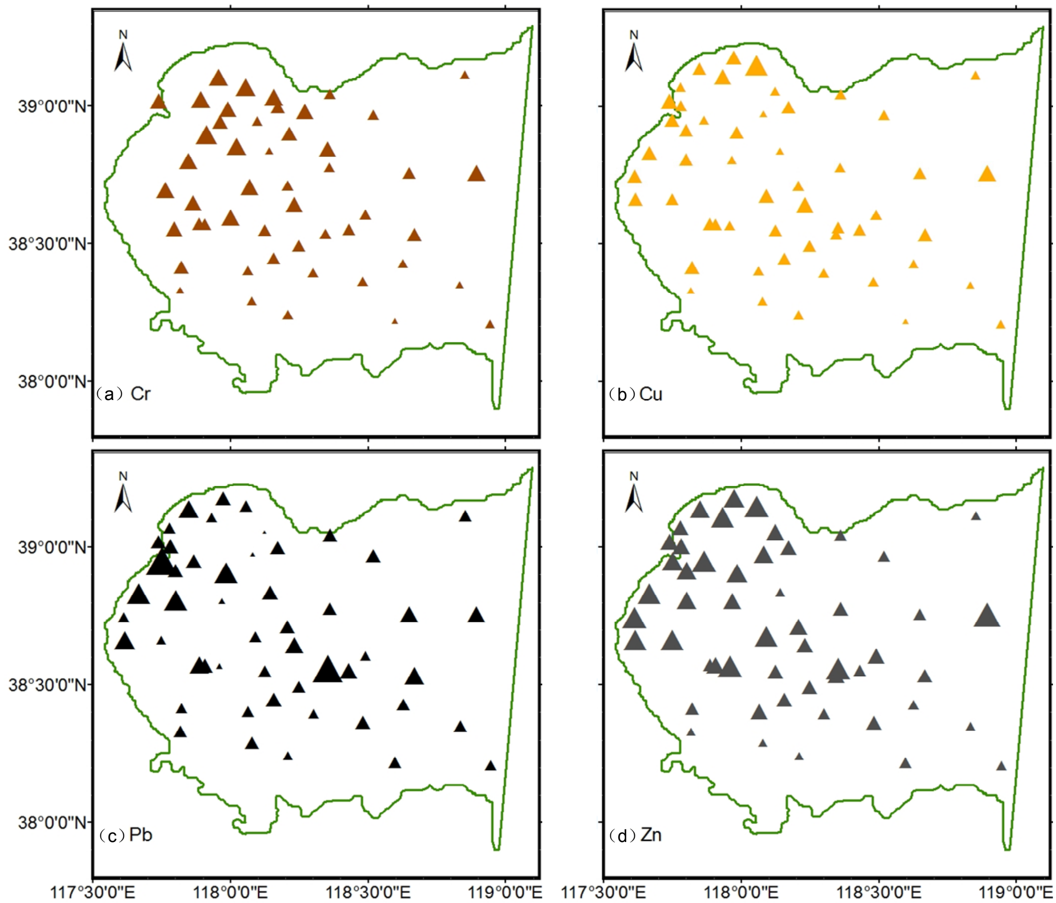

Figure 2. Trace metal distributions in the Bohai Bay. (The size of triangles indicates the value of concentration. The triangle's size should not be compared between figures) (Li and Li, 2008; Peng et al., 2009; Zhang et al., 2011; Zhou et al., 2013)

2) Residual circulation

Tidal force is the dominant force driving the movement of the water and the transport of the contaminant in the Bohai Bay. Tide is the oscillation of water level accompanied by the water flowing back and forth, with which the contaminant and the sediments on the sea bed also oscillate. However, in terms of long run, their transports are determined by the residual circulation of the tide.

In recent decades, especially in the last ten years, large scale land reclamations have been carried out in this region along with the economy development around the Bohai Bay. Those projects have significantly changed the shoreline around the Bohai Bay. In order to confirm the effect of the changed shoreline on the tide and residual current, the topography and shoreline in the years 2003 and 2010 were used respectively to examine the potential differences in the residual current in the Bohai Bay caused by the land reclamation. Figure 3 presents the residual current in these two years, respectively, and shows no significant change in residual currents in the offshore region of the bay. Most of the changes of the flow concentrate near the regions around the reclamation. In this sense, we can conclude that the residual flow pattern in the Bohai Bay did not change significantly during the past decades. Therefore, the distributions of trace metals in the Bohai Bay sediments are the consequence of the long-term ocean water circulation.

It is seen that the water from the Liaodong Bay and the central part of the Bohai Sea flows into the Bohai Bay near the north bank of the Bohai Bay. However, this current cannot go far enough once it enters the Bohai Bay and part of it turns south, and flows out of the bay near the center of it. On the mouth of the bay, this flow pattern forms a vortex, on the center of which the speed of the residual is slow. Another relative larger vortex can be found due south off Caofeidian. This is a counterclockwise vortex, reaching Tanggu on the west bank of the bay. With its large range, water in this vortex can flow into the bay along the north bank and reaches the region near Tanggu and west bank of the bay. Then, it flows along the south bank to the east direction and turns to northeast converging to a current coming from the Yellow River estuary. After that, the current directs to the northeast and comes out of the Bohai Bay near the center of the bay with the current from the north of the Bohai Bay. East off the Tanggu, the other branch of current from the Caofeidian turns to north and enter the small bay on the north of Tanggu. This current travels along the shoreline and gets to the west on the Caofeidian, where it converges to the flow from the east and forms a vortex in the northwest of the Bohai Bay.

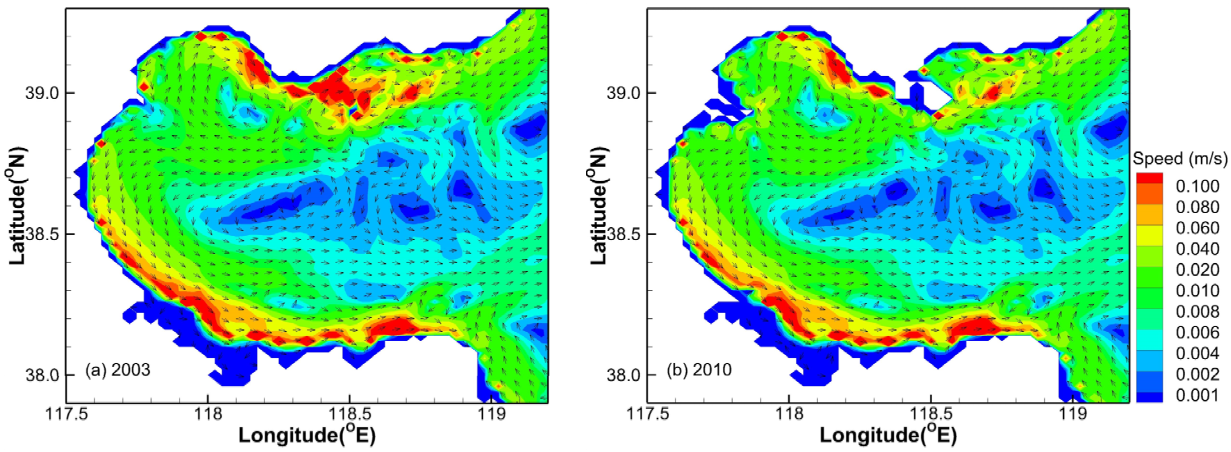

Figure 3. Tidal residual flows.

The circulation pattern presented in Figure 3 was also recognized by other researchers. Zhao et al. (1995) indicated that there are mainly two vortexes in the Bohai Bay with water flowing into the bay along the bank in the north and south and flowing out of the bay in the middle part of the mouth of the bay. The simulation result by Xu et al. (2006) suggested the existence of a vortex in the northwest of the bay and a flow from the Yellow River estuary entering the bay and then directing to the northeast and flowing out of the bay in the middle part of the mouth.

Generally, there are three vortexes in the northwest, the center and the mouth of the Bohai Bay, with weak current found in the center of them. The locations of vortex regions coincide with higher concentrations of trace metals, which may indicate a relation between them.

3) Particle tracking simulation

According to the Annual Report of Oceanic Environment in the Bohai Sea 2008 (SOA, 2009), Yongding River and Jian River located on the northwest of the Bohai Bay, Ziya River on the west and Dakou River on the south discharged water with worse condition. Considering the residual currents calculated previously and the locations of the four river outfalls, we inferred that the two areas with higher concentrations of trace metals are related to the discharge from these rivers. Four cases (Table 1) with the contaminant discharged into the Bohai Bay through the four outlets respectively were calculated using particle-tracking model and the transport of the contaminant from them were studied.

Table 1. Particle-Tracking cases.

Case	Outlet Name	Position Longitude(°E)	Latitude(°N)
1	Jian River	118.060	39.215
2	Yongding River	117.810	39.070
3	Dakou River	117.860	38.271
4	Ziya River	117.593	38.667

With the outfalls located in the northwest of Bohai Bay, Case 1 and Case 2 have similar pattern of contaminant transport. For Case 1, in which contaminant is discharged from Yongding River, a biggest outfall of Tianjin and Beijing, the flows and flume of contaminant turn left after discharged and flow northward along the shoreline and into the small bay in the northwest of the Bohai Bay, where concentration of trace metals is higher. After reaching the most north, the flow and contaminant continue flowing southward along the shoreline and get to the west off Caofeidian in Tangshan. Then, some of them go into the center of the Bohai Bay which is in the southeast off Caofidian, while others stay near Caofeidian. The rest of the particles converge into the flow from east and go back to the east of Tanggu, where the flow of particles goes separately, with one branch flowing north and forming a vortex in the northwest of Bohai Bay, and the other branch flowing south along the west bank of the Bohai Bay. The particles which are falling into the vortexes spend a relatively long time in them before escaping. Therefore, near the centers of the vortexes, the regions with high density of particles, which means high concentration of contaminant, can be found. The particles escaping from the vortex in northwest of the bay may converge to the flow from the east and continuing to travel southward along the west bank to the south of the Bohai Bay. However, the density of the particles (concentration of contaminant) in this branch is much smaller than that which stay in the vortex in northwest.

As the condition in the northwest of the Bohai Bay, particles entering the center of the Bohai Bay southeast off Caofeidian, also spend a long time in it. However, in this area, the fact does not only due to the vortex but also because of the low speed residual current which is shown in Figure 3. The low speed of residual current may indicate a weak transport condition, due to which more and more contaminant comes into the area but few of them can escape and a high concentration emerges there. The particles accumulating there produce another region with more particles. In the control of tidal force, some particles there continue to flow to southeast direction and turn to northeast off the north of the Yellow River estuary.

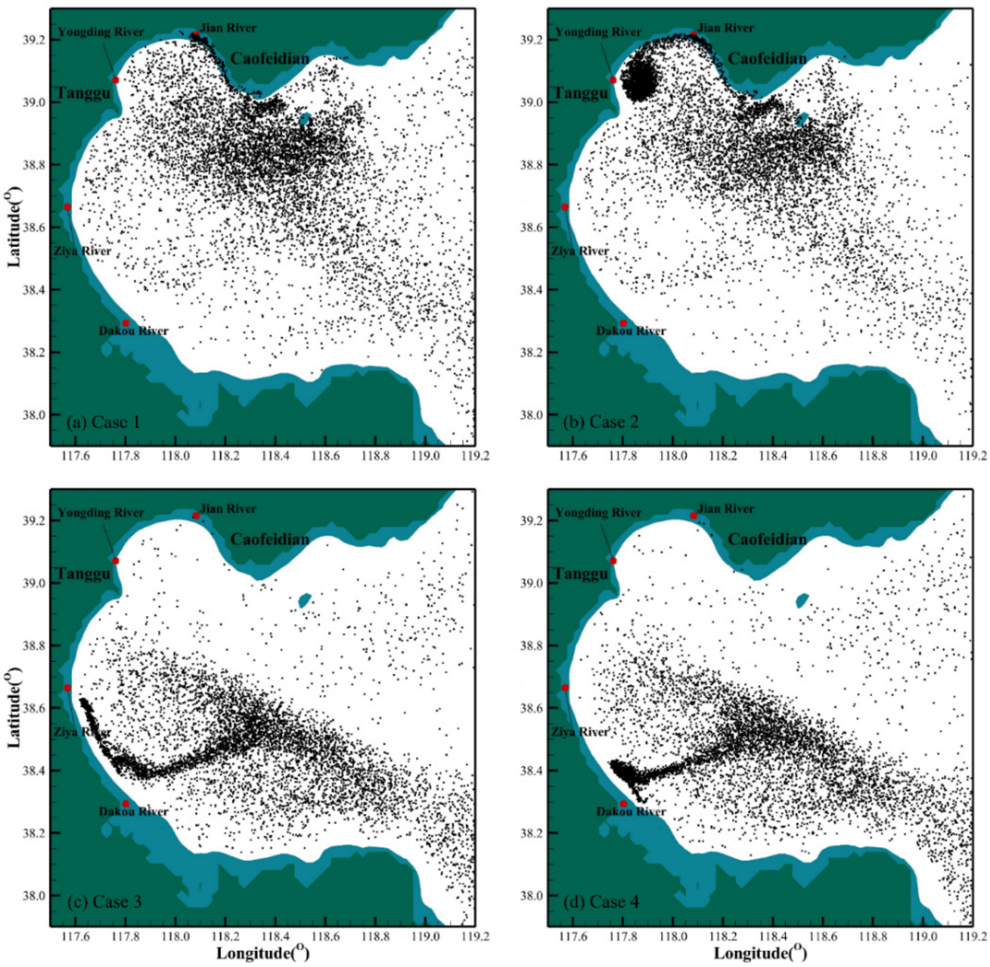

Figure 4. Distribution of particles after 2 years.

Case 3 and Case 4 have similar flow patterns. Particles discharged from Ziya River flow to the south with the current from the north along the west bank of the Bohai Bay. When the particles get to the place not far away from the outlet of Dakou River, most of them turn left and go up to the center of the Bohai Bay with a flow which is a part of the vortex in the center of the Bohai Bay. In the vortex, a lot of particles are trapped and hover there. In this region, the particles may go to two different directions separately. One branch goes to west and get to the west bank of the bay and then they converge with the flow from the north and form a vortex in the west of the bay. The other branch goes to southeast and get to the north off Yellow River estuary. Then, some of the particles turn right and go along the south bank and back to Dakou River estuary, forming a circulation in the south of the Bay. The other particles may continue flowing southward and get to the region east off the Yellow River estuary.

  / ISSN 1562-6865 (Online) - ISSN 1063-7710 (Print)

Generally, the results of the four cases using the particle-tracking method agree with the pattern of residual current and they confirm that the contaminants entering from the wastewater outfalls can get to the regions with higher concentrations of trace metals in the sediments. The particles that spend longer time in the northwest and the center of the Bohai Bay may further indicate the idea that the high concentrations of trace metals in the two regions are related to the four wastewater outfalls mentioned above and the emerging vortexes.

4) Distribution of ^{210}Pb and ^{7}Be in core samples

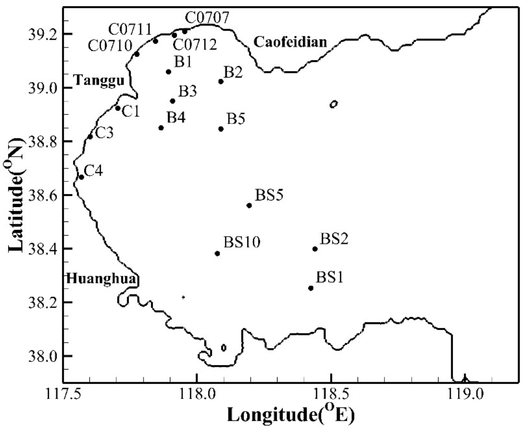

Figure 5. Stations of sediment cores sampling.(B1-B5 reference to Feng et al. (2010), BS1, BS2, BS5 and BS10 reference to Hu et al. (2011), C1, C3 and C4 reference Qin et al. (2006) and C0707, C0710, C0711, C0712 references to Wang et al. (2014)).

Since the trace metals usually bound to the sediment particles and deposit on the sea bed, the concentrations of trace metals in the sediments are related to the sedimentation process. Natural radionuclides such as the ^{238}U decay series radionuclide ^{210}Pb, have been used to estimate sedimentation conditions (Du et al., 1990; Hirschberg et al., 1996; Feng et al., 1998; Sommerfield et al., 1999; Woodruff et al., 2001; Su and Huh, 2002; Mabit et al., 2008; Feng et al., 2010). With a half-life time of 22.3 years, ^{210}Pb is a useful tracer for century-long sedimentation. The means to estimate the sedimentation rate can be found in Feng et al. (2010). In this section, the hydrodynamic condition represented by the vertical profile of the radionuclide will be discussed and the correlation among the profile, hydrodynamic condition and the concentration of trace metals in the sediments will also be studied.

The locations of sediment cores and vertical distributions of radionuclides from published archives (Qin et al., 2006; Feng et al., 2010; Hu et al., 2011; Wang et al., 2014) are summarized in Figure 5 and Figure 6.

Figure 6 shows the distributions of ^{210}Pb in the sediment cores sampled from the sites indicated in Figure 5. Among them, Figure 6 (a)-(i) present those of sediment cores sampled in the sea and Figure 6 (j)-(p) present those in the intertidal zones. Generally, in the sediment cores sampled in the sea, the activity of ^{210}Pb ranges from 0 to 60 except Station BS8. With steady sedimentation, ^{210}Pb shall have an exponential decaying profiles in the sediment cores. As shown in Figure 6, decaying ^{210}Pb profiles can be found in different levels of sedimentation at Stations B1, B2, B4, B5, C0710, C0711 and C0712 in the northwest of the Bohai Bay and Stations C4 and BS5 in the northwest and center of the Bohai Bay in the past decades with some disturbance, occasionally. Actually, when comparing the trace metal distributions shown in Figure 2, it can also be found that these stations were located at the northwest and center of the Bohai Bay, where the relative high trace metal concentrations in the sediment, and the vortexes and low speed residual currents can be found. In the northwest of the Bohai Bay, the upper 5cm of sediment core in Station B3 and upper 15cm of that in Station B5 also show steady-state sedimentation. These two stations are located near the navigation channel to the Port of Tianjin where there was many nautical constructions and anthropogenic activities that obviously disturbed the sedimentation considering no excess ^{210}Pb activities in the deep sediment cores. Stations C0707, C0710, C0711 and C0712 are located in the intertidal zone in the northwest of the Bohai Bay. Excess ^{210}Pb activities were found at varying depths at these stations except Station C0707. Like the situations of the stations in northwest of the Bohai Bay, these ^{210}Pb profiles suggest a decades-long steady-state sedimentation.

Sediment cores in Stations C1 and C3 did not show excess ^{210}Pb (Figure 6), indicating that there is no net sedimentation in these areas. Considering the locations of the two stations on the south of the Tanggu, this may be related to the activity of engineering and strong hydrodynamic condition in the intertidal zone. However, Station C4 is located further south among the three stations and shows, excess ^{210}Pb activities, indicating a certain degree of sediment accumulation.

In the center of the Bohai Bay, the sediment core at Station BS5 shows a relatively stable decay of activity of ^{210}Pb (Figure 6). Comparing with other three stations (BS1, BS2, and BS10) in this region and considering the slow speed of residual flow near Station BS5, it indicates a weak hydrodynamic condition near the Stations BS5 where there is a region with higher concentrations of trace metals in the sediments. Station BS1 and BS2 are not far from Yellow River estuary. Historically, the change of the Yellow River estuary has affected the sedimentation in the area, which is also reflected by ^{210}Pb activity.

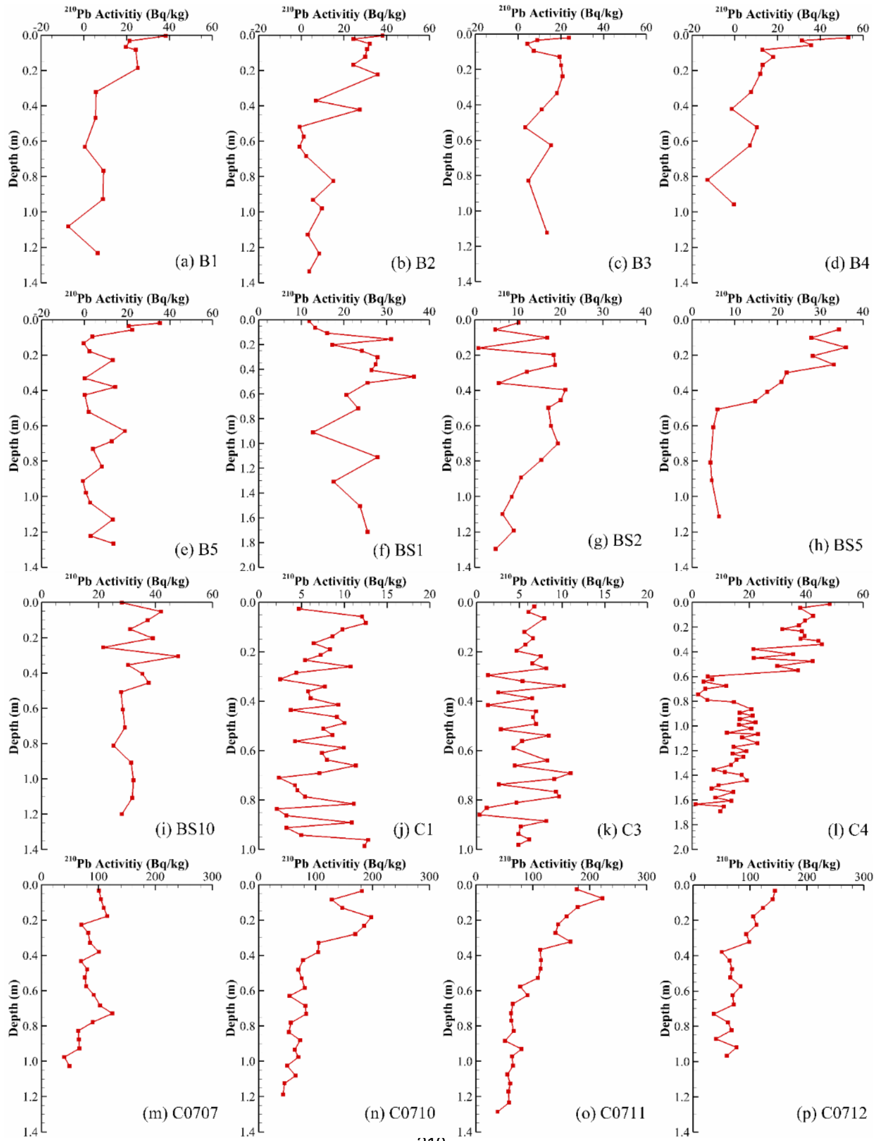

Figure 6. The distribution of ^{210}Pb in the sediment cores.

5 DISCUSSIONS AND CONCLUSIONS

The analysis on the distribution of trace metals shows that there are three regions with higher concentrations of trace metals in the Bohai Bay which are located in the northwest, center and mouth of the bay. It is interesting that the residual flow pattern and the result of the particle-tracking model show that, there is a vertex in the three regions, respectively. The contaminant entering the bay through the outlets of the polluted rivers can get to the northwest and center of the bay with the long-term transport and stays there for a long time due to the circulated flows and weak hydrodynamic conditions in these regions. This phenomenon indicates that the higher concentrations of trace metals in the sediments may have some relations to the vertexes in these regions.

Through the contaminant can get to the two of the regions, the concentrations of trace metals are also related to the sedimentation conditions in these regions. Fortunately, the radionuclide in the sediment cores can help us with the aspect. The distributions of ^{210}Pb in sedimentation cores show that the regions with higher concentrations of trace metals and near the vertexes of residual currents have the exponential decay of activity of excess ^{210}Pb, indicating the relatively steady sedimentation in these regions. However, in other regions, such as near the south bank of the bay, in which the trace metal concertation is lower and the contaminant did not stay for long, there is no sediment core with stable exponential decay of activity of excess ^{210}Pb being found. This means that the regions with higher concentrations of trace metals in the sediments

  / ISSN 1562-6865 (Online) - ISSN 1063-7710 (Print)

may have relatively weaker hydrodynamic conditions for their locations near the center of the vertexes in the Bohai Bay.

Moreover, Figure 7 shows the distribution of averaged current speed in the Bohai Bay. It can be found that the higher concentrations of trace metals are not located in the area with the strongest hydrodynamic condition. As the averaged current speed in the region off the south of the Caofeidian is relatively stronger, even though the contaminant from the northwest of the Bohai Bay can be accumulated there, the concentrations of heavy metals in this region are not very high.

The aforementioned analysis shows that the locations of regions with higher concentrations of trace metals in the sediments, the sediment cores with stable exponential decay of activity of excess ^{210}Pb and the residual current vertexes are closely correlated. It means that each of them is not independent and occasional. Since the concentrations of trace metals in the sediments are determined by the transport and sedimentation of them, the distribution of the trace metals in the sediment found in this paper should be the result of the water circulation calculated by the numerical models. On the other hand, with the distribution of trace metals in the sediments recording the information of the water circulation in the bay, the distribution pattern of trace metals in the sediments and the activities of ^{210}Pb in the sediment cores indicate that they can be well accounted by the water circulations calculated by the hydrodynamic model and particle-tracking model. Considering the facts mentioned above, we shall have enough confidence in the flow pattern calculated by the numerical models and it also indicates that the numerical models which we have developed can be well applied to the shallow sea like the Bohai Bay.

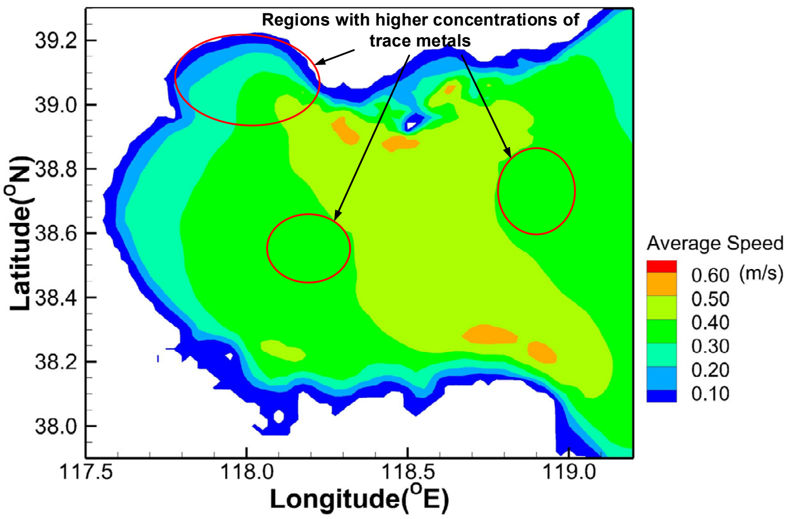

Figure 7. Averaged current speed in the Bohai Bay.

ACKNOWLEDGEMENTS

This study was supported in part by the Program of New Century Excellent Talents in University by the State Education Ministry of China (NCET-12-0406) (DY) and China Scholarship Council (YL).

REFERENCES

Bazzi, A. (2014). Heavy Metals in Seawater, Sediments and Marine Organisms in the Gulf of Chabahar, Oman Sea. *Journal of Oceanography and Marine Science,* 5(3), 20-29.

Du, R., Liu, G., Yang, S., Zhou, Y. & Zhang, B. (1990). Modern Sedimentation Rate and Sedimentation Process in Bohai Bay. *Marine Geology & Quaternary Geology,* 10(3), 15-22.

Feng, H., Cochran, J.K., Hirschberg, D.J. & Wilson, R.E. (1998). Small-Scale Spatial Variations of Natural Radionuclide and Trace Metal Distributions in Sediments from the Hudson River Estuary. *Estuaries,* 21(2), 263-280.

Feng, H., Jiang, H., Gao, W., Weinstein, M.P., Zhang, Q., Zhang, W., Yu, L., Yuan, D. & Tao, J. (2011). Metal Contamination in Sediments of the Western Bohai Bay and Adjacent Estuaries, China. *Journal of Environmental Management,* 92(4), 1185-97.

Feng, H., Zhang, W., Jia, L., Weinstein, M.P., Zhang, Q., Yuan, D., Tao, J. & Yu, L. (2010). Short- and Long-Term Sediment Transport in Western Bohai Bay and Coastal Areas. *Chinese Journal of Oceanology and Limnology,* 28(3), 583-592.

Gao, B., Lu, J., Hao, H., Yin, S., Yu, X., Wang, Q. & Sun, K. (2014). Heavy Metals Pollution and Pb Isotopic Signatures in Surface Sediments Collected from Bohai Bay, North China. *Scientific World Journal,* 2014, 6.

Gonzalez-Macias, C., Schifter, I., Lluch-Cota, D.B., Mendez-Rodriguez, L. & Hernandez-Vazquez, S. (2006). Distribution, Enrichment and Accumulation of Heavy Metals in Coastal Sediments of Salina Cruz Bay, Mexico. *Environmental Monitoring and Assessment,* 118(1-3), 211-30.

Hirschberg, D., Chin, P., Feng, H. & Cochran, J. (1996). Dynamics of Sediment and Contaminant Transport in the Hudson River Estuary: Evidence from Sediment Distributions of Naturally Occurring Radionuclides. *Estuaries,* 19(4), 931-949.

Hu, B., Li, G., Li, J., Yang, M., Wang, L.B. & Bu, R.Y.(2011). Spatial Variability of the (210)Pb Sedimentation Rates in the Bohai and Huanghai Seas and Its Influencing Factors. *Acta Oceanologica Sinica,* 33(6), 125-133.

Lei, Z., Qin, Y., Zheng, B., Jia, J. & Lei, K. (2011). Distribution and Pollution Assessment of Heavy Metals in Sediments from Typical Areas in the Bohai Sea. *Huanjing Kexue Xuebao,* 31(8), 1676-1684.

Li, R.W. & Li, Y. (2008). Environmental and Sedimentological Survey Along the Coast of Bohai Gulf. *Acta Sedimentologica Sinica,* 26(1), 128.

Li, X., Yuan, D. & Tao, J. (2011). *Study on Application of Random Walk Method to Calculate Water Exchange in Large-Scale Bay.* Applied Mathematics and Mechanics, 32, 621-634.

Li, Y., Guo, L. & Feng, H. (2015). *Status and Trends of Sediment Metal Pollution in Bohai Sea, China,* Current Pollution Reports, 1-12.

Li, Y., Yuan, D., Lin, B. & Teo, F.-Y. (2016). A Fully Coupled Depth-Integrated Model for Surface Water and Groundwater Flows. *Journal of Hydrology,* 542, 172-184.

Luo, W., Lu, Y., Wang, T., Hu, W., Jiao, W., Naile, J.E., Khim, J.S. & Giesy, J.P. (2010). Ecological Risk Assessment of Arsenic and Metals in Sediments of Coastal Areas of Northern Bohai and Yellow Seas, China. *Ambio,* 39(5-6), 367-375.

Mabit, L., Benmansour, M. & Walling, D., (2008). Comparative Advantages and Limitations of the Fallout Radionuclides 137 Cs, 210 Pb Ex and 7 Be for Assessing Soil Erosion and Sedimentation. *Journal of Environmental Radioactivity,* 99(12), 1799-1807.

Pempkowiak, J., Chiffoleau, J.F. & Staniszewski, A. (2000). The Vertical and Horizontal Distribution of Selected Trace Metals in the Baltic Sea Off Poland. *Estuarine, Coastal and Shelf Science,* 51(1), 115-125.

Peng, S.T., Yan-Di, H.U. & Bai, Z.P. (2009). Pollution Assessment and Ecological Risk Evalution for Heavy Metals in the Sediments of Bohai Bay. *Journal of Waterway & Harbor,* 30(1), 57-60.

Qin, Y.-w., Meng, W., Zheng, B.-h. & Su, Y.-b., (2006). Heavy Metal Pollution in Tidal Zones of Bohai Bay Using the Dated Sediment Cores. *Journal of Environmental Sciences(China),* 18 (3), 610-615.

Reddy, M.S., Basha, S., Sravan Kumar, V.G., Joshi, H.V. & Ramachandraiah, G. (2004). *Distribution, Enrichment and Accumulation of Heavy Metals in Coastal Sediments of Alang-Sosiya Ship Scrapping Yard, India,* Marine Pollutution Bulletin, 48(11-12), 1055-9.

SOA. (2009). *Annual Report of Oceanic Environment in the Bohai Sea 2008.*

SOA. (2010). *Annual Report of Oceanic Environment in the Bohai Sea 2009.*

Sommerfield, C., Nittrouer, C. & Alexander, C. (1999). 7 Be as a Tracer of Flood Sedimentation on the Northern California Continental Margin. *Continental Shelf Research,* 19(3), 335-361.

Su, C.-C. & Huh, C.-A., (2002). 210 Pb, 137 Cs and 239,240 Pu in East China Sea Sediments: Sources, Pathways and Budgets of Sediments and Radionuclides. *Marine Geology,* 183(1), 163-178.

Sweeney, A. & Sanudo-Wilhelmy, S.A. (2004). *Dissolved Metal Contamination in the East River-Long Island Sound System: Potential Biological Effects,* Marine Pollutution Bulletin, 48(7-8), 663-70.

Wang, F., Wang, H., Zong, Y., Anderson, T.J., Pei, Y.D., Tian, L.Z., Li, J.F. & Shang, Z.W. (2014). Sedimentary Dynamics Along the West Coast of Bohai Bay, China, During the Twentieth Century. *Journal of Coastal Research,* 294, 379-388.

Woodruff, J.D., Geyer, W.R., Sommerfield, C.K. & Driscoll, N.W. (2001). Seasonal Variation of Sediment Deposition in the Hudson River Estuary. *Marine Geology,* 179(1), 105-119.

Xing, F.W., Sun, J., Li, Y.Y., Yuan, D.K. & Tao, J.H. (2013). Numerical Simulation of Water Exchange in Bohai Sea with Age and Half-Life Time. *Proceedings of the 35th Iahr World Congress,* Iii and Iv, 7.

Xu, B., Yang, X., Gu, Z., Zhang, Y., Chen, Y. & Lv, Y. (2009). The Trend and Extent of Heavy Metal Accumulation over Last One Hundred Years in the Liaodong Bay, China. *Chemosphere,* 75(4), 442-6.

Xu, R., Zhao, B., Huang, J., Yang, Y. & Lei, F. (2006). The Mean Residual Circulations in the Bohai Sea. *Marine Sciences,* 30(11), 47-52.

Zhan, S., Peng, S., Liu, C., Chang, Q. & Xu, J. (2010). *Spatial and Temporal Variations of Heavy Metals in Surface Sediments in Bohai Bay, North China,* Bulletin of Environmental Contamination and Toxicology, 84 (4), 482-487.

Zhang, D., Zheng, X., Ying, H.E. & Guo, J. (2011). Pollution and Risk Assessment of Heavy Metals in Surface Sediment of South Bohai. *Environmental Pollution & Control,* 33(9), 8-10.

Zhao, B., Zhuang, G. & Cao, D. (1995). Circulation, Tidal Residual Currents and Their Effects on the Sedimentations in the Bohai Sea. *Oceanologia et Limnologia Sinica,* 26, 466-473.

Zhou, B., Liu, W., Liu, Y.G., Chu, J.Z. & Liu, S.J. (2013). Potential Ecological Risk Analysis of Heavy Metals in Surface Sediments from Typical Ecologically Regions of South Bohai Bay. *Marine Environmental Science,* 32(4), 533-537.

MODELLING TSUNAMI FOR COASTAL RECLAMATION: INFLUENCE OF COASTLINE REFLECTIVITY, COASTAL CHANNEL GEOMETRY AND ONSHORE STORAGE

JANET YI YEE LEE(1), JUAN CARLOS SAVIOLI(2), JACOB HJELMAGER JENSEN(3), CHI WEI CHENG(4) & CLAUS PEDERSEN(5)

(1,2,3,4,5) DHI Water & Environment (M) Sdn. Bhd., Petaling Jaya, Malaysia,
jyy@dhigroup.com; jcs@dhigroup.com; jhj@dhigroup.com; ccw@dhigroup.com; clp@dhigroup.com

ABSTRACT

Designing coastal development such as coastal reclamation in a tsunami prone area necessitates the assessment of potential tsunami impacts, specifically the evaluation of the tsunami-induced water level around the proposed development. The configuration of coastal settings is one of the most important elements in affecting tsunami-induced water level. Three different coastal settings have been identified to be influential: (1) the reflectivity of different types of the coast whether it is a sandy beach to dissipate tsunami wave energy or rocky headlands to reflect tsunami wave, (2) the geometry of a coastal channel in manipulating entrance of tsunami waters into the channel and (3) the capacity onshore along the coastal channel that allows water run-up inland. Thus, this paper discusses the influence of the three coastal settings: Coastline Reflectivity, Coastal Channel Geometry and Onshore Storage, on the assessment of tsunami-induced water level around a synthetic coastal reclamation island in northern Peninsular Malaysia, based on the 26 December 2004 tsunami event and numerical simulations using MIKE 21 HD. These three coastal settings should be well considered and developed in a tsunami model as they ultimately act as constructive inputs to the decision of the final design of a proposed reclamation.

Keywords: Coastal channel geometry; coastline reflectivity; Indian Ocean tsunami; onshore storage; reclamation.

1 INTRODUCTION

Reclamation, one of the developments in the coastal zone, is understood as an activity to create land from the sea or water bodies. The design and optimisation of the layout of the proposed reclamation often involve careful assessment in coastal hydraulics supported by meteorological analysis. The aspects to be considered include but not limited to tides, waves, winds, surges and sea level rise especially for extreme events to achieve a sustainable long-term usage of the reclaimed area. For a coastal reclamation located in a tsunami prone area, the evaluation of tsunami-induced water level is inevitable for protection against tsunami strike.

The coastal settings of the proposed reclamation and the existing shoreline in the vicinity of the development could play a significant role in affecting the build-up of the tsunami-induced water level around the proposed reclamation. Coastal settings may refer to sandy beaches, rocky headlands, tidal mudflats, mangrove areas, low-lying coastal floodplain, and artificial structures such as breakwaters, sheet piles, bunds, revetments or seawalls, etc. natural setup in the coastal environment.

This paper discusses the influence of manipulating the following three coastal settings in a tsunami model on the assessment of maximum tsunami-induced water levels in the vicinity of a synthetic reclamation, using numerical model MIKE 21 HD.

- Coastline Reflectivity: the reflectivity of different types of coast whether it is a beach-like coast (dissipating tsunami wave energy) or headlands (reflecting tsunami wave);
- Coastal Channel Geometry: the dimension and alignment of channel, the materials used for reclamation and the seabed materials manipulating entrance of tsunami waters into the channel;
- Onshore Storage: capacity on the land along the coastal channel to allow water run-up inland from the coastal channel.

1.1 Tsunami

A tsunami is a series of water waves generated by a geophysical event such as an earthquake that releases a large amount of energy rapidly into a water body. Tsunami waves travel over a long distance across the open oceans with little loss of energy towards the shore, where they shoal as they reach shallow water (Luger and Harris, 2010). The 26 December 2004 tsunami in the Indian Ocean, being the second largest global tsunami, is by far the most destructive tsunami ever in history and one of the worst natural catastrophes in human history (Nirupama et al., 2007). The tsunami struck after the 9.1-magnitude Sumatra-Andaman earthquake occurred off the north-west coast of Sumatra, Indonesia. The abrupt uplift of sea floor near the hypocentre resulted in the displacement of water above the sea floor, which subsequently triggered the Tsunami. This event has been selected as a basis for the present study.

1.2 Study area and synthetic reclamation

Penang, one of the Malaysian states hit by the December 2004 Tsunami, was selected as the study area. Two local areas in Penang Island were further selected in the present study (refer Figure 1):

- Area 1: Northeast of Penang Island facing Penang mainland;
- Area 2: West of Penang Island with a synthetic reclamation island.

Area 1 was selected for the case of Coastline Reflectivity, where the coastline of Penang mainland facing the northeastern coastline of the Penang Island provides a good platform to study the wave reflections off the coast and the subsequent wave superposition in the waters between northeastern Penang Island and its mainland. For this study, no synthetic reclamation is included in the model, however, the reflectivity of the Penang mainland should be considered, should a future reclamation were to take place in this area.

Area 2 was selected for the case of Coastal Channel Geometry and Onshore Storage. The modelling has included a synthetic reclamation island situated west of the Penang Island and a coastal channel (refer Figure 1). The west coast of Penang Island was chosen because this stretch of coastline directly faces the Tsunami wave propagation direction.

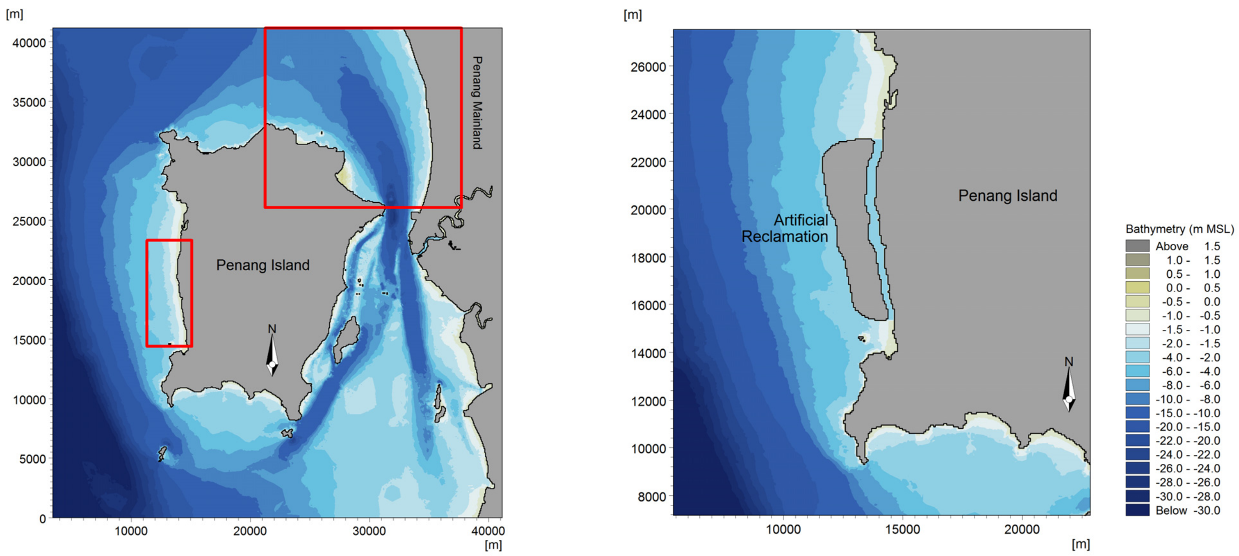

Figure 1. (Left) Penang Island and its mainland. Area 1 and 2 are highlighted in red. (Right) An artificial reclamation was created west of Penang Island.

1.3 Tsunami model

Tsunami modelling was carried out using DHI's existing tsunami model for the Indian Ocean. This model is based on two-dimensional MIKE 21 HD module and has been calibrated and validated by Pedersen et al. (2005). The December 2004 event, which is responsible for the onset of the Tsunami wave train to the study area, was inputted to the model as a 2D initial surface elevation map along the Andaman-Sumatra fault (see Figure 2). The initial surface elevation was generated by MIKE 21 Bathymetry Adjustment Tool, which applies the earthquake parameters.

The MIKE 21 HD module was applied for the following main justifications:

- To accurately initiate the Tsunami by imposing the sudden earthquake-induced elevated waters above the fault, through the application of an initial surface elevation map;
- To simulate the ocean response to the earthquake-induced surface elevations, to propagate the disturbance of the Tsunami waves from the fault to a coastal reclamation off Penang Island;
- To predict maximum water levels associated to the Tsunami in the local area of interest.

The present model uses an existing and calibrated bathymetry, covering Indian Ocean, South China Sea, Sulu Sea, Celebes Sea, Molucca Sea, Banda Sea, Flores Sea, Java Sea, part of the Philippine Sea and the East China Sea. The model is further refined in the waters of the Malacca Straits and near Penang Island using nested mode in order to accurately resolve the transformation of the Tsunami waves towards the area of interest. The seabed is resolved by nesting five bathymetries at increasing resolution: 5556, 1852, 617, 206 and finally 69 m where the study area is located.

The model has assumed a constant boundary level in Mean High Water Spring (MHWS) tidal condition (0.98 m MSL), based on the tidal conditions at Kedah Pier station (National Hydrographic Centre, 2016). It is noted that the tidal levels are important for the assessment of water levels, as the water depth on which the tsunami propagates constitute an important factor for the transformation of the Tsunami waves (i.e. the

 ©2017, IAHR. Used with permission / ISSN 1562-6865 (Online) - ISSN 1063-7710 (Print)

propagation speed, its attenuation and shoaling). The predicted tsunami-induced (or excess) water level from the modelling results, refers to the total water level as the tidal level used in the model.

In order to capture the passage of the Tsunami in the southern Penang waters, the Tsunami simulation covered a period of 6 hours and 40 minutes following the earthquake event of 26 December 2004.

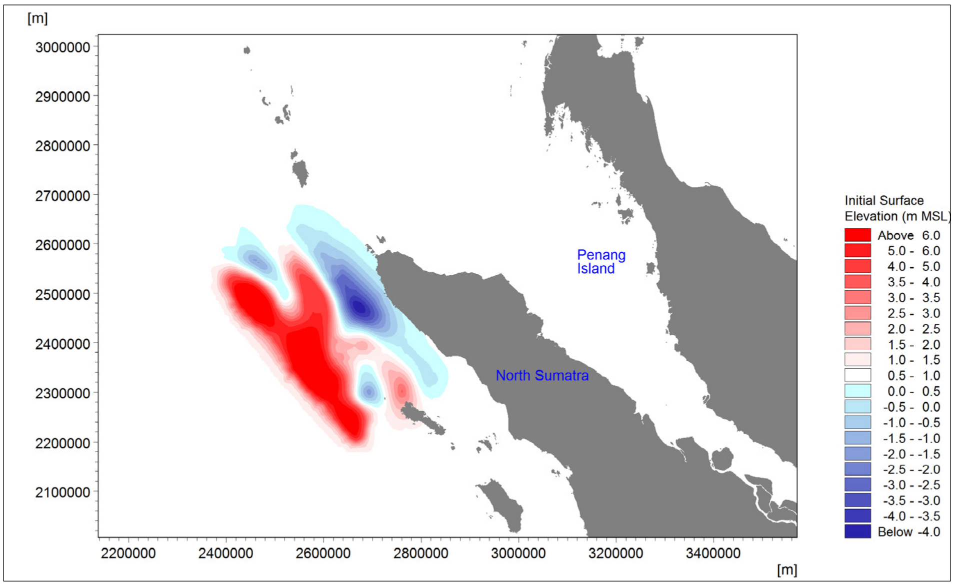

Figure 2. The 26 December 2004 tsunami event was applied in the tsunami model as an initial surface elevation map.

2 COASTAL SETTINGS IN MODELLING TSUNAMI

2.1 Coastline reflectivity

When the tsunami waves are approaching or reaching the coastline, a certain portion of the waves will be reflected off the land and propagating towards the sea. The intensity of the reflection could depend on the materials of the land boundaries in real life. MIKE 21 HD is able to reproduce the tsunami wave's reflection off its internal boundaries, i.e. land boundaries. Two types of land boundaries were set up in the model to evaluate the reflection pattern. Each type is specially designed to be distinct from the other.

- Fully reflective coastline. A stretch of coastline covered with extensive revetments or seawalls, which was inputted to the model as Manning coefficient, M=64 $m^{1/3}$/s, a relatively high number for minor energy dissipation. The land boundary will act as a vertical wall in the model;
- Alluvial coastline. A stretch of coastline comprises flat or gently sloping mud and sandy foreshores with a flat hinterland. This type of coastline tends to dissipate wave energy and thus limit wave reflections. In the model, it was inputted as a low Manning coefficient, M=5 $m^{1/3}$/s.

The coastline of the Penang mainland which is facing the Penang Island was selected for synthetic tests as this area is highly likely to reflect (if any) tsunami waves to the Penang Island (see Figure 3). The tests would determine the Tsunami wave transformation in distributing its wave energy in the waters between Penang Island and its mainland, i.e. superposition of the reflected first wave with the incoming second wave.

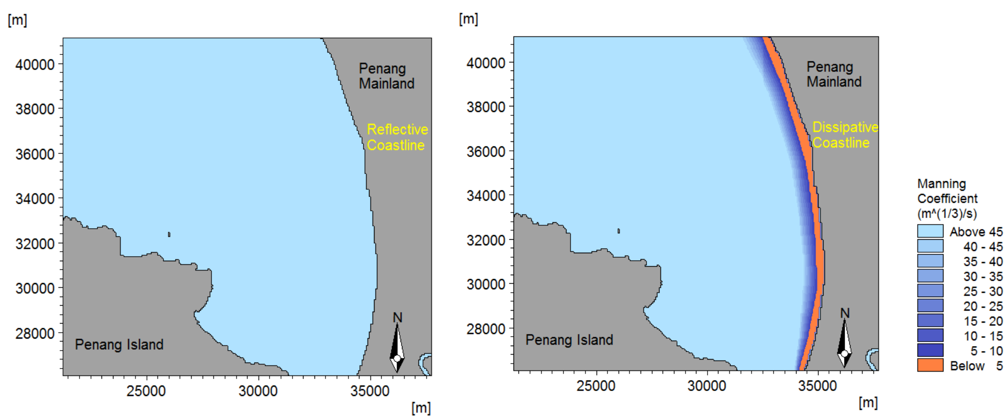

Figure 3. A typical Manning map to reproduce a reflective (left) and dissipative (right) Penang mainland's coastlines in the model.

2.2 Coastal channel geometry

Coastal channel between the existing land and the proposed reclamation is an element to be considered in designing the reclamation. The geometrical design of the channel, as well as the reclamation material and the seabed condition, may affect the water build-up within the channel. These elements can be represented as roughness or Manning coefficient, *M* map in the model (Gayer et al., 2008).

Generally, a lower Manning coefficient represents a restricted channel (which means the amount of water exchange is limited), revetment surface or a rougher seabed. In contrast, a higher Manning coefficient corresponds to a less restricted channel (with better water exchange) or a smoother seabed.

A total of three modelling cases were set up using different Manning maps: *M*=5, 32 and 64 $m^{1/3}/s$ in each of the tsunami models (see Table 1). An artificial reclamation was created west of the Penang Island for the modelling purposes (refer Figure 1). The alongshore length of the reclamation is approximately 7.5 km, with an average channel width of 400 m.

Table 1. Sensitivity tests using various Manning coefficient, *M* for the coastal channel.

No.	Local Project Area	Manning Coefficient, *M* ($m^{1/3}/s$)
1	Coastal channel between western Penang Island's coastline and that of the reclamation.	5 or 32 or 64
2	Areas other than the channel to represent a typical seabed condition.	64

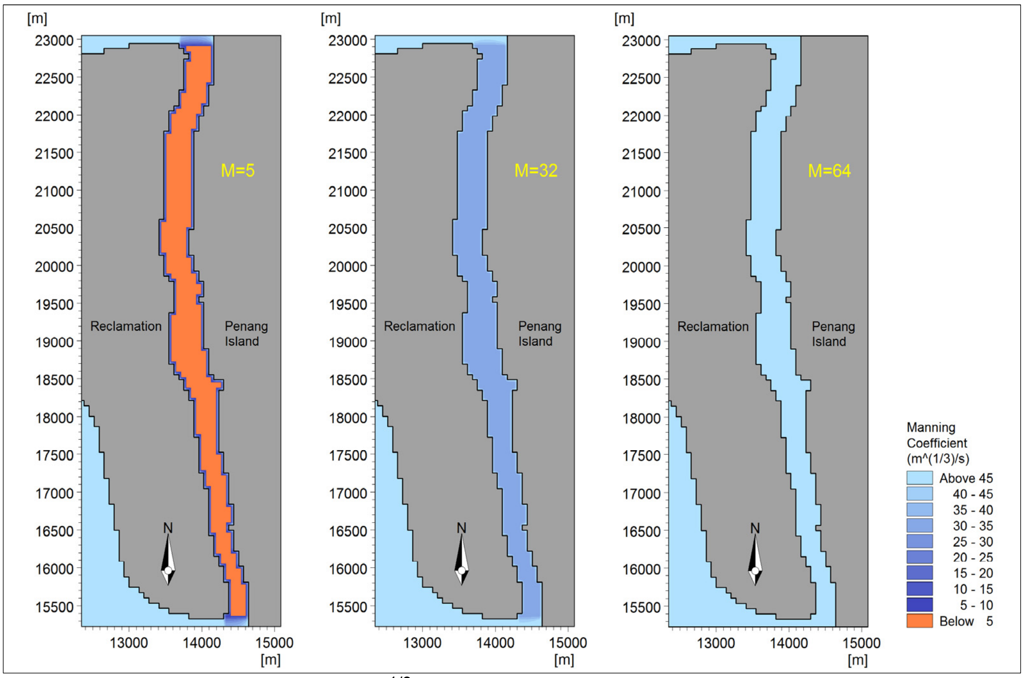

Figure 4. Modelling cases of *M*=5, 32 and 64 $m^{1/3}/s$ applied in the coastal channel to study the influence of channel geometry on the water build-up within the channel during the Tsunami impact.

2.3 Onshore storage

Tsunami-induced waters can surpass the coastline, propagate into the low-lying areas, and inundate significant onshore areas, depending on the magnitude of the tsunami and the local bathymetry and topography. A low-lying topography in the hinterland is susceptible to tsunami-induced inundation if it were to be situated immediately next to a proposed coastal channel between reclamation and existing land.

Two simulations were set up, to take into account the effect of including certain low-lying areas onshore in the tsunami model using the same artificial reclamation in Figure 1. The bathymetry was extended inland approximately 400 m from the shoreline with an alongshore distance of about 1.4 km (see Figure 5). This is to provide a capacity/storage onshore so that when water is reaching a certain land level, water run-up is allowed in the onshore areas, to mimic the inundation of hinterland by the tsunami. This is also important for a realistic assessment of design water level in the channel along the reclaimed islands.

The modelled reflective Penang mainland is observed to reflect a significant part of the incoming first wave energy back to the sea. Figure 6 shows the superposition of the first waves (reflected and incoming waves) and the superposition of the reflected first wave with the incoming second wave.

The wave transformation phenomena participating in the distribution of the Tsunami wave energy in the waters begin with the decomposition of the main Tsunami wave train into sub-wave trains. The first wave breaks into multiple smaller waves as it enters the waters behind Penang Island. As the first wave reflected off

  / ISSN 1562-6865 (Online) - ISSN 1063-7710 (Print)

Penang mainland’s coastline, it encounters the arrival of the second Tsunami wave train, hence superposition of both the waves occurs.

Conversely, the alluvial coastline is observed to be dissipating the Tsunami wave energy, thus limiting wave reflections off the shoreline (see Figure 7). The reflection patterns from both distinct settings in the Penang mainland’s coastline show that the evaluation of the tsunami-induced water levels is dependent on the actual coastline configuration and its corresponding setup in the tsunami model.

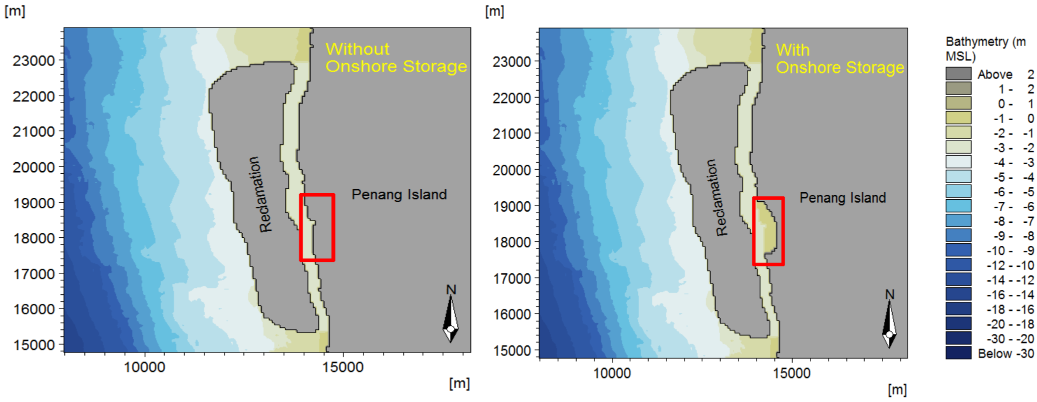

Figure 5. Without onshore storage (left) and with onshore storage (right) incorporated in the tsunami model.

3 RESULTS AND DISCUSSIONS

3.1 Coastline reflectivity

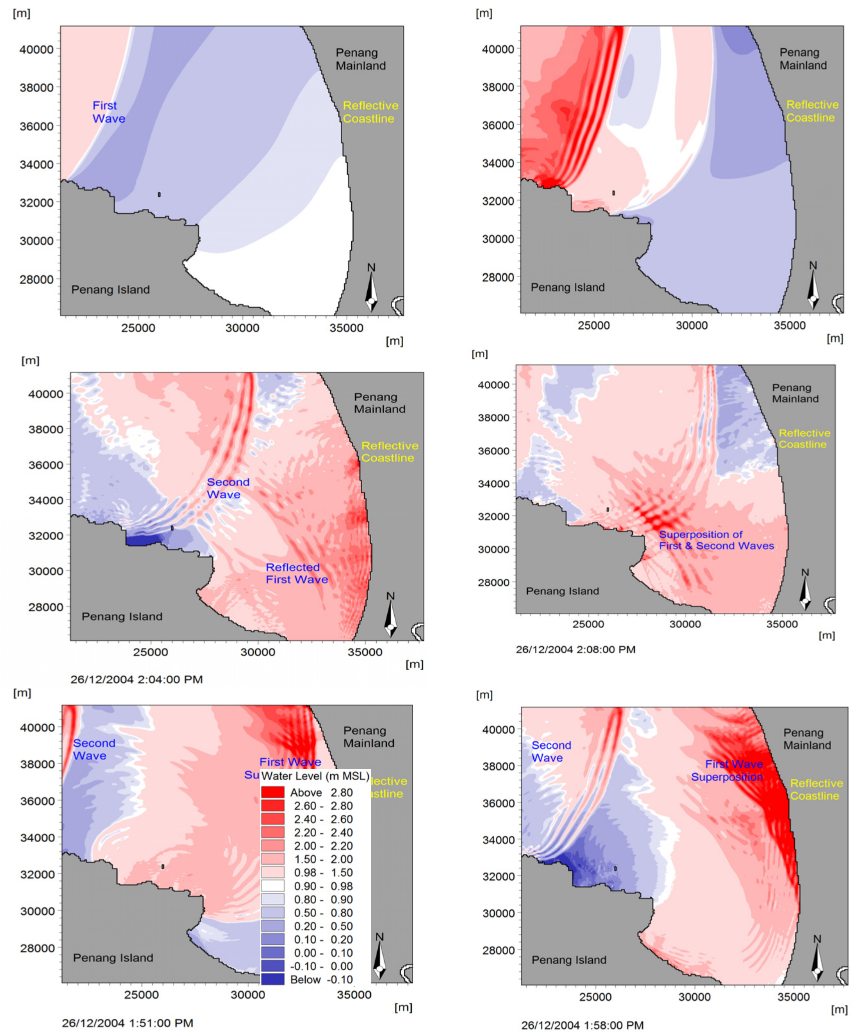

Figure 6. Snapshots of the Tsunami waves displaying wave reflections off Penang mainland which subsequently form wave superposition

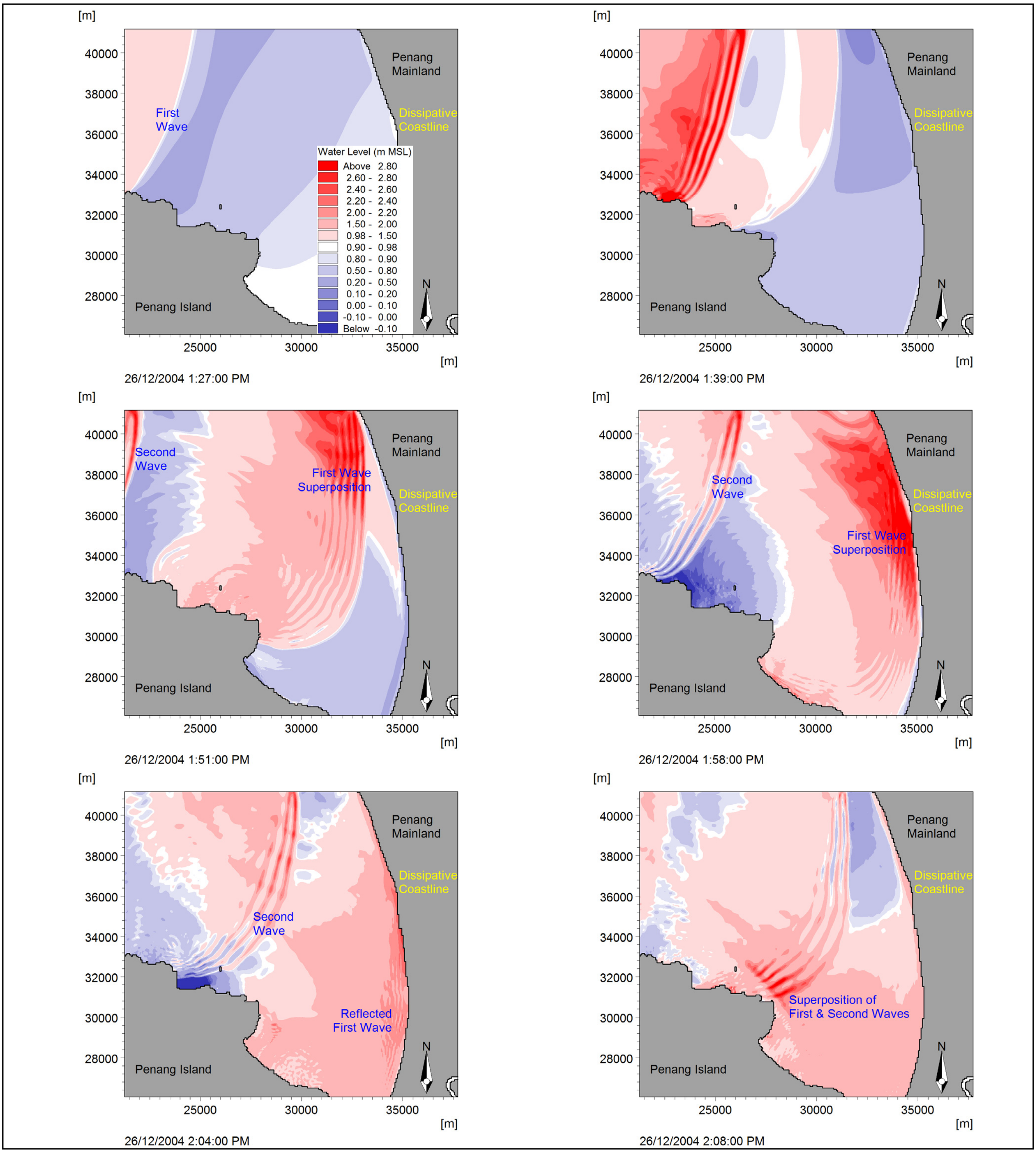

Figure 7. Snapshots of the Tsunami waves displaying wave energy absorbing coastline of Penang mainland. Wave reflections are thus weaker, forming a weaker superposition of waves.

3.2 Coastal channel geometry

For each modelling cases of M=5, 32 and 64 m$^{1/3}$/s, the statistical maximum tsunami-induced water level was computed. Figure 8 shows the differences of the maximum excess water levels between the case of M=5 and 64 m$^{1/3}$/s, as well as between the cases of M=32 and 64 m$^{1/3}$/s. Positive differences in red are related to the higher water level in the case of M=64 m$^{1/3}$/s.

Modelling results show that a relatively higher water level is seen in the coastal channel where M=64 m$^{1/3}$/s as compared to the case M=5 m$^{1/3}$/s, mainly due to the high roughness in the latter case, water is restricted to enter the coastal channel. Increased in the Manning Coefficient, M to 32 m$^{1/3}$/s has provided greater entrance, as seen in the difference map (Figure 8, right) that the positive changes were reduced as compared to the case M=5 m$^{1/3}$/s (Figure 8, left).

The results demonstrate that the build-up of Tsunami-induced water levels in a channel is dependent on the manipulation of Manning coefficient, *M*, which represents the channel geometry (dimension and alignment), seabed condition and reclamation materials. These factors are important in design, for instance in determining the design platform level of a reclamation island.

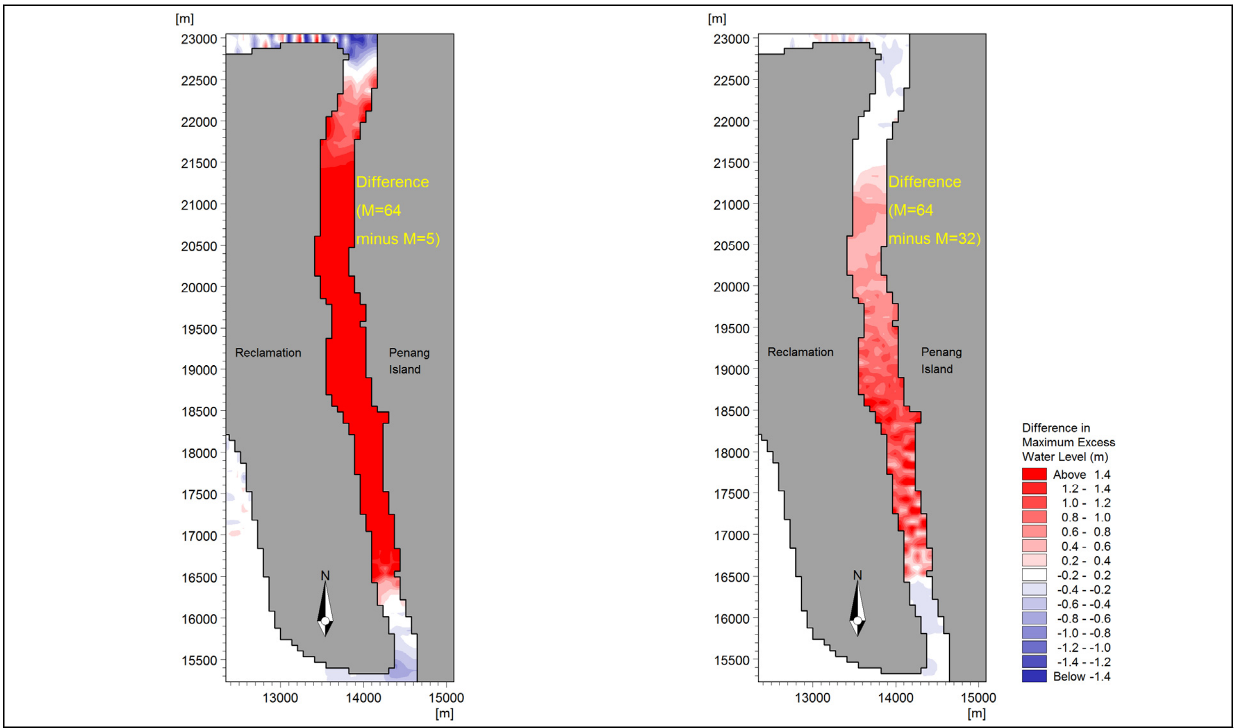

Figure 8. The difference in maximum tsunami-induced water levels, calculated from the case of *M*=64 $m^{1/3}/s$ subtracted by *M*=5 $m^{1/3}/s$ (left) and *M*=64 $m^{1/3}/s$ subtracted by *M*=32 $m^{1/3}/s$ (right) in the coastal channel.

3.3 Onshore storage

The statistical maximum tsunami-induced water level was computed. Figure 9 shows the differences of the maximum excess water levels between the case of including onshore storage and excluding onshore storage. Negative differences in blue are related to lower water level in the case of including onshore storage.

The modelling results show that the maximum Tsunami-induced water levels in the channel are generally lower when onshore storage is incorporated in the model. The availability of an onshore area allows water to inundate potential low-lying areas, thus making the tsunami assessment more realistic.

A relatively higher tsunami-induced water levels in the channel may be achieved when onshore storage is not included, as the water continuously build-up in the channel. It may not be a realistic approach, except that some artificial structures such as flood bunds are presence along the coastal channel.

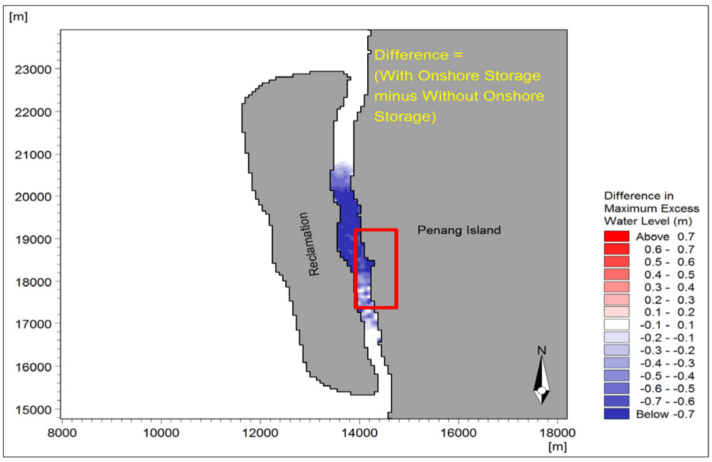

Figure 9. The difference in maximum tsunami-induced water levels, calculated from the case with onshore storage minus the case without onshore storage.

4 CONCLUSIONS

In a nutshell, the reflectivity of a coastline, which changes with the coastal conditions, has to be considered sensibly in making sure the model is reliable in simulating a Tsunami event, as it poses direct impacts on the assessment of tsunami-induced water levels around the reclamation and existing lands. The tsunami-induced water levels are also subjective to the coastal channel geometry modelled as roughness parameter between existing coastline and the synthetic reclamation. The incorporation of onshore storage in the model would result in a reduction in the tsunami-induced water levels in the coastal channel. It should be well noted that these elements ultimately act as a backbone in contributing to the final decision in designing coastal reclamation projects.

ACKNOWLEDGEMENTS

The authors would like to thank DHI Malaysia's staffs for their involvement and support in this project.

REFERENCES

Gayer, G., Nöhren, I., Leschka, S. & Kongko, W. (2008). Detailed Investigations of Tsunami Scenarios in Coastal Areas and Onshore. *International Conference on Tsunami Warning (ICTW)*, 1-8.

Luger, S. A. & Harris, R.L. (2010). Modelling Tsunamis Generated by Earthquakes and Submarine Slumps Using Mike 21. *International MIKE by DHI conference*, P017, 1-13.

National Hydrographic Centre. (2016). *Malaysia Tide Tables*. Royal Malaysian Navy, Book, Vol. 1.

Nirupama, N., Murty, T.S., Nistor, I. & Rao, A.D. (2007). *The Energetics of the Tsunami of 26 December 2004 in the Indian Ocean: A Brief Review*. The Indian Ocean Tsunami, Ed. T.S. Murty, U. Aswathanarayana and N. Nirupama, Taylor & Francis, Leiden, NL, 81-89.

Pedersen, N.H., Rasch, P.S. & Sato, T. (2005). Modelling of the Asian Tsunami off the Coast of Northern Sumatra. *Danish Hydraulic Institute Technical* Paper, 1-13.

FREE-SURFACE AND VELOCITY CHARACTERISTICS OF TIDAL BORE PROPAGATION AGAINST A SLOPE: EXPERIMENTS ON DECELERATING BORES

YOUKAI LI[1] & HUBERT CHANSON[2]

[1] The University of Queensland, School of Civil Engineering, Brisbane QLD 4072, Australia,
youkai.li@uq.net.au; h.chanson@uq.edu.au

ABSTRACT

A tidal bore is a hydraulic jump in translation occurring in the estuarine zone where the river has a funnel-shaped mouth. For a decelerating bore propagating upstream against a steep slope, its properties vary at different locations before it finally changes into an arrested bore: i.e. a stationary hydraulic jump. The present study conducted some novel and systematic research on the transformation of a decelerating bore into a stationary hydraulic jump in a relatively large channel with adverse slope. The arrested bore could be of different types: an undular jump with long shock waves, strong secondary waves and no breaking, a partially breaking jump with long shock waves and strong secondary waves, or a strongly breaking jump with short shock waves and weak secondary waves. All the experiments were repeated more than 25 times to yield some ensemble-averaged results in terms of the free-surface characteristics, velocity and turbulent Reynolds stresses. Physically, the decelerating bore propagation induced maximum free-surface and velocity fluctuations associated with the bore front passage, but there was a time lag between the occurrence of the maximum fluctuations, hinting some coupling effect between the free-surface elevations and turbulent velocity during the decelerating bore passage.

Keywords: Decelerating bores; physical modeling; arrested hydraulic jump; ensemble-averaging.

1 INTRODUCTION

A tidal bore is a positive surge of tidal origin, occurring in an estuary where the river has a funnel-shaped mouth, a large tidal range and low fresh water discharge (Chanson, 2011a; Lighthill, 1978). The bore is a hydrodynamic shock, sometimes called a hydraulic jump in translation (Henderson, 1966) (Figure 1). Field observations showed that tidal bores could highly enhance the turbulent process in estuaries inducing strong upward convection of riverbed materials and upstream advection of suspended sediments (Keevil et al., 2015; Chanson et al., 2011). The shape of the bore front is characterized by its Froude number, Fr_1, defined in a rectangular channel as:

$$Fr_1 = \frac{V_1 + U}{\sqrt{g \times d_1}} \quad [1]$$

where d_1 and V_1 are respectively the upstream initial flow depth and velocity immediately prior to the tidal bore passage, U is the bore celerity positive upstream and g is the gravity acceleration. The Froude number, Fr_1 is always greater than unity (Liggett, 1994; Henderson, 1966). For a tidal bore with Froude number slightly larger than unity, between 1 and 1.2-1.3, an undular bore is seen, characterised by a smooth rise of the free-surface, followed by a train of strong secondary free-surface undulations (Koch and Chanson, 2008; Treske, 1994) (Figure 1, Right). A tidal bore with Froude number between 1.2-1.3 and 1.5-1.8 is a breaking bore with weak secondary waves behind the bore front. When the bore Froude number is larger than 1.5-1.8, a breaking bore takes place: the bore front is characterised by an abrupt roller with air entrainment and highly turbulent motion (Leng and Chanson, 2015; Chanson, 2010) (Figure 1, Left).

When a tidal bore propagates upstream against a steep adverse slope, the bore may lose its celerity and transform into a stationary hydraulic jump. During the transformation process, the properties of the tidal bore slowly changes and may cause some erosion and scouring to the riverbed (MacDonald et al., 2009; Bellal et al., 2003). The formation of a bore propagating against a steep mobile-bed slope, its deceleration and vanishing may also be associated with a cyclic behaviour (Parker and Izumi, 2000; Grant, 1997; Parker, 1996). Pertinent studies included Chanson (2011b), MacDonald et al. (2009) and Carling (1995).

The deceleration of a tidal bore has yet been rarely studied to date. The experiments of Chanson (2011b) highlighted the complicated and slow transformation of a moving bore into a stationary hydraulic jump on an adverse steep slope. The present study aims to expand the work by conducting systematic laboratory experiments of the transformation of tidal bores into stationary hydraulic jumps for a broader range of flow conditions.

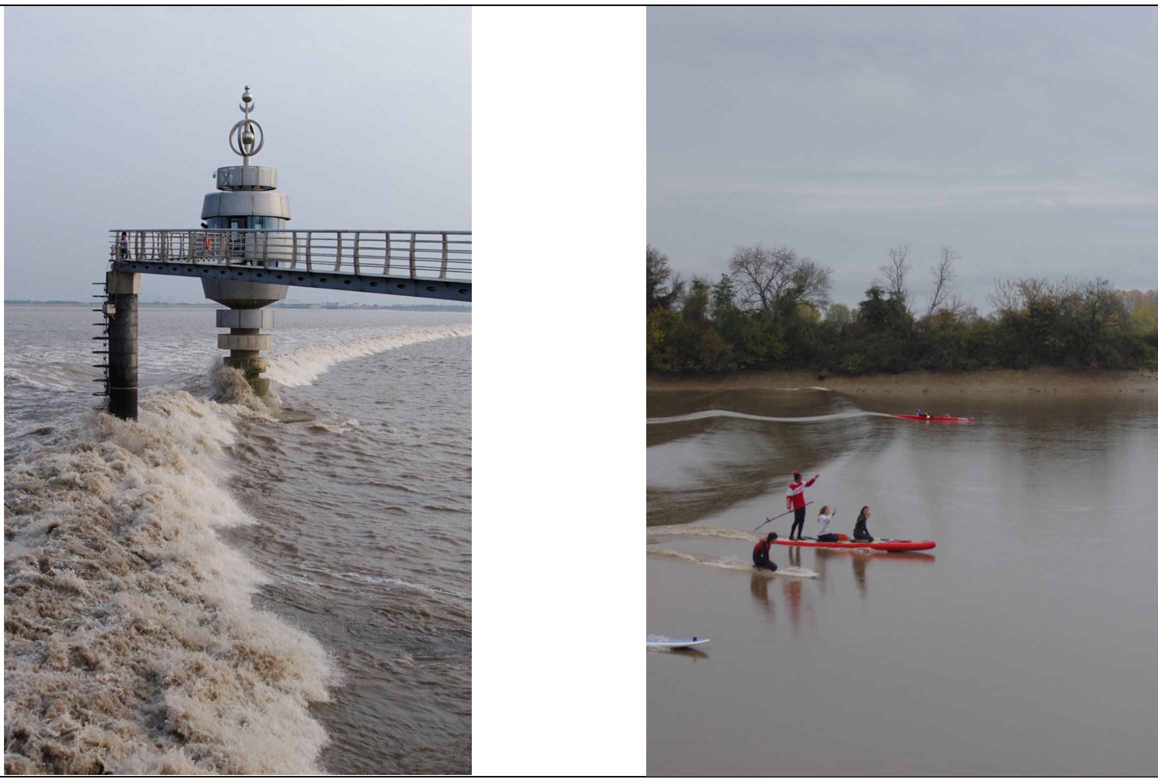

Figure 1. Photographs of tidal bores - Left: breaking tidal bore of the Qiantang River at Yanguan (China) on 23 September 2016; Right: undular tidal bore of the Dordogne River between Luchey and Port de Moulon (France) on 12 November 2016.

2 EXPERIMENTAL FACILITY, INSTRUMENTATION AND FLOW CONDITIONS

2.1 Facility and instrumentation

New experiments were conducted in a large tilting rectangular flume at the University of Queensland, Australia. The channel was 15 m long, 0.495 m wide and 0.465 m high. The channel bed was made of smooth PVC and the sidewalls were made of glass (Figure 2A). A constant head reservoir supplied the water to an upstream intake tank (1.43m×1.24m×1.0m), equipped with baffles and flow straighteners and connected to the start of the glass-walled channel by a smooth convergent section, enabling a quasi-uniform low-turbulence inflow into the glass-walled test section. The water discharge, Q was measured by a Venturi meter mounted in the water supply, designed based upon British Standard (British Standard, 1943) and calibrated on site with an error of less than 2%. The bed slope, $S_o = \sin\theta$, with θ, the angle between channel bed and the horizontal, could be finely adjusted by a mechanical screw jack system, with an estimated error of less than 1×10^{-4}.

A fast-closing Tainter gate was located at $x = x_{gate} = 14.17$ m, with x the longitudinal distance from the start of the glass-walled test section, leaving an opening h between the lower gate edge and invert (Figure 2B). At the location of the Tainter gate, the initial water surface was typically lower than h. The bore was initially generated using a temporary manually-controlled fast-closing adjunctive gate: it was shut down in less than 0.2 s, kept partially closed for 3-4 s and lifted up in less than 0.2 s.

The steady flow depths were measured using a pointer gauge. Measurements of unsteady water elevations were performed with 6 acoustic displacement meters (ADMs) Microsonic™ Mic+25/IU/TC, mounted above the channel centreline at x = 14.26 m (immediately downstream of Tainter gate), 13.85 m (immediately upstream of Tainter gate), 9.10 m, 8.10 m, 7.00 m and 6.10 m. All ADMs were sampled at 200 Hz. The water velocities were recorded by a Nortek™ Vectrino+ acoustic Doppler velocimeter (ADV) equipped with a side-looking probe (Probe ID: VCN 7999). The ADV control volume was located at x = 7.00 m on the channel centreline. The velocity range was ±2.5 m/s and the sampling rate was 200 Hz. The accuracy was ±0.5% of the velocity range. The vertical elevation of the ADV probe was controlled by a fine adjustment traverse mechanism connected to a Hafco™ M733 digimatic vertical scale unit. The error of the vertical position of the ADV probe was less than 0.025 mm. The accuracy of the longitudinal position along the channel was ±2 mm while the error of the transverse position was ±1 mm.

Two cameras were used to track the decelerating bore propagation against the steep slope. A dSLR camera Canon™ EOS 1200D (25fps; resolution: 640×480p) was placed at x=13.0 m on a tripod to record the tidal bore for a relatively short time span after its generation. The time origin was detected by the sound of gate closure. A camcorder Sony™ HDR-XR160 (25fps, 1400×1080p) followed the decelerating bore from the generation up to its transformation into a stationary hydraulic jump. For each flow condition, video recording was also performed at the final bore locations to track the oscillations of the arrested bore.

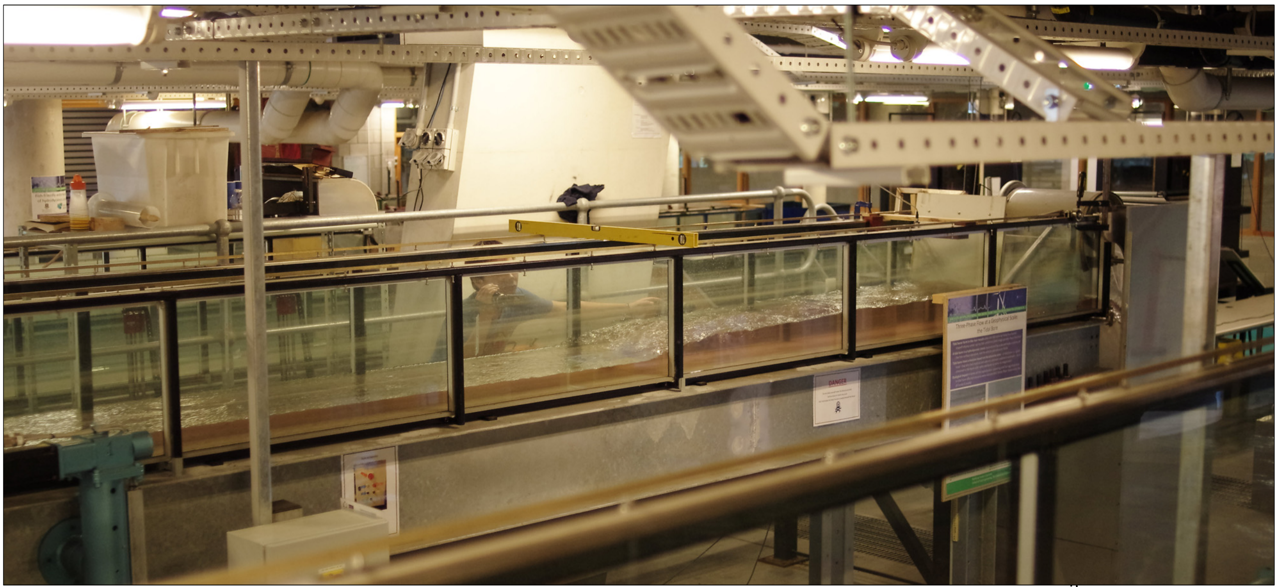

(A) Experimental channel - Initial bore propagation shortly after gate closure - Q = 0.039 m^3/s, d_1 = 0.065 m, S_o = 0.0068 - Red arrow points to bore front, bore propagation from right to left.

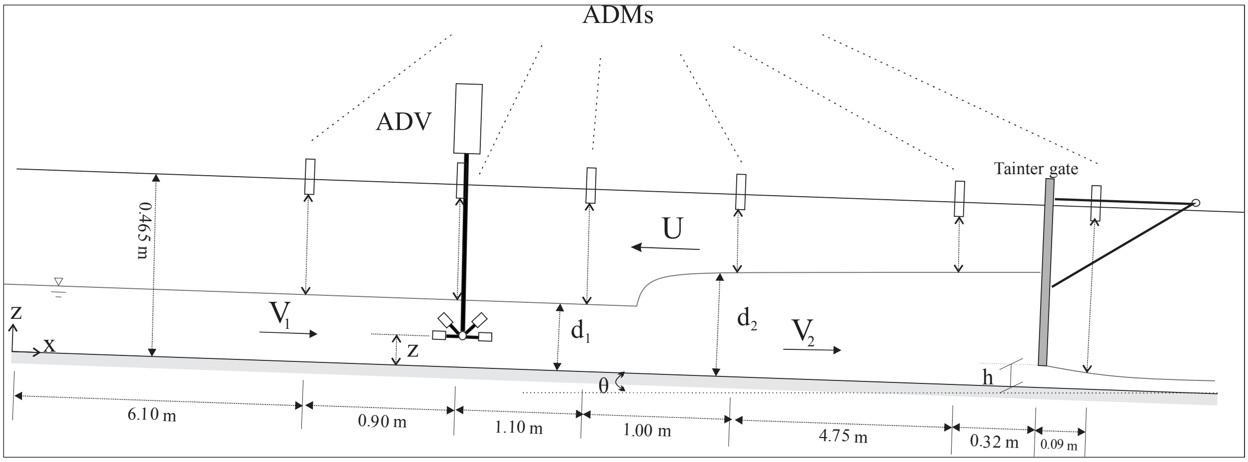

(B) Schematic diagram of the experimental channel facility and instrumentation setup (not to scale) - At x = 7.00 m, the ADM was immediately above the ADV control volume.

Figure 2. Experimental facility of decelerating bore investigation at the University of Queensland.

2.2 Experimental flow conditions

Two initial flow rates Q = 0.039 and 0.061 m^3/s and two bed slopes S_o = 0.0068 and 0.0110 were selected, following a series of preliminary tests to ensure that the bore front was arrested between x = 0 m and x= 6.10 m. Table 1 lists the experimental flow conditions, where the initial flow depth, d_1, the bore celerity, U, the initially-steady supercritical flow Froude number, Fr_o and the bore Froude number, Fr_1 were observed at x = 7.00 m, and x_s is the position of the bore front. In Table 1, only the final position of the arrested bore is shown, and B is the channel width.

The velocity profiles in the initially steady flow on the tilted bed showed the presence of a developing boundary layer. In the developing turbulent boundary layer, the longitudinal velocity component distribution followed a 1/8th power law. For all flow conditions, the initial flow was partially developed at x = 7.00 m (ADV sampling location). Using the von Karman momentum integral equation, the boundary shear stress was estimated to be τ_o = 1.2-1.8 Pa at x =7.00 m for all experiments.

For all experiments, the instrumentations started recording the initially steady flow conditions for 60 s before the bore generation. The data acquisition stopped after the bore became arrested. Each series of experiments was repeated more than 25 times to perform some ensemble-average analysis following Leng and Chanson (2016) as well as Chanson and Docherty (2012).

Table 1. Decelerating bore experiments (d_1, U, Fr_o, Fr_1 are flow conditions at x = 7.0m).

Reference	Q (m^3/s)	S_o	d_1 (m)	U (m/s)	Fr_o	Fr_1	x_s (Final) (m)	Remarks
Present study	0.039	0.0110	0.059	0.037	1.76	1.79	3.55	B = 0.495 m Smooth PVC bed
		0.0068	0.066	0.037	1.47	1.52	4.60	
	0.061	0.0110	0.074	0.019	1.95	1.96	5.15	
		0.0068	0.085	0.039	1.59	1.62	3.45	
Chanson (2011b)	0.035 to 0.06	0.009 to 0.027	0.040 to 0.072	0.002 to 0.22	--	1.71 to 2.83	--	B = 0.50 m smooth PVC bed

3 FLOW PATTERNS

3.1 Presentation

Visual, photographic and video observations were carried out to document the basic flow patterns of decelerating bores against the adverse slope. Immediately after gate closure, the bore was breaking for all investigated flow conditions (Table 1). The breaking bore process was characterised by a marked turbulent roller with some air bubble entrainment region following the bore font (Figure 2A).

As a bore propagated upstream against the steep slope, its properties slowly varied, and the bore Froude number decreased with increasing distance from the gate. For comparison, preliminary experiments in the same channel with the same flow rate and a horizontal slope (S_o = 0) showed little changes in bore characteristics along the 15m long flume, as shown by Yeow et al. (2016). As the bore decelerated, its shape evolved with time depending upon the initial flow and new boundary conditions. The bore could remain strongly breaking up to bore arrest. For other flow conditions, the arrested bore could be an undular jump with long shock waves, strong secondary waves and no breaking, or a partially breaking jump with long shock waves and strong secondary waves.

3.2 Bore celerity

The decelerating bore propagations were tracked, yielding the bore front arrival time at different longitudinal locations and the corresponding bore celerities. Figure 3 shows typical dimensionless bore celerity U/V_c data as a function of the dimensionless distance from the Tainter gate $(x_{gate}-x)/x_{gate}$, where V_c is the initially steady critical flow velocity. Their corresponding dimensionless bore locations are shown in Figure 3B, where d_c is the initially steady critical flow depth. In Figure 3, g is the gravity acceleration, and B is the channel width (B = 0.495 m). All tidal bores were arrested before they reached the upstream intake structure, as shown by the vertical line in Figure 3.

Immediately after the gate closure, the newly generated bore grew quasi-instantly, reached a maximum celerity at a short distance from the gate and then propagated further upstream with a decreasing celerity (Figure 3A). The bore celerity decreased rapidly to less than half the initial value, as the result of a combination of both adverse channel slope, adjunctive gate removal and boundary friction. For each flow condition, the fluctuations in decelerating bore arrival times became larger between different repeats at the locations farther away from the Tainter gate (Figure 3B). The whole transformation from a decelerating bore to a stationary hydraulic jump took about 350-450 s. In comparison, the bore took less than 20 s to travel through the whole horizontal channel length, for the same initial flow rate. Compared to the tidal bore propagation in a horizontal channel (S_o = 0), the transformation of a decelerating bore was a much slower process, as discussed by Chanson (2011b), who observed a tidal bore transformation into a stationary hydraulic jump in 300-600 s in a 12 m long 0.5 m wide channel. The entire process would take longer at full scale in a natural river flow condition and the duration should be scaled up according to a Froude similitude.

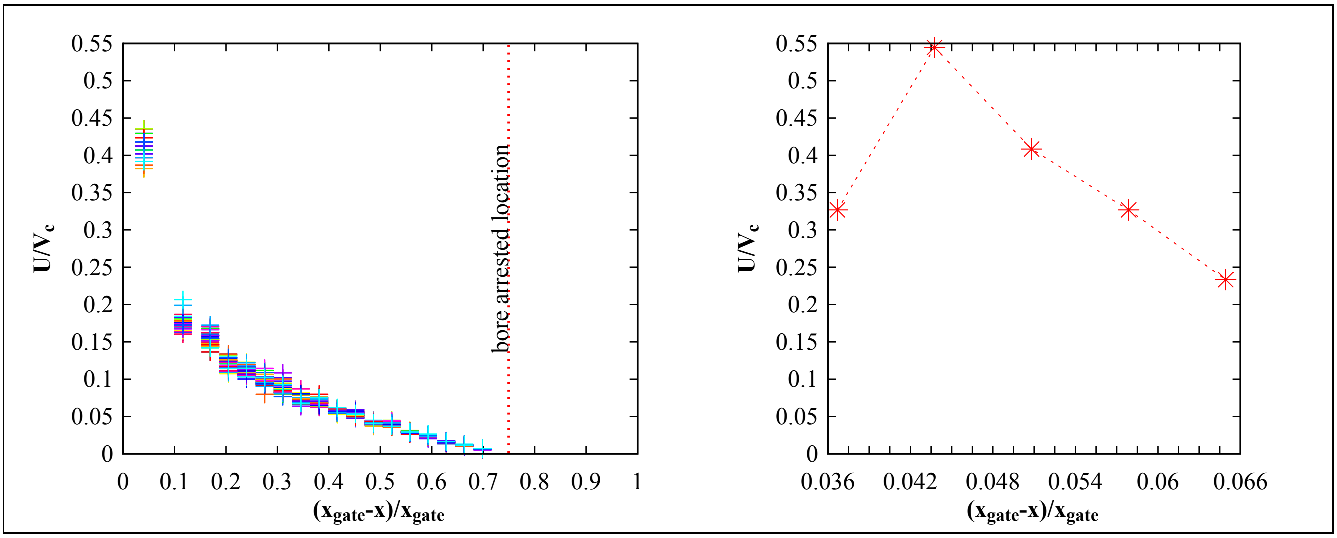

(A) Longitudinal variation in bore celerity - Inset (Right): bore celerity immediately after gate closure.

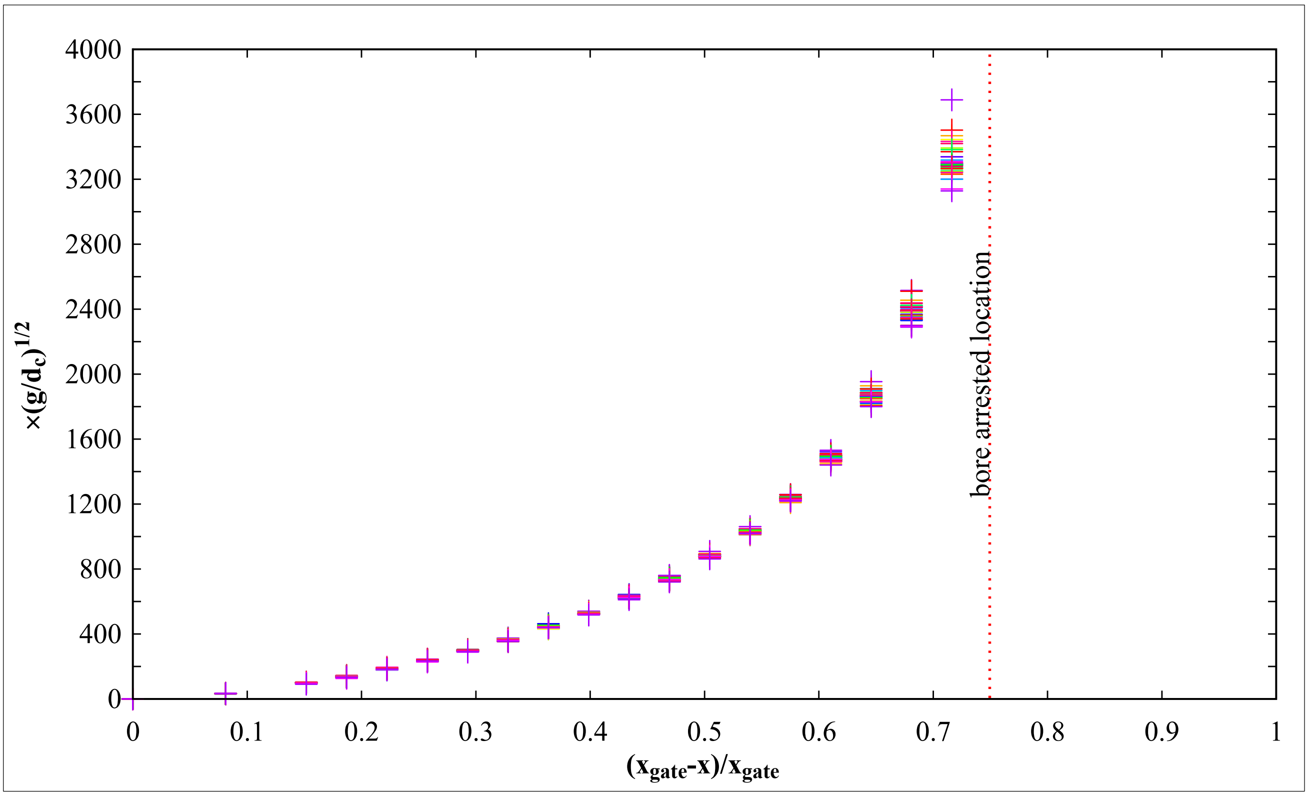

(B) Time-variation of the bore front location x_s.

Figure 3. Propagation characteristics of a decelerating bore. Ensemble-average results - Flow condition: Q = 0.039 m^3/s, S_o = 0.0110, h = 0.065 m, Fr_1 = 1.79 at x = 7.00 m; x_{gate} = 14.17 m, $(x_s)_{final}$ = 3.55 m, d_c = 0.086 m, V_c= 0.9172 m/s.

3.3 Free-surface properties

As the tidal bore is a highly unsteady and turbulent process, a time-average method is not applicable to analyze the free-surface characteristics during the bore passage. A series of ensemble-average measurements were performed for all four flow conditions. For each flow condition, the experiment was repeated more than 25 times on the same day. The median free-surface elevation d_{50} and the difference between the third and first quartiles (d_{75}-d_{25}) were derived from the experimental data. The difference between the third and first quartiles (d_{75}-d_{25}) characterised the instantaneous free-surface fluctuations. Typical results are presented in Figure 4. Herein, the time t = 0 corresponded to the gate closure.

For x > 6.10 m, the decelerating bores all propagated as breaking bores. The passage of the roller was associated with the abrupt increase in the water surface. A train of secondary waves followed the bore front and the water depth after bore passage kept slowly rising because of the backwater effect induced by the closed Tainter gate opening at the downstream end of the channel. For the experiment with the smaller slope (S_o = 0.0068), the well-marked secondary waves developed with time. With both small and large slopes, the secondary wave periods became longer with time at a fixed location. The bore passage was also associated with large free-surface fluctuations (d_{75}-d_{25}), which reached maximum values shortly after the bore roller toe passage (Figure 4).

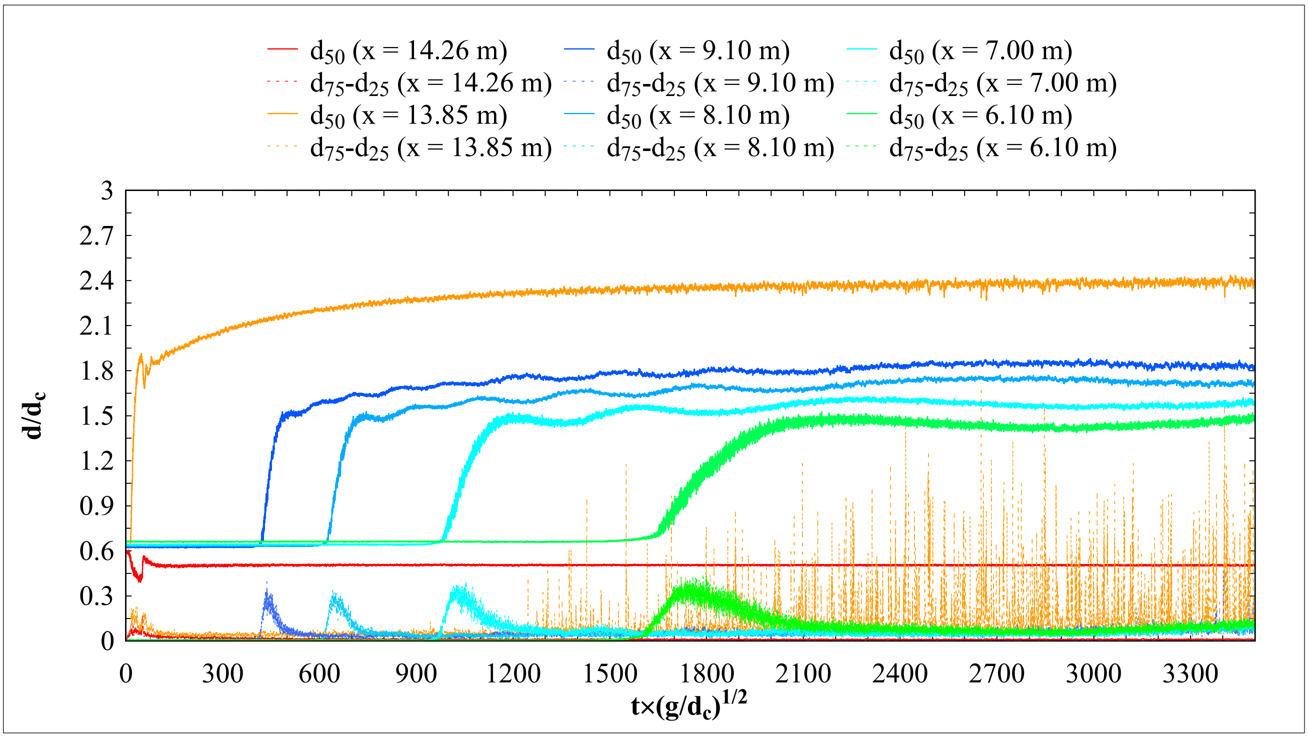

Figure 4. Time-evolutions of ensemble-averaged median free-surface elevations d_{50} and free-surface fluctuations (d_{75}-d_{25}) at different longitudinal locations along the channel - Experimental flow conditions: 32 runs, Q = 0.061 m^3/s, S_o = 0.0110, h = 0.100 m, Fr_1 = 1.96; d_c = 0.116 m.

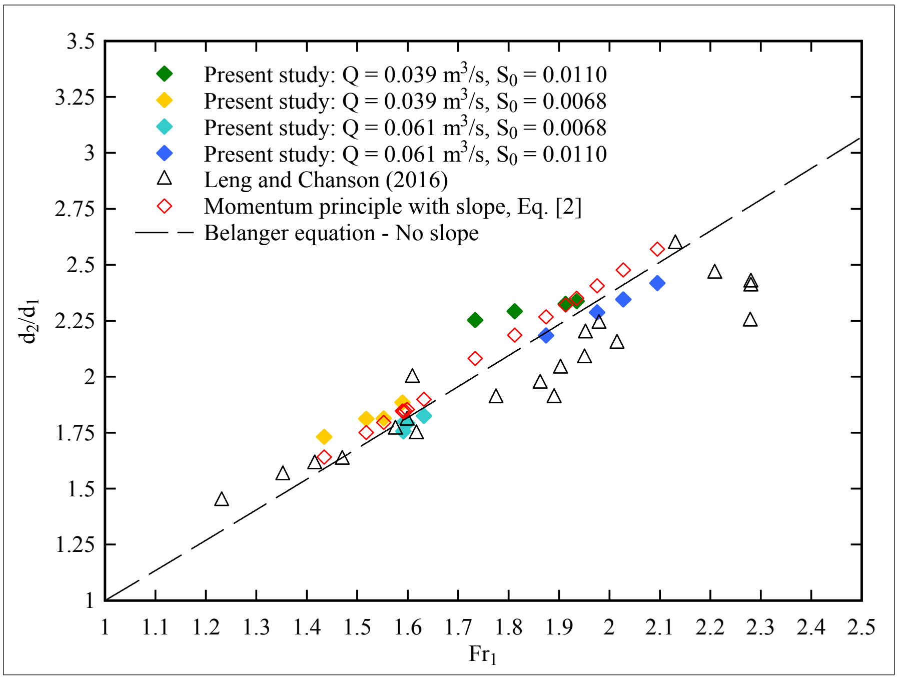

Figure 5. Dimensionless conjugate depth d_2/d_1 as a function of local bore Froude number Fr_1 - Comparison with horizontal slope data (Leng and Chanson, 2016), the momentum principle (Eq. [2]) and the Bélanger equation.

For a smooth rectangular channel, the application of the equations of conservation of mass and momentum in their integral form gives an analytical solution of the conjugate flow properties, namely the ratio of conjugate depth as a function of the Froude number and bed slope (Chanson, 2012). It yields:

$$\frac{d_2}{d_1} = \frac{1}{2} \times \left(\sqrt{(1-\varepsilon)^2 + 8 \times \frac{Fr_1^2}{1-\varepsilon}} - (1-\varepsilon) \right) \quad [2]$$

where d_1 and d_2 are initial and conjugate flow depths, respectively, and ε is a dimensionless coefficient defined as:

$$\varepsilon = \frac{Vol \times S_o}{B \times d_1^2 \times (Fr_1^2 - 1)} \quad [3]$$

with B, the channel width and Vol, the control volume encompassing the bore front, such as for weight force, W = ρ×g×Vol. Eq. [2] implies that the ratio of conjugate depths increases with increasing bed slope for a given Froude number. For a smooth horizontal rectangular prismatic channel, Eq. [2] yields to the classical Bélanger equation.

Eq. [2] is compared to the experimental results in Figure 5, as well as to the Bélanger equation and laboratory data in a smooth horizontal channel (Leng and Chanson, 2016). All the data showed a monotonic increase in conjugate depth ratio with increasing Froude number. Since $S_o << 1$ in the present experiments, the slope effect was small. For a given flow rate, a larger bed slope would yield both larger bore Froude number and larger conjugate depth ratio d_2/d_1 within the experimental flow conditions

4 VELOCITY MEASUREMENTS

Unsteady water velocity measurements during decelerating bores were conducted at the longitudinal location x = 7.00 m. The output data were the longitudinal, transverse and vertical velocity components: V_x, V_y and V_z. Here, V_x is parallel to the channel bed and positive downstream; V_y is parallel to the horizontal and positive towards left sidewall; V_z is normal to the channel bed and positive upwards. Figure 6 presents typical results of ensemble-average analysis. For all the flow conditions, the bore Froude number Fr_1 was larger than 1.5 at x = 7.00 m and the decelerating bores had a breaking roller on the channel centreline. With the passages of the bore front, the longitudinal velocity, V_x presented a marked deceleration by around 50% of the initially steady flow velocity (Figure 6A). The vertical velocity component, V_z had some slight perturbation associated with the bore front passage, although not as strong as the longitudinal velocity deceleration. Since the bore celerity, U only had an amplitude of 0.02 to 0.04 m/s at x = 7.00 m, the deceleration rate was much slower than that of a breaking bore in horizontal channel (Leng and Chanson, 2016; Koch and Chanson, 2009). The longitudinal velocity components always remained positive during the whole process. No velocity reversal was observed, contrarily to observations on a horizontal slope (Koch and Chanson, 2009). The finding was consistent with the instantaneous velocity measurements by Chanson (2011b) in a decelerating bore.

For all flow conditions, V_y and V_z had a mean value of zero, before the decelerating bore arrived at x = 7.00 m (Figure 6B and 6C). The longitudinal flow velocity component, V_x presented sharp decrease at all vertical elevations during the bore front passage. At the same time, the vertical flow component, V_z experienced some initial increase during the bore front passage and then some decrease after the bore crest passage. All the ensemble-averaged velocity components V_x, V_y and V_z presented an oscillating trend linked to the free-surface curvature induced by the secondary waves, especially for decelerating bores with the smallest Froude numbers. These characteristics were similar to the undular bore experiments in a horizontal channel by Leng and Chanson (2016) and Koch and Chanson (2008), as well as the stationary undular hydraulic jump experiments of Lennon and Hill (2006) and Chanson and Montes (1995).

The turbulent velocity fluctuations of V_x, V_y and V_z all experienced maximum values shortly after the bore front passage. The peak of velocity fluctuations at vertical elevation close to the bed appeared earlier than at higher elevations close to the free surface. The largest velocity fluctuations were observed close to the bed. Tidal bore experiments in a horizontal channel by Leng and Chanson (2016) exhibited the same features. These features differed from those of stationary hydraulic jump experiments with Froude numbers larger than 3.1 by Chachereau and Chanson (2011), indicating that some longitudinal velocity fluctuations increase with increasing distance from the bed.

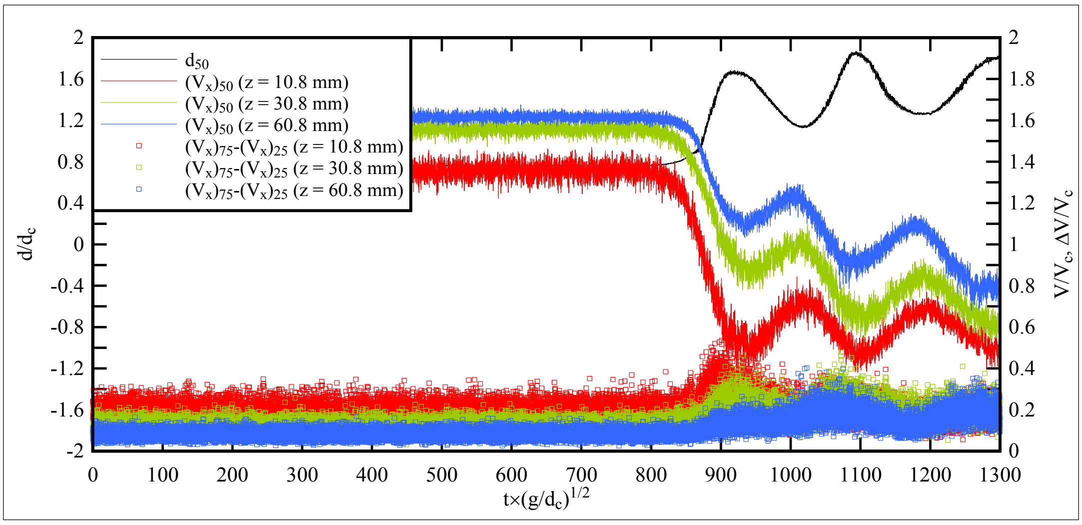

(A) Longitudinal velocity component.

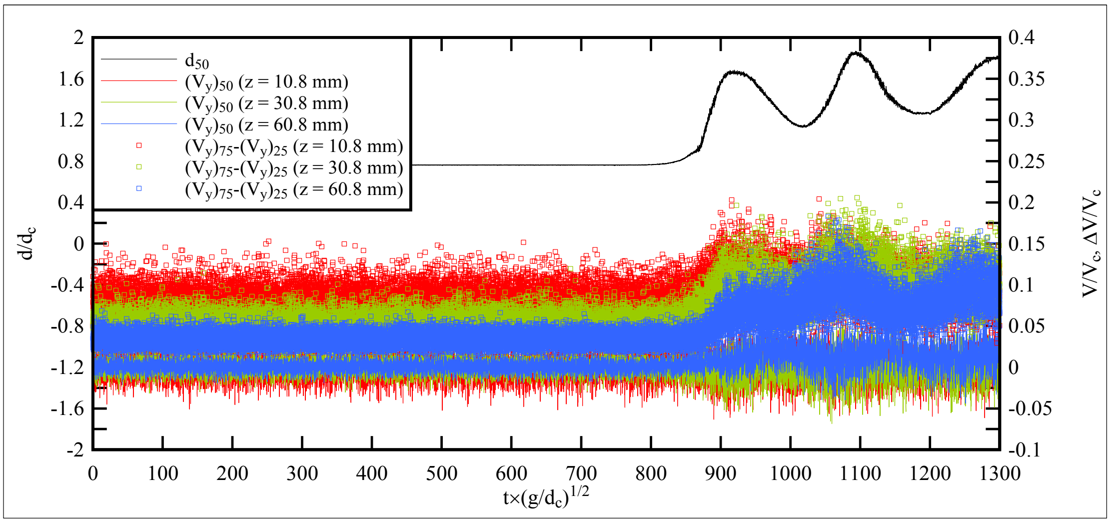

(B) Transverse velocity component.

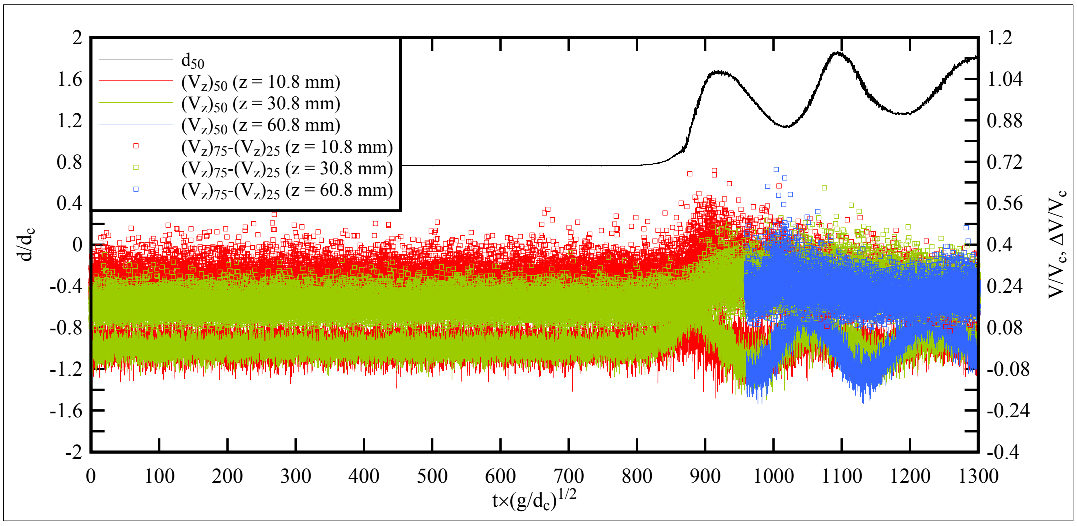

(C) Vertical velocity component.

Figure 6. Ensemble-averaged time variations of the median longitudinal, transverse and vertical velocity components and their velocity fluctuations (V_{75}-V_{25}) at different vertical elevations z for decelerating bores locally synchronized at x = 7.00 m - Flow condition: Q = 0.039 m^3/s, S_o = 0.0068, h = 0.080 m, Fr_1 = 1.52 at x = 7.00 m; d_c = 0.086 m, V_c = 0.9174 m/s.

5 CONCLUSIONS

The present work focused on the instantaneous and ensemble-averaged free-surface and velocity characteristics for decelerating bores against an adverse steep slope, and the transformation process of the travelling bore into a stationary hydraulic jump. For each flow condition, the experiment was repeated more than 25 times to enable ensemble-averaged measurements. The process of a decelerating bore and its transformation into an arrested bore was very slow, normally taking more than 300 s, compared to less than 20 s for a bore to travel through the entire horizontal channel. Both instantaneous free-surface measurements and ensemble-average analyses were conducted based on the data collected at six longitudinal locations. The shape of the decelerating bore gradually varied as it propagated upstream. The arrested bore could be an undular jump with long shock waves and strong secondary waves, a partially breaking jump with long shock waves and strong secondary waves, or a strongly breaking jump with short shock waves and weak secondary waves. The decelerating bore passage was observed with a marked rise in free-surface and some decrease of longitudinal velocity, as well as relatively large free-surface and velocity fluctuations. The time lag between maximum free-surface fluctuations and first wave crest increased with further distance from downstream gate. The bore front passage caused a significant rise in all the velocity components at all vertical elevations. At vertical elevations closer to the bed, the velocity fluctuations had an earlier response to the decelerating bore arrival and larger fluctuation amplitudes than at an upper elevation.

Overall, the present study presented seminal features of the slow and complicated process of decelerating bores with intense turbulence. The current experiment may be compared to in-situ tidal and tsunami bore process in estuarine zones. The varying characteristics of decelerating bores should be considered in the hydraulic structure designs in areas affected by tidal bores and tsunami bores.

ACKNOWLEDGEMENTS

The authors thank Ms Xinqian Leng, Mr Gangfu Zhang and Dr Hang Wang (The University of Queensland) for their assistance and advice. The technical assistance of Jason Van Der Gevel and Stewart Matthews (The University of Queensland) are acknowledged. The financial assistance of the Australian Research Council (ARC DP120100481) are acknowledged.

REFERENCES

Bellal, M., Spinewine, B., Savary, C. & Zech, Y. (2003). Morphological Evolution of Steep-Sloped River Beds in the Presence of a Hydraulic Jump: Experimental Study. *Proceeding 30th IAHR Biennial Congress*, Thessaloniki, Greece, C (2), 133-140.

British Standard (1943). *Flow Measurement*, British Standard Code BS 1042:1943, British Standard Institution, London.

Carling, P.A. (1995). Flow-Separation Berms Downstream of a Hydraulic Jump in a Bedrock Channel. *Geomorphology*, 11(3), 245-253.

Chachereau, Y. & Chanson, H. (2011). Bubbly Flow Measurements in Hydraulic Jumps with Small Inflow Froude Numbers. *International Journal of Multiphase Flow*, 37(6), 555-564.

Chanson, H. (2010). Unsteady Turbulence in Tidal Bores: Effects of Bed Roughness. *Journal of Waterway, Port, Coastal, and Ocean Engineering*, 136(5), 247-256.

Chanson, H. (2011a). *Tidal Bores, Aegir, Eagre, Mascaret, Pororoca: Theory and Observations*. World Scientific, 1-201.

Chanson, H. (2011b). Turbulent Shear Stresses in Hydraulic Jumps and Decelerating Surges: An Experimental Study. *Earth Surface Processes and Landforms*, 36(2), 180-189.

Chanson, H. (2012). Momentum Considerations in Hydraulic Jumps and Bores. *Journal of Irrigation and Drainage Engineering,* 138(4), 382-385.

Chanson, H. & Docherty, N.J. (2012). Turbulent Velocity Measurements in Open Channel Bores. *European Journal of Mechanics B/Fluids*, 32, 52-58.

Chanson, H. & Montes, J.S. (1995). Characteristics of Undular Hydraulic Jumps. Experimental Apparatus and Flow Patterns. *Journal of Hydraulic Engineering*, 121(2), 129-144.

Chanson, H., Reungoat, D., Simon, B. & Lubin, P. (2011). High-Frequency Turbulence and Suspended Sediment Concentration Measurements in the Garonne River Tidal Bore. *Estuarine Coastal and Shelf Science,* 95(2-3), 298-306.

Grant, G.E. (1997). Critical Flow Constrains Flow Hydraulics in Mobile-Bed Streams: a New Hypothesis. *Water Resources Research*, 33(2), 349-358.

Henderson, F.M. (1966). *Open Channel Flow*. MacMillan, 1-522.

Keevil, C.E., Chanson, H. & Reungoat, D. (2015). Fluid Flow and Sediment Entrainment in the Garonne River Bore and Tidal Bore Collision. *Earth Surface Processes and Landforms*, 40(12), 1574-1586.

Koch, C. & Chanson, H. (2008). Turbulent Mixing beneath an Undular Bore Front. *Journal of Coastal Research*, 24(4), 999-1007.

Koch, C. & Chanson, H. (2009). Turbulence Measurements in Positive Surges and Bores. *Journal of Hydraulic Research*, 47(1), 29-40.

Leng, X. & Chanson, H. (2015). Breaking Bore: Physical Observations of Roller Characteristics. *Mechanics Research Communications*, 65, 24-29.

Leng, X. & Chanson, H. (2016). Coupling between Free-surface Fluctuations, Velocity Fluctuations and Turbulent Reynolds Stresses during the Upstream Propagation of Positive Surges, Bores and Compression Waves. *Environmental Fluid Mechanics*, 16(4), 695-719.

Lennon, J.M. & Hill, D.F. (2006). Particle Image Velocimetry Measurements of Undular and Hydraulic Jumps. *Journal of Hydraulic Engineering*, 132(12), 1283-1294.

Liggett, J.A. (1994). *Fluid Mechanics*. McGraw-Hill, 1-495.

Lighthill, J. (1978). *Waves in Fluids*. Cambridge University Press, 1-504.

MacDonald, R.G., Alexander, J., Bacon, J.C. & Cooker, M.J. (2009). Flow Patterns, Sedimentation and Deposit Architecture under a Hydraulic Jump on a Non-Eroding Bed: Defining Hydraulic Jump Unit Bars. *Sedimentology*, 56, 1346-1367.

Parker, G. (1996). *Some speculations on the relation between Channel Morphology and Channel Scale Flow Structures. in Coherent Flow structures in Open Channels*. John Wiley, Chichester, UK, 423-458.

Parker, G. & Izumi, N. (2000). Purely Erosional Cyclic and Solitary Steps Created by Flow over a Cohesive Bed. *Journal of Fluid Mechanics*, 419, 203-238.

Treske, A. (1994). Undular Bores (Favre-Waves) in Open Channels - Experimental Studies. *Journal of Hydraulic Research*, 32(3), 355-370.

Yeow, S.C., Chanson, H. & Wang, H. (2016). Impact of a Large Cylindrical Roughness on Tidal Bore Propagation. *Canadian Journal of Civil Engineering*, 43(8), 724-734.

Proceedings of the 37th IAHR World Congress
August 13 – 18, 2017, Kuala Lumpur, Malaysia

THE RESPONSE OF SALTWATER INTRUSION TO THE RIVERBED DEGRADATION IN THE PEARL RIVER ESTUARY

HUAZHI ZOU(1), SHUNCHAO YU(2) & LIANGLIANG ZHANG(3)

(1, 2) Key Laboratory of the Pearl River Estuarine Dynamics and Associated Process Regulation, Guangzhou, China,
zouhuazhi@163.com; 65729016@qq.com
(3) Pearl River Hydraulic Research Institute, Guangzhou, China,
604832092@qq.com

ABSTRACT

In order to study the impact of the riverbed degradation on the saltwater intrusion in the Pearl River Estuary (PRE), a three-dimensional baroclinic numerical model with high-resolution grids was firstly set up based on the Finite Volume Coastal Ocean Model (FVCOM) and calibrated against measured data. Results indicate that the numerical model can properly capture the dynamic processes of saltwater intrusion in both well mixed and stratified rivers. Secondly, numerical experiments of saltwater intrusion in the PRE were carried out by inputting several sets of data of topographic survey in different years. Results show that the large-scale riverbed degradation leads to an obvious increase in the strength of the saltwater intrusion in the PRE and the scenario of saltwater intrusion is worse in stratified rivers than that in well mixed rivers even though they have similar change of water depth. Finally, the hydrodynamic characteristics of saltwater intrusion were analyzed according to simulated results from different numerical experiments and synchronous measured data. It seems that the larger water depth due to the riverbed degradation will enhance the vertical circulation along the longitudinal direction especially in the stratified rivers. As a result, both the upstream intrusion of near bottom high-salinity water and the downstream diffusion of surface diluted water are accelerated. These increased the amount of upstream transportation of salinity and thus greatly contributed to the worse scenario of saltwater intrusion in the PRE.

Keywords: Estuary; circulation; saltwater intrusion; numerical model; riverbed degradation.

1 INTRODUCTION

The Pearl River Delta (PRD) is located in the Guangdong Province of China and encompasses several cities such as ZhongShan, Zhuhai, Shenzhen, Hong Kong and Macau with a total area of 26,820km^2. It is a plain formed by the Network of the Pearl River (NPR) which includes more than one hundred interconnected Rivers. After flowing through the delta, the NPR finally enters into the South China Sea (SCS) through the Pearl River Estuary (PRE) which is comprised of eight outlets and two bays (see Figure 1). In the dry season, saltwater can abnormally intrude into the upstream freshwater zone of NPR through the PRE and thus jeopardize the freshwater supply of cities in the PRD region. The hydrological records indicate an increase in the frequency and strength of saltwater intrusion in the last 30 years. It becomes one of the most important causes of freshwater shortage of cities such as ZhongShan, Zhuhai, Shenzhen, HongKong and Macau.

With the shortage of freshwater, the problem of saltwater intrusion in the PRE has aroused wide public concern (Hu and Mao, 2012; Yuan et al., 2012). In the last 30 years, great efforts have been carried out to study the dynamic mechanism of saltwater intrusion and explore the key cause of worse scenario of saltwater intrusion in the PRE. The PRE is a typical multi-branch estuary. Its topography and dynamics of rivers, outlets and bays are different from each other. The spatial distribution of saltwater intrusion in the PRE has been analyzed according to in situ measured data. Results show that the dynamic processes and mechanism of saltwater intrusion in rivers and outlets are different from each other too (Gong and Shen, 2011; Ou, 2009). According to hydrologic records, the Modaomen River, which is one of the main channel of NPR and the important freshwater supply resources of Zhuhai and Macau, usually presents the worse scenario of saltwater intrusion compared to other rivers of the NPR (Chen et al., 2014; Bao et al., 2009). Further researches indicate that it also presents a different dynamic process from other rivers during a semi-month lunar tide cycle (Lu et al., 2013; Chen et al., 2011). Thus, the great mass of researches on saltwater intrusion in the PRE is focused on the Modaomen River. According to measured data, the saltwater intrusion in the Modaomen River starts and continuously intrudes upward at neap tide, and reaches its peak during middle tide but not during spring tide. Some researchers consider that this phenomenon is due to the vertical circulation related to the density and stratification (Lu et al., 2013; Chen et al., 2011), and others attribute it to wind speed and direction (Wang et al., 2012).

Although the saltwater intrusion in estuary is mainly induced by the imbalance between the forcing from river discharge and ocean tide, evidences indicate that it is greatly influenced by the coupled effect of topography, wind, sea level, etc. Recent researches show that the large-scale riverbed degradation due to erosion, sand drawing and channel dredging plays the more important role for the worse scenario of saltwater intrusion than sea level rising in the PRE (Li, 2013; Zhang et al., 2008). It becomes the key cause of worse scenario of saltwater intrusion during the last 30 years in the PRE (Kong and Chen, 2015; Han et al., 2010; Jia et al., 2006). The trend of riverbed degradation seems not stopping due to the decrease of sediment load and continuous influence of human activities.

Numerical model has several advantages over field measurement and physical model, for example, convenience, efficiency and cost. It becomes one of the most used methods in the study on estuary dynamics. The major component of this study is to set up and validate a three-dimensional baroclinic numerical model with high-resolution grids to simulate the dynamics of saltwater intrusion in the PRE. Based on this model, several numerical experiments of saltwater intrusion in the PRE were carried out according to several sets of data of topographic survey in different years. With the simulated results and historical measured data, both the dynamic mechanism of saltwater intrusion and influence of riverbed degradation on saltwater intrusion were then properly analyzed. The results may be significant to the prevention of saltwater intrusion and the future management for the PRE.

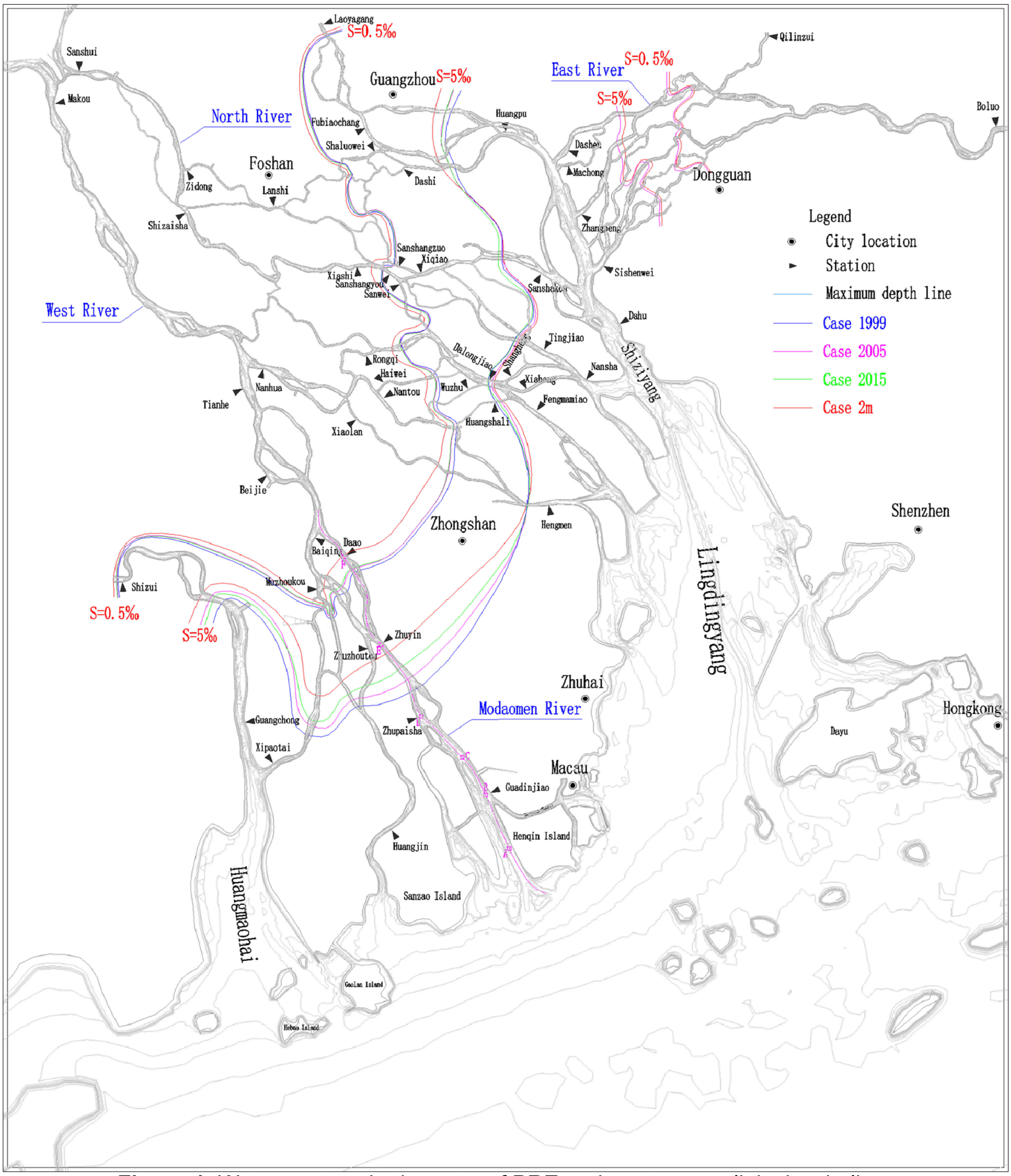

Figure 1. Water system, bathymetry of PRE and upstream salinity borderline.

2 NUMERICAL MODEL AND VALIDATION

2.1 FVCOM introduction

The combined water system of the PRE includes the NPR with more than one hundred interconnected Rivers, two bays with complicated bathymetry, and more than forty islands with curved shorelines are as shown in Figure 1. Though great efforts have been made and a number of numerical models have been developed and applied to estuaries in the last 30 years, a computationally efficient and accurate numerical model that can be competent to the simulation of saltwater intrusion in the PRE is still a challenge. A three-dimensional, unstructured grid, Finite-Volume, primitive equation Community Ocean Model (FVCOM) is developed by the Marine Ecosystem Dynamics Modeling Laboratory (MEDML) at the School for Marine Science and Technology, University of Massachusetts- Dartmouth. Unlike the differential form used in finite-difference and finite-element models, FVCOM discretizes the integral form of the governing equations. Since these integral equations can be solved numerically by flux calculation (like those used in the finite difference method) over an arbitrarily-sized triangular mesh (like those used in the finite element method), the finite-volume approach is better suited to guarantee mass conservation in both the individual control element and the entire computational domain. From a technical point of view, FVCOM combines the best attributes of finite-difference methods for simple discrete coding and computational efficiency and finite-element methods for geometric flexibility. In addition, the FVCOM code has been parallelized using a single processor data approach. This would further improve its computational efficiency. With continuous improvement of more than fifteen years, it has been widely applied and recognized as one of the most advanced and robust model (Bricheno et al., 2016; Lai et al., 2015; Wang et al., 2012).

Considering the complexity of water system and its outstanding advantages such as baroclinic equations, good mass conservation, geometric flexibility and computational efficiency, FVCOM is quite suited for the simulation of the dynamics of saltwater intrusion in the PRE. For conciseness purpose, its technical information will not be presented in this paper. Readers can refer to the user manual for details.

2.2 Computational domain and grid

For the convenient availability and input of boundary conditions such as river discharge and salinity, six upstream boundaries were placed at hydrometric stations: Shizui, Wuzhou, Shijiao, Laoyagang, Qilinzui and Boluo (see Figure 2). Also, the open sea boundary was set at the continental shelf of the South China Sea (SCS) with depth up to about 200m, where diluted water from the PRE was almost unacted on salinity during dry season. The whole computational domain covers the entire NPR, two estuarine bays and offshore area with a total area of 112×10^3 km^2.

As shown in Figure 2, computational grids are properly arranged according to bathymetry and shorelines. For narrow rivers, channels, shoals and islands, further optimization has been done to fit the curved shorelines and changing topography. Within the open sea regions, coarser grids were used to save computational time. The whole computational domain consists of 340,281 triangular cells and 190,039 grid points. The horizontal resolution of computational grids has a gradual and large-scale variety from 30m in rivers to 4km at the open sea boundary. For vertical grid, it was set to be 15 depth averaged layers.

2.3 Boundary and initial condition

The model is mainly driven by river discharge, tide and wind. The upstream boundary conditions are specified with the hourly series of river discharge, which are available from corresponding hydrometric stations: Shizui, Wuzhou, Shijiao, Laoyagang, Qilinzui and Boluo (see Figure 2). The open sea boundary conditions were calculated from eight main tidal constituents: M2, S2, K1, O1, N2, K2, P1 and Q1. Since the section of upstream boundary is far away from the outlets, its flow is unidirectional and its salinity has a constant value of zero. The salinity at open sea boundary is almost unaffected by diluted water during the dry season, its salinity can be given as a constant of 34.6‰. The direction of prevailing monsoon in the estuarine area is east-north during the dry season. The wind speed and direction were inputted to numerical model according to hourly data from two weather stations at Hong Kong and Macau. The wind speed and direction are plotted in Figure 3 during the last fifteen days of simulation.

The initial condition of salinity plays a very important role in the numerical simulation of saltwater intrusion. However, it is rather difficult to get a three-dimensional and synchronous salinity field for such a large computational domain. In this paper, the surface salinity field is firstly calculated from the remote sensing data based on the relationship between CDOM (Colored Dissolved Organic Matter) and salinity (Bowers and Brett, 2008). Then, the salinity field for under-surface layers is interpolated according to the vertical relationship with surface salinity, which was estimated from measured data and experiences. Since the initial condition of salinity is given as a horizontal non-constant field according to a reasonable surface salinity, the vertical salinity will reach a reliable condition in fewer run time. Practices prove that this method is workable and time saving. In addition, both water level and velocity were started from cold, namely the mean sea water level and zero velocity are given as initial conditions.

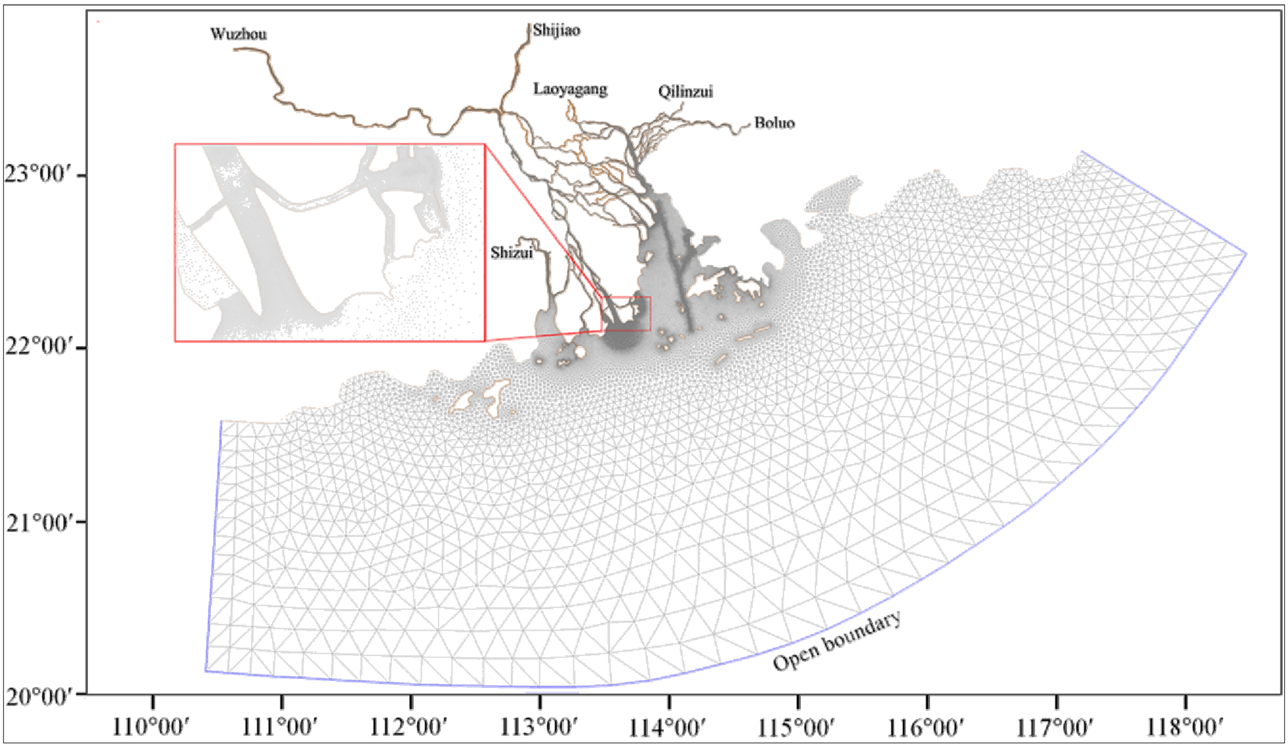

Figure 2. Computational grid.

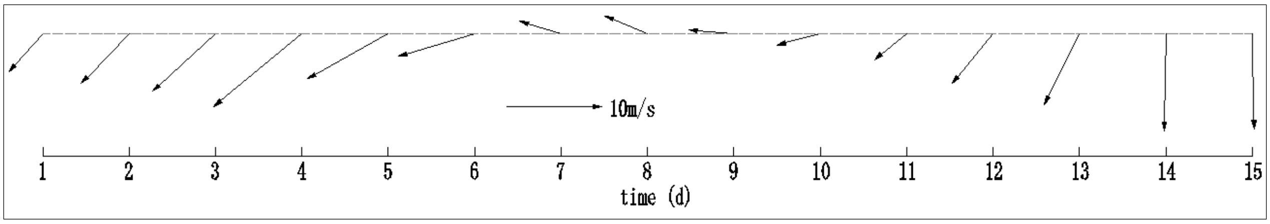

Figure 3. Wind speed and direction.

2.4 Model validation

Although FVCOM has been verified through comparisons with analytical solutions, other popular models and field measured data with successful application to a number of estuaries and continental shelf, further parameter calibration and validation is still necessary for its application in the PRE. In previous researches, this model has been successfully validated and applied to the PRE (Chen et al., 2014; Zou et al., 2013). Considering that this study will mainly focus on the rivers in the NPR, further validations for dynamics of the NPR were carried out in this paper. An hourly time series of measured data with more than forty stations were used to validate the model. The locations of stations are shown in Figure 1. The components of measured data include water level, sectional discharge, and stratified salinity.

Simulated time series of water level, sectional discharge, and stratified salinity were compared with measured data. For conciseness purpose, only several plots of important stations are presented in this paper. Figure 4 and Figure 5 are the comparisons of water level and sectional discharge, respectively. Figure 6 is the comparisons of surface and bottom salinity at different stations. As shown in figures, simulated results agree well with measured data. These indicate that the used model can properly simulate the hydrodynamics of saltwater intrusion in the rivers of NPR.

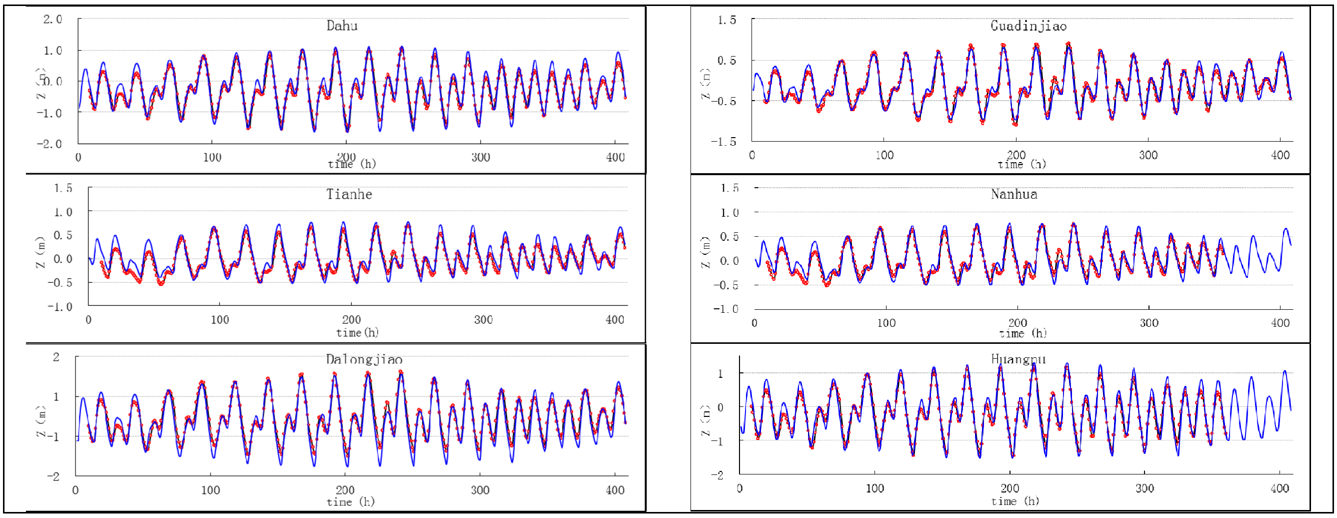

Figure 4. Water level (red dashed line for measured data and blue line for simulated results).

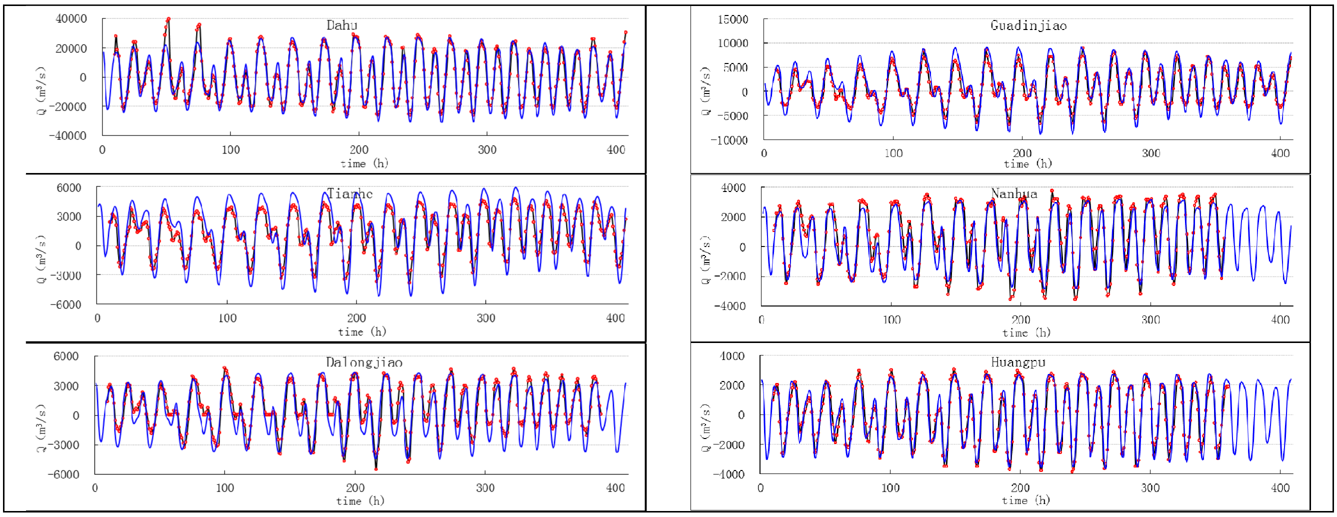

Figure 5. Sectional discharge (red dashed line for measured data and blue line for simulated results).

3 CASE STUDY

Since the NPR includes too many rivers and their riverbeds are dynamically changing due to erosion, deposition and human activities, it is very difficult to obtain a synchronous bathymetric data of the whole NPR. In the last 20 years, three sets of large scale bathymetric data are available: (1) data of 1999 covers almost all rivers in the NPR, including the West River, North River, and East River; (2) data of 2004-2006 covers the main rivers of West River, North River and most of branches; (3) data of 2015 covers the main rivers of West River and North River. According to these three sets of bathymetric data, the riverbed of the NPR demonstrated a continuous degradation and the water depth increased with an average value of 1.45m in the main rivers of the NPR during 1999~2015. In order to evaluate the influence of riverbed degradation on saltwater intrusion, the above three sets of bathymetric data were inputted into the numerical model for case study. Considering the obvious decrease of sediment load from rivers and continuous impact of human activities, the degradation of NPR will be continued at least in the coming decade. Based on the bathymetric data of 1999, an additional case study with a uniform value of 2m of riverbed degradation has also been carried out to evaluate the response of saltwater intrusion to future riverbed degradation. Thus, four case studies were carried out in this paper. For convenience, they are named as case 1999, case 2005, case 2015 and case 2m, respectively. All case studies were run for four months with the same boundary and initial conditions and the results of last fifteen days were used for analysis.

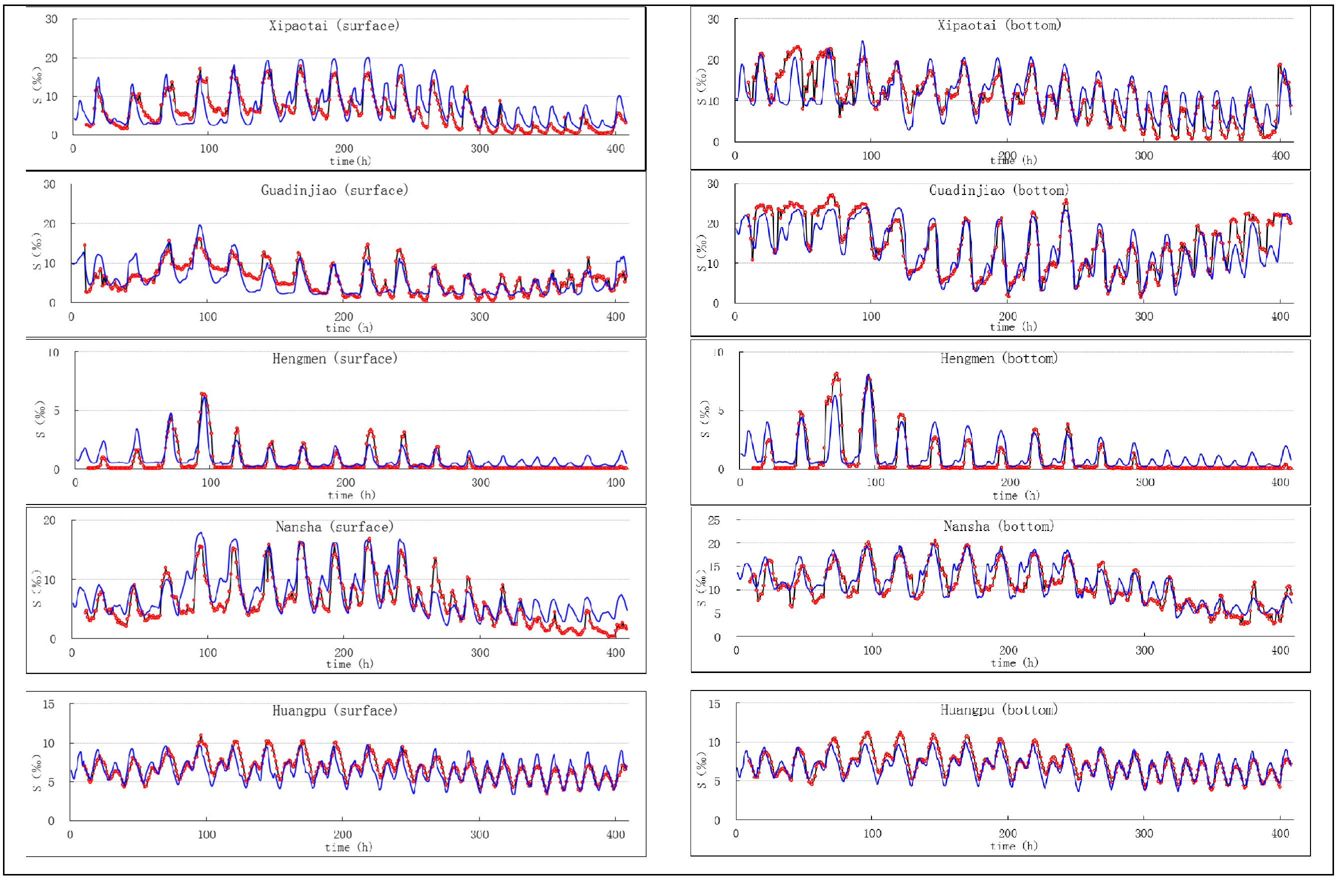

Figure 6. Surface and bottom salinity. (red dashed line for measured data and blue line for simulated results).

4 RESULT AND ANALYSIS

Since the water intakes are placed in rivers of the NPR, the upstream salinity borderline of 0.5‰ and 5‰, which indicates the maximum distance of saltwater intrusion during the last fifteen days of simulation, were plotted for comparison (see Figure 1). During one tidal cycle of neap and middle tide, the hourly sets of longitudinal distributions of surface and bottom salinity alone the maximum depth line of Modaomen River are plotted in Figure 7~Figure 10 for case 2005 and case 2m. The location of the maximum depth line is shown in Figure 1 and the tidal level at Guadinjiao station is plotted in Figure 11 during neap and middle tide.

Figure 1 shows that the salinity borderlines of 0.5‰ and 5‰ entirely moved upstream due to the riverbed degradation from 1999 to 2015. It is clearly included that the deeper water depth leaded to the worse scenario of saltwater intrusion in the NPR. Comparisons indicate that the increased upstream distance of salinity borderlines of 0.5‰ is obviously smaller than that of salinity borderlines of 5‰, which partially presents the index of mixing area in rivers. It should be concerned that the Modaomen River indicates a larger increased distance of salinity borderlines than other rivers even though the value of riverbed degradation is the same in case 2m. In order to investigate the mechanism of this phenomenon, the following analysis will mainly focus on the Modaomen River.

As shown in Figure 6, different rivers demonstrate different characteristic of saltwater intrusion during a semi-month lunar tide cycle of 15 days. Since the Shiziyang is a typical tide dominated outlet, its process of saltwater intrusion has a good relevance to tidal process and its range of salinity corresponds to tidal range. For both surface and bottom layers, salinity start to increase from neap tide and reach its maximal value during spring tide at the Dahu station. The hydrodynamic of Modaomen River is dominated by river discharge. According to the time series of salinity at the Guadinjiao station, the surface salinity starts to increase from neap tide. This is similar to the Dahu station. However, the bottom salinity maintains at a higher value all the time during neap tide and the vertical distribution of salinity is obviously stratified. Both surface and bottom salinity reach its maximal value during the middle tide instead of the spring tide, and then decrease during spring tide. This is obviously different from Shiziyang. Combining the results of Figure 7 and Figure 8, it is found that the density circulation may play the key role for the saltwater intrusion during the neap tide at the Guadinjiao station. The saltwater wedge is the main form of saltwater intrusion in the Modaomen River.

During the neap tide, the tidal range is about 0.86m at the Guadinjiao station. It presents a weaker force of tide. According to Figure 7 and Figure 8, although the surface salinity isoline of 0.5‰, 2‰, 5‰ and 10‰ all moves upward with the influence of riverbed degradation in the Modaomen River, the salinity near the outlet is decreased. In addition, the bottom salinity demonstrates an obvious increase alone the Modaomen River. It means that the larger water depth due to riverbed degradation may obviously enhance the circulation along the longitudinal direction in the Modaomen River. As a result, both the upstream intrusion of bottom saltwater wedge and the downstream diffusion of surface diluted water are accelerated. It increased the amount of upstream transportation of salinity and thus greatly contributed to the worse scenario of saltwater intrusion in the Modaomen River.

During the middle tide, the tidal range is about 1.44m at the Guadinjiao station. According to Figure 9 and Figure 10, both the surface and bottom salinity are increased continually with the enhancement of tidal force. Meanwhile, the vertical stratification of salinity gradually becomes weaker. This means that the density circulation may no longer plays the key role for the saltwater intrusion during the middle tide and the tidal force will contribute more to the saltwater intrusion with the increase of tide range. In addition, an obvious upstream intrusion of bottom high-salinity water from the branch has been observed from Figure 10 (as shown by the red ellipse) during middle tide. These are the reasons why the salinity reaches its maximal value during the middle tide instead of spring tide in the Modaomen River. According to Figure 9 and Figure 10, both surface and bottom salinity isolines moved upward with the influence of riverbed degradation in the Modaomen River during middle tide. Meanwhile, the upstream intrusion of bottom high-salinity water from the branch has been obviously enhanced.

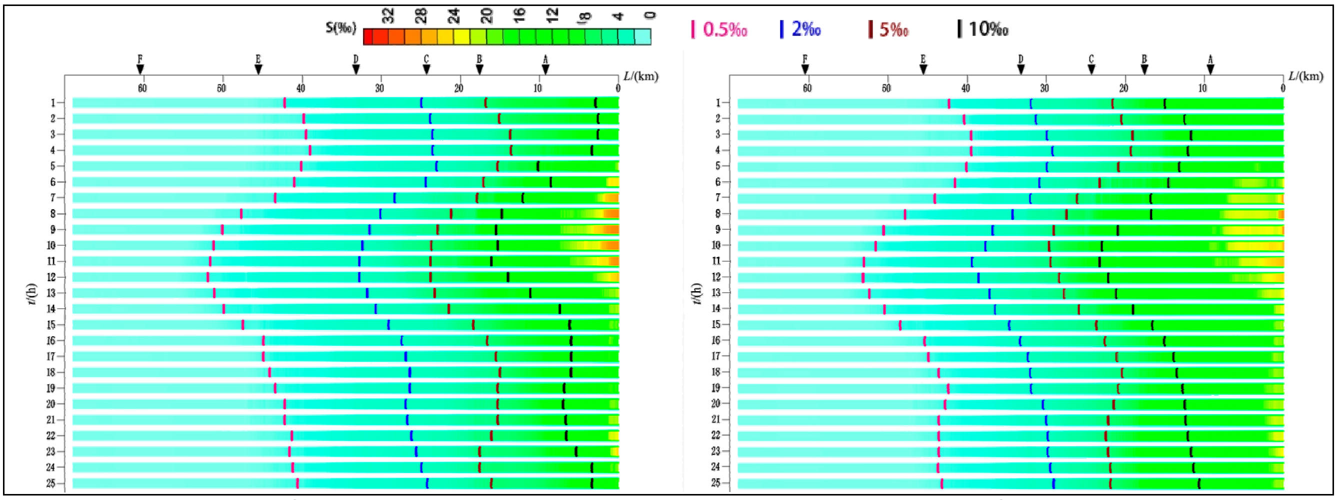

(a) Case 2005 (b) Case 2m

Figure 7. Hourly longitudinal distribution of surface salinity alone the maximum depth line of Modaomen River during neap tide.

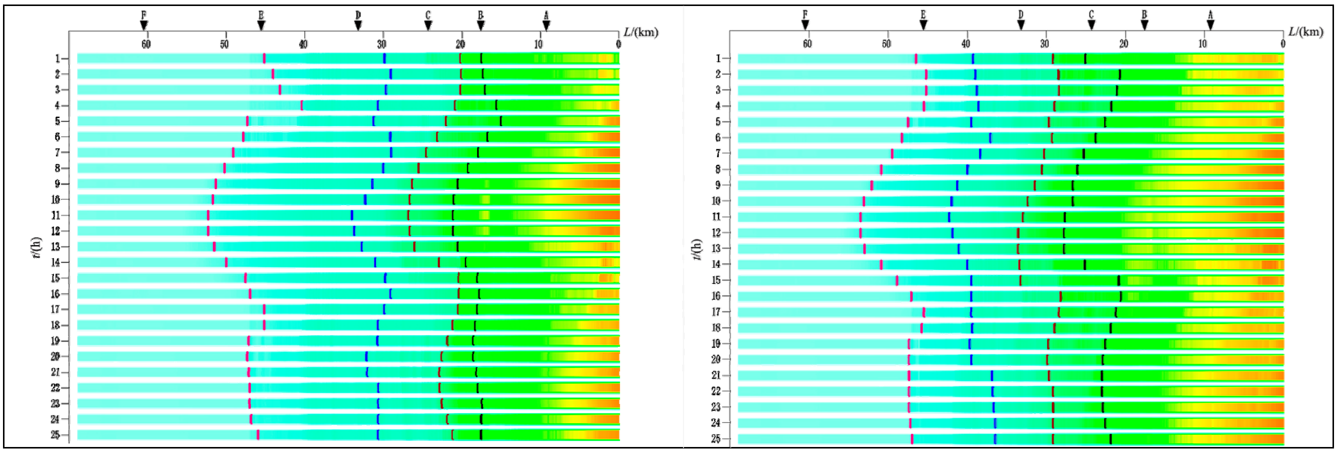

(a) Case 2005 (b) Case 2m

Figure 8. Hourly longitudinal distribution of bottom salinity alone the maximum depth line of Modaomen River during neap tide.

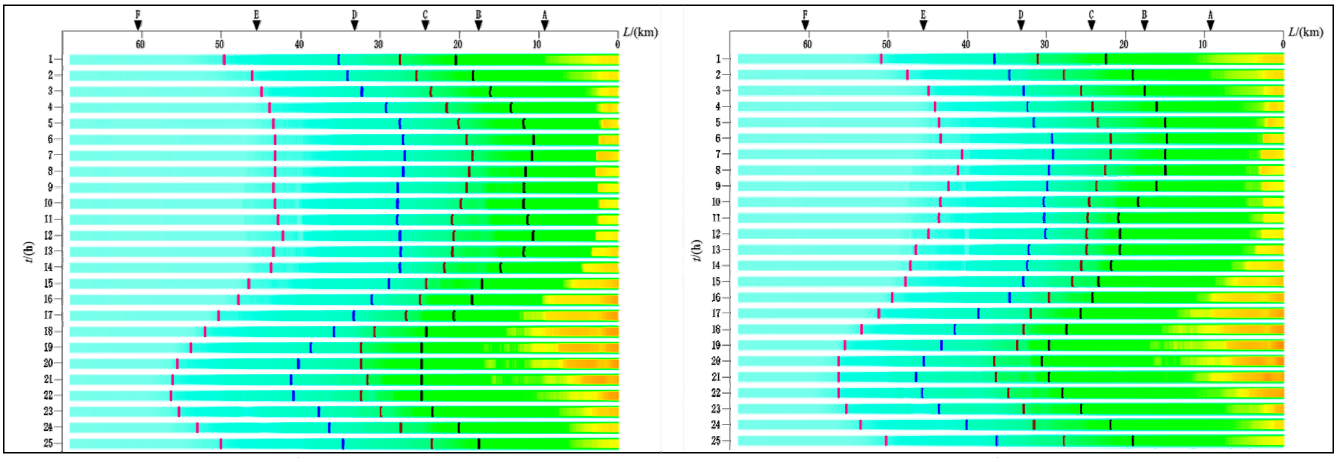

(a) Case 2005 (b) Case 2m

Figure 9. Hourly longitudinal distribution of surface salinity alone the maximum depth line of Modaomen River during middle tide.

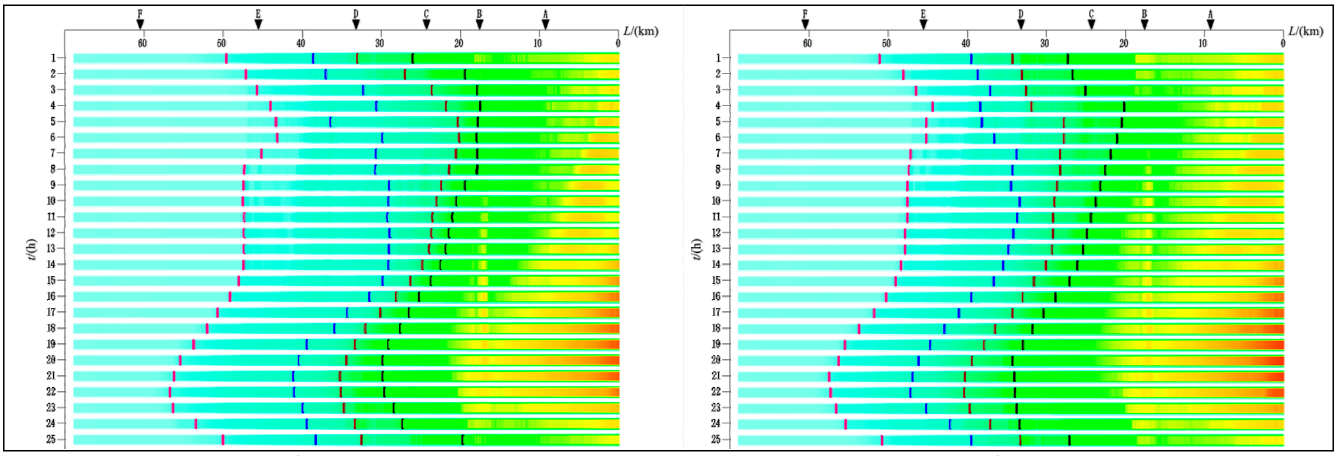

(a) Case 2005 (b) Case 2m

Figure 10. Hourly longitudinal distribution of bottom salinity alone the maximum depth line of Modaomen River during middle tide.

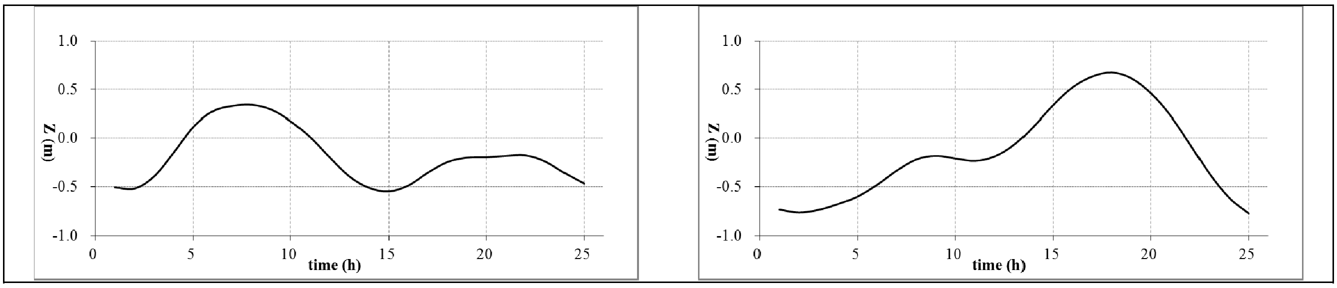

(a) Neap tide (b) Middle tide

Figure 11. Tide at Guadinjiao station during neap and middle tide.

5 CONCLUSIONS

A three-dimensional baroclinic numerical model with high-resolution grids was successfully established and applied to simulate the dynamics of saltwater intrusion in the PRE. Validations against measured data indicate that the used model can properly simulate the dynamic process of saltwater intrusion. Based on this model, numerical experiments were carried out to simulate the dynamic process of saltwater intrusion and evaluate the influence of riverbed degradation on saltwater intrusion in the PRE. Results show that the key dynamic factors leading to saltwater intrusion in the Modaomen River are changing with different tide range. Comparisons indicate that the riverbed degradation leads to an obvious increase in the strength of the saltwater intrusion in the PRE and the scenario of saltwater intrusion is worse in stratified rivers than that in well mixed rivers even though they have similar change of water depth. It seems that the larger water depth due to the riverbed degradation will obviously enhance the vertical circulation along the longitudinal direction especially in the stratified rivers. As a result, both the upstream intrusion of near bottom high-salinity water and the downstream diffusion of surface diluted water are accelerated. These increased the amount of upstream transportation of salinity and thus greatly contributed to the worse scenario of saltwater intrusion in the PRE.

ACKNOWLEDGEMENTS

The research reported herein was funded by the National Science Foundation of China (Grant No. 51409286), the Special Commonweal Research Foundation of the Ministry of Water Conservancy of China (Grant No. 201501010).

REFERENCES

Bao, Y., Liu, J.B., Ren, J., Xu, W.M. & Qi, Z.M. (2009). Research of Law and Dynamic Mechanism for Strong Saline Water Intrusion in Modaomen Waterway. *Science China Physics, Mechanics & Astronomy*, 39(10), 1527-1534.

Bowers, D.G. & Brett, H.L. (2008). The Relationship between CDOM and Salinity in Estuaries: an Analytical and Graphical Solution. *Journal of Maring Systems*, 73(1-2), 1-7.

Bricheno, L.M., Wolf, J. & Islam, S. (2016). Tidal Intrusion within a Mega Delta: an Unstructured Grid Modelling Approach. *Estuarine, Coastal and Shelf Science*, 182(A). 12-26.

Chen, R.L., Liu, C. & Gao, S.Y. (2011). Analysis of the Mechanism on the Saltwater Intrusion in Modaomen Estuary. *Chinese Journal of Hydrodynamics*, 26(3), 312-317.

Chen, W.L., Zou, H.Z. & Dong, Y.J. (2014). Hydrodynamic of Saltwater Intrusion in the Modaomen Waterway. *Shuikexue Jinzhan*, 25(5), 713-723.

Gong, W.P. & Shen, J. (2011). The Response of Salt Intrusion to Changes in River Discharge and Tidal Mixing during the Dry Season in the Modaomen Estuary, China. *Continental Shelf Research*, 31(7), 769-788.

Han, Z.Y., Tian, X.P. & Liu, F. (2010). Study on the Causes of Intensified Saline Water Intrusion into Modaomen Estuary of the Zhujiang River in Recent Years. *Journal of Marine Sciences*, 28(2), 52-59.

Hu, X. & Mao, X.Z. (2012). Study on Saltwater Intrusion in Modaomen of the Pearl Estuary. *Shuili Xuebao*, 43(5), 529-536.

Jia, L.W., Luo, Z.G. & Yang Q.S. (2006). Impacts of Huge Amount of Sand Dredging on Riverbed Morphology and Tidal Dynamics of the Lower Reaches of the Dongjiang River and the Dongjiang River Delta. *Acta Geographica Sinica*, 61(9), 985-994.

Kong, L. & Chen, X.H. (2015). Analysis on the Influence Factors of Saltwater in Pearl River Estury. *Water Resource Protection*, 31(6), 94-97.

Lai, Z.G., Ma, R.H., Chen, C. & Beardsley, R.C. (2015). Impact of Multichannel River Network on the Plume Dynamics in the Pearl River Estuary. *Journal of Geophysical Research Oceans*, 120(8), 5766-5789.

Li, C.C. (2013). My Opinion on salt Tide in the Pearl River Estuary. *Tropical Geography*, 33(4), 496-499.

Lu, C., Yuan, L.R., Gao, S.Y., Chen, R.L. & Su, B. (2013). Experimental Study on the Relationship between Tide Strength and Salt Intrusion Length. *Advances in Water Science*, 24(3), 251-257.

Ou, S.Y. (2009). Spatial Difference about Activity of Saline Water Intrusion in the Pearl (Zhu Jiang) River Delta. *Scientia Geographica Sinica*, 29(1), 89-92.

Wang, B., Zhu, J.R., Wu, H., Yu, F.J. & Song, X.J. (2012). Dynamics of Saltwater Intrusion in the Modaomen Waterway of the Pearl River Estuary. *Science China (Earth Sciences)*, 55(11), 1901-1918.

Yuan, L.R., Yang, Q.S. & Chen, R.L. (2012). Relationship between Sub-tidal Salt Intrusion Length and Tidal Amplitude in the Modaomen Estuary of Xijiang River. *Journal of Sichuan University (Engineering Science Edition)*, 44(2), 183-187.

Zhang, W., Yan, Y.X., Zhu, Y.L. & Yang, M.Y. (2008). Impact of Sand Excavation and Waterway Regulation on Hydrodynamics of Pearl Networks. *Shuili Xuebao*, 39(9), 1098-1104.

Zou, H.Z., Liu, G., Wang, L. & Chen, Y.X. (2013). The Dynamic Response of Salt-water Intrusion to Tidal Phase and Range in the Pearl River Estuary. *35th IAHR Congress*, 6(1), 1-12.

Proceedings of the 37th IAHR World Congress
August 13 – 18, 2017, Kuala Lumpur, Malaysia

MAPING TIDAL RESIDUAL CURRENTS AND SUSPENDED SEDIMENT PATTERN IN THE YONGJIANG ESTUARY, CHINA USING A NUMERICAL MODEL

YU KUAI[1], JIANFENG TAO[2], QING ZHANG[3] WEIQIU CHEN[4] & WEIQI DAI[5]

[1, 2] State Key Laboratory of Hydrology-Water Resources and Hydraulic Engineering, Hohai University Nanjing, China,
kuaiyu@hhu.edu.cn
[1, 2, 3, 4, 5] College of Harbor, Coastal and Offshore Engineering, Hohai University Nanjing, China,

ABSTRACT

A 2D tidal current and suspended sediment model which takes the Yongjiang River and the out sea area as the key research area are presented in this paper. The numerical model is employed to carry out the simulation of tidal hydrodynamics and sediment dynamics of the concerned area in the second half of June 2015. A good agreement is found between the in situ measured data and the simulated results. Analysis on the computed residual current and sediment transport pattern shows that, the residual current generally causes transport from northwest to southeast in the sea area, and seaward transport in the river. The sediment transport pattern is almost in accordance with the residual current pattern except local regions near the river mouth. The sediments are transported into the Yongjiang River by the flood current and the net sediment transport is landward near the river mouth. The local distinctions between the residual current and sediment transport pattern at the Yongjiang Estuary are due to the time lag between the hydrodynamic and sediment transport processes.

Keywords: Yongjiang Estuary; residual current; suspended sediment transport; sediment transport pattern.

1 INTRODUCTION

Yongjiang Estuary is located on the east coast of Zhejiang Province, China and south of Hangzhou bay (Figure 1). The Yongjiang River with meandering shoreline is narrow and shallow, of which the channel width is about 210-400m. In the concave bank of the river bend, there is usually a deep channel with the depth of approximately 5-10 m, which is the same as the water depth at the entrance of the estuary. As for the rest of the areas of the river, the water depth is within 5m. There is the Jintang Channel which connects the Hangzhou bay in the north and the Cezi Channel, Luotou Channel and Chuanshan Channel in the east outside the Yongjiang River (Chen, 1989). According to the classification criterion set by Xiong and Zeng (2008), Yongjiang Estuary belongs to the bending transition estuary, which is featured by curved horizontal shapes and strong river discharge. The tidal wave at Yongjiang estuary is dominated by standing wave and has the characteristics of progressive one as well, and the sediment concentration contained at this kind of estuary is relatively high.

A series of studies on Yongjiang Estuary have been carried out by scholars. It is found that the tide in the Yongjiang River and the Jintang Channel is irregular semidiurnal tide, and due to the interconnected channels and complex topography in the sea area, the tidal wave deformation and tide level characteristics in this area are quite different from the Hangzhou Bay and other sea areas in Zhejiang Province. The tidal waves at the Yongjiang Estuary are not only single standing waves or progressive waves have the features of both kinds of these two waves (Chen, 1989; Yang et al., 1989; Zhang, 1993). The sediments coming from the upstream of the Yongjiang River are rare and the sediments in the Yongjiang River mainly come from the sea area. According to the in situ measured data, the suspended and bed materials are both primary clayey silt (Yan, 2011; Chen et al., 2012; Jiang et al., 2013). The aforementioned research results are mostly based on multi-station or multi-section observation data and show the basic hydrodynamic and sediment characteristics at the Yongjiang Estuary. With the development of the social economics, human activities at the Yongjiang Estuary have become increasingly frequent, and it is necessary to have a clearer understanding of the hydrological sediment spatial and temporal distribution and transport features. Numerical modeling can help to describe the hydrological sediment processes more specifically and give the corresponding spatial and temporal distribution characteristics at the research area as well, so it plays an irreplaceable role in quantitative forecasting researches and applications.

A 2D tidal current and suspended sediment model based on in situ measured data in 2015 was established. The model takes the Yongjiang River and the sea area as the key research area and the residual current and sediment transport pattern at the Yongjiang Estuary were analyzed. The research results can be adopted as a reference to study the tidal current and sediment transport pattern and fluvial process at the similar tidal estuary.

  / ISSN 1562-6865 (Online) - ISSN 1063-7710 (Print)

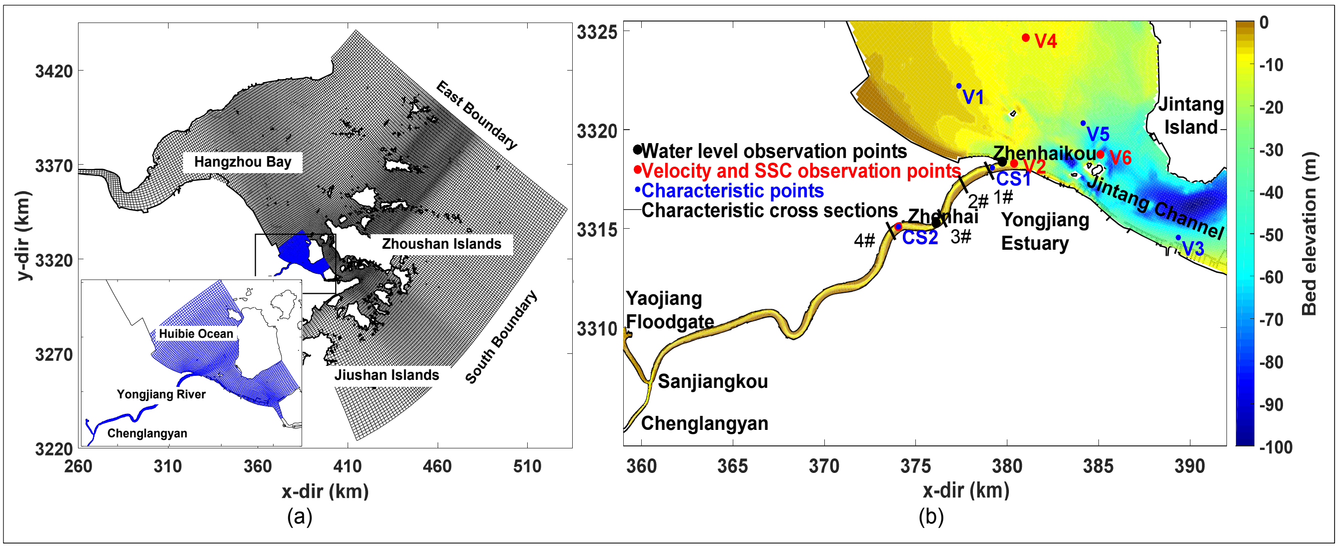

Figure 1. Numerical grids (a) and the location of the Yongjiang Estuary (b).

2 NUMERICAL MODEL

2.1 Basic equations

Since Yongjiang Estuary is a very shallow and vertically well-mixed estuary, with horizontal scales of more than two orders of magnitude greater than the vertical scales, and horizontal transport is of primary interest, the depth-averaged transport equations can be used for this modeling purpose. As the grain size of the bed material at the Yongjiang Estuary is very fine, and the median particle diameter at the bed is quite close to the one suspended, it can be considered that the cohesive sediments are transported as suspended load only at this area.

The continuity equation is given by:

$$\frac{\partial \zeta}{\partial t}+\frac{1}{G_\xi G_\eta}\frac{\partial[G_\eta(d+\zeta)U]}{\partial \xi}+\frac{1}{G_\xi G_\eta}\frac{\partial[G_\xi(d+\zeta)V]}{\partial \eta}=0 \qquad [1]$$

The equations for conservation of momentum are given by:

$$\frac{\partial(HU)}{\partial t}+\frac{1}{G_\xi}\frac{\partial(HUU)}{\partial \xi}+\frac{1}{G_\eta}\frac{\partial(HVU)}{\partial \eta}+\frac{HUV}{G_\xi G_\eta}\frac{\partial G_\xi}{\partial \eta}-\frac{HVV}{G_\xi G_\eta}\frac{\partial G_\eta}{\partial \xi}-fHV=-\frac{gH}{G_\xi}\frac{\partial \zeta}{\partial \xi}+\frac{1}{G_\xi}\frac{\partial(H\tau_{\xi\xi})}{\partial \xi}+\frac{1}{G_\eta}\frac{\partial(H\tau_{\eta\xi})}{\partial \eta}+\frac{H\tau_{\xi\eta}}{G_\xi G_\eta}\frac{\partial G_\xi}{\partial \eta}-\frac{H\tau_{\eta\eta}}{G_\xi G_\eta}\frac{\partial G_\eta}{\partial \xi}+\frac{\tau_{s\xi}-\tau_{b\xi}}{\rho} \qquad [2]$$

$$\frac{\partial(HV)}{\partial t}+\frac{1}{G_\xi}\frac{\partial(HUV)}{\partial \xi}+\frac{1}{G_\eta}\frac{\partial(HVV)}{\partial \eta}+\frac{HUV}{G_\xi G_\eta}\frac{\partial G_\eta}{\partial \xi}-\frac{HUU}{G_\xi G_\eta}\frac{\partial G_\xi}{\partial \eta}+fHU=-\frac{gH}{G_\eta}\frac{\partial \zeta}{\partial \eta}+\frac{1}{G_\xi}\frac{\partial(H\tau_{\xi\eta})}{\partial \xi}+\frac{1}{G_\eta}\frac{\partial(H\tau_{\eta\eta})}{\partial \eta}+\frac{H\tau_{\eta\xi}}{G_\xi G_\eta}\frac{\partial G_\eta}{\partial \xi}-\frac{H\tau_{\xi\xi}}{G_\xi G_\eta}\frac{\partial G_\xi}{\partial \eta}+\frac{\tau_{s\eta}-\tau_{b\eta}}{\rho} \qquad [3]$$

Transport of the suspended sediment in the model is based on the advection-diffusion equation.

$$\frac{\partial(HS)}{\partial t}+\frac{1}{G_\xi}\frac{\partial(HUS)}{\partial \xi}+\frac{1}{G_\eta}\frac{\partial(HVS)}{\partial \eta}=\frac{1}{G_\xi}\frac{\partial}{\partial \xi}\left(\upsilon_s\frac{H}{G_\xi}\frac{\partial S}{\partial \xi}\right)+\frac{1}{G_\eta}\frac{\partial}{\partial \eta}\left(\upsilon_s\frac{H}{G_\eta}\frac{\partial S}{\partial \eta}\right)+E-D \qquad [4]$$

where t is time step; ξ and η are orthogonal curvilinear coordinates; G_ξ and G_η are lame coefficients; ζ is tidal level; U and V are depth-averaged flow velocities in ξ and η directions, respectively; H is total water depth; d is still water depth; $f=2\omega\sin\varphi$ is Coriolis parameter (ω is rotational-angular velocity of the earth and φ is latitude of the research area); g is gravitational acceleration; ρ is water density; $\tau_{\xi\xi}$, $\tau_{\xi\eta}$, $\tau_{\eta\xi}$ and $\tau_{\eta\eta}$ are turbulent shear stress; $\tau_{s\xi}$ and $\tau_{s\eta}$ are surface wind induced shear stress; $\tau_{b\xi}$ and $\tau_{b\eta}$ are bed bottom shear stress; S is depth averaged Suspended Sediment Concentration (SSC); υ_s is sediment diffusion coefficient; E and D are sediment erosion flux and deposition flux respectively.

2.2 Model setup

In order to precisely simulate the flow and suspend sediment transport at the Yongjiang Estuary and save computing time as well as memories, two nested models of two different spatial resolutions were established.

The landward boundaries of the big model were set at the Chenglangyan Station in Fenghua River and the Yaojiang Floodgate in Yaojiang River. The seaward boundaries of the big model start form the 123°E in the east direction, the Jiushan Islands in the south direction and the north band of the Hangzhou Bay in the north direction. The computational domain of the small model starts from the Chenglangyan Station at the upstream as well. The seaward boundaries of the small model are located at the junction of the Jintang Channel and the Luotou Channel in the south direction and north of Huibie Ocean in the north direction (Figure 1.a). The grids in the sea area of the big model are sparser compared to the ones in the river, the resolutions of which are approximately 400m*400m and 100m*30m, respectively. Likewise the resolutions of the grids in the small model are 100m*100m in the sea and 30m*10m in the river.

The initial water level for the big model is set to the average water level at the boundary grid points, and the initial current velocity was set to be 0. As suspended sediment transport calculation to take more time to stabilize than hydrodynamic calculation, the initial SSC was set to be a constant value.

Along the open boundaries of the big model, the flow computation is driven by 13 main tidal constituents (M2、S2、N2、K2、K1、O1、P1、Q1、MF、MM、M4、MS4、MN4) given by the TPXO.3 global tidal model (Egbert and Erofeeva, 2002), and the corresponding tide level was calculated by the following formula.

$$\zeta(t) = A_0 + \sum_{k=1}^{13} f_k H_k \cos[\omega_k t + (\nu_0 + u)_k - G_k] \quad [5]$$

where A_0 is averaged sea level, H_k、G_k、f_k、ω_k、$(\nu_0 + u)_k$ correspond to amplitude, epoch, nodal factor, angular velocity and initial phase of the k-th tidal constituent, respectively. The seaward tidal level boundary condition for the small model was driven from the big model, and the landward boundary of the model was given by the measured discharge at the Chenglangyan Station (Figure 2). The suspended sediment was considered to be equilibrium transported at the seaward boundaries and driven from the measured concentration at the landward boundary. At the closed boundaries, the normal component of the current velocity and SSC gradient were set to 0.

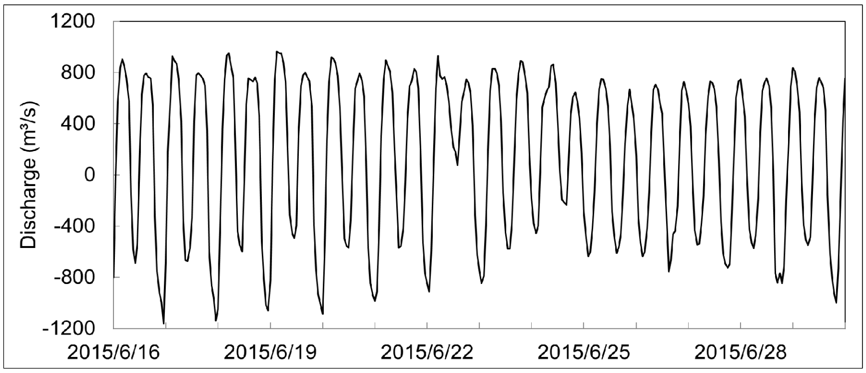

Figure 2. Measured discharge process at the Chenglangyan Station.

In the models, Manning coefficient, n was set to be 0.018~0.02(s $m^{-1/3}$). The setting velocity of sediment was set to be one of the floccules particles with the maximum size (0.037mm), which is 0.5mm/s. The deposition and resuspension flux were computed by the widely adopted Partheniades-Krone (1965) formulas (Partheniades, 1965), in which the critical shear stress was set to be 1000N/m^2 for deposition (Edmonds and Slingerland, 2009), and 0.5~0.6 N/m^2 for erosion according to the measured data and lab experiment. Based on the density of the bed material, the erosion parameter was set to be 0.0001～0.0004 kg/m^2s.

2.3 Model validation

The model simulates the tidal current and suspended sediment transport from 16th to 30th June, 2015 (including a complete process of spring, mid and neap tide). Based on the recorded data at the stations (Figure 1.b), the flow and sediment calculation results during the spring and neap tide period were validated (Figure 3).

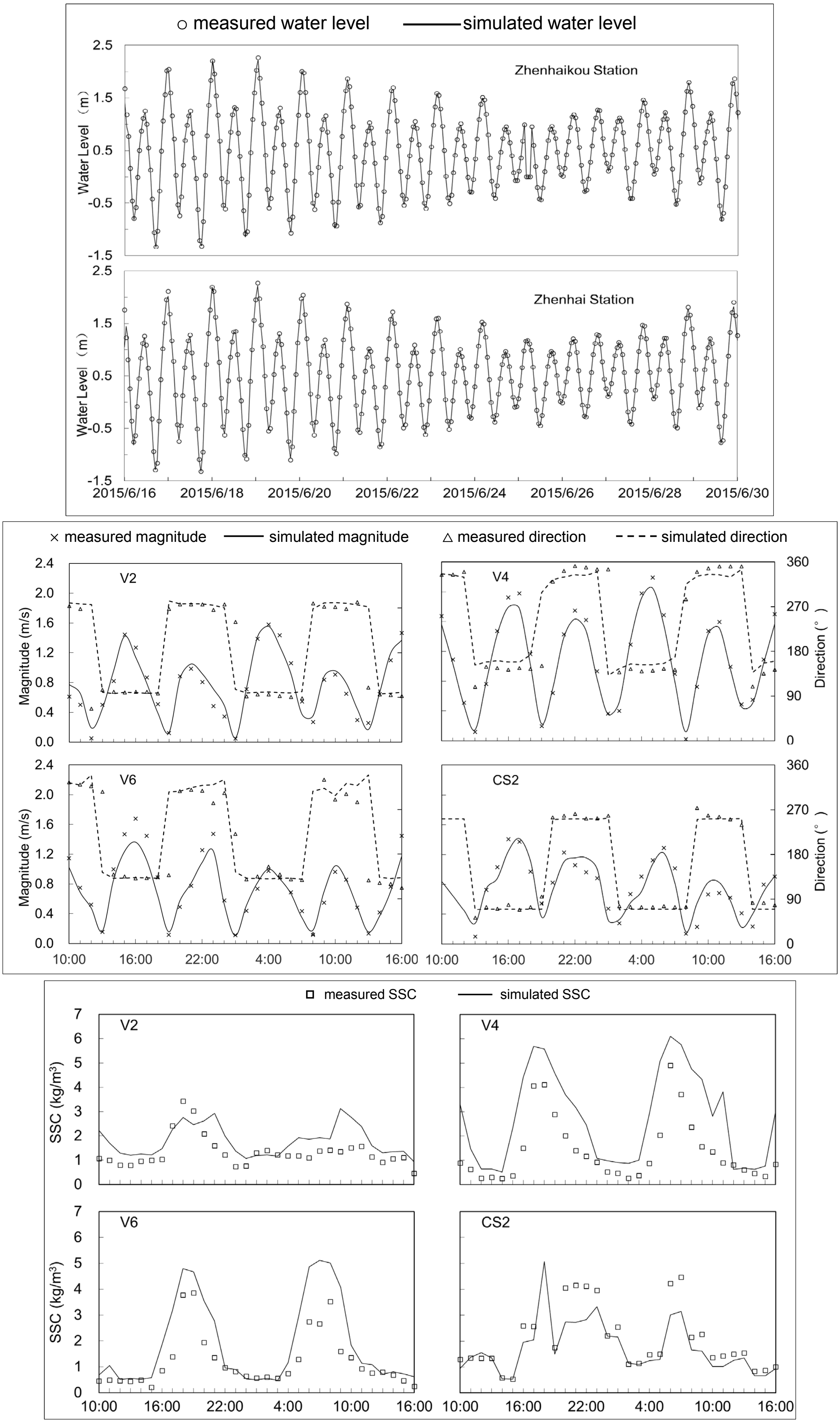

Figure 3. Comparison between model results and measured data for water level, velocity and SSC.

Figure 4 shows the flow and SSC field at the Yongjiang Estuary at the flood and ebb tide moment during the spring tide. During the flood tide period, partial tide current moves through the Jintang Channel into the Yongjiang River. During the ebb tide period, the current at the sea area veers firstly, and along with the water level falling, the tidal current and upstream runoff in the Yongjiang River discharge into the sea together. The maximum flood tide velocity at the Zhenhaikou station appears about 2 hours before the high tide. Similarly, the maximum ebb tide velocity occurs about 2 hours before the low tide. The maximum flow velocity appears neither at the same time with the crest value of the tidal level, nor with the middle tidal level, which means that the tidal wave has both the characteristics of progressive wave and standing wave at this area. This conclusion agrees well with previous research results (Chen, 1989; Yang et al., 1989; Zhang, 1993). The current in Yongjiang River is reciprocating current. The tidal current at the Yongjiang Estuary during the neap tide period is similar to it during the spring tide period in direction, and the overall flow pattern is consistent with the measured data. During the flood tide period, the tidal current with low SSC transports from the southeast through the Jintang Channel to the north, and the minimum SSC is less than 0.5kg/m^3; and during the ebb tide period, the tidal current with high SSC transports through the Huibie Ocean and north Jintang Channel to the south sea area, and the maximum SSC is over 5.0kg/m^3. Hence, the SSC is higher at the north side of the Jintang Channel, which is in accordance with the measured suspended sediment distribution pattern, further showing the rationality and reliability of the simulated results.

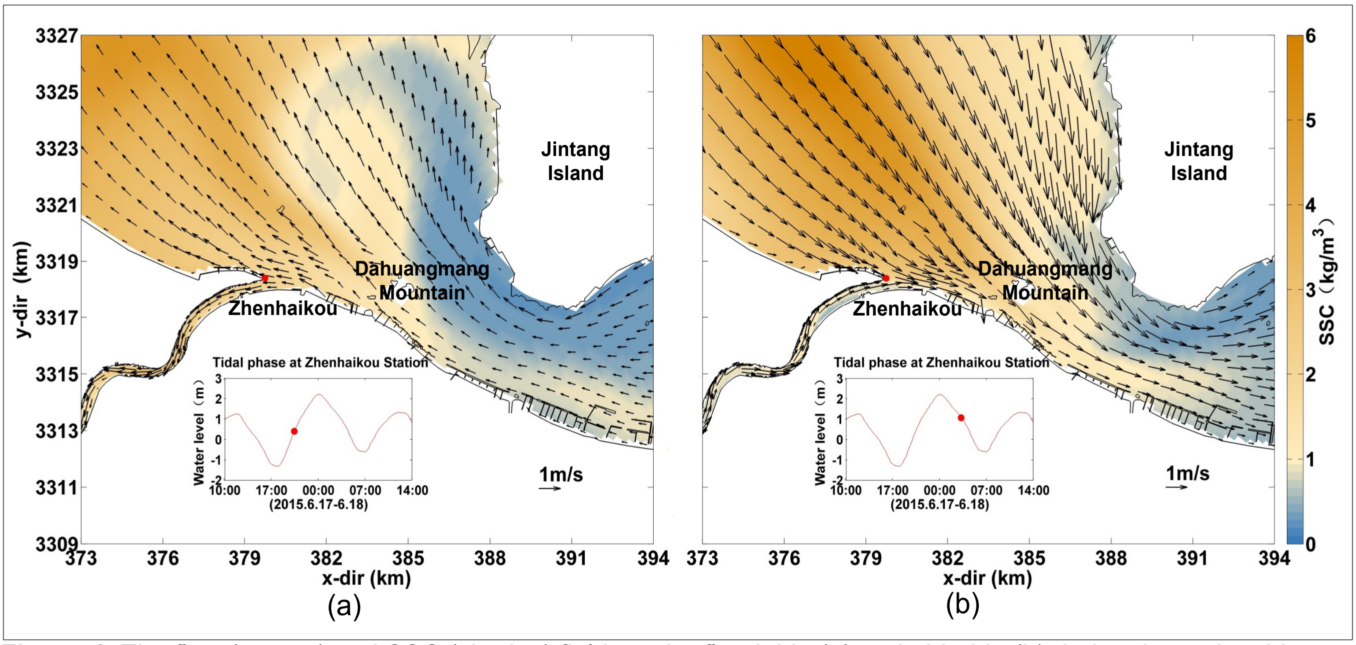

Figure 4. The flow (arrows) and SSC (shades) fields at the flood tide (a) and ebb tide (b) during the spring tide.

3 METHOD

3.1 Residual current calculation

The tidal dynamic is very strong at the Yongjiang Estuary, and the SSC distribution is supposed to be related to the transport caused by tidal residual currents. Thus, the tidal residual current can indicate the tendency of the flow and sediment transport to some extent. The Lagrangian Residual Velocity (LRV) which represents the time averaged net displacement of a water particle during n tidal periods (Zimmerman, 1979) can be driven from the Stokes formula, and be expressed by combining the Eulerian Residual Velocity (ERV) and the Stokes drift velocity as follows:

$$\vec{u}_L = \vec{u}_E + \vec{u}_S \qquad [6]$$

The ERV represents the time averaged velocity of a fix point in the field during n tidal periods (Abbott, 1960) and can be expressed as below:

$$\vec{u}_E = \frac{1}{nT}\int_{t_0}^{t_0+nT}\vec{u}dt \qquad [7]$$

The Stokes drift velocity can be driven from the Longuet-Higgins formula (Longuet-Higgins, 1969) and is defined as:

$$\vec{u}_S = \frac{1}{nT}\int_{t_0}^{t_0+nT}\left(\int \vec{u}\,dt \cdot \nabla\vec{u}\right)dt \qquad [8]$$

where T is the time of one tidal period, n is the number of the tidal periods, and $\vec{u}$ is the instantaneous velocity at the calculation point.

3.2 Sediment transport rate calculation

As the calculation of the tidal residual current does not take the time lag between sediment transport and flow movement into account, the sediment transport direction could be opposite to the residual current direction locally. Thus, the residual current calculation results can only be an indication to the suspended sediment net transport. As a consequence, it is still necessary to calculate the sediment net transport patterns in the research area, and the net sediment discharge rate unit width can be expressed as:

$$Q_s = \frac{1}{nT}\int_{t_0}^{t_0+nT} H\vec{u}S dt \qquad [9]$$

where H is the local overall water depth, and S is the instantaneous depth averaged SSC.

4 RESULTS AND ANALYSIS

The Zhenhaikou Station is located just outside the mouth of the Yongjiang River, therefore, the data here can well reflect the tidal level characteristics of the adjacent sea area. According to the statistics of the all year round water level data at the Zhenhaikou Station in 2015, the tidal range cumulative frequency of the spring, mid and neap tide during the second half of June were 10%, 50% and 75% respectively, so it can be considered to be the combination of three typical tidal type. As the impact of the upstream discharge is greater during the flood season, this article only takes this condition into account, and the computation results only represent the features during this season.

4.1 Residual current field

Figure 5 illustrates the tidal averaged ERV and LRV field during the spring and neap tide. It can be seen from the figure that, apart from the little differences at the river mouth, the tidal induced LRV and ERV field at this area are almost the same.

During the spring tide period, as the hydrodynamic at the ebb tide outweighs that at the flood tide, the overall residual current directs to southeast at the sea area. Outside of the river mouth, one part of the tidal current affected by the river discharge turns to southwest, and the other part forms a clockwise circumfluence near the Dahuangmang Mountain. At the southwest part of the Jintang Island, there is a local flood flow dominant area, which is in accordance with previous studies based on field measurements (Wang and Chen, 1989), and between this area and the ebb flow dominant area at the west part of the Jintang Channel, there is a weak anticlockwise circumfluence. Consider the magnitude of the residual current, it can reach over 0.4m/s at the middle part north to the river mouth and it is only about 0.1m/s at the shoal places. Near the west bank of the Jintang Channel, the residual current is relatively stronger and can rise to more than 0.3m/s. At the east side of the Dahuangmang Mountain the residual current is weaker than the one at the west part. In the Yongjiang river channel, caused by the upstream runoff, the residual current transports seaward and can reach 0.35m/s near the river mouth.

Like the spring tide period, the residual current during the neap tide period shows similar transport tendency. Since the hydrodynamic is relatively weaker during the neap tide period, the magnitude of the residual current is approximately 0.1m/s less than the one during the spring tide period. Besides, the clockwise circumfluence at the Dahuangmang Mountain is not as obvious as it is during the spring tide and the anticlockwise circumfluence is closer to the Jintang Island as well.

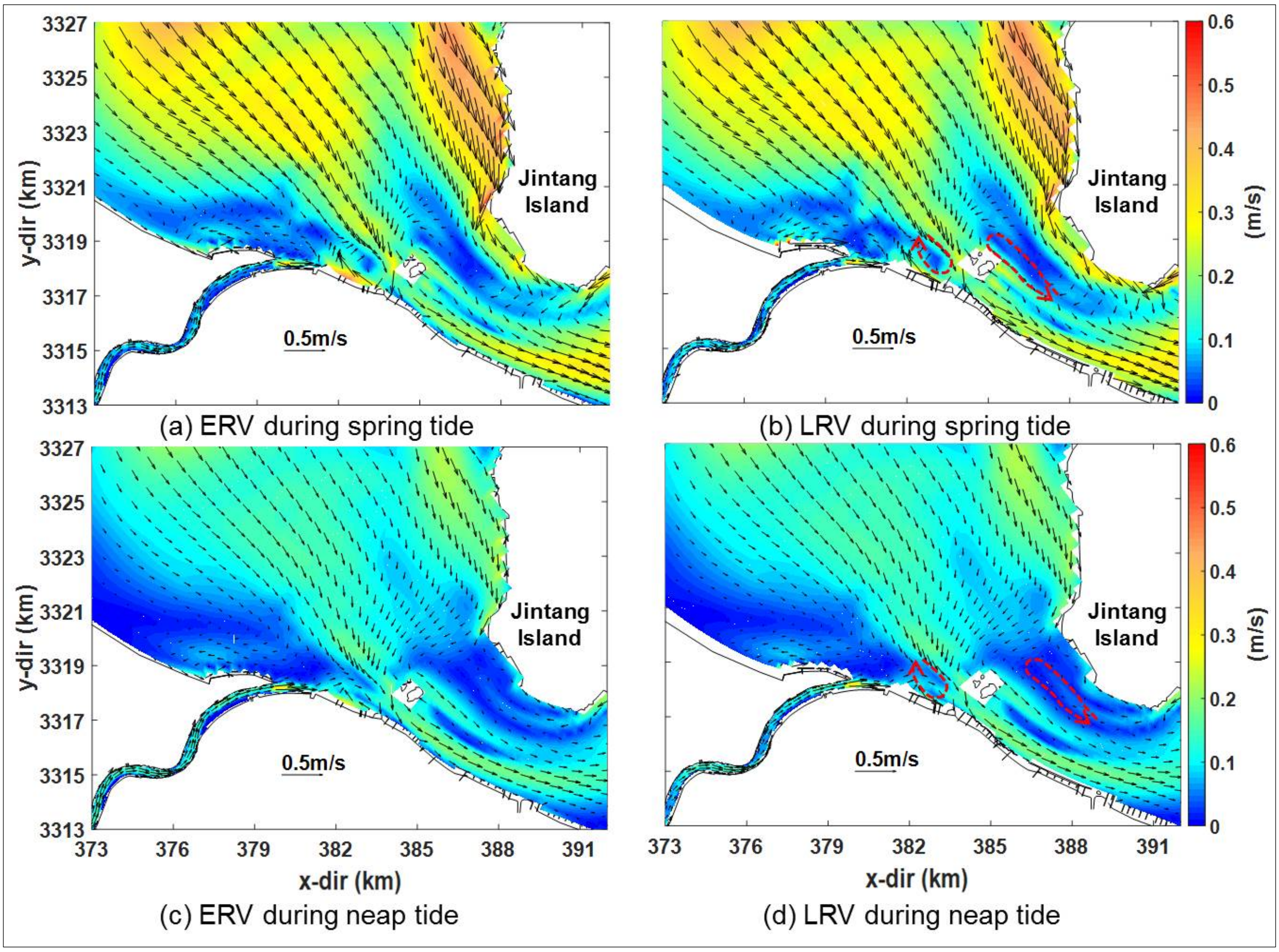

Figure 5. Tidal averaged residual current fields (the shades indicate the magnitude of the residual current velocity).

4.2 Sediment transport pattern

Figure 6 indicates the sediment transport rate unit width at the Yongjiang Estuary during the spring and neap tide based on Eq. [9], and the sediment discharge during one whole tide period (including two flood tide and ebb tide processes) at the given cross sections in the Yongjiang River is shown in Table 1. Compared to Figure 5, the overall sediment transport direction at the sea area is similar to the residual current direction that is from north to south.

Table 1. Sediment discharges at the characteristic cross sections.

Cross section	Sediment discharges in spring tide (10^6kg/24h50min)			Sediment discharges in neap tide (10^6kg/24h50min)		
	Flood tide	**Ebb tide**	**Net**	**Flood tide**	**Ebb tide**	**Net**
1#	177.56	-76.13	101.43	10.54	-7.18	3.35
2#	78.78	-53.54	25.24	3.69	-5.82	-2.13
3#	75.57	-67.75	7.82	4.14	-10.67	-6.53
4#	37.25	-45.87	-8.62	2.60	-10.27	-7.68

During the spring tide, the suspended sediments mainly gather in the deep channel and transport to southeast in the Jintang Channel and the net sediment transport rate can reach up to 25kg/ (m · s). However, at the north side of river mouth, the suspended sediments transport the opposite direction of the overall patterns. As the north-entering sediments transport to the Dahuangmang Mountain (about the same place of the clockwise circumfluence), one part turn back and transport northward coming into the Yongjiang River, which causes the sediment transport pattern to be landward at the river mouth, and this is just the opposite direction of the residual currents in this area. The northward transporting sediment at the north side of the river mouth is in a small quantity, of which the transport rate unit width is less than 5kg/ (m · s). From the 1~3# cross sections in the river, the sediment transports to the upstream and the magnitude is much larger near the river mouth than it is in the upstream areas.

During the neap tide period, the overall sediment transport shows similar pattern as it is during the spring tide period. However, as the hydrodynamic during the neap tide is relatively smaller, the tidal averaged sediment transport rate in this period is one order smaller in magnitude than it in the spring tide period. Like the residual current field, the sediment transport capability is weak at the southwest side of the Jintang Island and there is an anticlockwise circumfluence as well. Compared to the sediment transport during the spring tide period, the sediment still moves landward at the river mouth during the neap tide period, but the transport rate is much smaller. The net sediment stops transporting landward at the 2# cross section, and the net sediment discharge turns to be close to it in the spring tide period at the 4# cross section.

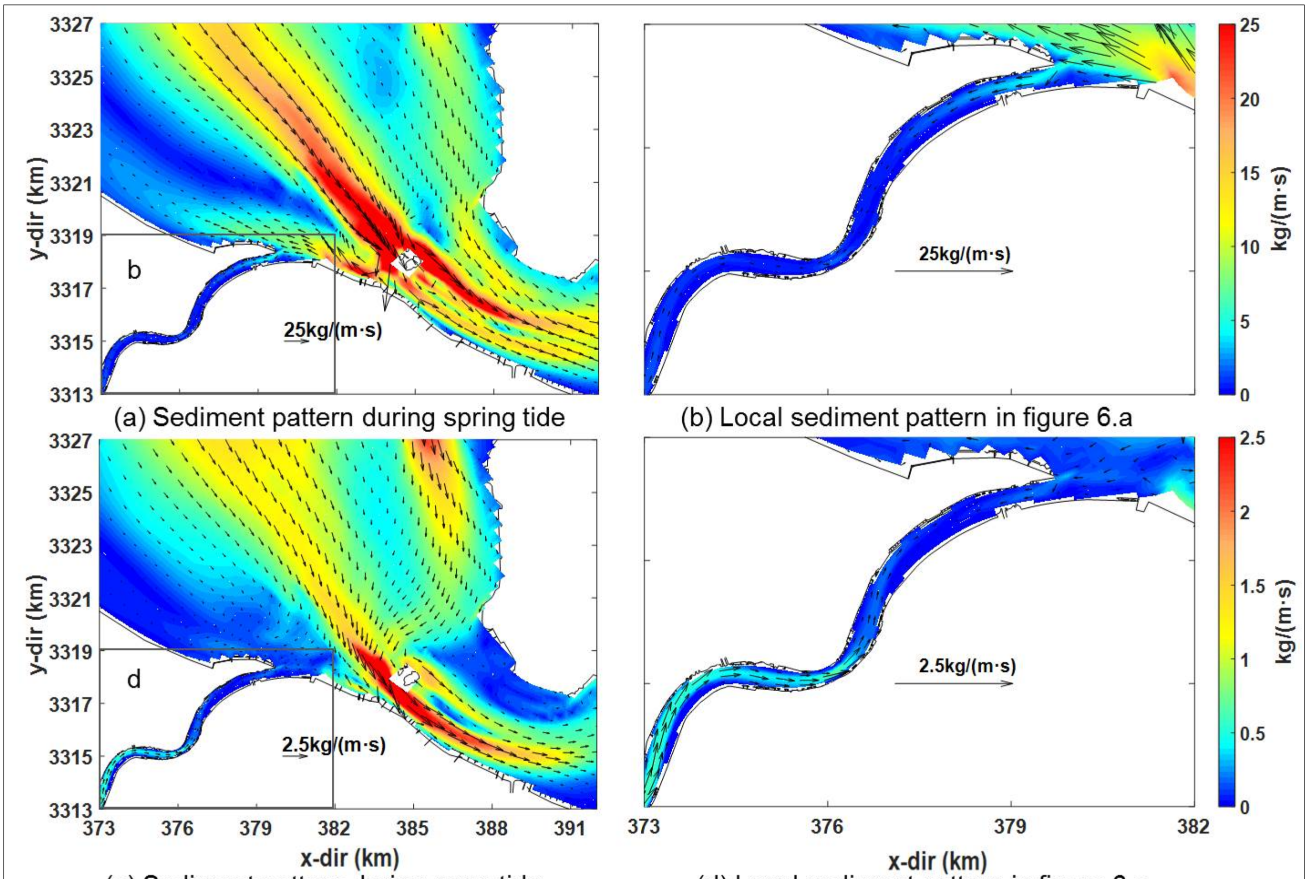

Figure 6. The tidal averaged sediment transport rate unit width (the shades indicate the magnitude of the transport rate).

4.3 Difference analysis

In order to analyze the local differences between the residual current and sediment transport pattern, the flow velocity and SSC processes (Figure 7) of five characteristic points (Figure 1.b) during the spring and neap tide were taken to study the relation between tidal current and sediment transport. Around the V1 point at the north sea area, during the spring tide, as the increase of the ebb tide velocity, the SSC rises as well, and peaks at the maximum value about 2~3h after the maximum ebb velocity point; during the spring tide period, the depth averaged SSC falls gradually as the water level and flood tide velocity increase, and there is a sharp decrease in the SSC at the maximum flood tide velocity point, after which the SSC continues to decrease steadily and reaches to the bottom value at the minimum flood tide velocity point. At the V5 point, the crest value of the SSC appears when the minimum flood or ebb tide velocity occurs, and the SSC magnitude is relatively small at both the maximum flood and ebb tide velocity points, so the sediment transport pattern is similar to the residual current pattern around the V5 point, that is entering in the north and leaving in the south. At the V3 point, during the neap tide period, although the SSC in the flood tide period is larger than it in the ebb tide period, the duration of the ebb tide is longer than it of the flood tide and the ebb tide velocity is relatively larger. During the spring tide period, the crest value of the SSC appears about 2h after the maximum ebb tide velocity occurring and the SSC keeps decreasing during the flood tide period. As a consequence, the sediment transport is the same direction as the ebb tide current that is from northwest to south east.

At the CS1 point in the river near the mouth, during the spring tide period, there are two SSC crest values in one tide period, and they appear 1h after the maximum flood and ebb tide velocity occurring respectively.

The lowest SSC appears at about 1~2h after the minimum flood and ebb tide velocity points. During the neap tide period, the SSC crest value appears around the maximum flood tide velocity point, but at the maximum ebb tide velocity point, the SSC is quite small. Thus, it can be concluded that, affected by the upstream runoff, the residual current in the river is seaward, but as the overall SSC during the flood tide period is larger than it in the ebb tide period, the sediments near the river mouth transport landward. At the CS2 point in the Yongjiang River, the SSC crest value appears 1~2h after the minimum ebb tide velocity occurring during both spring and neap tide. The tidal averaged SSC is almost the same during the flood and ebb tide period, but the ebb tide velocity is apparently larger than the flood tide velocity, so the sediments around the CS2 point transport seaward during the neap tide.

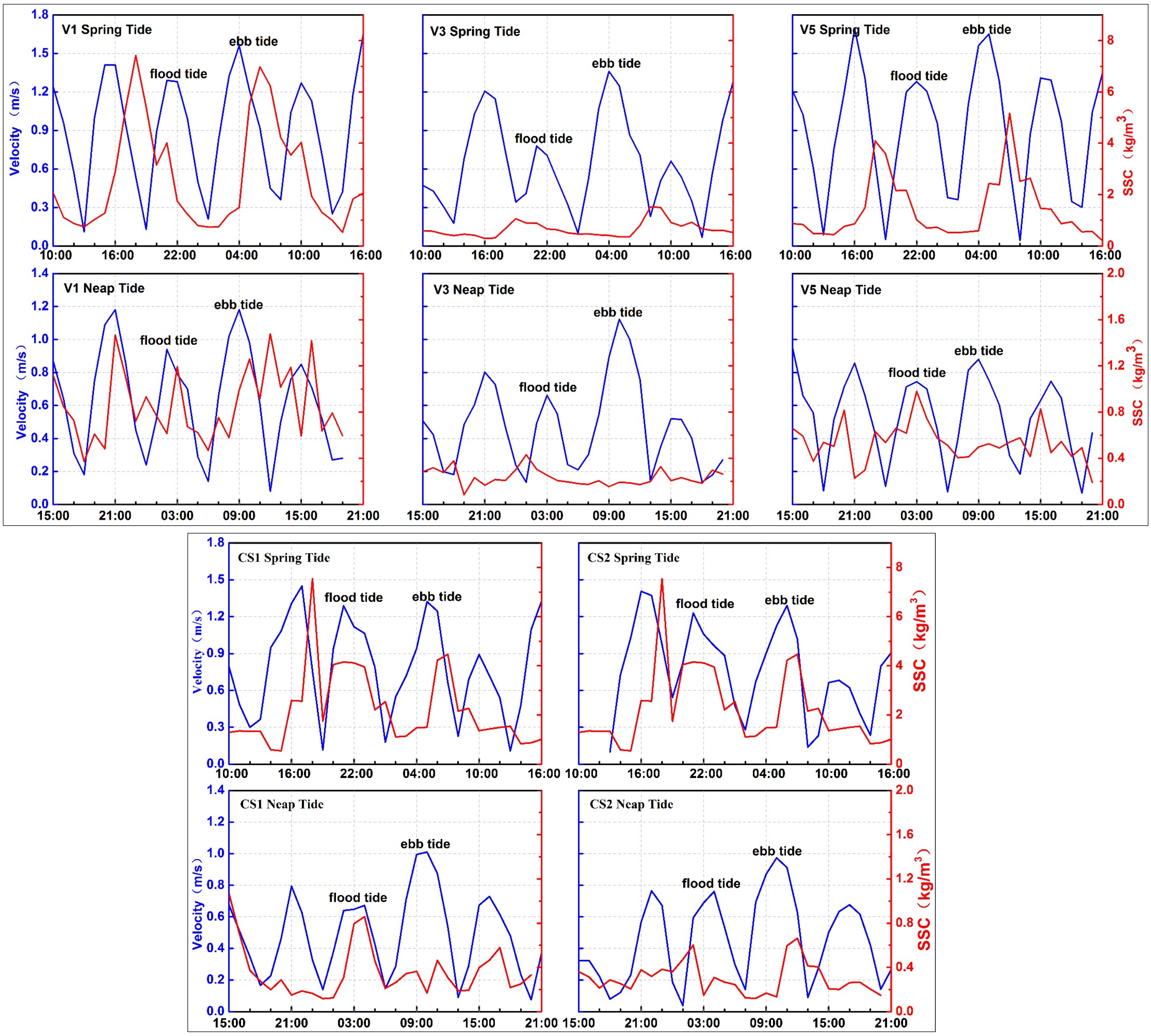

Figure 7. The hydrodynamic (blue) and sediment transport (red) processes during the spring and neap tide.

Comparing the residual current field, the sediment transport pattern and the hydrodynamic and sediment transport processes at the characteristics points, it can be concluded that the overall sediment transport direction is from the northwest to the southeast at the sea area, and because of the time lag between the suspended sediment and tidal current processes, there are local differences between the sediment transport and the residual current direction.

5 CONCLUSIONS

According to the simulated tidal current and suspended sediment field at the Yongjiang Estuary, the residual current field and sediment transport patterns were calculated and analysed, and the conclusions are as follows:

(1) The overall residual current transport direction is from northwest to southeast outside the Yongjiang River. There is a clockwise circumfluence beside the Dahuangmang Mountain and an anticlockwise circumfluence at the south side of the Jintang Island. In the Yongjiang River, because of the upstream runoff, the residual current transport seaward;
(2) The suspended sediments at the Yongjiang Estuary mainly comes from the northern sea area and the overall sediment transport pattern at the sea area is entering in the north and leaving in the south. Carried by the flood tide current, the sediments transport from the sea area to the Yongjiang River, which makes the sediments transporting landward near the river mouth;
(3) The local differences between the sediment transport and residual current directions is mainly because of the time lag between the hydrodynamic and sediment transport processes.

REFERENCES

Abbott, M.R. (1960). Boundary Layer Effects in Estuaries. *Mar. Res*, 18, 83-100.
Chen, G.X. (1989). Characteristics of Tidal Wave and Level of the Jintang Channel and the Adjacent Sea Area. *Marine Science Bulletin,* 4, 1-9.
Chen, J., Ji, M. & Zhang, H. J. et al. (2012). Analysis of Water and Sediment Characteristics during Flood and Low Water Period of Yong River. *Hydro-Science and Engineering,* (05), 48-54.
Edmonds, D.A. & Slingerland, R.L. (2009). Significant Effect of Sediment Cohesion on Delta Morphology. *Nature Geoscience,* 3(2), 105-109.
Egbert, G.D. & Erofeeva, S.Y. (2002). Efficient Inverse Modeling of Barotropic Ocean Tides. *Journal of Atmospheric and Oceanic Technology,* 19(2), 183-204.
Jiang, W.Z., Ma, H.L. & Wang, Z. (2013). Analysis on Flow-Sediment Characteristics and Suspended Sediment Transport in Yongjiang River and the Jintang Channel. *Science Technology and Engineering,* (11), 3162-3166.
Longuet-Higgins, M.S. (1969). On the Transport of Mass by Time-Varying Ocean Currents. *Deep Sea Research & Oceanographic Abstracts,* 16(5), 431-447.
Partheniades, E.A. (1965). Erosion and Deposition of Cohesive Soils. *World Journal of Biological Psychiatry the Official Journal of the World Federation of Societies of Biological Psychiatry,* 2(4), 190-192.
Wang, K.S. & Chen, G.X. (1989). Features of Flow Field of the Jingtang Channel. *Marine Science Bulletin,* (04), 10-19.
Xiong, S.L. & Zeng, J. (2008). Study on Classification Index and Fluvial Processes of Tidal Estuaries. *Journal of Hydraulic Engineering,* (12), 1286-1295.
Yan, W.W. (2011). Water and Sediment Characteristics and their Scouring and Silting Law in the Three Rivers of Ningbo. *Hydro-Science and Engineering,* (04), 143-148.
Yang, Z.Q., Xu, W.Y. & Wang, K.S. (1989). A Numerical Study of Tidal Wave of the Jintang Channel and the Adjacent Water Area. *Marine Science Bulletin,* (04), 20-26.
Zhang, W.L. (1993). A study of the Tidal Types in the Waters nearby the Mouth of the Yongjiang River. *Journal of Hangzhou University (Natural Science Edition),* (02), 229-237.
Zimmerman, J.T.F. (1979). On the Euler-Lagrange transformation and the Stokes' Drift in the Presence of Oscillatory and Residual Currents. *Deep Sea Research Part a Oceanographic Research Papers,* 26(5), 505-520.

Proceedings of the 37th IAHR World Congress
August 13 – 18, 2017, Kuala Lumpur, Malaysia

MODELING OF COLLOIDAL SULFURIN SALINITY-STRATIFIED URBAN STREAMS

SHIN MIURA[1], TETSUO HOTTA[2], HITOSHI NEGISHI[3], YASUSHI TSURUTA[4]
& TADAHARU ISHIKAWA[5]

[1, 2, 3, 4] CTI Engineering Co., Ltd., Tokyo, Japan,
miura@ctie.co.jp
[5] Tokyo Institute of Technology, Tokyo, Japan,
workishikawa0612@yahoo.co.jp

ABSTRACT

The generation of sulfide and colloidal sulfur was modelled for the tide-affected reach of urban streams. Field measurements conducted in the Meguro River, which flows through a highly urbanized area of the Tokyo Metropolis, suggested a change in the chemical form of sulfur in the river: In the saline underwater, anoxic conditions developed due to oxygen consumption by organic substances discharged from the outfall of a sewer system, and sulfide was generated by the action of sulfur-reducing bacteria. The deep water was transported to the shallow upstream reach by adverse tide flow, where the sulfide was oxidized rapidly, resulting in colloidal sulfur. A series of laboratory experiments were done to quantify the sulfide generation rate in a still-water column containing samples of bed sediment and saline water collected in the river. Experimental results were used to formulate empirical relations for the dependence of sulfide generation rate on the ignition loss of bed sediment and the COD of river water. A numerical model was developed for the variation in concentration of sulfide and colloidal sulfur in river water based on the experimental results and previously reported values. A practical model for numerical simulation of sulfur behavior in the tide-affected river reach was constructed by combining this model for the water with a two-dimensional (longitudinal /vertical) unsteady flow model. A numerical simulation was performed for the hydraulic conditions of the Meguro River during two weeks in the summer of 2008, when the sulfide concentration became very high due to a high level of organic sediment deposition from an intense rain runoff. The calculation results showed good agreement with the longitudinal distribution of sulfide concentration obtained from field measurements, two weeks after the rain runoff.

Keywords: Tide-affected reach of urban stream; milky water; behavior of sulfur; field measurement; numerical model.

1 INTRODUCTION

Water quality in urban rivers in the Tokyo Metropolis was improved significantly by the completion of a sewer system for domestic wastewater and the control of industrial effluent, as well as by the dredging of sludge in the channels, after the water was severely polluted by rapid urbanization in 1960s and 1970s. However, as most of the sewer system is a “combined system,” organic sediment deposited in the system is discharged to the river channels with excess water during intense rain runoff, which causes short-term water problems.

One striking phenomenon observed in the tide-affected downstream river reach has been the milky water with malodor, which appears when the saline water rises from the water’s depth to the surface during flood tide. The substance causing the milky color was identified as colloidal sulfur, and the source of malodor was hydrogen sulfide. Due to the similarity with the water problems found in a shallow inner bay with organic sludge on the bottom (Hansen et al., 1978; Horiguchi et al., 1991; Tanaka et al., 1997), the phenomenon is considered due to the high concentration of sulfide in the bottom water, generated by chemical reaction of the organic matter discharged from the combined sewer with the sulfate contained in seawater under the anoxic conditions existing in the bottom water layer (Miura et al., 2008).

In this study, the rate of generation of sulfide and colloidal sulfur was investigated using field measurements obtained in the Meguro River, which flows through the highly urbanized area of Tokyo, as well as from a series of laboratory experiments that quantified the sulfide generation rate in a still-water column containing samples of bed sediment and saline water collected in the same river. A practical model for the numerical simulation of sulfur behavior in river streams was constructed by combining the results from the field study with those from a two-dimensional (longitudinal/vertical) unsteady flow model proposed by Yamamoto and Igarashi (2003). A numerical simulation was conducted under the hydraulic conditions of the Meguro River during the two weeks in the summer of 2008, when sulfide concentrations became very high after intense rain runoff caused a significant amount of organic sediment deposition. The results were compared with the field data for the longitudinal distribution of sulfide.

2 FIELD OBSERVATIONS

2.1 Study site

The Meguro River extends for 8.0 km through a densely populated area of South Tokyo to the Tokyo Bay [Figure 1(a)]. The river flows into a canal system surrounded by reclaimed land that was constructed in the 20th century. The river has a total watershed of 45.8 km^2, including the upstream subsurface tributary basins. Rainwater collects through the combined sewer system, and is discharged occasionally from the outfalls to the river channel with domestic wastewater when total flow rate exceeds the capacity of main sewer lines. The discharged water carries organic sediments that were deposited in the conduits of the sewer system before the rain events. Figure 1(b) shows the site of this study, which covers the most downstream river reach of approximately 7 km, where milky water periodically appears. The eight red circles represent the measurement stations located at approximately 1000-meter intervals within 6 km of the reach.

Figure 2 shows the longitudinal channel bed profile along the deepest line of the downstream river reach, in which KP (Kilo Post) indicates the distance from the river mouth. The water depth changes suddenly at 4.0 KP. The channel bed downstream from the inflection point is nearly flat near –3.0 A.P.m (A.P.; the average ebb tide level in Tokyo Bay), while the bed elevation upstream from the point is higher than 0.0 A.P.m. In the days of no rainfall, river discharge is very low, and saltwater usually reaches the inflection point. Five measurement stations were located in the deep river reach, two were in the upstream shallow reach, and one was in the downstream canal.

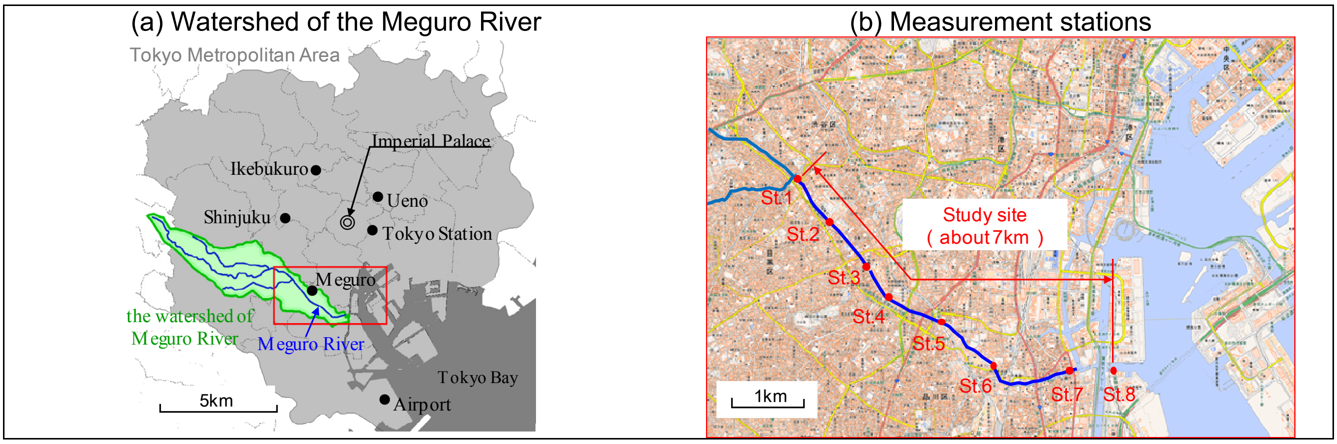

Figure 1. Study site.

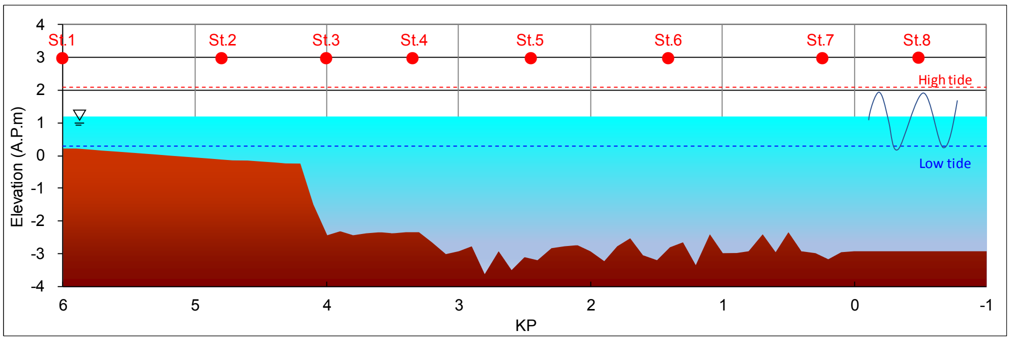

Figure 2. Longitudinal bed profile of the Meguro River.

2.2 Field measurements

Vertical profiles of water temperature, salinity, pH, DO, and ORP were obtained using a water quality meter (Horiba W-23XD) on the channel center line at the eight stations marked with the red circles in Figure 1(b). The measurements were obtained 13 times from August 2006, to March 2008. River water was sampled at three depths (water surface, 50-cm deep, and just above the river bed) at St. 4 and St. 8 and from the surface at St. 1, four times after the measurement of June 2007, and COD and sulfide were analyzed in the laboratory.

Figure 3 shows a portion of the data obtained at St. 1, St. 4 and St. 8 in August 2007, when river discharge was very low due to lack of rainfall for 14 days. DO saturated freshwater flowed in the shallow channel at St. 1. A clear interface of salinity stratification was observed at St. 4 of 3.4 KP (red line), while the salinity at St. 8 located in the canal near the river mouth (blue line) had a mild profile. The salinity at St. 8 was lower than the seawater salinity (~32 psu) because the river mouth of Meguro River is located in the canal system surrounded by reclaimed land [Figure 1(b)].

The pH, DO, and ORP profiles had the same tendency as the vertical salinity distribution: they showed a sharp variation near the density interface at St. 4. The water below the interface was almost anoxic, and ORP was less than –200 mV, which indicates that a reduction process prevailed. The low pH observed in the lower layer of St. 4 may be the result of anoxic chemical reactions. The sulfide concentration was very high in the bottom water layer, probably due to reduction of the sulfate contained in the saline water under the anoxic condition.

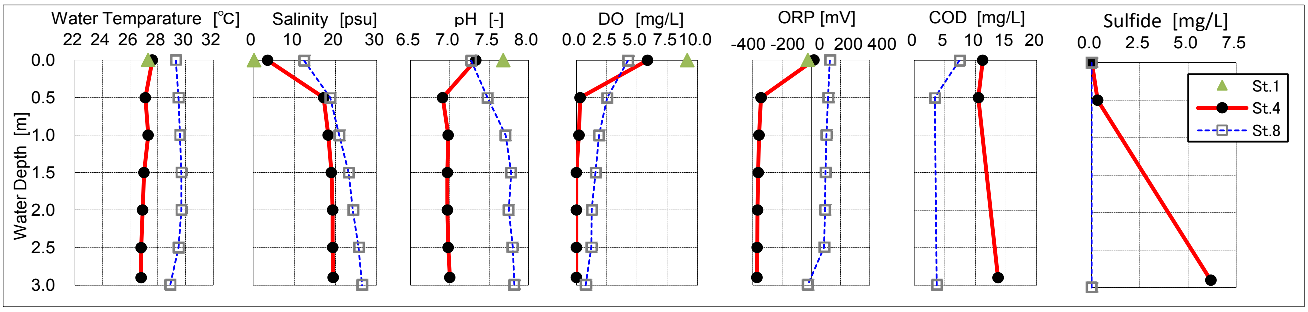

Figure 3. Vertical distribution of water quality at St. 1, St. 4, and St. 8.

2.3 Mechanism of colloidal sulfur

Generation of sulfide and colloidal sulfur was proposed as shown in Figure 4, based on the observations along with the diagram proposed by Garrels and Christ (1965), who classified the form of sulfur in water based on pH vs. ORP using the Nernst equation (Nernst, 1889). Due to the prevailing anoxic conditions in the bottom water layer caused by the oxidization of organic matter, sulfate-reducing bacteria generated ionic hydrogen sulfide (HS^-) from the sulfate (SO_4^{2-}) abundant in saline water during the process of organic substance decomposition [(1) → (2)]. A portion of the ionic hydrogen sulfide further combined with ionic hydrogen (H^+) to produce hydrogen sulfide (H_2S), decreasing pH [(2) → (3)]. Contact of anoxic bottom water with oxygen-rich surface water under the action of wind and tide returned the ionic hydrogen sulfide to sulfate [(2) → (4)], followed by conversion of hydrogen sulfide into colloidal sulfur [(3) → (5)].

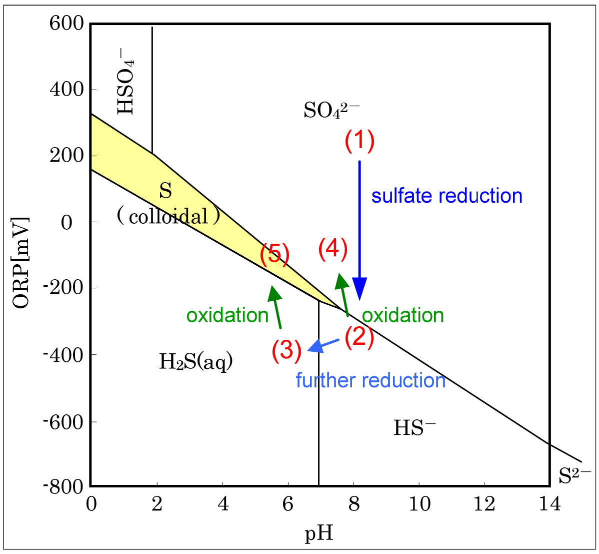

Figure 4. Chemical reactions of sulfur in river water (Garrels and Christ, 1965).

The field measurement data indicated that the process could be illustrated as shown in Figure 5, in which tide variation was the only external force considered for simplicity: (a) organic substances carried by flood water during a storm settled in the reach just after the step down of the riverbed due to flow velocity reduction; (b) after the storm, saltwater intruded into the channel, resulting in density stratification, and the bottom water just above the organic sludge became anoxic because of oxygen consumption by organic substances together with the lack of downward oxygen transport by the density interface; (c) as a result, sulfide was generated from sulfate by the activity of sulfur-reducing bacteria under anoxic conditions; (d) denser saline water containing sulfide was brought to the shallow upstream channel by adverse flow during flood tide; and (e) the swift favorable flow from the shallow reach during ebb tide enhanced mixing of the sulfide-rich saline water with the oxygen-rich surface water, causing sulfide oxidization to colloidal sulfur.

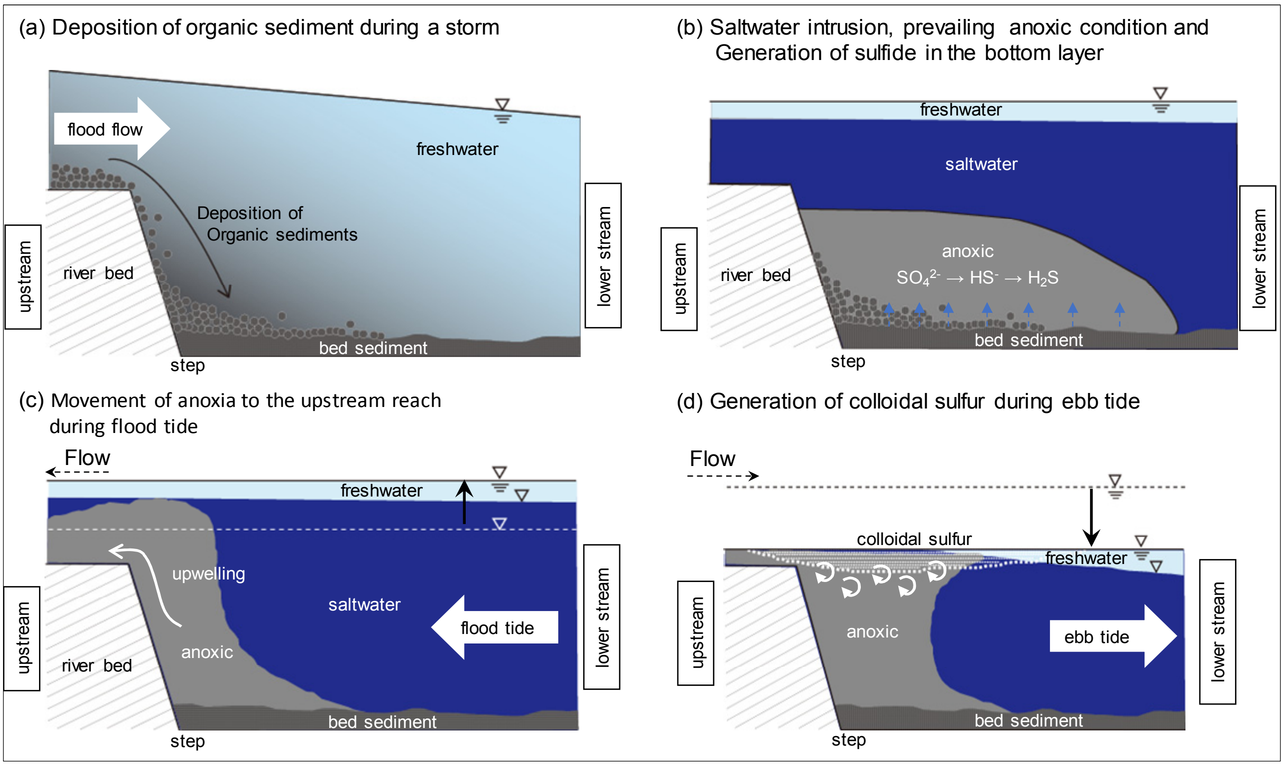

Figure 5. Illustration of the process of sulfide and colloidal sulfur generation in the river.

3 MODELING

3.1 Model structure

A model containing four variables (concentrations of sulfide, C_{sulf} and colloidal sulfur, C_{cols}, dissolved oxygen, C_{DO}, and chemical oxygen demand, C_{cod}) was used. Although the sulfide was divided between two components (HS^- and H_2S) (Figure 5), it was treated as one component in the following formulation for simplicity. The time variation rate of each factor in a control volume of flowing water were written as Eq. [1] – Eq. [4].

Sulfide
$$\frac{DC_{Sulf}}{Dt} = \alpha_S \theta_S^{T-20} e^{-\gamma_{DO} C_{DO}} \frac{A}{V} + \alpha'_S C_{COD} - K_s C_{Sulf} \quad [1]$$

Sulfur
$$\frac{DC_S}{Dt} = K_s C_{Sulf} - D_s C_s \quad [2]$$

DO
$$\frac{DC_{DO}}{Dt} = R_{RA}\theta_{RA}^{T-20}(C_{SO} - C_{DO})\frac{A}{V} - R_{KC}\theta_{KC}^{T-20} C_{COD}\frac{C_{DO}}{C_{DO0} + C_{DO}} - \frac{1}{2}K_s C_{sulf} - R_{KB}\theta_{KB}^{T-20}\frac{A}{V}\frac{C_{DO}}{C_{DO0} + C_{DO}} \quad [3]$$

COD
$$\frac{DC_{COD}}{Dt} = -f_C \theta_C^{T-20} C_{COD}\frac{C_{DO}}{C_{DO0} + C_{DO}} + W_{COD}\theta_{COD}^{T-20}\frac{A}{V} - \frac{1}{\Delta y} V_{COD} C_{COD} \quad [4]$$

where *D/Dt* means substantial differentiation, C_{so} is saturated dissolved oxygen (mg/L), C_{DO0} is DO value at which reaction rate was halved (mg/L), *T* is water temperature (°C), and *A* is horizontal area (m^2) and *V* is volume (m^3) of calculation mesh.

The meaning and unit of other parameters used in the equations are listed in Table 1. The DO balance equation (Eq. [3]) was proposed by Yamamoto and Igarashi (2003), and the value of the parameters, with the exception of K_s (rate of sulfide oxidization to produce colloidal sulfur), were presented. The three terms on the right side of the sulfide balance equation (Eq. [1]) represent the production by bed sediments, production in water, and decay by oxidization, respectively. The form of the first term was assumed following Hotta et al. (2002), and the values of parameters, with the exception of α_s, were obtained from previously reported studies. The two terms on the right side of the colloidal sulfur balance equation (Eq. [2]) represent production by sulfide oxidization and decay due to further oxidization to sulfate ion.

Table 1. Settings of parameters.

	Meanings	Set Value	Unit	Setting Basis
α_s	production rate of sulfide in bed sediment	setting from Eq.[9]	$g/m^2/day$	laboratory experiments
α_s'	production rate of sulfide in water	setting from Eq.[10]	$g/m^3/day/mg\text{-}COD$	laboratory experiments
K_s	oxidation reaction rate of sulfide	setting from Eq.[11]	day^{-1}	existing reports
D_s	reduction rate of sulfur colloid	2.0	day^{-1}	field observation
R_{RA}	reaeration coefficient	0.05	day^{-1}	general value
R_{KC}	dissolved oxygen consumption rate by COD matter	$0.10C_{COD}+2.09$	$mg\text{-}O_2/mg\text{-}COD/day$	laboratory experiments
R_{KB}	dissolved oxygen consumption rate by bed sediment	2.82～6.96	$mg\text{-}O_2/m^2/day$	laboratory experiments
θ_s	water temperature correction coefficient: production rate of sulfide	1.05	-	same as COD
θ_{RA}	water temperature correction coefficient: reaeration	1.05	-	general value
θ_{KB}	water temperature correction coefficient: dissolved oxygen consumption rate: COD matter	1.05	-	general value
θ_{KC}	water temperature correction coefficient: dissolved oxygen consumption rate: bed sediment	1.05	-	general value
θ_C	water temperature correction coefficient: organic decomposition rate	1.05	-	general value
θ_{COD}	water temperature correction coefficient: COD dissolution rate from bed sediment	1.05	-	general value
γ_{DO}	production rate correction coefficient by DO	2.0	mg/l	model validation
f_c	organic decomposition rate	0.025	day^{-1}	general value
W_{COD}	COD dissolution rate from bed sediment	0.030	$mg\text{-}COD/m^2/day$	general value
V_{COD}	settling velocity of COD	0.30	m/day	model validation

The equations contained four unknown parameters, α_s, α_s', Ks and D_s, which were dependent on the site conditions. The K_s value was considered to be roughly proportional to DO and weakly influenced by the water temperature. Eq. [5] was obtained from a report published by the Tokyo metropolitan government (1979). The value of D_s (decay rate of colloidal sulfur) was assumed to be 2.0 day^{-1}, based on the average duration of milky water observed in the Meguro River. The other unknown parameters, α_s and α_s', were determined by laboratory experiments using samples of bed sediment and river water collected in the Meguro River, because these parameters are the most essential ones for understanding and modeling the phenomenon.

$$Ks = 1.470C_{DO}\, 1.068^{T-20} \qquad [5]$$

3.2 Laboratory experiments to identify sulfide-generation rate

Saline water was sampled just above the river bed at St. 3, St. 6, and St. 7; the sludge deposited on the channel bed also was sampled at the deepest point in the cross-section of St. 3 and St. 6 in August 30, 2007 when organic sludge was deposited in the channel after a storm, even though sludge deposition was not found at St. 7.

Figure 6 shows the experimental apparatus; the body was a Perspex cylinder (20 cm inner diameter and 100 cm height) sealed at the top and bottom by rubber caps and paraffin film. For Experiment-1, sampled sludge was deposited at a depth of 30 cm, followed by filling the cylinder with sampled river water that had been fully aerated for DO saturation. The DO, pH, and ORP were measured continuously at half depth of the water column using water quality meters (Tohken Engineering RT530), and water was sampled occasionally through thin plastic tubes at 1/3 and 2/3 depth to analyze COD and sulfide concentration. For Experiment-2, the cylinder was filled only with aerated sampled river water. The DO and pH were measured at half depth of the water column, and water samples were collected occasionally at the same depth with a thin plastic tube.

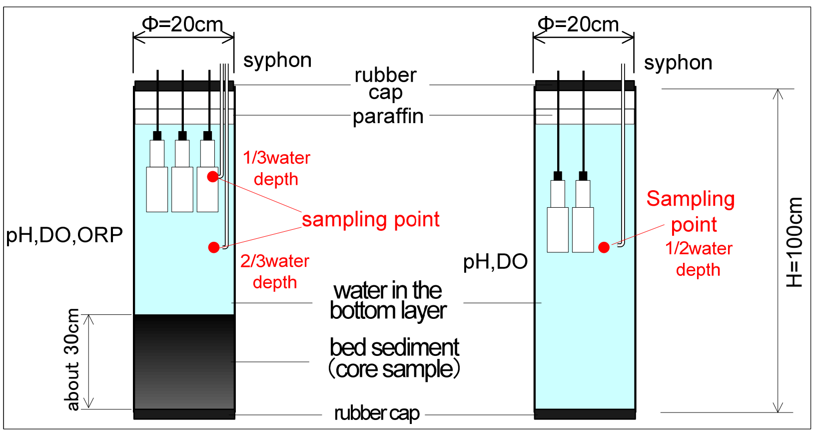

(a) Experiment- 1 (with sediment and river water)
(b) Experiment- 2 (with river water only)

Figure 6. Experimental apparatus.

Figure 7 shows the results from Experiment-1 for the materials sampled at St. 3 and St. 6. In the experiment involving St. 3, which is located just after the inflection point of river bed elevation, DO decreased rapidly to zero in the first two days, and ORP dropped sharply after anoxic conditions developed, while pH changed from mildly alkaline to neutral or weakly acidic. The sulfide concentration increased steadily from zero on the second day to 12 mg/L on the ninth day. The rate of sulfide generation was calculated as 1.74 g/m^2/day. In contrast, the experiment involving St. 6, located in the middle river reach, revealed that the duration to reach anoxic conditions was longer, and the final production of sulfide was lower than that from St. 3. The rate of sulfide generation was calculated as approximately 0.45 g/m^2/day.

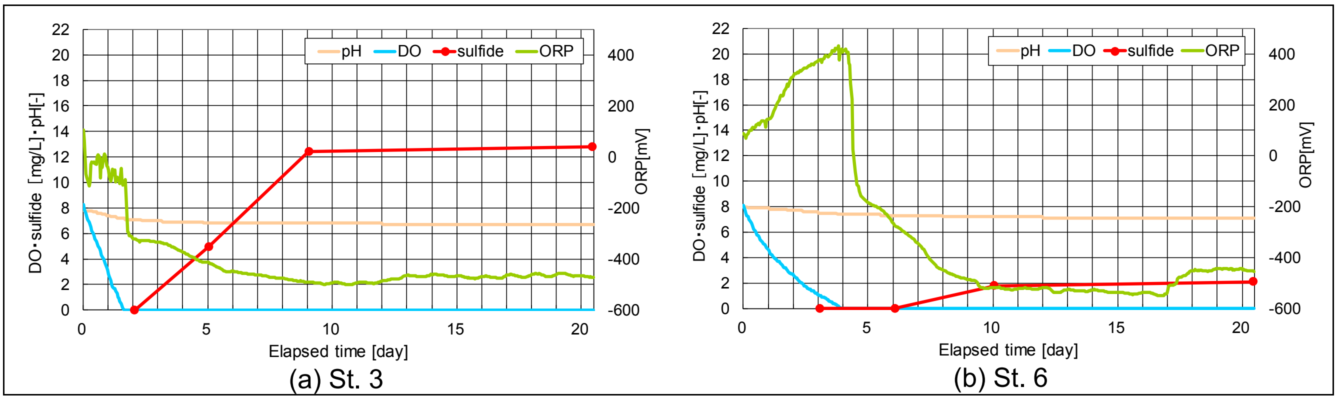

Figure 7. Change in water quality over time from experiment- 1.

Combining the results from the two experiments (sludge + water, water only) allowed calculation of the rates of sulfide generation by sludge and by water. The two red dots in Figure 8(a) indicate the correlation of sulfide generation rate by sludge, α_s, with ignition loss of the sediment, while the black dots indicate the results of same experiments for the sludge collected in the canals along the coast of Tokyo Bay near the river mouth of Meguro River (Tokyo metropolitan government, 1979). The results enabled creation of an empirical equation for α_s as expressed by Eq. [6]. Figure 8(b) shows the results for the correlation between sulfide generation rate with water only, α_s', and COD concentration in the water, which resulted in Eq. [7].

Bed sediment $\alpha_s = 0.124e^{0.171x}$ x: ignition loss (%) [6]

Water $\alpha'_s = 0.012C_{COD} + 0.017$ [7]

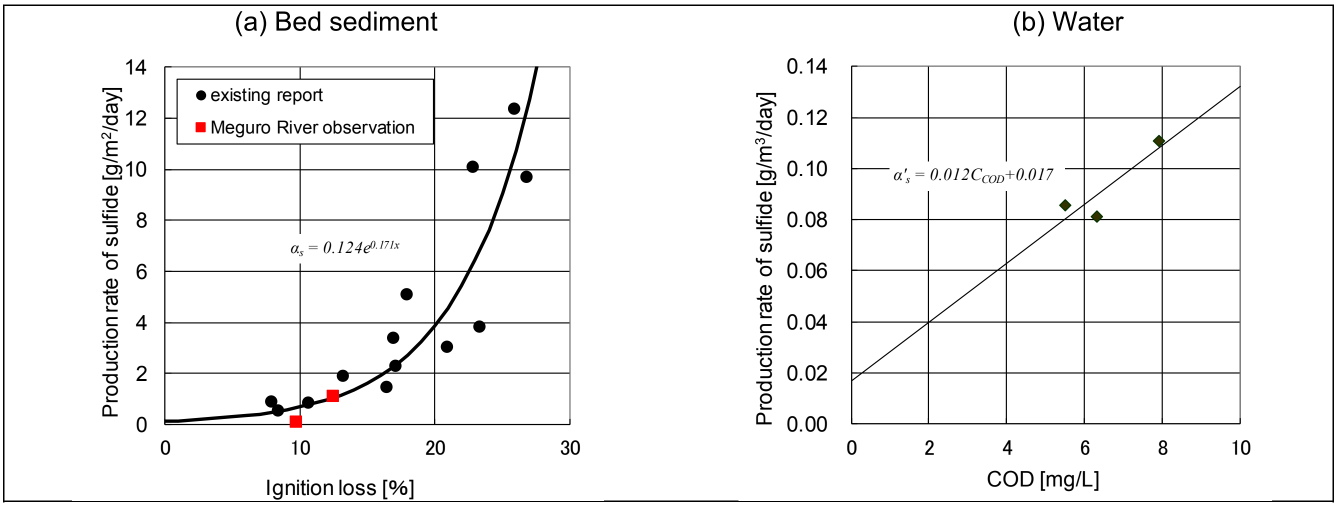

Figure 8. Correlation of the rate of sulfide generation.

4 NUMERICAL SIMULATION

4.1 Calculations

Numerical simulation was performed for hydraulic conditions during the two weeks from July 31 to August 13, 2007. Sulfide was not detected in the study area in measurements obtained on July 31. A storm brought

34.0 mm of precipitation on the same day, after which dry weather occurred for two weeks until the next river water measurement on August 13.

The river reach was 5.4 km long from 5.4 KP to the river mouth, including the riverbed inflection point (see Figure 2). A regular rectangular grid system was adopted for the calculation; one grid was Δx = 100 m and Δy = 0.2 m in the longitudinal and vertical planes, respectively. The total number of calculation points was 54 x 40 = 2160.

The unsteady flow model was used, but the boundary conditions for the calculation were simplified because of limitations of the field data. The average values for flow rate and water quality parameters as observed on dry weather days at the upstream boundary were used and were considered constant. The water surface level at the downstream boundary was provided from the hourly data at the nearest tide-gauge station, but the water quality parameters used were obtained from the values measured on August 13.

Meteorological factors (air temperature, solar radiation, cloud cover, wind velocity and humidity) for the upper boundary conditions (at the water surface) were those obtained from the hourly data at the nearest weather station. The lower boundary conditions (at the bed sediment surface) needed for the calculations were rate of DO absorption by the bed sediment and ignition loss necessary to estimate sulfide production rate using Eq. [6]. The DO absorption was provided by the experimental data described in Section 3-2. The ignition loss was provided from another experiment for ignition loss of sediment collected from the channel bed at every 50 m on August 13, 2007.

The initial conditions for the water quality parameters were obtained by interpolating the values from field observations on July 31; the initial hydraulic conditions were assumed stationary with the flat-water surface at the initial tide level. The time increment for calculations was 5 sec.

4.2 Results and discussions

Figure 9 shows calculated sulfide concentrations on August 13 as a color contour map in the longitudinal/vertical plane. Unusually high sulfide concentrations appeared in the bottom water layer just downstream from the down step of channel bed. Close examination of the calculation results indicated that the high sulfide concentration was generated by the high ignition loss of bed sediment in the reach together with flow stagnation that caused stable chemical reactions under the anoxic conditions.

The thin slanted lines near the water surface in the figure indicate the calculation grids where colloidal sulfur concentration exceeded 0.25 mg/L. The double arrow above the figure shows the reach where milky water was observed. These two agree fairly well. The thin black circles in the figure show the position of water samples used to obtain sulfide concentration. The data were compared with the calculated results shown in Figure 10. The calculated values were much lower than those measured at St. 5, which suggests that the estimate of downstream advection was too low in the model. The calculated value is also smaller at St. 3, where the sulfide concentration abruptly changed with depth, which may have been caused by an error in salinity stratification. The hydraulic model must be improved to discover the cause of and eliminate these errors.

Despite the limitations, the calculation results agree well with the field data for trends in sulfide concentration, which implies that this model has the ability to describe sulfur behavior in the tide-affected urban river.

In the model presented in this study, the sulfur originated from the reduction of sulfate contained in the saltwater under anoxic conditions in the bottom water layer. The model performance suggests that the measures to increase DO in the bottom layer, such as addition of water with supersaturated oxygen, can suppress the generation of sulfide and colloidal sulfur.

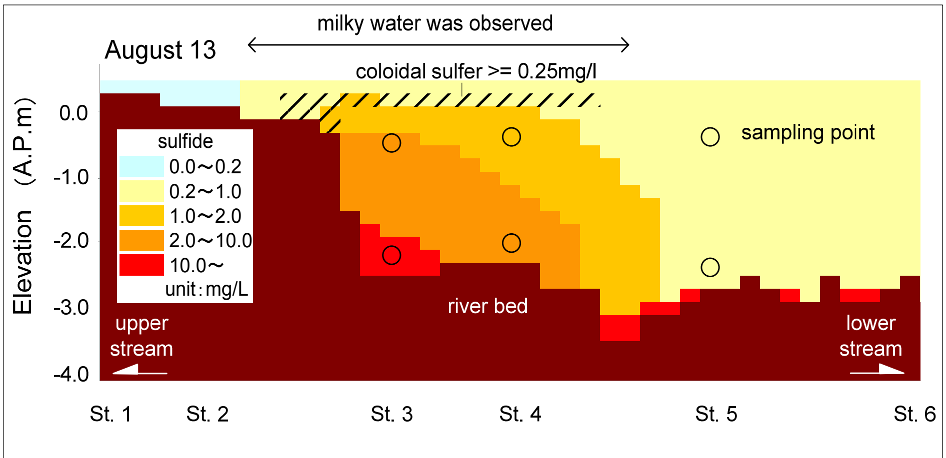

Figure 9. Changes in sulfide (from calculation results).

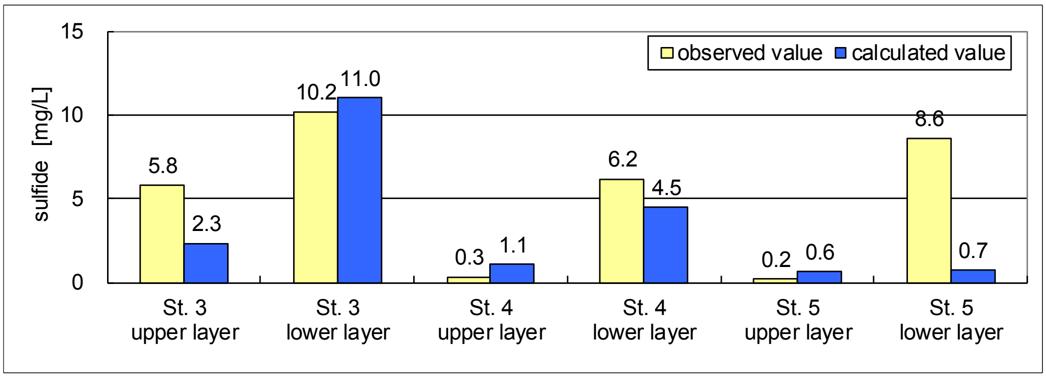

Figure 10. Comparison between observational data and calculation results.

5 CONCLUSIONS

A practical model for the behavior of sulfur in a tide-affected urban river reach was developed based on field measurements and the previously reported data. The results of numerical simulations using the model agreed fairly well with field measurements, although some limitations were observed. The results suggested that sulfate reduction in anoxic bottom water was the origin of the colloidal sulfur in the rivers and that injection of supersaturated water to increase DO in the bottom water would improve water quality. However, the hydraulic module model must be improved to represent the transport of dissolved substances more accurately. Upgrading and verifying the model through comprehensive field measurements is planned so that it can be used to predict the effect of measures to improve water quality.

ACKNOWLEDGEMENTS

The authors would like to thank the River Works Division of Shinagawa Ward, Tokyo Metropolitan Government for their support of the field survey and data collection.

REFERENCES

Garrels, R. M., & Christ, C. L. (1965). *Solutions, Minerals, and Equilibria*. Harper & Row, New York and John Weatherhill, Inc., 217.

Hansen, M.H., Ingvorsen, K. & Jonson, B. (1978). Mechanisms of Hydrogen Sulfide Release from Coastal Marine Sediments to the Atmosphere. *Limnology and Oceanography*, 23(1), 68-71, 1978.

Horiguchi, T., Horie, T., Kikuchi, M. & Kojima, S. (1991). Observation and Research on Odor Generation in Canal. *Annual Journal of Coastal Engineering, JSCE*, 38, 901-905.

Hotta, T., Amano, M., Yamashita, Y., Chen, F.Y. & Shoji, H. (2002). Observation on Malodor Gas Generation in Coastal Area. *Annual Journal of Coastal Engineering, JSCE*, 49, 1101-1105.

Miura, S., Negishi, H. & Hotta, T. (2008). Generation of White Turbid Water and Construction of Water Quality Prediction Model in Meguro River. *The 63th JSCE Annual Meeting Japan Society of Civil Engineers*, 167-168.

Tanaka, M., Markus, A. & Bando, K. (1997). Development of Numerical Model Including Biochemical Reaction of Blue Tides. *Annual Journal of Coastal Engineering, JSCE*, 44, 1096-1100.

W. Nernst (1889). Die elektromotorische Wirksamkeit der Ionen, Z. phys. Chem., 4, 129-181.

Yamamoto, A. & Igarashi, T. (2003). Study on Parameter Setting in Dam Reservoir Water Quality Simulation, Report of water resources environment research institute, Water Resources Environment Center, 78-83.

Proceedings of the 37th IAHR World Congress
August 13 – 18, 2017, Kuala Lumpur, Malaysia

HYDROLOGICAL EVOLUTION DUE TO ARTIFICIAL INTERVENTION AND CLIMATE CHANGE IN PEEL-HARVEY ESTUARY

PEISHENG HUANG[1], MATTHEW R. HIPSEY[2] & DYLAN PRITCHARD[3]

[1,2,3] School of Earth and Environment, The University of Western Australia, Crawley WA 6009, Australia
peisheng.huang@uwa.edu.au; matt.hipsey@uwa.edu.au; 21320099@student.uwa.edu.au

ABSTRACT

The impacts of an artificial channel Dawesville Cut, constructed in 1994, in order to increase the ocean flushing, and predicted future climate changes on the hydrology of a eutrophic shallow coastal estuary Peel-Harvey Estuary are examined with validated hydrodynamic models. The results suggested that the construction of the Dawesville Cut successfully improved the ocean flushing and reduced the water retention time inside the estuary. However, the Cut also introduced more saline water into the estuary and thus enhanced the water stratification. The impacts are more significant in wintertime when the estuary received strong fresh runoffs from three major inflow rivers. The combined impacts of climate change, including less runoffs, precipitation, higher sea levels and air temperature, largely increased the water retention time as well as the salinity inside the estuary, while reducing the water stratification. Both the Dawesville Cut and the climate change pushed the salt-wedge further toward the upstream of rivers, which could substantially change the riverine ecology.

Keywords: Estuary, salt-wedge; water retention; stratification; climate change.

1 INTRODUCTION

Salt-wedge, formed as the freshwater coming from catchment runoffs overlays denser saltwater from ocean, and water retention time are two major hydrological characters of an estuary and also the main drivers of the estuarine ecosystems (Watanabe et al., 2014; Bruce et al., 2014; Jovanovic et al., 2017). It is common in estuaries with high populations in their catchments that the water is eutrophic and sediment acts as a sink of nutrients. Once the water stratification persists for a considerable period, oxygen depletion occurs in these nutrient-rich estuaries and establish hypoxia in the bottom boundary layer, thus threat the aquatic ecosystem health (Hipsey et al, 2013; Cottingham et al, 2015; Nezlin et al., 2009). The characters of salt-wedge could be modified by both artificial interventions and climate change, and need be examined before providing a management strategy of an estuary.

Peel-Harvey Estuary is a shallow coastal estuary-wetland system located in Southwestern Australia (Figure 1). It connects to the ocean through small channels and is weakly tidal forced. Long-term monitoring data of water hydrology and quality are available, which shows that this wetland system suffered from heavy anthropogenic eutrophication in the past decades and experienced degraded water quality. The severity of the eutrophication problem led to the construction of an artificial channel, namely Dawesville Cut, built in 1994 with purpose to increase the flushing the estuarine waters and thus improve the eutrophication statues (Brearley, 2005). Although monitoring data showed the water nutrient and phytoplankton concentrations have been successfully reduced by the construction of the channel (Water and Rivers Commission, 1998), some other research suggested a decline of the aquatic community (Wildsmith et al., 2009). The situation could be further complicated by climate change that resulted in decreasing precipitations and runoff. Knowledge of the long-term effects of climate change as well as the artificial channel on the hydrology is important to the management of this estuary because of its high social and ecological values, yet still waiting for much investigations.

In this study, we investigated the hydrological evolution in Peel-Harvey Estuary due to the artificial channel and climate change. More specifically, we aim to parse the following questions:

(1) How the salt-wedge dynamics response to the artificial channel and climate change? E.g., How the water stratifications evolve due the intrusion of seawater? How far will the salt-wedge be pushed upstream due to climate change in future?
(2) How the water retention time responses to climate change? E.g., How the spatial pattern of water retention time varies in response to the construction of the artificial channel and changes in future with climate change?

2 METHODS

2.1 Study Site

Peel-Harvey estuary is located approximately 75km south of Perth in Western Australia. It is a coastal estuary-wetland system listed under the Ramsar convention for wetlands of international significance. The estuary comprised of two shallow lagoons (the Peel Inlet, a circular inlet to the north and the Harvey estuary, an oblong lagoon attached to the Peel Inlet at its north-eastern edge) with a combined area of approximately 136 km^2 and connected to the ocean via two channels: the Mandurah Channel, a natural but narrow 5 km long channel and Dawesville Channel, which is an artificial channel of about 2.5 kilometers long, 200 meters wide and between 6 and 6.5 meters deep, built in 1994 [Bicknell, 2006; EPA, 2008] (figure 1). The coastal catchment of the estuary is drained by three major river systems: the Serpentine, Murray and Harvey Rivers (Figure 2), including some minor drains. Approximately 95% of runoff from the total catchment area enters the estuary via the three rivers in the wet season (Kelsey et al., 2011).

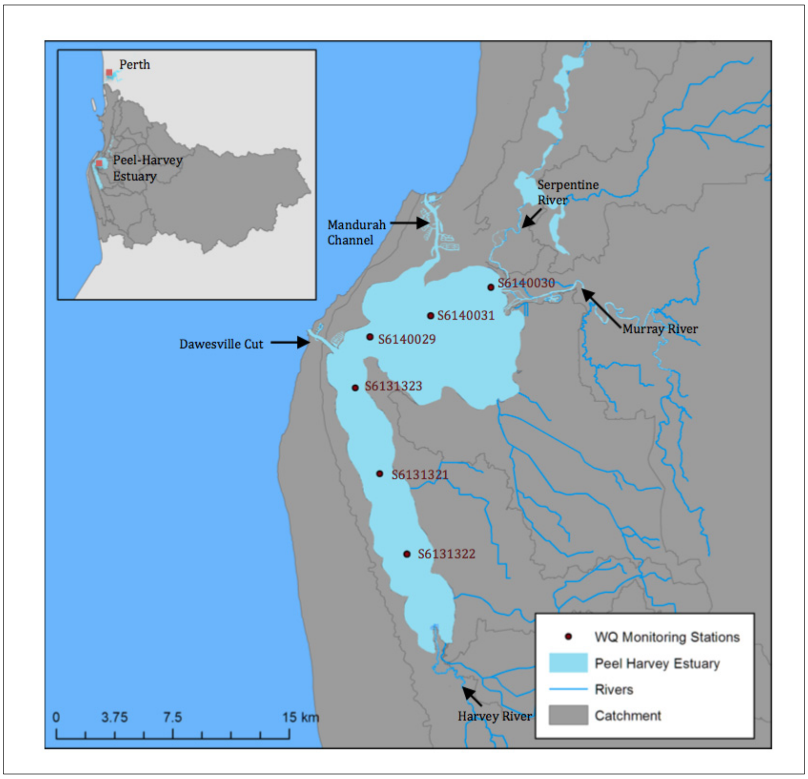

Figure 1. Peel-Harvey Estuary and the water quality monitoring stations.

2.2 Data Sources

Water quality monitored at 3 gauging stations in Peel Inlet and another 3 gauging stations in Harvey Estuary were obtained from the Department of Water through Water Information Reporting (WIR) and were used in this study to set up the model conditions and validate model results. Water quality parameters considered in this study were salinity and water temperature with sampling frequency changing over time from two samples per season, approximately monthly in the summer months and fortnightly in the winter months.

Daily flow data was collected from 1990 to 2008 for all three rivers where these rivers were all assigned salinity values of zero to replicate freshwater inflows. Water temperatures of the inflows were obtained using a regression between available field temperatures and daily air temperatures. Tidal forcing data since 1970s with frequency of every 5 minutes were obtained from Department of Transport at the gauging station of Fremantle. Meteorological data with hourly frequency was collected from BoM. Meteorological data includes north-south and east-west components of wind, air temperature, downward incoming shortwave radiation, relative humidity, cloud cover and precipitation.

2.3 Models

The estuary hydrodynamics was simulated with TUFLOW-FV, a 2D/3D flexible-mesh, finite volume hydrodynamic model (BMTWBM, 2013). The model solved the conservative integral form of the non-linear shallow water equations, advection and dispersion effects on salinity and temperature, and also included surface heat exchange and thermodynamics to simulate the influence of meteorological conditions on the water body, while the vertical mixing process was modeled with the General Ocean Circulation Model (GOTM)

(Umlauf & Burchard, 2003). The model was forced with boundary conditions at the three rivers, ocean, and from surface meteorology.

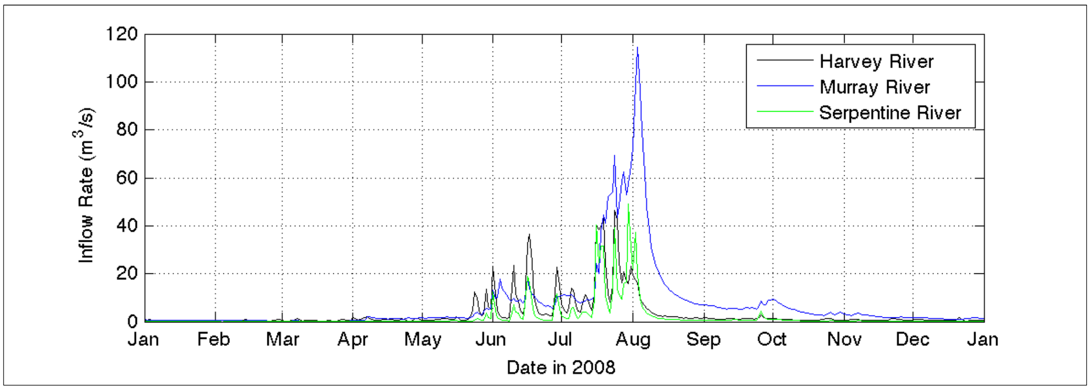

Figure 2. Inflow rates at three major rivers in 2008.

The hydrodynamic model was first ran and validated in year 2008. This year was selected because it represents a neutral year of rainfall and runoffs, i.e., not a particularly wet or dry year compared to annual history data (Ruibal-Conti, 2014). After the model has been validated with field monitoring data, two modeling scenarios were run: (1) “Dawesville Cut Scenario”, which is identical to the simulation in 2008, except with the Dawesville Cut closed and an initial condition interpolated from filed data in 1994 to represent water conditions before the cut; (2) “Future (in 50 years time) Scenario” to study the impact of climate change on hydrology in future, which is similar to the simulation in 2008 but uses boundary condition scales where all river inputs are decreased to 33% of the 2008 inflows and precipitation levels were decreased to 75% of the 2008 precipitation (Smith & Power, 2014), tidal levels are uniformly increased by 0.2 m using modest estimates of sea level rise into the future as in Kuhn et al (2011), and air temperature increases by 1.5° C as in IPCC Fifth Assessment Report (Collins & Knutti, 2013).

3 RESULTS AND DISCUSSIONS

3.1 Model Validations

Salinity and water temperature at the surface and bottom levels at 6 monitoring sites were taken to validate the model performance in year 2008. As shown in Figure 3, the salinity shows distinct seasonal variations at all sites in response to the temporal variation of inflows. In summer time (October – March) when the inflow rates were very low, the water was well mixed with the salinity that reached over 40 psu due to strong evaporations and shallow depth, and the temperature reached 27 degrees. Little difference of salinity and temperature was found between the surface and bottom layers. While in winter time (April – September) the salinity dropped quickly with inflow discharges increased to up to 118 m3/s (figure 2). The strong inflows created salt-wedges that can be seen from the salinity differences between the surface and bottom layers. At sites S6131323 and S6140029 that are close to the Dawesville Cut, strong tidal signals can be found at both the surface and bottom layers, and clear density stratification of up to 10 psu difference can also be observed. At site S6131322 and S6140030 that are close to the fresh inflows, the water salinity drop to nearly 0 psu at surface water, and ~10psu at the bottom. The water temperature dropped to ~12 degrees in winter time, however negligible difference was observed between the surface and bottom layers, indicating that the density stratification in Peel-Harvey Estuary is dominated by the salt wedge.

The model reproduced the seasonal variations of salinity as well as the salinity stratification, i.e. the salt wedge evolution with time and space. The regression coefficients for salinity at 6 sites vary between 0.92 and 0.95 with maximum MAE (Mean Absolute Error) of 2.86 psu, and minimum MEF (Model Efficiency Factor) of 0.84. While for water temperature the regression coefficients vary between 0.94 and 0.98 with maximum MAE of 1.49 degrees, and minimum MEF of 0.75.

3.2 Impact of Dawesville Cut on the estuary hydrology

3.2.1 Water retention time

The major target of the Dawesville Cut was to improve the ocean flushing thus to reduce the water retention time inside the estuary and improve the water quality. Figure 4 compares the monthly averaged water retention in a dry month (February) and in a wet month (August), where we can see that the Cut significantly improves the water retention time. In the dry month when the estuary received minor river flushing due to low runoff, the Dawesville Cut plays an important role in enhancing the ocean flushing especially in the area adjacent to the channel. The monthly average water retention time in the center of Harvey branch

  / ISSN 1562-6865 (Online) - ISSN 1063-7710 (Print)

estuary was largely improved from over 80 days to about 38 days, and from about 65 days to ~40 days in the Peel Inlet due to the Cut in the dry season. In the wet season (August), large improvement of water retention time inside the estuary was also found. The monthly average water retention time in the center of Harvey branch estuary was reduced from about 68 days to about 32 days, and from about 50 days to 22 days in the Peel Inlet due to the Cut in the wet season.

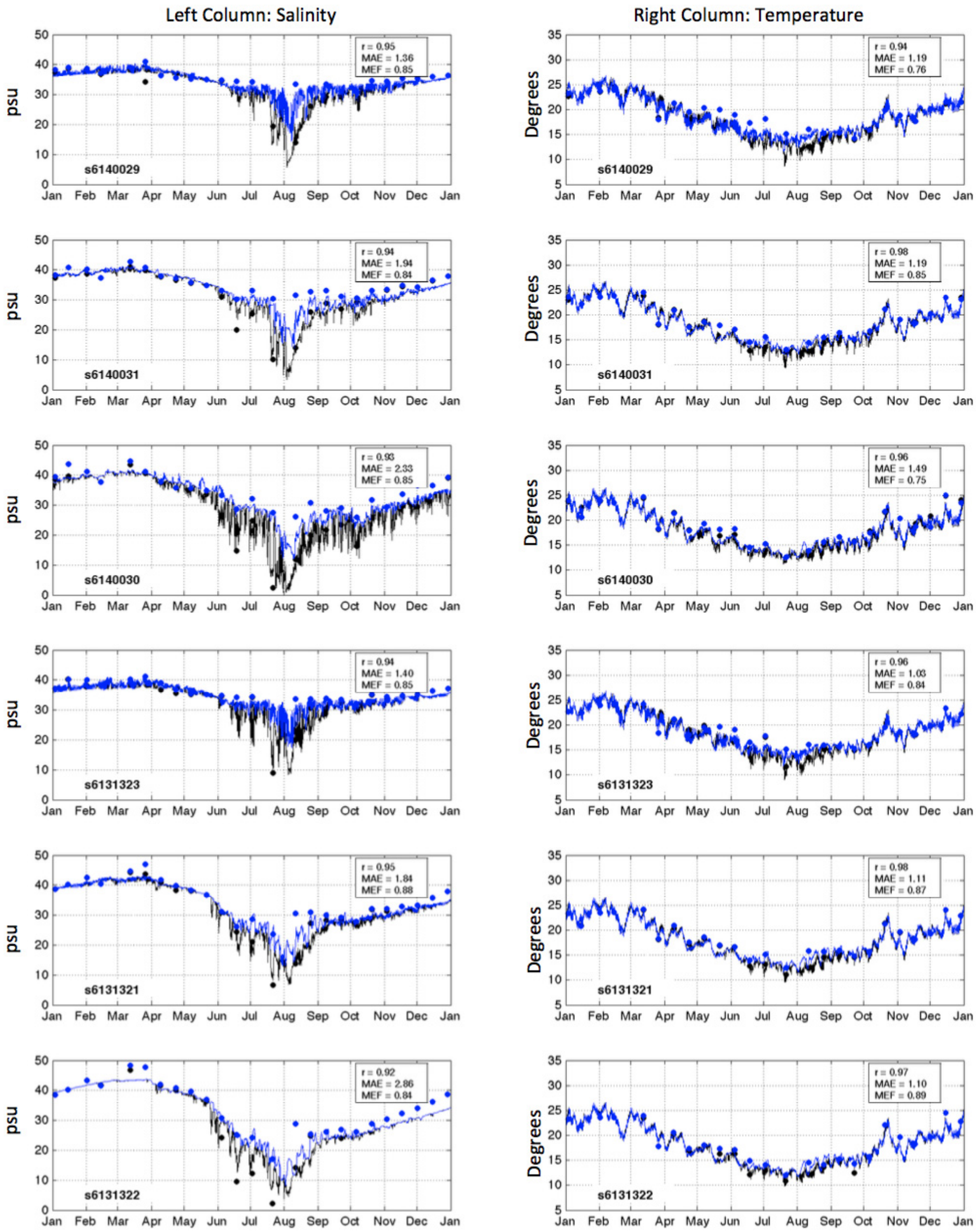

Figure 3. Measured vs. modelled (left) salinity and (right) temperature at 6 monitoring sites in year 2008. Black and blue dots represent measured data at surface and bottom water, respectively; while black and blue lines represent modelled data at surface and bottom water, respectively.

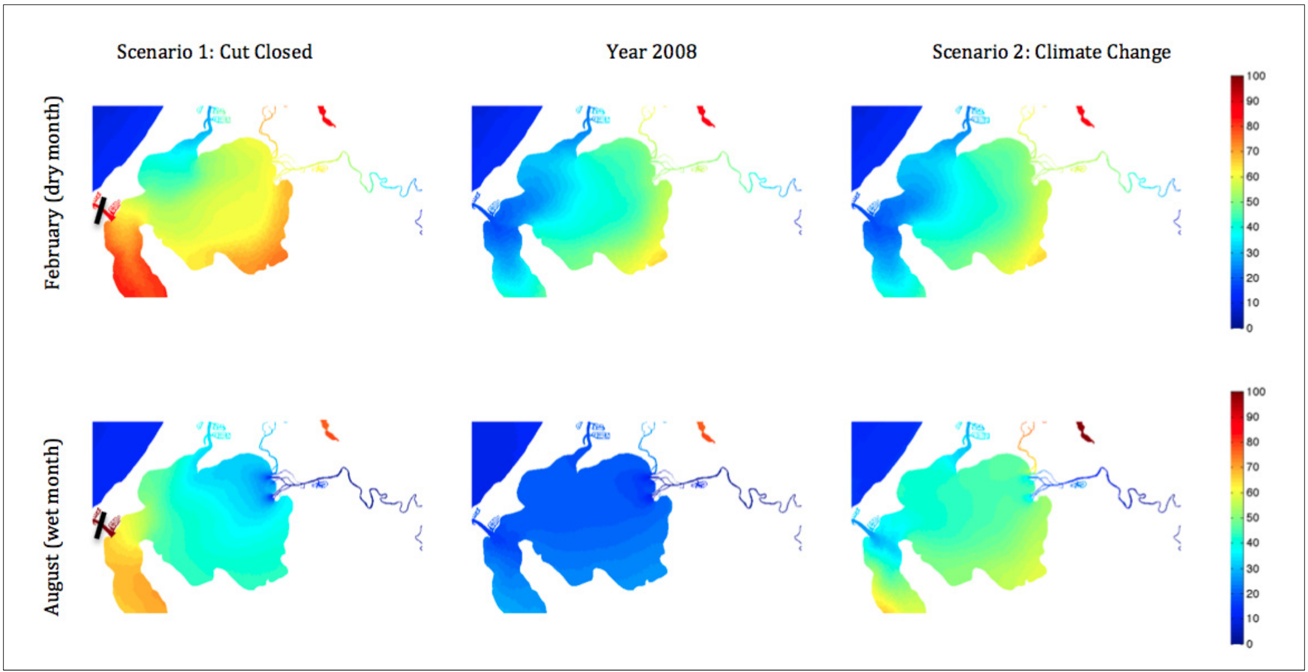

Figure 4. Monthly-averaged water retention time in Peel-Harvey Estuary.

3.2.2 Salinity and Water Stratification

Although the Dawesville Cut greatly reduced the water retention time, it also introduced more saline water into the estuary (Figure 5) and substantially changed the salt-wedge pattern inside the estuary in wet seasons when inflow rates were high (Figure 2). The average surface salinity in August increased from ~8 psu to ~17 psu in Peel Inlet, and from ~5 psu to ~20 psu in Harvey branch due to the construction of Dawesville Cut. While in the dry month, the water is very saline both before and after the cut, however small difference at the area adjacent to the Mandurah Channel can still be found.

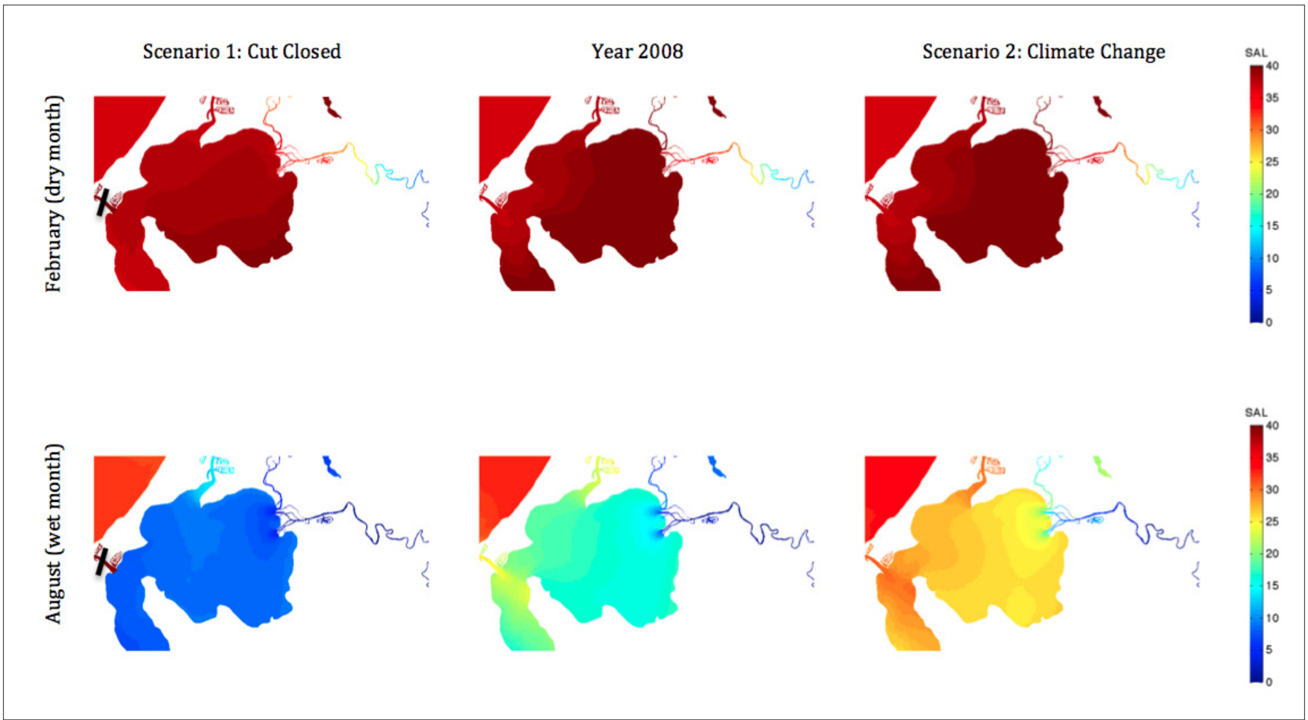

Figure 5. Monthly-averaged surface salinity in Peel-Harvey Estuary.

The spatial salt-wedge pattern also has been largely modified by the Dawesville Cut in the wet season (Figure 6). The salinity difference between the surface and bottom layers, i.e., the salt wedge created by the salinity stratifications, is only significant at the area adjacent to Mandurah Channel and at the mouth of Murray

River before the construction of Dawesville Cut, whereas after the Cut, significant salinity difference of up to 10 psu can be observed in both the Peel Inlet and Harvey branch estuary, indicating that the water stratification has been greatly enhanced. Intrusion of salt wedge toward the upstream in Murray River can also be found. While in dry season, no significant salinity stratification has been found before and after the Cut.

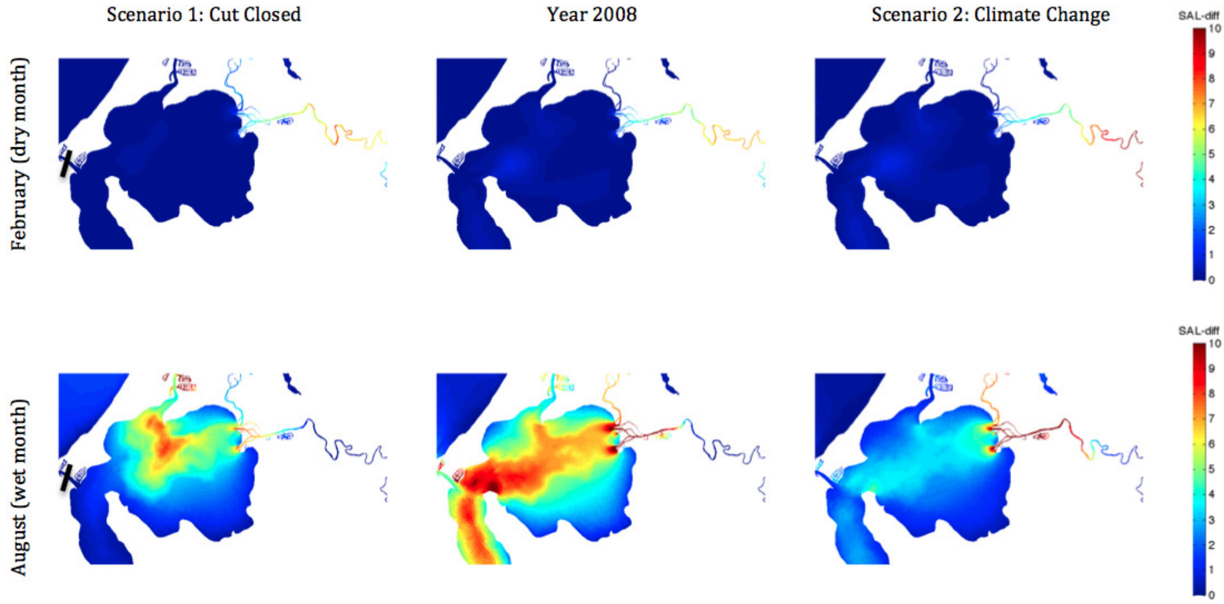

Figure 6. Monthly-averaged salinity difference between surface and bottom layers in Peel-Harvey Estuary.

Curtain views of the salinity stratifications along Dawesville Cut to Murray River provide another view of salinity stratification and salt wedge intrusion due to the construction of Dawesville Cut (Figure 7). Similar to previous plots, the difference of salinity curtain is more significant in winter time when the inflow rates were high. The salinity at the bottom of Peel Inlet increased by about 10 psu after the Cut, and the salt wedge in Murray River (where salinity difference between surface and bottom water is higher than 2 psu) moved ~ 2.9 km further upstream in winter time. The difference of salinity stratification in dry season is not as significant as wet season, but slight salt wedge intrusion into the upstream of Murray River can also be observed.

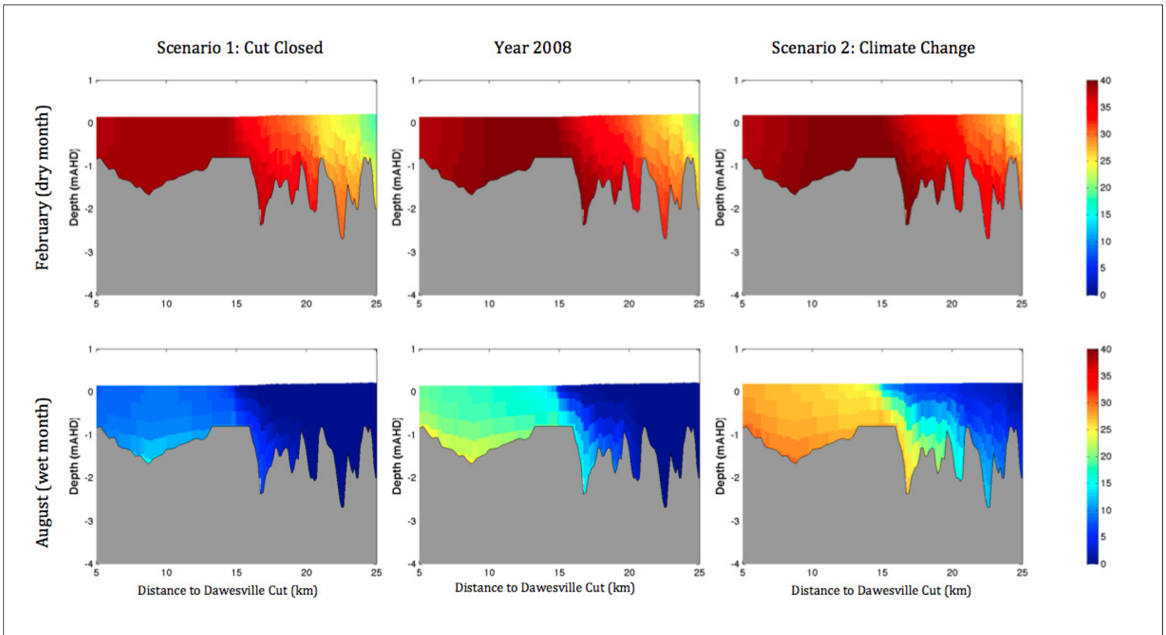

Figure 7. Curtain view of monthly-averaged salinity stratification from Dawesville Cut to Murray River.

It has been found in many eutrophic coastal estuaries that water stratifications cause water quality problems at the near-bottom layer because it restricts vertical mixing between oxygen depleted bottom waters and oxygen saturated upper water (Paerl et al., 1998; Roberts et al., 2012). Recent research also suggested that salinity variability could act as a disturbance by producing unstable habitats (Van Diggelen and Montagna, 2016). Our modelling results suggested that the construction of the Dawesville Cut created strong salinity stratification in winter time, and also more annual salinity variations in the area close to the cut, as well as in Harvey branch and some parts of the Peel Inlet (Figure 3, 5). This hydrological change could have a negative impact on the aquatic system although the flushing time has been improved by the Cut, and we recommend further study of the change of dissolved oxygen in the bottom water of Peel-Harvey Estuary due to the construction of the Dawesville Cut.

3.3 Impact of Climate Change on the estuary hydrology

3.3.1 Water retention time

The impacts of climate change on the water retention time are negligible in dry season due to rare inflows, while in wet season the reduction of runoff and rise of sea level clearly increased the water retention inside the estuary with difference of over 30 days can be found (Figure 4). Areas adjacent to the Mandurah channel and Dawesville Cut are less influenced by the climate change due to high flushing effect of tides.

3.3.2 Salinity and Water Stratification

Climate change increased the average water salinity in the wet season (Figure 4), and, interestingly, reduced the water stratification inside the estuary (Figure 5). The monthly averaged salinity in August increased by about 9 psu at the center of Peel Inlet; while the salinity difference between the surface and bottom layers decreased from ~7.0 psu to 3.5 psu. No significant difference of salinity and their difference inside the estuary was found in the dry season. However, the salt wedge in Murray River had been pushed further upstream in both seasons.

The push up of the salt-wedge is better illustrated in Figure 7 where it shows the curtain views of monthly averaged salinity. The bottom salinity in the Peel Inlet increased by ~7psu due to the climate change in future. The salt wedge in Murray River (where salinity difference between surface and bottom water is higher than 2 psu) moved ~ 4.0 km further upstream in winter time. In dry season, the salinity stratification is less significant, but saline water in further upstream of Murray River was found due to rare inflows.

4 CONCLUSION

Modeling experiments were carried out using validated hydrodynamic models to examine the impacts of the artificial channel Dawesville Cut and possible future climate change on the water retention time and salt wedge patterns in the Peel-Harvey Estuary. Our results suggested that the construction of the Dawesville Cut in 1994 successfully improved the ocean flushing and reduced the water retention inside the estuary. However, the Cut also introduced more saline water into the estuary and thus enhanced the water stratification. The impacts are more significant in winter time when the estuary received strong fresh runoffs from three major inflow rivers. The combined impacts of climate change, including less runoffs, precipitation, higher sea levels and air temperature, largely increases the water retention time as well as the salinity inside the estuary, while reducing the water stratification. Both the construction and the climate change pushed the salt-wedge further toward the upstream of rivers, which could substantially change the riverine ecology. Further study of the effects of the hydrological changes on the aquatic ecosystem are recommended to get comprehensive evaluations of the impacts of the artificial channel and climate change in this shallow coastal estuary.

5 REFERENCES

Bicknell. C. (2006). *Review of Sand Bypassing at Dawesville and Mandurah*. Department of Planning and Infrastructure.

BMTWBM. (2013). TUFLOW FV Science Manual. Available from: http://www.tuflow.com/Download/ TUFLOW_FV/ Manual/ FV_Science_Manual_2013.pdf

Bruce, L.C., Cook, P.L.M., Teakle, I. & Hipsey, M.R. (2014). Hydrodynamic controls on oxygen dynamics in a riverine salt wedge estuary, the Yarra River estuary, Australia. *Hydrology and Earth System Sciences*, 18(4): 1397-1411.

Brearley, A. (2005). Ernest Hodgkin's Swanland: Estuaries and Coastal Lagoons of South-Western Australia, first edition. University of Western Australia, Perth, 549 pp.

Collins, M. and Knutti, R. (2013). Chapter 12: Long-term Climate Change: Projections, Commitments and Irreversibility. IPCC Fifth Assessment Report, pp. 1029-1101.

Cottingham, A, Hesp S.A., Hall N.G., Hipsey M.R., Potter I. C. (2014). Marked deleterious changes in the condition, growth and maturity schedules of Acanthoparagus butcheri (Sparidae) in an estuary reflect environmental degradation. *Estuarine, Coastal and Shelf Science*, 149, 109-119.

EPA (2008). *The Water Quality Improvement Plan for the Rivers and Estuary of the Peel-Harvey System – Phosphorus Management*. Western Australia. P V.

Hipsey, M., Bruce, L., & Kilminster, K. (2013). *A 3D hydrodynamic-biogeochemical model for assessing artificial oxygenation in a riverine salt-wedge estuary*. University of Western Australia, 1-7.

Jovanovic, D., Coleman R., Deletic A., and McCarthy D. (2017). Spatial variability of E. coli in an urban salt-wedge estuary. *Marine Pollution Bulletin*, 114, 114-122.

Kelsey, P., Hall, J., Kretschmer, P., Quinton, B. and Shakya, D. (2011). *Hydrological and nutrient modelling of the Peel-Harvey catchment*, Water Science Technical Series, Report No.33, Department of Water, Western Australia, 234 pp.

Nezlin, N.P., Kamer, K., Hyde, J., & Stein, E.D. (2009). Dissolved oxygen dynamics in an eutrophic estuary, Upper Newport Bay, California. *Estuarine, Coastal and Shelf Science*, 82,139-151.

Ruibal-Conti A.L. (2014). Connecting land to the ocean: a retrospective analysis of nutrient flux pathways within the Peel-Harvey catchment-estuary system. *PhD thesis*, University of Western Australia.

Umlauf, L. and Burchard, H. (2003). A generic length-scale equation for geophysical turbulence models. *Journal of Marine Research*, 61, 235–265.

Van Diggelen, A.D. and Montagna, P.A. (2016). Is salinity variability a benthic disturbance in estuaries? *Estuaries and Coasts*, 39, 967-980.

Watanabe, K., Kasai A., Antonio E.S., Suzuki K., Ueno M., Yamashita Y. (2014). Influence of salt-wedge intrusion on ecological processes at lower trophic levels in the Yura Estuary, Japan. *Estuarine, Coastal and Shelf Science*, 139, 67-77.

Water and Rivers Commission (1998). *Dawesville Channel Monitoring Programme*. Technical Review. Report WRT 28, Perth, Western Australia.

Wildsmith M.D., Rose T.H., Potter I.C., Warwick R.M., Clarke K.R., Valesini F.J. (2009). Changes in the benthic macroinvertebrate fauna of a large microtidal estuary following extreme modifications aimed at reducing eutrophication. *Marine Pollution Bulletin*, 58, 1250-1262.

Proceedings of the 37th IAHR World Congress
August 13 – 18, 2017, Kuala Lumpur, Malaysia

SEDIMENTARY AND HYDRODYNAMIC PROCESSES OF TIDAL BORES: SILTATION OF THE ARCINS CHANNEL, GARONNE RIVER (FRANCE)

DAVID REUNGOAT(1), XINQIAN LENG(2)& HUBERT CHANSON (3)

(1) Université de Bordeaux, I2M, Laboratoire TREFLE, Pessac, France,
d.reungoat@i2m.u-bordeaux1.fr
(2) The University of Queensland, School of Civil Engineering, Brisbane QLD 4072, Australia,
xinqian.leng@uqconnect.edu.au
(3) The University of Queensland, School of Civil Engineering, Brisbane QLD 4072, Australia,
h.chanson@uq.edu.au

ABSTRACT

A tidal bore is a hydraulic jump in translation propagating upstream in an estuarine channel when a macro-tidal flood tide enters a funnel shaped river mouth with shallow waters.The tidal bore of the Garonne River (France) was extensively investigated in the Arcins channel in 2015, focusing on the temporal evolution of hydrodynamics and sediment processes during spring tide period. The tidal bore had a marked effect on the velocity field, including a rapid flow deceleration and flow reversal. Maximum flow deceleration between -0.65 m/s^2 to almost -1.4 m/s^2 were observed. The early flood flow motion was very energetic with large fluctuations in all velocity components. The suspended sediment concentration (SSC) data showed very large instantaneous SSC levels, in excess of 100 kg/m^3, during the passage of the tidal bore front, as well as large SSCs during the first hour of the flood tide for the entire observations. The work culminates a 5-year research project at the same site, showing a progressive siltation of the Arcins channel during the last three years.

Keywords: Tidal bores; field measurements; suspended sediment processes; channel siltation; Garonne River.

1 INTRODUCTION

A tidal bore is a compressive wave of tidal origin, which propagates upstream as the tidal flow rises. It may be observed when a macro-tidal flood tide enters a funnel shaped river mouth with shallow waters (Tricker, 1965; Chanson, 2011). A related application is the tsunami-induced bore propagating in rivers (Tanaka et al., 2012). The occurrence of tidal and tsunami-induced bores has a significant impact on the natural systems. Their impact on sedimentary processes was documented in the field and in laboratory (Faas, 1995; Khezri and Chanson, 2015). It is understood that the bore propagation is associated with intense scouring and suspension of bed materials (Greb and Archer, 2007; Furgerot et al., 2016) (Fig. 1A). In cohesive sediment river systems, the erosional processes may be linked to the rheological properties of sediment deposits, and field observations suggested that the bore passage induces some surface erosion immediately, followed by delayed bulk erosion (Faas, 1995; Keevil et al., 2015).

Herein new field measurements were repeated systematically at the same site in the Garonne River (France) on 29 August, 30 August, 31 August and 1 September 2015 and on 27 October 2015. Instantaneous velocity measurements were performed continuously at high-frequency (200 Hz) prior to, during and after each afternoon tidal bore. Instantaneous sediment concentration and suspended sediment flux data were derived from careful calibration of acoustic backscatter and checked against water sample concentrations.

2 INVESTIGATION SITE, INSTRUMENTATION AND METHODOLOGY

Field measurements were performed in the tidal bore of the Garonne River in the Arcins channel, close to Lastrene (France), at a site previously used (Chanson et al., 2011; Reungoat et al., 2014; Keevil et al., 2015). The Arcins channel is 1.8 km long, 70 m wide and about 1.1 to 2.5 m deep at low tide, between the Arcins Island and the right bank (Fig. 1A). The bathymetric data indicated a progressive siltation of the Arcins channel at the sampling site between 2012 and 2015 (Fig. 1B). Although the tides were semi-diurnal, the tidal data indicated slightly different periods and amplitudes typical of diurnal inequality. Detailed field measurements were conducted under spring tide conditions between 29 August and 1 September 2015, and on 27 October 2015, while additional observations were performed on 28 August 2015, 26 October and 28 October 2015. The tidal range was between 5.85 m to 6.32 m, and the tidal bore Froude numbers between 1.18 and 1.7 (Reungoat et al., 2016). All measurements were started prior to the passage of the tidal bore and ended at least one hour after the bore passage.

(A) Looking downstream on 28 October 2015 - The ADV unit was fixed to the pontoon next to the right bank.

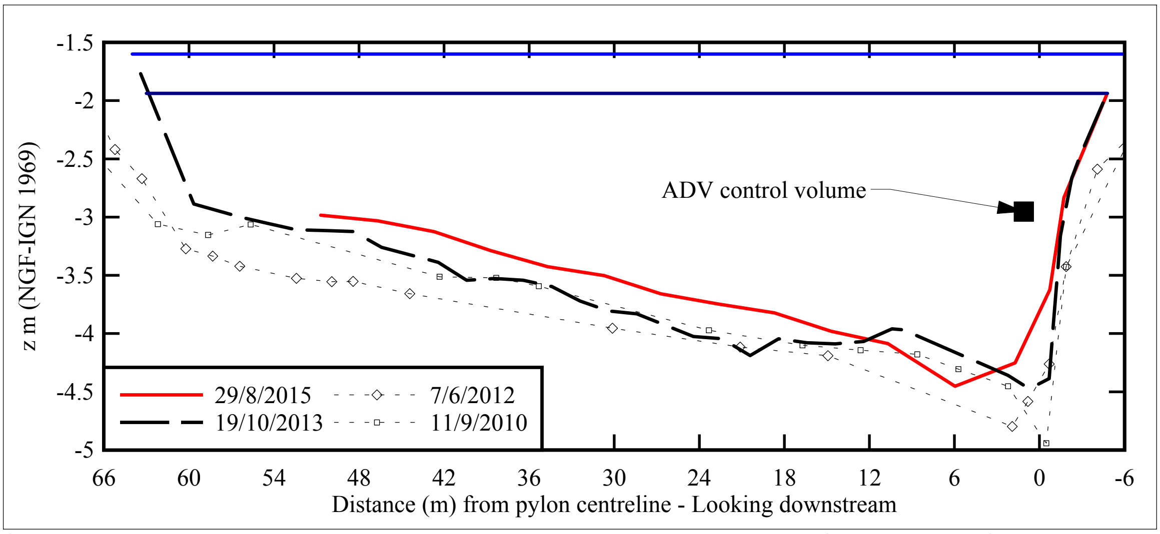

(B) Surveyed cross-section on 29 August 2015 with the initial water level (dark blue line), conjugate water depth (blue line) and ADV control volume - Comparison with the surveyed data in 2013, 2012 and 2010.

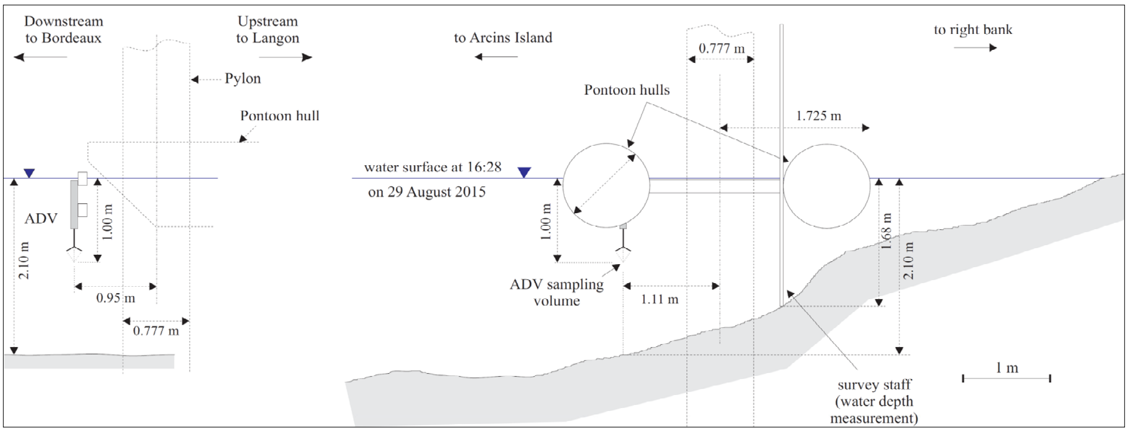

(C) Undistorted dimensioned sketch of the ADV mounting and sampling location relative to the bed and free-surface about 2 minutes prior to the tidal bore passage on 29 August 2015.

Figure 1. Tidal bore investigation site in the Arcins channel, Garonne River (France) in August-October 2015.

Free surface elevations were recorded continuously using a survey staff, while instantaneous velocity components were measured using a Nortek^{TM} ADV Vectrino+ equipped with a down-looking head. The ADV unit was fixed beneath a heavy pontoon and its control volume was located 1.0 m below the free-surface (Fig. 1). The ADV power setting (High- or Low) was selected after preliminary tests, to optimise the acoustic backscatter response of the ADV unit with the Garonne River sediment (Reungoat et al. 2016). The ADV system was sampled continuously at 200 Hz. The velocity signal post-processing included the removal of communication errors, the removal of average signal to noise ratio (SNR) data less than 5 dB, the removal of average correlation values less than 60% and despiking using the phase-space thresholding technique

(Goring and Nikora, 2002; Wahl, 2003). The percentage of good samples ranged between 60% and 90% for the entire data sets.

Garonne River bed materials were collected at the end of ebb tide, next to the right bank. The soil sample consisted of soft cohesive mud and silty materials. A series of laboratory tests were conducted to characterise the particle size distribution, rheometry and backscatter properties. Water samples were also collected prior to and shortly after the tidal bore about 0.2 m below the water surface. The water samples were dried in an oven, set at 40 °C, to measure the mass of dry sediments and the sample sediment concentration. Further details are reported in Reungoat et al. (2016).

3 BASIC FLOW PATTERNS

3.1 Free-surface observations

On 28 August 2015 afternoon, no tidal bore was observed. On 29, 30, 31 August, 1 September and 27 October 2015, tidal bores were formed at the downstream end of the Arcins channel. The bore extended rapidly across the entire channel width as a breaking bore in this very shallow region. The tidal bore was undular at the sampling location further upstream, although it was breaking close to the left bank (Fig. 1A). While the bore was undular, the free-surface elevation rose very rapidly during the bore passage: i.e., by 0.3 m to 0.5 m in the first 10 s. The tidal bore propagated up to the upstream end of the channel for the entire channel length. The bore passage was always followed by a series of strong whelps lasting for several minutes, with a wave period about 1 s (Fig. 2). For all field studies, the whelps were observed between one to three minutes after passage of the bore. In August-September, the free-surface wave motion was seen about three minutes after the front. In October, these whelps were seen about a minute after the bore front: that is, with a delay comparable to that observed in October 2013 at the same site. Figure 2 illustrates the well-formed whelp motion on 27 October 2015. The water depth data showed large free-surface fluctuations with a period about 1.3 to 1.5 s between 56270 s and 56310 s (Fig. 2B).

The tidal bore shape was characterised by its Froude number, $Fr_1 = (V_1+U)/(g \times A_1/B_1)^{0.5}$, where V_1 is the initial flow velocity positive downstream, U is the bore celerity positive upstream, g is the gravity acceleration, A_1 is the initial flow cross-section area and B_1 is the initial free-surface width, which were derived from bathymetric surveys conducted daily. The Froude number ranged from 1.2 to 1.7, consistent with the undular nature of the bore, except on 31 August 2015. On 31 August 2015, the bore front was undular on the channel centreline and towards to the right bank, but breaking close to the left bank. For the secondary waves, the relationships between Froude number, dimensionless wave amplitude and wave length data, followed closely by past field and laboratory observations and the results were close to a solution of the Boussinesq equation. During the late ebb tide, the current velocity decreased in the Arcins channel with time. The tidal bore had a marked effect on the velocity field (see below), with a rapid flow deceleration and flow reversal during the bore passage.

The application of the equations of conservation of mass and momentum in their integral form gives an analytical solution of the conjugate flow properties, namely the ratio of conjugate cross-section areas as a function of the Froude number and cross-section shape (Chanson, 2012). It yields:

$$\frac{A_2}{A_1} = \frac{1}{2} \times \frac{\sqrt{\left(2 - \frac{B'}{B}\right)^2 + 8 \times \frac{\frac{B'}{B}}{\frac{B_1}{B}} \times Fr_1^2} - \left(2 - \frac{B'}{B}\right)}{\frac{B'}{B}} \qquad [1]$$

where A_2 is the new cross-sectional area: $A_2 = A_1 + \Delta A$ (Fig. 3A), B and B' are characteristic widths defined based upon the cross-sectional shape (Chanson, 2012). The observations are reported in Figure 3B and Table 1 in terms of the ratio of conjugate cross-sectional areas A_2/A_1 as a function of the Froude number Fr_1. The data in this study (filled square symbols) were compared with the momentum principle solution (Eq. (1)) (open circles) and previous field data (solid symbols) (Fig. 3B). For completeness, the Bélanger equation, which was developed for a smooth rectangular channel, is included (thin solid line). Figure 3B shows a good agreement between Equation (1) and the field data. It highlights further the improper application of the Bélanger equation in natural irregular-cross-section channels.

Table 1. Tidal bore properties at the sampling location during the 2015 field measurements in the Arcins channel (Garonne River, France).

DATE	Fr_1	U (m/s)	d_1 (m)	A_1 (m^2)	B_1 (m)	□d (m)	A_1/B_1	B_2/B_1	B/B_1	B'/B_1	A_2/A_1
29/08/2015	1.18	4.23	1.685	101.4	67.6	0.338	1.50	1.034	1.019	1.012	1.23
30/08/2015	1.34	4.25	1.25	72.8	64.3	0.470	1.13	1.048	1.017	1.019	1.42
31/08/2015	1.70	4.79	1.122	56.6	65.1	0.496	0.87	1.068	1.032	1.025	1.59
01/09/2015	1.38	4.45	1.28	74.9	64.5	0.440	1.16	1.048	1.024	1.017	1.39
27/10/2015	1.33	4.61	1.24	88.0	65.9	0.480	1.34	1.049	1.019	1.017	1.37

(A) View from the right bank looking downstream about 30 s after the bore passage - Arrow points to whelps.

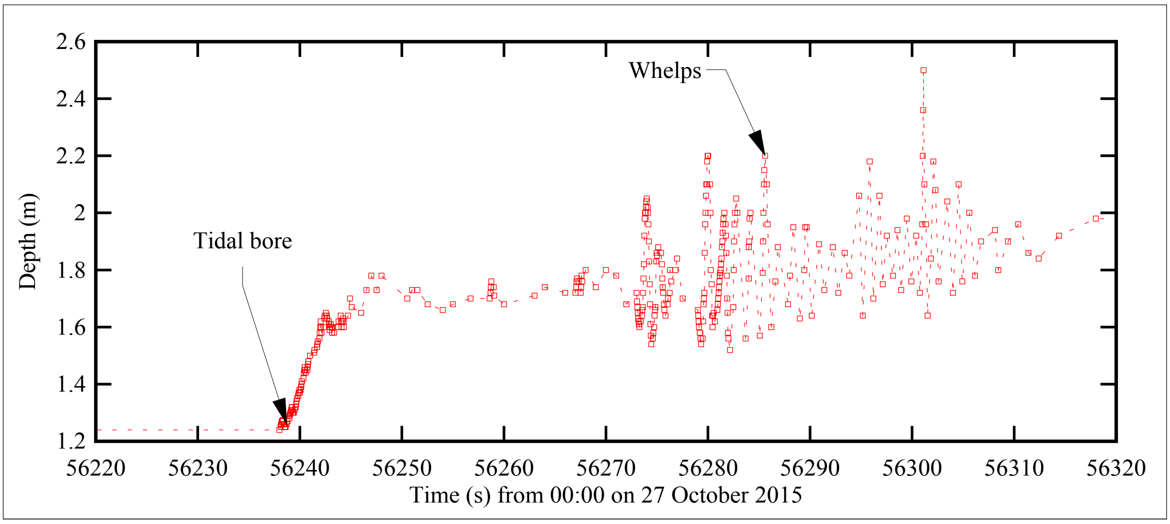

(B) Water depth observations at the survey staff.

Figure 2. Well-formed whelp motion observed about a minute after tidal bore passage on 27 October 2015.

3.2 Velocity measurements

Velocity measurements were conducted continuously at high frequency prior to, during and after the tidal bore. Figure 4 shows a typical data set, where the longitudinal velocity component, V_x is positive downstream, the transverse velocity component, V_y is positive towards the left bank and the vertical velocity component, V_z is positive upwards. In Figure 4A, the time-variations of the water depth are included as well as surface velocity data on the channel centre. During the late ebb tide, the current velocity in the Arcins channel decreased with time. Immediately prior to the bore, the surface velocity dropped down to the range between +0.2 m/s and +0.3 m/s at the channel centre. Lower instantaneous velocities were recorded by the ADV unit close to the left bank. The tidal bore occurrence had a marked effect on the velocity field, as illustrated in Figure 4. A rapid flow deceleration and flow reversal were observed during the bore passage, followed by large and rapid fluctuations of all velocity fluctuations during the early flood tide. The maximum flow deceleration ranged from -0.65 m/s^2 to less than -1.4 m/s^2 (Table 2). A number of data are summarised in Table 2, regrouping basic flow properties prior to the bore (a couple of minutes prior to the bore), as well as flow properties recorded during the very early flood tide (i.e. 20 s after bore passage), early flood tide free-surface wave motion period and flood tide (i.e. one hour after bore passage).

The bore passage was associated with large fluctuations of all velocity components, lasting throughout the flood tide. The flood flow was very energetic. About 100 s to 300 s after the bore front, some strong free-surface oscillation motions were observed (Fig. 3), associated with large oscillations of both horizontal and vertical velocity components with periods about 1.3 s to 1.5 s (Table 2). Such velocity oscillations were closely linked to the free-surface curvature and its induced vertical motion.

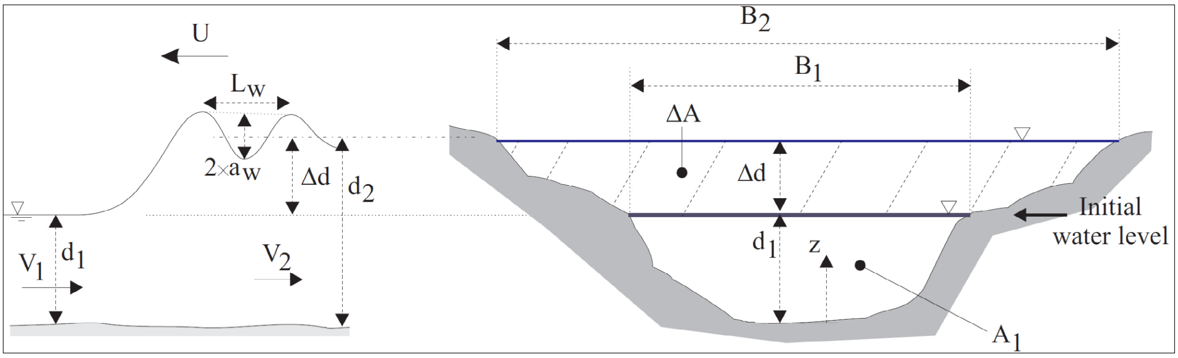

(A) Definition sketch of a tidal bore propagating in a natural irregular-cross-section channel.

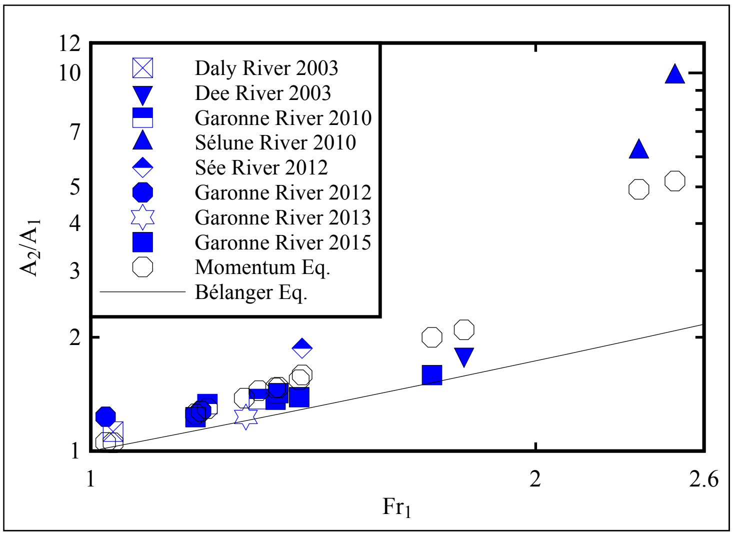

(B) Relationship between conjugate cross-sectional area ratio, A_2/A_1 and Froude number, Fr_1 in tidal bores - Comparison between field observations (blue symbols), momentum principle solution (Eq. (1), black hollow circles) and the Bélanger equation (thin solid line).

Figure 3. Free-surface characteristics of the tidal bore of the Garonne River at Arcins in August, September and October 2015 - Comparison with past field observations.

The turbulent properties were estimated before and after the tidal bore passage. A few basic characteristics are summarised in Table 2. After the rapid deceleration, the data in this study showed large velocity fluctuations during the very early flood tide, as first reported by Chanson et al. (2011). Dimensionless velocity fluctuations, $v'/|\overline{V_x}|$ ranged from 10% to 30% for all velocity components, where v' is the standard deviation of a velocity component and $|\overline{V_x}|$ is the magnitude of time-averaged longitudinal velocity. Typical data are illustrated in Figure 4 with the tidal bore passage about t ~ 327,550 s and quantitative observations are reported in Table 2.

The velocity fluctuations were large during the flood tide and large fluctuations were recorded for the first two hours. For example, dimensionless velocity fluctuations, $v'/|\overline{V_x}|$ ranged from 6% to 18% one hour after the bore passage in August-September-October 2015 (Table 2). The horizontal turbulence ratio, v_y'/v_x' was between 0.42 and 0.85, with the vertical turbulence ratio, v_z'/v_x' being between 0.35 and 0.5. Such values were comparable to laboratory observations in straight prismatic rectangular channels (Nezu and Nakagawa, 1993;Nezu, 2005). Overall, v_z'/v_x' was about two-thirds of the horizontal turbulence intensity, v_y'/v_x' and such a finding indicated some turbulence anisotropy during the flood tide motion behind the tidal bore.

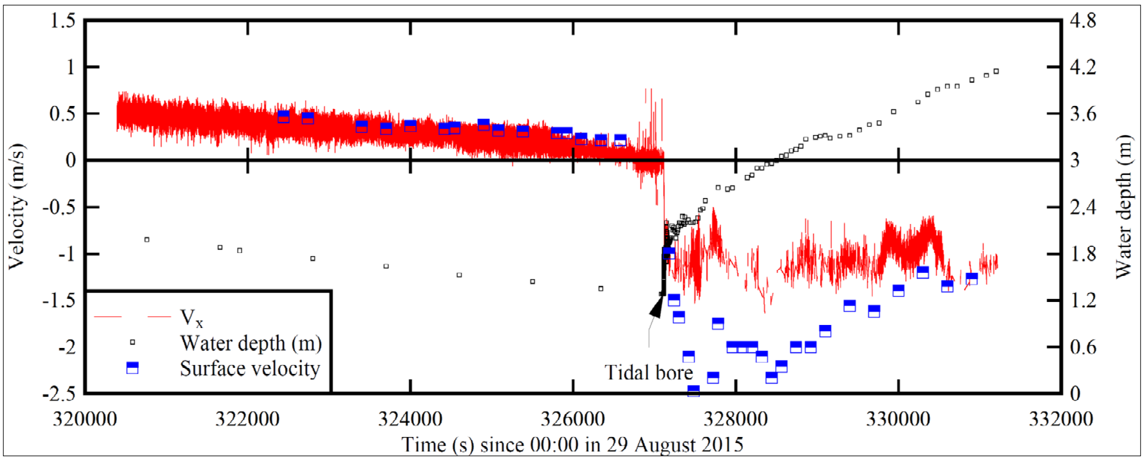

(A) Water depth and longitudinal velocity component - Comparison between ADV data (sampling rate: 200 Hz) and surface velocity data.

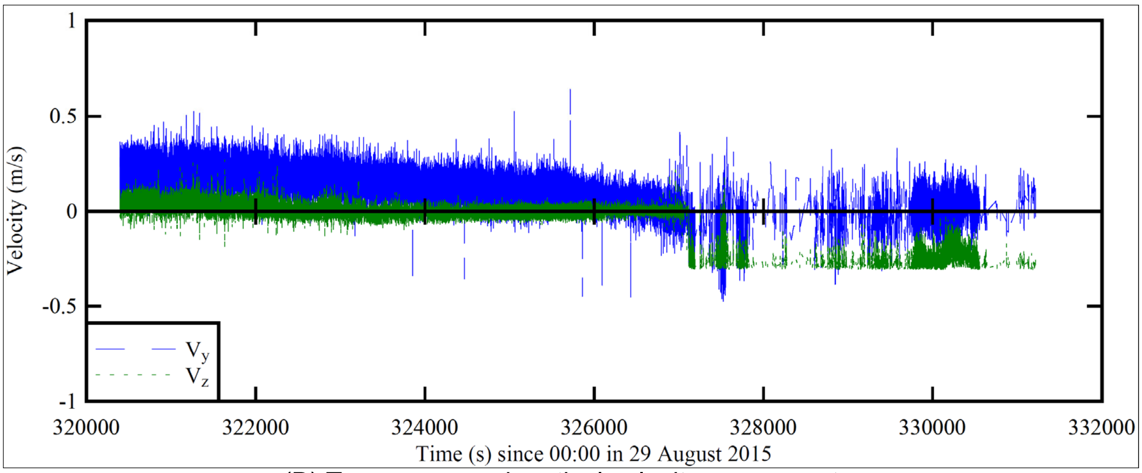

(B) Transverse and vertical velocity components.

Figure 4. Water depth and instantaneous velocity data as functions of time during the Arcins channel tidal bore on 1 September 2015 for the entire data set.

4 SUSPENDED SEDIMENT CHARACTERISTICS

The time-variations of the suspended sediment concentration (SSC) were deduced from the acoustic backscatter amplitude data, after a daily calibration. In addition, water samples were collected next to the surface before and after tidal bore (Fig. 5) and the data were analysed in laboratory subsequently. Typical data sets are presented in Figure 6 together with the water depth and the sediment concentrations of water samples. The SSC data showed some low SSC level at the end of the ebb tide: that is, SSC <2 kg/m^3 to 10 kg/m^3 typically. The passage of the tidal bore was associated with a very rapid increase in SSC levels together with large and rapid fluctuations in SSC estimates. Immediately after the bore, the colour of the water was dark brown, as seen in Figure 5. During the mid flood tide, the SSC estimates tended to decrease about 30-45 minutes after the bore passage. For all field studies, maximum SSC levels were observed about 500-600 s after the bore passage, with maximum instantaneous SSC estimates up to 90-130 kg/m^3, while the water sample analysis yielded maximum SSCs larger than 60 kg/m^3 (Fig. 6B).

The SSC data, indicating some large sediment concentration during the tidal bore as well as during the first hour of the flood tide, were consistent with visual observations of murky water during the bore event. They were also comparable to previous field observations in several natural systems (Chanson et al., 2011;Fan et al., 2012;Keevil et al., 2015;Furgerot et al., 2016). All the field data highlighted the massive suspended sediment load after the tidal bore passage. Figure 7 regroups the present results by showing the time-average suspended sediment flux per unit area as a function of the time-average suspended sediment concentration for the first hour after the tidal bore. In Figure 7, the tidal bore data are compared to field data recorded in large rivers during major floods, including the Brisbane, Missouri and Yellow Rivers. The comparative results emphasised the large suspended sediment fluxes in the Garonne River tidal bore.

Table 2. Velocity properties in the Arcins channel immediately prior to, during and immediately after the tidal bore during the 2015 field measurements in the Arcins channel (Garonne River, France).

DATE	29/08/2015	30/08/2015	31/08/2015	01/09/2015	27/10/2015
Froude number, Fr_1	1.18	1.34	1.70	1.38	1.33
Initial flow conditions					
Initial water depth (m) ([1])	1.685	1.25	1.12	1.28	1.24
Initial surface velocity (m/s) ([2])	+0.29	+0.21	+0.18	+0.22	+0.22
Initial velocity, $\overline{V_x}$ (m/s) ([3])	+0.094	+0.105	+0.005	0.0	+0.066
Bore passage					
Maximum deceleration $(\partial \overline{V_x} / \partial t)_{max}$ (m/s^2) ([3])	-1.2	-1.4	-0.883	-0.739	-0.645
Very early flood tide (T_{bore}+20s)					
$\overline{V_x}$ (m/s) ([3])	-0.82	-0.83	-0.83	-0.84	-0.81
$\overline{V_y}$ (m/s)	+0.02	-0.06	-0.06	-0.04	-0.06
$\overline{V_z}$ (m/s)	-0.11	-0.14	-0.20	-0.22	-0.16
v_x' (m/s)	0.085	0.098	0.047	0.068	0.054
v_y' (m/s)	0.046	0.079	0.070	0.039	0.058
v_z' (m/s)	0.026	0.032	0.031	0.028	0.026
Early flood tide wave motion					
Time after bore passage (s)	180	170	170	175	50
Velocity amplitude, V_x (m/s) ([3])	0.165	0.255	0.138	0.135	0.175
Velocity amplitude, V_z (m/s)	0.10	0.11	0.102	0.07	0.10
Velocity oscillation period (s)	1.5	1.31	1.47	1.46	1.33
Flood tide (T_{bore}+3600s)					
$\overline{V_x}$ (m/s) ([3])	-0.91	-1.02	-1.27	-0.90	-1.20
v_x' (m/s)	0.088	0.173	0.116	0.088	0.116
v_y' (m/s)	0.074	0.073	0.061	0.063	0.059
v_z' (m/s)	0.044	0.060	0.060	0.034	0.041

Notes: ([1]): at survey staff; ([2]): surface data at channel centre; ([3]): ADV data.

Figure 5. Photograph of sediment-laden water samples collected on 27 October 2015 respectively at 14:00, 15:05 [before bore], 15:55, 15:59, 16:17 [after bore] (from right to left)- Tidal bore passage at 15:40- All samples were thoroughly mixed prior to the photograph.

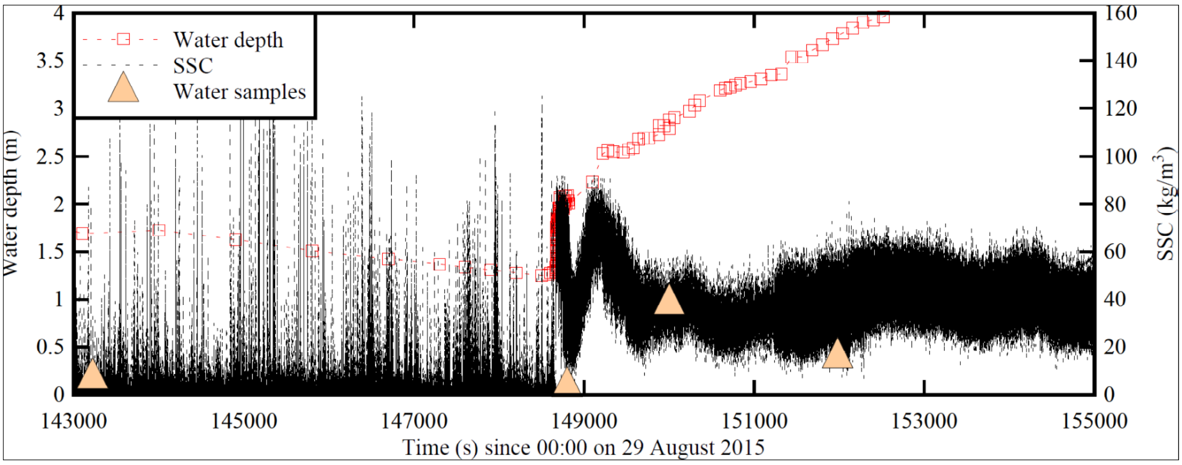

(A) 30 August 2015.

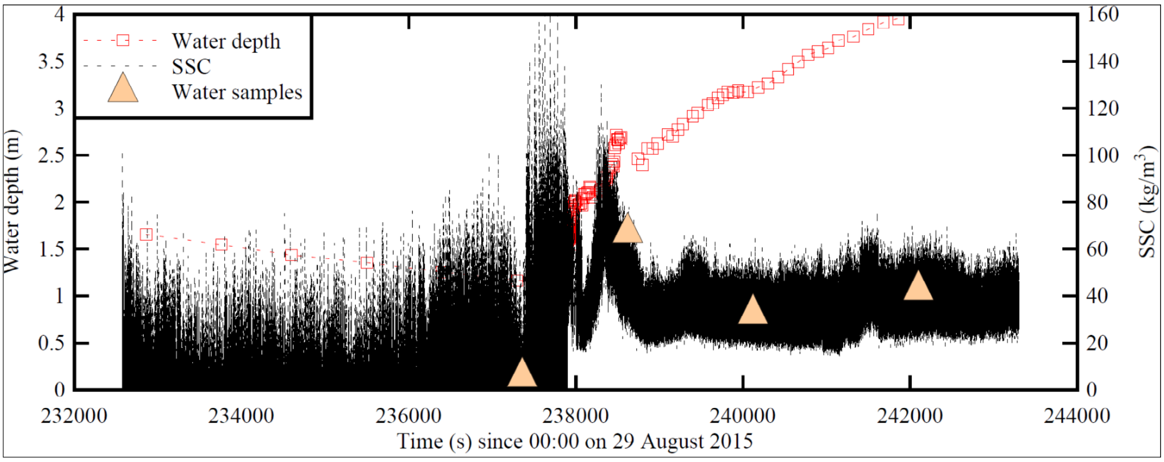

Figure 6. Suspended sediment concentration (SSC) and water depth data as functions of time during the Arcins channel tidal bore - Comparison between SSC estimates derived from ADV acoustic backscatter amplitude and water samples.

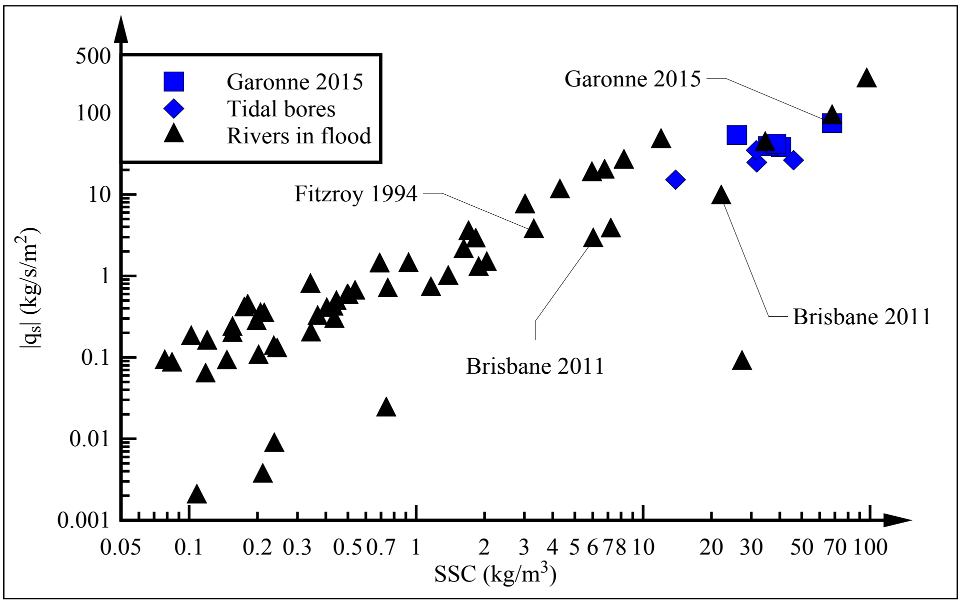

Figure 7. Time-average suspended sediment flux per unit area $\overline{q_s}$ (kg/m^2/s) as function of the mean time-average suspended sediment concentration $\overline{SSC}$ during the first hour of the flood tide after the tidal bore - Comparison between present tidal bore data (Garonne 2015, blue square symbols), past tidal bore data (blue diamond symbols) and observations of major flood river data (Amazon, Mississippi, Nile, Brisbane, Fitzroy and Yellow Rivers).

4.1 Discussions

Since 2010, the Arcins channel is believed to have experienced some progressive siltation (Keevil et al. 2015). In 2013, a build-up of low natural bar of hard materials was observed at the upstream end of the Arcins channel. In 2015, two low natural bars of relatively hard materials were noted, at both upstream and downstream ends of the channel. At the upstream end, the bar was established across the entire Arcins channel width: it was possible to walk to the Arcins Island in less than knee-deep waters. At the downstream end, surfers had barely enough water to surf the bore without damaging their board fins. At the sampling site, some siltation of both left and right banks was observed. It is conceivable that recent major floods of the Garonne River in 2012 and 2013 scoured the main river channel, located at the west of Arcins Island, thus reducing the flow into Arcins channel particularly at low tides and enhancing channel siltation.

5 CONCLUSIONS

The tidal bore of the Garonne River (France) was extensively investigated in the Arcins channel between year 2010 and 2015. The 2015 field study aimed to comprehend the temporal evolution of hydrodynamics and sediment processes in a tidal bore affected estuarine zone during a spring tide period, by conducting comprehensive observations encompassing hydrodynamics, turbulence and sediment transport.

The tidal bore had a marked effect on the velocity field, including a rapid flow deceleration and flow reversal during the bore passage, followed by large and rapid fluctuations of all velocity fluctuations during the early flood tide. The maximum flow deceleration ranged from -0.65 m/s^2 to almost -1.4 m/s^2. The early flood flow motion was very energetic with large fluctuations in all velocity components. The suspended sediment concentration (SSC) data showed very large instantaneous SSC levels during the passage of the tidal bore front (in excess of 100 kg/m^3), as well as substantially large SSC estimates during the early flood tide for all the entire observations.

This study is the first detailed characterisation of turbulent sedimentary processes in a tidal bore affected channel with such a fine temporal and spatial resolutions: i.e., continuous sampling at 200 Hz in a small control volume O (5 mm). The work culminates a 5-year research project at the same site, showing a progressive siltation of the Arcins channel during the last three years.

ACKNOWLEDGEMENTS

The authors thank all the people who participated in the field works. They acknowledge the helpful inputs of Professor Pierre Lubin (University of Bordeaux, France). The financial assistance of the AgenceNationale de la Recherche (ProjetMascaret ANR-10-BLAN-0911) is acknowledged.

REFERENCES

Chanson, H. (2011). *Tidal Bores, Aegir, Eagre, Mascaret, Pororoca: Theory and Observations*. World Scientific, Singapore, 220.

Chanson, H. (2012). Momentum Considerations in Hydraulic Jumps and Bores. *Journal of Irrigation and Drainage Engineering*, ASCE, 138(4), 382-385.

Chanson, H., Reungoat, D., Simon, B. & Lubin, P. (2011). High-Frequency Turbulence and Suspended Sediment Concentration Measurements in the Garonne River Tidal Bore. *Estuarine Coastal and Shelf Science*, 95(2), 298-306.

Faas, R.W. (1995). Rheological Constraints on Fine Sediment Distribution and Behavior: The Cornwallis Estuary, Novia Scotia. *Proceding of Canadian Coastal. Conference*, Dartmouth, Nova Scotia, 301–314.

Fan, D., Cai,G., Shan, S., Wu, Y., Zhang, Y. & Gao, L. (2012). Sedimentation Processes and Sedimentary Characteristics of Tidal Bores along the North Bank of the Qiantang Estuary. *Chinese Science Bulletin*, 57(13), 1578-1589.

Furgerot, L., Mouaze, D., Tessier, B., Perez, L., Haquin, S., Weill, P. & Crave, A. (2016). Sediment Transport Induced by Tidal Bores. Estimation from Suspended Matter Measurements in the Sée River (Mont-Saint-Michel Bay, Northwestern France). *Comptes Rendus Géoscience*, 348(6), 432-441.

Goring, D.G. & Nikora, V.I. (2002). Despiking Acoustic Doppler Velocimeter Data. *Journal of Hydraulic Engineering*, ASCE, 128(1), 117-126.

Greb, S.F. & Archer, A.W. (2007). Soft-Sediment Deformation Produced by Tides in a Meizoseismic Area, Turnagain Arm, Alaska. *Geology*, 35(5), 435-438.

Keevil, C.E., Chanson, H. & Reungoat, D. (2015). Fluid Flow and Sediment Entrainment in the Garonne River Bore and Tidal Bore Collision. *Earth Surface Processes and Landforms*, 40(12), 1574-1586.

Khezri, N. & Chanson, H. (2015). Turbulent Velocity, Sediment Motion and Particle Trajectories Under Breaking Tidal Bores: Simultaneous Physical Measurements. *Environmental Fluid Mechanics*, 15(3), 633-651.

Nezu, I. (2005). Open-Channel Flow Turbulence and its Research prospect in the 21st Century. *Journal of Hydraulic Engineering*, ASCE, 131(4), 229-246.

Nezu, I. & Nakagawa, H. (1993). *Turbulence in Open-Channel Flows.* IAHR Monograph, IAHR Fluid Mechanics Section, Balkema Publ., Rotterdam, Netherlands, 281.

Reungoat, D., Chanson, H., & Caplain, B. (2014). Sediment Processes and Flow Reversal in the Undular Tidal Bore of the Garonne River (France). *Environmental Fluid Mechanics*, 14(3), 591-616.

Reungoat, D., Leng, X. & Chanson, H. (2016). *Hydrodynamic and Sedimentary Processes of Tidal Bores: Arcins Channel, Garonne River in August-September-October 2015*. *Hydraulic Model Report No. CH102/16*, School of Civil Engineering, University of Queensland, Brisbane, Australia, 270 (ISBN 978-1-74272-155-2).

Tricker, R.A.R. (1965). *Bores, Breakers, Waves and Wakes*. American Elsevier Publ. Co., New York, USA.

Wahl, T.L. (2003). Despiking Acoustic Doppler Velocimeter Data. Discussion. *Journal of Hydraulic Engineering*, ASCE, 129(6), 484-487.

INVESTIGATION OF WIND SPEED PROJECTIONS IN THE PERSIAN GULF USING DIFFERENT RESOURCES OF CMIP5 DATA

TAHEREH ALINEJHAD-TABRIZI[1], NASSER HADJIZADEH-ZAKER[2] & BAHAREH KAMRANZAD[3]

[1, 2] Graduate Faculty of Environment, University of Tehran, Tehran, Iran,
t.alinejhad@ut.ac.ir; nhzaker@ut.ac.ir
[3] Iranian National Institute for Oceanography and Atmospheric Science, Tehran, Iran,
kamranzad@inio.ac.ir

ABSTRACT

Assessment of climate change impacts on the wind field is a primary concern for environmental policy analysts all over the world. The aim of this study was to assess the Coupled Model Inter-comparison Project (CMIP) phase 5 results in wind speed, and to investigate the wind speed projections in the Persian Gulf at the end of 21st century. Two models from CMIP5 were selected and their results were compared quantitatively for the period 1986 to 2005, with ECMWF wind field as a reliable data in the study area. Results showed that CMIP5 wind speed in the Persian Gulf are underestimated and a regression or other complex approaches are required for modifying CMIP5 wind speed before being used as input data for climate change impact assessment. Variation of wind speed in the Persian Gulf were also evaluated using data for two Representative Concentration Pathways for the period 2081 to 2100. Time series of the annual averages of the wind speeds and statistical analysis indicate a decreasing trend in the point of study. Also, variation of statistical parameters such as maximum and minimum values showed an insignificant reduction compared to the period 1986 to 2005, which can lead to larger variation in wave characteristics and change in sediment transportation in the coastal areas.

Keywords: Climate change; RCPs; ECMWF; CMIP5; Persian Gulf.

1 INTRODUCTION

Climate change is defined as any long-term change in the patterns of average weather of a specific region or the whole Earth, which is generally accepted as one of the most important constrains in the assessment of long-term changes in coastal and marines (Bonaldo et al., 2015; Casas-Prat et al., 2015; Salles et al., 2011). Its impact is explicated through changes in the earth surface temperature, precipitation, wind speed, sea surface level, storm patterns and etc. (DHI, 2012). Changes in the wind climate may result in the increase in the frequency or magnitude of extreme events or causing the changes in wave activity and also increasing the risk of flooding, coastal erosion, changing the available renewable energy amount, changing the marine environment, etc. (Bonaldo et al., 2015; Cousino et al., 2015; Kamranzad et al., 2015; Grabemann et al., 2014). These changes result in a threat in coastal areas due to the fact that the coastal areas are heavily occupied by human activities, such as coastal cities, ports, infrastructures, industries, public utilities, tourist developments, fishing communities, etc. (Nicholls and Kebede, 2012). All of the above will most likely present the biggest planning and engineering challenges for future adaptation to these changes in coastal and offshore areas, therefore assessment of the impact of climate change on wind field would provide coastal managers with data to make better, more economical and sustainable decisions.

Many factors have to be taken into account in the investigation of how future global warming will cause climate change. The Intergovernmental Panel on Climate Change (IPCC) Fifth Assessment Report (AR5) is based on a new set of scenarios called Representative Concentration Pathways (RCPs) (IPCC, 2007). General circulation models (GCMs) are developed for simulation of global climate response due to different scenarios. They are an important tool for the assessment of climate change impacts (Fowler et al., 2007). Some studies assessed Coupled Model Inter-comparison Project 5 (CMIP5) for different data in different areas (Elguindi et al., 2014; Miao et al., 2014; Geil et al., 2013). Also, the effects of climate change on wind patterns has been assessed in many studies using different global or regional climate models, which illustrate the increasing or decreasing of wind speed in different areas in the world (Kamranzad et al., 2013; Deepthi and Deo, 2010; Pereira de Lucena et al., 2010;). Despite all these studies regarding assessment GCMs and projected future changes in climate wind, there are no comprehensive studies that assess the result of these models based on new set of scenarios, over the Persian Gulf.

In this paper, wind fields from two models by phase 5 of Coupled Model Inter-comparison Project (CMIP5) were examined to determine how well these generations of GCMs perform in the Persian Gulf. For this purpose, data obtained from IPSL-CM5A-MR and CMCC-CM models were compared, quantitatively with those of local assimilated wind field, i.e., ECMWF-ERA-Interim for the period 1986 to 2005, in the location in the middle of Persian Gulf (figure 1). In addition, in order to assess the effects of climate change on wind

  / ISSN 1562-6865 (Online) - ISSN 1063-7710 (Print)

regime in the Persian Gulf at the end of 21st century, IPSL and CMCC projection data were used based on two greenhouse gas presentative concentration pathways (RCP4.5 and RCP8.5).

2 METHODOLOGY

2.1 Study area

The Persian Gulf is an extension of the Indian Ocean through the Strait of Hormuz and lies between Iran to the northeast and the Arabian Peninsula to the southwest. It has many fishing grounds, extensive coral reefs, and abundant pearl oysters, and it is also important for the oilfields on its shore. Its strategic location has made it an ideal place for human development over time. Therefore, specifying the wind field variation caused by the climate change seems to be necessary in this area. Assessment of the effect of climate change on wind field was carried out in a point in the middle Persian Gulf, this point is located far from the coastline, because numerical models have limited ability to produce the reliable data near the coastal areas due to the complicated orography. Also, the selection of the point of study was also based on the spatial resolution of the models used and their availability.

Figure 1. Study Area.

2.2 Data resources

In climate change research, scenarios describe plausible trajectories of different aspects of the future that are constructed to investigate the potential consequences of anthropogenic climate change. The Intergovernmental panel on climate change (IPCC) Fifth Assessment Report (AR5) published in 2013-14. Its findings are based on a new set of scenarios that replace the Spatial Report on Emissions Scenarios (SRES) standards employed in two previous reports. The new scenarios are called Representative Concentration Pathways (RCPs). An RCP contains a set of starting values and the estimated emissions up to 2100, based on assumptions about economic activity, energy sources, population growth and other socio-economic factors. Coupled Model Inter-comparison Project phase 5 (CMIP5) identifies four RCPs. The high scenario, RCP8.5, predicts an increase of $8.5\frac{\mathrm{W}}{\mathrm{m}^2}$ by 2100, there are also two intermediate scenarios, RCP4.5, RCP6.0, and a low scenario, RCP2.6, in which radiative forcing reaches a peak in the middle of the twenty first century before decreasing to $2.6\frac{\mathrm{W}}{\mathrm{m}^2}$ by 2100 (Taylor et al., 2012). The CMIP5 data set, obtained from the Earth system Grid Federation (https://pcmdi.llnl.gov/projects/esgf-llnl/), include two RCPs based on the limiting access to the data of the studied models, RCP4.5 and RCP 8.5. We selected and evaluated two GCMs (IPSL, CMCC) based on their resolution and data availability.

In order to evaluate the impact of climate change on the variation of wind field over the Persian Gulf, two models were selected based on their data availability. The IPSL-CM5A model with 6-hourly temporal resolution and spatial resolutions of 3.75 degrees longitude and 1.875 latitude, prepared by the Pierre Simon Laplace Institute (IPSL) were used as first model and The Centro Euro-Mediterranean sui Cambiamenti Climatic Climate Model CMCC-CM with 6-hourly temporal resolution and spatial resolutions of 0.75 degrees longitude and 0.7484 latitude as second model, were used.

In order to assess the CMIP5 wind field, local wind field was obtained from the European Centre for Medium-Range Weather Forecasts (ECMWF). It contains the wind vector at 10 meters above the sea level with 0.125 degree and 6-hourly spatial and temporal resolutions, respectively. This model has already been investigated in the study area and its accuracy is confirmed (Moeini et al., 2010).

3 RESULTS & DISCUSSION

3.1 Evaluation of CMIP5 in the Persian Gulf

In order to evaluate the CMIP5 results in the Persian Gulf, two models from CMIP5 were selected based on their availability, and were compared with ECMWF wind field as a reliable wind field in the study area (Moeini et al., 2010). Comparison was carried out in a point in the middle of Persian Gulf (figure 1). This point was selected based on the spatial resolution of models, far from the coastal areas, where the data are available. Each of the selected models of CMIP5 were compared quantitatively in the point of study for the period of 1986 to 2005. Seasonal average wind speeds were obtained and shown in figure 2. According to this figure, in comparison to ECMWF, CMIP5 wind speeds are underestimated. However, the trends of all wind data seem to be similar. Also, it seems that wind speed obtained from CMCC model is closer to that of the local model, quantitatively.

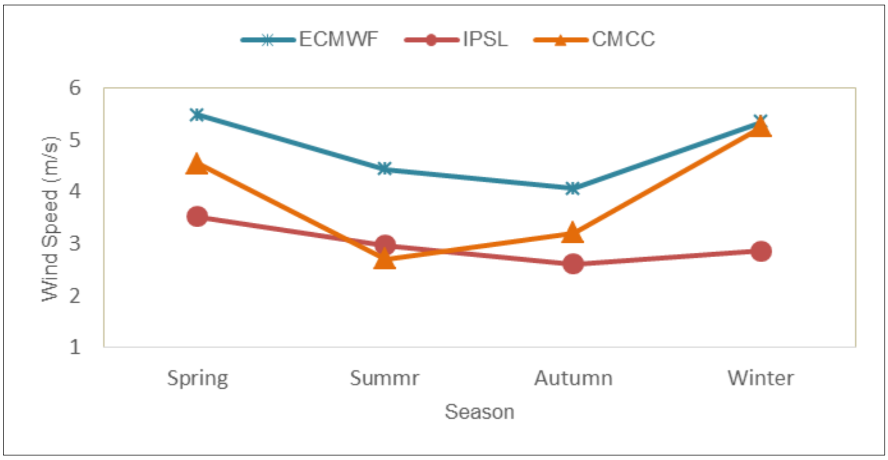

Figure 2. Seasonal average wind speed (1986-2005).

In addition, wind directions were assessed using wind roses as shown in figure 3, which illustrates that generally, CMIP5 wind direction is consistent with that of ECMWF, while the magnitude of wind speed is required to be modified. All three wind roses show properly Shamal wind direction as the most well-known wind in the study area (Perrone, 1981).

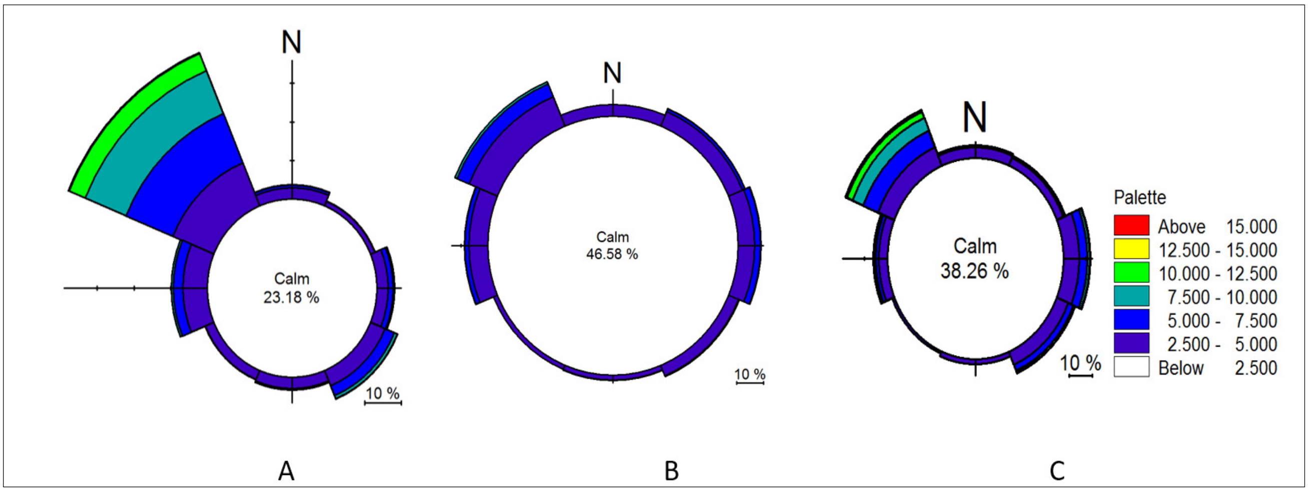

Figure 3. Wind roses for A) ECMWF, B) IPSL and C) CMCC (1986-2005).

According to figure 4 which shows the monthly average of IPSL, CMCC and ECMWF wind speeds from 1986 to 2005, the highest wind speed for ECMWF occur in February and June, which implies the dominance of winter and summer-time Shamal winds, respectively in the study area (Reynolds, 1993). IPSL and CMCC Models also show similar results, except in quantitative terms, in which results are inconsistent and are required to be downscaled. Furthermore, it is concluded from this figure that CMCC represents more accurate results in the study area compared to IPSL, however, it needs reforming or downscaling.

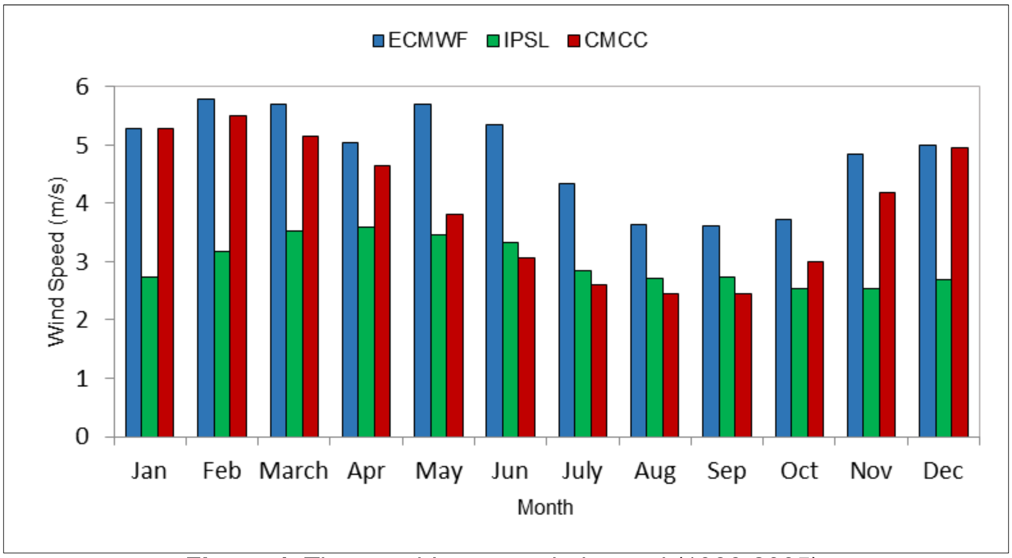

Figure 4. The monthly mean wind speed (1986-2005).

Regarding the mentioned difference between CMIP5 and local wind data, CMIP5 wind speed requires modification before being used in this area for climate change impact assessments. It is also mentioned by the previous studies done in this area (Alinejhad et al., 2016). In addition, it was concluded that CMCC provides more accurate results in comparison with IPSL. Therefore, it is suggested that the CMCC results be used for climate change research in the Persian Gulf.

3.2 Impact of climate change on the wind field in the Persian gulf

Evaluation of wind speed variation was done using RCPs and historical experience obtained from CMIP5 wind field. For this purpose, annual average of CMIP5 wind speeds were calculated and was assessed for the present (control) period from 1986 to 2005 and also in two RCPs (RCP 4.5, RCP 8.5) for the future from 2081 to 2100. Assessment was done using time series and statistical analysis, as shown in figure 5. The trend lines have been fitted to wind speeds driven from CMCC and IPSL. It indicates a global decreasing trend in both models for both RCPs.

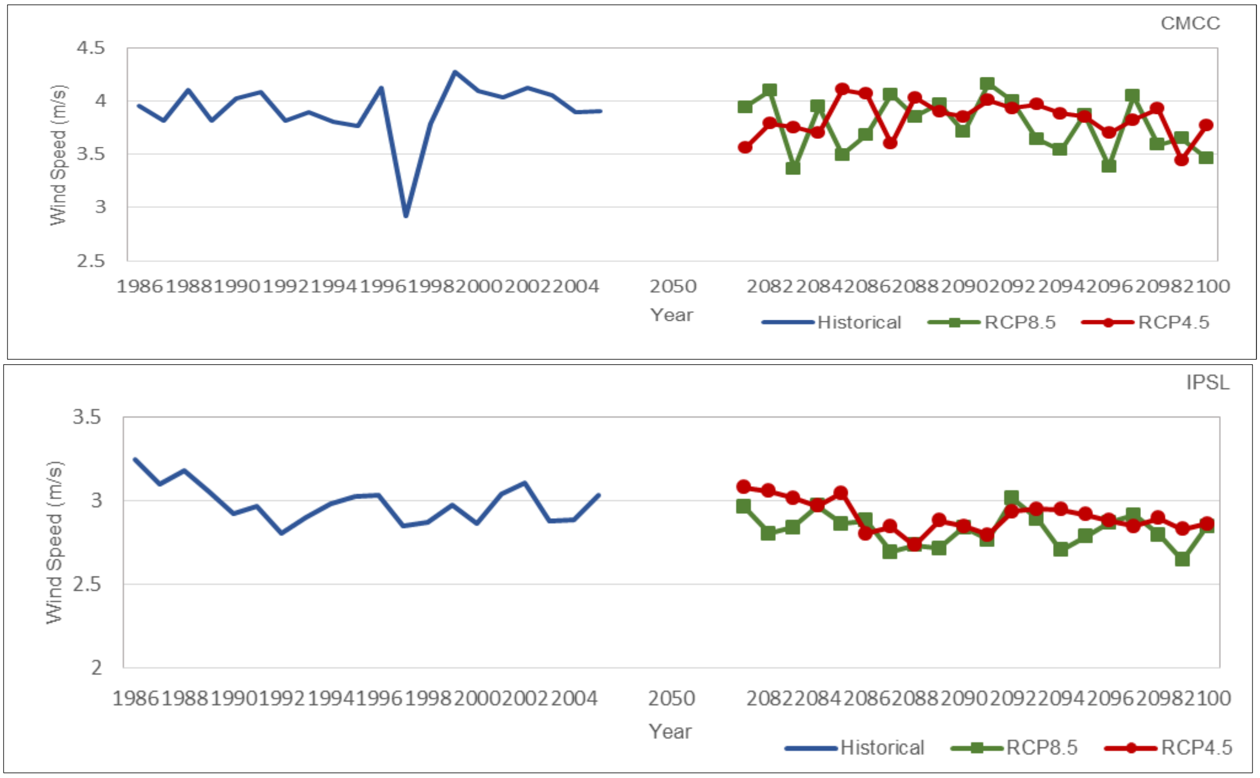

Figure 5. Wind speed variation using CMIP5.

Furthermore, the maximum, minimum and standard deviation of the wind speed, for control (1986-2005) and future (2081-2100) periods were obtained using CMCC results, and shown in Table 1. Since CMCC results are more consistent with the values of the local model, the results of this model were used for the comparison. According to this table, there is an insignificant change in the average wind speed; however, even small changes in average wind speeds can lead to large variations in the wave characteristics and sedimentation in the area.

Table 1. Statistical changes in wind speed in the future than the current.

	Historical	**RCP4.5**	**RCP8.5**	**Average future changes compared to current (%)**
Max	18.29	17.01	16.67	-7.96
Min	0.01	0.01	0.02	-1.24
STD	2.79	2.72	2.62	-4.24

4 CONCLUSIONS

Two models from CMIP5 were selected and compared with ECMWF as a reliable wind field in the Persian Gulf in order to evaluate the CMIP5 wind data in the area of study. Comparison of seasonal average wind speeds show that CMIP5 wind speed is underestimated. In addition, directional analysis using wind roses was done. Results show that CMIP5 models indicate similar directions to local wind field with lower magnitude. This means that CMIP5 wind speed needs an overall correction in the amount of wind speed, while the dominant wind direction is somewhat similar for both wind fields and this should be considered in the studies of climate change in the region.

Moreover, variation of wind speed was also investigated. For this purpose, time series of annual averages of wind speeds were calculated and statistical analysis were carried out. Results indicated a decreasing trend in both RCPs (RCP4.5, RCP8.5) in the point of study for both CMIP5 models (IPSL and CMCC) from 2081 to 2100. Although, the reduction is small, it may lead to large variation in wave and current regime and change in sediment transportation in ports.

REFERENCES

Alinejhad-Tabrizi, T, Hadjizadeh-Zaker, N. & Kamranzad, B. (2016). Assessment of Cmip5 Wind Field in the Persian Gulf. *International Conference on Coasts, Ports and Marine Structures*.

Bonaldo, D., Benetazzo, A., Sclavo, M. & Carniel, S. (2015). Modelling Wave-Driven Sediment Transport in a Changing Climate, a Case Study for Northern Adriatic Sea (Italy). *Regional Environmental Change*, 15(1), 45-55.

Casas-Prat, M., McInnes, K.L., Hemer, M.A. & Sierra, J.P. (2015). Future Wave-Driven Coastal Sediment Transport along the Catalan Coast (NW Mediterranean). *Regional Environmental Change*, 16(6), 1739-1750.

Cousino, L.K., Becker, R.H. & Zmijewski, K.A. (2015). Modeling the Effects of Climate Change on Water, Sediment, and Nutrient Yields from the Maumee River Watershed. *Journal of Hydrology: Regional Studies*, 105, 14.

Deepthi, R. & Deo, M.C. (2010). Effect of Climate Change on Design Wind at the Indian Offshore Locations. *Ocean Engineering*, 37(11), 1061-1069.

Elguindi, N., Grundstein, A., Bernardes, S., Turuncoglu, U. & Feddema, J. (2014). Assessment of CMIP5 Global Model Simulations and Climate Change Projections for the 21st Century using a Modified Thornthwait Climate Classification. *Climate Change*, 122(4), 523-538.

Erichsen, A., Rugbjerg, M., Mangor, K. & Deigaard, R. (2012). *How to Obtain Sustainable Adaptation in Marine Areas,* Marine Climate Change Guidelines, DHI, 1-80.

Fowler, H.J., Blenkinsop, S. & Tebaldi, C. (2007). Review Linking Climate Change Modelling to Impacts Studies: Recent Advances in Downscaling Techniques for Hydrological Modeling. *International Journal of Climatology*, 27(12), 1547-1578.

Geil, L.K., Serra, Y.L. & Zeng, X. (2013). Assessment of CMIP5 Model Simulations of the North American Monsoon System. *American Meteorological Society*, 26(22), 8787-8801.

Grabemann, I., Groll, N., Moller, J. & Weisse, R. (2014). Climate Change Impact on North Sea Wave Conditions: a Consistent Analysis of Ten Projections. *Ocean Dynamics*, 65(2), 255-267.

IPCC, (2007). *Towards New Scenarios for Analysis of Emissions, Climate Change, Impacts, and Response Strategies : Technical Summary*, IPCC Expert meeting report, Noordwijkerhout, The Netherlands, Intergovernmental Panel on Climate Change, 1-34.

Kamranzad, B., Etemad-Shahidi, A., Chegini, V. & Hadadpour, S. (2013). Assessment of CGCM 3.1 Wind Field in the Persian Gulf. *Journal of Coastal Research*, 65(sp1), 249-253.

Kamranzad, B., Etemad-Shahidi, A., Chegini, V. & Yeganeh-Bakhtiary, A. (2015). Climate Change Impact on Wave Energy in the Persian Gulf. *Ocean Dynamics*, 65(6), 777-794.

Miao, C.H., Duan, Q., Sun, Q., Huang, Y., Kong, D., Yang, T., Ye, A., Di, Z. & Gong, W. (2014). Assessment of CMIP5 Climate Models and Projected Temperature Changes over Northern Eurasia. *Environmental Research Letter,* 9(5), 1-12.
Moeini, M.H., Etemad-Shahidi, A. & Chegini, V. (2010). Wave Modeling and Extreme Value Analysis off the Northern Coast of the Persian Gulf. *Applied Ocean Research*, 32(2), 209-218.
Moeini, M.H., Etemad-Shahidi, A., Chegini, V. & Rahmani, I. (2012). Wave Data Assimilation using a Hybrid Approach in the Persian Gulf. *Ocean Dynamics*, 62(5), 785-797.
Nicholls, R.J., & Kebede, A.S. (2012). Indirect Impacts of Coastal Climate Change and Sea-Level Rise: The UK Example. *Climate Policy*, 12(sup01), S28-S52.
Pereira de Lucena, A.F., Szklo A.S., Schaeffer, R. & Dutra, R.M., (2010). The Vulnerability of Wind Power to Climate Change in Brazil. *Renewable Energy*, 35(5), 904-912.
Perrone, T.J. (1981). *Winter Shamal in the Persian Gulf*, Naval Environmental Prediction Research Facility, Monterey CA, I.R.-79-06, 1-23.
Reynolds, R.M. (1993). Physical oceanography of the Gulf, Strait of Hormuz, and the Gulf of Oman-Results from the Mt Mitchell expedition. *Marine Pollution Bulletin*, 27, 35-59.
Salles, T.B., Griffiths, C.M., Dyt, C.P. & Li, F. (2011). Australian Shelf Sediment Transport Responses to Climate Change-Driven Ocean Perturbations. *Marine Geology*, 282(3), 268-274.
Taylor, K.E., Stouffer, R.J. & Meehl, G.A. (2012). An overview of CMIP5 and the Experiment Design. *Bulletin of the American Meteorological Society*, 93(4), 485-498.

Proceedings of the 37th IAHR World Congress
August 13 – 18, 2017, Kuala Lumpur, Malaysia

EVALUATION ON RELATIONSHIP BETWEEN PARTICULATE TOTAL MERCURY IN SEAWATER AND SUSPENDED SOLIDS PARTICLE SIZE DISTRIBUTION IN MINAMATA BAY, JAPAN

SHINICHIRO YANO(1), TAKAAKI TANINAKA(2), EDISTRI NUR FATHYA(3), SATOSHI MATSUMOTO(4), AKITO MATSUYAMA(5), AKIHIDE TADA(6) & HERAWATY RIOGILANG(7)

(1) Dept. of Urban and Environmental Engineering, Kyushu University, Fukuoka, Japan,
yano@civil.kyushu-u.ac.jp
(2, 3, 4) Dept. of Maritime Engineering, Kyushu University, Fukuoka, Japan,
(5) Mercury Analysis Technique Section, National Institute for Minamata Disease, Japan
(6) Division of System Science, Nagasaki University, Japan
(7) Dept. of Civil Engineering, Sam Ratulangi University, Indonesia

ABSTRACT

Minamata disease was officially confirmed in Japan, in 1956. Although 60 years have passed, it has been concerned about influence of mercury released into natural environments on human health around the world. To manage risks of mercury in marine environment especially, to understand mercury dynamics is necessary. In order to develop a numerical model to predict mercury fate, we have been carrying out monthly in-situ measurement of mercury concentration in seawater from 2006 for acquisition of fundamental data. From October 2010, we have carried out seawater sampling in five layers at three observation points in Minamata Bay around the maximum ebb tide to measure mercury concentration, and also in-situ measurement of suspended solids (SS) particle size distribution by the LISST-100X. It is the only instrument which can observe particle size spectrum of SS in in-situ seawater directly. Yano et al. (2013) found out the weakly correlation between particulate total mercury (THg) concentration and SS particle size distribution by using the data from 2010 to 2011. However, there was a problem for reliability because of subjective method to divide data into groups. In this study, we used a cluster analysis by the Ward method to divide SS particle size distribution data. Secondly, we attempted to judge the best grouping using the entropy method. This method can determine the optimal number of group, into which the shape of particle size distribution is categorized, by entropy. Thirdly, we confirmed statistical significance of relationship between each group and P-THg concentration with both of Bartlett test and Kruskal-Wallis test. Finally, we tried to determine relationship between P-THg concentration and SS particle size fraction. As a result of this study, the followings were found: (1) The most optimal group number of SS particle size distribution was determined as 6 groups; (2) Statistically significant correlation between the P-THg concentration and SS particle size distribution was seen; and, (3) It can be seen from the present relationship between particulate THg concentration and SS particle size fraction that particulate THg depends on source of SS and mixing condition with SS from rivers and other possible sources.

Keywords: Mercury; particle size distribution; suspended solids.

1 INTRODUCTION

The Minamata disease tragedy which occurred 60 years ago was caused by toxic methylmercury pollution discharged from a chemical factory in Minamata Bay, Japan (Minamata City Government, 2014). Furthermore, this has been resolved by dredging projects of highly mercury contaminated (total Hg>25ppm) bottom sediment over around 2.1 km^2 coastal area of the bay. The project which was conducted by Kumamoto prefectural government and Japanese government was held on 1977 to 1990. 0.58 km^2 area of the bay was reclaimed by around 1.5 million ton of bottom sediments in the project. (Balogh et al., 2015). Recently, Tomiyasu et al. (2006) and Matsuyama et al. (2014) found that the trace mercury (total Hg<10ppm) remained in the bottom sediment in the bay. Also, Tomiyasu et al. (2000) reported that the trace mercury (total Hg<3ppm) has dispersed in the outer sea area, the Yatsushiro Sea, from the measurement result of bottom sediment sampling.

Normally, mercury in (sea) water can be categorized into particulate and dissolved components. They are separated by filter of 0.45μm pore size. Also, concentration of mercury is discussed by using methylmercury (MeHg) and total mercury (THg). Methylmercury is a kind of organic mercury and can be separated into mono-MeHg and di-MeHg. In natural environment, mono-MeHg is normally dominant in seawater. On the other hand, THg means the total of inorganic mercury and organic one. In Minamata Bay, Matsuyama et al. (2011) clarified that particulate THg concentration was higher than the dissolved one in seawater. Thus, to develop the numerical model to simulate and to predict mercury fate in the bay and in the outer sea area, bottom sediment transport model should be firstly developed.

The concentration of particulate component (unit: ppm), which is the rate of mass of THg to the mass of suspended solids (SS), may be affected by particle size distribution of SS, in other words, specific surface area of SS, because the component can bond the surface of SS. Especially, the information is very important for numerical modeling of particulate Hg fate. However, the relationship between them had not been clarified before Yano et al. (2013). They conducted *in-situ* measurement of particulate THg concentration and particle size distribution of SS simultaneously. The relationship between groups of patterns of SS particle size distribution and concentration of particulate THg was evaluated by the entropy method (Forrest and Clark, 1984; Orpin and Kostylev, 2006; Okada et al., 2009) However, grouping of the particle size distribution pattern was conducted by subjective way using only the following statistical factors: median diameter, D_{50}, standard deviation, σ, and kurtosis of SS particulate size distribution curve of each sample. Thus, it should be considered to group those SS samples by an objective way. In the present research, we try to group SS particle size distribution patterns by statistical objective method, the Ward cluster method and to clarify the relationship between particulate THg concentration and characteristics of SS particle size distribution.

2 IN-SITU MEASUREMENT FOR MERCURY CONCENTRATION AND SS GRAIN SIZE DISTRIBUTION IN SEAWATER

Water sampling has almost been conducted monthly after 2006 at three sites shown in Figure 1. Mean water depth of Sta.1, 2, and 3 are 22m, 14.9m, and 13.5m, respectively. Sea water samples were collected from 5 layers (surface, -6m, -10m below water surface, +1m and +10cm from sea bottom) at Sta.1 and 2, and from 4 layers (except for -10m below water surface) at Sta.3. Concentration of particulate THg and MeHg, dissolved THg and MeHg, and SS were detected from water samples. Concentration of mercury was detected by the same method in Matsuyama et al. (2011). Sampling was carried out for 2 hours around maximum ebb tide in spring tide. Also, vertical profiles of salinity, water temperature, dissolved oxygen, turbidity, and others, were measured by multiple water quality meter (AAQ1183, Alec Electrics Co. Ltd., Japan).

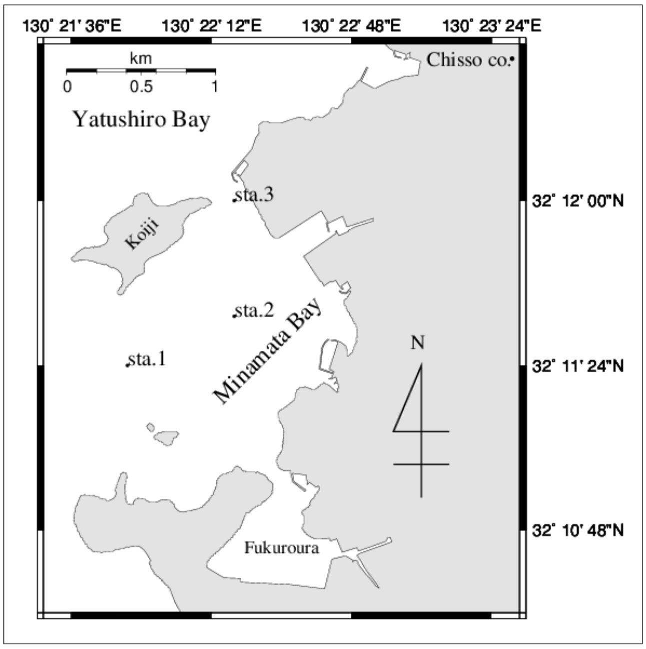

Figure 1. Measurement stations in Minamata Bay.

In addition, from October 2010, vertical profile of grain size distribution of SS has been measured by LISST-100X (Sequoia Scientific Co. Ltd, USA), which was a type for measurement range 2.5-500μm in our *in-situ* measurement. The LISST is the only equipment to measure SS grain size distribution directly by laser diffractometry in a field. It can show volumetric concentration of SS for 36 log scale fractions in the measurement range. Sampling rate was set as 1Hz. The equipment was unloaded from water surface to sea bottom with speed of about 0.2 m/s by humans. Depth meter was attached in this equipment, thus it can measure the vertical profile of grain size distribution of SS. In this paper, we analyzed measurement data for 6 days: 20th Aug., 14th Oct., and 18th Nov., in 2012 and 1st Feb., 16th Mar., and 28th Jun., in 2014. Also, we omitted the data in the water surface layer and bottom layer (: 10cm above sea bottom), because the effects of sun light scattering in water surface and re-suspension of bottom sediments due to device's attaching on the bottom. Thus, we used a total of 48 pairs of sample of particulate THg and SS grain size distribution.

3 ANALYSIS OF MEASUREMENT DATA

3.1 Grouping of SS grain size distribution data

Firstly, we used a cluster analysis by Ward method to classify SS particle size distribution data (N=48). Figure 2 shows the dendrogram of all data by the Ward method. Next, we attempted to determine suitable number of groups by the entropy method as mentioned below.

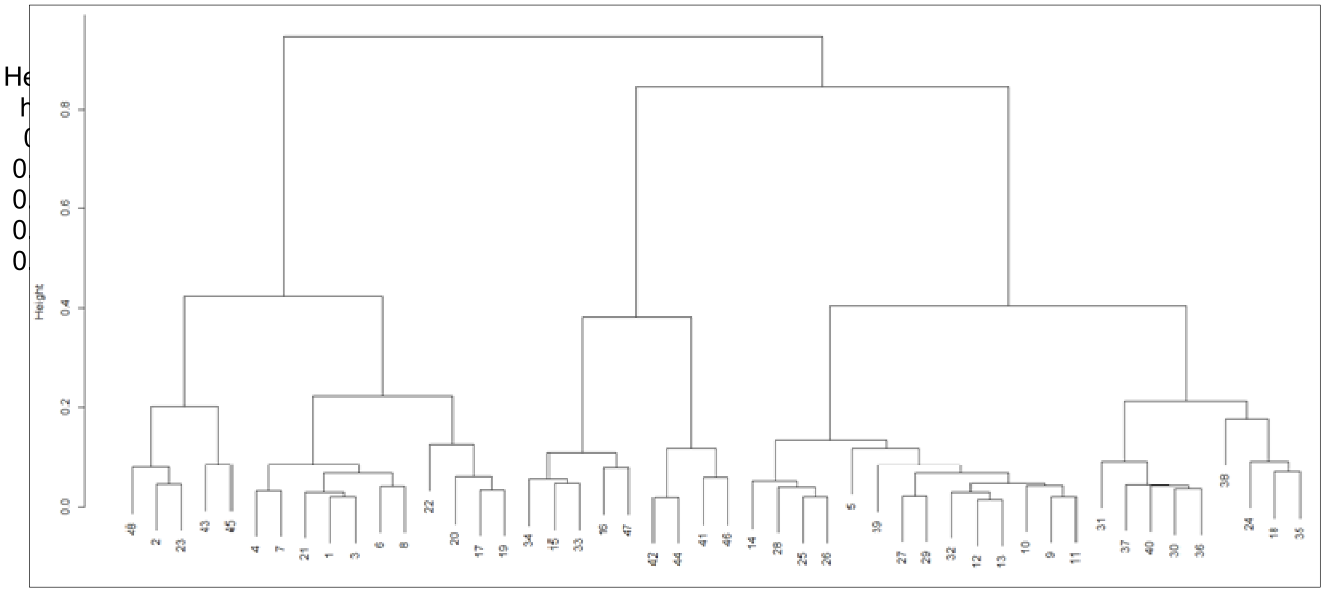

Figure 2. Dendrogram for all data of SS particle size distribution.

The inequality statistic, I_T is expressed as Eq. [1] in the multivariate case for N samples.

$$I_T = \sum_{j=1}^{J} Y_j \sum_{i=1}^{N} Y_i \log NY_i \qquad [1]$$

where, Y_j: frequency value of SS grains in size interval j, J: number of size intervals, N: number of samples, Y_i: frequency value of SS grains in size interval j that are in sample i, such that:

$$Y_j = \sum_{i=1}^{N} Y_{ij}, Y_i = \frac{Y_{ij}}{Y_j} \ , \qquad [2]$$

Y_{ij}: proportion of the total population of all samples in (i, j). When N samples are separated into R groups, between-group of samples inequality, I_B can be estimated from:

$$I_B = \sum_{j=1}^{J} Y_j \sum_{r=1}^{R} p_{jr} \log\left(\frac{p_{jr}}{N_r / N}\right) \qquad [3]$$

where:

$$p_{jr} = \frac{\sum_{i \in r} Y_{ij}}{Y_j} \qquad [4]$$

and N_r: number of samples in the r-th group.

All samples should be separated into suitable groups that have minimizing I_T and maximizing I_B. The measure of efficiency of the grouping, which means maximizing between-group inequality, I_B and minimizing inequality, I_T can express the characteristics of original data set, can be obtained from

$$R_s = \frac{I_B}{I_T} \cdot 100 \qquad [5]$$

The R_s statistic tends to close to 100% in the case of a large number grouping ($R \rightarrow N$).

The relationship between the number of groups R and R_s is shown in Figure 3. Decision method for most suitable number of groups has been proposed, for example, C-H variance ratio criterion (Calinski and Harabasz, 1974), K-mean method, and others. We can select the largest value of R_s under normal condition. But, this means there is a loss of the original merit of grouping to be able to separate into the suitable small number groups. We selected the way to select the number for small increasing rate of R_s in the present paper (Okada et al., 2009). As a result, R=6 was selected as the most suitable number of grouping for this data set. Figure 4 shows representative SS particle size distribution of each group.

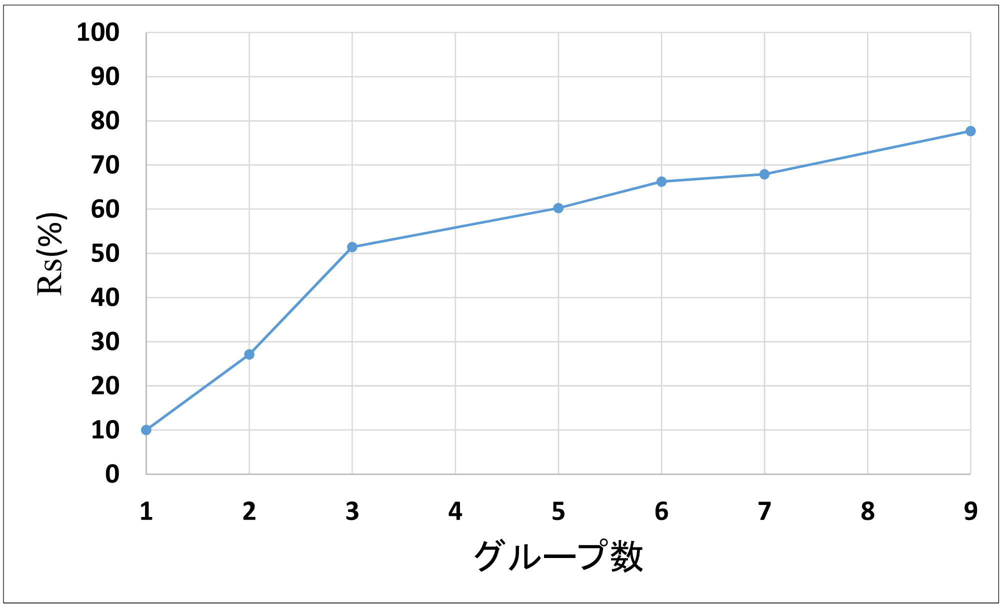

Figure 3. Dendrogram for all data of SS particle size distribution.

3.2 Evaluation of statistical significance

Figure 5 shows relationship between SS particle size distribution pattern group and particulate THg concentration. We attempted to evaluate the statistical significance of the result. Firstly, Kolmogorov-Smirnov test was carried out to check the null hypothesis “the sample distribution accords with the normal distribution.” The p-value was shown as 0.038 from the test with 5% of the significant level. Thus, the null hypothesis was rejected, and we can say that the sample distribution does not accord with the normal distribution. Therefore, we attempted the Kruskal-Wallis test to confirm the null hypothesis “the representatives of all groups have no significant difference.” Since the p-value was 0.010 (<0.05), it was confirmed that the representative value of each group has a significant difference. Also, we attempted Bartlett test with the null hypothesis “variance of each grope is same.” The result showed p=0.0014 (<0.05). Thus, it was confirmed that variance of each group was significantly different with others.

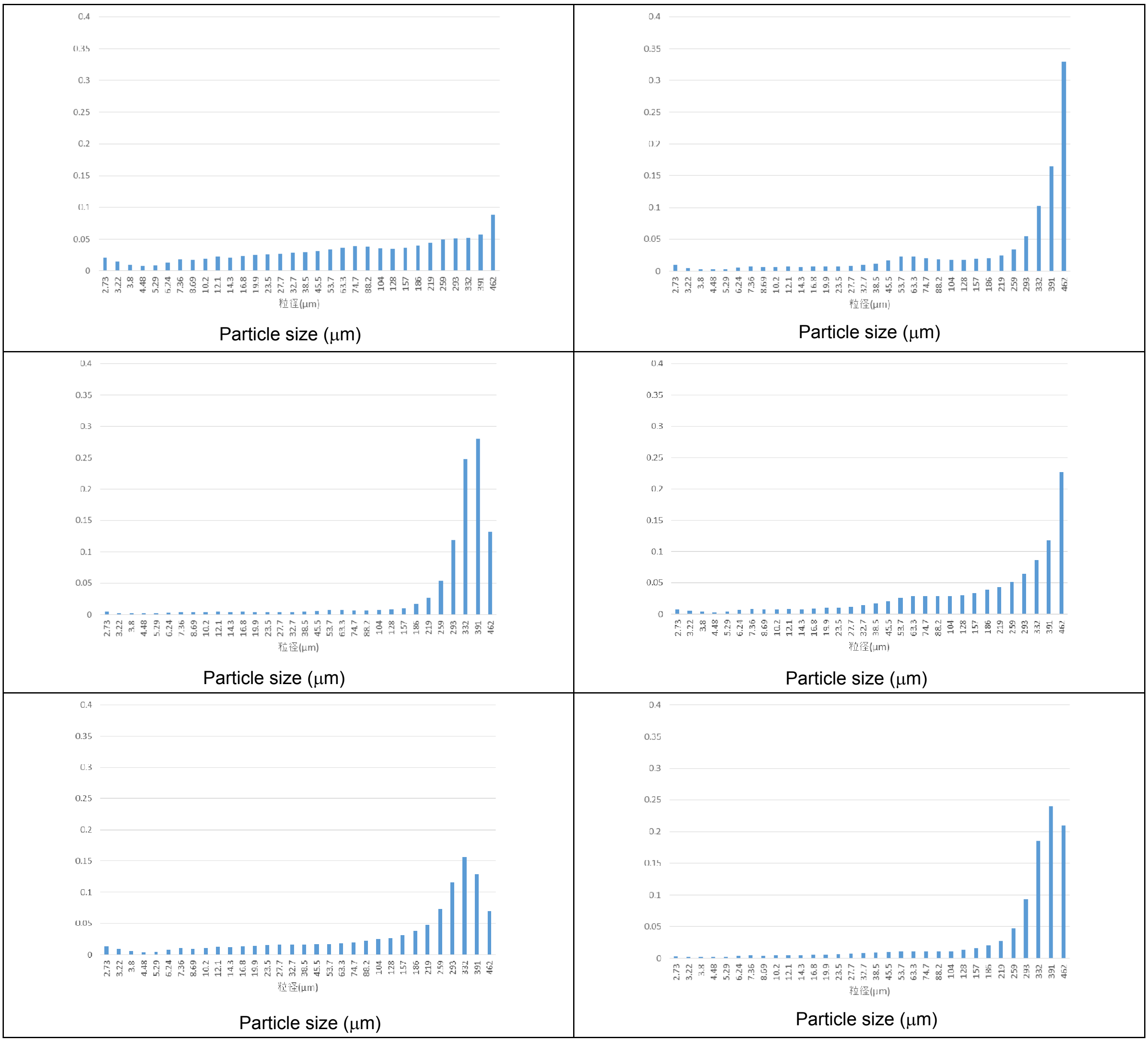

Figure 4. Representative SS particle size distribution in each group (in the case of 6 groups).

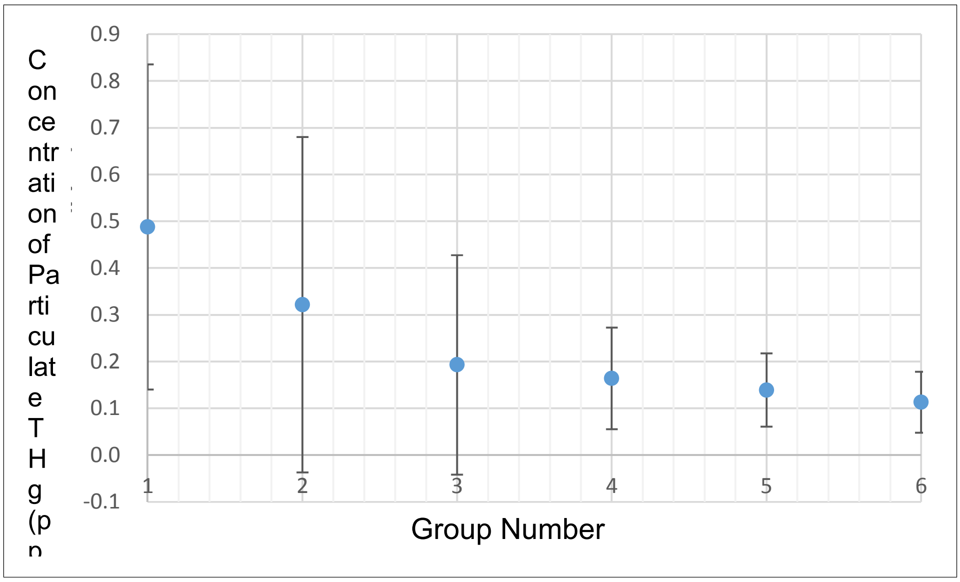

Figure 5. Relationship between SS particle size distribution pattern group and particulate THg concentration (mean±standard deviation).

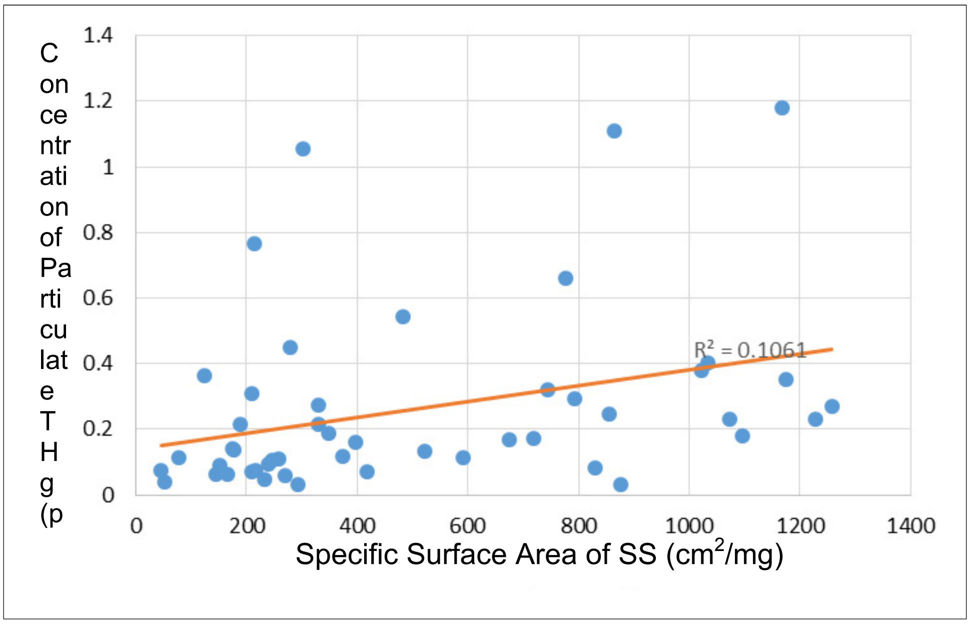

Figure 6. Relationship between specific surface area of SS and particulate THg concentration for all data.

3.3 Evaluation of relationship between specific surface area of SS and particular THg concentration

Figure 6 shows relationship between SS specific surface area and particulate THg concentration for all data (N=48). Figure 7 shows relationship between mean specific surface area of SS and mean particulate THg concentration in each grope (R=6). The specific surface area was calculated from the assumption that all particles have complete sphere shape. Grouping (Figure 7) can show stronger positive correlation than all data (Figure 6).

Finally, estimation of concentration of particulate THg from SS particle size distribution was developed. We divided the measurement range of SS particle size for LISST-100X (: 2.5-500μm) into six ranges: i) 2.73-6.24μm, ii) 7.36-16.8 μm, iii) 19.9-38.5 μm, vi) 45.5-88.2 μm, v) 104-219 μm, and vi) 259-462 μm in median value of each range. Concentration of particulate THg can be expressed by linear correlation, Eq. [6] was obtained from the mean values of the grouping result. Since negative coefficients are shown in the equation, it means that concentration of particulate THg cannot be decided by only SS particle size distribution. However, it also suggests that development of fractional SS transport model is necessary for numerical simulation for particle Hg fate.

$$Part.THg = 1.31X_1 + 6.15X_2 - 14.20X_3 + 19.41X_4 - 8.32X_5 + 0.63X_6 \qquad [6]$$

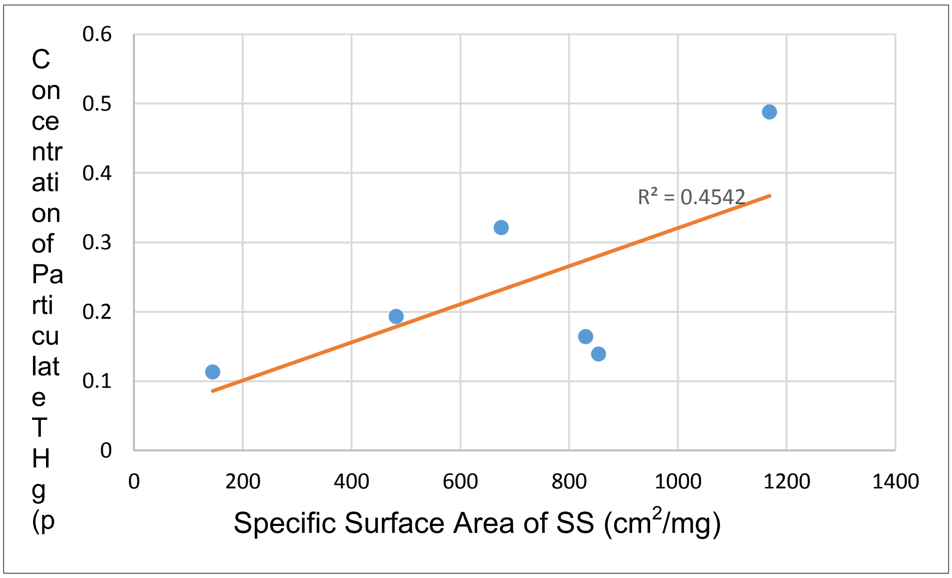

Figure 7. Relationship between mean specific surface area of SS and mean particulate THg concentration for 6 groups.

4 CONCLUSIONS

The results of objective statistical analysis of SS grain size distribution and particulate THg concentration data in Minamata Bay show the followings:

1. Correlation between characteristics of SS grain size distribution and particulate total mercury (THg) was clarified;
2. Concentration of particulate THg shows positive correlation to specific surface area of SS; and
3. Evaluation of concentration of particulate THg from fractions of grain size of SS was obtained.

It suggests that fractional SS transport modeling, which can classify into several fractions of SS grain size, is necessary in numerical modeling of particulate mercury dynamics and fate.

ACKNOWLEDGEMENTS

The study was supported by JSPS KAKENHI Grant Number 24360200.

REFERENCES

Balogh, S. J., Tsz-Ki Tsui, M., Blum, J.D., Matsuyama, A., Woerndle, G.E., Yano, S. & Tada. A. (2015). Tracking the Fate of Mercury in the Fish and Bottom Sediments of Minamata Bay, Japan, Using Stable Mercury Isotopes. *Environmental Science &Technol*ogy, 49(9), 5399–5406.

Calinski, T. & Harabasz, J. (1974). A Dendrite Method for Cluster Analysis. *Communications in Statistics-theory and Methods*, 3(1), 1-27.

Forrest, J. & Clark, N.R. (1989). Characterizing Grain Size Distributions: Evaluation of a New Approach using a Multivariate Extension of Entropy Analysis. *Sedimentology*, 36(4), 711-722.

Matsuyama, A., Eguchi, T., Sonoda, I., Tada, A., Yano, S., Tai, A., Marumoto, K., Tomiyasu, T. & Akagi, H. (2011). Mercury Speciation in the Water of Minamata Bay, Japan. *Water, Air and Soil Pollution*, 218(1-4), 399-412.

Matsuyama, A., Yano, S., Hisano, A., Kindaichi, M., Sonoda, I., Tada, A. & Akagi, H. (2014). Reevaluation of Minamata Bay, 25 years after the Dredging of Mercury-Polluted Sediments. *Marine Pollution Bulletin*, 89(12), 112-120.

Minamata City Government (2007). *Minamata Disease –Its History and Lesson*. Minamata City, 103. (In Japanese)

Okada, T., Mong Trinh, N.T. & Furukawa, K. (2009). Proposal for Seabed Sediment Map Based on Whole Shape of Particle-Size Distributions, in Tokyo Bay. *Proceedings of Civil Engineering in the Ocean, JSCE*, 25, 401-406. (In Japanese)

Orpin, A.R. & Kostylev, V.E. (2006). Towards a Statistically Valid Method of Textual Sea Floor Characterization of Benthic Habitats. *Marine Geology*, 225(1), 209-222.

Tomiyasu, T., Nagano, A., Yonehara, N., Sakamoto, H., Rifardi, Oki, K. & Akagi, H. (2000). Mercury Contaminant in the Yatsushiro Sea, South-Western Japan: Spatial Variations of Mercury in Sediment. *Science of the Total Environment,* 257(2), 121-132.

Tomiyasu, T., Matsuyama, A., Eguchi, T., Fuchigami, Y., Oki, K., Horvat, M., Rajar, R. & Akagi, H. (2006). Spatial Variations of Mercury in Sediment of Minamata Bay. Japan. *Science of the Total Environment*, 368(1), 283-290.

Yano, S., Hisano, A., Riogilang, H., Kawase, H., Tai, A., Matsuyama, A. & Tada, A. (2013). In-site Measurement for Relationship among Grain Size Distribution of Suspended Solid and Bottom Sediment and Particulate Total Mercury in Minamata Bay, Japan. *Proceedings of 2013 IAHR World Congress*, A11420.

EXAMINATION AND RECALIBRATION OF EMPIRICAL FORMULAS FOR COMPUTING SHOALING WAVE HEIGHTS

WINYU RATTANAPITIKON[1] & SUWIMOL KANOKRATTANANUKUL[2]

[1,2] Civil Engineering Program, Sirindhorn International Institute of Technology, Thammasat University, Pathum Thani, Thailand,
winyu@siit.tu.ac.th

ABSTRACT

The present study concentrates on the computation of shoaling wave heights based on simple empirical formulas. During the past decades, various simple empirical formulas have been proposed for computing wave shoaling. No direct literature has been made to describe clearly the applicability and accuracy of the existing empirical formulas. This study is undertaken to examine the accuracy of five empirical formulas for computing regular wave shoaling. The formulas are developed empirically from the computed results of nonlinear wave models. One formula is in a form of implicit equation, while the others are in the form of explicit equations. Forty cases of measured shoaling wave heights from four sources of published experimental data are used to examine the formulas. The data covers a range of deepwater wave steepness from 0.002 to 0.069. The accuracy of the formulas is also compared with that of a linear wave theory. It is found that the linear wave theory gives a reasonable overall prediction of shoaling wave heights. Three empirical formulas give better prediction than that of a linear wave theory. The formulas, that give better prediction than that of a linear wave theory, are selected to be recalibrated. The calibrated formulas give slightly better accuracy than the best existing formula. Considering accuracy and simplicity of the formulas, only one formula is recommended to be used for computing the shoaling of regular wave heights.

Keywords: Wave shoaling; empirical formula; offshore; linear wave; nonlinear wave.

1 INTRODUCTION

Wave height is an essential required factor for many coastal engineering applications such as the design of coastal structures and the study of coastal processes. When waves propagate to the nearshore zone, wave profiles steepen and become asymmetric where eventually waves break. The transformation of wave heights in an offshore zone can be determined from a wave shoaling model (or formula). During past decades, various models or formulas have been proposed for computing wave shoaling. There are varieties of equations, which can be used for simulating wave propagation. The equations vary from simple equations (e.g. linear wave and empirical formulas) to complex equations (e.g. Navier-Stokes, Mild-slope, and Boussinesq equations).

For convenience, most engineers prefer the simplest formula or model (which does not give bad accuracy) for practical work. There are 2 simple formulas, which may be suitable for computing wave shoaling in practice, i.e. linear wave formula and empirical formula. Applicability of linear wave formula has been investigated by many researchers (Svendsen and Brink-Kjaer, 1972; Shuto, 1974; Sakai and Battjes, 1980; Isobe, 1985). It is well-known that the linear wave theory gives an underestimation on wave heights at the location of large Ursell parameter near the breaking point. However, no direct literature has been made to describe clearly the applicability and accuracy of the existing empirical formulas. Moreover, as there exist several empirical formulas, it is not clear which formula should be used for computing shoaling wave heights. Hence, the main objective of this study is to examine the accuracy of some selected empirical formulas for computing regular wave shoaling and find out a suitable one. The accuracy of the empirical formulas was also compared with a wildly-used formula (linear wave formula) for computing wave shoaling.

This paper is divided into three main parts. The first part is review of linear wave formula and the selected existing empirical formulas for computing wave shoaling. The second part is the examination of the existing formulas for identifying the suitable one. The third part describes the formula recalibration.

2 EXISTING FORMULAS

Brief reviews of a widely-used formula (linear wave formula) and the selected empirical formulas for computing shoaling wave heights are described below.

(a) Airy (1845), hereafter referred to as A45, introduced the linear wave theory (1st order Stokes wave theory) to describe the propagation of small amplitude wave on horizontal bed. Because of the simplicity of the theory and not bad accuracy, the theory was widely used for practical work. The wave height transformation was computed from the energy flux conservation law. The energy flux conservation for computing wave shoaling in the offshore zone can be written as:

$$F_{x1} = F_{x2} \quad [1]$$

where F_x is the energy flux. The energy flux based on linear wave theory can be expressed as:

$$F_x = \frac{1}{8}\rho g H^2 c_g = \frac{1}{8}\rho g H^2 c \frac{1}{2}\left(1+\frac{2kh}{\sinh 2kh}\right) \quad [2]$$

where ρ is the water density, g is the acceleration due to gravity, H is the mean wave height, c_g is the group velocity, c is the phase velocity, k is the wave number, and h is the water depth. The wave shoaling can be computed from the energy flux conservation equation (Eq. [1]) by substituting the formula of the energy flux (F_x) at deepwater and any position in the offshore zone as:

$$\frac{1}{8}\rho g H_o^2 c_{go} = \frac{1}{8}\rho g H^2 c_g \quad [3]$$

or

$$H = \frac{H_o}{\sqrt{(\tanh kh)\left(1+\frac{2kh}{\sinh 2kh}\right)}} \quad [4]$$

where H_o is the deepwater wave height, and c_{go} is the deepwater group velocity.

(b) Sakai and Battjes (1980), hereafter referred to as SB80, determined wave shoaling based on Cokelet's (1977) wave theory. The results were plotted in form of a graph showing relationship among H/H_o, H_o/L_o, and h/L_o. Le Roux (2007) recast the graph into the following equations:

$$H = H_o A \exp\left(B\frac{H_o}{L_o}\right) \quad [5]$$

in which

$$A = \begin{cases} 0.5875\left(\frac{h}{L_o}\right)^{-0.18} & for\ \frac{h}{L_o} \le 0.0844 \\ 0.9672\left(\frac{h}{L_o}\right)^{-0.18} - 0.5013\frac{h}{L_o} + 0.9521 & for\ 0.0844 < \frac{h}{L_o} \le 0.6 \\ 1 & for\ \frac{h}{L_o} > 0.6 \end{cases} \quad [6]$$

$$B = 0.0042\left(\frac{h}{L_o}\right)^{-2.3211} \quad [7]$$

where $L_o = gT^2/2\pi$ is the deepwater wavelength, and A and B are coefficients.

(c) Iwagaki et al. (1982), hereafter referred to as I82, determined wave shoaling based on cnoidal wave theory. They related nonlinear shoaling coefficient with several dimensionless parameters (i.e., linear shoaling coefficient, relative depth, and deepwater wave steepness) were studied and fitted the results with the following formula:

$$H = \frac{H_o}{\sqrt{(\tanh kh)\left(1+\frac{2kh}{\sinh 2kh}\right)}} + 0.0015 H_o \left(\frac{h}{L_o}\right)^{-2.8}\left(\frac{H_o}{L_o}\right)^{1.2} \quad [8]$$

in which the variables H_o, L_o, and k are calculated based on linear wave theory.

(d) Kweon and Goda (1996), hereafter referred to as KG96, recalibrated the formula of I82 with the computed results from the formula of Shuto (1974). After recalibration, the formula is modified to be:

$$H = \frac{H_o}{\sqrt{(\tanh kh)\left(1+\frac{2kh}{\sinh 2kh}\right)}} + 0.0015H_o\left(\frac{h}{L_o}\right)^{-2.87}\left(\frac{H_o}{L_o}\right)^{1.27} \quad [9]$$

(e) Tajima and Madsen (2002), hereafter referred to as TM02, determined wave shoaling based on modified Boussinesq-type model of Nwogu (1993) for various wave and bottom slope conditions. They related the computed wave heights with the wave heights calculated from linear wave theory, and fitted the results with the following formula:

$$H = \frac{H_o}{\sqrt{(\tanh kh)\left(1+\frac{2kh}{\sinh 2kh}\right)}}\left[1+A_1\exp\left(-A_2\frac{h}{L_o}\right)\right] \quad [10]$$

in which

$$A_1 = [2.2+2\tanh(55m)]\tanh\left[\left(1.6m^{-1.5}+25\right)\frac{H_o}{L_o}\right]+30m^{0.1}\frac{H_o}{L_o} \quad [11]$$

$$A_2 = 9.5\left(\frac{H_o}{L_o}\right)^{-0.5}+10 \quad [12]$$

where m is the beach slope.

(f) Wang et al. (2008), hereafter referred to as W08, determined wave shoaling based on nonlinear (Boussinesq-type) wave model of Lynett and Liu (2004) for various wave conditions. They related the ratio of nonlinear and linear shoaling coefficients with the Ursell parameter, and fitted the results with the following formula:

$$H = \frac{H_o}{\sqrt{(\tanh kh)\left(1+\frac{2kh}{\sinh 2kh}\right)}}\left[1+0.80\tanh\left(\frac{U_r}{1070}\right)^{1.06}\right] \quad [13]$$

where $U_r = HL^2/h^3$ is the local Ursell parameter. Eq. [13] is an implicit equation because U_r is a function of H. Therefore, Eq. [13] has to be solved by iteration method.

In total, there are 6 formulas to be considered in this study. The formulas can be classified in to 2 groups based on the theories used in the development, i.e. linear wave (formula of A45), nonlinear wave (formulas of SB80, I82, KG96, TM02, and W08). Most of the formulas (except W08) were expressed in the form of explicit equations. The formula of W08 contains implicit equation, which had to be solved by iteration method.

The 5 empirical formulas were derived by fitting dimensionless parameters to data determined from the wave models. The formula of Tajima and Madsen (2002) was verified with one case of measured regular waves, while the other formulas were not verified with the measured regular wave shoaling. As the empirical formulas were not verified or verified with limited conditions of regular wave shoaling, it is not clear whether the existing formulas are applicable for computing regular wave shoaling for a wide range of wave conditions. The main objective of the next section is to verify the empirical formulas with a wide range of wave conditions.

3 FORMULA EXAMINATION

Many researchers (Battjes and Janssen, 1978; Baldock et al., 1998; Rattanapitikon et al., 2003) showed that wave models, developed based on linear wave theory, give satisfactory results, even when the assumptions of linear wave theory (e.g. small amplitude, sinusoidal wave, flat-bed, and non-breaking) had been violated. This shows that the violations havd not much effect on the prediction of wave height transformation. In addition, the empirical formulas of Kweon and Goda (1996), and Tajima and Madsen (2002) were used to compute the shoaling of irregular waves, in which the profiles were much different from that of periodic waves assumed in the models (or formulas) development. Therefore, it might be expected that the selected formulas may be applicable for general periodic waves, even when their assumptions are violated. There are many ways to test the validity of the theories (or formulas), e.g. mathematical validity, analytical validity, and physical validity (Dean and Dalrymple, 1991). The present study concentrated on the physical validity of the formulas (how well the prediction of the formulas agrees with actual measurements). Hence, in the present study, the selected formulas (developed based on linear wave or nonlinear waves) were examined with the experimental data generated with either Stokes or cnoidal waves at the wavemakers.

The measured data of wave height transformation in the offshore zone are used to verify the formulas. Experimental data from 4 sources, including 40 cases, have been collected for examination of the formulas. A summary of the collected experimental data is given in Table 1. Either Stokes or cnoidal waves were generated in the experiments of Hansen and Svendsen (1979), while the Stokes waves were generated in the other experiments. The experimental data cover a wide range of wave conditions ($0.002 \le H_o / L_o \le 0.069$). The experiments were performed under fixed plane beach of slope (m) ranging between 0.03 to 0.05.

Table 1. Summary of collected experimental data used to examine the wave shoaling formulas.

Sources	Abbreviation	No. of cases	No. of data	H_o / L_o	Beach slopes
Iwagaki and Sakai (1969)	IS69	8	48	0.003-0.056	0.05
Hansen and Svendsen (1979)	HS79	17	359	0.002-0.069	0.03
Nagayama (1983)	N83	12	104	0.025-0.055	0.05
De Serio and Mossa (2006)	DM06	3	11	0.002-0.051	0.05
Total		40	522	0.002-0.069	0.03-0.05

The basic parameter for determination of the overall accuracy of the formulas is the root-mean-square relative error (ER), which is defined as:

$$ER = 100\sqrt{\frac{\sum_{i=1}^{nm}(H_{ci} - H_{mi})^2}{\sum_{i=1}^{nm} H_{mi}^2}} \qquad [14]$$

where i is the wave height number, H_{ci} is the computed wave height of number i, H_{mi} is the measured wave height of number i, and nm is the total number of measured wave heights. The small value of ER indicates good overall accuracy of the formula.

The measured wave heights in the offshore zone from 4 sources (shown in Table 1) are used to examine the accuracy of each formula. The errors (ER) of the 6 formulas for 4 data sources are shown in Table 2. The results can be summarized as follows.

a) The linear wave formula (A45) gives a reasonable overall prediction of shoaling wave heights (ER = 9.4%).
b) Two empirical formulas (TM02 and SB80) give less accuracy than that of linear wave formula and should be used with care in practice.
c) The overall accuracy of the formulas in descending order are the formulas of W08, KG96, I82, A45, TM02, and SB80. Comparing among the 5 empirical formulas, the formula of W08 gave the best prediction (ER = 5.7%), while the formula of SB80 giving the worst prediction (ER = 16.3%). This shows that it is possible to use empirical formula for computing shoaling wave heights.
d) Although, the formula of W08 gives the best overall prediction, it is in the form of an implicit equation. The equation has to be solved by iteration method and may not be convenient for using in practice.

Table 2. The root-mean-square relative error (ER) of existing and modified formulas for each data source and all data (measured data from 4 sources shown in Table 1).

Sources	No. of data	A45	SB80	I82	KG96	TM02	W08	I82C	W08C
IS69	48	11.8	12.3	5.1	4.9	9.7	6.5	5.3	6.0
HS79	359	9.1	18.1	8.2	7.6	12.8	5.6	5.5	5.6
N83	104	8.0	5.4	5.0	5.0	8.5	5.8	5.2	5.6
DM06	11	12.5	27.5	12.7	11.0	11.1	5.2	4.7	6.3
All data	522	9.4	16.3	7.6	7.1	11.7	5.7	5.4	5.6

4 FORMULA RECALIBRATION

The main objective of this section is to recalibrate some existing formulas. As the formulas of SB80 and TM02 contain many constants, it seems to be difficult to recalibrate the formulas. Therefore, only the top 3 formulas were selected to be recalibrated with the collected experiments, i.e. W08, KG96, and I82. However, the general form of KG96 is the same as that of I82. Hence only 2 existing formulas were selected to recalibrate, i.e. the formulas of I82 and W08. The general forms of I82 and W08 are shown in Eq. [15] and [16].

$$H = \frac{H_o}{\sqrt{(\tanh kh)\left(1+\frac{2kh}{\sinh 2kh}\right)}} + K_1 H_o \left(\frac{h}{L_o}\right)^{K_2} \left(\frac{H_o}{L_o}\right)^{K_3} \quad [15]$$

$$H = \frac{H_o}{\sqrt{(\tanh kh)\left(1+\frac{2kh}{\sinh 2kh}\right)}} \left[1 + K_4 \tanh\left(\frac{U_r}{K_5}\right)^{K_6}\right] \quad [16]$$

where K_1 to K_6 are constants. The default values of K_1 to K_6 are 0.0015, -2.8, 1.2, 0.80, 1070, and 1.06, respectively.

The measured data shown in Table 1 were used to calibrate the constants (K_1 to K_6). The calibrations are conducted by gradually adjusting the coefficients K_1 to K_6 until the minimum error (ER) of each formula was obtained. The optimum values of K_1 to K_6 are 0.0015, -2.8, 1.3, 0.80, 900, and 1.1, respectively. Substituting the corresponding constants into Eq. [15] and [16], where the calibrated formulas become:

$$H = \frac{H_o}{\sqrt{(\tanh kh)\left(1+\frac{2kh}{\sinh 2kh}\right)}} + 0.0015 H_o \left(\frac{h}{L_o}\right)^{-2.8} \left(\frac{H_o}{L_o}\right)^{1.3} \quad [17]$$

$$H = \frac{H_o}{\sqrt{(\tanh kh)\left(1+\frac{2kh}{\sinh 2kh}\right)}} \left[1 + 0.80 \tanh\left(\frac{U_r}{900}\right)^{1.1}\right] \quad [18]$$

Eq. [17] and [18] are hereafter referred to as I82C and W08C, respectively. The errors of the calibrated formulas are shown in the last 2 columns of Table 2. The results can be summarized as follows:

a) The calibrated formulas give slightly better accuracy than that of the best existing formula (W08).
b) The accuracy of W08C is not improved significantly. The proposed constants are almost the optimal values.
c) The accuracy of I82C is improved significantly. Comparing among the selected formulas, the formula of I82C gives the best prediction. The formula of I82C is an explicit formula, which can be used to compute shoaling wave heights directly.
d) Considering accuracy and simplicity of the existing and the calibrated formulas, the formula of I82C is recommended to be used for computing the shoaling of regular wave heights.

5 CONCLUSIONS

This study concentrates on empirical formulas for computing shoaling wave heights. The empirical formulas were introduced to facilitate engineers for design works and preliminary study of coastal processes in an offshore zone. During the past decades, several empirical formulas have been proposed for computing shoaling wave heights. Most of the formulas were developed empirically from computed results of nonlinear wave models, which were not calibrated or calibrated with a limited experimental data. No direct literature has been made to describe clearly the applicability and accuracy of each formula. The main objective of this study is to examine the accuracy of 5 empirical formulas for computing regular wave shoaling. Forty cases of measured shoaling wave heights from four sources of published experimental data are used to examine the formulas. The data obtained cover the range of deepwater wave steepness from 0.002 to 0.069. The accuracy of the formulas was also compared with an often-used formula (linear wave formula). It was found that the formula of W08 gives the best prediction, while the linear wave formula gives a reasonable overall prediction of shoaling wave heights. Two empirical formulas (SB80 and TM02) give less accuracy than that of linear wave formula and should be used with care in practice. Although, the formula of W08 gives the best overall prediction, it is in the form of an implicit equation, which may not be convenient for using in practice. The formulas, that give better prediction than that of linear wave theory, were selected to be recalibrated. The calibrated formulas give slightly better accuracy than that of the best existing formula. Considering accuracy and simplicity of the existing and the calibrated formulas, the formula of I82C is recommended to be used for computing the shoaling of regular wave heights.

REFERENCES

Airy, G.B. (1845). Tides and Waves. *Encyclopedia Metropolitan*, London, Article, 192, 241–396.

Baldock, T.E., Holmes, P., Bunker, S. & Van Weert, P. (1998). Cross-Shore Hydrodynamics within an Unsaturated Surf Zone. *Coastal Engineering*, 34(3), 173-196.

Battjes, J.A. & Janssen, J.P.F.M. (1978). Energy Loss and Set-Up due to Breaking of Random Waves. *Proceedings of the16th Conference on Coastal Engineering*, 569-587.

Cokelet, E.D. (1977). Steep Gravity Waves in Water of Arbitrary Uniform Depth. *Philosophical Transactions of the Royal Society of London A: Mathematical, Physical and Engineering Sciences*, 286(1335), 183-230.

Dean, R.G. & Dalrymple, R.A. (1991). *Water Wave Mechanics for Engineers and Scientists*. World Scientific Publishing Co. Pte. Ltd, 368.

De Serio, F. & Mossa, M. (2006). Experimental Study on the Hydrodynamics of Regular Breaking Waves. *Coastal Engineering*, 53, 99–113.

Hansen, J.B. & Svendsen, I.A. (1979). *Regular Waves in Shoaling Water - Experimental Data*, Series Paper 21, Inst. Hydrodyn. and Hydraulic Engineering, Tech. Univ. Denmark.

Isobe, M. (1985). Calculation and Application of First-Order Cnoidal Wave Theory. *Coastal Engineering*, 9, 309–325.

Iwagaki, Y. & Sakai, T. (1969). *Studies on Cnoidal Waves (seventh report) - Experiments on wave shoaling*, Dis. Pre. Research Institute Annals, No. 12B, Kyoto Univ., 569–583 (in Japanese).

Iwagaki, Y., Shiota, K. & Doi, H. (1982). Shoaling and Refraction Coefficients of Finite Amplitude Waves. *Coastal Engineering Japan*, 25, 25–35.

Kweon, H.M. & Goda, Y. (1996). A Parametric Model for Random Wave Deformation by Breaking on Arbitrary Beach Profiles. *Proceedings of the 25th Coastal Engineering Conference, ASCE*, 578–587.

Le Roux, J.P. (2007). A Simple Method to Determine Breaker Height and Depth for Different Deepwater Height/Length Ratios and Sea Floor Slopes. *Coastal Engineering*, 54, 271–277.

Lynett, P. & Liu, P.L.F. (2004). A Two-Layer Approach to Water Wave Modeling. In *Proceedings of The Royal Society of London A: Mathematical, Physical and Engineering Sciences,* 460(2049), 2637-2669.

Nagayama, S. (1983). Study on the Change of Wave Height and Energy in the Surf Zone, *Bachelor Thesis*. Civil Engineering, Yokohama National University, Japan.

Nwogu, O. (1993). Alternative Form of Boussinesq Equations for Nearshore Wave Propagation. *Journal of waterway, port, coastal, and ocean engineering*, 119(6), 618-638.

Rattanapitikon, W., Karunchintadit, R. & Shibayama, T. (2003). Irregular Wave Height Transformation using Representative Wave Approach. *Coastal Engineering Journal*, 45, 489-510.

Sakai, T. & Battjes, J.A. (1980). Wave Theory Calculated from Cokelet's Theory. *Coastal Engineering*, 4, 65–84.

Shuto, N. (1974). Nonlinear Long Waves in a Channel of Variable Section. *Coastal Engineering Japan*, 17, 1–12.

Svendsen, I.A. & Brink-Kjaer, O. (1972). Shoaling of Cnoidal Waves. *Proceedings of the 13th Coastal Engineering Conference, ASCE*, 365–383.

Tajima, Y. & Madsen, O.S. (2002). Shoaling, Breaking and Broken Wave Characteristics. *Proceedings of the 28th Coastal Engineering Conference, ASCE*, 222–234.

Wang, B., Chadwick, A.J. & Otta, A.K. (2008). Derivation and Application of New Equations for Radiation Stress and Volume Flux. *Coastal Engineering*, 55, 302–318.

DETERMINING OBSERVATIONAL LOCATIONS IN THE GEUM RIVER ESTUARY

NAM-HOON KIM[1] & JIN HWAN HWANG[2]

[1,2] Department of Civil and Environmental Engineering, Seoul National University, Seoul, Korea,
nhkim0426@snu.ac.kr; jinhwang@snu.ac.kr

ABSTRACT

An artificial gate located at the mouth of the Geum River in Korea is operated to discharge freshwater irregularly to the coastal sea depending on the reservoir water level during the ebb time. It controls the regions of freshwater influence along with generating the salinity front. In order to manage such a coastal bay to sustain environmentally sound conditions, monitoring or field observations are necessary. For the operation of long-term monitoring or cost-effective field measurement, the deploying locations of the monitoring or sampling equipment's should be determined reasonably to represent the whole characteristics of the bay. However, no standard method to determine the optimal locations of monitoring or sampling has been proposed so far. Therefore, this study demonstrates how an objective analysis method with an inverse distance weighting function can be used to draw salinity maps from several points which can be used for optimized monitoring and sampling locations.

Keywords: Observational locations; salinity distribution; objective analysis; Geum River Estuary.

1 INTRODUCTION

Appropriate determination of the observational locations is important in understanding the environmental processes and operating management program in the coastal area (Hwang et al., 2014). Generally, field observations should be performed to identify the physical characteristics of water circulation in a bay (Chang et al., 2015). However, measurement locations of the field observations are hard to be determined considering the numbers of observational points, actual locations and sampling time. In particular, along with the optimal locations and sampling times, the physical characteristics of the estuary are not easy to be considered to find the best observational locations. If we want to find the best or optimal measurement points from the limited observational data, we need to construct data-map to reflect the real physical conditions. As the first step to reconstruct realized data, interpolation techniques should be selected appropriately. Therefore, the present paper is aimed to study the following:

(a) Evaluation of an interpolation technique, which can reproduce the true value.
(b) Proposing a protocol to determine the numbers of the observational locations.

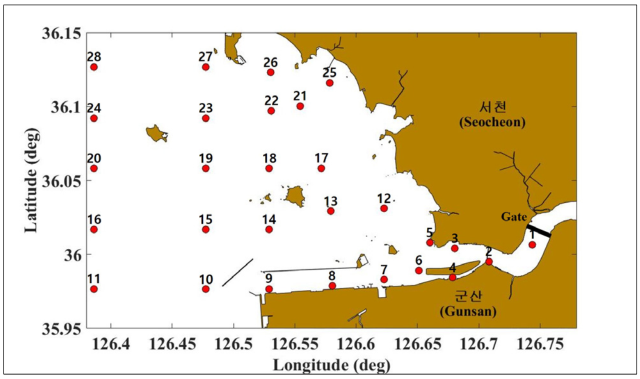

Figure 1. 28 Positions of True Salinity.

2 METHODS

The Geum River Estuary is located at the mouth of one of the rivers in Korea and categorized as the well-mixed condition because of the strong semidiurnal tide (Park et al., 2014; Kim et al., 2016). Therefore, horizontal gradient of salinity is large and sometimes, even a front can develop (Hwang et al., 2011). In this bay, salinities were measured using a Conductivity, Temperature, Depth sensor (CTD, Sea-Bird Electronics, Inc.) at 28 points (Figure 1). Assuming that the data measured at 28 points are true values, it is possible to construct a salinity map for the region of interest using interpolation technique. From 28 measured points, we selected the reduced numbers of measurement and reconstruct new salinity map. This new constructed map with smaller numbers of measurement points is again compared with the true salinity map constructed with 28 points measurements. To interpolate data and construct the map, an objective analysis scheme of the type proposed by Barnes (1964) was used to produce the salinity field in Geum River Estuary. This scheme can interpolate the whole region of interest by repeatedly applying an inverse distance dependent weighting function to two or more passes (loops) based on irregularly distributed salinity observations (Barnes, 1973; Koch et al., 1983; Sinha et al., 2006). If a variable $S(x_m, y_m)$ is observed at a location designated by m, then the first pass at grid point g is described by:

$$S_g^1 = \frac{\sum_{m=1}^{N} w_m S(x_m, y_m)}{\sum_{m=1}^{N} w_m} \qquad [1]$$

where the m^{th} weight applied to the observation at g is given by:

$$w_m = \exp\left[-\left(\frac{d_{mx}^2}{c_x^2} + \frac{d_{my}^2}{c_y^2}\right)\right] \qquad [2]$$

where the distance between the grid point and the m^{th} observation is designated by the variable d_m and the length scale, c_x and c_y , control the rate of fall-off of the weighting function with a different length scale in each of the x and y directions. It means that the weight approaches zero asymptotically, there is no need to specify a radius of influence. However, the number of observations, *N* should be chosen large enough so that the observations far away from the grid point receive a small weight. The length scales c_x and c_y were determined by using the Levenberg-Marquardt algorithm and control over the filtering (smoothing) properties of the analysis (Sinha et al., 2006).

The second pass is given by:

$$S_g^2 = S_g^1 + \frac{\sum_{m=1}^{N} w_m^{'} \left[S(x_m, y_m) - S^1(x_m, y_m) \right]}{\sum_{m=1}^{N} w_m^{'}} \qquad [3]$$

where the weighting function $w_m^{'}$ is given by:

$$w_m^{'} = \exp\left[-\left(\frac{d_{mx}^2}{\gamma c_x^2} + \frac{d_{my}^2}{\gamma c_y^2}\right)\right] \qquad [4]$$

The results from the first pass provide the background field which is the same as the original location, $S^1(x_m, y_m)$ and γ is a numerical convergence parameter that controls the difference between the weights on the first and second passes for the range of 0 to 1. It should be noted that the Barnes Objective Analysis (BOA) method does not incorporate a prediction error and instead relies on direct comparisons between estimates and observations to quantify errors (Rogowski et al., 2012).

The closeness between selected points and true values can be evaluated in terms of the expected error. Note that several possible choices for “error” evaluation are possible. An obvious choice is the Root Mean Square Error (RMSE) between estimated salinity points and the true salinity points (Rogowski et al., 2012). Consider the estimated salinity values $\left(\hat{S}_1, \hat{S}_2, \hat{S}_3, \ldots, \hat{S}_M\right)$ and corresponding true values $(S_1, S_2, S_3, \ldots, S_M)$, the RMSE for measuring points is calculated as:

$$\mathrm{RMSE} = \sqrt{\frac{1}{M}\sum_{i=1}^{M}\left(\hat{S}_i - S_i\right)^2} \qquad [5]$$

3 RESULTS

Salinities were interpolated from the irregularly spaced observation data for the area where we are interested. The observational locations were evaluated in terms of the RMS error between the estimated salinity points and the true salinity points in April, May and June 2016 (Figure 2). The number of observational locations can be iteratively modified by removing the positions with the smallest RMS error. If we take a salinity map obtained from 28 points as a true value, the minimum RMS error increases as the number of positions decreases regardless of which optimal number of locations are determined in three different months. The important point here is that there may not always be a unique set of observational location. In many observational location problems, there may be several possible sets and number of observational locations which are sufficient to the locations of present study. Figure 3-5 show an example of salinity map based on true and estimated (15 points) values using BOA. The bold line means 30 psu of the front which can move back and forth due to the tidal variation. The estimated salinity is similar to true salinity even if 10 or more points are excluded in the ocean side and 1 or 2 points inside the salinity front are excluded. Although the shape of the contour line for ocean side is slightly different, it can be seen that the shape of the overall contour line, difference between true and estimated salinity and position of the 30 psu front are very well estimated by using BOA. Present study is a result of having a good reference on determining the number of observational locations in the design of optimal monitoring network to understand the physical characteristics of the freshwater influences.

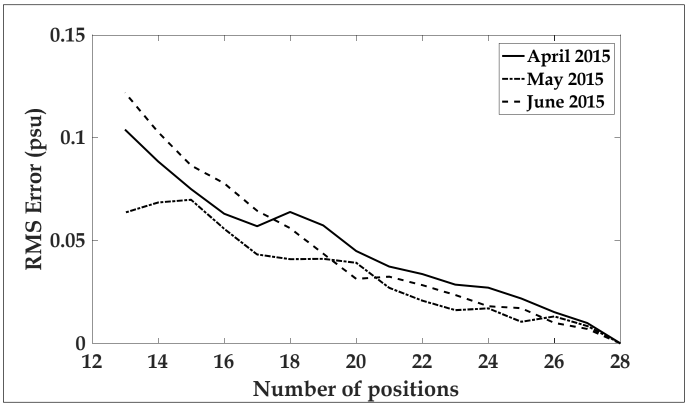

Figure 2. The RMS error from 13 to 28 (true).

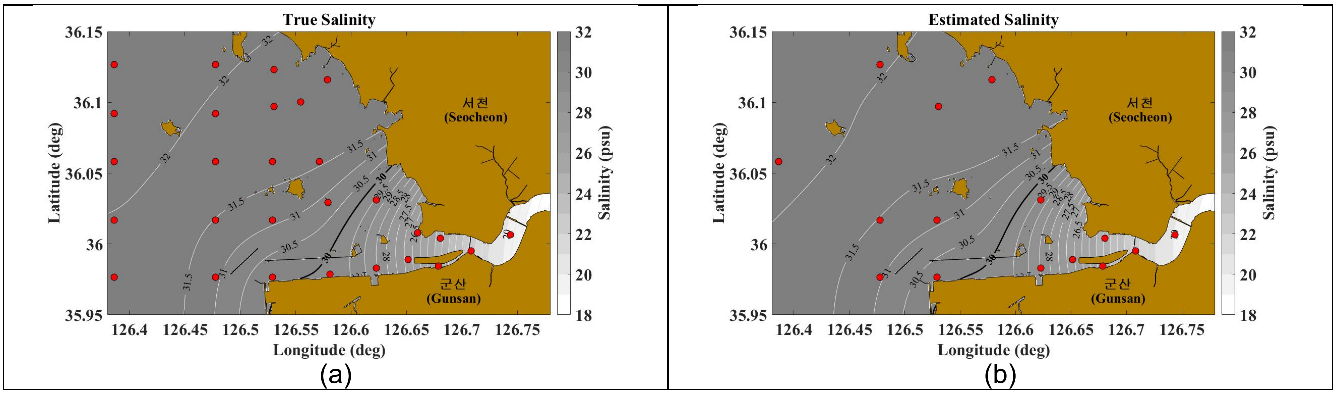

Figure 3. The spatial distribution of (a) true and (b) estimated salinity in April 2015.

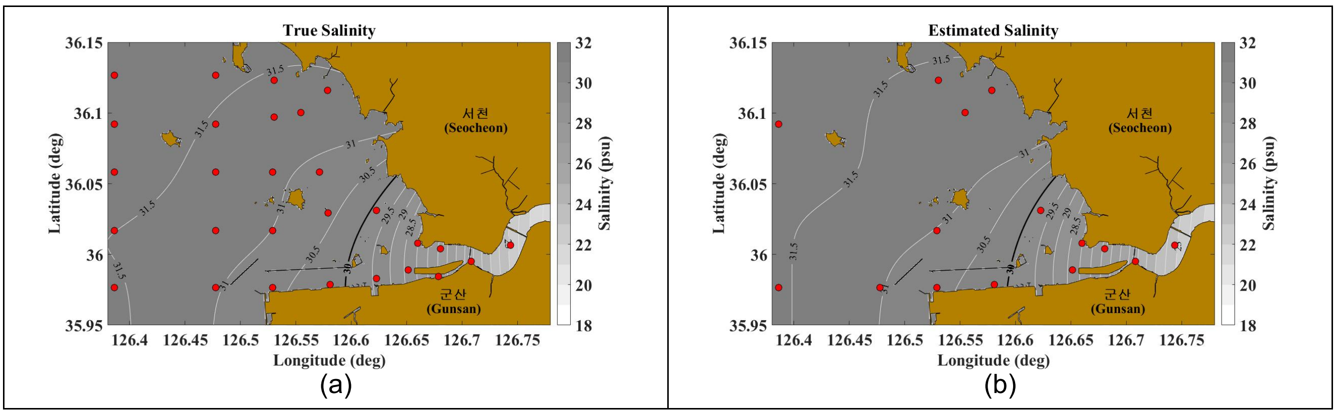

Figure 4. The spatial distribution of (a) true and (b) estimated salinity in May 2015.

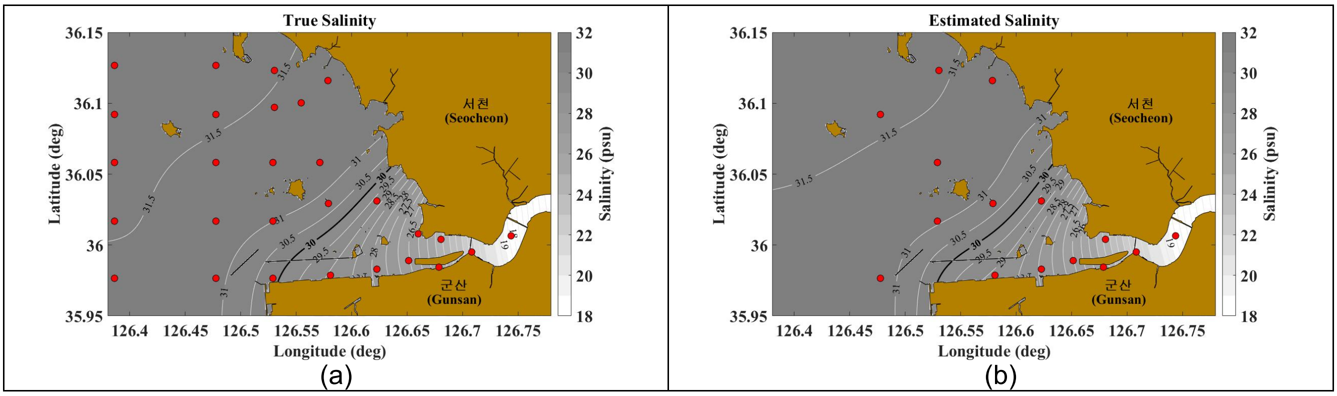

Figure 5. The spatial distribution of (a) true and (b) estimated salinity in June 2015.

4 CONCLUSIONS

In this study, the following conclusions were drawn for the determination of observational locations that can effectively reflect the characteristics of spatial distribution for salinity based on the data set acquired from the Geum River Estuary.

(a) To determine the number of observational location, it is effective to use the BOA method to obtain a result close to the true value. It is important to note that the authors are not emphasizing that the BOA method is the ideal interpolation technique. It was chosen because it is a common and easy to implement interpolation method that worked well for this application.

(b) The RMS error from the true value increases as the number of observational location decreases. In order to determine the exact optimized observational location, an additional cooperation with various techniques such as cost function and optimization technique should be performed.

Future work would be a proposal of more reliable process combining optimization technique and cost function based on numerical model because the number of observational locations in this study was evaluated by using 28 measurement points assuming the true value.

ACKNOWLEDGEMENTS

This research was a part of the project titled “Development of integrated estuarine management system”, funded by the Ministry of Oceans and Fisheries, Korea and the National Research Foundation of Korea (NRF) Grant (No. 2015R1A5A 7037372) funded by MSIP of Korea.

REFERENCES

Barnes, S.L. (1964). A Technique for Maximizing Details in a Numerical Weather Map Analysis. *Journal of Applied Meteorology*, 3(4), 396-409.

Barnes, S.L. (1973). *Mesoscale Objective Map Analysis using Weighted Time-Series Observation*, NOAA Technical Memorandum ERL NSSL-62, National Severe Storms Laboratory, Norman, OK 73069, 60, NTIS COM-73-10781].

Chang, Y.S., Hwang, J.H. & Park, Y.G. (2015). Numerical Simulation of Sediment Particles Released at the Edge of the Viscous Sublayer in Steady and Oscillating Turbulent Boundary Layers. *Journal of Hydro-environment Research*, 9(1), 36-48.

Hwang, J.H., Ahn, J.E., Park, Y.G., Jang, D.M. & Kim, B.R. (2011). The Growth of the Bulge Near a River Mouth. *Journal of Coastal Research*, 64, 1048-1052.

Hwang, J.H., Sy, P.V., Choi, H.J., Chang, J.S. & Kim, Y.H. (2014). The Physical Processes in the Yellow Sea. *Ocean and Coastal Management*, 102, 449-457.

Koch, S. E., DesJardins, M. & Kocin, P. J. (1983). An Interactive Barnes Objective Map Analysis Scheme for use with Satellite and Conventional Data. *Journal of Climate and Applied Meteorology*, 22(9), 1487-1503.

Kim, N.-H., Hwang, J.H. & Ku, H. (2016). Stratification of Tidal Influenced Navigation Channel. *Journal of Coastal Research*, 75(sp1), 63-67.

Park, Y.G., Kim, H.Y., Hwang, J.H., Kim, T., Park S., Nam, J.H. & Seo, Y.G. (2014). Dynamics of Dike Effects on Tidal Circulation around Saemangeum, Korea. *Ocean and Coastal Management*, 102, 572-582.

Rogowski, P., Stolkin, R. & Bruno, R. (2012). Optimization of the Spatial Distribution of Oceanographic Sensors in a Highly Variable Estuarine Environment. *Journal of Marine Environmental Engineering*, 9(3), 211-224.

Sinha, S., Narkhedkar, S. & Mitra, A. (2006). Barnes Objective Analysis Scheme of Daily Rainfall over Maharashtra (India) on a mesoscale grid. *Atmosfera*, 19(2), 109-126.

LABORATORY STUDY OF WAVE-INDUCED SETUP OVER FRINGING REEFS UNDER THE EFFECT OF TIDAL CURRENT

YU YAO [1], WENRUN HE [2], RUICHAO DU [3] & CHANGBO JIANG [4]

[1,2,3,4] School of Hydraulic Engineering, Changsha University of Science and Technology, Changsha, Hunan, China,
[1] Key Laboratory of Coastal Disasters and Defence of Ministry of Education, Nanjing, Jiangsu, China,
[4] Key Laboratory of Water-Sediment Sciences and Water Disaster Prevention of Hunan Province, Changsha, China.
yaoyu821101@163.com

ABSTRACT

Recent field studies on coral reef hydrodynamics have increasingly recognized the importance of tide in dominating the reef regional circulation. In this study, a series of laboratory experiments were performed in a wave-current flume to investigate the maximum wave-induced setup on the reef flat in the absence/presence of the tidal current. Experimental results were reported for a variety of regular wave and steady current conditions by using an idealized fringing reef model. Wave setup was found to reduce along the reef flat when shoreward current was present, but such decline was not obvious with seaward current. Compared to the absence of current, the maximum wave setup on the reef flat was consistently smaller during the shoreward current (flood tide) whereas it was always larger during the seaward current (ebb tide). Moreover, wave setup on the reef flat decreased with increasing flowrate of shoreward current while it increased with increasing flowrate of seaward current. Tidal current affecting the magnitude of wave setup on the reef flat were due to the changes of both bottom friction and momentum advection in the surfzone momentum balance.

Keywords: Wave breaking; wave setup; tidal current; fringing reef.

1 INTRODUCTION

Wave interactions with fringing coral reefs have been the primary focus of near-shore hydrodynamic studies over the decades. A typical fringing reef is characterized by a seaward sloping reef face and an inshore shallow reef flat. Corals commonly grow to mean low tide levels and may impose a shallow water control on the waves reaching reef flats. Similar to the wave transformation over a shallow shelf, ocean waves first shoal on a fore-reef slope and then break near the reef edge, dissipating their energy and generating a rise of mean sea level known as "wave setup", a phenomenon first described by Munk and Sargent (1948). The maximum setup usually occurs on the reef flat where it can drive flow across a shallow reef flat, through a deeper lagoon, and finally exits to the open sea through a channel, thus building up a two-dimensional horizontal (2DH) regional circulation in the reef area (Lowe et al., 2009). The 2DH reef-lagoon-channel system are crucial to the transport of organisms, nutrient and sediments (Hench et al., 2008).

Astronomical tides modulate all of the hydrodynamic processes over coral reefs (Hearn, 2011). Traditionally, the tide effect was simply represented by the variation of the reef-flat water level in previous field studies of wave setup (e.g., Lugo-Fernández et al., 1998; Hearn, 1999; Jago et al., 2007; Vetter et al., 2010 and many others). Until recently, the mechanics of water level variation (tide level modulation) in determining wave breaking and setup over reefs were addressed by Becker et al. (2014) using a semi-analytical model accounting for the measurements at three fringing reef sites. More recently, Lowe and Falter (2015) presented a global survey of the wave and tidal conditions experienced by coral reefs, and found that roughly one-third of reefs worldwide could be considered as tide-dominated, which means that not only the tidal level, but also the tidal current could possibly control the 2DH circulation. Subsequently, Lowe et al. (2015) conducted field experiment to investigate the hydrodynamics of a strongly tidally forced tropical intertidal reef platform in northwestern Australia, and they used a one-dimensional numerical model to solve the nonlinear shallow water equations with rapid (sub to supercritical) flow transitions.

To date, most existing laboratory investigations (e.g., Seelig, 1983; Demirbilek et al., 2007; Yao et al, 2013) of waves and reef hydrodynamics have generally ignored the currents, focusing only on the waves. A pioneer study of both wave setup and wave-generated flow on the reef flat were carried out by Gourlay (1996). He showed that the wave setup generally decreased with the increasing reef-flat water depth but the wave-generated flow increased with the water depth until a peak value, then it decreased. However, Gourlay's experiments only modeled the wave-driven current in the context of a 2DH wave basin and the effects of ambient currents such as tides, were still not considered.

In this study, to reveal the wave setup dynamics under the combined effect of waves and tidal currents, we performed laboratory experiments to investigate the maximum wave-induced setup on the reef flat in the absence/presence of the tidal current under a series of incident wave conditions. The regular waves, rather than the spectral waves were tested because there are well established theories in the literature to account for their interactions with the currents. We used a wave-current flume to isolate the waves and the tidal currents from other reef currents such as those driven by wind or buoyancy (Monismith, 2007) in a well-controlled environment. Since tide cycle usually has a much larger time scale than wave cycle, we modelled the tide effect through a constant current generated by a pump. The rest of the paper is organized as follows. The laboratory setting, instrumentation, and experimental procedures are introduced in Section 2, followed by an analysis of the measured wave setup under combined wave and current conditions in Section 3. Further discussion on the results is given in Section 4. Major conclusions drawn from this study are summarized in Section 5.

2 EXPERIMENTAL SETTINGS AND INSTRUMENTS

The schematic layout of the experimental arrangement is shown in Figure 1. Laboratory experiments were conducted in a wave flume 40 m long, 0.50 m wide and 0.8 m high at Hydraulics Modeling Laboratory, Changsha University of Science and Technology, P.R. China. A servo-controlled wave maker was placed at one end of the flume to generate the designed waves. At the other end, a sloping beach covered with porous materials was mounted to absorb the wave energy and reduce reflection. To establish an idealized two-dimensional reef-model that replicates a fringing reef, a plane slope of approximate 1:6 was built with the PVC plates at 27.3 m from the wave maker and was truncated to platform when it reached 0.35 m above the flume bottom. The flat was 7 m in cross-shore length with its width matching up the flume width. The end of reef flat was again connected to the flume bottom by a PVC slope, thus there was a “lagoon” region laying between the reef flat and the final beach. The entire model was firmly held by stainless steel rods attached to the two walls of the flume. To prevent water escaping or coming out from gaps between the model and wall of flume, plastic clay was used to fill the gaps up. Meanwhile, the slots between adjacent plates or between slope and flume bottom were sealed up by adhesive tapes. An iron pipe with 300 mm in diameter was established to connect both the bottom of lagoon and the bottom near the wave maker to model the channel. A timing pump was set on the middle of the pipe to generate the designed steady current in the pipe, and the pump could eventually force a circulation in the “reef-lagoon-channel” system through the connecting pipe. An electromagnetic flowmeter (SIEMENS Ltd., Denmark) was installed to the pipe to show the real-time flow rate.

The designed regular wave conditions were a combination of four incident wave heights, H= 0.04 m, 0.06 m, 0.08 m, and 0.1 m; three wave periods, T= 1.0 s, 1.5 s, and 2.0 s and two reef-flat submergences, h_r=0.05 m and 0.1 m. To examine the effect of a tidal current, we first tested both shoreward current (flood tide) and seaward current (ebb tide) with a constant flow rate of Q=20 m^3/h generated by the pump under all above wave conditions. We then tested a series of shoreward and seaward flow rates (Q=±14 m^3/h, ±18 m^3/h, ±22 m^3/h and ±26 m^3/h) by adjusting the pumping capacity under a typical wave condition of H_0=0.08 m, T=1.5 s and h_r=0.05 m. The corresponding range of reef-flat current speed was 0.078~0.29 m/s. For comparison purpose, we also tested all the waves without the presence of pumped current, i.e., Q=0. The laboratory reef profile was designed to mimic a natural reef site typically found at the Republic of the Marshall Islands. The reef dimensions, the water depth over the reef flat, and the incoming waves and tidal currents were selected according to the Froude similarity with a geometric scale factor of 1:20. The corresponding scale factor for both time and velocity was 1:4.5. Thus, the prototype reefs in this study were 140 m for reef-flat width, 1.0 ~2.0 m for reef-flat submergence, 0.8~2.0 m for incident wave height, 4.5~9.0 s for wave period and 0.35~1.3 m/s for tide current speed, which were in general fell in the ranges observed by Becker et al. (2014).

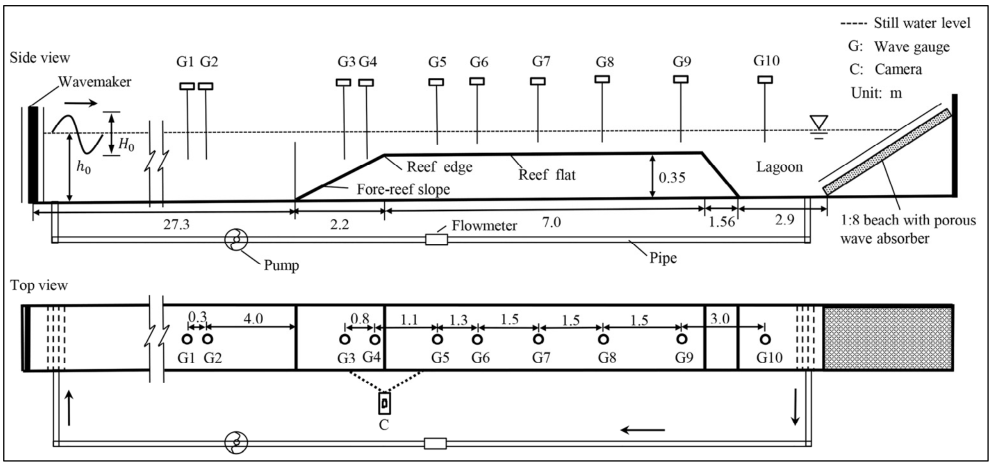

Figure 1. Experimental settings

In the shallow region on the reef flat, five Ultralab sensors (G5~G9, General Acoustics Ltd.) were used to measure water surface elevations, and they were almost equally spaced. An additional sensor (G10) was placed in the lagoon to monitor the lagoon water level. However, in order to measure waves in the surf zone near the reef edge, where the acoustic sensors cannot work well due to the effect of air bubbles in water, two resistance-type probes (G3 and G4) (RBR, Canada) were installed on the fore-reef slope near the reef edge. In addition, two probes (G1 and G2) were placed upstream of the fore-reef to separate incident waves from reflected waves using a two-point method. All the wave gauges were sampled at 50 Hz through a data acquisition system. During the experiments, each wave condition was repeated three times to ensure repeatability. Based on our pilot tests, waves and current in the flume could reach a quasi-steady state about 10 minutes after the start of the wave maker. Therefore, wave gauges were sampled for 12 minutes and only the last 100 wave cycles in each measured wave record were used to calculate the wave setup. A waiting time of several minutes between two subsequent runs were imposed to avoid possible effects of residual waves and currents in the flume. Additionally, a video camera (Logitech Pro 249 C920) was placed on the side of the flume to capture the surfzone process associated with wave breaking around the reef edge. The frame acquisition rate of the camera was 30 Hz. Note that for subsequent analysis, wave breaking before reef slope was observed in some cases because the wave steepness was too large due to the increased seaward current and those cases were discarded. Meanwhile, for the reef-flat submergence of 0.10 m with very small wave height, waves may propagate over the reef flat without breaking and these cases were ignored as well.

3 DATA ANALYSIS

3.1 Visualization of wave transformation in absence/presence of current

In these experiments, we observed that plunging breaker occurred near the reef edge under most of the tested wave conditions. Using the typical wave condition (H_0=0.08 m, T=1.5 s, h_r=0.05 m), Figure 2 compares the representative features of the surfzone process around the reef edge under both shoreward and seaward currents but with the same flow rate of Q=20 m^3/h, also included are those without current. Four different phases were displayed starting from the moment when lip of breaker hit the water surface (t/T= 0). For all cases, the breakers stroke the reef edge at t/T=0. while at t/T=1/4 , the splash-up jet due to plunging breaker hit the water ahead of it, producing air-water mixture of foam, bubbles and some subsequent white-capping. After one half wave period (t/T=1/2), the broken waves propagated across the surfzone as fully turbulent bores with a turbulent roller in the front. For the last phase (t/T=3/4), the bore was mostly dissipated and transmitted waves reformed on the reef flat. Strong reverse flow could be observed during this period before the next incoming wave arrived.

When examining the presence of tidal current, we found that, compared to the case without current, the breaking point at t/T=1/4 moved further shoreward with the shoreward current while it moved seaward with the seaward current. Meanwhile at t/T=1/2, wave breaking resulted in a larger turbulent roller for the case with the seaward current compared with that with shoreward current, whereas the surfzone width decreased as the current varied from shoreward to seaward as indicated at t/T=3/4.

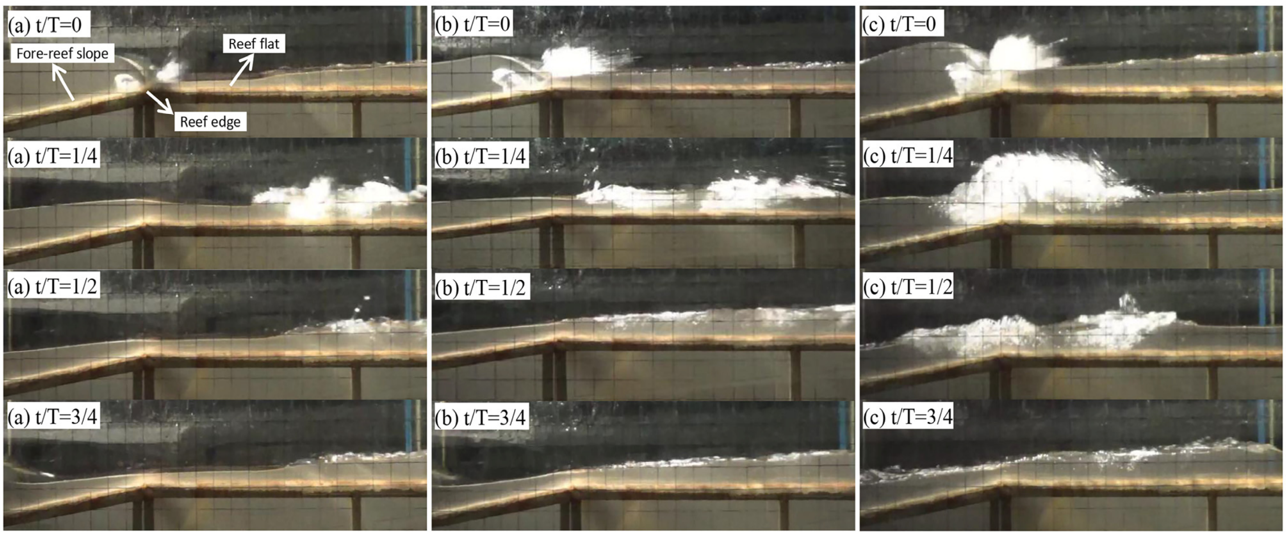

Figure 2. Breaking waves around the reef edge under different wave phases (t/T) (a) shoreward current; (b) without current; (c) seaward current.

3.2 Mean water level (MWL) across the reef profile in absence/presence of current

Ten wave gages (G1 to G10) were used in our experiments, enabling us to construct reasonably detailed wave setup profiles across the reef models by linear interpolation. Figure 3 shows that the mean water level

(MWL) across the reef profile varied with different incident waves and currents. Two representative reef-flat submergences (h_r), wave heights (H_0), wave periods (T) as well as current flowrates (Q) were examined.

For all cases, the setdown in the water in front of the fore-reef (G1 and G2) was related to the conservation of mass in a closed flume: the gain of water mass in the region with wave-induced setup must be balanced by the loss of water mass in the region with wave-induced setdown. On the fore-reef slope (G4), the mean water level further decreased due to wave shoaling. In the surf zone (G5), there was a monotonic increase of MWL due to wave breaking. The peak wave setup always appeared at G6. After the peak (G7~G9), the setup became more or less constant on the reef flat for the case with seaward current and it eventually decreased in the lagoon (G10). For the case with shoreward current, wave setup decreased all the way along the reef flat until the lagoon. Overall, wave setups on the reef flat were consistently larger for the seaward current than the shoreward, and those setups in absence of current lied between them.

When examining the effects of different wave and current conditions, Figure 3 shows that wave setups were larger for smaller still water depth (Figures 3a and 3b), larger wave height (Figures 3c and 3d), and larger wave period (Figures 3e and 3f). However, for the effect of current, Figures 3g and 3h suggest that larger flowrate on the reef flat caused a smaller wave setup for shoreward current but larger wave setup for seaward current. In other words, the discrepancy of wave setups between the shoreward and the seaward currents increased with the increasing magnitude of the current flowrate.

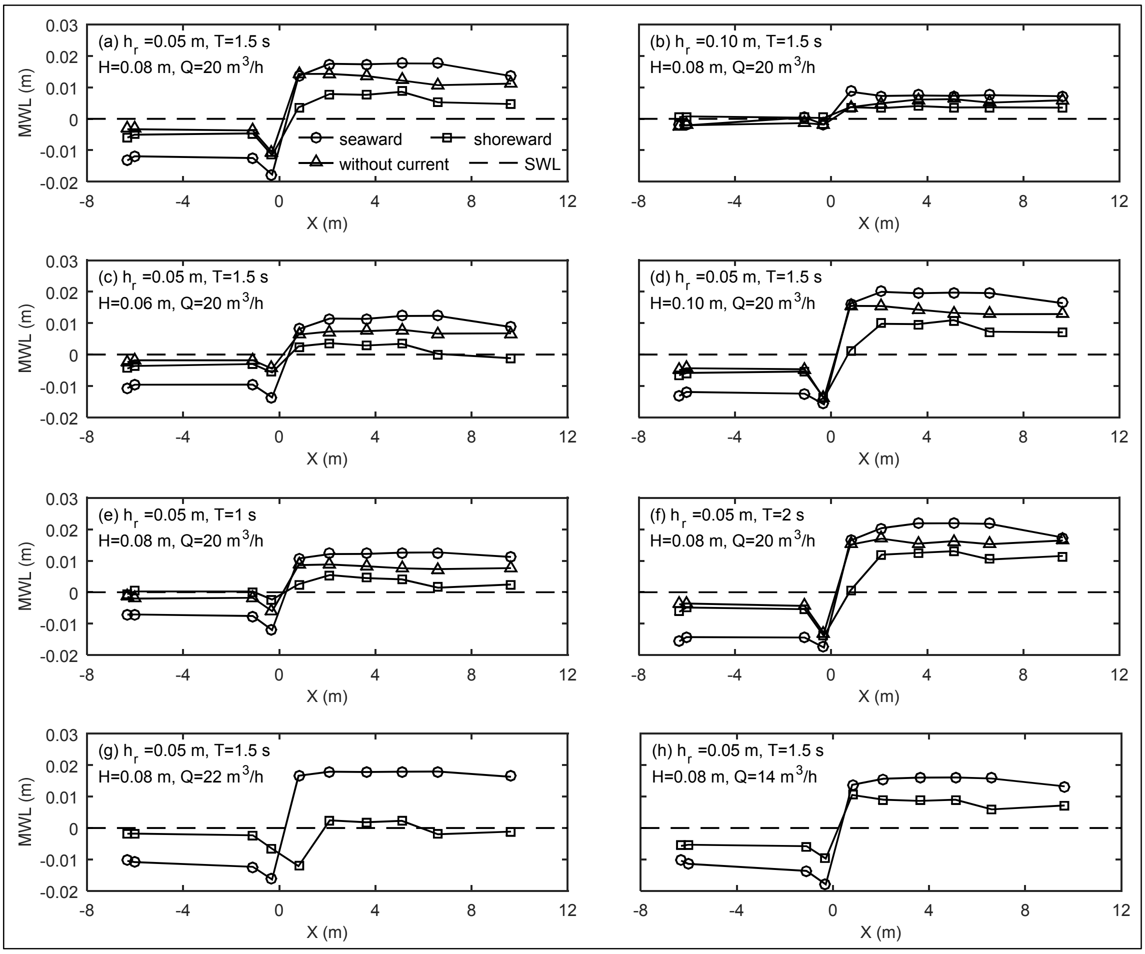

Figure 3. Mean water level across the reef profile with different waves and currents (X=0 indicates the location of reef edge with positive x pointing shoreward).

3.3 Variation of wave setup with incident waves in absence/presence of current

The above analysis shows that the MWL always reached maximum around G6 on the reef flat, thus the wave setup at G6 is a good representative of the maximum setup ($\overline{\eta}_r$) on the reef flat. Figures 4a and 4b show this wave-induced setup as a function of deep water wave height (H_0) and wave periods (T) for the two reef-flat submergences (h_r), respectively. Note that we included in this figure for all tested cases with both shoreward and seaward currents of Q=20 m^3/h and without currents.

For both reef-flat submergence, the wave-induced setup on the reef flat increased almost linearly with increasing H_0. The relationship between $\overline{\eta}_r$ and T was less obvious. However, by comparing the setup with similar H_0, it could be found that $\overline{\eta}_r$ in general, increased with increasing T. These trends were generally in agreement with the observations of Gourlay (1996) without considering the tidal current. As for the effect of reef-flat submergence, we found that wave setup was generally larger with h_r=0.05 m than h_r =0.10 m, suggesting that the reef-flat submergence was still a key parameter to control the wave setup on the reef flat in the presence of current. Meanwhile, among the cases with different current conditions, we again observed an increasing wave setup from the shoreward current to the seaward current, and the setups in absence of current staying between them. The magnitude of $\overline{\eta}_r$ raised significantly as Q increased from +20 m^3/h (shoreward) to -20 m^3/h (seaward) for h_r=0.05 m. However, this growth was less significant as h_r reached 0.10 m.

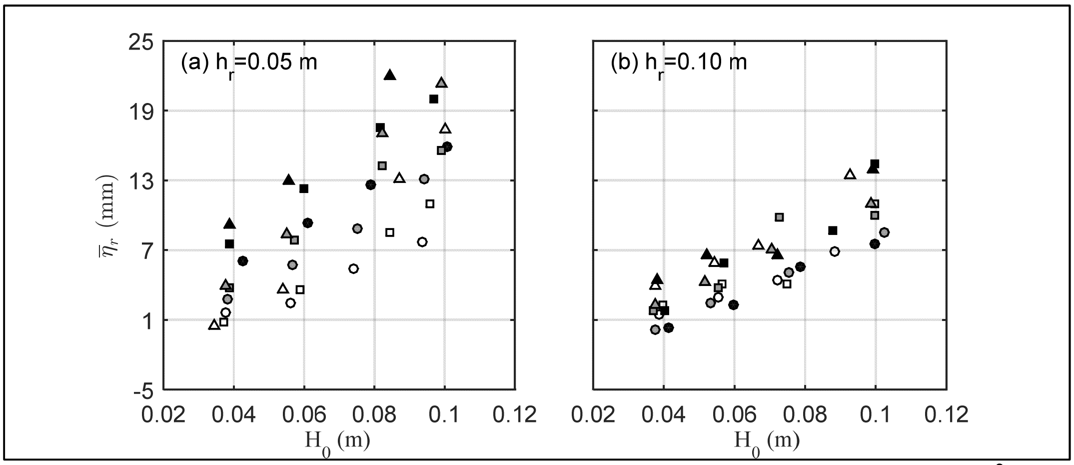

Figure 4. Variation of wave setup ($\overline{\eta}_r$) with incident waves in presence of current of Q=20 m^3/h (White: shoreward current, grey: without current, black: seaward current; circular: T=1 s, square: T=1.5 s, triangle: T=2 s).

3.4 Variation of wave setup with current flowrate

Finally, the effect of flowrate on the wave setup ($\overline{\eta}_r$) was examined systematically under the aforementioned typical wave conditions (H_0= 0.08 m, T=1.5 s and h=0.40 m). A series of steady flowrate ranging from Q= -26 m^3/h to 26 m^3/h were examined. The corresponding wave setups were compared in Figure 5. Figure 5 suggested that $\overline{\eta}_r$ decreased almost linearly with increasing Q for the shoreward current, while it increased linearly for the seaward current. Again, for the same Q, $\overline{\eta}_r$ was consistently smaller with shoreward current than that with seaward, and the difference in wave setups between the two types of current enlarged with increasing Q. A linear fit of the variation of $\overline{\eta}_r$ with Q gives the determination of coefficient R^2=0.90.

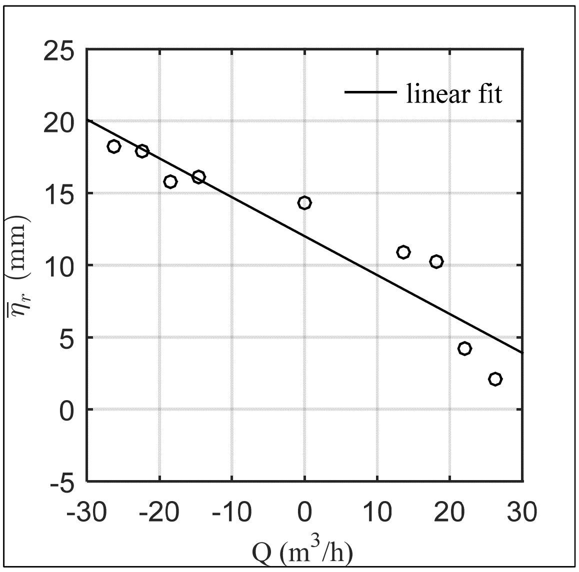

Figure 5. Variation of wave setup ($\overline{\eta}_r$) with current flow rate (Q) (H_0= 0.08 m, T = 1.5 s and h_r = 0.05 m).

4 DISCUSSION

The 1D depth-integrated wave-averaged momentum equation was conventionally used to interpret the reef-top hydrodynamics, it can be written as (Monismith, 2007)

$$g\frac{\partial\bar{\eta}}{\partial x}+\frac{3g}{16(\bar{\eta}+h)}\frac{\partial H^2}{\partial x}+\frac{\partial}{\partial x}\frac{q^2}{\partial(\bar{\eta}+h)^2}+\frac{C_D q|q|}{(\bar{\eta}+h)^3}=0 \qquad [1]$$

where $\bar{\eta}$ is the deviation of mean water level from still water level, q is the reef-top current per unit width, h is the local water depth, C_D is the bottom drag coefficient and g is the gravity acceleration. On LHS of Eq. [1], the first term is the pressure gradient, the second term is the radiation stress gradient in which we have used the linear wave approximation, the third term is the momentum advection and the last term is the bottom friction in which we have assumed a quadratic frictional law.

It was well recognized that under pure wave action, the dominated balance in the surf zone is the balance between pressure gradient (shoreward increase) and radiation stress (shoreward decrease), thus a wave setup is generated similar to wave breaking on the traditional plane beach. After the surf zone where wave breaking ceases, the pressure gradient associated with the induced setup normally balances the friction term on the reef flat which could force current on the reef flat to the lagoon and finally to the open sea via the channel. Hearn (2011) (his figure 1) has shown the variations of each term in Eq. [1] across a 1DH typical reef configuration. It showed that in the surf zone, both the friction term and advection term (although less important) change reversely across the reef with the radiation stress term. Thus, when the shoreward tidal current was present, more radiation stress gradient was used to compensate the raise of both friction and advection terms since they are proportional to the flow rate, q in Eq. [1]. Consequently, less radiation stress gradient was balanced with the pressure gradient, resulting in a reduction of wave setup, and vice versa for the seaward current. A quantitative analysis of each term in Eq. [1] based on current experimental data will be reported elsewhere.

Indeed, most natural coral reefs are composed of hard calcium carbonate skeletal material and covered by a wide variety of benthic organisms, and the coral community on a reef flat is more like a layer of porous material. Although, the dominant physical process in the surf zone for our experiments was wave breaking because of the very smooth reef surfaces that we used, we still anticipate that more radiation stress would balance the increased friction term (because C_D increases) in Eq. [1] at realistic reef sites, thus more reduction of the maximum wave setup on the reef flat should be found compared to our laboratory experiments. Reproducing hydraulic roughness and porosity of natural reef flats at model scale will be attempted in our future studies.

5 CONCLUSIONS

A series of laboratory experiments were conducted in a wave-current flume to examine the effect of tidal current on wave-induced setup over a submerged idealized fringing reef. Different combinations of regular waves and steady currents were examined and the results were also compared with those in absence of the current. Data analysis showed that the surfzone process (breaking location, breaking intensity and surfzone width) were altered when the current was present. Wave setup reduced along the reef flat with shoreward current, but such variation was not obvious with seaward current. The maximum wave setup on the reef flat in the presence of current increased with increasing incident wave height and wave period, but decreased with increasing reef-flat water depth. Compared to the case without current, the maximum wave setup on the reef flat was consistently smaller during the shoreward current (flood tide) while it was always larger during the seaward current (ebb tide). With the shoreward current, wave setup decreased when the flowrate of current increased. Whereas with the seaward current, wave setup increased with the growth of current flowrate. This study suggests that the tidal current plays an important role in determining the magnitude of wave setup on the reef flat due to its change in both bottom friction and momentum advection in the surfzone momentum balance. Subsequent investigation will concentrate on an analytical model to further interpret the experimental results, the details will be reported in a subsequent paper.

ACKNOWLEDGEMENTS

This study was supported financially by the National Natural Science Foundation of China (No.51679014 and No.51309035), the Specialized Research Fund for the Doctoral Program of Higher Education (No. 20134316120004), the Open Foundation of Key Laboratory of Coastal Disasters and Defence of Ministry of Education (No.201602) and the Open Foundation of Key Laboratory of Port, Waterway and Sedimentation Engineering of the Ministry of Transport (No. Yn216002).

REFERENCES

Becker, J.M., Merrifield, M.A. & Ford, M. (2014). Water Level Effects on Breaking Wave Setup for Pacific Island Fringing Reefs. *Journal of Geophysical Research: Oceans*, 119(2), 914-932.

Demirbilek, Z., Nwogu, O.G. & Ward D.L. (2007). Laboratory Study of Wind Effect on Runup over Fringing Reefs. *Report 1: Data report*, *Coastal and Hydraulics Laboratory Technical Report ERDC/CHL-TR-07-4*, U.S. *Army Engineer Research and Development Center, Vicksburg, MS.*

Gourlay, M.R. (1996). Wave Set-Up on Coral Reefs. 1. Set-Up and Wave-Generated Flow on an Idealised Two Dimensional Horizontal Reef. *Coastal Engineering*, 27(3-4), 161-193.

Hench, J.L., Leichter, J. & Monismith, S.G. (2008). Episodic Circulation and Exchange in a Wave‐Driven Coral Reef and Lagoon System. *Limnology and Oceanography*, 53(6), 2681-2694.

Hearn, C.J. (1999). Wave-breaking hydrodynamics within coral reef systems and the effect of changing sea level. *Journal of Geophysical Research*, 104 (C12), 30007-30019.

Hearn, C.J. (2011). *Hydrodynamics of Coral Reefs*. Hopley D (ed) Encyclopedia of modern coral reefs, Springer, Berlin, 563–573.

Jago, O.K., Kench, P.S. & Brander, R.W. (2007). Field Observations of Wave‐Driven Water‐Level Gradients across a Coral Reef Flat. *Journal of Geophysical Research: Oceans*, 112(C6).

Lugo-Fernandez, A., Roberts, H. H. & Wiseman Jr, W. J. (1998). Tide Effects on Wave Attenuation and Wave Set-Up on a Caribbean Coral Reef. *Estuarine, Coastal and Shelf Science*, 47(4), 385-393.

Lowe, R.J., Falter, J.L., Monismith, S.G. & Atkinson, M.J. (2009). Wave-Driven Circulation of a Coastal Reef–Lagoon System. *Journal of Physical Oceanography*, 39(4), 873-893.

Lowe, R.J., Leon, A.S., Symonds, G., Falter, J.L. & Gruber, R. (2015). The Intertidal Hydraulics of Tide‐Dominated Reef Platforms. *Journal of Geophysical Research: Oceans*, 120(7), 4845-4868.

Lowe, R.J. & Falter, J.L. (2015). Oceanic Forcing of Coral Reefs. *Annual review of marine science*, 7, 43-66.

Munk, W. H., & Sargent, M. C. (1948). Adjustment of Bikini Atoll to Ocean Waves. *Eos, Transactions American Geophysical Union*, 29(6), 855-860.

Monismith, S. G. (2007). Hydrodynamics of Coral Reefs. *Annu. Rev. Fluid Mech.*, 39, 37-55.

Seelig, W.N. (1983). Laboratory Study of Reef-Lagoon System Hydraulics. *Journal of waterway, port, coastal, and ocean engineering*, 109(4), 380-391.

Vetter, O., Becker, J. M., Merrifield, M. A., Pequignet, A. C., Aucan, J., Boc, S.J. & Pollock, C.E. (2010). Wave Setup over a Pacific Island Fringing Reef. *Journal of Geophysical Research: Oceans*, 115(C12).

Yao, Y., Huang, Z., Monismith, S.G. & Lo, E.Y. (2012). Characteristics of Monochromatic Waves Breaking Over Fringing Reefs. *Journal of Coastal Research*, 29(1), 94-104.

HYDRODYNAMIC MODELLING OF SINGAPORE AND MALACCA STRAITS FOR OPERATIONAL FORECAST AND MANAGEMENT

SERENE H. X. TAY[1], ALAMSYAH KURNIAWAN[2], SENG KEAT OOI[3] & VLADAN BABOVIC[4]

[1,4] Department of Civil and Environmental Engineering, National University of Singapore (NUS), Singapore
serenetay@nus.edu.sg; vladan@nus.edu.sg
[2] Ocean Engineering Program, Institut Teknologi Bandung (ITB), Bandung, Indonesia
alamsyah@ocean.itb.ac.id
[3] Tropical Marine Science Institute, National University of Singapore (NUS), Singapore
sk.ooi@nus.edu.sg

ABSTRACT

Geographically located between Indian Ocean and South China Sea, the straits of Singapore and Malacca are one of the world's busiest maritime trading routes. In addition to shipping operations, more facilities and infrastructure have been constructed near the coast of Singapore in the recent years, and they are heavily dependent on sea water for different purposes such as cooling and desalination. Therefore, coastal water quality management is becoming one of Singapore's national interests. One of the tools to help achieving this is a high spatial resolution localized model that represents the Singapore coastal water condition accurately. Previous studies show the seasonal pattern in the throughflow of straits of Singapore and Malacca that is not induced locally, but rather caused by wind and pressure forcing applied on large basin scale water bodies; South China Sea and Indian Ocean, respectively. In order to account for this non-tidal flow in a localized model of high spatial resolution, several types of modelling approaches have been introduced previously such as multi-scale and multi-domain modelling. One of these approaches includes nesting of the local detailed model in a large domain model to obtain forcing condition at the nested boundaries. This paper will evaluate the various nested boundary conditions to simulate the hydrodynamics in Singapore and Malacca straits accurately for operational forecast and management. The optimum boundary condition setting of the nested model in Singapore Strait is found to be one with boundary condition of current velocity prescribed in the Eastern and Western boundaries and water level in the Southern boundary.

Keywords: Hydrodynamic; modelling; coastal; Singapore Strait; Malacca Strait.

1 INTRODUCTION

Local detailed hydrodynamic model is useful for studies in which operational forecast and coastal management is involved in highly in-homogenous coastline such as Singapore (Figure 1) whereby the coastline is occupied with different activities and industries from east to west. The degree of detail in this type of model is defined by the spatial resolution. A high spatial resolution model i.e. fine grid model is able to describe the land outline and bathymetry with higher precision, thus enhancing the representation of the modelled environment and the accuracy of the simulated hydrodynamics.

In Singapore coastal waters, hydrodynamic condition of sea state are defined by a combination of tidal and non-tidal water flow. Non-tidal flow in this region is mainly induced by the varying wind and air pressure of the large seasonal monsoon system. With the focus on Singapore coastal waters, several studies such as Kurniawan et al. (2011), Kurniawan et al. (2015) and Tay et al. (2016) have carried out using large scale domain model to model tidal and non-tidal (such as surge) flow in Singapore Strait accurately. However, the spatial resolution of these large domain models is low (between 300 m and 3 km) in Singapore Strait. These work have been carried out on large scale domain because Ooi et al. (2009) have shown that the non-tidal flows in vicinity of Singapore especially during Northeast monsoon can only be properly simulated in a model that covers the entire South China Sea basin. In Malacca Strait, Tay et al. (2015) and Tay et al. (2016) have shown that the local non-tidal flow are mainly driven by sea level anomalies in Indian Ocean.

Due to its computational cost, development of a high spatial resolution model that covers a large domain of the entire South China Sea such as in Kurniawan et al. (2015) and Tay et al. (2016) is infeasible. Nesting or offline coupling becomes a preferable option to develop such high spatial resolution model. Nesting is a modelling technique in which hydrodynamic result of a larger spatial domain model is fed to a smaller domain model (also known as nested model) as boundary forcing. This allows both the tidal and non-tidal flow that can only be simulated by using the large domain model such as Tay et al. (2016) to be incorporated into the small domain grid model which can be of higher spatial resolution. Hasan et al. (2016) has studied model accuracy of different spatial scales of hydrodynamic models, including nested models in Singapore coastal waters. However, their work did not describe the sensitivity of different types of nested boundary conditions, i.e. water level or current velocity.

This paper will focus on the effect of different nested boundary conditions on the nested model results in Singapore Strait based on both tidal and non-tidal forcing from the large domain model. As Tay et al. (2015) has illustrated that the effect of non-tidal forcing is not apparent in the velocity and water levels, but plays a big role in the volume flux transport through Malacca Strait. Besides water level, this paper will also evaluate the nested model results based on the volume flux transport through different sections of Singapore Strait. An optimum nested boundary setting for high spatial resolution model in Singapore Strait under operational forecast and management will be recommended.

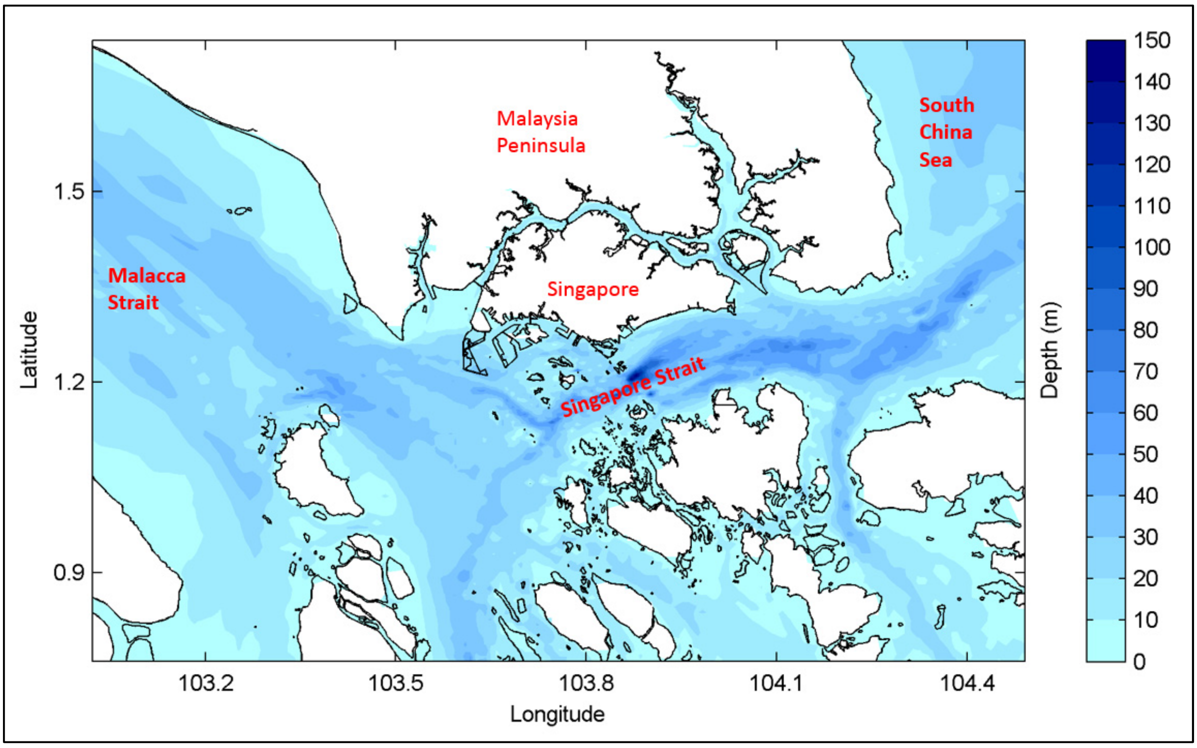

Figure 1. Map and bathymetry of Singapore coastal waters

2 MODELLING APPROACH

In this study, 2D depth-averaged models were set up in Delft3D modelling environment. As mentioned earlier, nesting modelling technique will be applied in this study. Prior to simulating the nested model, the large domain model (also known as overall model) will be simulated. The overall model used in this study was based on Tay et al. (2016) which has a domain grid extent encompassing the entire South China Sea. It is driven by tide and non-tidal forcing in form of water level prescribed on the open boundaries and wind and pressure on the water surface. Details of the model set up and validation can be found in Tay et al. (2016). This overall model will be driven with two types of forcing: (1) tidal forcing only, and (2) combined tidal and non-tidal forcing in this study. The simulation period in this study is from 01 July 2014 to 31 December 2014.

Domain of the nested model used in this study covers western Singapore Strait and southern Malacca Strait as shown in Figure 2. Figures 1 and 2 also illustrate the model bathymetry which is based on local navigation chart and historical hydrographic surveys and nested boundaries, respectively. Spatially varying grid of the nested model (a total of 33,284 grid cells) was schematized in a way whereby the areas close to the open boundaries were of lower resolution of about 2 km while the area of near southwestern Singapore Island, were of higher resolution of 150 to 200 m. Bed roughness was represented by uniform Manning friction coefficient of 0.026 m1/3/s. Time step of model was 1 minute, and it took about 4.5 hour computational time for a half year simulation on an Intel Core i7-2600 (quad core) 3.4 GHz CPU PC.

As shown in Figure 2, there were three main nested boundaries: 'Western boundary', 'Southern boundary' and 'Eastern boundary'. The main objective of this study is to evaluate the effect of different nested boundary conditions i.e. water level or current velocities, at these three boundaries on the simulated flow. Table 1 presents the description of eight combinations of boundary condition allocated at each nested boundaries and their corresponding case name.

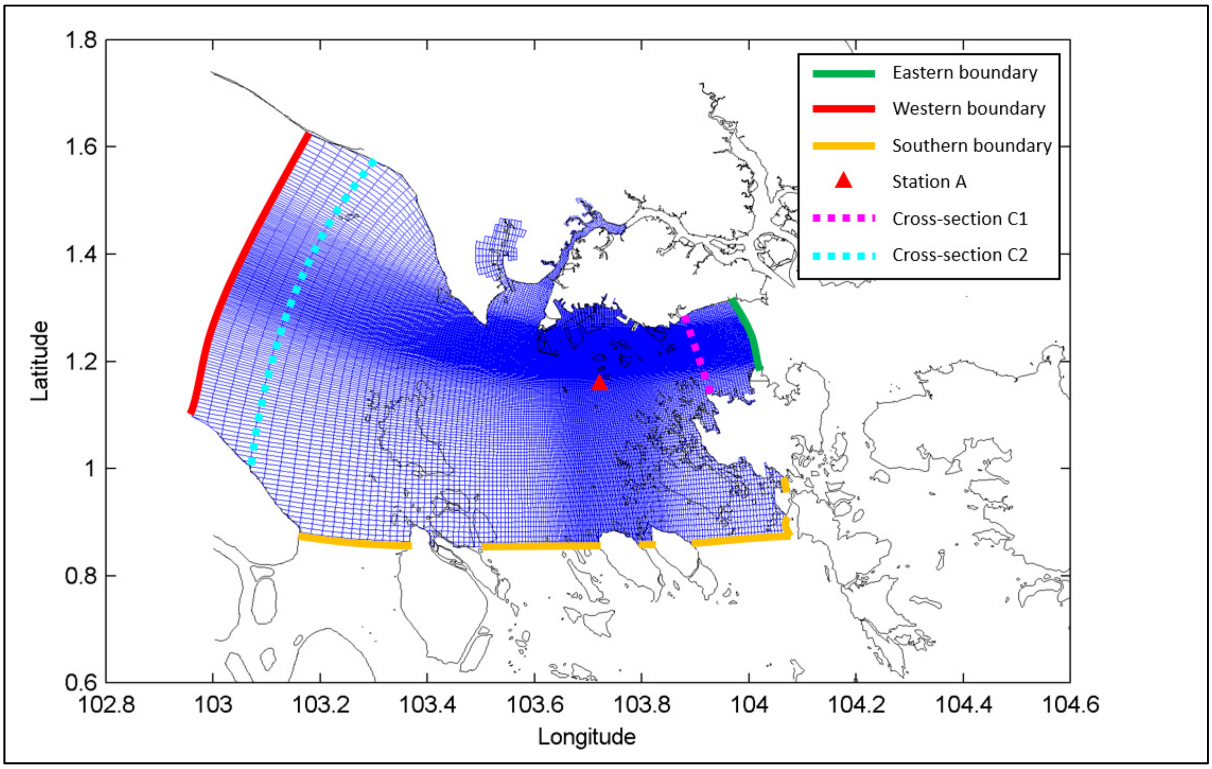

Figure 2. Model grid with nested boundaries and water level station and cross sections

Table 1. Model cases with different combinations of nested boundary condition at three nested boundaries

Case Name	Western boundary	Southern boundary	Eastern boundary
B02	Water level	Water level	Water level
B03	Water level	Current velocities	Water level
B04	Current velocities	Water level	Water level
B05	Water level	Water level	Current velocities
B06	Current velocities	Water level	Current velocities
B07	Current velocities	Current velocities	Water level
B08	Water level	Current velocities	Current velocities
B09	Current velocities	Current velocities	Current velocities

3 RESULTS AND DISCUSSION

The eight model cases were evaluated based on Root Mean Squared Error (RMSE) and Correlation Coefficient (CC) of the nested model and overall model. Simulated flow variables such as water level at Station A and flux transport through cross section C1 and C2 representing flow Singapore Strait and Malacca Strait, respectively, were evaluated.

Table 2 presents the RMSE and CC of water level at Station A computed by all eight model cases under the two types of forcing: (1) tidal forcing only and (2) combined tidal and non-tidal forcing. It is shown that the cases B02, B03 and B04 give the lowest RMSE (less than 0.055 m) among the eight cases for both types of forcing. These three model cases have water level as their nested boundary condition on the Eastern boundary. Most cases give relatively low RMSE (less than 0.08 m) and high CC (more than 0.998) except case B09 which has RMSE of more than 3 m.

Table 3 presents the RMSE and CC of cumulative flux transport through cross section C1 computed by all eight model cases under the two types of forcing: (1) tidal forcing only and (2) combined tidal and non-tidal forcing. Details of the large differential of model result induced by these two types of forcing can be found in Tay et al. (2016). Figure 3 presents the cumulative flux transport timeseries through cross section C1 of all eight model cases compared to the overall model under tidal forcing only. Cases B02, B03 and B04 show great deviation from overall model with the high negative cumulative flux transport which means overestimation of westward flow of more than 9 times in the nested model at the end of six months. Under combined tidal and non-tidal forcing (Figure 4), these three models underestimate the eastward flow (positive cumulative flux transport) by more than 40 percent compared to the overall model. It is noted that these three model cases that have the highest RMSE in terms of cumulative flux transport through C1 are also the ones with the lowest RMSE in terms of water level representation shown earlier. This demonstrates that water level assessment alone is not sufficient to evaluate the accuracy of a nested model. In terms of cumulative flux transport representation through C1, cases B05 and B06 show the lowest RMSE and highest correlation for both types of forcing.

Table 2. RMSE and CC of water level at Station A under two types of forcing

Case	Tidal forcing only		Combined tidal and non-tidal forcing	
	RMSE (m)	CC	RMSE (m)	CC
B02	0.054	0.998	0.055	0.998
B03	0.053	0.998	0.053	0.998
B04	0.051	0.998	0.052	0.998
B05	0.055	0.998	0.057	0.998
B06	0.069	0.998	0.071	0.998
B07	0.065	0.997	0.064	0.998
B08	0.075	0.997	0.076	0.997
B09	3.827	0.329	13.378	0.220

Table 3. RMSE and CC of cumulative flux transport through cross section C1 under two types of forcing

Case	Tidal forcing only		Combined tidal and non-tidal forcing	
	RMSE (m^3)	CC	RMSE (m^3)	CC
B02	8.887E+10	0.787	1.663E+11	0.914
B03	8.515E+10	0.797	1.579E+11	0.931
B04	4.835E+10	0.824	1.096E+11	0.985
B05	5.530E+09	0.942	1.614E+10	1.000
B06	5.526E+09	0.942	1.605E+10	1.000
B07	3.429E+10	-0.487	4.483E+10	0.997
B08	7.168E+09	0.885	1.467E+10	1.000
B09	7.441E+09	0.819	3.918E+10	0.996

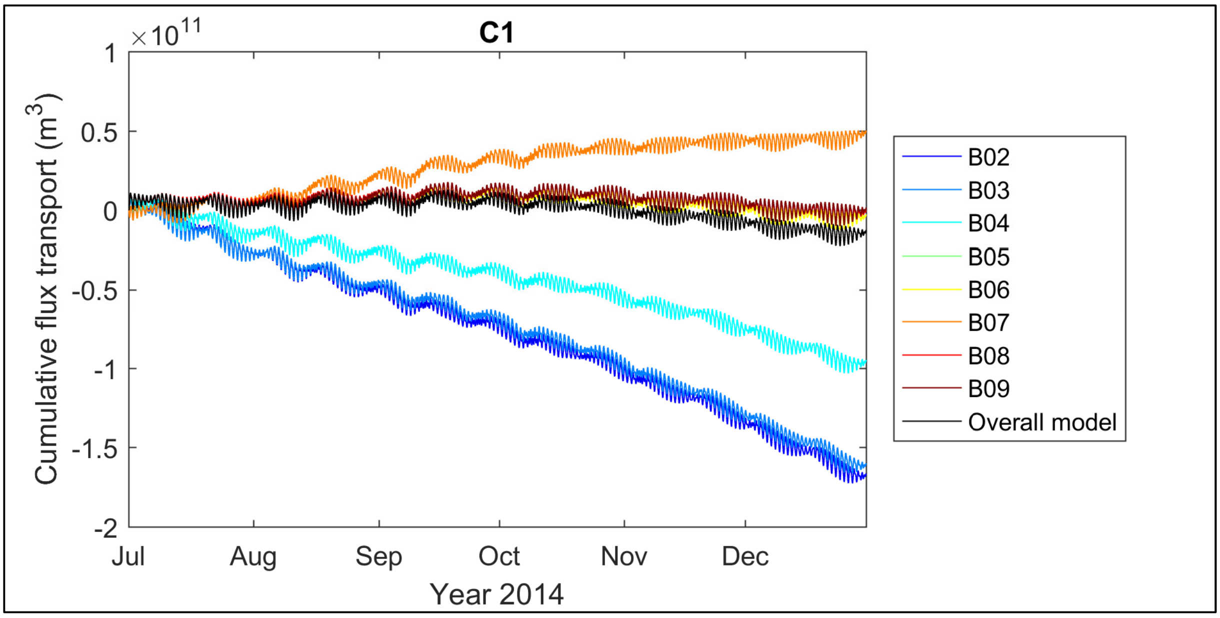

Figure 3. Cumulative flux transport through cross section C1 under tidal forcing

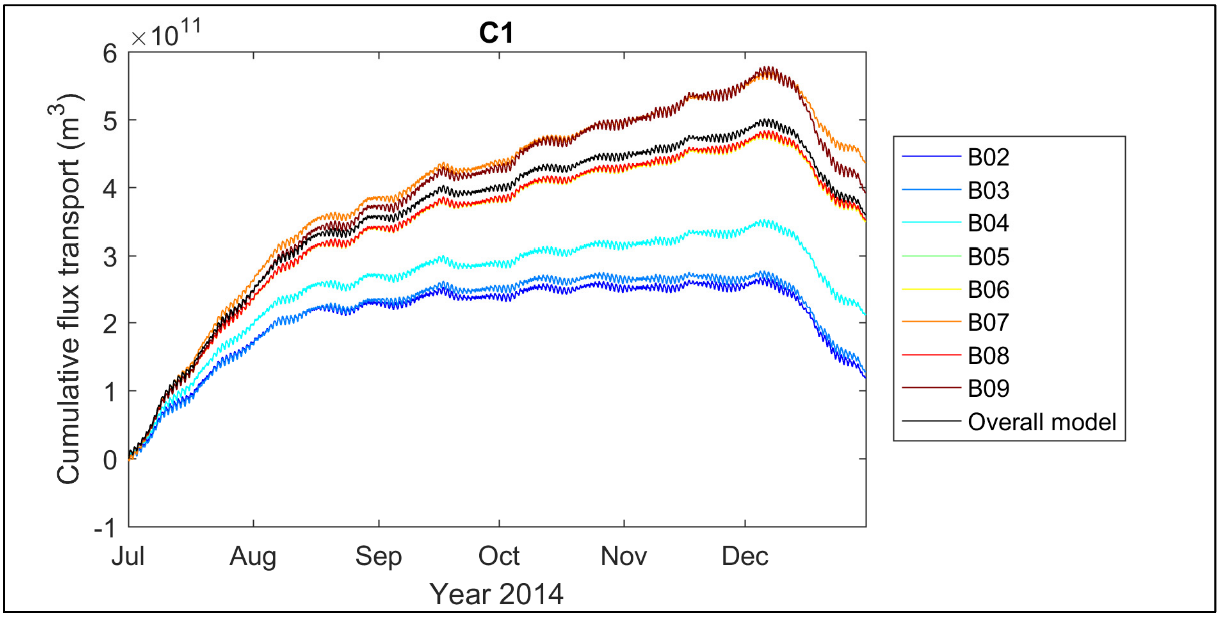

Figure 4. Cumulative flux transport through cross section C1 under combined tidal and non-tidal forcing

Table 4 presents the RMSE and CC of cumulative flux transport through cross section C2 computed by all eight model cases under the two types of forcing: (1) tidal forcing only and (2) combined tidal and non-tidal forcing. Figure 5 and Figure 6 present the cumulative flux transport timeseries through cross section C2 of all eight model cases compared to the overall model under tidal forcing and combined tidal and non-tidal forcing, respectively. Case B03 gives the highest RMSE and negative correlation which indicates opposite flux flow direction from the overall model under tidal only forcing. Cases B04 and B06 are the two model cases with the lowest RMSE for cumulative flux transport through C2. Under tidal forcing (Figure 5), model cases B04, B06, B07 and B09 have cumulative flux transport through C2 close to the overall model and all of them have current velocity as their nested boundary condition at Western boundary. Other model cases (B02, B03, B05 and B08) underestimate the eastward flow through C2 under both types of forcing. Under combined tidal and non-tidal forcing, case B09 overestimates the eastward flow while cases B04, B06 and B07 show the similar net eastward flow compared to the overall model.

Table 4. RMSE and CC of cumulative flux transport through cross section C2 under two types of forcing

Case	Tidal forcing only		Combined tidal and non-tidal forcing	
	RMSE (m^3)	CC	RMSE (m^3)	CC
B02	7.531E+10	0.763	1.454E+11	0.992
B03	1.278E+11	-0.866	2.042E+11	0.963
B04	2.190E+09	1.000	3.553E+09	1.000
B05	3.010E+10	0.998	7.768E+10	0.998
B06	3.230E+09	1.000	2.547E+09	1.000
B07	1.092E+10	1.000	4.927E+09	1.000
B08	2.922E+10	0.994	5.385E+10	0.999
B09	8.875E+09	0.999	9.691E+10	0.993

Based on the assessment of modelled variables which are water level at station A and flux transport through C1 and C2 presented earlier, case B06 provides the best flow representation among the eight cases. Though it does not provide the lowest RMSE for all three variables in the assessment, it is perpetually among the top three cases with the lowest RMSE. It is noted that case B06 applies current velocity as nested boundary condition at Western and Eastern boundaries and water level at Southern boundary. It is noted that the nested model used in Hasan et al. (2016) covers the eastern Singapore Strait and is driven by current velocity in the east and south boundaries and water level in the west boundary of the model domain. Interestingly, the three model cases (B05, B06 and B08) that give the lowest RMSE in terms of cumulative flux transport through C1 (Singapore Strait) have current velocity as their nested boundary condition at the Eastern boundary. This could imply that the throughflow in Singapore Strait may be mainly governed by its eastern boundary i.e. South China Sea. This is consistent with the findings of Tay et al. (2016) in which the sea level anomalies in Singapore Strait have been shown to be highly correlated to that in east coast of Malaysia Peninsula where it is exposed to the South China Sea.

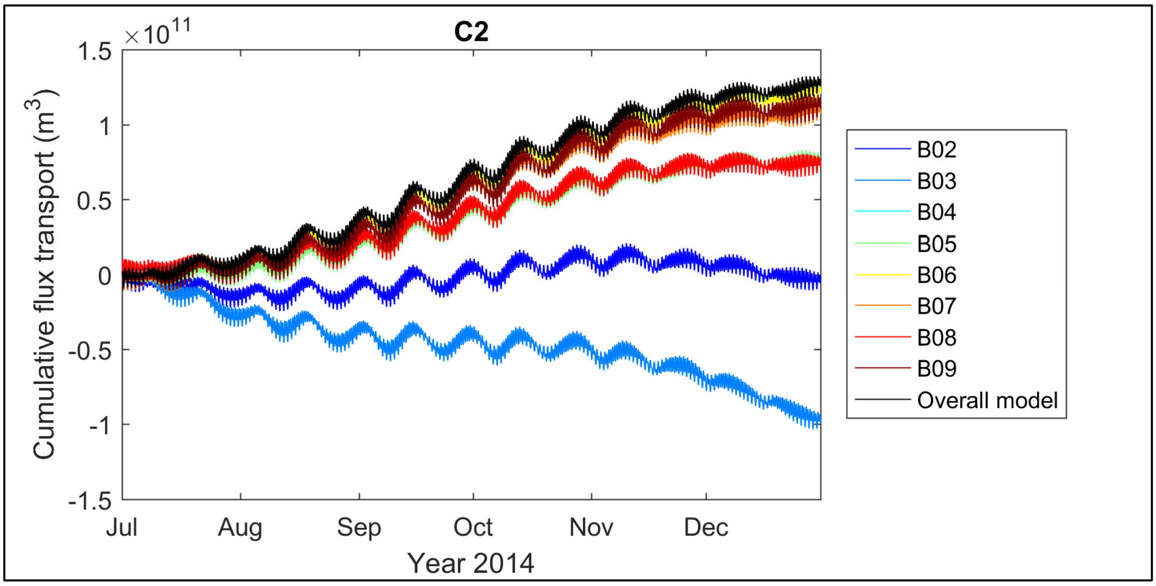

Figure 5. Cumulative flux transport through cross section C2 under tidal forcing

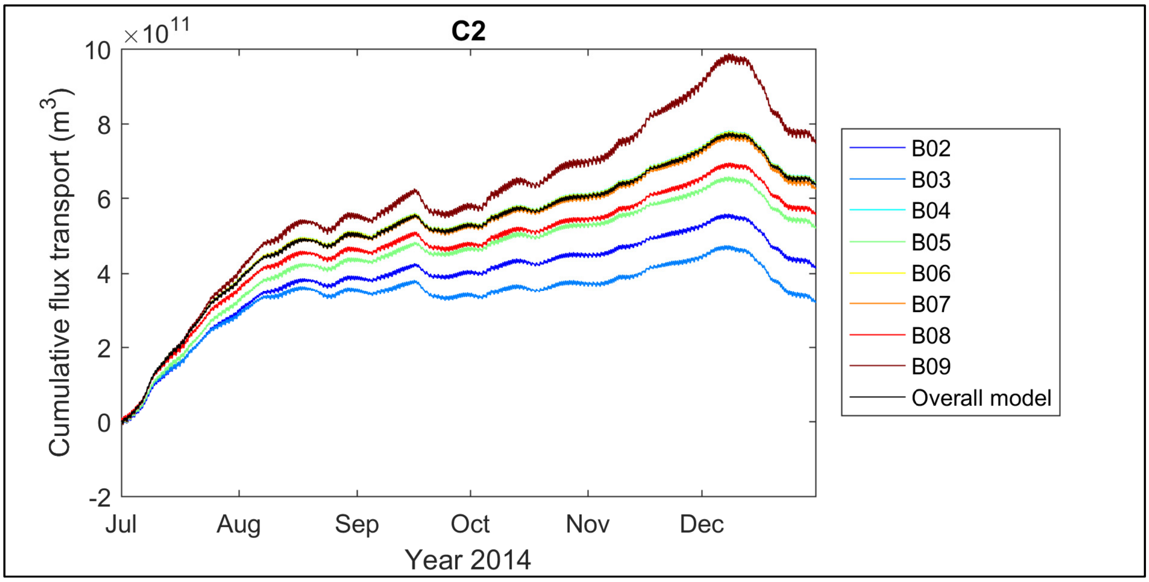

Figure 6. Cumulative flux transport through cross section C2 under combined tidal and non-tidal forcing

4 CONCLUSIONS

Local detail hydrodynamic model often relies on large scale model for open boundary forcing and one common method is nesting. This paper has evaluated the sensitivity of applying different nested boundary conditions on the hydrodynamics simulated in the nested model in Singapore coastal waters. The evaluation was carried out by computing the root mean squared error and correlation coefficient of water level in the western Singapore Strait and flux transport through the middle of Singapore Strait and southern Malacca Strait. A total of eight combinations of nested boundary conditions varying in three nested boundaries were tested. Results show that water level alone is not a reliable variable to assess the quality of the flow representation. It has to be complimented with momentum-dependent variable such as volume flux transport to provide a good assessment of the flow representation accuracy. Based on the assessment, the optimum boundary condition setting of the nested model in Singapore Strait is found to be one with boundary condition of current velocity prescribed in the Eastern and Western boundaries and water level in the Southern boundary. With a good flow representation of high spatial resolution in Singapore coastal waters, this detail hydrodynamic serves as a useful tool for operational forecast and also a basis for future morphological studies and environmental impact assessment in the coastal environment.

ACKNOWLEDGEMENTS

The authors would like to thank Eunice Delores Tan Mei Hua from Jurong Town Corporation (JTC) who built the nested model as part of her Master's programme in National University of Singapore (NUS). The authors would also like to acknowledge PUB, Singapore's National Water Agency for the partial funding of this work.

REFERENCES

Hasan, G.M.J., van Maren, D.S. & Ooi, S.K. (2016). Hydrodynamic Modeling of Singapore's Coastal Waters: Nesting and Model Accuracy. *Ocean Modelling*, 97, 141-151.

Kurniawan, A., Ooi, S.K., Hummel, S. & Gerritsen, H. (2011). Sensitivity Analysis of the Tidal Representation in Singapore Regional Waters in a Data Assimilation Environment. *Ocean Dynamics*, 61, 1121-1136.

Kurniawan, A., Tay, S.H.X., Ooi, S.K., Babovic, V. & Gerritsen, H. (2015). Analyzing the Physics of Non-Tidal Barotropic Sea Level Anomaly Events Using Multi-Scale Numerical Modelling in Singapore Regional Waters. *Journal of Hydro-Environment Research*, 9, 404-419.

Ooi, S. K., Zemskyy, P., Sisomphon, P., Gerritsen, H. & Twigt, D. J. (2009, August). The Effect of Grid Resolution and Weather Forcing On Hydrodynamic Modelling of South East Asian Waters. In *Proc XXXIII IAHR Congress, Vancouver*, 9-14.

Tay, S. H., Kurniawan, A. L. A. M. S. Y. A. H., Ooi, S. K. & Babovic, V. L. A. D. A. N. (2015). Modelling Sea Level Anomalies in Malacca Strait. In *36th IAHR Congress. The Hague*.

Tay, S.H.X., Kurniawan, A., Ooi, S.K. & Babovic, V. (2016). Sea Level Anomalies in Straits of Malacca and Singapore. *Applied Ocean Research*, 58, 104-117.

Proceedings of the 37th IAHR World Congress
August 13 – 18, 2017, Kuala Lumpur, Malaysia

AN ITERATIVE NEUMANN BOUNDARY CONDITION METHOD AND ITS APPLICATION IN THE SIMULATION OF BREAKING INTERNAL SOLITARY WAVES

HAI ZHU(1), LINGLING WANG(2), HONGWU TANG(3), QUNLIANG YANG(4) and J.J.R WILLIAMS(5)

(1,2,3) College of Water Conservancy and Hydropower Engineering, Hohai University, Nanjing, China
(1)Nanjing Hohai Science and Technology Co. Ltd, Nanjing, China
h.zhu@hhu.edu.cn
(2,3) State Key Laboratory of Hydrology-Water Resources and Hydraulic Engineering, Hohai University, Nanjing, China
Engineering and Materials Science, Queen Mary, University of London, London, UK
(4) China Water Resources Pear River Planning Surveying & Designing Co. Ltd, Guangzhou, China
(5)Engineering and Materials Science, Queen Mary, University of London, London, UK

ABSTRACT

Breaking internal solitary waves and corresponding breaking mechanisms have great impact on the mixing in the interior of oceans and lakes, on sediment re-suspension and nutrients transport. The interaction between fully nonlinear MCC (Miyata-Choi-Camassa) internal solitary waves and topographic slopes are modelled by direct numerical simulation. In the present study, immersed boundary method is employed to model the no-slip boundary of the topographic slopes and a novel iterative Neumann boundary condition enforcement strategy is proposed to ensure local scalar conservation near the boundary. Three typical breaking types (collapsing, plunging and surging) are observed during the internal solitary waves shoaling process. General characteristics for shoaling internal solitary waves, such as the evolution of flow field, density field and wave energy variation are monitored and analyzed. Both collapsing and plunging breaker are found to be more energetic than surging breaker but the high bed stress area caused by surging breaker is more widely distributed and it may have greater environmental impacts on coastal regions.

Keywords: Internal solitary waves; shoaling ISW; wave breaking; immersed boundary method.

1 INTRODUCTION

Internal solitary waves (ISWs) widely exist in oceans (Moum et al., 2007; Duda et al., 2004) where they are usually generated from tide-topography interaction. Nonlinear ISWs are also ubiquitous in seasonal stratified lakes and wind force are usually the primary driven forces (Sakai and Redekopp, 2010). Even in relatively small lakes, internal waves re-occur frequently and can have potential ecological consequences for metalimnetic phytoplankton populations (Pannard et al., 2011). Shoaling ISWs and the corresponding breaking mechanisms have great impact on the mixing in the interior of oceans and lakes, on sediment re-suspension and nutrients transport. Very large subaqueous sand dunes have been observed on the upper continental slope in the South China Sea that are believed to be generated by episodic, shoaling deep-water internal solitary waves (Reeder et al., 2011). Intensive in-situ observations of nonlinear internal waves on the Portuguese shelf showed that internal waves provided an important source of vertical mixing (Jeans and Sherwin, 2001). Numerous laboratory experiments have been carried out to study the shoaling process of ISWs. Helfrich (1992) observed that the shoaling of a single ISW can break and produce multiple turbulent surges, resulting in significant vertical mixing occurring everywhere inshore of the breaking location. The shoaling and breaking of an internal solitary wave of depression on a uniform slope were studied experimentally by Michallet and Ivey (1999). They pointed out that even if the mixing efficiency was low for a particular ISW shoaling process, the regular nature of the breaking event was important for the mixing and transport of benthic materials over long periods of time. Internal solitary wave evolution was performed on steep and inverse uniform slopes by Chen et al. (2007) and a mirror-image model was hypothesized to describe the physical features of shoaling waves.

Numerical simulations have also been widely applied to investigate ISW-slope interaction. Bourgault et al. (2005) carried out field scale numerical simulation of ISW-slope interaction and confirmed theoretical predictions of the location where internal wave breaks. Aghsaee et al. (2010) observed three distinct breaking processes, surging, plunging and collapsing breakers for ISWs (DJL model) in their two-dimensional directional numerical simulation. In the present study, nonlinear ISWs of Miyata-Choi-Camassa theory (Camassa et al., 2006) shoaling in a two-layer fluid system are used as an extension to earlier numerical work. Cartesian grid systems are the most commonly used mesh system in the modelling of geophysical flows due to their easy implementation. Bourgault et al. (2014) simulated sediment re-suspension and nepheloid layers induced by shoaling long ISWs using z-coordinates. If a complex geometry or irregular domain is encountered, Cartesian coordinates can no longer deal with the bottom topography accurately by itself (Even if the mesh is refined near the topographic boundary, approximation errors of a stepwise topography still exist). One way to solve this problem is to transform from the Cartesian coordinates to the terrain-following sigma coordinates. For example, Aghsaee et al. (2012) studied the boundary layer dynamics of shoaling ISWs on relatively mild slopes with a sigma-coordinate system. Zeng and Li (2014) used sigma-coordinate to model the free surface variation for an open channel flow. However, the sigma-coordinate system has difficulties in simulating baroclinic flows over steep topography because of pressure gradient errors. On the other hand, immersed boundary methods (IB methods) are very flexible in dealing with Fluid-Solid-Interaction (FSI) problems with complex solid boundaries. This approach was first proposed by Peskin (1972) to simulate blood flows in the leaflet of a human heart using Cartesian coordinates. The main flaw of IB method lies in the non-conservative mass across the immersed boundary that may cause unrealistic simulated results. In the present work, a novel iterative Neumann boundary condition enforcement strategy that has effective scalar conservativeness is applied to deal with the complex topographies in ISW-slope interaction.

The main aim of the present study is to investigate the shoaling and breaking characteristics for fully nonlinear ISWs in a two-layer fluid system by IB method. The paper is organized in the following manner: Numerical models and the detailed implementation of a novel scalar boundary condition setup for the IB method is given in Section 2. Section 3 is devoted to model validation. In Section 4, both the density fields and energy budgets of shoaling ISWs are analyzed. Conclusions are given in the last section.

2 NUMERICAL MODELS

2.1 Hydrodynamic model

A three-dimensional direct numerical simulation (DNS) has been employed in the present study to explore the detailed dynamics of ISW-slope interaction. The physical process is governed by the incompressible Navier-Stokes equations:

$$\frac{\partial u_i}{\partial x_i}=0 \qquad [1]$$

$$\frac{\partial u_i}{\partial t}+\frac{\partial\left(u_i u_j\right)}{\partial x_i}=-\frac{1}{\rho}\frac{\partial p}{\partial x_i}+\frac{\partial}{\partial x_i}\left(\nu\frac{\partial u_i}{\partial x_j}\right)+f_i \qquad [2]$$

where t is the time variable, u_i is the velocity component, x_i is the Cartesian coordinate, ρ is the density of the fluid, p is the pressure, ν is the kinematic viscosity and f_i is the body force modelling the gravitational acceleration g in the vertical direction. The Einstein summation convention and notation are used here. The ISW is intended to be generated in a viscous fluid, so ν is not omitted in the present simulation.

One of the factors that drives the ISWs' propagation is the density difference inside the fluid, and thus mass transfer between the two-layer water system is taken into account. The scalar transport equation that governs the advection-diffusion effect is as follows:

$$\frac{\partial c}{\partial t}+\frac{\partial\left(u_i c\right)}{\partial x_j}=\frac{\partial}{\partial x_j}\left(k\frac{\partial c}{\partial x_j}\right) \qquad [3]$$

where c is the volume concentration of saline water in the fluid. k is the molecular diffusivity coefficient of the solute.

2.2 Numerical methods

Adams-Bashforth scheme of second order accuracy is used in time marching and a second order central difference scheme is used in space for the momentum equation discretization. The pressure Poisson equation is solved by a preconditioned pressure conjugated gradient method. The above numerical methods were originally developed by Thomas and Williams (1995). Once the correct velocity field is obtained, the scalar transport equation is then solved. In time a conservative explicit second order Runge–Kutta scheme is used to discretize the advection-diffusion equation (Eq. [3]). The advection term itself is discretized by a second order upwind difference scheme while the diffusion term is discretized using second order central differences. The superbee flux limiter is used in the upwind scheme to ensure that the solutions are total variation diminishing (TVD). Generally, flux limiters are used to avoid the spurious oscillations (wiggles) that would occur with high order spatial discretization schemes due to shocks, discontinuities or sharp changes in the solution domain. The function for the superbee flux limiter is $\psi(r)=\max\left[0,\min(2r,1),\min(r,2)\right]$, where r is the ratio of upwind-side gradient of the concentration c to downwind-side gradient of c on the solution mesh (Roe, 1986).

2.3 Immersed boundary methods with scalar transport problem

A direct-forcing IB method developed by Ji et al. (2012) is adopted here and extended in the present work to deal with scalar transport problems. Computational costs of this iterative IB method is comparable to those of conventional IB methods but has a more accurate body force distribution approach. Detailed validation of the method and its further applications can be referred to Ji et al. (2012) and Bai et al. (2014).

(a) (b)

Figure 1. Immersed boundary Γ and a boundary cell P. Point M is the intersection point between the immersed boundary and the Cartesian grid.

Although the Dirichlet-type boundary condition for the velocities or scalar at the immersed boundary can be straightforwardly specified, the treatment of Neumann-type boundary at the immersed boundary is more complex. An iterative Neumann-type boundary for the scalar transport will be specified as follows. As shown in Figure 1a, the control volume P crossed by the immersed boundary Γ is defined as a boundary cell. The scalar value at point P is calculated as follows (in two-dimensional case without considering diffusion effect):

$$\frac{c_P^{n+1} - c_P^n}{\Delta t} = F_e + F_w + F_n + F_s \qquad [4]$$

where c_P^n is the scalar of point P at the previous time step and F is the scalar flux at the cell face, for instance the flux across the east face is:

$$F_e = u_e c_e \Delta x \qquad [5]$$

where u_e and c_e are the velocity and scalar at point e, respectively, and Δx is the length of the control volume. In a FSI case, with the solid inside the IB and the fluid is outside, the scalar value at the new time step can be calculated as:

$$c_P^{n+1} = c_P^n + (F_e + F_w + F_n + F_s)\Delta t \text{ AND } F_e = 0 \qquad [6]$$

For the boundary cell P, it is easy to understand that the scalar value at point P only depends on the flux at face w, n, and s, and there is no contribution to c_P from face e. The immersed boundary method can only guarantee the velocities at the IB points equal to or very close to zero (in a very extreme case the velocity at the intersection point M between immersed boundary and Cartesian grid can be zero) but usually the velocity at point e is nonzero, resulting in the unphysical flux exchange ($F_e \neq 0$) between across the immersed boundary for the scalar transport equation. Special boundary conditions for the scalar must be enforced at the boundary cells to ensure local mass conservation.

In Figure 1b the solid curve is the immersed boundary and the dashed curve, called a mask, is its extension in the outer normal direction with a distance Δx . Point P is one of the Cartesian grids adjacent to the immersed boundary. Zero gradient boundary condition ($\partial c_{P_{IB}} / \partial n = 0$) should be applied on the immersed boundary if there is no source or sink of the scalar C at the boundary. For instance, the scalar value of the IB point $c_{P_{IB}}$ is set to be the same as that of point P'. However, this will cause unrealistic scalar accumulation at the surrounding Cartesian grids during the distribution process.

Instead of setting $c_{P_{IB}} = c_{P'}$ and distributing its value to the neighboring Cartesian grids, we set the boundary condition directly on the Cartesian grids closest to the immersed boundary, that is $c_P = c_{P'}$ (where $c_{P'}$ can be calculated by interpolation) in the present study. It should be noted that the value of c_P itself is used during the interpolation process to obtain $c_{P'}$, so iteration is needed to get the correct value of $c_{P'}$. The detailed process are as follows,

a) INITIALIZATION

Locating the Cartesian grids immediately adjacent to the IB.

Locating the mask points coordinates which is $\Delta d = MIN(\Delta x, \Delta y)$ (grid length scale) away from the IB points in the out normal direction of the IB boundary Γ.

b) LOOP BEGINS

Iter = 0

$c_{P'} = I(\mathrm{c}_i)$ Tri-linear interpolation using scalar values at surrounding grid points.

$c_P = c_{P'}$ Enforcement of Neumann BC.

iter= iter+1

c) LOOP ENDS if $|c_P - c_{P'}| \le e$, e is a small tolerance and can be set as 10^{-6} if C is in the order of 1.

3 MODEL VALIDATION

3.1 Validation of iterative Neumann BC

In order to validate the above boundary condition configuration strategy for scalar transport, laminar flow past a two-dimensional stationary circular cylinder was used for verification purpose. The computational domain was W/D=5, L_1/D=10, L_2/D=20 and Re=100, where W is the span-wise width of the domain, D is the diameter of the cylinder and L_1 and L_2 are the stream-wise lengths before and after the cylinder centre respectively. The scalar value was set as 1.0 inside the cylinder while it is initialized as 0.0 elsewhere outside the cylinder, see Figure 2a. Details of the validation cases are shown in Table 1.

Table 1. Validation cases of iterative Neumann BC.

Case No.	Scalar BC	Δx (m)	Time step (s)
1	Not specified	1/128	0.001
2	Outside IB	1/128	0.001
3	Both sides of IB	1/128	0.001

The total computational time steps were 3000 for all the three cases. In case 1, the scalar boundary condition was not enforced. In case 2, the iterative scalar BC was only enforced outside of the immersed boundary while it was enforced both inside and outside in case 3. As it is clearly shown in Figure 2b, scalar is transported from inside the immersed boundary to the outside, which is unrealistic. In Figure 2c, no scalar is advected from inside of the cylinder, indicating that the scalar field outside of the immersed boundary is not interfered with the flow information inside of the immersed boundary. It should be noted that the total scalar value inside of the immersed boundary becomes smaller in case 2 because the zero-gradient boundary condition enforced outside the immersed boundary acts like a sink to the scalar inside. If correct scalar fields are required on both inside and outside of the immersed boundary, the proposed iterative zero-gradient scalar boundary condition should be enforced on both sides of the immersed boundary, as shown in Figure 2d. There is no significant scalar exchange across the immersed boundary and the local scalar (both inside and outside) is conserved.

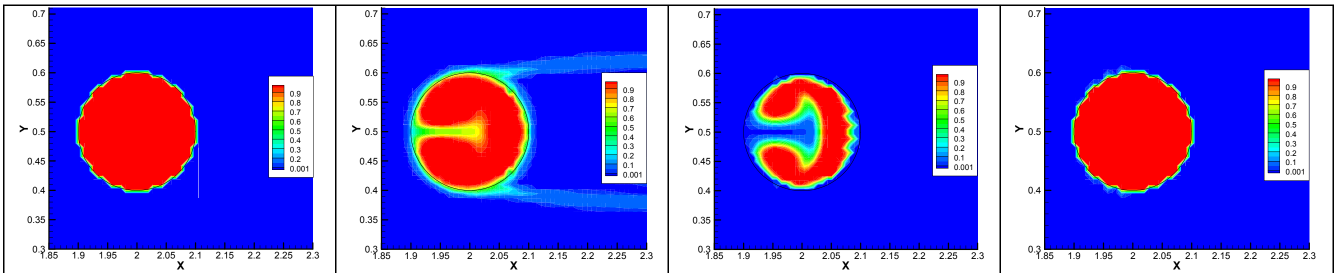

(a) Initial scalar field (b) Case 1 (c) Case 2 (d) Case 3

Figure 2. Scalar fields for the three test cases after 3000 time steps. The scalar was computed on the Cartesian grid, so that after the treatment of the flow visualization software, there exists a stair case presentation of the scalar field near the immersed boundary.

3.2 Validation of the scalar transport model

The typical lock-exchange flow experiment of Shin et al. (2004) was chosen to validate the present scalar transport model. Figure 3 is a schematic view of the lock-exchange flow experimental configuration. The computational domain has a dimension of $2m \times 0.2m \times 0.2m$ ($L \times H \times W$) and was separated to two compartments by a gate in the middle. The left compartment was filled with heavier fluid of density $\rho_2 = 1007.05 kg / m^3$ while the right part of the computational domain was filled with lighter fluid of density $\rho_1 = 1000 kg / m^3$. Once the gate is removed, the system will lose the hydrostatic instability. The grid resolution is $N_x = 768, N_y = 128, N_z = 32$ and a standard Smagorinsky sub-grid model was employed to the present large eddy simulation case.

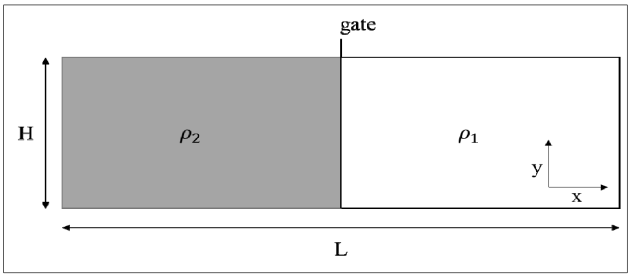

Figure 3. Schematic view of lock-exchange flow.

Figure 4 shows the density field evolution process of the lock-exchange flow between experiment and present simulation and good agreement was achieved. It should be noted that obvious K-H billows can be observed in numerical simulation (Figure 4a and b) while in the experiment K-H billows are indistinct. The main reason is due to the three-dimensional structures of the shear interface. In numerical simulation, the density field can be extracted in the cross section while the camera photo of the experiment can only show the mixture of structures of all scales in z direction. Figure 5 is the position of the heavy front of the lock-exchange flow changing with time and it shows that the numerical results agree well with the experiment.

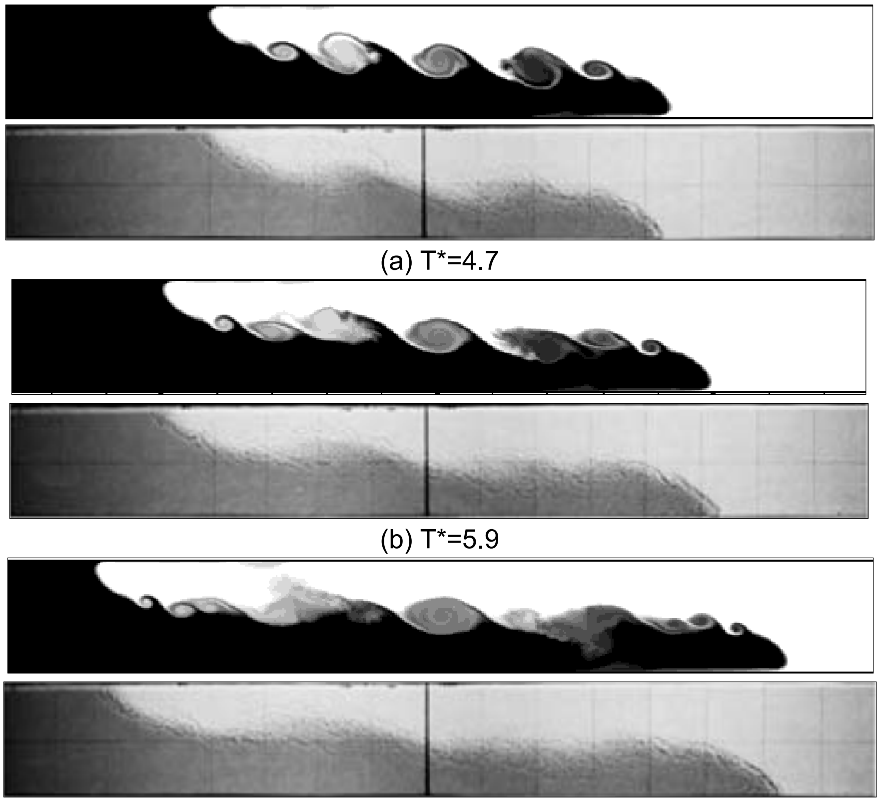

(a) T*=4.7

(b) T*=5.9

(c) T*=7.0

Figure 4. Comparison between experiment (up) and numerical simulation (down) of lock-exchange flow evolution.

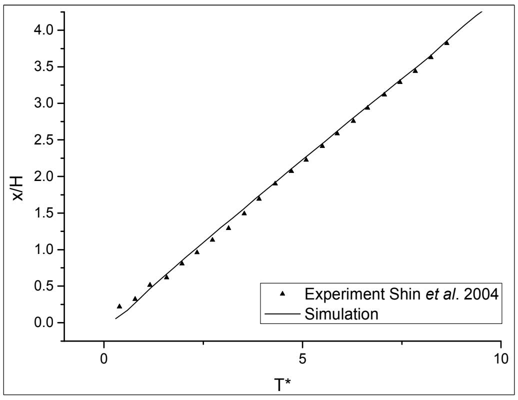

Figure 5. The position of the heavy front *vs* time.

4 NUMERICAL SIMULATION OF BREAKING ISWS

4.1 Simulation setup

In order to generate single clean ISWs without any oscillatory wave tails, the fully nonlinear MCC theory was employed to generate ISWs with large amplitude instead of the so-called “step-pool” method which is commonly used in experiments. The initial flow field of incident ISWs was configured according to the analytical solution of Miyata-Choi-Camassa (MCC) equation (Camassa et al., 2006) in a two-layer fluid system as shown in Figure 6. The numerical wave tank has a dimension of 24m×1m×1m (*L*×*H*×*W*). The upper layer thickness was set to be 0.25m and the lower layer thickness was set to be 0.75m. The density difference between the two layers was 30kg/km^3. The average angle of continental shelves is around 0.03-0.07 (Lamb, 2014) while steeper slopes are often encountered in lakes (Michallet and Ivey, 1999). For very mild slopes, fission process occurs in the ISW-slope interaction instead of breaking (Aghsaee et al., 2010). In the present study, three computational cases with different topographic slopes were chosen to ensure that breaking will occur (Case A: *s*=0.1, Case B: *s*=0.25 and Case C: *s*=0.4). In all the three cases, the amplitude of the incident ISW was kept to be 0.15m. The top boundary and lateral walls were set to be free-slip and the immersed boundary method was used to represent the no-slip uniform slopes. The grid resolution was 2304×384×32 in stream wise, vertical and span wise direction respectively to obtain a grid independent result.

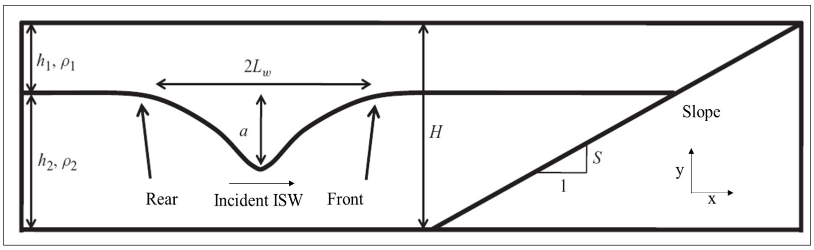

Figure 6. Numerical wave tank for ISW-slope interaction.

4.2 Typical breaking types for ISW-slope interaction

In the present study, three typical breakers are found for shoaling ISWs, namely collapsing breaker, plunging breaker and surging breaker, which is consistent with the work of Aghsaee et al. (2010). The main characteristics of a collapsing breaker is the formation of several vortices (separation bubbles) in the lower layer fluid increasing the steepening of the rear interface which does not reach vertical before breaking. The separation bubbles can interact with each other and increase local turbulence (Figure 7a). They can propagate far away onshore in a form of so-called turbulent boluses. For plunging breakers, the rear interface of the ISW becomes vertical first and then overturns in the onshore direction, inducing Rayleigh-Taylor instability (Figure 7b). Only one major separation bubble forms in the bottom boundary layer for plunging breaker. For the surging breaker (Figure 7c), boundary layer separation and overturning do not play a major role before the wave trough reaches the slope. In our simulation, we found that for a surging breaker, the lower layer fluid transported to the upper layer by an intense upslope flow rather than by the boluses like in the collapsing breaker.

Vertical distributions of horizontal velocities at critical water depth (location on the slope where the upper layer and lower layer thickness is equal) are shown in Figure 8 at different times for the above cases. Before wave breaking, obvious velocity differences exist between upper layer and lower layer fluid. However, velocity distributions tend to be more uniform after wave breaking for collapsing (Figure 8a at T=13.99, where the non-dimensional time scale T= t/(L_w/C_0), in which L_w is the wave length and C_0 is the linear wave phase speed) and plunging breaker (Figure 8b at T=13.37) but velocity difference is still significant for surging breakers

(Figure 8c at T=12.13), indicating that the collapsing and plunging breaker are much more energetic than surging breaker.

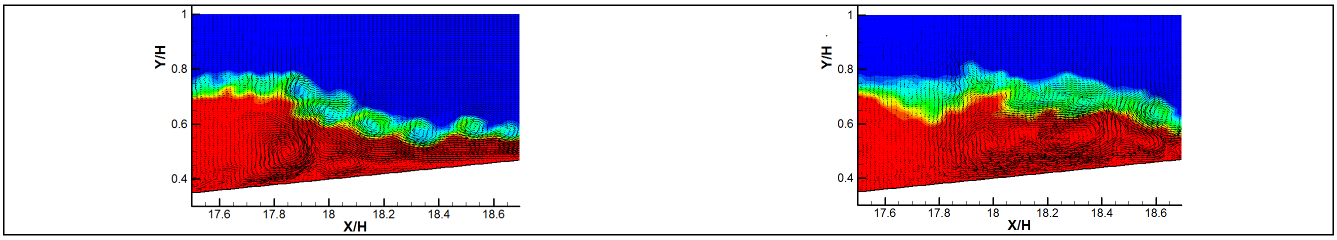

(a) Collapsing breaker (Case A) at T=9.36 and T=9.98.

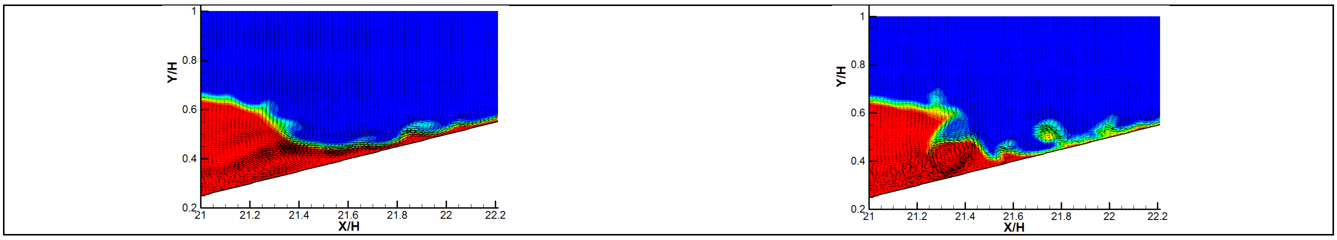

(b) Plunging breaker (Case B) at T=10.53 and T=10.76.

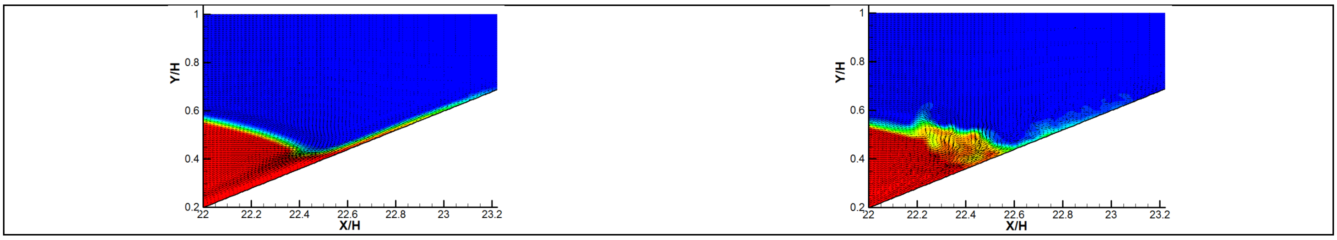

(c) Surging breaker (Case C) at T=15.44 and T=16.85.

Figure 7. Three typical ISW breaking types.

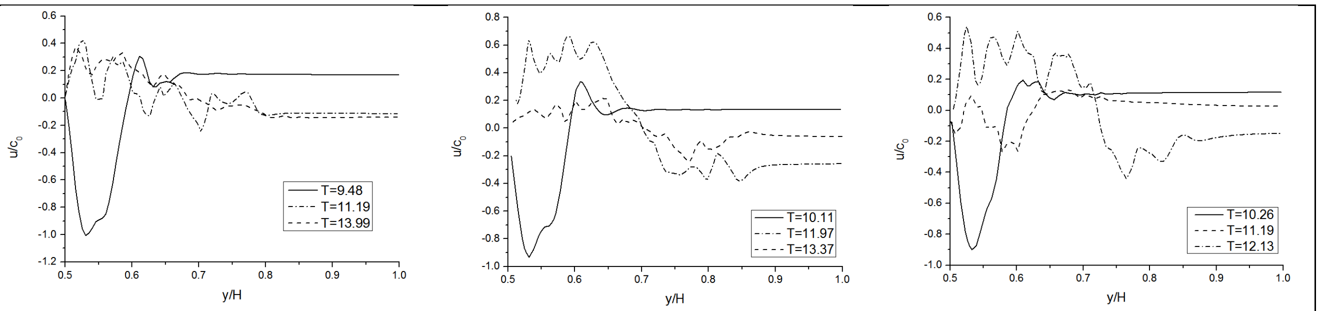

(a) Collapsing breaker (b) Plunging breaker (c) Surging breaker

Figure 8. Velocity distributions at critical water depth for three typical ISW breaking types.

4.3 Flow fields of breaking ISWs

Boundary layer separation is commonly observed under the bottom of ISWs of the depression type due to the impact of an adverse pressure gradient. For shoaling ISWs, the separation mechanism can be enhanced and the global instability (vortex shedding) may be induced. The shedding vortices can modify the ISW breaking mechanism, increase the bottom shear stress and thus enhance sediment re-suspension (Aghsaee et al., 2012). In order to illuminate how such coherent vortices can affect the sediment re-suspension mechanism, the flow fields of the three breaking types (cases A, B and C, when the maximum velocity gradient occurs) were compared. For the three cases, the incident wave amplitudes are the same but they interact with different topographic slopes, resulting in collapsing, plunging and surging breakers on the slope respectively. Velocity vector fields and velocity gradient fields are plotted in Figure 9. It should be noted that the coordinates of the strain rate tensor $(\partial u/\partial y + \partial v/\partial x)/2$ has been converted in order to calculate the velocity gradient $(\partial u^*/\partial y^*)$ in the normal-slope direction. Evident boundary layer separation bubbles can be observed in cases A and B (Figure 9a and b), but for the surging breaker in case C, the scale of separation region is much smaller. For both collapsing and plunging breakers, the highest velocity gradients occur beneath the separation bubbles (pointed by the black arrows in Figure 9), indicating much higher bed shear stress. The length scale of the intense bed shear stress region is around 0.1H for the collapsing breaker and

0.2H for the plunging breaker and it is much longer for surging breaker. However, in our laboratory scale simulations, the maximum bed shear stress, τ_b on the slope during the ISW shoaling process is around 26.78×10^{-3} N/m^2 and 24.72×10^{-3} N/m^2 for the collapsing and plunging breakers, respectively, which are about twice of the value for surging breakers (τ_b =12.09×10^{-3} N/m^2). This may suggest that collapsing and plunging breakers have the ability to re-suspend heavier sediments.

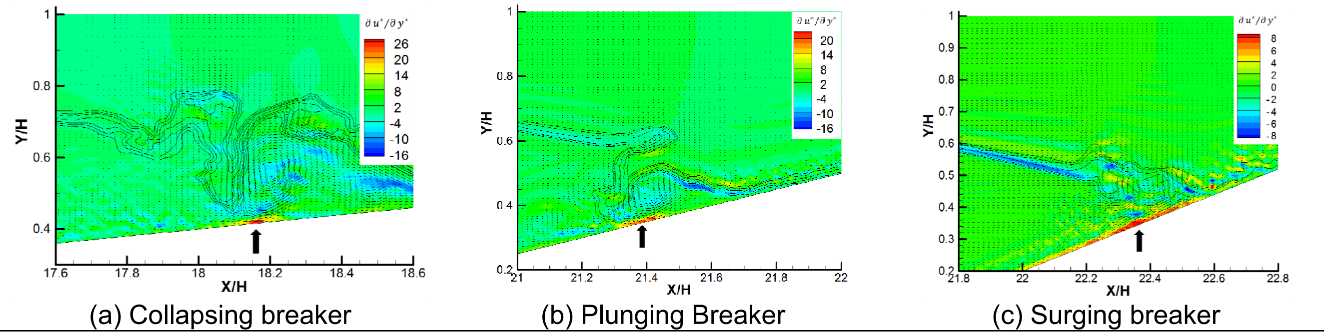

Figure 9. Velocity vector fields and velocity gradient fields for cases A, B and C. The solid lines are iso-pycnoclines of the density fields. (u* is the velocity parallel to the slope and y* is the outer normal direction of the slope).

4.4 Energy budgets for breaking ISWs

In order to investigate the energy transformation during ISW shoaling process, the kinetic energy (KE), available potential energy (APE) and pseudo energy (PSE, the sum of KE and APE) of the whole system are monitored for all the cases. APE and KE are defined as follows:

$$APE = \int_V (\rho - \bar{\rho}_r) g y dV' \quad [7]$$

$$KE = \frac{1}{2}\int_V \rho U^2 dV' \quad [8]$$

in which ρ and $U = u^2 + v^2 + w^2$ are the density and velocity of a fluid element, $\bar{\rho}_r$ is a background monotonic reference density profile, y is the vertical coordinate and V the finite volume of the system.

Simulation results of the present work show that during the shoaling process, collapsing breakers are most energetic (Figure 10a) and can lose around 50% of the PSE. The PSE drops dramatically during collapsing breaking. Plunging breakers can lose 20% PSE (Figure 10b) while surging breakers are least energetic and less than 10% of the energy is converted to heat or mixing during the shoaling process (Figure 10c).

Fast Fourier transform (FFT) of the vertical variation of the horizontal velocities at the critical water depth (where the upper layer thickness and lower layer thickness are equal) reveals that there exists a universal energy spectrum characterizing -3 slope for all the three breaking types (Figure 11). The -3 slope is only valid in the range of lower wave numbers, indicating larger scale motions. Compared with the famous -5/3 slope of the velocity spectra in inertial subrange for fully developed isotropic turbulence, this -3 slope is very similar to the nature of stratified turbulence.

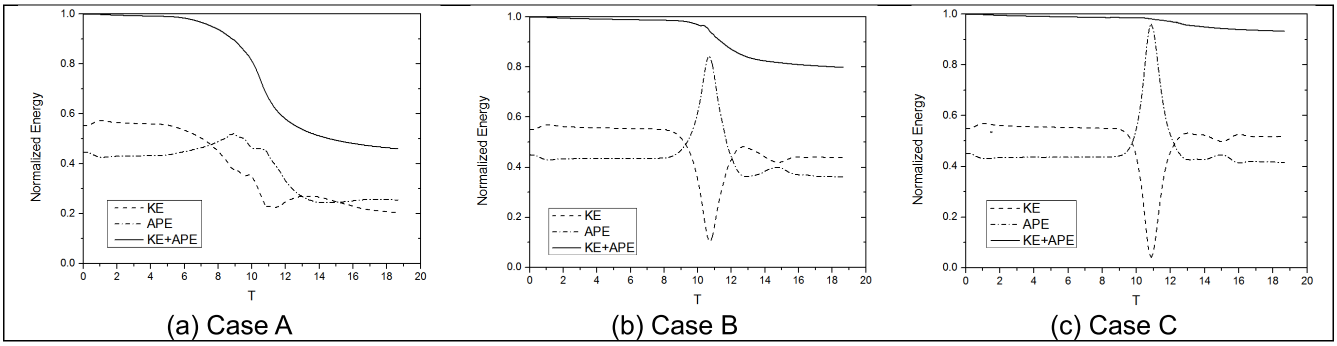

Figure 10. Energy budgets for collapsing, plunging and surging breakers.

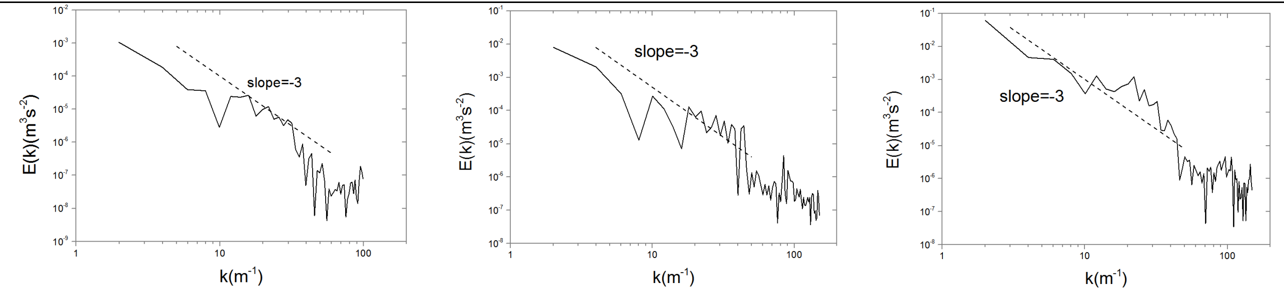

(a) Case A, T=13.99 (b) Case A,T=13.37 (c) Case A, T=12.13

Figure 11. Kinetic energy spectrum of case A, B and C at critical depth.

5 CONCLUSIONS

The shoaling process of fully nonlinear internal solitary waves of Miyata-Choi-Camassa (MCC) type in a two-layer fluid system has been carried out by direct numerical simulations. The immersed boundary (IB) method was applied to model the no-slip topographic slope boundary to avoid stepwise approximation errors in the z-coordinate and pressure gradient errors in sigma-coordinates. An innovative Neumann-type boundary condition enforcement strategy has been proposed to satisfy local scalar conservation for the IB method. Three breaking types (collapsing, plunging and surging breaker respectively) have successfully been modeled for the interaction between MCC internal waves and uniform slopes. During collapsing and plunging breaking process, the momentum between upper layer and lower layer fluid is well mixed compared with that of surging breaker. However, the high stress region on the topographic slope for surging process is more widely distributed than for the other two breaking types. Collapsing breakers can lose up to half of the pseudo-energy (PSE) during the breaking process and plunging breakers can lose around 20% of the PSE. Surging breakers are least energetic and can only lose less than 10% of the PSE. The present study shows that the kinetic energy spectrum has a universal slope of -3 for all the three typical types of breakers during lower wave number region, which is consistent with the velocity spectra of stratified turbulence.

ACKNOWLEDGEMENTS

The authors acknowledge the support from the National Natural Science Foundation of China (Grant Nos. 51609068, 51479058), National Key Research and Development Program of China (Grant No. 2016YFC0401703), the Fundamental Research Funds for the Central Universities (Grant No. 2016B00414), China Postdoctoral Science Foundation (Grant No.2016M601710) and the State Key Program of National Natural Science of China (Grant No.51239003).

REFERENCES

Aghsaee, P., Boegman, L., Diamessis, P.J. & Lamb K.G. (2012). Boundary-Layer-Separation-Driven Vortex Shedding Beneath Internal Solitary Waves of Depression. *Journal of Fluid Mechanics*, 690, 321-344.
Aghsaee, P., Boegman, L. & Lamb, K.G. (2010). Breaking of Shoaling Internal Solitary Waves. *Journal of Fluid Mechanics*, 659, 289-317.
Bai, X., Avital, E.J., Munjiza, A. & Williams, J.J.R. (2014). Numerical Simulation of a Marine Current Turbine in Free Surface Flow. *Renewable Energy*, 63, 715-723.
Bourgault, D., Kelley, D. E. & Galbraith, P.S. (2005). Interfacial Solitary Wave Run-Up in the St. Lawrence Estuary. *Journal of Marine Research*, 63(6), 1001-1015.
Bourgault, D., Morsilli, M., Richards, C., Neumeier, U. & Kelley, D.E. (2014). Sediment Resuspension and Nepheloid Layers Induced by Long Internal Solitary Waves Shoaling Orthogonally on Uniform Slopes. *Continental Shelf Research*, 72, 21-33.
Camassa, R., Choi, W., Michallet, H., Rusås, P.O. & Sveen, J.K. (2006). On the Realm of Validity of Strongly Nonlinear Asymptotic Approxima-Tions for Internal Waves. *Journal of Fluid Mechanics*, 549, 1-23.
Chen, C., Hsu, J.R., Cheng, M., Chen, H. & Kuo, C. (2007). An Investigation on Internal Solitary Waves in a Two-Layer Fluid: Propagation and Reflection from Steep Slopes. *Ocean Engineering*, 34(1), 71-184.
Duda, T. F., Lynch, J. F., Irish, J. D., Beardsley, R. C., Ramp, S. R., Chiu, C. S. & Yang, Y. J. (2004). Internal Tide and Nonlinear Internal Wave Behavior at the Continental Slope in the Northern South China Sea. *IEEE Journal of Oceanic Engineering*, 29(4), 1105-1130.
Helfrich, K.R. (1992). Internal Solitary Wave Breaking and Run-up on a Uniform Slope. *Journal of Fluid Mechanics*, 243, 133-154.
Jeans, D.R.G. & Sherwin, T.J. (2001). The Evolution and Energetics of Large Amplitude Nonlinear Internal Waves on the Portuguese Shelf. *Journal of Marine Research.* 59(3), 327-53.
Ji, C., Munjiza, A. & Williams, J.J.R. (2012). A Novel Iterative Direct-Forcing Immersed Boundary Method and its Finite Volume Applications. *Journal of Computational Physics*, 231(4), 1797-1821.

Lamb, K.G. (2014). Internal Wave Breaking and Dissipation Mechanisms on the Continental Slope/Shelf. *Annual Review of Fluid Mechanics*, 46, 231-54.

Michallet, H. & Ivey, G.N. (1999). Experiments on Mixing due to Internal Solitary Waves Breaking on Uniform Slopes. *Journal of Geophysical Research*, 104(C6), 13467-13477.

Moum, J. N., Klymak, J. M., Nash, J. D., Perlin, A. & Smyth, W. D. (2007). Energy Transport by Nonlinear Internal Waves. *Journal of Physical Oceanography*, 37(7), 1968-1988.

Sakai, T. & Redekopp, L.G. (2010). A Parametric Study of the Generation and Degeneration of Wind-Forced Long Internal Waves in Narrow Lakes. *Journal of Fluid Mechanics*, 645, 315-344.

Shin, J.O., Dalziel, S.B. & Linden, P.F. (2004). Gravity Currents Produced by Lock Exchange. *Journal of Fluid Mechanics*, 521, 1-34.

Pannard, A., Beisner, B. E., Bird, D. F., Braun, J., Planas, D., & Bormans, M. (2011). Recurrent Internal Waves in a Small Lake: Potential Ecological Consequences for Metalimnetic Phytoplankton Populations. *Limnology and Oceanography: Fluids and Environments*, 1(1), 91-109.

Peskin, C. (1972). Flow Patterns Around Heart Valves: A Numerical Method. *Journal of Computational Physics*, 10(2), 252–271.

Reeder, D.B., Ma, B.B. & Yang, Y.J. (2011). Very Large Subaqueous Sand Dunes on the Upper Continental Slope in the South China Sea Generated by Episodic, Shoaling Deep-Water Internal Solitary Waves. *Marine Geology*, 279(1), 12-18.

Roe, P.L. (1986). Characteristic-Based Schemes for the Euler Equations. *Annual Review of Fluid Mechanics,* 18(1), 337-365.

Thomas, T.G. & Williams, J.J.R. (1995). Turbulent Simulation of Open Channel Flow at Low Reynolds Number. *International Journal of Heat and Mass Transfer*, 38(2), 259-266.

Zeng, C. & Li, C.W. (2014). Measurements and Modeling of Open-Channel Flows with Finite Semi-Rigid Vegetation Patches. *Environmental Fluid Mechanics*, 14(1), 113-134.

Proceedings of the 37th IAHR World Congress
August 13 – 18, 2017, Kuala Lumpur, Malaysia

EAST CHINA SEA WAVE HEIGHT TRENDS ANALYSIS USING 20CR REANALYSIS

LINGLI WU[(1)], TENG WU[(2)] & XING LI[(3)]

[(1,2)] Jiangsu Key Laboratory of Coast Ocean Resources Development and Environment Security, Hohai University, Nanjing, China,
lingliwu036@163.com; wuteng@hhu.edu.cn
[(3)]Fishery Engineering Research Institute of Chinese Academy of Fishery Sciences, Beijing , China
lixinghhu@163.com

ABSTRACT

This study investigates long-term significant wave heights trends in the East China Sea (ECS). The H_s–SLP relationship in each domain is represented by a multivariate regression model with lagged dependent variable, which is calibrated and validated using the ERA-Interim reanalysis of H_s and SLP over the period 1981–2010. The 6-hourly H_s time series at each grid point was homogenized for discontinuities identified in the regional mean series. The homogenized wave heights were then used to assess wave height trends over the period 1911-2010. For comparison, the wave height trends derived from the inhomogenized wave heights were also shown. The reconstructed wave heights trends are also compared with the trends as derived from ERA40 dynamical wave reanalysis data sets.

Keywords: East China Sea; wave height trend; statistical downscaling; Mann-Kendall test

1 INTRODUCTION

Under the circumstance of climate warming (IPCC, 2013), the global mean sea level has risen over the 20th Century (Rhein et al., 2013), and the change of ocean wave height is also affected (X. L. Wang et al., 2010). Thus, wave height modeling is of great importance since increased wave heights on top of the rising sea level could not only increase the risk of coastal flooding, but also impact the offshore industries.

There are two approaches to project ocean wave heights: dynamical downscaling and statistical downscaling. Dynamical downscaling involve using climate-model-simulated atmospheric variables to drive an ocean wave model while statistical downscaling relies on statistical relationships between selected large scale predictors and regional scale predictands (Planton et al., 2008; Mori et al., 2010; Hemer et al., 2013a; Hemer et al., 2013b). Since dynamical approach was found to be not as good as the statistical methods in terms of reproducing the observed climate and interannual variability of the predictand (X. L. Wang et al., 2010), several works were done with statistical downscaling (Lazarus et al., 2013; Xiaolan L. Wang et al., 2012). The general principle is to establish a link between the simulated large scale and the finer scale of extreme events using one or a combination of statistical models calibrated on observational datasets. Observations of ocean wave heights are available only for the last few decades at limited buoy locations around the globe, in addition to some volunteer ship observations which are limited to major ship routes. Satellite data for wind speed and wave height have global coverage, however, they only span over the last couple of decades [Young et al., 2012), which hampers reliability of trend estimates, especially for extremes. Until recently, reanalysis of the atmosphere was limited to span over the second half of the 20th century. The 20th century reanalysis (20CR) (Compo et al., 2011) is the first reanalysis data set that spans over the past 140 years (1871–2010). Thus, this data set makes it possible to assess East China sea wave height trends on a centennial scale, which would be helpful for related decision making.

As the west part of the Pacific Ocean, East China Sea (ECS) is one of China's three biggest marginal seas. It connects with the Sea of Japan through Korea Strait and opens in the north to the Yellow Sea. Yangtze River, the longest river of China, also flows into it. Surrounded by most of the peninsula and the islands, ECS is also an important natural resource of oil and gas production, tourism and recreation, commerce, navigation and fisheries. However, the information on potential long-term changes of wave height in the ECS is fragmented and incomplete. The number of studies on ECS waves covers only a short period of time (Chen et al., 2013; Wu et al.,2015). This study aims to make wave height trends assessment on a centennial scale on ECS by a statistical reconstruction of historical wave heights using the mean sea level pressure (SLP) fields of the 20CR ensemble. The rest of this article is structured as follow: The data sets and methodologies used in this study are described in Sections 2. Section 3 presents the two series of wave height climate which are derived from the 20CR reconstructed wave height series before and after homogenization, in comparison with that derived from ERA40 and ERA-Interim wave reanalysis data sets. Historical wave height trends derived from 20CR are described in Section 4. Finally, the results and some concluding remarks are given in Section 5.

2 DATA AND METHODOLOGY

2.1 Data

We use the ERA-Interim Reanalysis (Dee et al., 2011) of the atmosphere (SLP) and ocean significant wave heights (H_s) for the period 1981–2010 to calibrate and validate the statistical relationship between the predictand H_s and its SLP-based predictors (Wang et al., 2012). The model calibration period is from 1981 to 2000 and the evaluation period is from 2001 to 2010. Using the best chosen model (with the best set of predictors) in Wang's research, we also use the 30-yr (1981–2010) data from the ERA-Interim Reanalysis to recalibrate the best model, which is then used to reconstruct H_s. Then, the 20CR ensemble of SLP fields for the period 1871–2010 (Compo et al., 2011) are used to derive time series of the predictors to reconstruct the corresponding significant wave heights (H_s) in the ECS. Since the 20CR ensemble of SLP fields are available on a 2°-by-2°lat/long grid, this study uses the ERA-Interim SLP data on this grid, and the H_s data, on a 1°-by-1°lat/long grid. All the SLP and H_s data are 6-hourly instantaneous values. The unit is hPa for SLP and m for H_s.

To find out the seasonal difference of ocean wave height variations, we model the 6-hourly H_s in four seasons: JFM (January-February-March), AMJ (April-May-June), JAS (July-August-September), and OND (October-November-December). And JFM refers to winter and JAS refers to summer in this paper.

2.2 Wave modeling method

We use the multivariate regression model of the form (Wang et al., 2012) as in Eq. [1]:

$$H_t = a + \sum_{k=1}^{K} b_k X_{k,t} + \sum_{p=1}^{P} c_p H_{t-p} + u_t \qquad [1]$$

where H_t is the Box-Cox transformed H_s at a target wave grid point, $X_{k,t}$ are the K SLP-based predictors that are retained for the wave grid point, P is the order of lags of the predictand, and the residuals u_t can generally be modeled as an M-order autoregressive process, AR(M). u_t is a white noise process if M = 0. The detailed reason of the selection of model and predictors is described in (Wang et al., 2012). The main difference of the model used in this article is that the predictor is based on semi-enclosed regional scale while Wang's is based on global scale.

Due to different wave surge influence to Sea level pressure (SLP) based predictor according to different SLP field choosing, the same model may have different projection performance. Therefore, the first thing is to select a suitable SLP field, the predictor domain (PD) to make the projection. We calculated the model performance to compare PD1 and PD2. We also added the global scale projection result (W14) of Wang et al. (2012) to make sure that the regional scale predictor performs better than that based on global model. Since the model skill with the PD2 got the best results, PD2 was chose to make the H_s reconstructions. We compared the model performance mainly by the hit rate (HR) and root mean square errors (RMSEs).

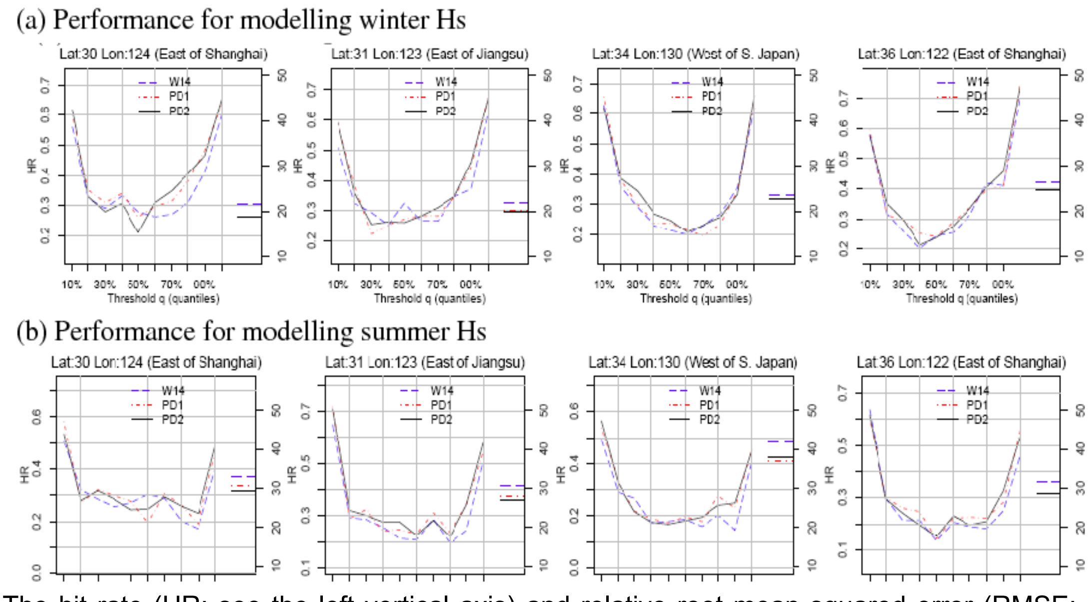

Figure 1. The hit rate (HR; see the left vertical axis) and relative root mean squared error (RMSE; see the right vertical axis) of the model with the indicated predictor-domains (PD1 and PD2) for winter (JFM) and summer (JAS) significant wave heights (Hs) at eight different grid points in ECS. A hit rate is the ratio of the number of hits to the number of observations in the category.

  / ISSN 1562-6865 (Online) - ISSN 1063-7710 (Print)

For the hit rate (HR) shown in Figure 1, a hit is defined as the occurrence when the forecast value and the corresponding observed value fall within the same category. We used the 5th, 10th…, and 95th percentiles of the observed values to define 20 categories for calculating the hit rates to assess the model skill in predicting Hs in each category. A hit rate is the ratio of the number of hits to the number of observations in the category.

The relative RMSE is the RMSE expressed in percentage of the corresponding 2001-2010 mean Hs (i.e., the mean of the validation period). The RMSEs are defined in Eq. [2].

$$RMSE = \sqrt{\frac{1}{N}\sum_{t=1}^{N}(H_s(t) - \widehat{H}_s(t))^2} \qquad [2]$$

The four grid points chosen in the East China Sea are: (30°N, 124°E) (East of Shanghai), (31°N, 123°E) (East of Jiangsu), (34°N, 130°E) (west of Japan) and (36°N, 122°E) (East of Shanghai). We could see that the model skill is higher in the cold seasons (winter and fall) than in the warm seasons (summer and spring), which is also true in the global setting of Wang et al. (2014) as represented by the parameter W14, as shown in Figure 1. W14 stands for the result of the global predictor domain of Wang et al. (2014). We could find that the improvement of our regional model settings over the global model setting is noticeable.

Having the best skilled model of ECS with the corresponding best predictors derived with the PD2, we used the 30-year period data (1981–2010) of SLP and Hs from the ERA-Interim to recalibrate the best model which is also performed in Wang et al. (2012). Then, the recalibrated model was used to reconstruct the ECS significant wave height. Namely, the predictors were derived from each part of the 20CR ensemble of 6 hourly SLP and then were fed to the calibrated best model to hindcast Hs at 6 hourly time scale.

3 RECONSTRUCTED WAVE HEIGHT SERIES COMPARISON（BEFORE AND AFTER HOMOGENIZATION）

Figure 2 shows the climatological mean fields of annual mean (Havg) and annual maximum (Hmax) significant wave heights in ECS as derived from the reconstructed 20CR ensemble-mean Hs and derived from the ERA40 dynamical wave reanalysis before homogenization.

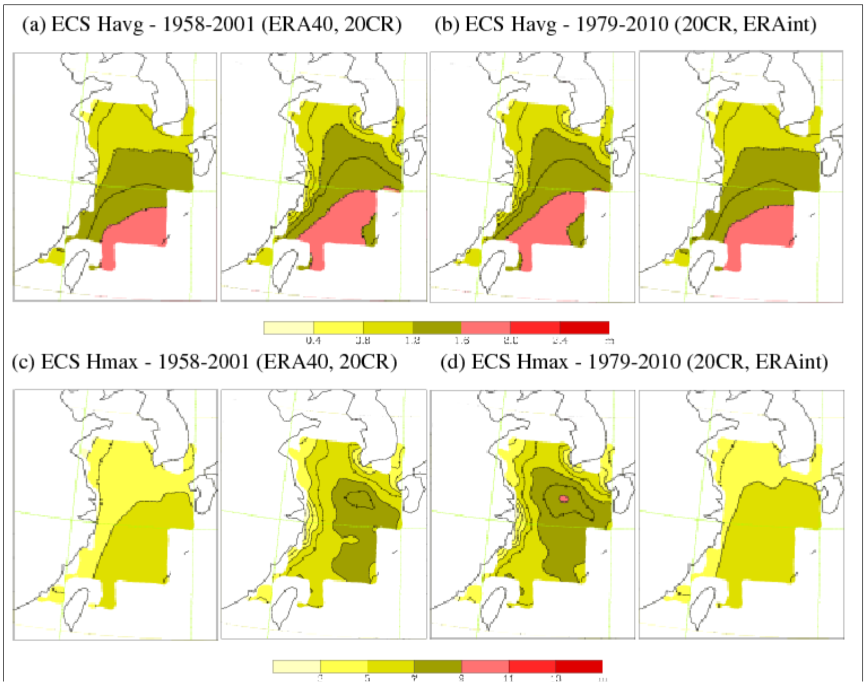

Figure 2. The climatological mean fields of annual mean (Havg) and annual maximum (Hmax) significant wave heights in the East China Sea (ECS), as derived from the 20CR ensemble mean, the ERA40 and ERA-Interim dynamical wave reanalysis before homogenization.

As Wang et al. (2014) had described that the 20CR data may have partial inhomogeneities in the early decades due to the very low amount and intensity of observations available for assimilation. Following Wang's method, we detected the sudden changes and completed the homogenization process.

Figure 3 shows the climatological mean fields of annual mean (Havg) and annual maximum (Hmax) significant wave heights in ECS as derived from the reconstructed 20CR ensemble-mean Hs and derived from the ERA40 dynamical wave reanalysis after homogenization. Comparing with the results shown in Figure 2, the statistical reconstructions presented the annual mean and maximum wave height climates fairly well after homogenization (Figure 3).

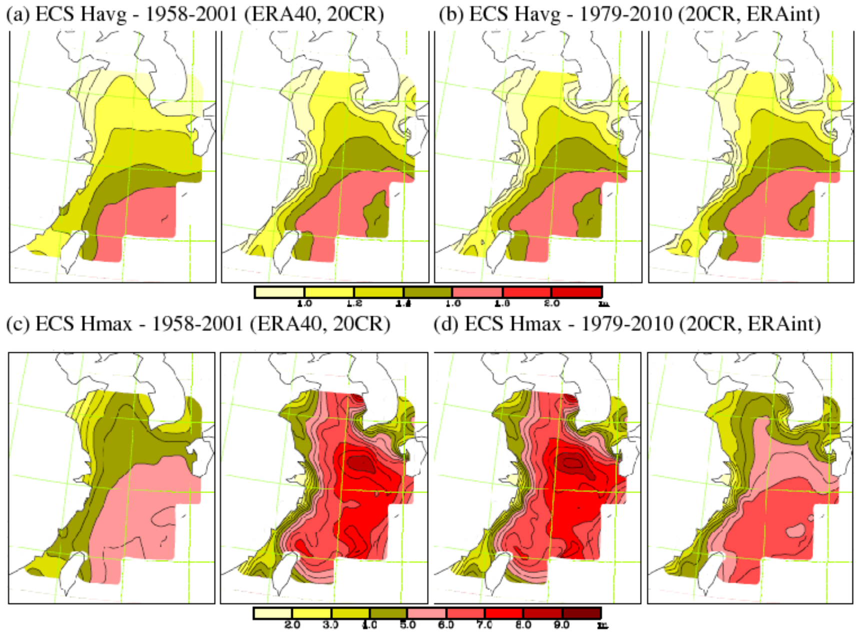

Figure 3. The climatological mean fields of annual mean (Havg) and annual maximum (Hmax) significant wave heights in the East China Sea (ECS), as derived from the 20CR ensemble mean, the ERA40 and ERA-Interim dynamical wave reanalysis after homogenization.

However, the reconstructions slightly overestimated the annual mean and maximum wave heights in ECS especially compared with ERA40 (Figure 3a and 3c). This is partly because the statistical reconstructions are derived from the ERA-Interim reanalysis, which has better resolution than the ERA40. Within the resolution scope of the ERA40 and ERA-Interim models, significant wave heights especially extreme series are better reproduced with a higher resolution. This is evidently described by J.-R. Bidlot's comparison in ECMWF Report Series and is also presented in the results that the reconstructed annual wave height climate is more similar to its ERA-Interim counterpart than to its ERA40 counter part (compare Figure 3a and 3c with 3b and 3d). Thus, the ERA-Interim annual mean wave height climate largely determines the reconstructed annual mean wave height climate.

4 HISTORICAL WAVE HEIGHT TRENDS

From the inhomogenized and homogenized 6 hourly significant wave heights, we picked up the annual and seasonal mean and maximum values of Hs at each grid point in ECS.

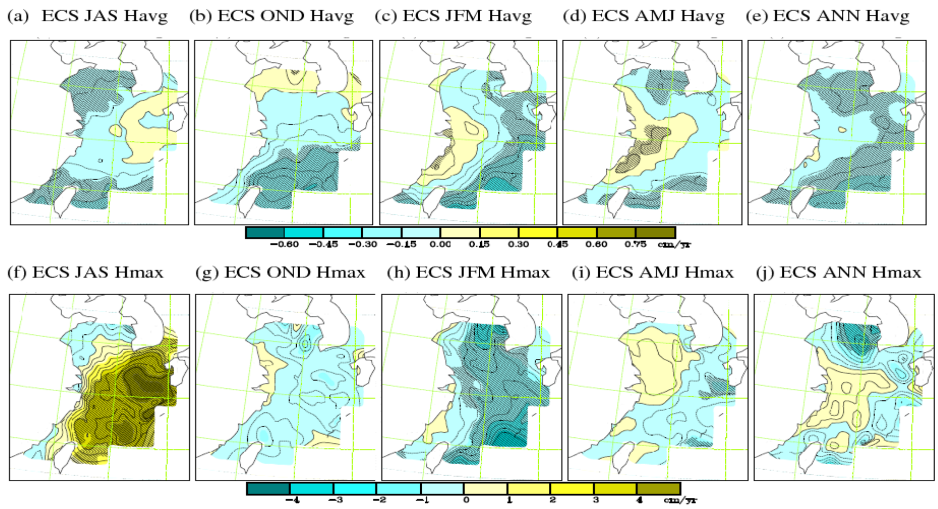

Figure 4. Maps of trends estimated from the homogenized ECS significant wave heights Hs. Havg represent seasonal and annual mean Hs and Hmax represent seasonal and annual maximal Hs. The trends are estimated for the ensemble mean series of the Hs statistics (Havg or Hmax). Stippling denotes areas where the significant trends exceed 5% level.

  / ISSN 1562-6865 (Online) - ISSN 1063-7710 (Print)

We used the trend analysis method of Wang and Swail (2001) to assess trends in Hs time series, which are not asymmetrically distributed. This method is based on Mann-Kendall test for trend against randomness (Mann, 1945; Kendall, 1955) and an iterative procedure is applied to display the effect of lag-1 autocorrelation on trend analysis. This nonparametric method with no distributional assumption for the data is less sensitive to gross errors and has been found to have the best performance compared with the other trend estimate methods (Zhang and Zwiers, 2004). Therefore, we chose to use this method on each sequence of Hs statistics at each grid point in East China Sea. Figure 4 shows the trend analysis results derived from homogenized 6 hourly Hs series in ECS while Figure 5 shows the results of inhomogenized series. For the inhomogenized series, no significant trends are detected in the seasonal mean/maximum of significant wave heights in four seasons (Figure 5).

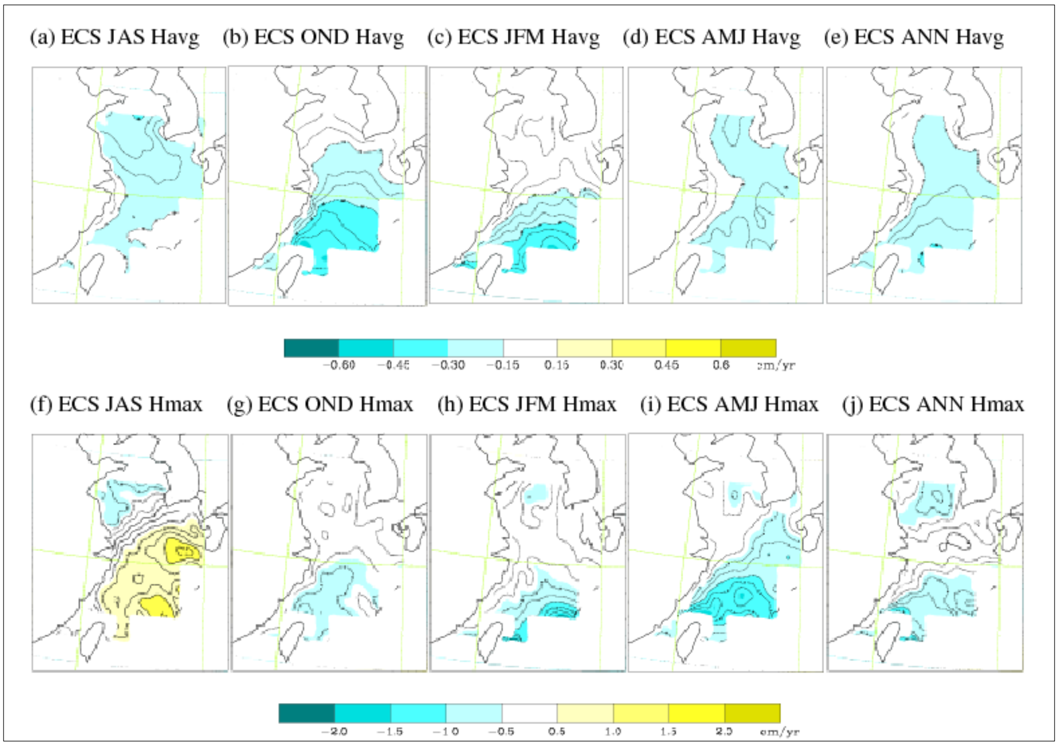

Figure 5. Maps of trends estimated from the inhomogenized ECS significant wave heights Hs. Havg represent seasonal and annual mean Hs and Hmax represent seasonal and annual maximal Hs. The trends are estimated for the ensemble mean series of the Hs statistics (Havg or Hmax). Stippling denotes areas where the significant trends exceed 5% level.

Figure 5 shows that the homogeneities greatly improve the estimate of wave height trends. In the East China Sea, as shown in Figure 4a-4e, the annual/seasonal mean of significant wave heights shows a significant decreasing trend over the period of 1911-2010, with the decrease being largest and most extensively significant in winter, and least extensively significant in summer. However, the seasonal maximum of significant wave heights shows a significant increasing trend in East China Sea in summer (Figure 4f) and also shows small increases in the west region of the East China Sea in spring (Figure 4i). These increases were accompanied with a significant decreasing trend in winter maximum Hs (Figure 4h), and with little change in autumn (Figure 4g). Trends in the annual mean of significant wave heights in the East China Sea are predominantly negative. Trends in the annual maximum of significant wave heights are predominantly negative in the upper and east part of East China Sea, positive in the central and west part of the East China Sea (Figure 4j).

5 CONCLUSIONS

The 20CR ensemble of 6 hourly SLP fields and a multivariate regression model with lagged dependent variable to represent the H_s -SLP relationship at each grid point were used to reconstruct 6 hourly significant wave heights (Hs) in the East China Seas over the period of 1871 to 2010. We used the ERA-Interim data of Hs and SLP over the period of 1981–2010 to calibrate and assess the multivariate regression model. The result demonstrated that our statistical reconstructions of 6 hourly Hs fairly well represented the seasonal mean and maximum significant wave height climates of the East China Sea as displayed by the ERA40 and ERA-Interim reanalysis.

We have examined temporal homogeneity for the ECS mean series of the ensemble mean of the reconstructed consecutive monthly mean Hs and have homogenized the 6 hourly Hs time series for the period

1911–2010 at each grid point in ECS for the few discontinuities identified in the respective regional mean series of the ensemble mean of the reconstructed consecutive monthly mean Hs. Then, we have derived seasonal mean and maximum Hs from the homogenized 6 hourly Hs data and have used a nonparametric trend analysis method to estimate historical trends of seasonal and annual mean and maximum Hs in East China Sea.

We also derived seasonal mean and maximum Hs from the inhomogenized 6 hourly Hs data and estimated historical trends for comparison. It was found that homogenization greatly improve the trend estimate of significant wave height in the East China Sea, although it does not differ much in the climatological mean fields.

And for homogenized series, the trend analysis results showed that the significant wave height trends calculated in the period 1911–2010 are mainly negative except that the seasonal maximum wave heights have apparently increased in summer in the East China Sea. Since the East China Sea is subject to a lot of tropical cyclone activity such as typhoon in spring and summer, the increasing trend in seasonal maximum wave heights might demonstrated an increase in tropical cyclone activity in the East China Sea. These might help increase the public awareness of coastal hazards in this area.

ACKNOWLEDGEMENTS

Supported by the National Natural Science Foundation of China (Grant No. 51409080), Open Fund of Jiangsu Key Laboratory of Coast Ocean Resources Development and Environment Security (Hohai University)(Grant No.JSCE201507)，Major State Basic Research Development Program of China (Grant No. SOED1505) and Open Fund of the Key Laboratory of Ocean Circulation and Waves, Chinese Academy of Sciences (Grant No.KLOCW1505). The authors are grateful to Jean Bidlot of ECMWF and the ERAInterim reanalysis team for providing us the wave and SLP data of the ERAInterim reanalysis, and to the team and supporting programs/offices/agencies of the Twentieth Century Reanalysis Project (see Compo et al., 2011) for making the 20CR data available. Request for the ERA-Interim wave and SLP data should be addressed to ECMWF, and for the 6 hourly SLP of the Twentieth Century Reanalysis, to Gil Compo (compo@colorado.edu).

REFERENCES

Compo, G.P., Whitaker, J.S. & Sardeshmukh, P.D.(2011). The Twentieth Century Reanalysis Project. *Quarterly Journal of the Royal Meteorological Society*, 137, 1-28.

Chen,Y.P., Xie,D.M., Zhang,C.K. & Qian, X.S.(2013). Estimation of Long-Term Wave Statistics in The East China Sea. *Journal of Coastal Research*, 65,177-182.

D. P. Dee, S. M. Uppala, A. J. Simmons, P. Berrisford, P. Poli, S. Kobayashi, U. Andrae, M. A. Balmaseda, G. Balsamo, P. Bauer, P. Bechtold, A. C. M. Beljaars, L. Van De Berg, J. Bidlot, N. Bormann, C. Delsol, R. Dragani, M. Fuentes, A. J. Geer, L. Haimberger, S. B. Healy, H. Hersbach, E. V. Hólm, L. Isaksen, P. Kållberg, M. Köhler, M. Matricardi, A. P. Mcnally, B. M. Monge-Sanz, J.-J. Morcrette, B.-K. Park, C. Peubey, P. De Rosnay, C. Tavolato, J.-N. & Thépaut, F. Vitart. (2011) . The ERA-Interim Reanalysis: Configuration and Performance of the Data Assimilation System. *Quarterly Journal of the Royal Metrological Society*, 137, 553-597.

Hemer, M. A., Fan, Y., Mori, N., Semedo, A. & Wang, X.L. (2013a). Projected Changes Wave Climate from a Multi-Model Ensemble. *Nature Climate Change*, 3, 471-476.

Hemer, M. A., Mcinnes, K. L. & Ranasinghe, R. (2013b). Projections of Climate Change-Driven Variations in the Offshore Wave Climate Off South Eastern Australia. *International Journal of Climatology*, 33, 1615–1632.

IPCC (2013). *Summary For Policymakers, In Climate Change 2013: The Physical Science Basis. Contribution Of Working Group I To The Fifth Assessment Report Of The Intergovernmental Panel On Climate Change*. Edited By T. F. Stocker et al., Cambridge Univ. Press, Cambridge, U. K., 3–29.

Kendall M.G. (1955). *Rank Correlation Methods*, Charles Griffin, London, U. K., 196.

Lazarus,S.M., Wilson,S.T., Splitt, M.E. & Zarillo, G.A.(2013). Evaluation of a Wind-Wave System for Ensemble Tropical Cyclone Wave Forecasting. Part II: *Waves. Weather and Forecasting*, 28(2), 316-330.

Mann, H. B. (1945). Non-Parametric Tests Against Trend. *Econometrica*, 13, 245-259.

Mori, N., Yasuda, T., Mase, H., Tom, T. & Oku, Y. (2010). Projection of Extreme Wave Climate Change Under Global Warming. *Hydrological Research Letters*, 4, 15-19.

Planton, S., M Déqué, Chauvin, F. & Terray, L. (2008). Expected Impacts of Climate Change on Extreme Climate Events. *Comptes Rendus Geoscience*, 340(9), 564-574.

Rhein, M., Rintoul, S.R., Aoki, S.,Campos, E. & Chambers D.(2013). *Observations: Ocean, in Climate Change 2013: The Physical Science Basis. Contribution Of Working Group I To The Fifth Assessment Report Of The Intergovernmental Panel On Climate Change*. Edited By T. F. Stocker et al., Cambridge Univ. Press,Cambridge, U. K, 256-315.

Wang, X. L. & Swail, V. R. (2001). Changes of Extreme Wave Heights in Northern Hemi- Sphere Oceans and Related Atmospheric Circulation Regimes. *Journal of Climate*, 14(10), 2204-2221.

Wang, X. L., Swail, V. R. & Cox, A. (2010). Dynamical Versus Statistical Downscaling Methods for Ocean Wave Heights. *International Journal of Climatology*, 30(3), 317-332.

Wang, X. L., Feng, Y. & Swail, V. R. (2012). North Atlantic Wave Height Trends as Reconstructed from the 20th Century Reanalysis. *Geophysical Research Letters*, 39(18), 1-6.

Wang, X. L., Feng, Y. & Swail, V. R. (2014). Changes in Global Ocean Wave Heights as Projected using Multimodel CMIP5 Simulations. *Geophysical Research Letters*, 41, 1026-1034.

Wu,S.P., Liu,C.Y. & Chen,X.P. (2015). Offshore Wave Energy Resource Assessment in The East China Sea. *Renewable Energy*, 76, 628-636.

Young, I. R., Vinoth, J., Zieger, S. & Babanin A.V. (2012). Investigation of Trends in Extreme Value Wave Height and Wind Speed. *Journal of Geophysical Research*, 117(11), 1-13.

Zhang, X. & F. Zwiers (2004). Comment on “Applicability of Prewhitening to Eliminate the Influence of Serial Correlation on the Mann-Kendall Test” by Sheng Yue and Chun Yuan Wang. *Water Resources Research*, 40(3), 1-5.

Proceedings of the 37th IAHR World Congress
August 13 – 18, 2017, Kuala Lumpur, Malaysia

ESTIMATION OF WAVE PROPAGATION VELOCITY ON A CHANNEL WITH SMOOTH AND ROUGH BED

DAVIDE WÜTHRICH(1), MICHAEL PFISTER(2), IOAN NISTOR(3) & ANTON J. SCHLEISS(4)

(1) Laboratoire de Constructions Hydrauliques (LCH), Ecole Polytechnique Fédérale de Lausanne (EPFL), Lausanne, Switzerland, davide.wuthrich@epfl.ch
(2) Laboratoire de Constructions Hydrauliques (LCH), Ecole Polytechnique Fédérale de Lausanne (EPFL), Lausanne, Switzerland and Civil Engineering Department, Haute Ecole d'Ingénierie et d'Architecture de Fribourg (HEIA-FR, HES-SO), Fribourg, Switzerland, michael.pfister@epfl.ch
(3) Department of Civil Engineering, University of Ottawa, 161 Louis-Pasteur, Ottawa, ON, Canada K1N 6N5, inistor@uottawa.ca
(4) Laboratoire de Constructions Hydrauliques (LCH), Ecole Polytechnique Fédérale de Lausanne (EPFL), Lausanne, Switzerland, anton.schleiss@epfl.ch

ABSTRACT

Natural hazards such as tsunamis, impulse waves and dam-break waves are rare, but extremely destructive. In recent times, more importance was given to structures that could withstand such events, however, uncertainties still exist in the estimation of wave velocities. This project focuses on the estimation of wave front celerity in a laboratory environment for both smooth and rough beds and the results are successfully compared to previous studies and design codes. Based on the experimental data an expression for the wave celerity is presented and discussed. The influence of bed roughness on the propagation velocity is also investigated and a dependence on the bed friction is observed, pointing out the need for further studies.

Keywords: Tsunami; impulse wave; dam-break wave; wave front celerity; bed roughness.

1 INTRODUCTION

In the past, the impacts of hydrodynamic waves on structures were considered extremely rare events and wave induced forces were typically neglected in the design process. In nature, the sudden release of a large amount of water can be found in impulse waves and tsunamis. Dam-break waves have similar behaviours and their solid theoretical background is widely used to describe the behaviour of hydrodynamic waves. Some recent catastrophic events that took place in the Indian Ocean (2004), in Chile (2010) and in Japan (2011, Figure 1), with large damages and casualties have shown that measures had to be taken to guarantee human safety and reduce reconstruction costs in coastal areas.

Figure 1. Tsunami propagating inland during the Japan 2011 event (Keystone, 2011).

Nowadays, the newly released design codes put emphasis on the importance of hydrodynamic forces in the design process and the role of engineers and researchers is becoming fundamental to alleviate the consequences of such events. In most design codes all over the world, hydrodynamic forces are computed using the wave front propagation celerity, however, its estimation is covered by high incertitude. In the past, many studies were carried out investigating the magnitude of wave celerity, including both experimental (Matsutomi and Okamoto, 2010; Shafiei et al., 2016; Wüthrich et al., 2017) and field surveys (Rossetto et al., 2007; Fritz and Okal, 2008; Chock et al., 2012). Nevertheless, the consistent amount of formulae available in literature showed that disagreement still exists in the evaluation of the front celerity (Nistor et al., 2009). As the force proportional to the squared value of the velocity, these uncertainties are amplified in the computation, resulting into large differences in magnitude of the resulting forces. A more precise estimation of wave velocities is therefore necessary to improve the design process, taking into account the influence of bed roughness, whose values are assumed to play an important role.

2 EXPERIMENTAL SET-UP

For the present study, tsunami generation was achieved through the sudden release of a known volume of water from an upper basin into a lower tank and then into the channel. Similar wave generation techniques were previously used by Chanson et al. (2002), Lukkunaprasit et al. (2009), Meile et al. (2011), Rossetto et al. (2011) and Wüthrich et al. (2017). In the current facility, different released volumes resulted into waves with various equivalent impoundment depths, d_0 ranging between 0.40 m and 0.82 m if a classical dam-break waves is considered. This corresponded to waves with different hydrodynamic properties, mainly wave height and celerity. The waves propagated in a horizontal channel with a length of 15.5 m and a width of 1.5 m. The smooth surface was represented by painted wooden panels, whereas for the tests over rough bed, an artificial carpet was added; the latter had a thickness of 7 mm. The Darcy-Weissbach friction factors for both channels were deducted through free surface profiles leading to average values of $f \approx 0.02$ and $f \approx 0.04$ for the smooth and rough configurations respectively, corresponding to roughness values $\varepsilon = 1.4$ mm and $\varepsilon = 2.4$ mm. These values are consistent with the findings of Choufi et al. (2014) for similar materials. The facility used in the present study is shown in Figure 2 for both smooth and rough configurations. Both dry bed surges and wet bed bores were produced in the present study. The initial still water depth, h_0 was controlled through a sill located at the downstream end of the channel. The propagating surges and bores were investigated in terms of wave height, using 7 Ultrasonic distance Sensors (US) located at x = 2.00, 10.10, 12,10, 13.10, 13.35, 13.60 and 13.85 m from the channel inlet. These were sampled at a frequency of 12.5 Hz with a precision of ±0.5mm.

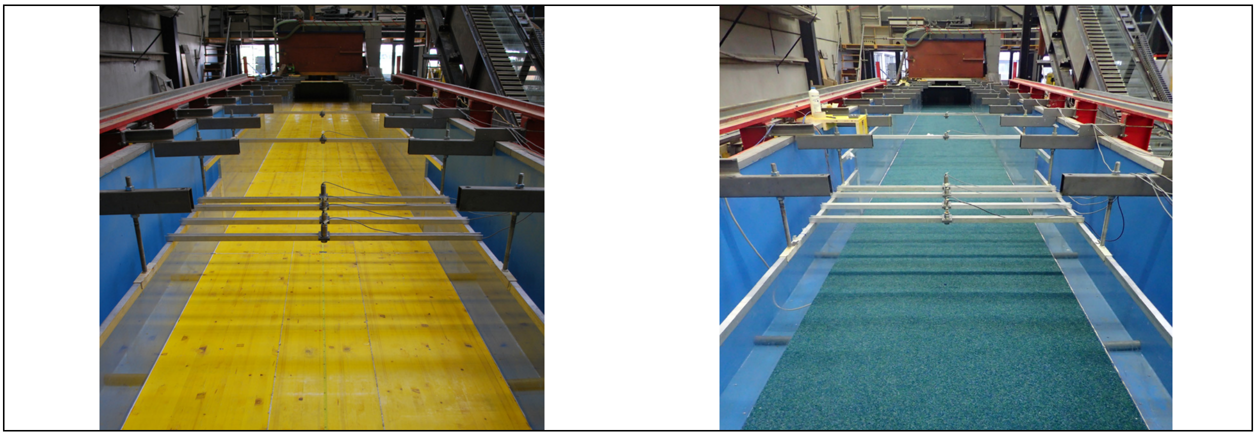

Figure 2. Figure of the experimental set-up: (left) smooth bed, (right) rough bed.

The tested waves reached heights of 0.30 m and front celerity of 3.5 m/s at model scale. If a 1:30 Froude scaling ratio is assumed, these values corresponded to typical configurations observed in coastal areas subject to tsunami hazard. The arrival of the wave was set when a water depth of 0.01 m was measured. Knowing the spatial repartitions Δx of the US sensors, an estimation of the wave propagation celerity was obtained through the ratio $\Delta x/\Delta t$.

3 METHODOLOGY

This project specifically focused on the estimation of wave front velocities in laboratory environment and results were compared to previous studies and existing design codes. The study is based on an experimental approach and the details of the 18 tests performed are presented in Table 1 along with some key parameters of the reproduced waves.

Table 1. Experimental program carried out for the present study.

Bed condition	Friction factor f	d_0 [m]	h_0 [m]	U [m/s]	h_{max} [m]	N. of repetitions
dry	0.02	0.82	-	3.57	0.20	3
dry	0.02	0.63	-	3.10	0.17	2
dry	0.02	0.40	-	2.35	0.13	2
dry	0.04	0.82	-	2.85	0.22	3
humid	0.04	0.82	0.001 m	2.89	0.23	1
wet	0.01	0.82	0.05 m	2.73	0.27	5
wet	0.04	0.82	0.05 m	2.74	0.28	2

4 VISUAL OBSERVATIONS

Both dry bed surges and wet bed bores were investigated in the present study. The difference in behaviour between surges and bores on smooth horizontal bed has been widely investigated in previous studies, including Ramsden (1996), Chanson (2004) and Wüthrich et al. (2016; 2017). Dry bed surges are characterized by a constant increase of water depth without aeration, whereas bores have a turbulent aerated front propagating along the channel. Surges are associated with higher velocities, whereas bores have greater wave heights. The same differences between surges and bores were also observed on the rough condition, as shown in Figure 3. Nevertheless, dry bed surges propagating on rough bed had higher wave heights and slower velocities compared to the smooth condition. Furthermore, the propagating front was more aerated. For wet bed bores, the difference in behaviour between the smooth and the rough condition was, visually, very small.

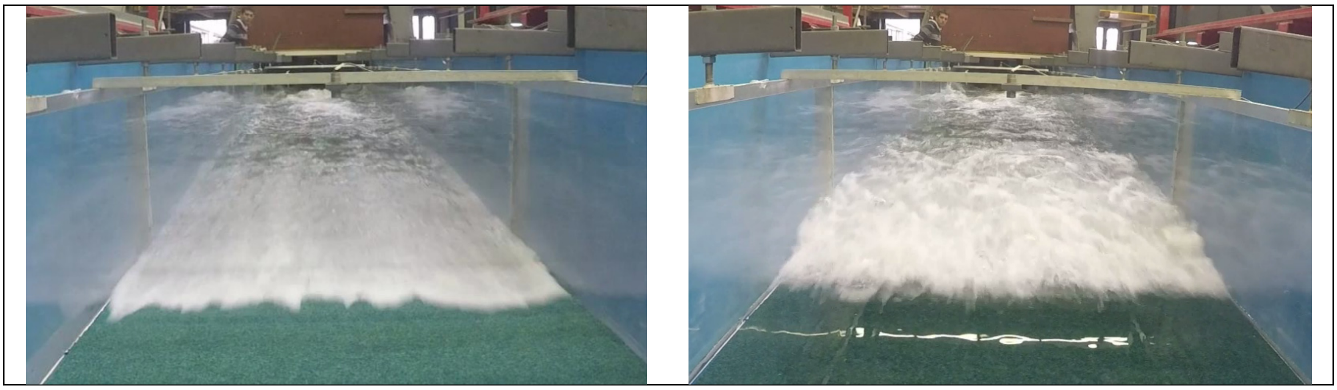

Figure 3. Dry bed surge (left, d_0 = 0.82m) and wet bed bore (right, d_0 = 0.82m, h_0 = 0.05m) on rough bed.

5 RESULTS

It was shown by Wüthrich et al. (2017) that the surges produced through the vertical release technique were similar to the classical dam-break scenario on smooth bed described by the theory of Ritter (1892). The latter assumed the sudden removal of a gate in front of an infinite reservoir under ideal fluid conditions, producing a wave propagating over a smooth horizontal surface. The longitudinal wave profiles obtained when the dry bed surge reached x = 13.85 m (location of US 7) were successfully compared to the theoretical solutions proposed by Ritter (1892) and Chanson (2009), as shown in Figure 4. Unfortunately, the smooth bed condition is merely theoretical and the influence of bed friction was implemented by Dressler (1952; 1954) and Whitham (1955). The profiles obtained for the experiments over rough bed were compared to these theoretical solutions in Figure 4, where a good match can be observed with Whitham (1955) and Chanson (2009). The results were also compared with the experimental data of Schoklitsch (1917), where some differences can be observed, most probably attributed to the difference in surface roughness.

For wet bed bores, no differences were observed between the smooth and the rough conditions in terms of wave profiles (herein not shown) and wave front celerity (Figure 6b), showing that both scenarios were well described by the theory of Stoker (1957). These findings suggested that for the tested roughness values, the initial still water depth, h_0 had a greater influence on the resulting wave than friction.

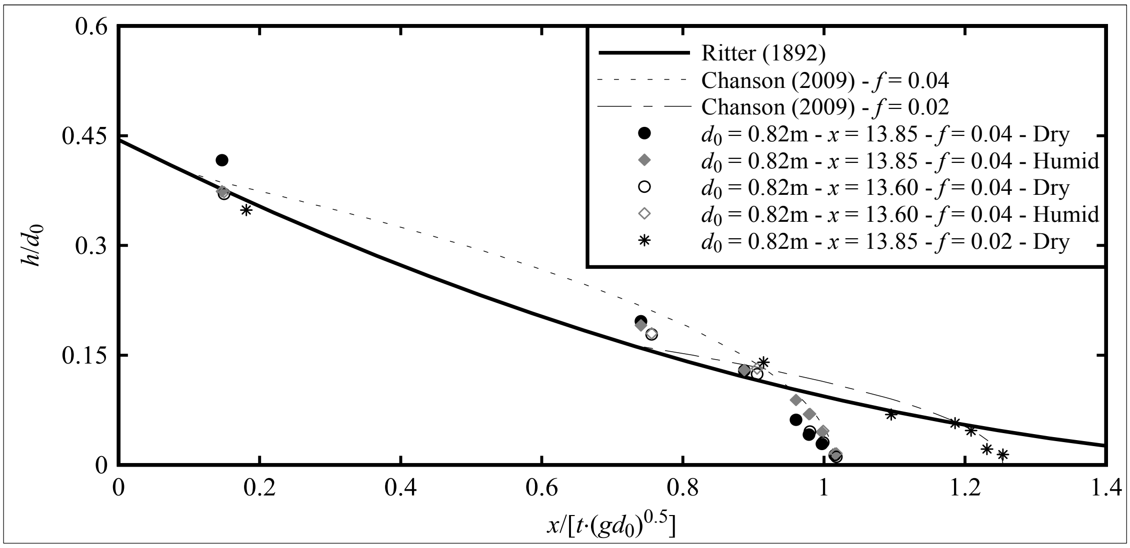

Figure 4. Comparison of longitudinal wave profiles for smooth and rough beds with theoretical solutions.

For engineers designing structures resistant to hydrodynamic loads, it is fundamental to determine the celerity U of the incoming wave. While for wet bed bores velocities can be precisely predicted using the Stoker (1957) theory, great incertitude still exists in the evaluation of front celerity for dry bed surges (Nistor et al. 2009, Wüthrich et al. 2017). For dry bed surges, it is commonly assumed in the literature that:

$$U = \alpha\sqrt{gd_0} \quad [1]$$

where U is the wave front celerity, d_0 the equivalent impoundment depth and α is a parameter whose value is covered by high uncertainties. The velocity coefficient, α can also be expressed as a dimensionless velocity:

$$\alpha = \frac{U}{\sqrt{gd_0}} \quad [2]$$

and various values of α can be found in literature; the most relevant ones are presented in Table 2. The same values are presented graphically in Figure 5 and compared to the experimental results of the present study.

Table 2. Coefficient α in Eq. [1] and [2].

Reference	α
Iizuka and Matsutomi (2000)	1.1
Kirkoz (1983)	$\sqrt{2}$
Ritter (1892), FEMA55 (2000)	2
Murty (1977)	1.83
Bryant (2008)	1.67
Matsutomi and Okamoto (2010)	0.66
Shafiei et al. (2016)	1.7
Wüthrich et al. (2017)	1.25

For the tests carried out in the present study on the smooth channel, the best approximation was found with a coefficient α = 1.3 (Figure 5). As previously discussed, this value slightly underestimated the waves with higher values of d_0 and overestimated the lower ones.

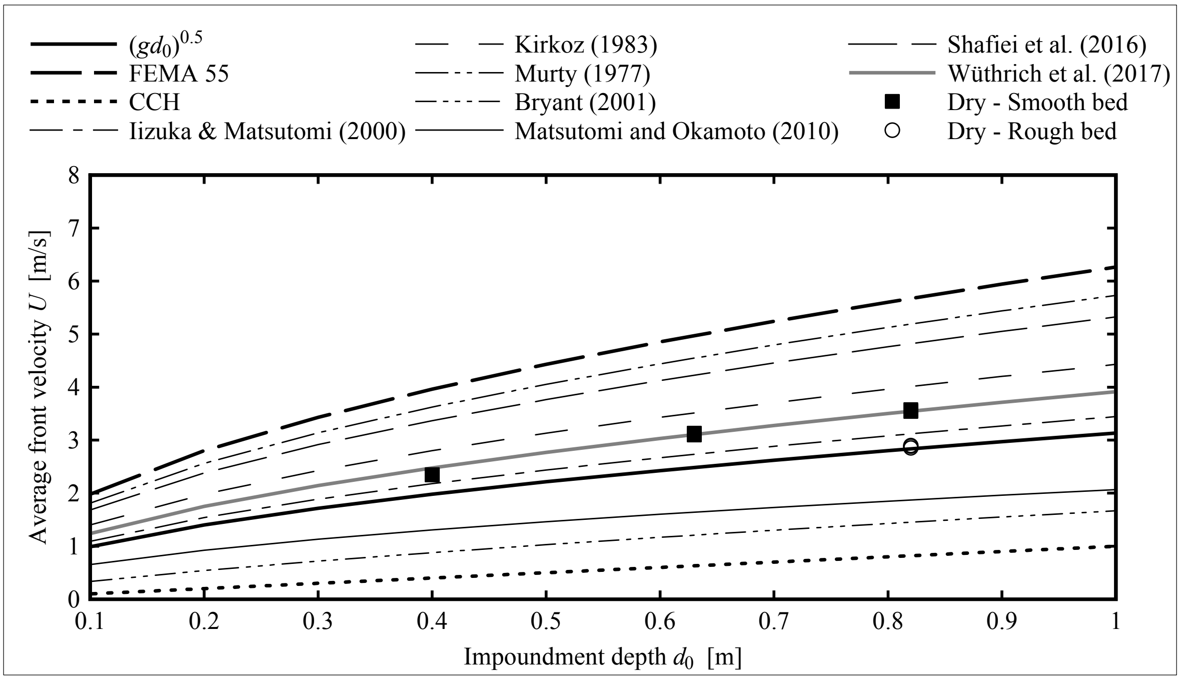

Figure 5. Comparison of experimental data with previous existing formulae.

The values presented in Table 2 and Figure 5 for the smooth configuration, were also compared to the experimental tests obtained for the rough bed. A significant influence of roughness was observed and lower celerity values were measured over rough bed, leading to an overestimation of the celerity values up to 25 % for a coefficient α = 1.3. These findings clearly indicated a dependence of α on the friction factor f that should be taken into account in the prediction of the incoming wave celerity. For wet bed bores, the roughness was shown to have a less significant influence and the same celerity values were recorded for both smooth and rough scenarios. Both behaviours are presented in Figure 6, in which the values of α were plotted as a function of the friction factor, f. The decreasing behaviour of α for larger values of f confirms its dependence on the bed roughness for dry bed surges. In this preliminary study, only two roughness values were tested, implying that only an overall indication of this relationship can be drawn; further studies are therefore necessary to implement it.

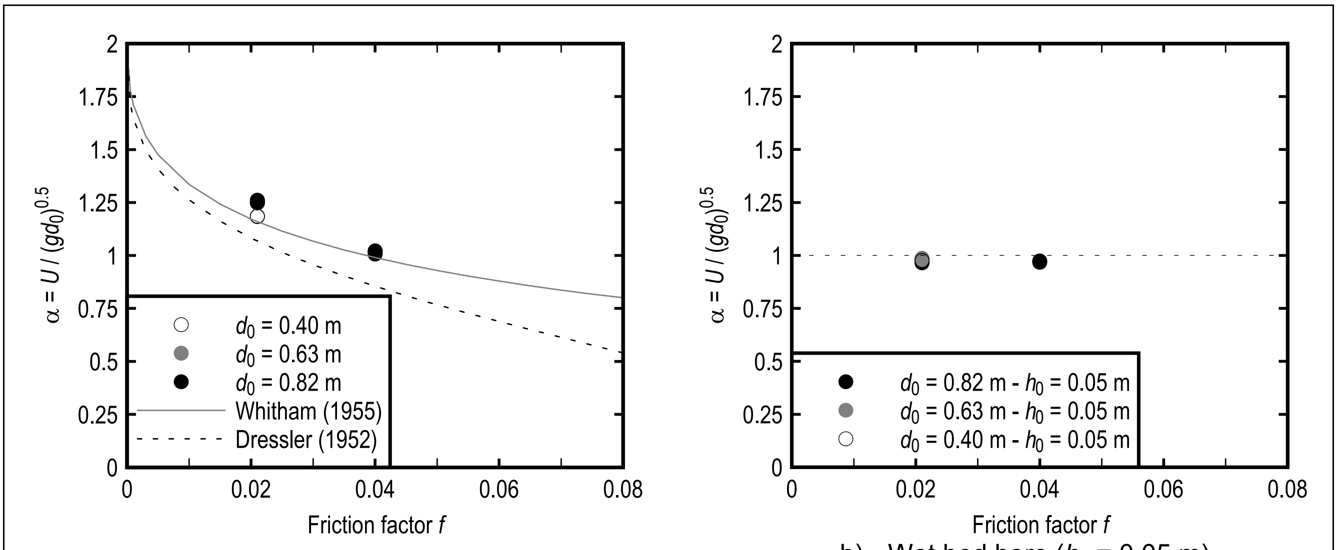

Figure 6. Velocity coefficient α as a function of friction factor f for both dry bed surges and wet bed bores.

The experimental points were also compared to some existing theories found in literature, mainly in Dressler (1952; 1954) and Whitham (1955). Dressler (1952) solved the Saint-Venant equations using a perturbation method assuming a constant friction factor, leading to the Eq. [3] (readapted by Chanson, 2004).

$$\frac{U}{\sqrt{g \cdot d_0}} = \frac{2}{3}\left(1 + \frac{x}{t \cdot \sqrt{g \cdot d_0}}\right) + F_1 \cdot \frac{f}{8}\sqrt{\frac{g}{d_0}} \cdot t \qquad [3]$$

where F_1 is a first order correction factor for the flow resistance, whose value is expressed in Eq. [4].

$$F_1 = -\frac{108}{7\left(2 - \frac{x}{t \cdot \sqrt{g \cdot d_0}}\right)^2} + \frac{12}{2 - \frac{x}{t \cdot \sqrt{g \cdot d_0}}} - \frac{8}{3} + \frac{8\sqrt{3}}{189} \cdot \left(2 - \frac{x}{t \cdot \sqrt{g \cdot d_0}}\right)^{\frac{3}{2}} \qquad [4]$$

An analogous solution was proposed by Whitham (1955), solving the Saint-Venant equations using an adaptation of the Polhausen Method (Chanson, 2004), leading to Eq. [5].

$$\frac{U}{\sqrt{g \cdot d_0}} = \frac{2}{1 + 2.90724\left[\left(\frac{f}{8}\right)\sqrt{\frac{gt^2}{d_0}}\right]^{0.4255}} \qquad [5]$$

For both theories, on a completely smooth surface ($f = 0$), a celerity value equal to the propagation of the forward characteristic in the Ritter (1892) theory can be assumed, implying $\alpha = 2$. An asymptotic behaviour toward this value can be observed in Figure 6a for $f \to 0$ leading to a vertical tangent. For large roughness values ($f \to \infty$), zero velocity should be expected, implying $\alpha = 0$, even if this scenario is physically impossible. This represents a limitation for both theories of Whitham (1955) and Dressler (1952; 1954) that are no longer valid for large tip regions, i.e. for large roughness values (Chanson, 2004). Figure 6 shows a relative good match for low friction factors with both theories, however, differences become more important for rougher surfaces and Whitham (1955) theory represented the experimental tests better.

6 CONCLUSIONS

In the design phase of structures resistant to hydrodynamic loading, the estimation of the approaching velocity is fundamental. Previous studies and field surveys showed that the disagreement and high incertitudes still exist in the evaluation of this parameter. The present study was based on an experimental approach and it focused on the evaluation of wave front celerity. Waves were reproduced in a large scale facility through a vertical release technique and both a smooth and a rough surface were tested. Produced waves were investigated in terms of wave height using Ultrasonic Distance Sensors located along the channel, allowing the estimation of the average wave celerity. The wave profiles were shown to be in agreement with existing theories in the domain of dam-break waves for both smooth and rough horizontal beds. While no influence of bed roughness was observed for wet bed bores, results clearly showed a dependence of the wave celerity on the friction factor for dry bed surges. For the two tested roughness values, lower celerity were observed for higher roughness, suggesting that friction should be considered when estimating the approaching velocity of a tsunami inland. The experimental points showed good agreement with previous theoretical solutions found in the literature. Nevertheless, only two values were investigated, pointing out the need of a more extensive experimental work to validate these preliminary results.

ACKNOWLEDGEMENTS

The research reported herein was funded by the Swiss National Science Foundation SNSF (grants 200021_149112/1 and 200021_149112/2).

NOTATION

d_0	equivalent impoundment depth [m]
f	Darcy-Weissbach friction factor
F_1	first order correction of flow resistance in Eq. [3]
g	gravity constant [m/s^2]
h	wave height [m]
h_0	initial still water depth [m]
h_{max}	maximum wave height [m]
t	time [s]
U	wave front celerity [m/s]
x	longitudinal coordinate along the channel [m]
α	velocity coefficient, defined as $U/(gd_0)^{0.5}$
Δt	increment in time [s]
Δx	Increment in distance [m]

REFERENCES

Bryant, E. (2008). *Tsunami: The Underrated Hazard*. Springer-Verlag Berlin Heidelberg, 1-330.

Chanson, H. (2004). *The Hydraulics of Open Channel flow: an Introduction*. *Elsevier*, Oxford, 1-585.

Chanson, H. (2009). Application of the Method 0f Characteristics to the Dam Break Wave Problem. *Journal of Hydraulic Research*, 47(1), 41–49.

Chanson, H., Aoki, S. & Maruyama, M. (2002). Unsteady Air Bubble Entrainment and Detrainment at a Plunging Breaker: Dominant Time Scales and Similarity of Water Level Variations. *Coastal Engineering*, 46(2), 139–157.

Chock, G., Robertson, I., Kriebel, D., Francis, M. & Nistor, I. (2012). Tohoku Japan Tsunami of March 11, 2011, Performance of structures. *American Society of Civil Engineers (ASCE)*, 1-14.

Choufi, L., Kettab, A. & Schleiss, A.J. (2014). Effet de la rugosité du fond d'un réservoir rectangulaire à faible profondeur sur le champ d'écoulement. *La Houille Blanche*, 5, 83-92.

Dressler, R.F. (1952). Hydraulic Resistance Effect upon the Dam-Break Functions. *Journal of Research of the National Bureau Standards*, 49(3), 217-225.

Dressler, R.F. (1954). Comparison of Theories and Experiments for the Hydraulic Dam-Break Wave. *International Association Scientific Hydrology*, 3(38), 319-328.

FEMA55 (2000). Coastal Construction Manual. *Federal Emergency Management Agency*, Washington DC, USA. Volume 2, 1-400.

Fritz, H.M. & Okal, E.A. (2008). Socotra Island, Yemen: Field Survey of the 2004 Indian Ocean tsunami. *Natural Hazards*, 46(1), 107-117.

Iizuka, H. & Matsutomi, H. (2000). Damage Due to Flood Flow of Tsunami. *Proceedings of the Coastal Engineering JSCE*, 47, 381–385.

Kirkoz, M. (1983). Breaking and Run-up of Long Waves, Tsunamis: their Science and Engineering. *Proceedings of the 10th IUGG International Tsunami Symposium*.

Lukkunaprasit, P., Thanasisathit, N. & Yeh, H. (2009). Experimental Verification of FEMA P646 Tsunami Loading. *Journal of Disaster Research*, 4(6), 410-418.

Matsutomi, H. & Okamoto, K. (2010). Inundation Flow Velocity of Tsunami on Land. *Island Arc*, 19(3), 443-457.

Meile, T., Boillat, J.L. & Schleiss, A.J. (2011). Water-Surface Oscillations in Channels with Axisymmetric Cavities. *Journal of Hydraulic Research*, 49(1), 73-81.

Murty, T.S. (1977). Seismic Sea Waves: Tsunamis. Department of Fisheries and the Environment Fisheries and Marine Service, Ottawa.

Nistor, I., Palermo, D., Nouri, Y., Murty, T. & M. Saatcioglu, M. (2009). Tsunami-Induced Forces on Structures. *Handbook of Coastal and Ocean Engineering*. Singapore, World Scientific, 261–286.

Ramsden, J.D. (1996). Forces on a Vertical Wall due to Long Waves, Bores, and Dry-Bed Surges. *Journal of Waterway, Port, Coastal, and Ocean Engineering,* 122(3), 134-141.

Ritter, A. (1892). Die Fortpflanzung der Wasserwellen. *Zeitschrift Verein Deutscher Ingenieure*, 36(33), 947–954.

Rossetto, T., Allsop, W., Charvet, I., & Robinson, D. (2011). Physical Modelling of Tsunami using a New Pneumatic Wave Generator. *Coastal Engineering*, 58(6), 517–527.

Rossetto, T., Peiris, N., Pomonis, A., Wilkinson, S.M., Del Re, D., Koo, R. & Gallocher, S. (2007). The Indian Ocean tsunami of December 26, 2004: Observations in Sri Lanka and Thailand. *Natural Hazards*, 42(1), 105-124.

Schoklitsch, A. (1917). *Über Dambruchwellen*, Sitzungberichte der Königlichen Akademie der Wissenschaften, Vienna, 126(2a), 1489-1514.

Shafiei, S., Melville, B.W. & Shamseldin, A.Y. (2016). Experimental Investigation of Tsunami Bore Impact Force and Pressure on a Square Prism. *Coastal Engineering*, 110, 1-16.

Stoker, J. J. (1957). Water Waves: The Mathematical Theory with Applications. *Intersciences*, 567.

Whitham, G. (1955). The Effects of Hydraulic Resistance in the Dam-Break Problem. *Proceedings of the Royal Society of London*. Series *A. Mathematical and Physical Sciences*, 227(1170), 399–407.

Wüthrich, D., Pfister, M., Manso, P., Constantinescu, G. & Schleiss, A.J. (2016). Surface Turbulence on Bores and Surges Propagating on Smooth and Rough Beds. *Proceedings of the 6th International Conference on the Application of Physical Modelling in Coastal and Port Engineering and Science (Coastlab16)*. Ottawa, Canada, 1-8.

Wüthrich, D., Pfister, M., Nistor, I. & Schleiss, A.J. (2017). Experimental Study of Tsunami-Like Waves on Dry and Wet Bed Generated with a Vertical Release Technique. *Journal of Waterway, Port, Coastal, and Ocean Engineering*. (Under review)

APPROPRIATE WATER QUALITY ENVIRONMENT FOR PROTECTING THE COASTAL ECOSYSTEM IN THE ARIAKE SEA, JAPAN

TOSHINORI TABATA(1), WATARU HAYASHI(2) EMI OTSUBO(3),
KAZUAKI HIRAMATSU(4) & MASAYOSHI HARADA(5)

(1,4,5) Faculty of Agriculture, Kyushu University, Fukuoka, Japan,
ttabata@bpes.kyushu-u.ac.jp; hiramatsu@bpes.kyushu-u.ac.jp; mharada@bpes.kyushu-u.ac.jp
(2) Graduate School of Bioresource and Bioenvironmental Sciences, Kyushu University, Fukuoka, Japan,
1ag12155@gmail.com
(3) Naigai Engineering Co., Ltd., Fukuoka, Japan,
mn3n7ksc61kdr@yahoo.co.jp

ABSTRACT

The resource of bivalve has been decreasing drastically since 1970s in the Ariake Sea located in Kyushu Island, Japan. Water quality of environment in the sea has been changed in decades. Eventhough, the data of water quality or the amount of bivalve catchment have been collected for more than 30 years, these data have never been assessed before. In this research, the change of decennial characteristics is assessed in order to identify the environmental change. Using kriging method, all data point of water quality items is interpolated into the entire area. Then, each area was classified into six groups by cluster analysis. The result showed that the water quality environment in the Ariake Sea have been significantly changed in these past 30 years. It was revealed that the amount of nutrient (DIN, DIP) and organic matter (COD) has been decreasing rapidly in this area. Then, the relationship between water quality items and bivalve catchment is investigated using Artificial Neural Network (ANN) model with sensitive analysis. ANN model reproduced the annual bivalve catchment well from 10 of annual average water quality items. Sensitive analysis was conducted to evaluate which water quality item is affecting the bivalve catchment the most. The result showed that decreasing amount of nutrients is inducing the decrease of bivalve catchment in Ariake Sea. This result coincides with the result from cluster analysis. In Japan, the technologies of waste water treatment or sewage coverage have been improved so much that the water qualities in the river become clean which means less nutrients in the water. There are water quality standard to protect the coastal area from eutrophication, but there are no standard to protect the area from oligotrophication in Japan. Therefore, appropriate standard of the water quality items must be established to protect coastal ecosystems in Japan.

Keywords: Kriging; cluster analysis; artificial neural network; sensitive analysis; water quality.

1 INTRODUCTION

The Ariake Sea is a semi-closed bay located in the Kyushu Island, Japan (Figure 1). It is surrounded by the Fukuoka, Saga, Nagasaki, and Kumamoto prefectures and is the biggest bay in the Kyushu Island. Vast quantities of nutrients flow into the sea, and due to its shape the retention period is long. Hence, the Ariake Sea is a homeostatic eutrophic area. Typically, eutrophic areas tend to suffer from the formation of red tides or the appearance of anoxic water mass leading to a decrease of fish production. However, owing to its unique character, the Ariake Sea has not suffered from any of these issues. In fact, seaweed (Nori) aquafarming has been increasing in the Ariake Sea, currently accounting for 40% of the Nori production in Japan. Moreover, because there are large areas of tidal flats (>200 km^2), many bivalves inhabit this area; in turn, the Ariake Sea has been renowned for bivalve production. Thus, the Ariake Sea was known for its high biological productivity.

Previously, the Ariake Sea has not suffered from environmental issues, despite the eutrophic nature of the area. However, its environmental deterioration is becoming a serious social problem with the recent occurrence of large red tides. Since 1985, the number of red tide outbreaks has exceeded 20/year. During the period 1998 - 2002, red tides occurred >30/year. Furthermore, numerous studies have been conducted on large anoxic water mass, which has also become a serious issue in the Ariake Sea (Hamada et al., 2008; Kajihara et al., 2003; Tsutsumi et al., 2007).

More recently, fish conservation has been required in the Ariake Sea. The destabilization of Nori products has also become a serious problem in recent years. The average production value was 20.8 billion yen/year during the period 1978 to 1989. After 1990, the production value varied from 13.1 billion to 23 billion yen/year with only few years exceeding the 20 billion yen/year level (Shutou et al., 2009). Catches of bivalves have been drastically decreasing. The catch of bivalves in the Ariake Sea was 70,000 to 110,000 tons/year during the late 1970s and early 1980s. These values decreased to 50,000 tons/year in 1984 and dropped below 20,000 tons/year in 1998. Now, the catch of bivalves is 1/10 the value during its peak period (Nakane, 2013).

Although many research have been conducted in the Ariake Sea (Tabata et al., 2013; Mizumukai et al., 2008; Shiratani et al., 2007), the catchment of bivalve or the environmental degradation have not been improved yet. In this research, the change of decennial characteristics of water quality in the Ariake Sea was assessed by cluster analysis in order to identify the environmental change. After identifying the water quality environment in this area, the relationship between water quality items and bivalve catchment was investigated using Artificial Neural Network (ANN) model with sensitive analysis. Then, the appropriate water quality environment in the Ariake Sea was discussed with the result of cluster analysis and sensitive analysis.

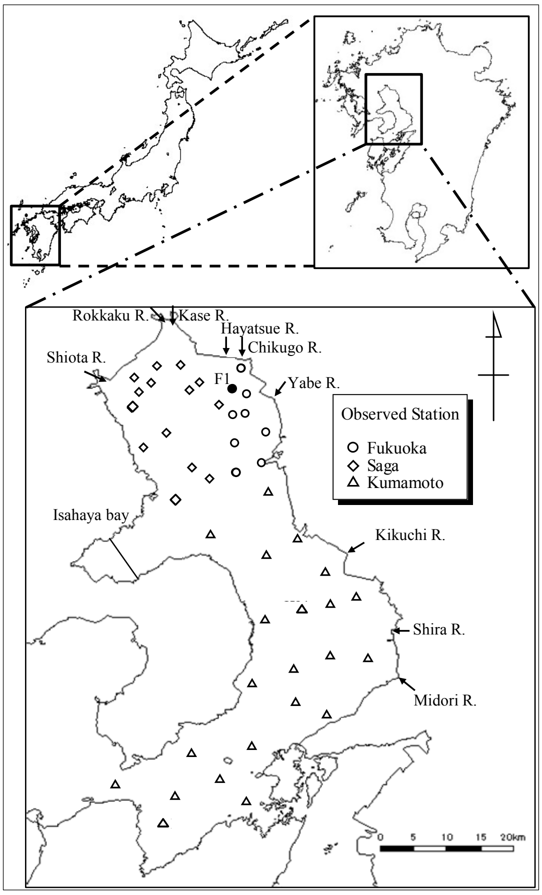

Figure 1. Location of the Ariake Sea, river inflow, and the observation station by coastal prefectures.

2 METHODS

2.1 Data

Once a month water quality surveys had been carried out over the past 30 years at multiple locations (Figure 1) in the four prefectures on the Ariake Sea coast. Furthermore, annual statistical surveys had been performed over the past 50 years, publishing catch volumes by species for each prefecture. Table 1 list the water quality attributes and observation periods for the data used in this study. As an example, Figure 2 shows the results of periodic shallow water surveys for location F1 in Figure 1 for April 1997 - March 2013. Location F1 is a survey point in Fukuoka Prefecture, but surveys for multiple water quality attributes identical to the ones in Figure 2 were also carried out in other prefectures. Moreover, Figure 3 indicates catch volumes for the Asari clam and other bivalves for each prefecture in the period of 1974-2012.

Table 1. The water quality attributes and observation periods for the data used.

Prefecture	Observed period	Water quality attributes
Fukuoka	1965-2013	transparency, water temperature, salinity, DO (Dissolved Oxygen), COD (Chemical Oxygen Demand), DIN (Dissolved Inorganic Nitrogen), NO_3-N (nitrate nitrogen), NO_2-N (nitrite nitrogen), NH_4-N (ammonium nitrogen), PO_4-P (phosphate phosphorus)
Saga	1972-2013	transparency, water temperature, salinity, DO, COD, DIN, NO_3-N, NO_2-N, NH_4-N, PO_4-P
Kumamoto	1974-2013	transparency, water temperature, salinity, DO, COD, DIN, NO_3-N, NO_2-N, NH_4-N, PO_4-P

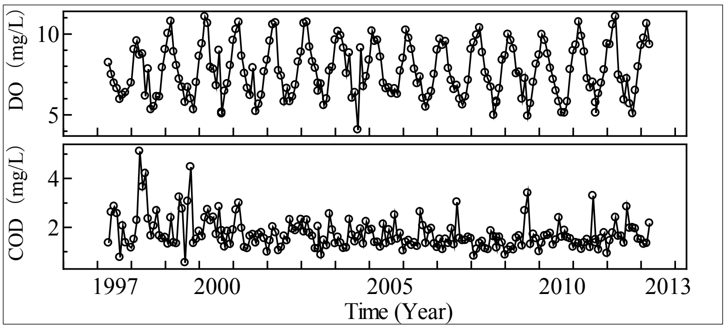

Figure 2. Results of the surveys from April 1997 to March 2013 performed at station F1.

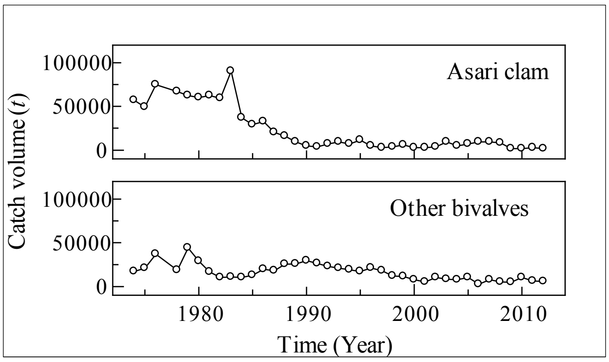

Figure 3. Catch volumes for the Asari clam and other bivalves for each prefecture in the period 1974-2012.

2.2 Cluster analysis with kriging

In order to identify the water quality characteristics in the Ariake Sea, cluster analysis which is used widely in evaluating the environment (Singh et al., 2004; Shrestha and Kazama, 2007) was conducted to the water quality data. However, it was insufficient to conduct a cluster analysis only with one point data. It is important to understand the distribution of environmental characteristics since the Ariake Sea is suffering from very complex issues. Therefore, point data of the water quality in the Ariake Sea was interpolated to the whole area using kriging method. Kriging is one of the interpolation methods in geostatistics. Matheron (1963) established this theory by expressing this spatial dependency using the variogram. This method is applied in environmental field, recently (Cao et al., 2017; Vasu et al., 2017). Using this technique, value of un-sampled point can be estimated from the measured value accurately.

First, variogram analysis was performed to explore the spatial distance. It begins with a graph of the sample semivariogram $\gamma(h)$, computed as:

$$\gamma(h) = \frac{1}{2N}\sum_{i=1}^{N}\left(Z(x_i + h) - Z(x_i)\right)^2 \quad [1]$$

where h is the separation distance, $Z(x_i+h)$, $Z(x_i)$ are the measured value of the water quality of i th point and N is the number of points. The value of semivariogram increase until certain distance and it can be confirmed that in a small separation distance, the data had a similar value. However, the value of sample semivariogram computed from just sample data was not continuous, so it was important to fit a smooth curve, which was called variogram models. Sample variogram were fitted to the spherical model which is often used in geostatistics. The formula of the spherical model is given that:

$$\gamma(h) = \begin{cases} C_0 + C\left(\dfrac{3h}{2a} - \dfrac{h^3}{2a^3}\right) & 0 < h \le a \\ C_0 + C & h > a \end{cases} \quad [2]$$

where a is range, C_0 is the nugget, (C_0+C) is the sill. Kriging is one of the interpolation methods in geostatistics. Using this technique, value of unsampled point can be estimated from measured value. In this method, the estimated value is given as:

$$\hat{Z}(x)=\sum_{i=1}^{n}\lambda_i Z(x_i) \quad [3]$$

where $\hat{Z}(x)$ is the estimated value, □ is the weight of the measured value and fulfill the non-bias condition as follows:

$$\sum_{i=1}^{n}\lambda_i = 1 \quad [4]$$

By at these steps, point data of each water quality will be interpolated into the whole area. To characterize decennial water environment, change in the sea, 10 years averaged water quality items were interpolated using this method.

Then, cluster analysis was performed with interpolated 10 water quality items (transparency, water temperature, salinity, DO, COD, DIN, NO_3-N, NO_2-N, NH_4-N, PO_4-P). Hierarchical cluster analysis was performed in the normalized data set by means of Ward's method. The Ward's method creates the cluster based on the indicator which quantitatively estimates the variance of data. Euclidian distance is used as the distance between each data. In case of clustering data set $S=\{y_1,y_2,\cdots,y_n\}$, Eq. [5] is used as an index to measure data variation.

$$\sum_{i=1}^{n}(y_i-\bar{y})^2,\bar{y}=\frac{1}{n}\sum_{i=1}^{n}y_i \quad [5]$$

When data set S is categorized into m clusters, the sum of squared deviations within each cluster is expressed as follows:

$$W_j=\sum\left(y_i^{(j)}-\bar{y}_j\right)^2,\bar{y}_j=\frac{1}{n}\sum_{i=1}^{n_j}y_i^{(j)}, j=1,2,\cdots m \quad [6]$$

where n_j is the number of data included in the j th cluster. Then, the total sum of square deviations of all m clusters can be calculated with following equation:

$$W_j=W_1+W_2+\cdots+W_m \quad [7]$$

This also indicates the variance of all categorized clusters $\{C_1,C_2,\cdots,C_m\}$. In particular, the total sum of square deviations of all clusters should be 0 when each data is taken as a cluster. In Ward's method, consolidation index $d(C_\alpha,C_\beta)$ can be obtained from equation below when combining cluster C_α and C_β:

$$d(C_\alpha,C_\beta)=W_{\alpha\beta}-W_\alpha-W_\beta \quad [8]$$

This represents the increment of the sum of square deviations caused by combining two clusters. In this method, after calculating this consolidation index, two clusters which had the smallest increment will be merged. The process was repeated until there is only one cluster.

2.3 Sensitive analysis using Artificial Neural Network model

There are limits to assessing the relation between bivalve catch volumes and marine environment using linear regression. An ANN model on the other hand allows for the representation of the mapping relationship between several environmental factors as a non-linear model, and has an extremely high capacity for pattern recognition (Hiramatsu et al., 1995). In other words, using a network that has learned through the use of known input and output as training data, an unknown output variable can be estimated for an input variable. An ANN is commonly divided into three or more layers: an input layer, a hidden layer, and an output layer. The input layer contains the input neurons, i.e. the input variables for the network. The output layer contains the desired output of the system and the hidden layer usually contains a series of nodes associated with transfer functions. Each layer of the ANN is linked by weights that have to be determined through a learning algorithm (Lee et al., 2003; Lek, 1999). The present study employed a 3-layered ANN model, consisting of an input layer, an intermediate layer and an output layer, as shown in Figure 4. The input variables used were from a total of 30 attributes comprising 10 annual average water quality attributes (transparency, water temperature, salinity, DO, COD, DIN, NO_3-N, NO_2-N, NH_4-N, PO_4-P) in the surface layer for all locations in Fukuoka, Kumamoto and Saga prefectures, as shown in Figure 1. Output variables were from a total of two variables, namely annual Ariake Sea catch volumes for the Asari clam and for other bivalves. The figure for the intermediate layer was determined through trial and error. Backpropagation learning method was utilized for determining parameters of ANN model. For the learning computations a total of 38 datasets were used dating from 1974-2012 (except 1977 due to lack of data). Firstly, all datasets were used as training data to study the network's learning accuracy. Then, the average root mean square error (RMSE) and the Nash-Sutcliffe index (NS) over 10 times were obtained to examine the estimation accuracy for bivalve catch volumes. After the ANN model was constructed the sensitive analysis was conducted. The detail of the sensitive analysis will be explained in the result section.

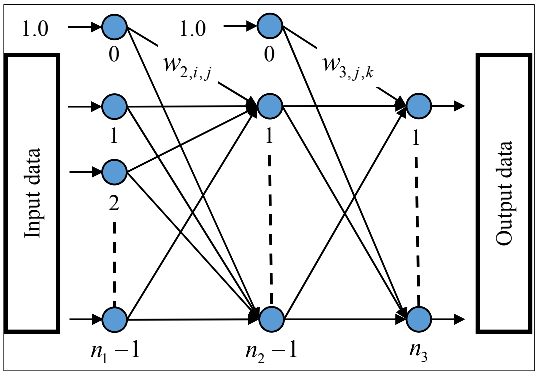

Figure 4. The image of 3-layerd ANN model.

3 RESULT AND DISCUSSION

3.1 Decennial water quality characteristics

Figure 5 shows the distribution of 10-year averaged PO_4-P in the 1990’s and 2000’s. The result of cross-validation showed that water quality items were interpolated accurately (RMSE=0.09□g-at/l). As it can be seen in Figure 5, PO_4-P was highly distributed near Chikugo river mouth (north-east part) in 1990’s. This was because the inflow amount from Chikugo River account for 60% of all inflow into the Ariake Sea, so the nutrient from land flowed into the sea. However, the distribution of high PO_4-P has moved to western side of the sea since the technologies of waste water treatment or sewage coverage have been improved in these 10 years in Japan. The Ariake Sea was characterized when classifying into 6 clusters. Figure 6 shows the distribution of 6 clusters divided by cluster analysis. Table 2 shows the averaged water quality items of each cluster. These result showed that the water quality in the Ariake Sea have improved. For instance, it is classified into cluster 4 in Kumamoto estuaries (south west part) in 1990’s. Then, it is classified into cluster C in 2000. According to Table 2, it can be said that the amount of nutrient has been decreased (DIN: from 4.27 to 3.08 □g-at/l). Also, transparency has increased (from 4.6m to 5.7m). Moreover, DO has also increased in the area (from 7.6 to 8.3 mg/l). On the other hand, water quality environment in Saga estuaries (north west part) have been decreasing (from cluster 2 to cluster E). This is because Saga prefecture input some nutrients into the Sea in order to increase the growth of Nori (edible seaweed cultivated in the area).

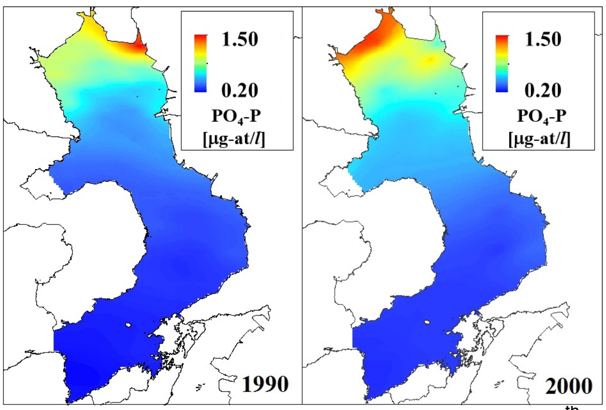

Figure 5. Distribution of 10-year averaged PO4-P in 1990th and 2000th.

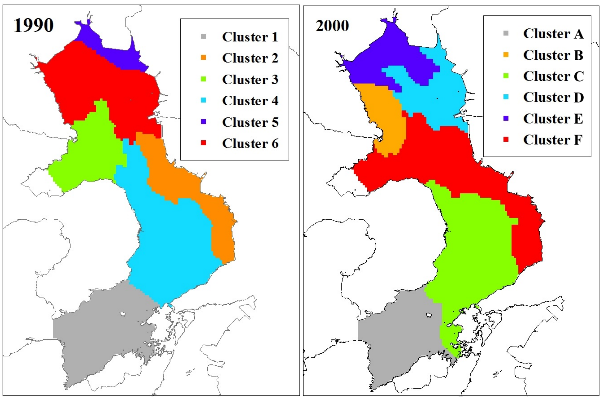

Figure 6. Results of cluster analysis in 1990's and 2000's.

Table 2. Average value of each water quality items in each cluster.

No.	1990th transparency (m)	DO (mg/l)	DIN (□g-at/l)	PO_4-P (□g-at/l)	No.	2000th Transparency (m)	DO (mg/l)	DIN (□g-at/l)	PO_4-P (□g-at/l)
1	6.9	7.6	3.74	0.23	A	8.3	7.5	2.78	0.28
2	2.5	7.6	5.27	0.38	B	2.3	7.6	6.22	0.66
3	4.0	8.0	5.69	0.41	C	5.7	8.2	3.08	0.32
4	4.6	7.8	4.27	0.31	D	1.8	8.2	8.70	0.74
5	0.8	7.6	22.8	1.14	E	1.2	7.9	11.2	1.11
6	1.8	7.9	10.8	0.70	F	3.3	7.7	4.47	0.48

3.2 Relationship between water quality items and bivalve catchment

Figure 7 shows learning results when all 38 datasets were used as training data. Moreover, results from a 10-fold cross validation showed that estimation accuracy for Asari clams was NS=0.701, RE=0.304 and for other bivalves NS=-0.373, RE=0.422. This indicates that for Asari clams good results were obtained both for learning and estimation accuracy. For other bivalves however, although learning results with high NS values were obtained, in cross validation no adequate computation accuracy was obtained as an estimation model with e.g. negative NS values. The reason for this may be that other bivalves were comprised of multiple species including the Tairagi calm and oysters, and it is surmised that pattern recognition is made difficult by the varying effects of water quality on each bivalve species. Anyway, Asari clams had high reproducibility using ANN model with water quality items. This result suggeseds that it is certain that decreasing catchment of Asari clams can be explained with the change of water qualities in the Ariake Sea.

The sensitivity of the output results to changes in input values was examined for the Asari clam, which obtained good results for learning and estimation. The water quality attributes defining the increase and reduction of catch volumes were thus selected, and their degree of impact was assessed. Firstly, the average water quality/catch volume data for the period 1974-1983, boasting high catch volumes in excess of 50,000 tonnes, were set as the reference values. Next, sensitivity of the output values was obtained for each water quality attribute by changing the input values by ±20%, ±10%, ±5% with regard to the reference value, that is to say, the degree of variability in Asari clam catch volumes was obtained. As an example of the calculated results, sensitivity to each water quality attribute in Kumamoto Prefecture is shown in Table 3. Results of the sensitivity analysis indicated that an increase in transparency, a decrease in salinity and a reduction of COD in Kumamoto Prefecture affect the reduction of catch volumes of the Asari clam. Since no characteristics for change over time in salinity could be detected, we focused on transparency and COD. Figures 8 and Figure 9 shows the relationship between Asari clam catch volume, transparency and COD for Kumamoto Prefecture respectively. Figure 10 indicates the change over time in transparency and COD in Kumamoto Prefecture. Figure 8 reveals that if transparency exceeds 4.4 m, catch volumes rapidly decline. When focusing on Figure 10 it can be seen that transparency shows a year-on-year upward trend and has exceeded 4.4 m since the latter half of the 1980's. It is clear from Figure 9 that Asari clam catch volumes rapidly decline when COD falls below 0.9 mg/L. According to Figure 10 COD has dropped sharply since the mid 1980's and has fallen below 0.9 mg/L, allowing us to confirm a relationship between Asari clam catch volumes and COD. The above shows that change in transparency over time and an excessive reduction in COD in the Kumamoto Prefecture coastal region affect the reduction of bivalve catch volumes. In general, the reasons described above were trends which are good for marine environments, but they have created an adverse effect for Asari clam catch volumes. The reason for this is that since the Asari clam feeds on phytoplankton in the water, it is surmised that in clear waters with extremely low levels of suspended solids, or in other words, in highly transparent waters, phytoplankton serving as feed is scarce. Because of this, Asari clam production capacity dropped and catch volumes were reduced. Similarly, in waters where COD is extremely low, levels of phytoplankton which the Asari clam feeds on are low, leading to reduced Asari clam catch volumes.

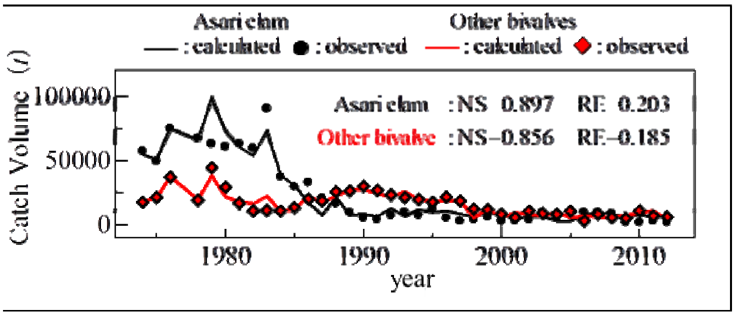

Figure 7. Learning results of the ANN model using all 38 datasets as training data.

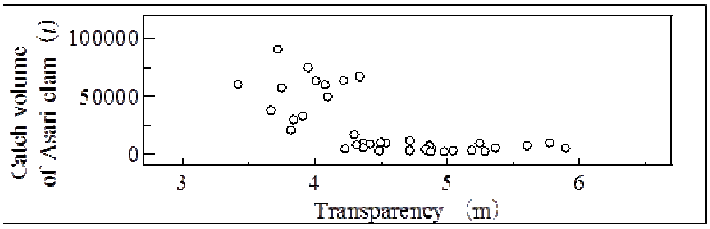

Figure 8. The relationship between Asari clam catch volume and transparency.

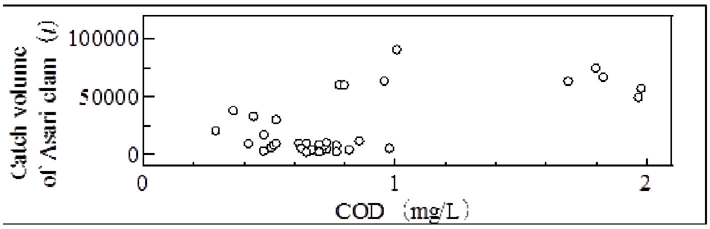

Figure 9. The relationship between Asari clam catch volume and COD.

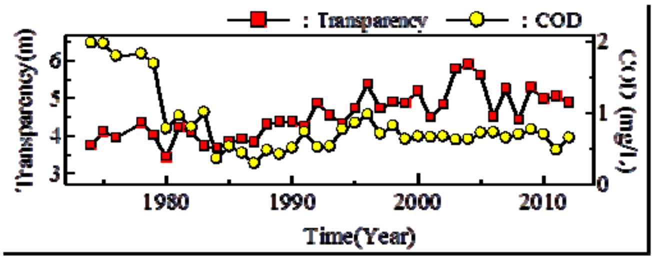

Figure 10. The change over time in transparency and COD in Kumamoto Prefecture.

Table 3. Sensitivity (%) of Asari clam catchment to each water quality attribute in Kumamoto Prefecture.

	-20%	-10%	-5%	+5%	+10%	+20%
Transparency	-0.86	-0.29	-0.07	-0.27	-1.33	-10.52
Water	-3.44	-2.16	-1.13	0.83	0.61	-9.43
Salinity	-3.77	-2.57	-1.42	1.23	1.50	-5.36
DO	-3.46	-2.20	-1.17	1.00	1.35	-3.01
COD	-3.66	-2.49	-1.38	1.40	2.45	2.59
DIN	-3.22	-1.98	-1.06	1.04	1.88	2.31
NO_3-N	-3.41	-2.18	-1.18	1.20	2.22	3.15
NO_2-N	-3.30	-2.04	-1.09	1.11	2.06	2.99
NH_4-N	-3.26	-2.01	-1.07	1.05	1.90	2.30
PO_4-P	-3.45	-2.22	-1.21	1.22	2.24	3.00

3.3 Appropriate water environment in the Ariake Sea

The result of cluster analysis showed that the nutrient level have been decreased in these 10 years. It seemed that the water quality environment in the Ariake Sea has improved. However, the result of sensitive analysis with ANN model showed that the decreasing nutrient was the main cause of decreasing catchment of bivalve. Therefore, these results indicated that appropriate nutrient level should be kept for sustainable fisheries. In Japan, since many region suffered from eutrophication, they focused on improving the technologies of waste water treatment or sewage coverage. As a result, the water qualities in the river become clean which means less nutrients in the water. Now, there are water quality standard to protect the coastal area from eutrophication, but there are no standard to protect the area from oligotrophication in Japan. Therefore, appropriate standard of the water quality items must be established to protect coastal ecosystems in Japan.

4 CONCLUSIONS

In this research, the appropriate water quality environment in the Ariake Sea is discussed. First, cluster analysis was conducted with interpolated water quality data. Using kriging method 10-year averaged water quality items (1990’s and 2000’s) were interpolated in to the entire area of the Ariake Sea with high accuracy. The area is categorized into 6 groups for both 1990’s and 2000’s. The result showed that nutrient level in the Ariake Sea has decreased in 10 years. Then, ANN model is constructed to represent the relationship between bivalve catchment and water quality. ANN model could learn the relationship between Asari clam and water quality well. After the construction of ANN model, sensitive analysis was performed to the model. Results suggested that the cause of the reduction in Asari clam catch volumes in recent years is because of increased transparency (more than 4.4 m) and reduced COD (less than 0.9 mg/L) in the coastal region of Kumamoto Prefecture. This is thought to be due to insufficient presence of phytoplankton, which the Asari clam feeds on, leading to a reduction in Asari clam catch volumes. As a conclusion, the appropriate water quality standard must be installed in the Ariake sea for protecting both water environment and sustainable fisheries.

ACKNOWLEDGEMENTS

The authors wish to thank the Ariakekai Laboratory of Fukuoka Fisheries and Marine Technology Research Center, the Saga Prefectural Ariake Fisheries Research and Development Center, and finally, the Kumamoto Prefectural Fisheries Research Center for providing data on the Ariake Sea.

REFERENCES

Cao, S., Lu, A., Wang, J. & Huo, L. (2017). Modeling and Mapping of Cadmium in Soils based on Qualitative and Quantitative Auxiliary Variables in a Cadmium Contaminated Area. *Science of the Total Environment*, 580, 430-439.

Hamada, K., Hayami, Y., Yamamoto, K., Ohgushi, K., Yoshino, K., Hirakawa, R. & Yamada, Y. (2008). Serious Hypoxia in the Head of the Ariake Sea in summer, 2006. *Oceanography Society in Japan*, 17(5), 371-377.

Hiramatsu, K., Shikasho, S. & Mori, K. (1995). Application of Multi-Layered Perceptron Model to the Estimation of Chlorinity Variations in a Tidal River. *The Japanese society of Irrigation, Drainage and Rural Engineering*, 178, 483-492

Kajihara, Y., Tomita, T., Nakano, T. & Isobe, M. (2003). Occurrence of Hypoxic Water in the Inner Area of Ariake Bay in the Summer of 2002. *Journal of the Japan Society of Civil Engineers*, 747(II-65), 187-196.

Lee, J.H.W., Huang, Y., Dciman, M. & Jayawardena, A.W. (2003). Neural Network Modelling of Coastal Algal Blooms. *Ecological Modelling*, 159, 179-201.

Lek, S. & Guegan, J.F (1999). Artificial Neural Networks as a Tool in Ecological Modeling. *Ecological Modelling*, 120, 65-73.

Matheron, G. (1963). Principles of Geostatistices. *Economic Geology*, 58(8), 1246.

Mizumukai, K., Sato, T., Tabeta, S. & Kitazawa, D. (2008). Numerical Studied on Ecological Effects of Artificial Mixing of Surface and Bottom Waters in Density Stratification in Semi-enclosed Bay and Open Sea. *Ecological Modelling*, 214, 251-270.

Nakane, T. (2013). Annual Change of Fishery Production in Ariake Bay. *Aquabiology*, 35(5), 447-456.

Shiratani, E., Kiri, H., Takaki, K., Hamada, K., Tanji, H. & Nakata, K. (2007). Research on Factors of Tide and Tidal Current Changes in the Ariake Sea. *Irrigation, Drainage and Rural Engineering Journal*, 252, 145-156.

Shutou, T., Matsubara, T. & Kuno, K. (2009). Nutrient State and Nori Aquaculture in Ariake bay. *Aquabiology*, 31(2), 168-170.

Shrestha, S. & Kazama, F. (2007). Assessment of Surface Water Quality using Multivariate Statistical Techniques: A Case Study of the Fuji River Basin, Japan. *Environmental Modelling & Software*, 22, 464-475

Singh, K.P., Malik, A., Mohan, D. & Sinha, S. (2004). Multivariate Statistical Techniques for the Evaluation of Spatial and Temporal Variations in Water Qualityof Gomti River (India)—A Case Study. *Water Research*, 38, 3980-3992

Tabata, T., Hiramatsu, K., Harada, M. & Hirose, M. (2013). Numerical Analysis of Convective Dispersion of Pen Shell Atrina Pectinata Larvae to Support Seabed Restoration and Resource Recovery in the Ariake Sea, Japan. *Ecological Engineering*, 57, 154-161.

Tsutsumi, H., Tsutsumi, A., Takamatsu, A., Kimura, C., Nagata, S., Tsukuda, M., Komorita, T., Takahashi, T. & Montani, S. (2007). Mechanisms for the Expansion of Hypoxic Water in the Inner Areas of Ariake Bay during Summer. *Oceanography in Japan*, 16(3), 182-202.

Vasu, D., Singh, S.K., Sahu, N., Tiwary, P., Chandran, P., Duraisami, V.P., Ramamurthy, V., Lalitha, M. & Kalaiselvi, B. (2017). Assessment of Spatial Variability of Soil Properties using Geospatial Techniques for Farm Level Nutrient Management. *Soil & Tillage Research*, 169, 25-34

Proceedings of the 37th IAHR World Congress
August 13 – 18, 2017, Kuala Lumpur, Malaysia

IMPACTS OF SEA LEVEL RISE ON A SEMI-ENCLOSED BAY INSIDE THE PEARL RIVER ESTUARY

YE YANG[1] & TING FONG MAY CHU[2]

[1,2] Department of Civil Engineering, The University of Hong Kong, Pokfulam, Hong Kong SAR, China,
yangye07@connect.hku.hk; maychui@hku.hk

ABSTRACT

Sea level rise is a global concern and threat to coastal regions. In the most prosperous estuarine region of China, the Pearl River Estuary, sea level is rising at a rate of 0.01 m/year. The Deep Bay is a semi-enclosed bay connected to the Pearl River Estuary, and its inner bay houses a Ramsar Convention wetland. Previous studies have determined that sea level rises at 0.3 and 0.5m and would respectively cause a 26.2% and 45.7% loss of the intertidal region of Ramsar site. This study employed a three-dimensional coastal model to evaluate the impacts of sea level rise on the hydrodynamics and salinity transport of the bay. The model was validated with observation data in the year of 2007, and hypothetical scenarios for the years 2037 and 2057 are simulated with sea level rises of 0.3 and 0.5m respectively. Simulation results show that the two levels of sea level rise would substantially increase the tidal effect, elevating the tidal prism by 9.8% and 15.0% and magnifying the tidal energy entering the bay by 21.0% and 41.4% respectively. The spatial distribution of salinity in the whole bay would also be substantially changed. The annually averaged salinity levels at bay mouth were 28.3, 28.8, and 29.1 psu respectively in 2007, 2037 and 2057. Those in the inner bay were respectively 9.7, 12.1, and 13.7 psu. Furthermore, the water age at the inner bay would be influenced the most with a 3-day increase. The water exchange ability in inner bay would decrease, potentially stressing the intertidal region with longer residence time of nutrients from the Shenzhen River. However, the current velocity in the intertidal region would decrease by 8.7% and 15.0%, possibly enhancing sediment deposition and thus minimizing the loss of intertidal region during sea level rise.

Keywords: Sea level rise; semi-enclosed bay; intertidal region; numerical model; pearl river estuary.

1 INTRODUCTION

As a result of global warming, sea-level rise (SLR) is threatening many coastal regions worldwide, and especially the region around the Pacific Ocean where a higher rising rate is expected (Nicholls and Cazenave, 2010). The rate of SLR has also been accelerating in recent years, making the coastal cities more vulnerable and raising a global concern (Yin et al., 2009). The vulnerable area to SLR has been estimated to cover 2% of the world's land area, but containing 13% of the world's urban population (McGranahan et al., 2007). Recently, some studies have been conducted to evaluate the impacts of SLR in estuarine regions. Chua and Xu (2014) employed an idealized numerical model to evaluate the response of estuarine circulation to SLR, and used the San Francisco Bay as a case study. Kuang et al. (2014) simulated the tidal levels, tidal wave propagations, flood and ebb tide velocities with potential future SLR in the Yangtze River Estuary, and further examined the impacts of SLR on the hydrodynamics. Yuan et al. (2015) simulated the hydrodynamics and salt transport processes in the Pearl River Estuary, and further estimated salt water intrusion in Jiaomen and Hongqili outlets. However, studies about the impacts of SLR on the water transport process in coastal regions, especially on semi-enclosed bays, are still limited.

Numerical modeling is a popular and effective method to examine the impacts of SLR on hydrodynamics and water transport processes, as it can simulate the scenarios with elevated sea-levels in an estuarine region. A semi-implicit estuarine, coastal, and ocean model was used to assess the influences of rising sea level on salt transport processes and estuarine circulation patterns in the Yangtze River Estuary (Qiu and Zhu, 2013). A Finite Volume Coastal Ocean Model was used to investigate the salt water intrusion length in the outlets of the Pearl River Estuary (Yuan et al., 2015). A three-dimensional semi-implicit Eulerian-Lagrangian finite-element model was established and applied to evaluate the impacts of SLR in the Tamsui River estuarine and the adjacent coastal system (Chen et al., 2015). Numerical modeling method has been shown to be effective in evaluating the impacts of SLR on the hydrodynamics and salt transport processes. However, further studies should be conducted to assess the SLR impacts on the transport processes of solute other than salt.

In this study, a numerical model would be generated for the whole Pearl River Estuary including a semi-enclosed bay and the Deep Bay. The model would been developed based on the field observations in the year of 2007, and future scenarios in the years 2037 and 2057 with, respectively, 0.3 m and 0.5 m elevated sea-levels. Different hydrodynamics and water transport indicators would be estimated for the different scenarios, giving results that would be useful for environmental engineers and managers to better protect semi-enclosed bays against SLR.

2 MATERIAL AND METHODS

2.1 Study area

The Pearl River Estuary is one of the largest estuaries in China and is located in the northern part of the South China Sea. It is the most prosperous estuarine region of China with several fast developing and densely populated cities such as Shenzhen and Hong Kong. According to a 72-year tidal record of 54 tide gauges in Hong Kong, the seal level in the Pearl River Estuary is estimated to be rising at 1 cm/year (Huang et al., 2004). It is higher than the medium SLR rate for global scale, which is 0.49 cm/year (IPCC, 2001), and thus making the coastal region in the Pearl River Estuary to be one of the most vulnerable regions.

The Deep Bay is a semi-enclosed bay inside of the Pearl River Estuary, which borders Shenzhen on the north and Hong Kong on the south (shown in Figure 1b). There is a Ramsar Conservation Site, Mai Po Nature Reserve, in the inner part of the bay. The intertidal wetland in the Ramsar Site is of international significance, as it hosts more than 55,000 migratory wading birds for each year. If the SLR was at the rate estimated by Huang et al. (2004), 26.2% and 45.7% of the intertidal wetland could be submerged and become sub tidal regions in the years of 2037 and 2057, if the wetland elevation remains the same. However, the fate of the intertidal wetland is also dependent on the sedimentation rate which is governed by the water transport process inside of the bay. The aquatic environment at the inner bay is also of great importance as it would influence the productivity of the benthic in-fauna at the tidal wetland, which is the vital food supply for migratory birds.

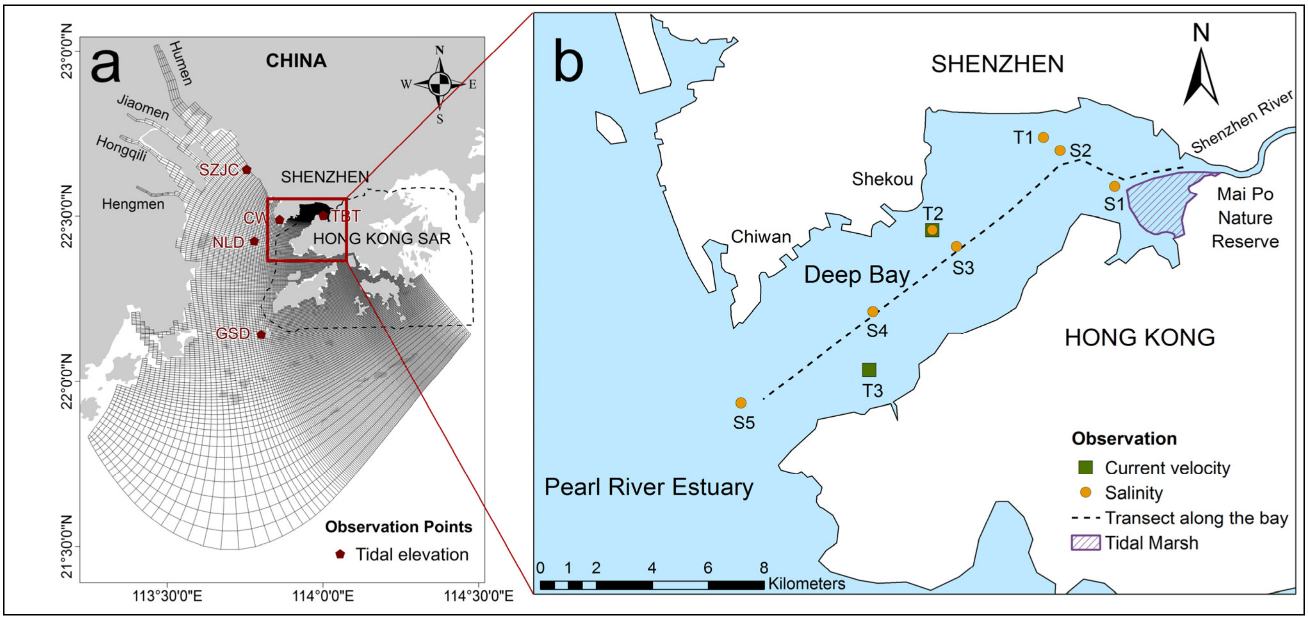

Figure 1. Study domain. (a) horizontal simulation grids and tidal gauges, (b) map of the Deep Bay and observation stations of current velocity and salinity.

2.2 Description and configuration of the numerical model

This study applied the Environment Fluid Dynamic Code (EFDC) (Hamrick, 1992; Hamrick and Wu, 1997) to simulate the hydrodynamics and water transport processes. EFDC can simulate drying and wetting processes in intertidal regions (Ji et al., 2001), and had been successfully applied in numerous estuarine regions worldwide to solve hydrodynamic and water quality problems (Xia et al., 2007; Xu et al., 2008; Yang et al., 2015). To accurately simulate the hydrodynamics and water transport in the Deep Bay with an extensive area of intertidal wetlands, a three-dimensional numerical model was generated.

The simulation domain covered the whole Pearl River Estuary as the hydrodynamics at the mouth region of the Deep Bay was dynamic and intricate due to the complicated bay bathymetry. The horizontal grids, as shown in Figure 1a, consisted of about 4500 active orthogonal curvilinear grids. To balance computational efficiency and accurate coastline interpretation, the grid size varied between fine to coarse from the Deep Bay to the adjacent sea. Sigma coordinate was used in the vertical direction with 10 evenly divided layers. The computational time step was set to be 5 s to ensure the maximum Courant number to be below 0.6.

2.3 Simulation scenarios for SLR

Three scenarios were developed to simulate the hydrodynamics and water transport with different sea levels. The real condition in the year of 2007 was simulated and used as a baseline. Two potential future SLR scenarios were developed with sea-level elevated by 0.3 m and 0.5 m, respectively, to represent the projected condition in the years of 2037 and 2057. The scenarios of baseline, 0.3 m and 0.5 m SLR were named as cases 2007, 2037 and 2057. In the case of 2037 and 2057, all the conditions were kept identical with the baseline except the sea-level at the sea open boundary. Each simulation was conducted for two years, and the first year was used as a warm-up while the second was used for analysis.

2.4 Hydrodynamic and water transport indicators

To better quantify the differences in hydrodynamics and water transport processes among the cases, stratification strength and water age were used as indicators in addition to current velocity, tidal prism, tidal energy flux and salinity. Stratification strength represents the change of salinity gradient in the vertical direction and thus the stratification condition inside of the bay. The square of the Brunt Väisälä Frequency, N^2, was calculated (Knauss, 1978) to quantify the stratification strength for each computational grid inside the bay as follows:

$$N^2 = \frac{g}{\rho}\frac{\partial \rho}{\partial z} \qquad [1]$$

where g is the gravitational constant, ρ is the water density, and $\frac{\partial \rho}{\partial z}$ is the vertical density gradient. N^2 was also averaged over the whole analysis simulation year to represent the general condition for each case.

Water age reflects the time scale for any dissolved substance to be transported from the boundary of an estuarine region to a given location inside of the estuarine. It had already been confirmed that the variations of nutrients and phytoplankton growth in estuarine regions are well correlated with the simulated water age from numerical models (Shen and Haas, 2004). Therefore, water age could be employed to indicate the change in water transport processes in estuarine regions when assessing the impacts of SLR. The definition of water age in the study of Takeoka (1984) had been applied in this study, and that the age of a water particle is the time which has elapsed since it entered the region of interests. The transport equations for calculating the age of water were firstly developed by Delhez et al. (2004), and they also have been successfully applied in the studies of Shen and Wang (2007) and Li et al. (2010).

3 RESULTS AND DISCUSSIONS

3.1 Model validation

The simulation results of tidal elevation were validated with hourly observations throughout the year 2007 at five tidal gauges inside of the Pearl River Estuary (locations shown in Figure 1a). The correlation coefficients between simulated and observed data ranged from 0.911 to 0.977, which confirmed the performance of this model in simulating the dynamics of tidal water movement.

Tidal current speed and direction were also validated at stations T2 and T3 (locations shown in Figure 1b) inside of the Deep Bay. The mean errors for the current velocity at surface and bottom layers of T2 and T3, range from -0.024 to 0.075 m/s, and the associated RMS errors range from 0.075 to 0.181 m/s. The correlation coefficients were from 0.461 to 0.718, which further confirmed the performance of this model in simulating the hydrodynamics.

The monthly observed salinity data at stations S1 to S5 inside the Deep Bay (locations shown in Figure 1b) was acquired from the Environmental Protection Department of Hong Kong. Comparisons were made between the observed and simulated salinity at these five stations in 2007, and some example comparisons are shown in Figure 2. The seasonal trends of salinity at both bay mouth and inner bay have been well captured, and the model could also well simulate the salinity stratification at the bay mouth.

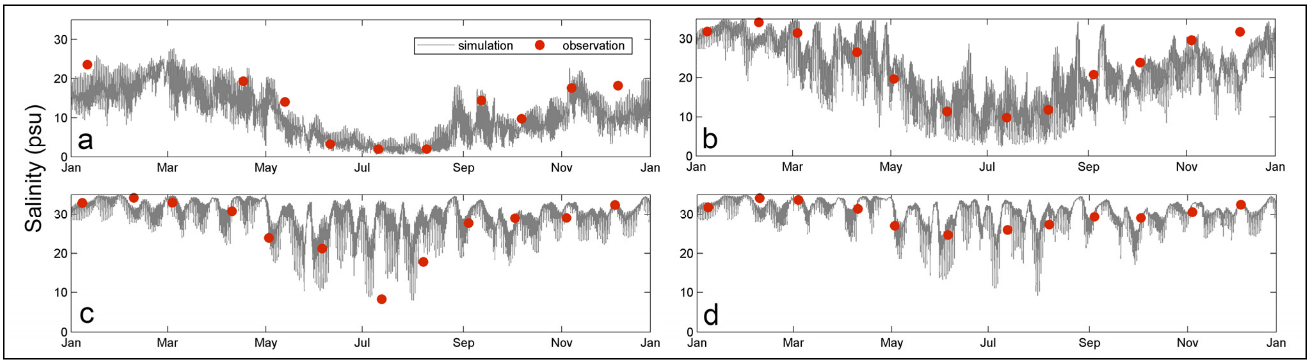

Figure 2. Comparison of simulated and observed salinity. (a) is the comparison in surface layer at S1, while (b), (c), and (d) are the comparisons in surface, middle and bottom layers at S5, respectively.

3.2 Impacts on hydrodynamics

The tidal prism, tidal currents, and tidal energy flux have been employed as hydrodynamic indicators to evaluate the SLR's impacts on hydrodynamics inside of the bay. Tidal prism indicates the volume of tidal water a bay and could inlet between a low tide and its subsequent high tide. The calculated tidal prism in cases of 2007, 2037 and 2057 are listed in Table 1. The tidal prism in 2037 increases by 9.1% with 0.3 m of SLR, and that in 2057 increases by 13.6% with 0.5 m of SLR. The incoming tidal energy represents the strength of the tidal force which governs the water transport process inside of the bay. With the rise of sea-level, the incoming tidal energy increases by 0.6 MW with 0.3 m SLR, and by 1.2MW with 0.5m SLR. The increase of incoming tidal energy is not strictly proportional to the SLR height, as the area transforming from intertidal into subtidal regions is different between each sea-level elevation, which would influence the change in tidal energy dissipation inside of the bay. The average salinity level for the whole bay increases with SLR, and increases from 28.3 psu to 28.8 psu when sea-level was elevated by the first 0.3 m, then to 29.1 psu with another extra 0.2 m SLR.

Table 1. Simulation results of tidal prism, incoming tidal energy and average salinity level for the whole bay in each case.

	Elevated sea-level (m)	Tidal prism ($\times 10^8$ m^3)	Incoming tidal energy (MW)	Average salinity level (psu)
2007	0	2.2	2.9	28.3
2037	0.3	2.4	3.5	28.8
2057	0.5	2.5	4.1	29.1

The spatial distributions of tidal current velocities during ebb and flood tide periods are shown in Figure 3. The overall patterns of current fields show minimal difference among the three cases. The only noticeable change in the current fields of 2037 and 2057 when comparing with that in 2007 is the slight reduction in current magnitude at the inner part of the bay. Using the current velocity at station S1 to represent the velocity around the intertidal mudflat, it was respectively decreased by 8.7% and 15.0% in magnitude for 2037 and 2057 comparing with that in 2007. The reduction of current velocity might benefit the sedimentation of suspended sediment and elevate the bathymetry of the intertidal mudflat and prevent it from being submerged by the rising sea-level.

The tidal energy fluxes in cases of 2007, 2037 and 2057 also present significant changes with SLR. The magnitude of tidal energy flux inside of the bay in 2037 and 2057 are significantly larger than that in 2007, which indicate a stronger tidal influence governing the hydrodynamics inside of the bay. The increase of tidal energy flux was mainly because of the increase of tidal prism with SLR. More tidal water would flush into the bay during flood tide, flush out of the bay during ebb tide, and the incoming tidal energy would also be consequently magnified.

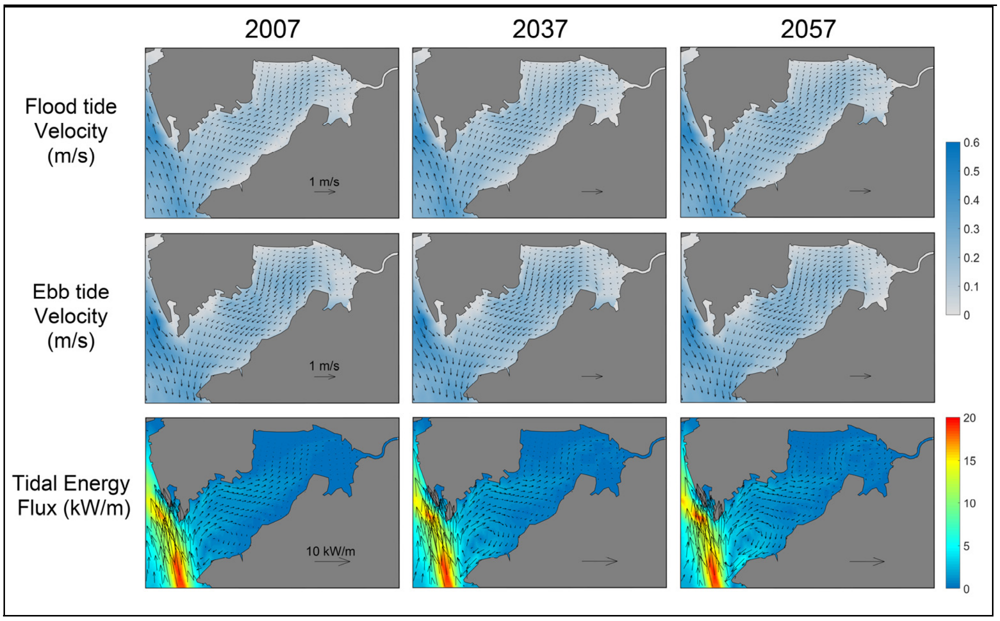

Figure 3. Spatial distribution of the simulated velocity and tidal energy flux in cases 2007, 2037 and 2057.

3.3 Impacts on water transport processes

Salinity, stratification strength, and water age have been used to indicate the water transport inside of the bay, and the spatial distributions of their yearly averages are shown in Figure 4.

The salinity gradient from the bay mouth to inner bay was about 25 psu in 2007, but has been reduced to around 20 psu in 2037 and 18 psu in 2057. The salinity levels at the bay mouth show less difference with SLR, but the impact of SLR was much more significant on the salinity at the inner bay which increases from 9.7 psu to 12.1, and 13.7 psu, respectively, in 2037 and 2057. The tongue of the saline water intrudes further upstream with the SLR along the northern coast of the bay while the salinity level along the southern coastline appears to be more resistant.

By comparing the stratification condition of each case in Figure 4, it could be found that the bay, especially the inner bay, becomes more stratified with the SLR. Shenzhen River is the main freshwater inflow for the bay. Its discharge into the inner bay is constant but the salinity level for the whole day is elevated. Therefore, the water at the inner bay becomes more stratified, which has an adverse impact on the circulation of water inside of the bay.

The spatial distributions of water age demonstrate the various water ages inside of the bay. In 2007, the time for the solute to transport from the outer part into the bay (i.e., the average water age for the whole bay) is 28.1 days on average, and it increases to respectively 28.8 and 29.2 days in 2037 and 2057. The increase in water age suggested a reduced water exchange ability of bay, which were probably a result of the increased stratification which inhibits the vertical mixing and thus the circulation of the bay. The inner bay is the most affected with an average increase of 3 days. The difference in the temporal variations of water age at the inner bay (i.e., station S1) among the cases is shown in Figure 5. The water age at the inner bay varies significantly over the year, and was larger in the dry season but smaller in the wet season. The impacts of SLR on the water age also show temporal difference, as the difference of water age reaches over 5 days during April and May between the cases of 2007 and 2057, but is less than 3 days during January and December. This should be mainly due to the seasonal difference of flow discharge from the Shenzhen River, which in the wet season is almost doubled than that in the dry season. In fact, the increase of tidal prism and tidal energy flux would improve the water exchange ability of the bay. However, the tidal energy flux only increased significantly at the outer and middle parts of the bay which can counteract the effect of increased stratification. Its increase was significantly less in the inner part of the bay.

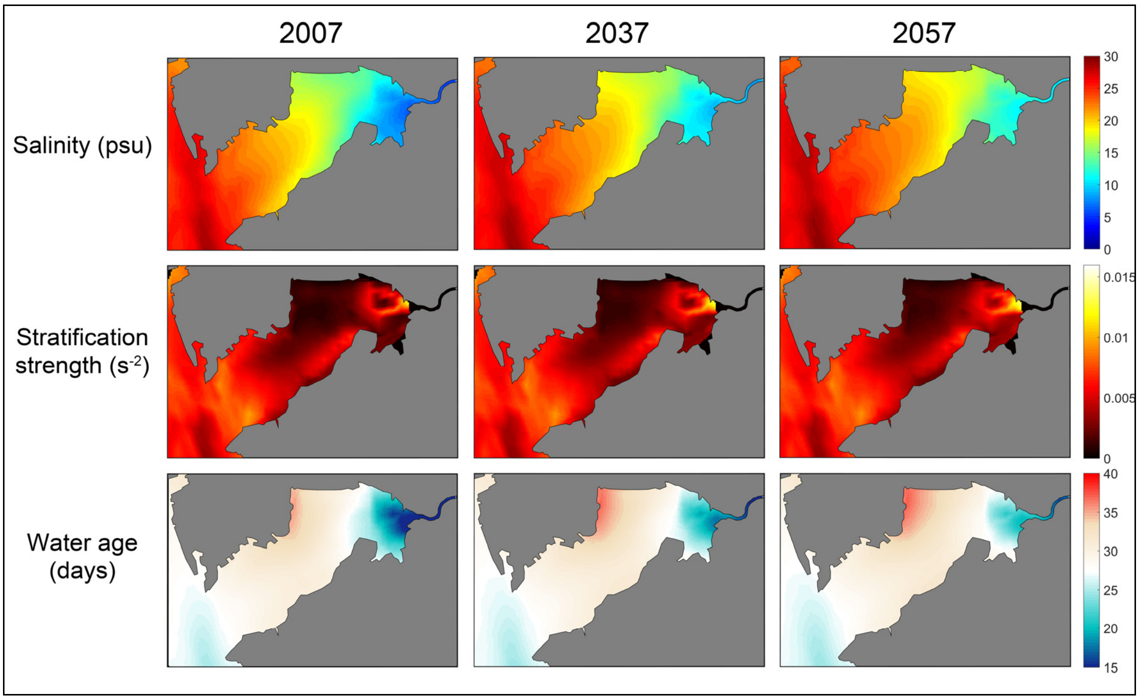

Figure 4. Spatial distribution of the simulated salinity, stratification strength, and water age in cases 2007, 2037 and 2057.

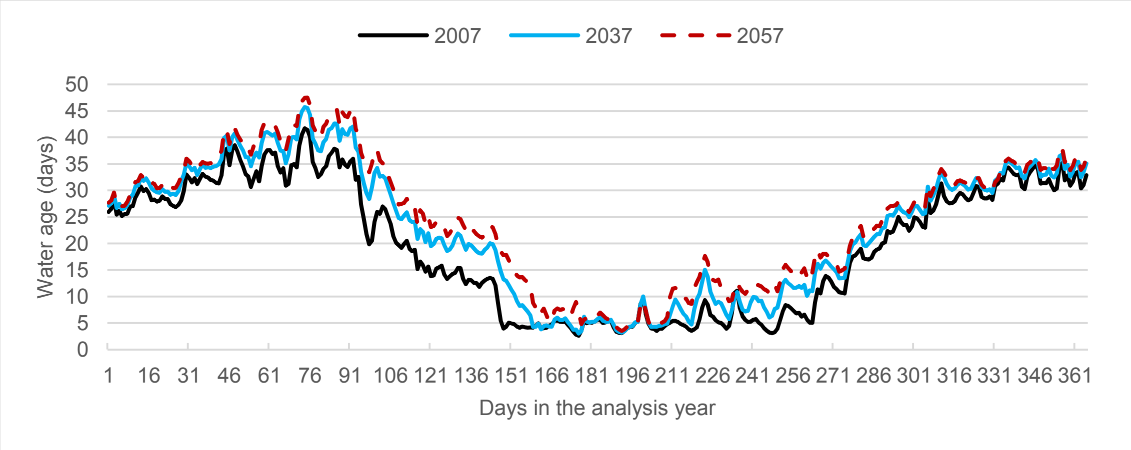

Figure 5. Temporal variations of water age at the inner bay.

3.4 Potential implications on aquatic environment

The SLR presents complicated impacts on the water transport processes inside of the bay. The most vulnerable regions of the bay to SLR is the inner part, where the salinity would increase but become more stratified, and the water age would also increase. The changes in salinity at inner bay might disturb the structure of the ecological environment in the tidal wetland ecosystem, as some species of fauna and flora are sensitive to the salinity level. Besides, some intertidal wetland might become subtidal with the SLR, which would threaten the flora and benthic fauna. The increased stratification and larger water age at the inner bay might also change the material circulation and the aquatic environment due to the longer residence time of the solute such as nutrients and pollutants. Some studies have already found that the nutrients loading from the upstream of the Shenzhen River have been increasing in the past decades (Xu et al., 2010). The possible increase in residence time of nutrient indicated by the water age in this study might pose more stress to the aquatic environment for eutrophication, as a larger water age would increase the activity of algae (Shen and Haas, 2004). More studies should be conducted to evaluate the possible water quality changes at the inner bay so that the aquatic environment can be better protected from the negative impacts of SLR in the future.

4 CONCLUSIONS

This study generated a three-dimensional numerical model to simulate the hydrodynamics and water transport process inside of the Deep Bay, Pearl River Estuary, China. The model has been validated with observed tidal elevation, current direction and velocity, and salinity, which confirmed the model's good performance in simulating the hydrodynamics and water transport process. Scenarios for potential future SLR have been designed to evaluate the changes in 2037 and 2057. Simulation results show that in 2037 and 2057, the tidal prism would be increased by 9.8% and 15.0%, and the incoming tidal energy flux would be magnified by 21.0% and 41.4%, respectively. These indicate that the tidal force governing the hydrodynamics of the bay has been substantially reinforced with the SLR. The tidal current field pattern inside of the bay would not change, but the current velocity slightly decreases at the inner bay. The yearly average salinity distribution would also substantially change as the saline water would intrude further upstream along the northern coastline. The salinity level changes at the bay mouth are relatively less, but that at the inner bay changes from 9.7 psu in 2007 to 12.1, and 13.7 psu, respectively, in 2037 and 2057. The stratification condition in the whole bay would also be enhanced with SLR, especially at the inner part. The water age of bay would also slightly increase in the whole bay scale, and most significantly at the inner part with a 3-day increase. The water exchange ability of the bay would reduce with the increase of both stratification and water age, and consequently the solute in water column at the inner bay would acquire a longer residence time in the future with SLR. This might lead to a series of environmental implications. Studies to evaluate the future changes in water quality due to SLR are needed to help protect the environment and ecosystem.

ACKNOWLEDGEMENTS

This work is funded by Seed Funding Programme for Basic Research of The University of Hong Kong (Project code: 201511159044).

REFERENCES

Chen, W.B., Liu, W.C., & Hsu, M.H. (2015). Modeling Assessment of a Saltwater Intrusion and a Transport Time Scale Response to Sea-Level Rise in a Tidal Estuary. *Environmental Fluid Mechanics* 15, 491-514.

Chua, V.P. & Xu, M. (2014). Impacts of Sea-Level Rise on Estuarine Circulation: An Idealized Estuary and San Francisco Bay. *Journal of Marine Systems* 139, 58-67.

Delhez, É.J., Heemink, A.W. & Deleersnijder, É. (2004). Residence Time in a Semi-Enclosed Domain from the Solution of an Adjoint Problem. *Estuarine, Coastal and Shelf Science,* 61, 691-702.

Hamrick, J.M. (1992). *A Three-Dimensional Environmental Fluid Dynamics Computer Code: Theoretical and Computational Aspects*. Virginia Institute of Marine Science, College of William and Mary, 126.

Hamrick, J.M. & Wu, T.S. (1997). *Computational Design and Optimization of the EFDC/HEM3D Surface Water Hydrodynamic and Eutrophication Models, Next Generation Environmental Models and Computational Methods*. Society for Industrial and Applied Mathematics, Philadelphia, PA, 143-161.

Huang, Z., Zong, Y. & Zhang, W. (2004). Coastal Inundation due to Sea Level Rise in the Pearl River Delta, China. *Natural hazards,* 33, 247-264.

IPCC. (2001). *The Scientific Basis*. Cambridge, United Kingdom and New York, NY. USA: Cam bridge University Press.

Ji, Z.G., Morton, M.R. & Hamrick, J.M. (2001). Wetting and Drying Simulation of Estuarine Processes. *Estuarine. Coastal and Shelf Science,* 53, 683-700.

Knauss, J.A. (1978). *Introduction to Physical Oceanography*. Prentice-Hall International, Inc, 320.

Kuang, C., Chen, W., Gu, J., Zhu, D.Z., He, L. & Huang, H. (2014). Numerical Assessment of the Impacts of Potential Future Sea-Level Rise on Hydrodynamics of the Yangtze River Estuary, China. *Journal of Coastal Research,* 30, 586-597.

Li, Y.P., Acharya, K., Chen, D. & Stone, M. (2010). Modeling Water Ages and Thermal Structure of Lake Mead Under Changing Water Levels. *Lake and Reservoir Management,* 26, 258-272.

McGranahan, G., Balk, D. & Anderson, B. (2007). The Rising Tide: Assessing the Risks of Climate Change and Human Settlements in Low Elevation Coastal Zones. *Environment and urbanization,* 19, 17-37.

Nicholls, R.J. & Cazenave, A. (2010). Sea-Level Rise and its Impact on Coastal Zones. *Science* 328, 1517-1520.

Qiu, C. & Zhu, J. (2013). Assessing the Influence of Sea Level Rise on Salt Transport Processes and Estuarine Circulation in the Changjiang River Estuary. *Journal of Coastal Research,* 31, 661-670.

Shen, J. & Haas, L. (2004). Calculating Age and Residence Time in the Tidal York River using Three-Dimensional Model Experiments. *Estuarine, Coastal and Shelf Science,* 61, 449-461.

Shen, J. & Wang, H.V. (2007). Determining the Age of Water and Long-Term Transport Timescale of the Chesapeake Bay. *Estuarine, Coastal and Shelf Science,* 74, 585-598.

Takeoka, H. (1984). Fundamental Concepts of Exchange and Transport Time Scales in a Coastal Sea. *Continental Shelf Research,* 3, 311-326.

Xia, M., Xie, L. & Pietrafesa, L. (2007). Modeling of the Cape Fear River Estuary plume. *Estuaries and Coasts,* 30, 698-709.

Xu, H., Lin, J. & Wang, D. (2008). Numerical Study on Salinity Stratification in the Pamlico River Estuary. *Estuarine, Coastal and Shelf Science,* 80, 74-84.

Xu, J., Yin, K.D., Lee, J.H.W., Liu, H.B., Ho, A.Y.T., Yuan, X.C. & Harrison, P.J. (2010). Long-Term and Seasonal Changes in Nutrients, Phytoplankton Biomass, and Dissolved Oxygen in Deep Bay, Hong Kong. *Estuaries and Coasts,* 33, 399-416.

Yang, Y., Chen, X.F., Li, Y.Y., Xiong, M. & Shen, Z.Y. (2015). Modeling the Effects of Extreme Drought on Pollutant Transport Processes in the Yangtze River Estuary. *JAWRA Journal of the American Water Resources Association,* 51, 624-636.

Yin, J., Schlesinger, M.E. & Stouffer, R.J. (2009). Model Projections of Rapid Sea-Level Rise on the Northeast Coast of the United States. *Nature Geoscience* 2, 262-266.

Yuan, R., Zhu, J. & Wang, B. (2015). Impact of Sea-Level Rise on Saltwater Intrusion in the Pearl River Estuary. *Journal of Coastal Research,* 31, 477-487.

  / ISSN 1562-6865 (Online) - ISSN 1063-7710 (Print)

DEVELOPMENT OF THREE-DIMENSIONAL WATER QUALITY MODEL AND ITS APPLICATION TO A LONG-NARROW BAY

SONGLIN HAN[(1)], SHUXIU LIANG[(2)] & ZHAOCHEN SUN[(3)]

[(1)] Changjiang River Scientific Research Institute, Wuhan, China
hansl86@qq.com
[(1,2,3)]State Key Laboratory of Coastal and Offshore Engineering, Dalian University of Technology, Dalian, China
sliang@dlut.edu.cn; zcsun@dlut.edu.cn

ABSTRACT

Water quality simulation in bays is an important foundation for water environmental planning and evaluation, pollution control and treatment. A water quality model involving phytoplankton kinetics, nitrogen and phosphorus cycles， DO and CBOD, was developed based on the three-dimensional hydrodynamic model in a long-narrow bay, in China. The model can simulate not only the physical processes of the water quality variables, but also the chemical and biological processes. To resolve the difficulty in parameters selection and determination, a parameters optimisation method based on data driven theory was developed. Then, the parameters were selected and optimised based on the measured data. The simulated results matched well with the measured data and reproduced the spatial-temporal variation of the water quality variables in Xiangshan bay, which verified the effectiveness of the model parameters optimisation method.

Keywords: Three-dimensional; water quality model; numerical simulation; Xiangshan Bay.

1 INTRODUCTION

Using water quality models to describe and simulate water quality in rivers, lakes and bays is an important foundation and prerequisite for water environmental planning and evaluation, pollution control and treatment. A large amount of researches have been conducted on the development of water quality models to study the characteristics of pollution transport in waters. For example, Skerratt (2013) developed a three-dimensional hydrodynamic, sediment and ecosystem dynamics mathematical model to study the changes in nutrients in the Derwent estuary. Based on an unstructured three-dimensional hydrodynamic model (FVCOM) and water quality model (WASP), Justice (2014) simulated the temporal-spatial changes of low-oxygen zones in the Inner Louisiana-upper Texas shelf.

However, it is challenging to establish and calibrate water quality models. Dynamic water quality models generally include tens of water quality variables and dozens of model parameters. For instance, the DYRESM water quality model developed by Schladow (1997) contains 13 state variables and 28 model parameters. The eutrophication module of the WASP (Ambrose et al., 2006) model, which has been widely applied, includes 8 state variables and 36 model parameters. The selection and determination of these parameters have been a focus of research. A number of parameter estimation procedures have been proposed, such as the trial and error method (Schladow et al., 1997), the adjoint method (Schartau et al., 2001; Shen et al., 1998) and the direct minimisation method (Shen, 2006; Matear, 1995). The function approximation method (Gutmann, 2001) is an effective approach to improve parameter estimation and uncertainty analysis of computational models. Use of learning machines to approximately replace the complex and time-consuming water quality models has been applied in several studies. For example, the neural network method was selected as the data-driven model to surrogate the water quality model for evaluation of parameter selection (Afshar et al., 2012; Zhang et al, 2009) and water quality management (Zou et al., 2012).

In the present study, the function of the approximation method was applied to surrogate the WASP model and the LS-SVM was used as the data-driven model. Then, the Particle Swarm Optimisation algorithm (PSO) was used to search for the optimal parameters. The results can provide guidance for selection of control parameters.

2 MATERIAL AND METHOD

2.1 Study area

The study area was XSB (121°25′E~122°00′E, 29°23′N~29°49′N) (as shown in Figure. 1), which is located along the central coast of Zhejiang Province, China. The bay is a semi-closed narrow-shaped bay with complex topography. It is 62.8 km long from the mouth of the bay to the head and varies in width from 20 km near the mouth to a minimum of 3 km in the middle of the bay. XSB is a strong-tide bay. There are several streams along the coastline and the total annual runoff is $1.2×10^9$ m^3.

Xiangshan Bay, the largest aquaculture base of Zhejiang province, has an excellent aquaculture condition. In the past three decades, the mariculture and harbour industries in the coastal areas developed rapidly, but a large amount of agricultural waste, industrial sewage and pollutants were discharged into the bay. Eutrophication has become a serious problem in the bay and red tides occasionally occur. Understanding the transport characteristics of water quality state variables can provide scientific guidance for water environmental protection.

The water quality indicators were monitored in XSB at the Ningbo Marine Environmental Monitoring Station from April to October in 2009. The monitoring frequency was twice per month, and there were 13 stations in the study area (as shown in Figure. 1). The monitored water quality indicators included water temperature T (℃), Seawater Transparency ST (m), pH, Salinity S (psu), Chemical Oxygen Demand COD (mg/L), Dissolved Oxygen DO (mg/L), Dissolved Oxygen Saturation DO% (%), Inorganic Phosphorus OPO_4 (mg/L), Nitrite NO_3 (mg/L), Nitrate NO_2 (mg/L), Ammonia NH_3 (mg/L) Silicate Si (mg/L) and Chlorophyll-a Chl-a (μg/L). The above measured data were used to analyse the relationship among the water quality indicators and to verify the water quality model.

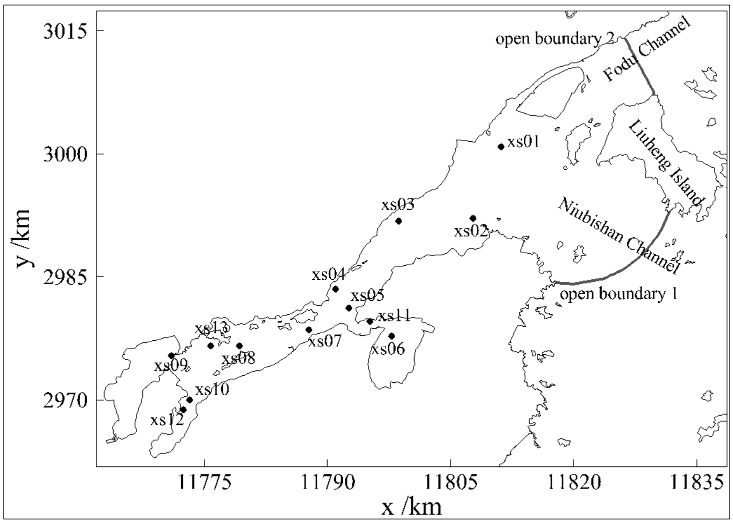

Figure 1. The study area of XSB and the monitoring stations.

2.2 Water Quality model

The dynamic water quality model was developed based on the EUTRO module of the WASP model (Ambrose et al., 2006). The hydrodynamic field was supplied by the improved FVCOM (Chen et al., 2006; Liang et al., 2014), which was successfully applied in our study area. The water quality model involves phytoplankton kinetics, the dissolved oxygen balance, and the nitrogen and phosphorus cycles. The water quality variables include DO, carbonaceous biochemical oxygen demand (CBOD), phytoplankton (PHYT), NH_3, NO_3+NO_2, organic nitrogen (ON), OPO_4 and organic phosphorus (OP). The kinetic process of the model is shown in Figure 2. The governing equations and parameters for describing the kinetic processes could be referred to the literature (Liang et al., 2014).

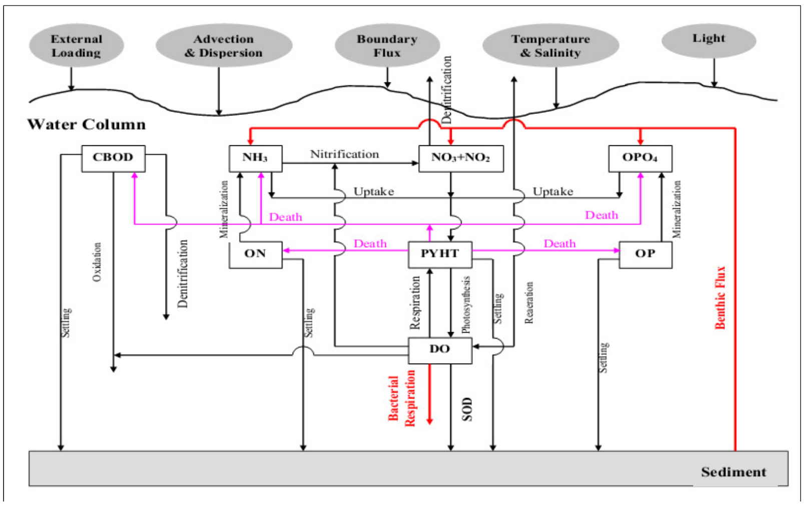

Figure 2. The water quality state variable interactions in the water quality model (Chen et al., 2006).

2.3 Data-driven method

Support vector machines (SVMs) (Vapnik, 1999) are powerful learning machines based on statistical learning methodology for classification and function estimation. The method was developed within the area of statistical learning theory and structural risk minimisation. The basic idea is mapping the input data into a higher dimensional space via nonlinear mapping and constructing an optimal separating hyperplane or regression equation in this space. LS-SVM, proposed by J.A.K suykens et al. (1999; 2002) is an extended version of the standard SVM. Different from the standard SVM, LS-SVM takes a squared loss function for the error variable and uses equality constraints instead of inequality constraints. As a result of these modifications, the problem changes from a Quadratic Programming (QP) problem into a linear system, which makes LS-SVM easier in terms of training. LS-SVM has been widely applied in fields of pattern recognition, classification and function estimation (Zhang et al., 2011; Pijush et al., 2012). A regression algorithm based on LS-SVM is called the least square support vector regression (LS-SVR). The detailed algorithm description could be referred to Suykens et al. (2002).

In actual application, we need to choose the appropriate kernel function and corresponding kernel parameters according to certain conditions. In our study, the RBF kernel was selected as the kernel function because it has been widely used in nonlinear function estimation and is suitable for most types of conditions. The width parameter of the RBF kernel function, σ and the regularisation factor, γ are kernel parameters that should be determined for model accuracy and reliability. They were optimised by the grid search method in our research, which was efficient for models with fewer parameters (Hsu et al., 2008).

3 WATER QUALITY MODEL IN XIANGSHAN BAY

3.1 Model setup

The hydrodynamic fields in the study area were simulated based on the FVCOM model and the detailed configuration of Liang et al. (2014), Han et al. (2014). The water quality was simulated by coupling with the hydrodynamic model. The calculation area and the mesh generation of the water quality model were consistent with the hydrodynamic model. The computation area included Xiangshan Bay, Fodu channel, and Niubishan Channel, and the open boundary was divided into two parts by Liuheng Island (Figure. 1). There were 18,645 elements and 9,958 nodes in the study area, and six sigma layers were adopted vertically. The initial conditions of the water quality state variables were obtained from the measured data via data interpolation. The inputs of land-based outlets and mariculture discharges along the coast were considered in the model. Based on the estimated waste loads from Huang (2010), the seasonal average waste loads were given. The model parameters could be referred to Liang et al. (2014). The numerical simulation time occurred from Jan. 1 to Nov. 1 in 2009. The output results from April to October were analysed.

3.2 Control parameter selection

The processes of control parameter selection are shown in Figure. 3. The data-driven model was established to describe the relationship between Chlorophyll-a and water environmental factors on the basis of the measured data. Using the model, the relationship between Chlorophyll-a and the water environmental factors was analysed by the Mean Impact Value (MIV) index. Then, parameter sensitivity analysis of the dynamic water quality model was conducted. According to the above results, the control parameters of each water quality variable were determined.

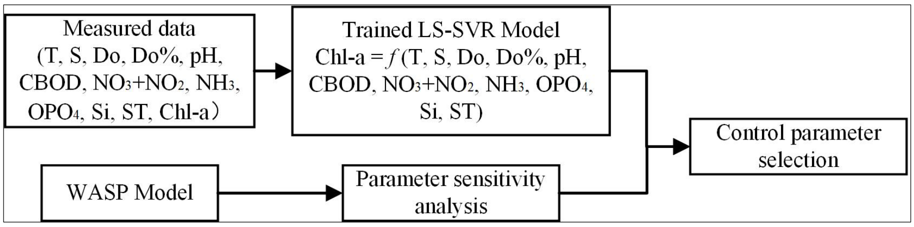

Figure 3. The flowchart of control parameter selection.

The MIVs of all of the water environmental factors to Chl-a in XSB are listed in Table. 1. The results showed that the highest MIV to Chl-a is CBOD. The second group included DO%, S, DO, and T, and the remaining factors had a lower influence. This result indicated that CBOD has a powerful ability to characterise Chl-a. This suggests that detrital phytoplankton carbon, produced as a result of algal death, is a principal source of CBOD. As photosynthesis occurs, the rate of DO is proportional to the growth rate of the phytoplankton. However, oxygen is diminished due to phytoplankton respiration. The higher MIV of DO and DO% to Chl-a suggested that photosynthesis is a major process changing DO. Water temperature and salinity have direct effects on phytoplankton growth and death. It can be concluded that the higher temperature and salinity as a whole are well suited for phytoplankton in XSB. The lower MIV of Nutrients to Chl-a may be due to the rich nitrogen and phosphorus in XSB, which is sufficient for phytoplankton intake (Liu et al., 2013).

Table 1. MIV of water environment factors to Chl-a in XSB.

No.	Environment factors	MIV	No.	Environment factors	MIV
1	CBOD	3.379	7	Si	-0.236
2	DO%	0.860	8	ST	0.195
3	S	0.802	9	pH	0.146
4	DO	0.616	10	NO_3	0.100
5	T	0.605	11	NH_3	-0.016
6	OPO_4	-0.240			

Parameter sensitivity analysis plays an important role in the parameter selection, optimisation and uncertainty analysis. Parameter sensitivity analysis of the water quality model in XSB was performed using the OAT (one-at-a-time) method. Ten of 36 parameters were selected for the analysis because these parameters were generally sensitive in most of the area. The assigned ranges of each parameter are listed in Table. 2.

Table 2. Parameters and assigned ranges used for sensitivity analysis.

Parameter No.	Name	Value	Assigned range	Unit	Description
1	k_{deox}	0.16~0.21	Max/min	d^{-1}	Deoxygenation rate at 20℃
2	k_{ni}	0.09~0.13	Max/min	d^{-1}	Nitrification rate at 20℃
3	k_{resp}	0.05~0.2	Max/min	d^{-1}	Phytoplankton respiration rate at 20℃
4	k_{deni}	0.09	±30%	d^{-1}	Denitrification rate at 20℃
5	k_{gr}	2	±30%	d^{-1}	Optimum phytoplankton growth rate at 20℃
6	k_{mort}	0.02~0.04	Max/min	d^{-1}	Mortality rate of phytoplankton at 20℃
7	k_{mine1}	0.075	±50%	d^{-1}	Organic nitrogen mineralisation at 20℃
8	k_{mine2}	0.22	±50%	d^{-1}	Organic phosphorus mineralisation at 20℃
9	*SOD*	0.2	±50%	$g\ m^{-2}\ d^{-1}$	Sediment Oxygen Demand at 20℃
10	I_S	200~500	Max/min	ly/day	Optimum light intensity

The effect of each parameter was estimated via changing this parameter and keeping all others fixed at their original values. Variations of the minimum, mean and maximum of the water quality state variables at 13 stations on July 20, 2009, were selected to evaluate the sensitivity degree of each parameter. The results are shown in Figure. 4. The grey, shadow, and white colour of the bars represent the minimum, mean and maximum of water quality at 13 measured stations, respectively. The left and right histograms represent the decreases and increases of the parameters in their assigned ranges, respectively.

It can be seen that the parameters have different effects on the water quality state variables. The parameters that affect phytoplankton concentration include the optimum phytoplankton growth rate (k_{gr}), phytoplankton respiration rate (k_{resp}), phytoplankton mortality rate (k_{mort}) and optimum light intensity (I_S). The changes in phytoplankton concentration also influence the other water quality state variables, such as DO, CBOD, NH_3, NO_3+NO_2, OPO_4, ON, and OP. In addition, CBOD was also affected by the deoxygenation rate (k_{deox}), and DO was affected by the Sediment Oxygen Demand (*SOD*). NO_3, NH_3, and ON (OPO_4 and OP) were sensitive to organic nitrogen mineralisation (k_{mine1}) (organic phosphorus mineralisation (k_{mine2})). This finding indicated that nitrogen (phosphorus) mineralisation decomposes organic nitrogen (phosphorus) into ammonia nitrogen (organic phosphorus), and this kinetic process was the major process for the nutrients in XSB.

In summary, the phytoplankton concentration has a close relationship with CBOD and DO, and these variables have the same sensitivity parameters. The parameters that affect phytoplankton also influence other water quality variables both directly and indirectly. Therefore, these parameters should be determined as a priority. Other parameters, such as k_{mine1} and k_{mine2}, have little influence on phytoplankton and can thus be optimised individually.

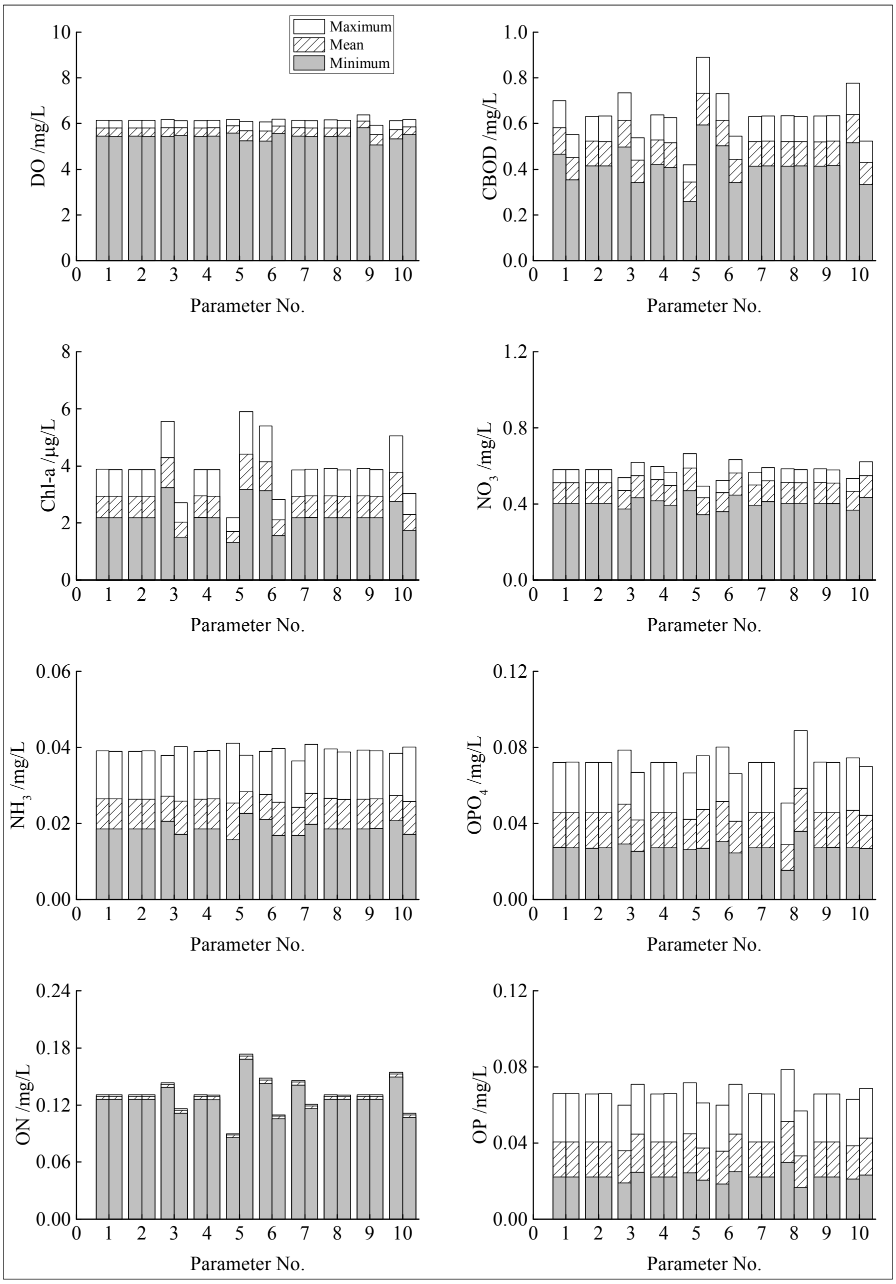

Figure 4. Sensitivity analysis results of parameters on July 20, 2009.

The control parameters of each water quality variable and the optimisation sequence are listed in Table. 3. Table. 3 shows that four parameters affect phytoplankton concentration, CBOD and DO and thus have to be optimised together.

Table 3. Parameters and assigned ranges used for sensitivity analysis.

Water quality variable	Control parameters
Chl-a, CBOD, DO	k_{gr}, k_{resp}, k_{mort}, I_S
CBOD	k_{deox}
DO	*SOD*
NH_3, NO_3, ON	k_{mine1}
OPO_4, OP	k_{mine2}

3.3 Parameter optimisation estimation

The PSO algorithm was utilised to optimise the control parameters of the water quality model. It is a population-based evolutionary algorithm that has been applied in optimisation problems in various fields (Poli, 2008). Like other evolutionary algorithms, PSO searches for the best parameter combination by iteratively trying to improve a candidate solution with regard to a given measure of quality. The optimisation objective function expressed the agreement between the measured data and the simulated results. In our study, the RMSE between simulation and measured data were calculated as the objective function.

For the WASP model, the input data generally included geometric data, initial and boundary conditions, and kinetic parameters. The output data are the simulated concentration of water quality state variables. When the geometric data, initial and boundary conditions are fixed, the simulated results and the simulated errors are related to the parameters. They became functions of the parameter values. By running the WASP model with different parameter values, the corresponding results are obtained. The data can be used to train the LS-SVR model to approximate the input-output response relationships between the parameters and outputs of the water quality model. Then, the LS-SVM model embedded in the PSO algorithm can perform parameter optimisation.

Figure 5 shows the comparison between the measured data and the simulated results with the optimised parameters. The verification area contrasted the measured data used in the process of parameter optimisation with the simulated data. The results showed a reasonable agreement between the measured data and simulated data. The RMSEs of Chl-a, CBOD, and DO were 3.64 μg/L, 0.57 mg/L, and 1.7 mg/L, respectively, which were similar to the results of the LS-SVR model. This finding indicated that the LS-SVR model has reliable precision. To verify the prediction accuracy and the computational stability of the model, the water quality model continued to simulate for another two months until Nov. 1, 2009. The results are shown in the predicted area in Figure 5 and showed the correct changing tendency of water quality variables with the measured data. However, the simulated results have large divergences from the measured values at some points. The cause of these divergences were analysed in the following discussions.

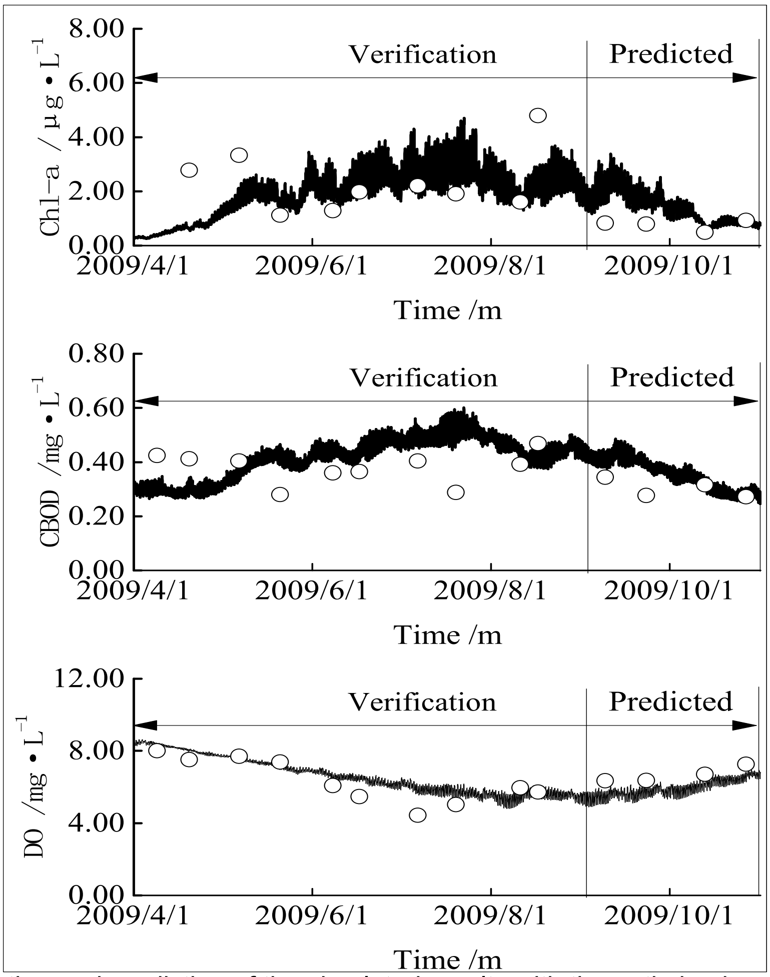

Figure 5. The verification and prediction of the simulated results with the optimised parameter (with the XS04 station used as an example).

Figure 6 shows the results of the measured and simulated concentrations of the eight variables at station XS04. The results indicated that the simulations were consistent with the measured data and reflected the seasonal variation of the water quality state variables.

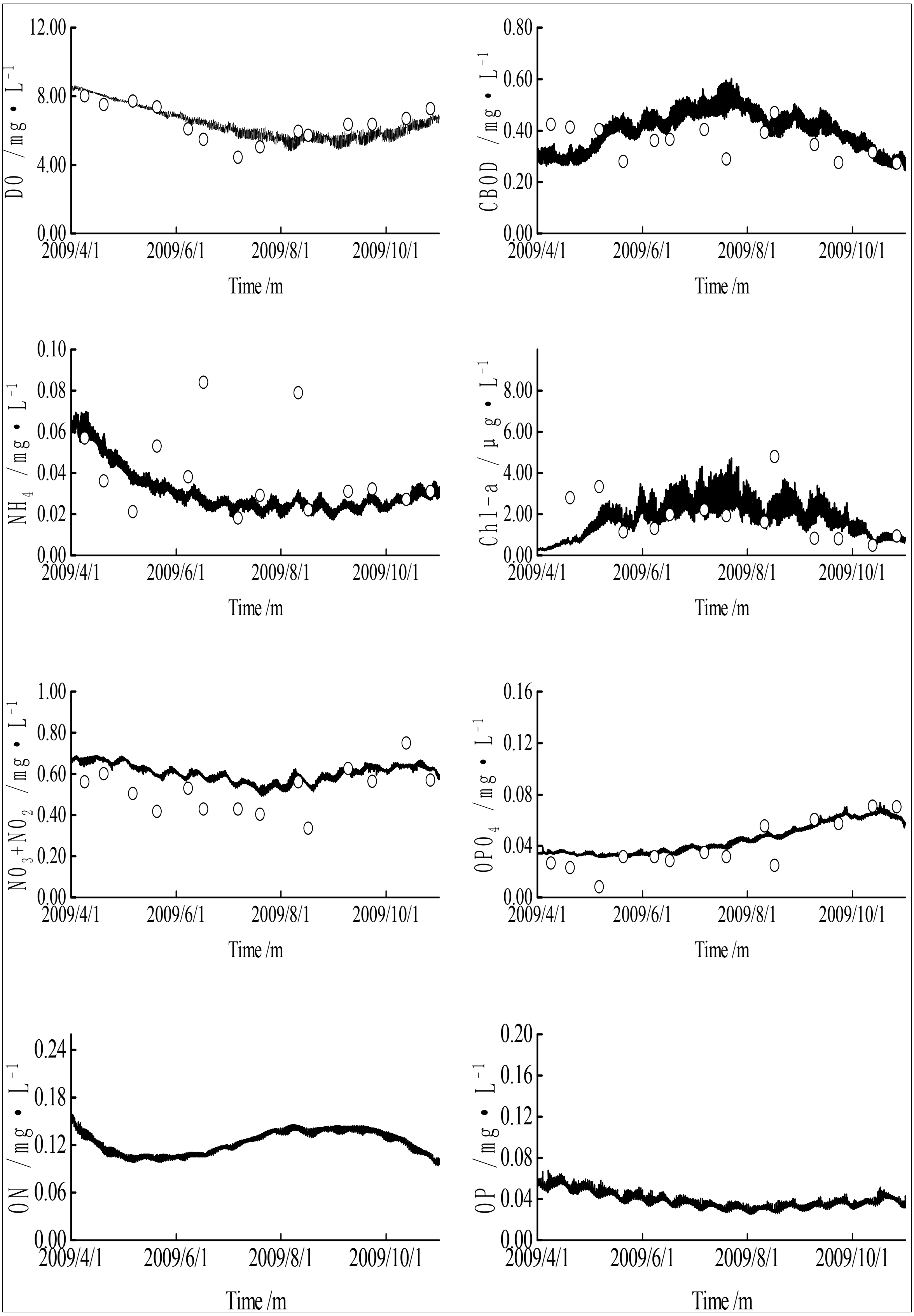

Figure 6. Time series of the model-simulated results and measured data for the eight water quality state variables at station XS04 (Open circles represent monitoring data, and black lines represent model results.

Figure 7 shows the distribution of Chl-a, DO, nutrients in Xiangshan Bay on July 20, 2009. It indicated that the highest concentration of DO was in the mouth of the bay and decreased from the mouth to the head of the bay. The concentration of Chl-a increased from the mouth to the head of bay. The highest concentration of CBOD, NH_3 and NO_3, OPO_4 occurred in the three sub-bay because of the land-based outlets and mariculture discharges in it.

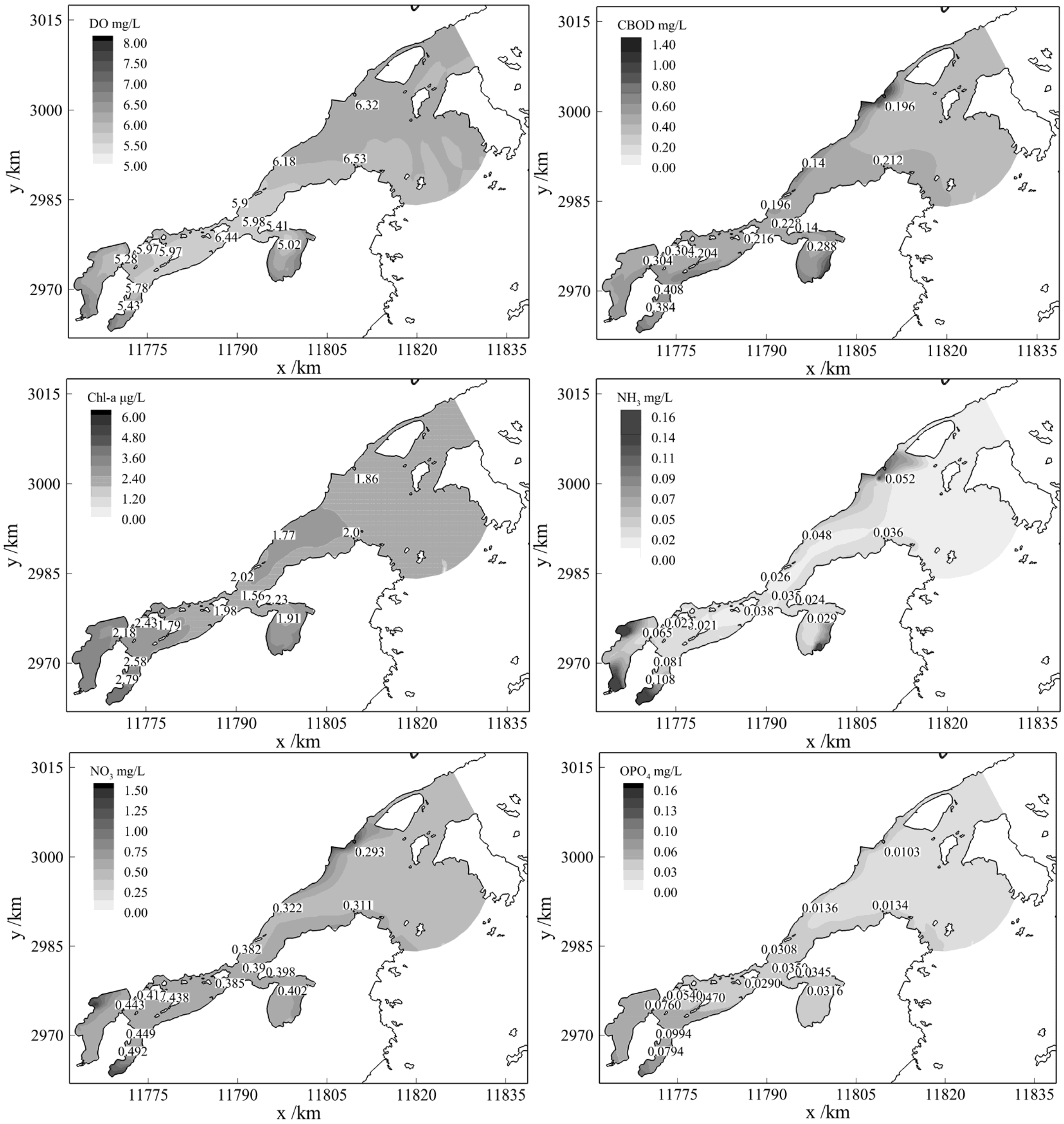

Figure 7. Distribution of Chl-a, DO, nutrients in Xiangshan Bay. (July, 20, 2009)

4 CONCLUSIONS

A water quality model involving phytoplankton kinetics, nitrogen and phosphorus cycles， DO and CBOD, has been developed based on the three dimensional hydrodynamic model. To resolve the difficulty in parameters selection and determination, a parameter optimisation method for a water quality dynamic model has been developed based on the data-driven LS-SVM model and the PSO algorithm. The method applied LS-SVM to study the eutrophication processes based on the measured data in the study area. Together with the results of parameter sensitivity analysis, the control parameters of the water quality state variables and the optimisation sequence of the parameters were determined. Then, the LS-SVM model has been developed to approximate the parameter-simulated results response relationship of the WASP model. The data-driven model has been embedded in the PSO algorithm for the parameter optimisation. The simulated results matched well with the measured data and reproduced the spatial-temporal variation of the water quality variables in Xiangshan bay, which verified the effectiveness of the model parameters optimisation method.

ACKNOWLEDGEMENTS

The research reported herein was funded by National Natural Science Foundation of China (Grant No. 51609022) and Open Project of State Key Laboratory of Coastal and Offshore Engineering (Grant No. LP1605).

REFERENCES

Ambrose, R. B., Wool, T. A. & Martin, J.L. (2006). *The Water Quality Analysis Simulation Program, WASP5, Part A: Model Documentation*, Environmental Research Laboratory Athens, Georgia.

Afshar, A. & Kazemi H. (2012). Multi Objective Calibration of Large Scaled Water Quality Model Using a Hybrid Particle Swarm Optimization and Neural Network Algorithm. *KSCE Journal of Civil Engineering*. 16(6), 913-918.

Chen, C., Beardsley, R. & Cowles, G. (2006). An Unstructured Grid, Finite-Volume Coastal Ocean Model (FVCOM) System. *Journal of Oceanography*, 19(1), 78 - 89.

Gutmann, H. M. (2001). A Radial Basis Function Method for Global Optimization. *Journal of Global Optimization*, 19(3), 201 - 227.

Hamilton, D. P. S. (1997). Prediction of Water Quality in Lakes and Reservoirs. *Part I — Model description*, *Ecological Modelling*, 96(1), 91 - 110.

Han, S.L., Liang, S.X. & Sun, Z.C. (2014). Numerical Simulation of Tides, Tidal Currents and Temperature-Salinity Structures in Xiangshan Bay Based on FVCOM. *Journal of Waterway and Harbor,* 5, 481-488.

Hsu, C., Chang, C. & Lin, C. (2008). *A Practical Guide to Support Vector Classification*, Department of Computer Science, National Taiwan University, Taipei 106, Taiwan.

Huang, X.Q., Wang, J.H. & Jiang, X. (2008). *Marine Environmental Capacity and Pollution Total Amount Control Research in Xiangshan Bay.* Beijing Oceanpress.

Justić D, Wang L. (2014). Assessing Temporal and Spatial Variability of Hypoxia over the Inner Louisiana–Upper Texas Shelf: Application of an Unstructured-Grid Three-Dimensional Coupled Hydrodynamic-Water Quality Model. *Continental Shelf Research*, 72(1), 163-179.

Liang, S., Han, S. & Sun, Z. (2014). Lagrangian Methods for Water Transport Processes in a Long-Narrow Bay- Xiangshan Bay, China. *Journal of Hydrodynamics, Series B*, 26(4), 558-567.

Liu, L., Ren, M. & Hua, M.M. (2013). Studies on the Ecology of Phytoplankton in summer in Western Xiangshan Bay I. Species Composition and Inter-Annual Variation. *Marine Sciences*, 5, 94-99.

Matear, R J. (1995). Parameter Optimization and Analysis of Ecosystem Models Using Simulated Annealing: A Case Study At Station P. *Journal of Marine Research*, 53(4), 571-607.

Ningbo Ocean & Fishery Bureau, (2008). *Aquaculture layout planning in Xiangshan Bay*, Ningbo.

Pijush, S. & Pradeep K. (2012). Multivariate Adaptive Regression Spline and Least Square Support Vector Machine for Prediction of Undrained Shear Strength of Clay. *International Journal of Applied Metaheuristic Computing (IJAMC)*, 3(2), 33-42.

Piotrowski, A. P. & Napiorkowski, J. J. (2013). A Comparison of Methods to Avoid Overfitting in Neural Networks Training in the Case of Catchment Runoff Modelling. *Journal of Hydrology*. 476(1), 97-111.

Poli R. (2008). Analysis of the Publications on the Applications of Particle Swarm Optimization. *Journal of Artificial Evolution and Applications*, 685175, 1-10.

Schladow, S.G. & Hamilton, D.P. (1997). Prediction of Water Quality in Lakes and Reservoirs: Part II - Model Calibration, Sensitivity Analysis and Application. *Ecological Modelling*. 96(1-3), 111-123.

Schartau, M., Oschlies, A. & Willebrand, J. (2001). Parameter Estimates of a Zero-Dimensional Ecosystem Model Applying the Adjoint Method. *Deep-Sea Research Part II*, 48(8), 1769 - 1800.

Shen, J. (2006). Optimal Estimation of Parameters for an Estuarine Eutrophication Model. *Ecological Modelling*. 191(3), 521 - 537.

Shen, J.A.Y.K. (1998). Application of Inverse Method to Calibrate Estuarine Eutrophication Model. *Journal of Environmental Engineering*, 124(5), 409-418.

Skerratt, J., Wild-Allen, K. & Rizwi, F. (2013). Use of a High Resolution 3D Fully Coupled Hydrodynamic, Sediment and Biogeochemical Model to Understand Estuarine Nutrient Dynamics under Various Water Quality Scenarios. *Ocean and Coastal Management*, 83(1), 52-66.

Suykens, J.A., Van, G.T. & De, B.J. (2002). *Least Squares Support Vector Machines*. World Scientific.

Suykens, J.A.K. & Vandewalle, J. (1999). Least Squares Support Vector Machine Classifiers. *Neural Processing Letters*, 9(3), 293-300.

Vapnik, V.N. (1999). An Overview of Statistical Learning Theory. *Neural Networks, IEEE Transactions On*, 10(5), 988-999.

Yang, H., Ding, J. & Wang, C.F. (2012). Study on the Water Quality Model of the Mesocosm Ecosystem in the Xiangshan Bay. *Marine Sciences*, 36(7),14-22.

Zhang, C., Zhang, T. & Yuan, C. (2011). Oil Holdup Prediction of Oil–Water Two Phase Flow Using Thermal Method Based on Multiwavelet Transform and Least Squares Support Vector Machine. *Expert Systems with Applications*, 38(3), 1602-1610.

Zhang, X., Srinivasan, R. & Van, L.M. (2009). Approximating SWAT Model Using Artificial Neural Network and Support Vector Machine. *Journal of the American Water Resources Association*, 45(2), 460-474.

Zheng, L., Chen, C. & Zhang, F.Y. (2004). Development of Water Quality Model in the Satilla River Estuary, Georgia. *Ecological Modelling*, 178(3-4), 457-482.

Zou, R., Dong, Y.Z. & Zhen, Z. (2012). Neural Network Modeling of the Eutrophication Mechanism in Lake Chenhai and Corresponding Scenario Analysis. *Acta Ecologica Sinica*, 32(2), 448-456.

Proceedings of the 37th IAHR World Congress
August 13 – 18, 2017, Kuala Lumpur, Malaysia

MODELLING THE IMPACTS OF TIDAL RANGE ENERGY STRUCTURES IN THE SEVERN ESTUARY AND BRISTOL CHANNEL, UK

NEJC ČOŽ(1), REZA AHMADIAN(2) & ROGER A. FALCONER(3)

(1,2,3) Hydro-environmental Research Centre, School of Engineering, Cardiff University, Cardiff, UK,
CozN@cf.ac.uk; AhmadianR@cf.ac.uk; FalconerRA@cf.ac.uk

ABSTRACT

With the increasing awareness about climate change and rising prices of fossil fuels, the demand for renewable energy is rapidly growing and so is the popularity of tidal energy production. To date, only a few small scale tidal power plants are in operation, however this is about to change. The number of studies on this topic is fast increasing. Severn Estuary is one of the most talked about sites when it comes to tidal range power production as it has one of the largest tidal ranges in the world. The Hydro-environmental Research Centre at Cardiff University has a rich legacy of research on the topic. In this paper the Delft3D software is used to develop a hydraulic model that will be used for future studies of tidal range structures at the department. The model is validated against observation data and compared to results from the literature. The Delft3D code has to be modified to accurately represent turbines and sluice gates. Simulations are performed both in 2D and 3D.

Keywords: Severn estuary; renewable energy; tidal power; hydraulic structures; Delft3D.

1 INTRODUCTION

The demand for renewable energy is rapidly growing. Although there is an increased interest in harvesting tidal power, only a few small-scale working tidal power plants are in operation to date. Places where tidal energy has the most potential are areas with a large tidal range - that is where the difference between low and high water levels is big enough to create a sufficient head difference to produce energy. One such place is along the west coast of the UK, where there is an exceptional tidal range in the Severn Estuary and Bristol Channel.

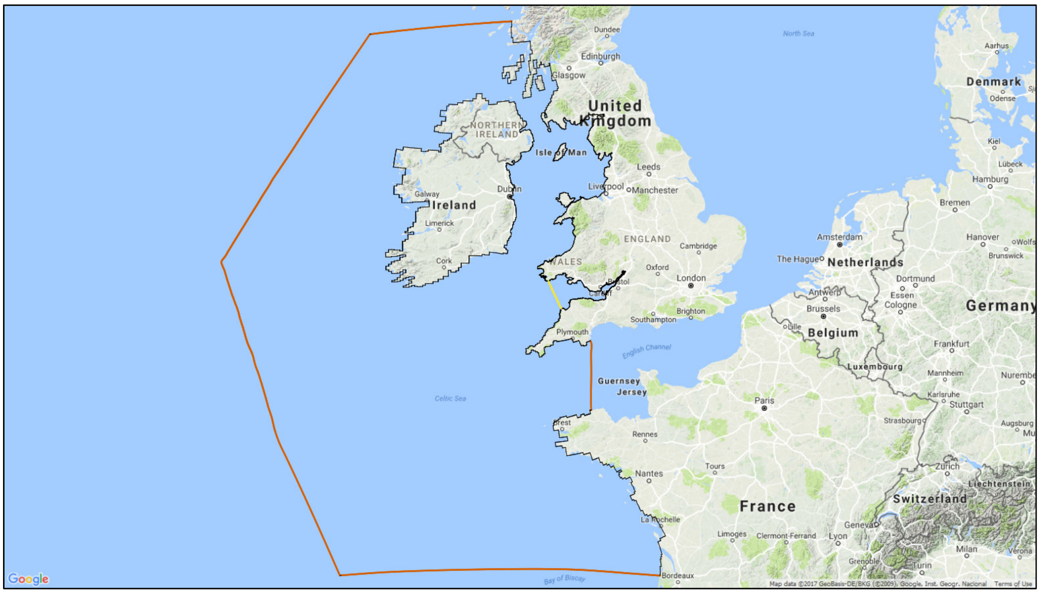

Figure 1. Study area - showing seaward boundaries of the Continental Shelf Model (orange) and Severn Estuary Model (yellow).

The study area (Figure 1) is situated off the west coast of the UK, with a particular interest in the Severn Estuary. The estuary has the second largest tidal range in the world which can be more than 14 m during the spring tides. The estuary is around 200 km long and relatively shallow. At its widest point, it measures approximately 14 km between Cardiff and Weston-super-Mare. This characteristic makes it an extremely attractive site for tidal power extraction, a number of proposals have been considered to date – these vary from the tidal barrage to a combination of various tidal lagoons and other tidal energy schemes (DECC, 2010).

Just recently a proposal for the Swansea Bay lagoon got backing from an independent review (Hendry, 2016) which paves the way for construction of the first tidal energy project in the estuary in the very near future. Other similar tidal schemes can therefore be expected to follow.

The objective of this study is to prepare a flexible but stable model/procedure that will be used for the tidal energy analysis at the Severn Estuary by the Hydro-environmental Research Centre (HRC) at Cardiff University. To date, much of the hydrodynamic analysis of tidal range structures in the estuary focused on the Severn Barrage proposal (to mention just a few Angelouduis and Falconer, 2016; Bray et al., 2016; Lin et al., 2010; Xia et al., 2010; Burrows et al., 2009). The calculations herein were performed with the Delft3D software suite. For comparison and validation of the new model, the same tidal barrage scheme was chosen to be used in this study. It acts as a sort of “development model” that in future will be used for hydraulic simulations of other tidal power projects proposed in the estuary

2 METHODOLOGY

2.1 Governing equations

Hydrodynamic processes in tidal estuaries are generally solved using the Navier-Stokes equations for incompressible fluid. Velocity field is more significant in the horizontal direction. The vertical acceleration can be neglected as it was smaller compared to gravity. Under these assumptions the vertical momentum equation can be reduced to the hydrostatic pressure equation. The set of partial differential equations (Eq. [1], [2] and [3]) in combination with an appropriate set of initial and boundary conditions was solved on a finite difference grid.

In this study the simulations were preformed both in two and three dimensions. A depth averaged approach was used for the 2D models, whilst 3D equations were solved using a sigma coordinate system (σ model) and hydrostatic pressure assumption. The σ-model represents the vertical dimension of the grid. It is divided into many layers (planes), which are not strictly horizontal but follow the shape of the bottom topography and free surface. Instead of fixed depth, the σ-layers are characterized by the proportion of the total depth.

$$\begin{aligned}\frac{\partial u}{\partial t}+\frac{u}{\sqrt{G_{\xi\xi}}}\frac{\partial u}{\partial \xi}+\frac{u}{\sqrt{G_{\eta\eta}}}\frac{\partial u}{\partial \eta}+\frac{\omega}{d+\varsigma}\frac{\partial u}{\partial \sigma}-\frac{v^2}{\sqrt{G_{\xi\xi}}\sqrt{G_{\eta\eta}}}\frac{\partial\sqrt{G_{\eta\eta}}}{\partial \xi}\\ +\frac{uv}{\sqrt{G_{\xi\xi}}\sqrt{G_{\eta\eta}}}\frac{\partial\sqrt{G_{\xi\xi}}}{\partial \eta}-f_v\\ =-\frac{1}{\rho_0\sqrt{G_{\xi\xi}}}P_\xi+F_\xi\\ +\frac{1}{(d+\varsigma)^2}\frac{\partial}{\partial\sigma}\left(\nu_V\frac{\partial u}{\partial\sigma}\right)+M_\xi\end{aligned} \qquad [1]$$

and

$$\begin{aligned}\frac{\partial v}{\partial t}+\frac{u}{\sqrt{G_{\xi\xi}}}\frac{\partial v}{\partial \xi}+\frac{u}{\sqrt{G_{\eta\eta}}}\frac{\partial v}{\partial \eta}+\frac{\omega}{d+\varsigma}\frac{\partial v}{\partial \sigma}-\frac{uv}{\sqrt{G_{\xi\xi}}\sqrt{G_{\eta\eta}}}\frac{\partial\sqrt{G_{\eta\eta}}}{\partial \xi}\\ +\frac{u^2}{\sqrt{G_{\xi\xi}}\sqrt{G_{\eta\eta}}}\frac{\partial\sqrt{G_{\xi\xi}}}{\partial \eta}-f_u\\ =-\frac{1}{\rho_0\sqrt{G_{\eta\eta}}}P_\eta+F_\eta\\ +\frac{1}{(d+\varsigma)^2}\frac{\partial}{\partial\sigma}\left(\nu_V\frac{\partial v}{\partial\sigma}\right)+M_\eta\end{aligned} \qquad [2]$$

where u, v and ω are flow velocities in ξ, η and σ direction respectively, ν_V is vertical eddy viscosity, P_ξ and P_η are pressure gradients, forces F_ξ and F_η represent the unbalance nature of horizontal Reynold’s stresses, M_ξ and M_η represent the contributions due to external sources or sinks of momentum and $\sqrt{G_{\xi\xi}}$ and $\sqrt{G_{\eta\eta}}$ are used for transformation of the coordinate system.

$$\begin{aligned}w=\omega+\frac{1}{\sqrt{G_{\xi\xi}}\sqrt{G_{\eta\eta}}}\left[u\sqrt{G_{\eta\eta}}\left(\sigma\frac{\partial H}{\partial\xi}+\frac{\partial\varsigma}{\partial\xi}\right)\right.\\ \left.+v\sqrt{G_{\xi\xi}}\left(\sigma\frac{\partial H}{\partial\eta}+\frac{\partial\varsigma}{\partial\eta}\right)\right]+\left(\sigma\frac{\partial H}{\partial t}+\frac{\partial\varsigma}{\partial t}\right)\end{aligned} \qquad [3]$$

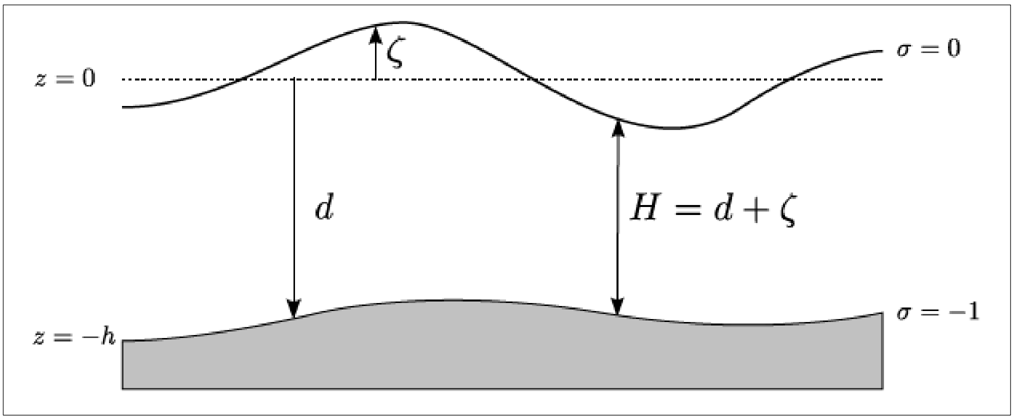

Figure 2. Definition of water level (ς), depth (d) and total depth (H) for σ-model (Deltares, 2014).

2.2 Hydraulic objects

Two different types of hydraulic objects were used: turbines and sluice gates. They were both represented as modified culverts with a user-defined transfer of flow between an intake and outfall points. They both adopt the same method as described in Bray et al. (2016). The discharge through sluice gates was calculated using an orifice equation for a completely submerged flow Eq. [4]. For the turbines, a so-called hill chart (Figure 3) was used to prescribe the discharge based on the head difference between the intake and outfall points.

$$Q = c_d A\sqrt{2gH} \quad [4]$$

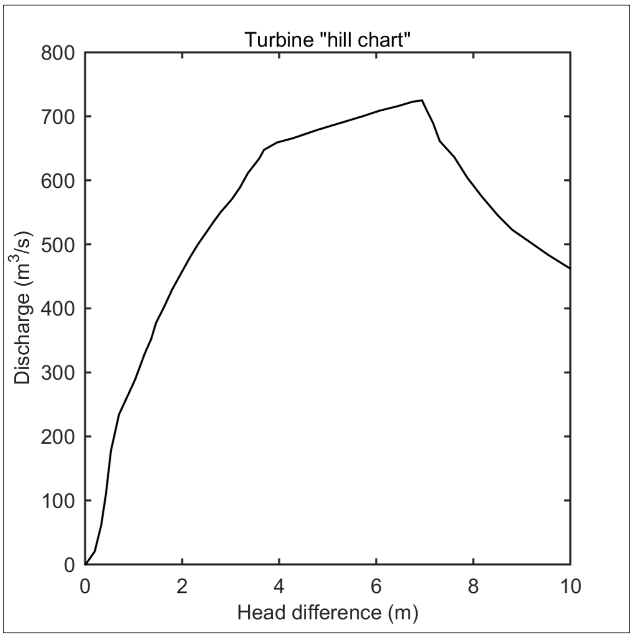

Figure 3. A hill chart for turbines used in this study.

2.3 Computational model

The hydrodynamic simulations were conducted using the Delft3D-FLOW, a hydrodynamic module of the Delft3D software suite developed by Deltares in the Netherlands. The model is capable of both two dimensional and three-dimensional unsteady flow simulations resulting from tidal and meteorological forcing. The governing equations were derived from three dimensional Navier-Stokes equations for incompressible flow (Eq. [1], [2] and [3]). A curvilinear staggered grid was used for the discretization of the partial differential equations which are solved using a finite difference altering direction implicit (ADI) solver to satisfy the second order accuracy of the solution (Deltares, 2014).

The open source aspect of the Delft3D suite is an important advantage as it allows the user to modify the code to better fit for individual study. In the simulations presented herein, the code was modified to represent the operation of tidal range structures (TRS) by implementing turbines and sluice gates. The procedure for TRS operation was developed in a similar manner as in Angeloudis and Falconer (2016) and will be only briefly described herein. The discharge through the turbines and sluice gates was calculated using a hill chart (Figure 3) and orifice equation (Eq. [4]) respectively. Furthermore, in a three-dimensional model the intake and outfall of a turbine and a sluice gate can be assigned to a specific vertical position (i.e. specific horizontal layer) to better represent the out coming jet. In this paper, we merely focus on the ebb-only generation scheme, where turbines are producing electricity only with the outgoing tide, however the model can be set up for other scenarios as well. The ebb-only scheme has distinctive phases of operation: holding low water – filling – and holding high water - generating. When the head difference was too small for efficient power production the gates were closed and no flow was let into the impoundment. During the filling phase the sluice gates were opened and the turbines were turned off (disconnected from the generator) allowing the incoming tide to fill in the impoundment. When the high-water level is reached all the gates were closed again and the energy generation stage does not start until the sufficient head difference was established.

As recent studies, have shown (Zhou et al., 2014; Adcock et al., 2011) an obstruction in the domain of such scale as a tidal barrage can have a direct impact on volume of water flowing into the domain and thus affecting the model's open boundary conditions. This motivated us to develop a model on two different scales: a large so called Continental Shelf Model (CSM), and a smaller Severn Estuary Model (SEM). CSM is represented with large and coarse grid that extends all the way from British West Coast to the edge of UK Continental Shelf and it covers approximately 850,000 m^2. The grid for SEM was cut at the entrance into the Bristol Channel and refined to a higher resolution – cells near the barrage were reduced from 250 x 250 m in CSM to around 100 x 100 m. The calculations were performed both in 2D and 3D. It was first set up to run in 2D, with and without the tidal barrage, and in both cases with the same boundary conditions – water levels time series for a typical 14 days neap-spring tidal cycle. The run without the barrage was used for calibration and validation purposes while the results from the second run with the barrage were used to set up boundary conditions of the smaller model. The edge of the SEM model was set at the entrance into the Bristol Channel.

This case study of the Severn Estuary tidal barrage acts as a development model for future tidal energy extraction analysis in the UK. The main objective was to establish a robust procedure for these kind of simulations, where the model can still be effortlessly transformed to accommodate other tidal energy schemes in the domain (for example Swansea Bay Lagoon, Bridgwater Bay lagoon, etc.). While the current paper only investigates an ebb-only generation scheme, the model can be easily refined to work with other schemes, such as two-way generation that is proposed for the Swansea Bay lagoon in Angeloudis and Falconer (2016).

3 RESULTS AND DISCUSSIONS

3.1 Validation of the continental shelf model

The initial CSM model was run in 2D and was validated against observed water levels and velocity data across the whole domain. The time series for the former were obtained from British Oceanic Data Centre (BODC), the velocity magnitudes and directions for the latter were collected from the Admiralty Charts. The velocity was in addition compared to results produced by the EFDC model from Bray et al. (2016).

From Figure 5 we can see that in some places Delft3D predicts even better results than EFDC model, especially at the incoming tide at the Site A. Site B is in deeper waters, therefore the speed magnitude was much smaller. Delft3D still shows much better fit during the incoming tide but it over predicts at the ebb. Figure 4 compares water levels at the observation point near Hinkley point. Delft3D slightly under predicts the tidal range of neap tides, however it showed very accurate results during the spring high and low waters. Similar results were observed at other observation points across the whole domain.

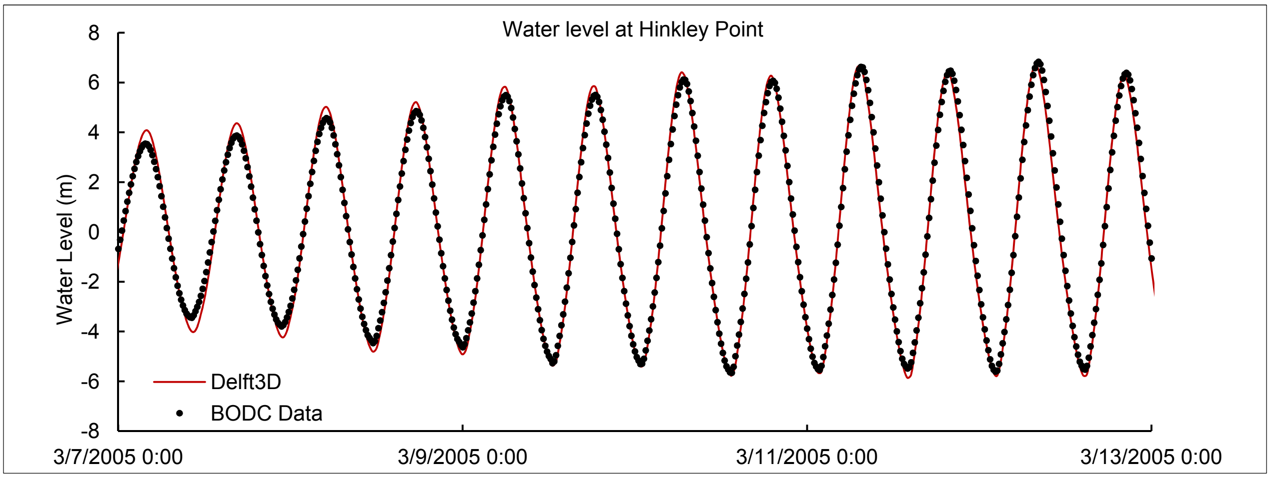

Figure 4. Water levels compared to observed data.

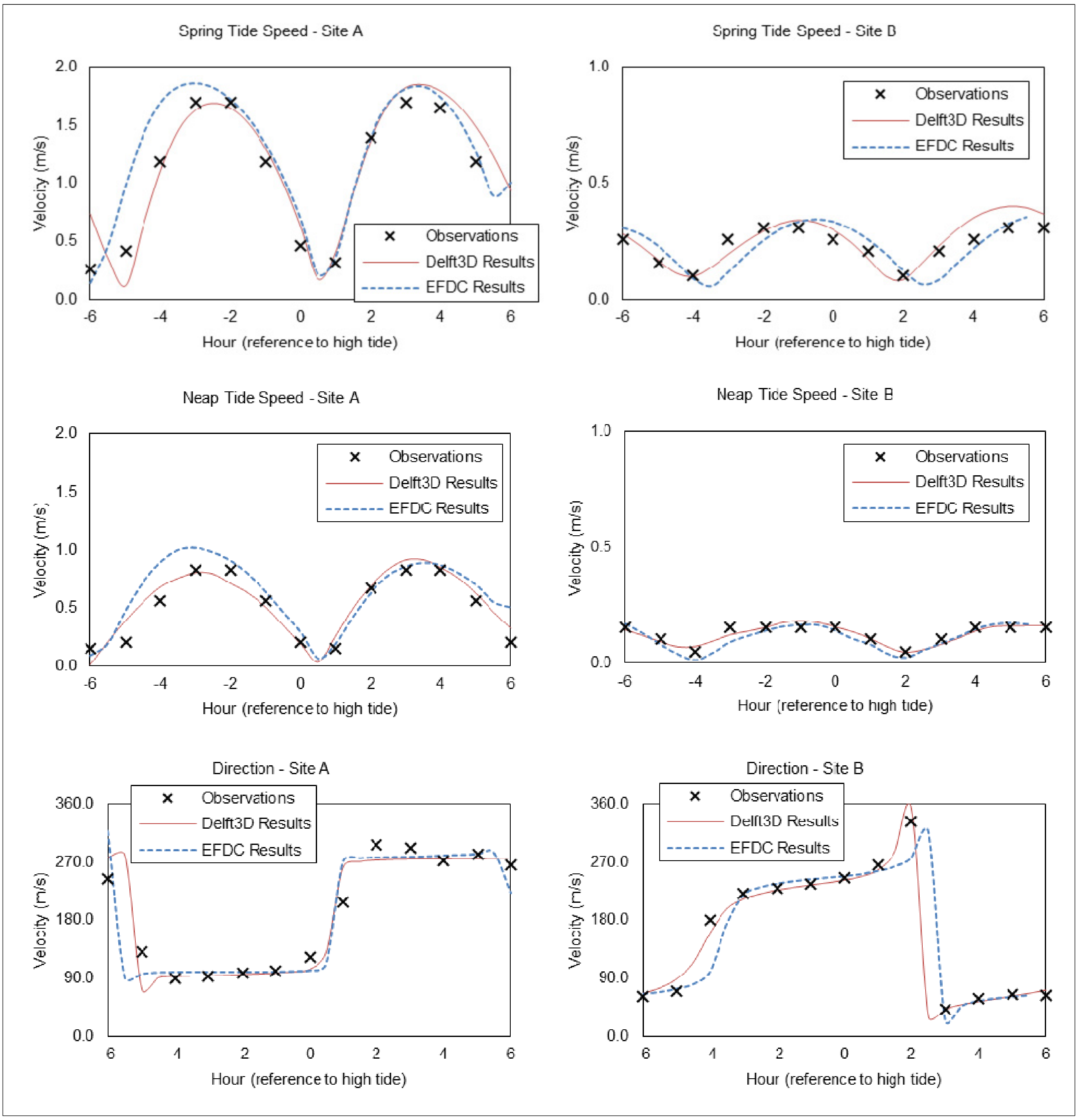

Figure 5. Comparisons between Delft3D results, EFDC results and observed data. Site A is situated in the middle of the Bristol Channel and site B in Celtic Deep.

3.2 Far field effects

Next the same model set-up was run again, but this time with the tidal barrage in place. To assess the impacts on the extreme water levels, maximum water elevations across the whole domain were calculated for both runs.

Figure 6 shows the comparison of the two. The results were consistent with the findings of Bray et al. (2016). The rise of the maximum water levels can be observed throughout the Bristol Channel and beyond. In the Irish Sea and Cardigan Bay the extent of increased maximum elevation was slightly smaller but of the same order of magnitude (5 cm – 15 cm) as predicted by Bray et al. (2016).

The open boundary of the smaller SEM model was at the entrance to the Bristol Channel and as we see from Figure 6, it falls well into the area that was affected by the barrage operation. Therefore, we extracted the water level time series along the channel entrance and set them as the open boundary conditions.

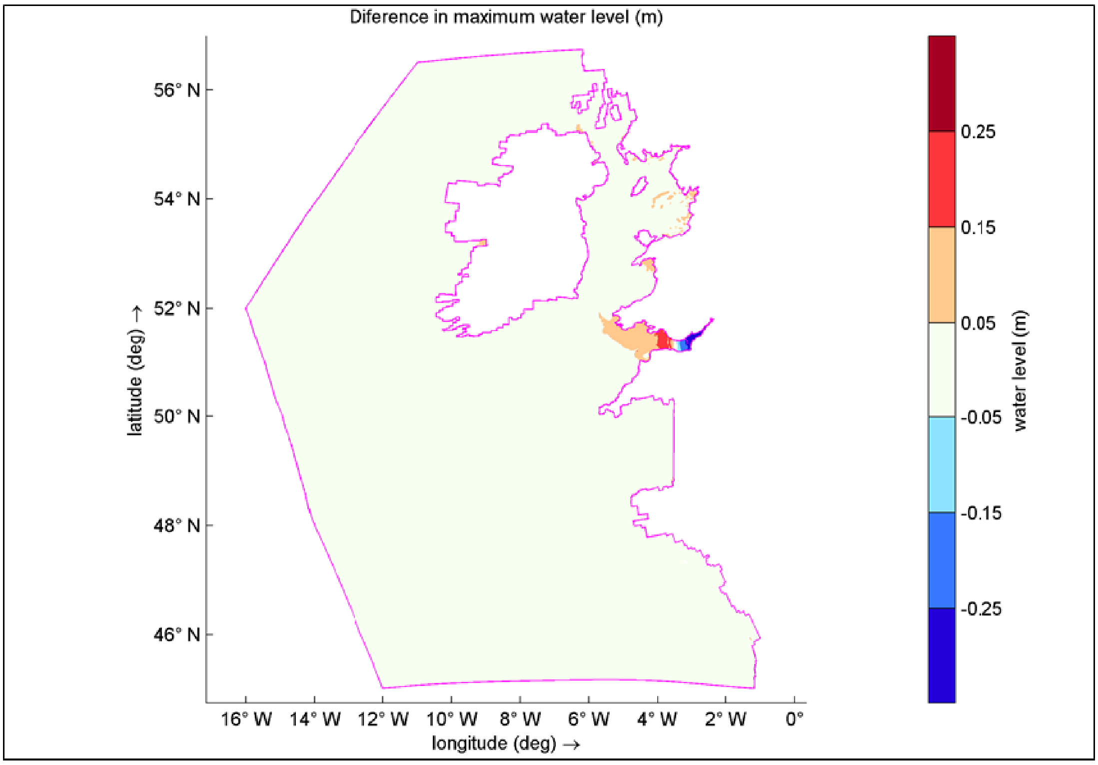

Figure 6. Maximum water elevation changes due to the barrage operation.

3.3 Severn Estuary Model with tidal barrage

To monitor the barrage operation two observation points were set-up at 5 kilometers upstream and downstream of the turbines. Figure 7 shows the time series of the water level for the whole duration of the simulation. Typical spring and neap tide cycles were cut out in Figure 8. The dotted lines were added to demonstrate the four distinctive phases of ebb-only operation mode. Figure 9 shows the sum of the discharge across the barrage over time. The discharge through turbines when generating is positive and negative during the filling stage.

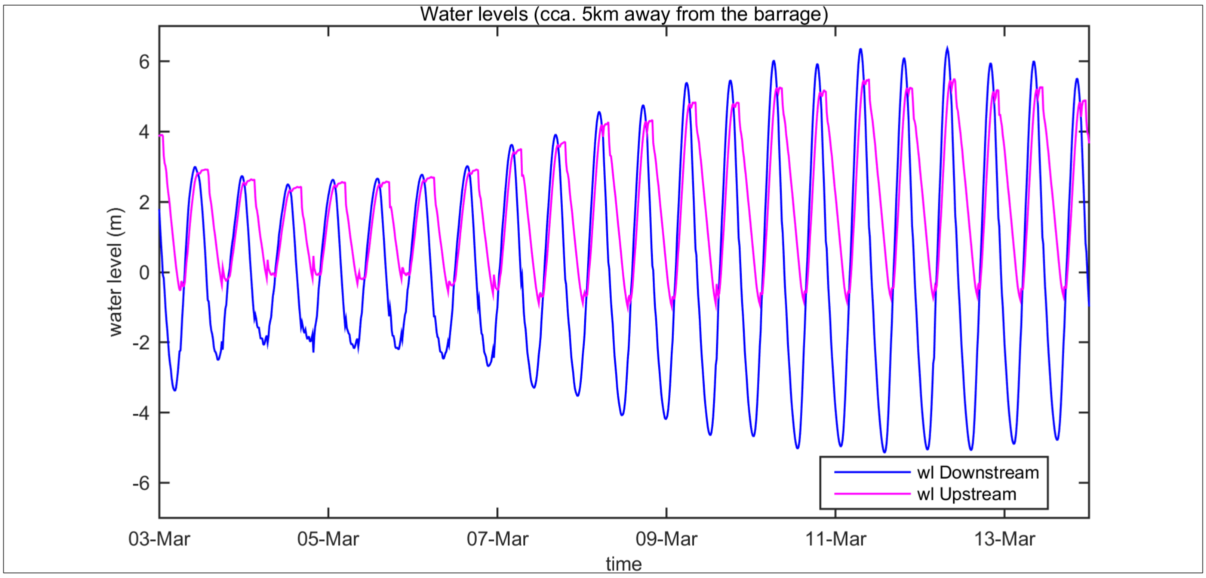

Figure 7. Water levels 5 kilometers upstream and downstream of the barrage.

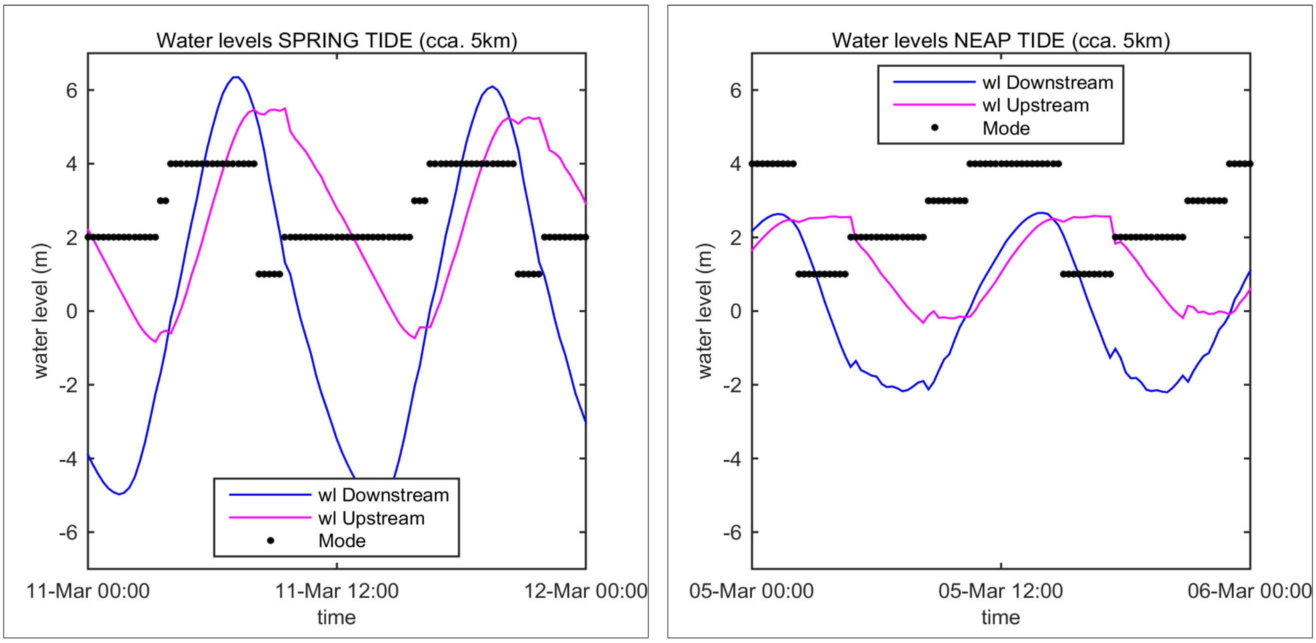

Figure 8. Ebb-only generation mode during a spring and neap tide. Mode: 1 – holding high water; 2 – generating; 3- holding low water; 4 – filling.

3.4 Velocities due to the barrage operation

Figures 9 and 10 show a snapshot of the velocity field during the barrage operation for a typical spring tide. The results were taken from the 2D (depth averaged) simulation. First one was recorded during the ebb tide and we can clearly see the discharge through turbines that were spread along the middle part of the barrage. In some places the magnitude of velocity exceeds 2.0 m/s. A jet of relatively fast flow can be seen in the northern part of the channel. Second recording is of the same tidal cycle but 5 hours later during the incoming tide when sluice gates along the whole width of the barrage were open. The flow through the middle part of the barrage was much less prominent but again a higher velocity flow was observed just west of the Flat Holm Island.

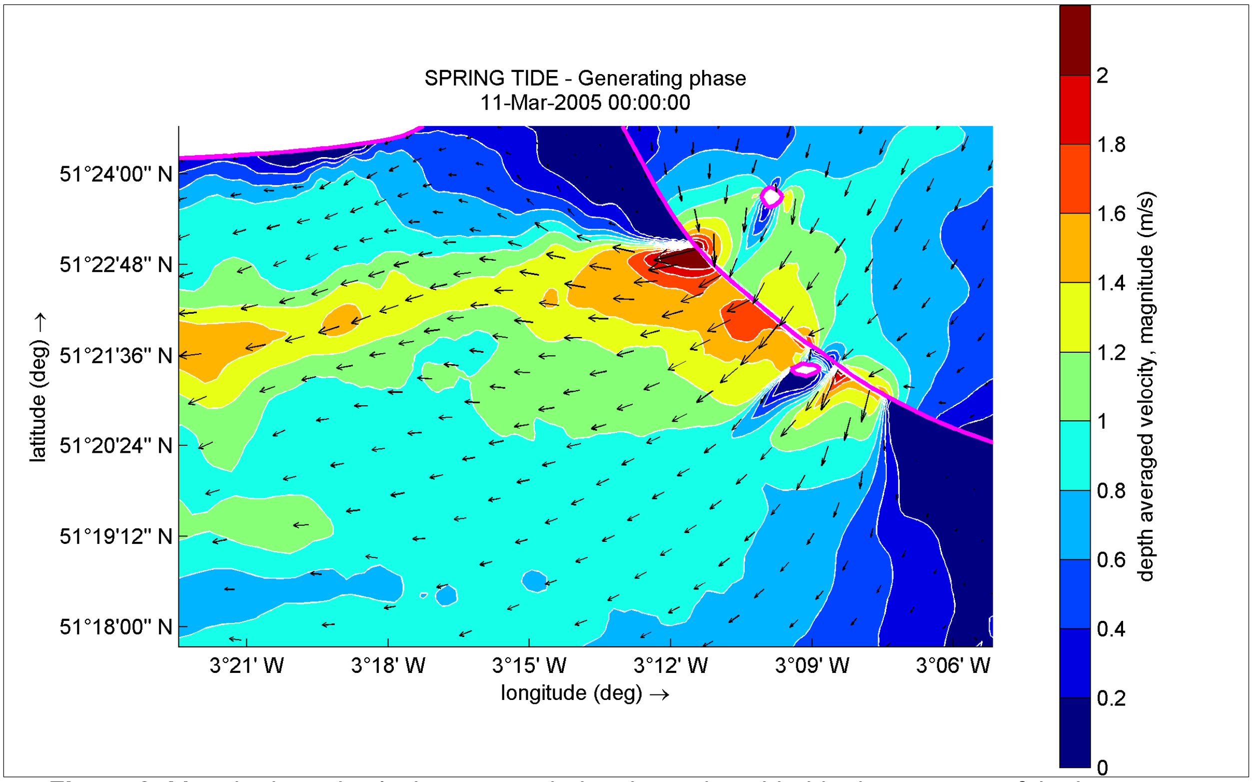

Figure 9. Magnitude and velocity vectors during the spring ebb tide downstream of the barrage.

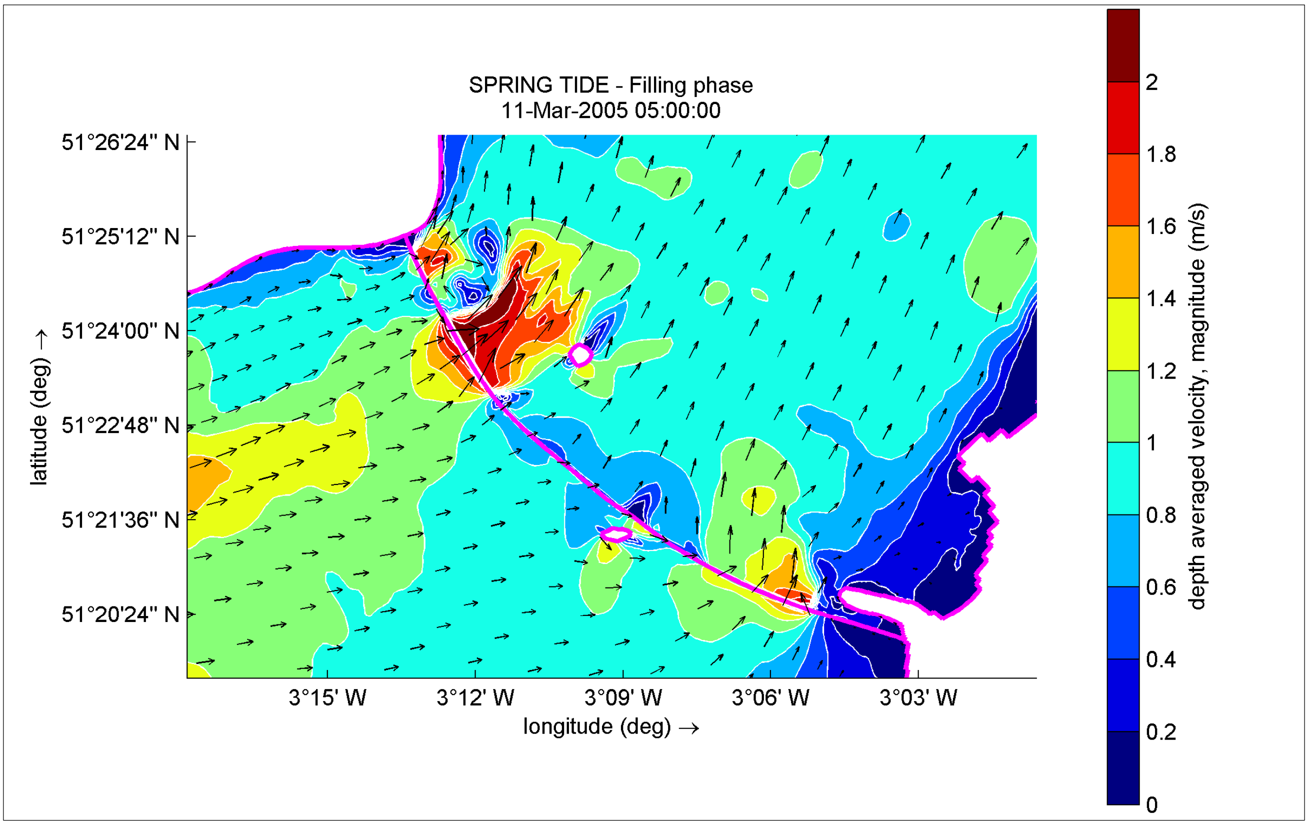

Figure 10. Magnitude and velocity vectors during the spring flood tide upstream of the barrage.

The model was run both in 2D and 3D and the comparison of the velocity profile is illustrated in Figure 11. Five layers were used for the 3D run and the turbines and sluices were assigned to vertical position of 12 m below the ordnance datum. The velocity profiles were taken at four places just downstream of the barrage during the generating phase. The advantage of a 3D model over 2D is evident from the figure – the depth averaged model under predicts the surface speed by almost 20% compared to the 3D model. A clear spike can be seen at the depth of 12 m, where the turbines are positioned.

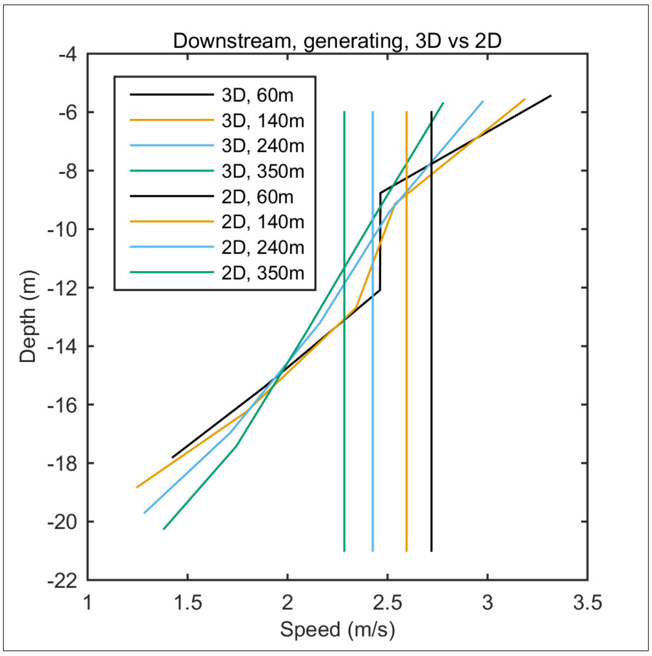

Figure 11. Comparison of velocity profiles between 2D and 3D simulation.

4 CONCLUSIONS

In this paper, a model for hydraulic simulation of tidal range structures is developed by using Delft3D software. The case study of tidal barrage in the Severn Estuary is examined using two scales of the model: a large-scale Continental Shelf model (CSM) and a smaller, higher resolution Sever Estuary model (SEM). Two simulations are performed with a 2D CSM model – with and without the barrage. The results of the first are used for validation purposes. The comparison of the two confirmed that the barrage causes significant changes to water levels even as far away as Cardigan Bay and Irish Sea. Using the extracted water elevations as boundary conditions another two simulations using the SEM are preformed, both with the barrage included, but one in 2D and the other in 3D. The barrage operation is presented with plots of water elevations and velocity fields just downstream and upstream of the barrage. In addition, a difference between 2D and 3D model is also presented. In general, the results have shown a good agreement with the studies from literature. This encourages us to continue using Delft3D and expand it to other tidal range projects in the Severn Estuary.

ACKNOWLEDGEMENTS

The research reported herein is funded by The Engineering and Physical Sciences Research Council (EP/L016214/1) and is part of a PhD research topic at Centre for Doctoral Training in Water Informatics: Science and Engineering (WISE CDT).

REFERENCES

Adcock, T.A.A., Borthwick, A.G.L. & Houlsby, G.T. (2011). The Open Boundary Problem in Tidal Basin Modelling with Energy Extraction. *Proceedings of the 9th European Wave and Tidal Energy Conference. Southampton*, UK, 1–7.

Angeloudis, A. & Falconer, R.A. (2016). Sensitivity of Tidal Lagoon and Barrage Hydrodynamic Impacts and Energy Outputs to Operational Characteristics. *Renewable Energy*, Available online: 27 August 2016, 1-15.

Bray, S., Ahmadian, R. & Falconer, R.A. (2016). Impact of Representation of Hydraulic Structures in Modelling a Severn Barrage. *Computers and Geosciences*, 89, 96–106.

Burrows, R., Walkington, I.A., Yates, N.C., Hedges, T.S., Wolf, J. & Holt. J. (2009). The Tidal Range Energy Potential of the West Coast of the United Kingdom. *Applied Ocean Research*, 31(4), 229-238.

Department of Energy and Climate Change (DECC). (2010). *Severn Tidal Power Feasibility Study: Conclusions and Summary Report power*.

Deltares. (2014). *Delft3D-FLOW*, User Manual, 1–684.

Hendry, C. (2016). *The Role of Tidal Lagoons*, Final Report, Greg Clark, the Secretary of State for Business, Energy and Industrial Strategy, 183.

Lin, B., Ahmadian, R. & Falconer, R. (2010). Hydro-Environmental Modeling of Proposed Severn Barrage, UK. *Proceedings of the ICE - Energy*, 163(3), 107–117.

Zhou, J., Pan, S. & Falconer, R.A. (2014). Effects of Open Boundary Location on the Far-Field Hydrodynamics of a Severn Barrage. *Ocean Modelling*, 73, 19–29.

Xia, J., Falconer, R.A. & Lin, B. (2010). Impact of Different Operating Modes for a Severn Barrage on the Tidal Power and Flood Inundation in the Severn Estuary, UK. *Applied Energy*, 87(7), 2374–2391.

DIFFUSE BACTERIA LOADING FROM INTERTIDAL MARSHLAND AND IMPACTS TO ADJACENT ESTUARINE WATER QUALITY

AMYRHUL ABU BAKAR[1], REZA AHMADIAN[2] & ROGER A. FALCONER[3]

[1,2,3] Hydro-environmental Research Centre, School of Engineering, Cardiff University, The Parade, Cardiff, UK,
AbuBakarA1@cf.ac.uk, AhmadianR@cf.ac.uk, FalconerRA@cf.ac.uk

ABSTRACT

The Loughor Estuary is a macro-tidal estuarine waterbody which is located on the North of the Bristol Channel, South West of the U.K. This estuary, with a shallow inlet, traps sand and mud from Carmarthen Bay, which are discharged from upstream catchments and resuspended through the tidal cycle in the estuary. Much of the estuary dries during low tides and forms an important site for shellfish beds. The water quality at this site of interest is potentially impaired by receiving bacterial overloading from multiple sources, including: sheep grazing on the intertidal marshland at the southern edge of the estuary. As the point source of bacteria generated from domestic and industrial inputs is well quantified through releases from the wastewater treatment works, the bacterial diffuse sources originating from the marshland during intertidal flooding are considered as being poorly quantified and could be one of the main contributors of the failure of this waterbody to comply with the guideline standards of the EU Shellfish Water Directive. Accurate computations of bacterial loading are required to establish a trade-off between managing livestock grazing practices and improving the water quality status. In this study, a developed two-dimensional hydrodynamic model has been extended to solve the transport process of bacteria within this waterbody. The bacteria loading from the marshland is computed based on the animal density and their faeces production rates during grazing over the drying areas. The bacteria released from the marshland and loading into the waterbody are treated as an instantaneous flush of a diffuse source after flooding during subsequent high tides. The transported bacteria concentrations within the shellfish water are evaluated for the exposure time and severity variables to the filter-feeding shellfish in this waterbody. The improved model for the quantification of diffuse bacteria loading from the intertidal marshland can be used for assessing the impacts of various sources and adopting the best management practices.

Keywords: Hydro-environmental modelling; faecal bacteria; diffuse source; Loughor Estuary; shellfish contamination.

1 INTRODUCTION

The shellfish waters in the European Union (EU) are identified as a protected area by the Water Framework Directive (WFD), with the EU member states being legally responsible to ensure that these protected areas achieve the compliance level with any defined standards and objectives in the directive (Stapleton et al., 2011). The filter-feeding shellfish, which are classified as economically important species to the community, can be easily polluted by the bacteria as they filter and retain this kind of pollutant from the water column (Kay et al., 2008). This bacteria-contaminated shellfish, if consumed raw or without being properly cooked, is known to cause infectious disease outbreaks, such as typhoid fever (Rippey, 1994; Potasman et al., 2002; Feldhusen, 2000). Such extreme infectious diseases can be very harmful to humans and could also lead to significant economic losses (Rabinovici et al., 2004).

Shallow inshore waters, such as those in estuarine and coastal areas, are often highly productive ecosystems which make these waters very suitable for commercial shellfish cultivation and harvesting (Almeida and Soares, 2012). This type of waterbody, however, is at high risk of exposure to bacterial contamination, which potentially enters the system from nearshore catchments as point or diffuse source inputs, dominated by human and animal activity (Chigbu et al., 2004; Gourmelon et al., 2010). While point source inputs of bacteria released from wastewater treatment works (WWTWs) can be well quantified (Burkhardt et al., 2000), diffuse source inputs of bacteria originating from livestock voiding faeces from inland waters and riparian areas are considered as poorly quantified (Stapleton et al., 2011).

The paper highlights the development of a numerical model to estimate the bacteria load from intertidal marshland in the Loughor estuary, with the diffuse source originating from animal grazing activity. The subsequent analyses established the impact of the transported bacteria on the water quality at shellfish harvesting sites. This is based on the hydro-environmental model developed by Bakar et al., (2017) to simulate the bacterial transport processes and predict water quality in the Loughor Estuary. Causse et al. (2015) have studied the bacteria mobilisation and transfer along montane agroecosystems streams, with the concentration and released processes of bacteria from livestock manures having been review by Ferguson et al. (2008) and Blaustein et al. (2015). The factors and rate of bacteria accumulation to different species of shellfish have been studied by Kershaw et al. (2013). Martins et al. (2006), Fiandrino et al. (2003), and Dabrowski et al. (2014) have applied numerical models to determine the impact of bacterial loading from different sources on the quality of shellfish flesh and with consideration being given to the accumulation process.

2 MATERIALS AND METHODS

2.1 Study area

The Loughor Estuary is a macro-tidal estuarine waterbody which is located along the Welsh side of the Bristol Channel, and in the south-west of the U.K. (see Figure 1). The tidal ranges during spring tides can reach a maximum of 7.5 m near Burry Port. Sands and muds are derived from resuspension in the coastal bay and inputs from upstream catchments respectively, with these sediments being trapped within the estuary due to a natural formation of a dune system along the south-west, which narrows at the inlet mouth (Elliott et al., 2012).

This macro-tidal estuary with the shallow bottom of sands and muds, is mostly dry during low tides and forms an important site for shellfish harvesting. There are two Shellfish Water Designation areas in this estuary, namely Burry Inlet (BI) North and South respectively, which are located north of the tidal channel between Llanelli and Burry Port and at northern edge of the intertidal marshland. Several bivalve mollusc species are present in these designation areas, including the commercially important species of common edible cockles and mussels (Youell et al., 2013a; 2013b).

The upstream catchments of this estuary are dominated by rural and agricultural activities, although there are developing areas at Llanelli and Burry Port, with important urban and industrial activities associated with these developments. Llanrhidian marshland at the southern edge of the estuary, which floods during high tides, was historically used as a grazing area. The main potential sources of bacterial pollution are treated and untreated effluents through wastewater treatment works (WWTWs), combined sewer overflows (CSOs) (Kay et al., 2008) and the raw flushing bacteria from surface runoff through the streams (Kay et al., 2005) or flooding at the intertidal marshland.

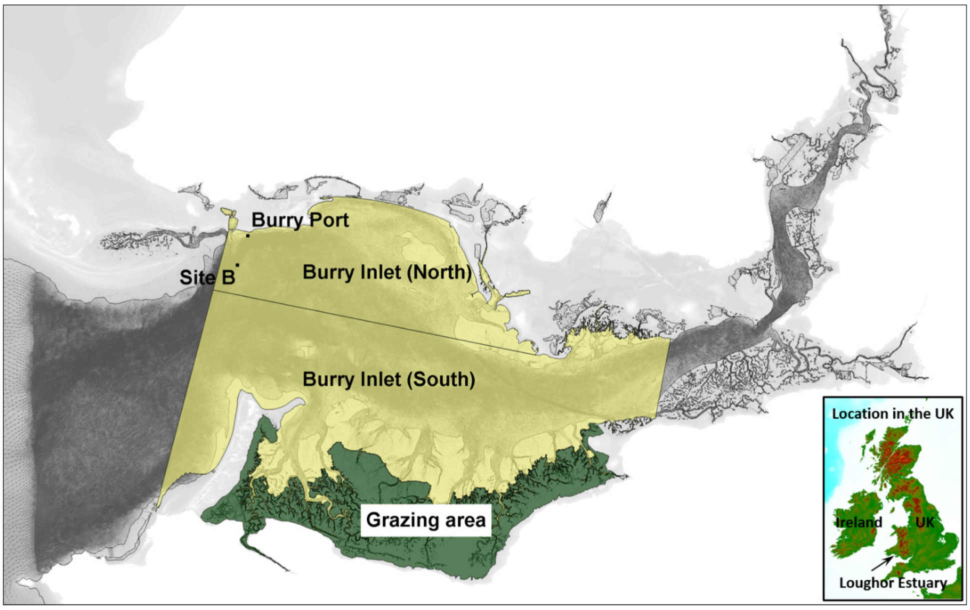

Figure 1. Location of animal grazing area over the intertidal marshlands and Shellfish Water Designation sites in the Loughor estuary.

2.2 Modelling details

A two-dimensional depth-averaged numerical model was implemented to solve the Shallow Water Equations (SWEs). The model was built to cover the Severn Estuary and Bristol Channel, with the modelling domain being extended to include the flooding area of the intertidal marshland in the Loughor Estuary. The resolution of the elements was refined from 100 m at the mouth of the estuary down to 10 m at sites of interest, such as the intertidal marshlands. The tidal time series was specified at the western open boundary, with the estimated stream discharges have been included for the realistic presentation of pollutants flushing from the upstream. The bottom friction parameter was used for calibrating the surface elevation and current in this model.

2.2.1 Hydrodynamic and transport model

The SWEs have been solved for the surface elevation and current flow patterns using the finite element method. The continuity and momentum conservation equations are solved respectively written in the following form:

$$\frac{\partial h}{\partial t} + \vec{u}.\overrightarrow{grad}(h) + h\,div(\vec{u}) = S_h \qquad [1]$$

$$\frac{\partial u_i}{\partial t} + \vec{u}.\overrightarrow{grad}(u_i) = -g\frac{\partial Z_s}{\partial x} + F_i + \frac{1}{h}\,div\left(hv_t.\overrightarrow{grad}(u_i)\right) \quad i = 1,2 \qquad [2]$$

where h is the water depth, $\vec{u}$ and u_i, i=1,2 are the two components of the horizontal velocity, g is the gravitational acceleration, Z_s is the surface elevation, S_h is the source/sink of water inputs, F_i, i=1,2 are the two components of source/sink of horizontal momentum including the bottom friction parameter, and v_t is the molecular or eddy viscosity of water that is calculated from the turbulence closure model.

The depth-averaged solute transport equation has been solved to model the bacteria transport using the finite volume method, in order to ensure the conservation of solute mass. The bacteria transport equation is solved for with the inclusion of a first-order kinetic decay rate and is written as:

$$\frac{\partial T}{\partial t} + \vec{u}.\overrightarrow{grad}(T) = \frac{1}{h}\,div\left(hv_T.\overrightarrow{grad}(T)\right) + k_b T \qquad [3]$$

where T is the bacteria concentration, v_T is the bacteria dispersion coefficient, k_b is the bacteria decay rate, which is also expressed as the T_{90} value, giving the equivalent time required for the inactivation of 90% from the total bacteria count.

2.2.2 Load estimation model

The diffuse bacteria loading, as a result of grazing animals at Llanrhidian intertidal marshland, was estimated as the product between bacteria production rates, the animal density, and the area of grazing. Sheep are the main animals grazing over this area and therefore constitute the only animals included in the model as the diffuse source of bacteria. The bacteria production rate was estimated to be equal to 4.04 x 10^8 cfu/sheep/hr (Causse et al., 2015). The sheep density grazing on the marshland during low tides was assumed at the constant value of 0.1 sheep/m^2 for the whole simulation period. Literature on the estimation of domestic livestock densities including sheep has also been reviewed (Ferguson et al., 2008). The grazing area by sheep is defined as the extension of the drying intertidal marshland, which resulted from the wetting-drying process of hydrodynamic model. This grazing area is variable in time depending on the tidal conditions with the maximum extension being approximately equal to 11.8 x 10^6 m^2 during low spring tides.

2.2.3 Bacteria release model

The bacteria release from the diffuse load at the intertidal marshland was modelled based on the calculation of bacteria concentration and the flooding rate once the grazing area became inundated. The bacteria concentration was calculated with reference to the cumulative bacteria number at the marshland just before the area flooded. The flooding rate was calculated at the threshold water depth of 0.1 m, and within 1 second. The bacteria load at the marshland was reset to zero once this pollutant source is flushed into the waterbody, with all the processes being iterative with the tidal cycles. The bacteria flux released from the marshland during flooding can be modelled as the product between bacteria concentration and the flooding rate. The release processes of bacteria from the manure matrix with the available models have been reviewed elsewhere (Blaustein et al., 2015).

2.2.4 Shellfish exposure model

The accumulation of the transported bacteria in the flesh of bivalve molluscs at the designation areas was modelled as the exposure time and bacteria severity variables. The exposure time of the bivalve molluscs was modelled as the time of shellfish flesh exposed to the bacteria over the threshold concentration of 100 cfu/ml. This threshold value was estimated as the concentration where filter-feeding shellfish begins to accumulate and depurate the bacteria in their flesh. A microcosm study has been conducted to estimate the bacteria accumulation rate and factors to the different shellfish species (Kershaw et al., 2013). The bacteria severity to the bivalve mollusc flesh was then modelled as the product of the exposure time to the transported bacteria concentration at the designated site in the waterbody. Several modelling approaches have also been proposed for the process of accumulation and depuration of bacteria to the filter-feeding shellfish (Martins et al., 2006; Fiandrino et al., 2003; Dabrowski et al., 2014).

3 RESULTS AND DISCUSSIONS

3.1 Hydrodynamic validation

The developed two-dimensional numerical model was calibrated for the hydrodynamic processes over the Severn Estuary and Bristol Channel, with the surface elevations and currents predicted by the refined model being validated at Burry Port and site B respectively, for the duration of six tidal cycles during 8th – 10th October 2014, namely 281 – 284 Julian Date (JD). The validated surface elevations during the spring tidal condition with a range of 7.5 m, compares well with the measured data as shown in Figure 2. The currents also showed good correlation with the measured data. However, the model failed to predict the maximum currents by about 0.5 m/s for the ebb tides, as shown in Figure 3. Considering the underpredicted result of maximum currents during ebb tides at site B, the modelled flow process would consequently reduce the transport rate of bacteria mass during flushing from the estuary. The measured currents for the site B data, however, were obtained from the Admiralty Chart 1167 of the 1977 survey, which might not represent the real conditions during the validation period. The estuary is also known to experience the active bed morphological changes, with the sediment accretion has narrowed the inlet's mouth between 1876 and 2000 (Elliott et al., 2012), and possibly reduced the modelled of maximum currents during ebb tides near the validation site. The validated currents informed that this estuary has the characteristics of a standing wave and with the ebb currents dominating at the lower tidal channel.

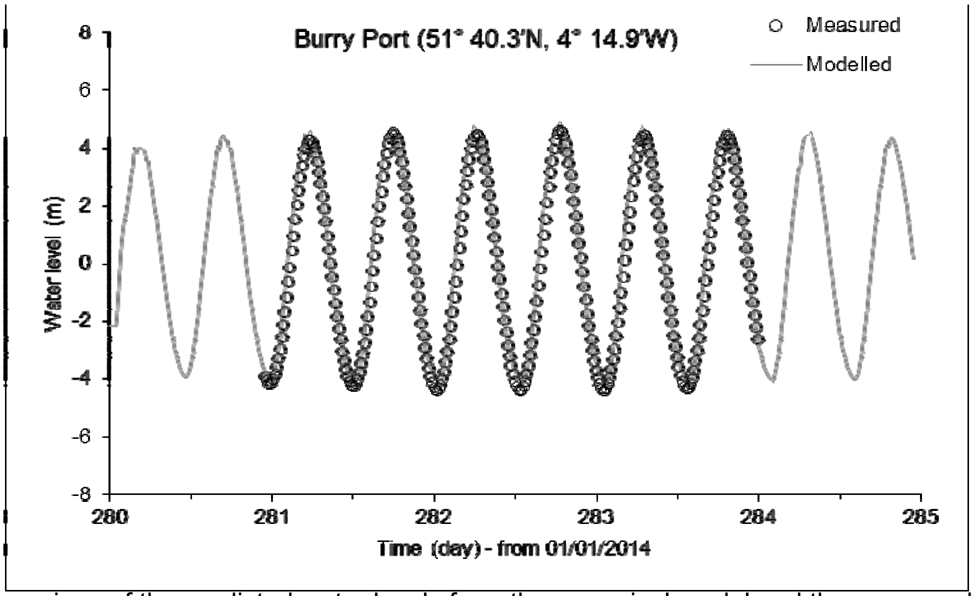

Figure 2. Comparison of the predicted water levels from the numerical model and the measured data at Burry Port.

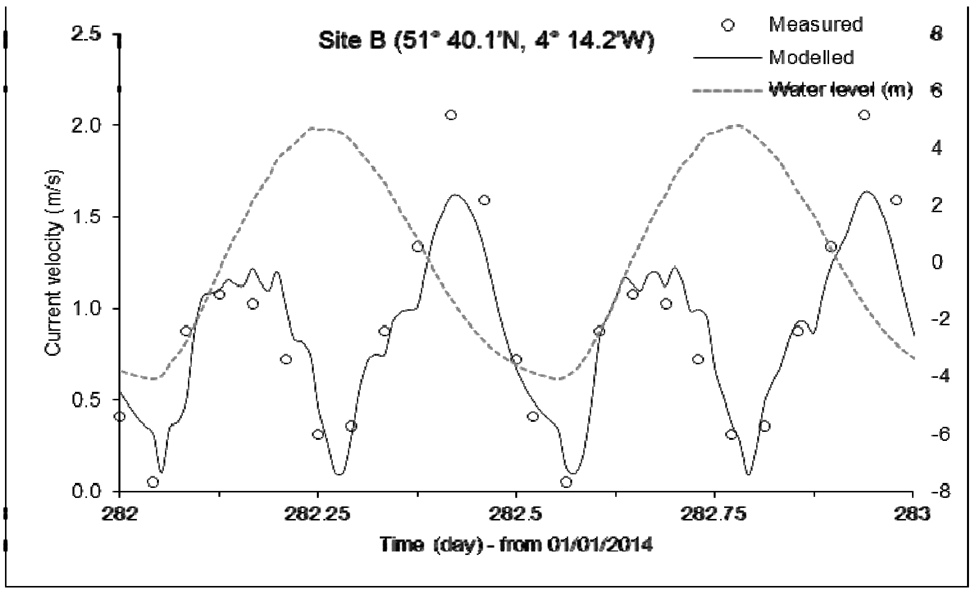

Figure 3. Predicted current velocities from the numerical model and the measured data at Site B.

  / ISSN 1562-6865 (Online) - ISSN 1063-7710 (Print)

3.2 Diffuse load at marshland

The diffuse load of bacteria from sheep grazing three hours after flooding of the intertidal marshlands is illustrated in Figure 4. The dry areas of the intertidal marshlands receive a constant bacteria load of 4.04 x 10^7 cfu/m^2/hr, with the total accumulated bacteria load being up to 4.85 x 10^8 cfu/m^2. The higher grazing areas at the south of the marshlands, which flood less frequently, retains more of the bacteria loads in comparison with the lower grazing areas adjacent to the waterbody.

The release of diffuse bacteria from the marshlands is variable in time as the result from the real-time wetting-drying processes and the associated hydrodynamics. The bacteria flux released into the waterbody during flooding and drying at the grazing areas is illustrated in Figure 5. The figure shows the diffuse bacteria primarily released during flood events at the marshland site, which peaks just before high water. The maximum release rates vary between each tidal cycle with the value as high as 3.5 x 10^{10} cfu/s. The bacteria release rate during flooding of the first tidal cycle was lower, as the result from the model cold start.

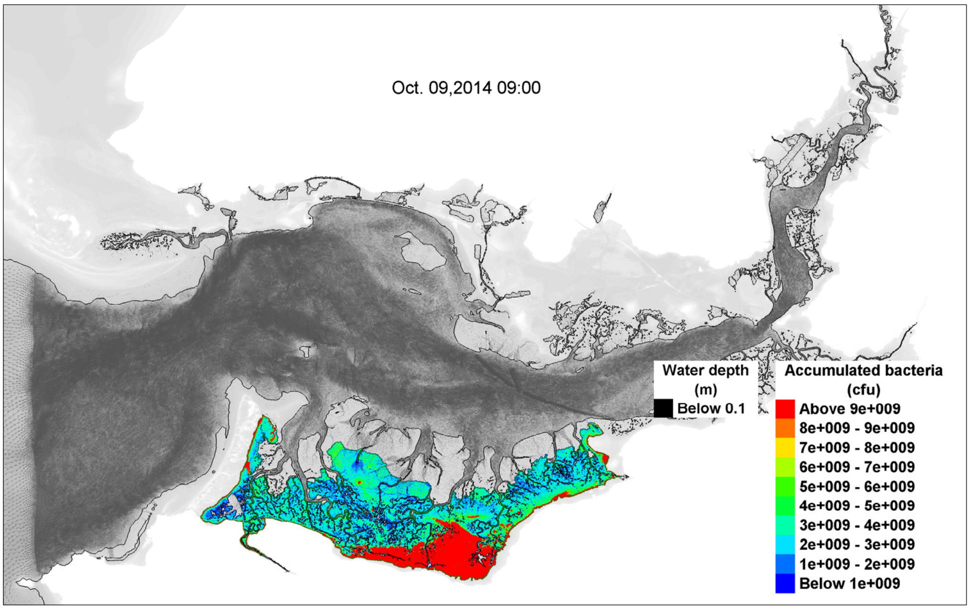

Figure 4. Diffuse bacteria loading from the marshland at HW + 3 hr at Burry Port.

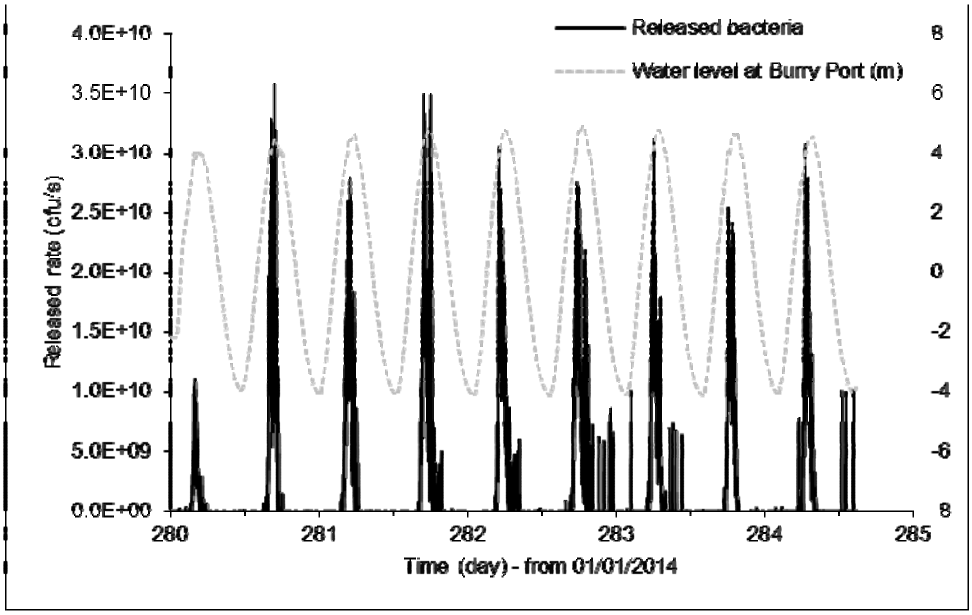

Figure 5. Water levels and flux of diffuse bacteria from the grazing areas during flooding.

3.3 Bacteria transport in estuary

The bacteria concentrations across the Loughor Estuary, as a result of sheep grazing over the intertidal marshland after five tidal cycles from the start of the model simulations, and at 3 hr after flooding are illustrated in Figure 6. The bacteria was only modelled as a conservative solute without considering the kinetic decay processes at this stage. The model results indicate that the bacteria is transported landward during the flood tide while it is flushed seaward into the estuary through tidal creeks during ebb tides. The transported bacteria distribution indicates that the area to the south and south-east of the marshland are retaining more of the load after flooding than the lower grazing area, with some proportional quantity being released into the adjacent estuary. This is consistent with the overall bacteria concentration observations across the estuary.

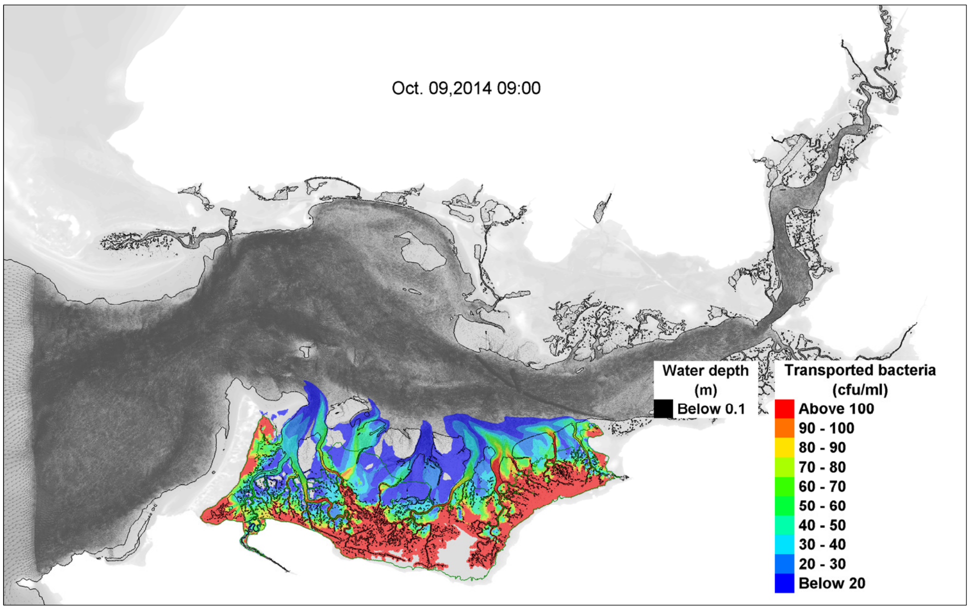

Figure 6. Transported bacteria in the estuarine water at HW + 3 hr at Burry Port.

3.4 Shellfish exposure to bacteria

The transported bacteria from the grazing area could be one of the most important sources of pollution at the designated waterbody sites. The shellfish flesh exposure time to bacteria and its severity after 3 hr from high water are illustrated in Figures 7 and 8, respectively. The results show that the exposure time cumulatively increases and decreases, respectively, with the fluctuation of the bacteria concentration over and below the threshold value. The bacteria severity to the shellfish flesh also behaves in a similar manner to the fluctuation of the bacteria concentration with exposure time, with the increment and decrement in severity, respectively, depending on the bacteria concentration in the water column and the bacteria concentration gradient between the flesh and the adjacent water. The resulting shellfish exposure time shows the increment above 90 s at the grazing area, where the higher bacteria retention load was expected to occur after flooding, and with the bacteria severity also increasing above 9000 cfu/ml*s at the same location.

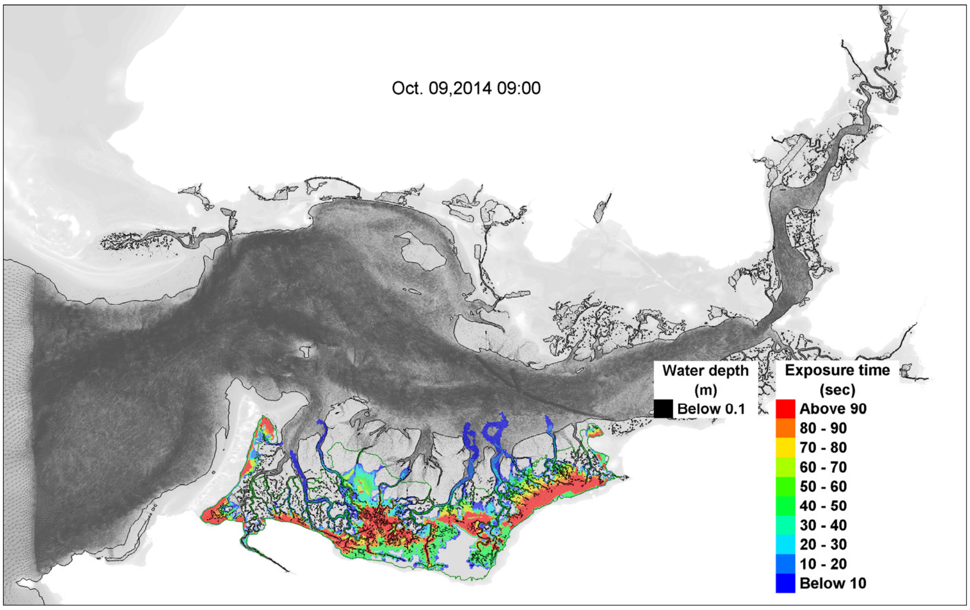

Figure 7. Bacteria exposure time to shellfish at HW + 3 hr at Burry Port.

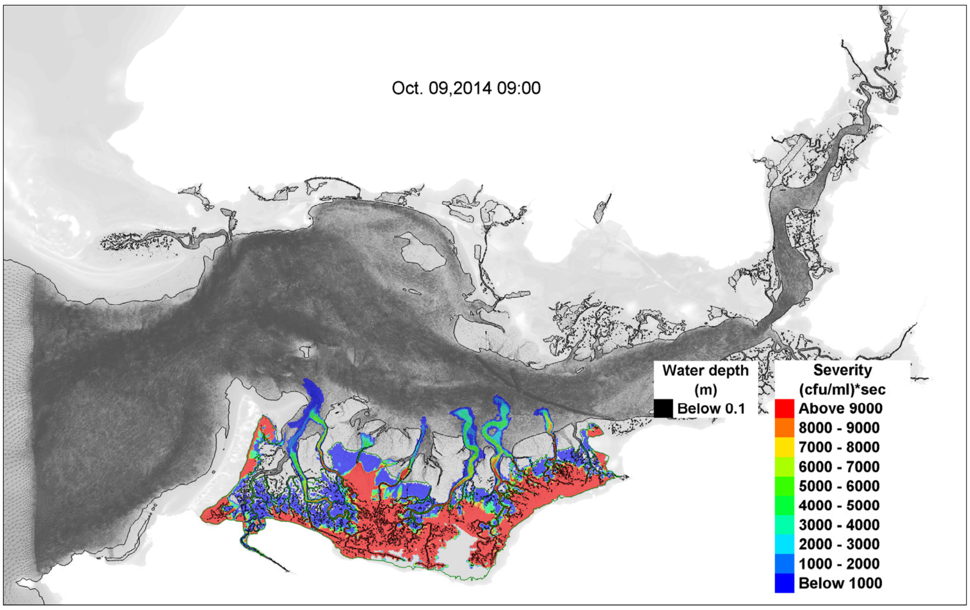

Figure 8. Bacteria severity to shellfish at HW + 3 hr at Burry Port.

4 CONCLUSIONS

The hydrodynamic processes, including surface elevations and depth mean currents, for the Loughor Estuary have been calibrated and validated against measured data. It was found that the model predictions generally correlated well with the measured data. The bacteria load over the grazing area has been estimated based on the sheep density and was assumed to be constant. It was observed that the less frequently flooded areas retained a higher load compared to the lower areas, due to the cumulative nature of bacteria deposition. The release of bacteria from flooded grazing areas to the water column was modelled to occur instantaneously. Along with the assumption of instantaneous flushing, it was also assumed that the total deposited bacteria was completely mixed over the water column of a constant water depth. The maximum release rate was observed just before high water, as a result of the maximum extension of flooding area. The transported bacteria in the estuarine waterbody was modelled as a conservative mass without considering any kinetic decay processes. Bacteria was transported and retained landward, then flushed seaward during the flood and ebb tides, respectively. The shellfish flesh exposure to bacteria at the designated waterbody sites was modelled as the variables of exposure time and severity, with inclusion of the accumulation and depuration processes being related to the bacteria fluctuation at threshold concentration. Further improvements in modelling the impact of diffuse bacteria loading from marshlands to the adjacent quality of the waterbody could be used to inform best management practices in the future.

ACKNOWLEDGEMENTS

The authors are grateful for the support provided by staff at the Centre for Research into Environment and Health (CREH) at Aberystwyth University, Natural Resources Wales, and Swansea City County Council. LIDAR data were used to refine the domain, with these data being provided by Natural Resources Wales and the Environment Agency. The authors are also grateful for the support provided by the Food Standards Agency which has made this research study possible.

REFERENCES

Almeida, C. & Soares, F. (2012). Microbiological Monitoring of Bivalves from the Ria Formosa Lagoon (South Coast Of Portugal): a 20 Years of Sanitary Survey. *Marine Pollution Bulletin*, 64(2), 252–262.

Bakar, A.A., Ahmadian, R. & Falconer, R.A. (2017). Modelling the Transport and Decay Processes of Microbial Tracers Released in a Macro-Tidal Estuary. *Water Research*, Under review.

Blaustein, R.A., Pachepsky, Y.A., Shelton, D.R. & Hill, R.L. (2015). Release and Removal of Microorganisms from Land-Deposited Animal Waste and Animal Manures: a Review of Data and Models. *Journal of Environmental Quality*, 44(5), 1338–1354.

Burkhardt, W., Calci, K.R., Watkins, W.D., Rippey, S.R. & Chirtel, S.J. (2000). Inactivation of Indicator Microorganisms in Estuarine Waters. *Water Research*, 34(8), 2207–2214.

Causse, J., Billen, G., Garnier, J., Henri-des-Tureaux, T., Olasa, X., Thammahacksa, C., Latsachak, K.O., Soulileuth, B., Sengtaheuanghoung, O., Rochelle-Newall, E. & Ribolzi, O. (2015). Field and Modelling Studies of Escherichia Coli Loads in Tropical Streams of Montane Agro-Ecosystems. *Journal of Hydro-environment Research*, 9(4), 496–507.

Chigbu, P., Gordon, S. & Strange, T. (2004). Influence of Inter-Annual Variations in Climatic Factors on Fecal Coliform Levels in Mississippi Sound. *Water Research*, 38(20), 4341–4352.

Dabrowski, T., Doré, W.J., Lyons, K. & Nolan, G.D. (2014). Numerical Modelling of Blue Mussel (Mytilus Edulis) Bacterial Contamination. *Journal of Sea Research*, 89, 52–63.

Elliott, M., Burdon, D., Callaway, R., Franco, A., Hutchinson, T., Longshaw, M., Malham, S., Mazik, K., Otto, Z., Palmer, D. & Firmin, C. (2012). Burry Inlet Cockle Mortalities Investigation 2009–2011, *Technical Report to the Environment Agency Wales,* YBB140-Tech(Final-2012), 1-337.

Feldhusen, F. (2000). The Role of Seafood in Bacterial Foodborne Diseases. *Microbes and Infection*, 2(13),1651–1660.

Ferguson, C.M., Charles, K. & Deere, D.A. (2008). Quantification of Microbial Sources in Drinking-Water Catchments. *Critical Reviews in Environmental Science and Technology*, 39(1), 1–40.

Fiandrino, A., Martin, Y., Got, P., Bonnefont, J.L. & Troussellier, M. (2003). Bacterial Contamination of Mediterranean Coastal Seawater as Affected by Riverine Inputs: Simulation Approach Applied to a Shellfish Breeding Area (Thau lagoon, France). *Water Research*, 37(8), 1711–1722.

Gourmelon, M., Caprais, M.P., Mieszkin, S., Marti, R., Wery, N., Jardé, E., Derrien, M., Jadas-Hécart, A., Communal, P.Y., Jaffrezic, A. & Pourcher, A.M. (2010). Development of Microbial and Chemical MST Tools to Identify the Origin of the Faecal Pollution in Bathing and Shellfish Harvesting Waters in France. *Water Research*, 44(16), 4812–4824.

Kay, D., Kershaw, S., Lee, R., Wyer, M.D., Watkins, J. & Francis, C. (2008). Results of Field Investigations into the Impact of Intermittent Sewage Discharges on the Microbiological Quality of Wild Mussels (Mytilus Edulis) in a Tidal Estuary. *Water Research*, 42(12), 3033–3046.

Kay, D., Wyer, M.D., Crowther, J., Wilkinson, J., Stapleton, C. & Glass, P. (2005). Sustainable Reduction in the Flux of Microbial Compliance Parameters from Urban and Arable Land use to Coastal Bathing Waters By a Wetland Ecosystem Produced by a Marine Flood Defence Structure. *Water Research*, 39(14), 3320–3332.

Kershaw, S., Campos, C.J.A., Reese, A., Mitchard, N., Kay, D. & Wyer, M. (2013). Impact of Chronic Microbial Pollution on Shellfish. *Cefas*, 1-75.

Martins, F., Reis, M.P., Neves, R., Cravo, A.P., Brito, A. & Venâncio, A. (2006). Molluscan Shellfish Bacterial Contamination in Ria Formosa Coastal Lagoon: a Modelling Approach. *Journal of Coastal Research*, 3(39), 1551–1555.

Potasman, I., Paz, A. & Odeh, M. (2002). Infectious Outbreaks Associated with Bivalve Shellfish Consumption: a Worldwide Perspective. *Clinical Infectious Diseases*, 35(8), 921–928.

Rabinovici, S.J., Bernknopf, R.L., Wein, A.M., Coursey, D.L. & Whitman, R.L. (2004). Economic and Health Risk Trade-Offs of Swim Closures at a Lake Michigan Beach. *Environmental Science and Technology*, 38(10), 2737-2745.

Rippey, S.R. (1994). Infectious Diseases Associated with Molluscan Shellfish Consumption. *Clinical Microbiology Reviews*, 7(4), 419–425.

Stapleton, C.M., Kay, D., Magill, S.H., Wyer, M.D., Davies, C., Watkins, J., Kay, C., McDonald, A.T. & Crowther, J. (2011). Quantitative Microbial Source Apportionment as a Tool in Aiding the Identification of Microbial Risk Factors in Shellfish Harvesting Waters: the Loch Etive Case Study. *Aquaculture Research*, 42(1), 1–20.

Youell, M., Osborn, H., Stuart, T., Evans, S. & Llewellyn-Davies, R. (2013a). *South West Area Shellfish Waters Investigation Project - (Shellfish) Waterbody Action Report Burry Inlet (North) November 2011 - March 2013,* Environment Agency Wales, 1-39.

Youell, M., Osborn, H., Stuart, T., Evans, S. & Llewellyn-Davies, R. (2013b). *South West Area Shellfish Waters Investigation Project - (Shellfish) Waterbody Action Report Burry Inlet (South) November 2011 - March 2013*, Environment Agency Wales, 1-46.

TWO-DIMENSIONAL OIL SPILL MODELLING FOR COASTAL WATERS

LAVINE WONG(1), MOHAMAD HIDAYAT BIN JAMAL(2) & AHMAD KHAIRI BIN ABD WAHAB(3)

(1, 2, 3) Department of Hydraulics and Hydrology, Faculty of Civil Engineering, Universiti Teknologi Malaysia, Skudai, Johor, Malaysia,
borneoangel91@gmail; mhidayat@utm.my; akhairi@utm.my
(2, 3) Centre for Coastal and Ocean Engineering (COEI),
Universiti Teknologi Malaysia Kuala Lumpur, Jalan Yahya Petra, Kuala Lumpur, Malaysia

ABSTRACT

Oil tanker accidents in seas cause serious problems to the marine environment, in particular when these accidents occur close to the estuary coastlines. The rate and importance of the processes change of a spilled oil depend on the oil spill volume, oil spill location, oil type, the speed and direction of wind and sea currents. Port of Tanjung Pelepas (PTP) being among the busiest port in Southeast Asia is located at the estuary of Pulai River and therefore subjected to oil spill occurrence although it may not be frequent. The objective of this study is to generate a trajectory for hypothetical spill accident at the river mouth and navigation channel and to determine the direction and percentage balance of spill trajectory using a numerical simulation method. The hydrodynamic modelling is calibrated and validated using tide and current data and the computed tide elevations and currents are in agreement with the field data. The hydrodynamic model is coupled with an oil spill model to predict the movement of oil slick on the surface. The observed spill trajectory is driven by current velocity and moves westwards in the estuary and 40 percent of the oil particles are left stranded after the simulated period of 36 hours. The prediction of the movement of spill is important so that the response team of PTP is able to initiate quick measures before further spreading of the oil in the area.

Keywords: Oil spill; Port of Tanjung Pelepas (PTP); spill trajectory; numerical model; Telemac2D.

1 INTRODUCTION

In recent years, the increase in areas of contamination of shoreline and water bodies by oil spills has been an ongoing major concern around the world. Oil exploration and transport, oil storage facilities, industrial discharge, and discharge from shipping water routes are some of the processes that have increase the risk of oil spill accidents (Chao et al., 2001). A major oil spill can contaminate coastal shoreline over time and aquatic environment for fishery and wildlife will suffer from long term damage if oil tracers are to be found in the water body system or consumed by these fishes. In general, oil spill accidents are harmful to the ocean environment and also to the health of mankind as indirect consumers of the ecological community. In a port harbor whereby there is continuous inflow of shipping vessels, any major contamination has the potential to foul harbor facilities and vessels, or contaminate the waterway, causing the disruption in waterway traffic or immediate halt of ships to proceed movement, especially at harbors located nearby the river mouth.

A large number of oil spill models have been used in the world today since the 19th century and all models aim to simulate the physical and chemical processes that transport and weather the oil in the sea. When an oil spillage occurs, the oil slick breaks up and become smaller particles under the actions of breaking waves and upper layer turbulence. These particles then advect and diffuse in the water column. Some of the particles will resurface while some form water-in-oil or oil-in-water emulsions. The effect of oil particles in water column has adverse effect to the environment if not treated within a short period of time as the spreading of oil will increase and also leaving tracers behind at coastal shores. Therefore, oil spill modeling is essential to predict the movement of oil particles in future circumstances when a spillage occur for a more effective containment or dispersion action to be taken by the authorities. Hence, the focus of this study is towards the study of movement of the predicted location of spilled oil on relatively calm water surface.

Telemac2D model was used to simulate the oil spill trajectories. The present work is a modeling study for a hypothetical oil spill that has high possibility to occur in the coastal waters of the Johor Estuary. The objectives of this study were as follows: (i) to simulate hydrodynamics of the coastal waters at PTP, (ii) to generate a trajectory for hypothetical spill accident at the estuary of Pulai River and at the navigation channel and (iii) to determine the direction and percentage mass balance of spill in the domain.

2 SITE DESCRIPTION

The climatic information was compiled during two seasons, which are during spring tide (12th to 15th October 2015) and neap tide (19th to 22nd October 2015). The average temperature of coastal waters at the area of location is 30^{o}C. Malaysia faced the northeast monsoon from October to March. This study does not take into account the wind factor. The domain covers the boundary from Pulau Kukup, Johor (1^{o} 20'N, 103^{o}25'E) to Raffles, Singapore (1^{o} 9.6'N, 103^{o}44.5'E) with PTP located at the centre of the model domain as shown in Figure 1. The Port of Tanjung Pelepas (PTP) is located at the estuary of Pulai River with a constant inflow of ship movement and subjected to oil spill accidents or discharges from the ships. Located approximately 10km southwest of PTP is Tanjung Piai (1° 15'50.64"N, 103°30'36.57"E) which has been designated as the Ramsar Convention's 1298th Ramsar Site where the ecological character of the area cannot be changed by human activity within or surrounding the area (Awang et al., 2014). Pulau Kukup on the other hand, is well known as mangrove wetland and has also been designated as Ramsar Site in 2013. Apart from the impending threat to the sensitive mangrove ecosystem due to sea level rise (Abd Wahab et al., 2016), any occurrence of oil spill that leaves tracers among these locations will have adverse effects on the rich biodiversity of the mangrove mudflats.

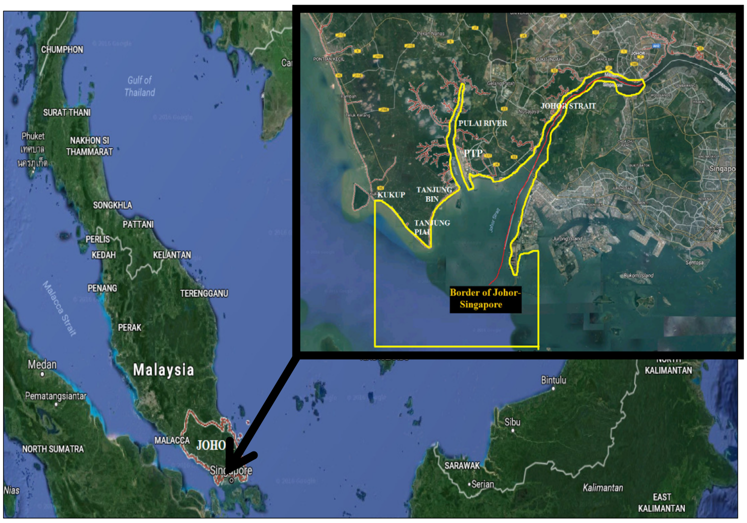

Figure 1. Location of PTP within the Johor region south of Malaysia.

3 NUMERICAL SIMULATION

3.1 Hydrodynamic model

The hydrodynamic simulation of process was carried out using the two-dimensional finite element open source model TELEMAC-2D (http://www.opentelemac.org). This model solves the depth-averaged free surface flow equations depending on the approximation in the calculation of the vertical velocity and the topography of the configuration. The computation of TELEMAC requires the building up of a numerical domain and mesh discretization whereby the density of mesh at the studied area has more intense density and the density gradually increases away from the study area. The finite element mesh was generated by the software BLUEKENUE, which is one of the pre-processor associated with the TELEMAC system. The bathymetric data was also loaded into the BLUEKENUE and applied onto the grid to assign each node in the map with an elevation data. The process of visualizing the output results was carried out using the software TECPLOT 360. The main results at each node of the computational mesh were the depth of water and the depth-averaged velocity components. Figure 2 and 3 show the discretization of the mesh and also model bathymetry of the model area. The bathymetry of the model was obtained by superimposing admiralty charts (MAL 5123, MAL 5128 and MAL 5129) and surveyed data that was conducted by Johor Port Authority in June 2015 to evaluate the impacts of nearby reclamations. The mesh was formed in a way whereby the density is coarser at the study area and the bathymetry of the domain varies with the depth from 0m (coastal shoreline) to 30m deep in the estuary or open sea.

3.2 Oil Spill Modelling

When oil is spilled on the water surface, it spreads due to inertia, gravity, viscous and surface tension force and the loss of oil is from the weathering processes which includes evaporation, dispersion, dissolution and sedimentation (Delgado et al., 2005; Aghajanloo et al., 2012; Wang et al., 2005). In the release of TELEMAC v7p0, a lagrangian/Eulerian oil spill model has been developed within the TELEMAC hydro-informatic system and the oil spill prediction is directly related to the quality of the hydrodynamic model (Goeury et al., 2014). The oil slick is represented by a large set of small hydrocarbon particles whereby each particle has an area, a mass, its element number, and its barycentric coordinates in this element associated to it (Goeury et al., 2012). The prediction of the oil slick transport on the surface of water column utilizes the Lagrangian approach whereas the Eularian advection-diffusion equation as in Eq. [1] governs the oil dissolution in the water. Where h is the water depth, v_t is the turbulent viscosity, C is the depth average pollutant concentration and σ_c represents the neutral Schmidt number, which is 0.72 (Issa et al., 2010).

$$\frac{\partial C}{\partial t} + u\nabla(\mathrm{C}) = \frac{1}{h}\nabla \cdot \left(\frac{h\nu_t}{\sigma_c}\nabla C\right) \qquad [1]$$

Generally, the transport and fate of spilled oil can be affected by physical, chemical and biological processes and the chemical and biological processes occur a long time after the spill of oil (Chao et al., 2001). The transport model in Telemac2D discusses on the advection and diffusion of oil particles and the weathering process in the system including spreading, evaporation, dissolution and volatilization as shown in Figure 4.

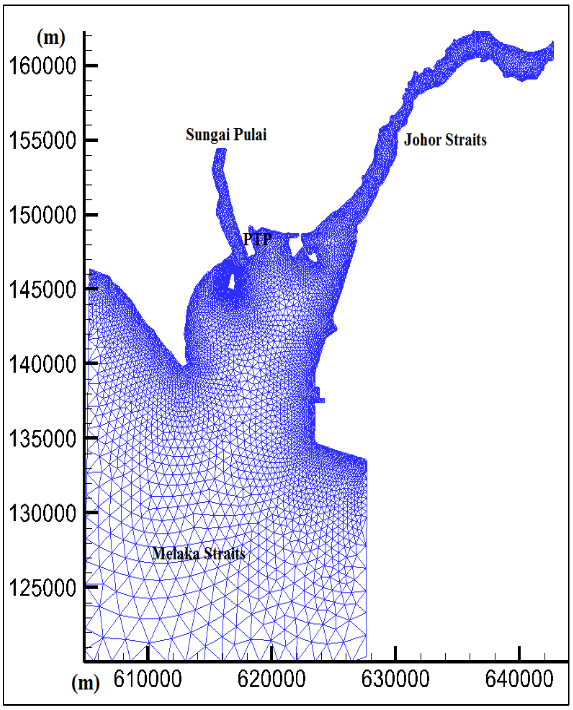

Figure 2. Mesh discretization.

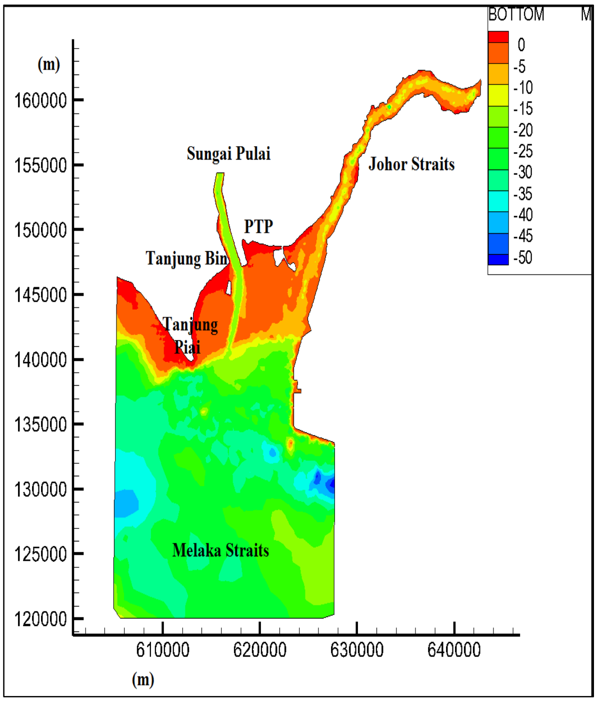

Figure 3. Model bathymetry.

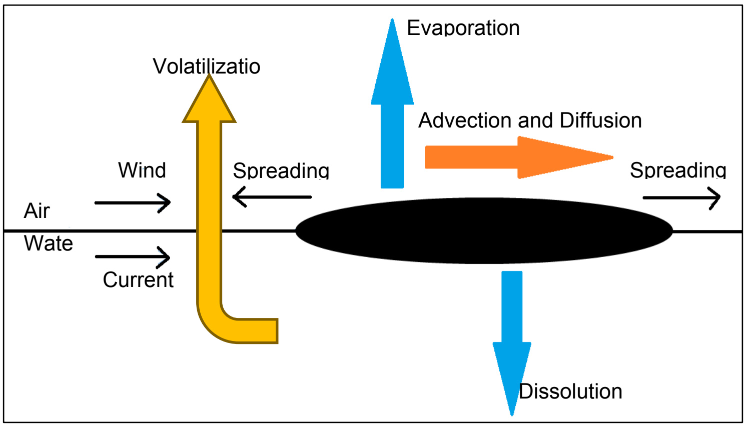

Figure 4. Fate and transport of oil slick processes.

4 RESULTS AND DISCUSSIONS

4.1 Hydrodynamic simulation

Prior to the modeling of oil spill, the result of the hydrodynamic simulation model was calibrated and validated against the measured data for water level variations and tidal currents at selected locations during both spring tide (13th to 15th October 2015) and neap tide (19th to 22nd October 2015). The model was calibrated with tidal levels from the water level data obtained from Jabatan Laut and current speed and direction from current meter at PTP waters. The located tide gauge and current meter is shown in Figure 5.

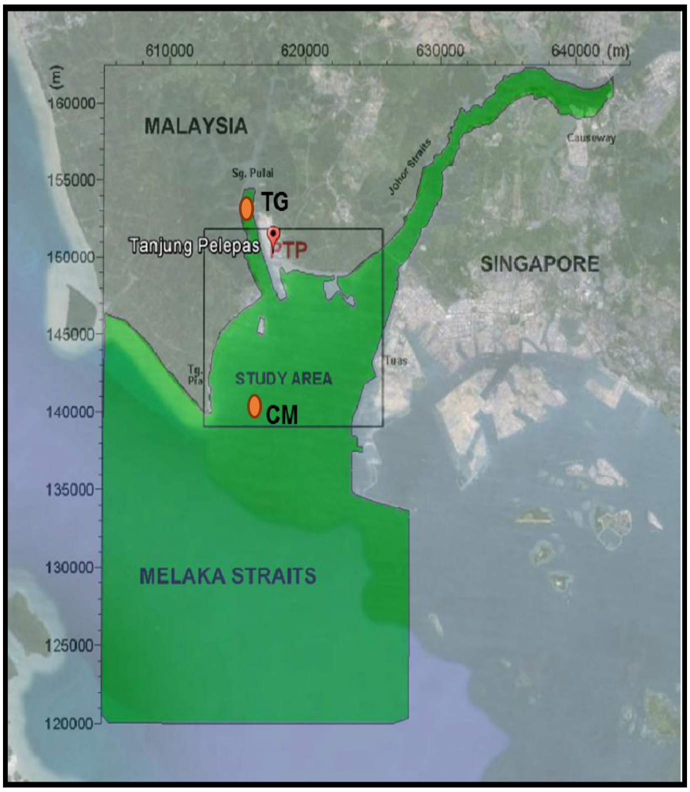

Figure 5. Location of tide gauge and current meter.

A comparison between the simulated results and observed data was done for calibration and validation purpose by comparing water level (Figure 6a and 6b), current magnitude (Figure 6c and 6d) and direction (Figure 6e and 6f) during spring and neap tide condition. The modelled and field data showed that the model reproduced the phase as well as the amplitude closely with the predicted tides. The simulated currents were slightly higher than the measured currents. In general, the water level in the estuary during spring tide is higher than tide level during neap condition. The current vector in Figure 7 shows that the current velocity during ebb tide is stronger than during flood tide. This phenomenon shows that the estuary has a good flushing system from the Pulai River into the sea.

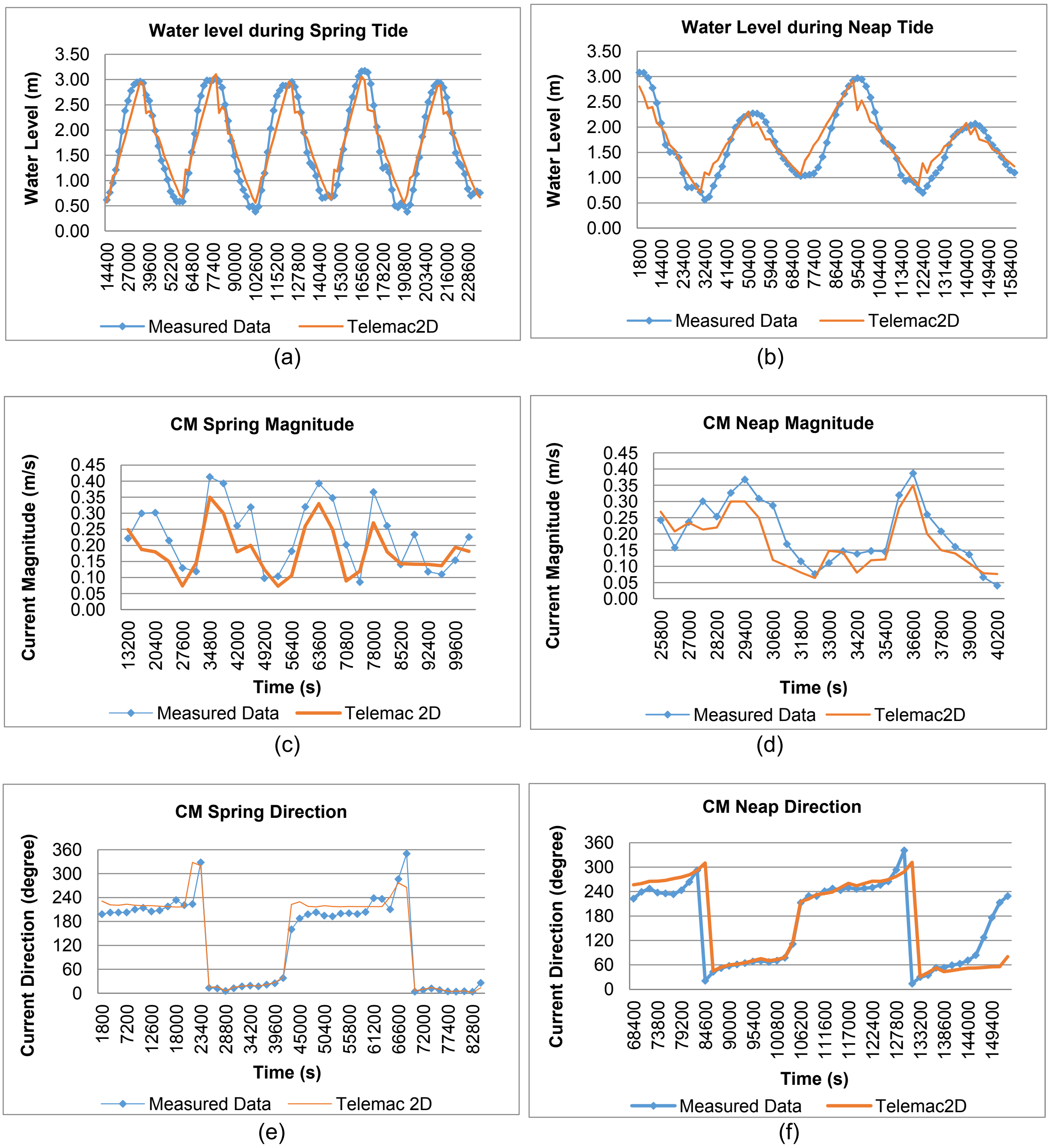

Figure 6. Calibration and validation curves for water level and current during spring and neap tide condition.

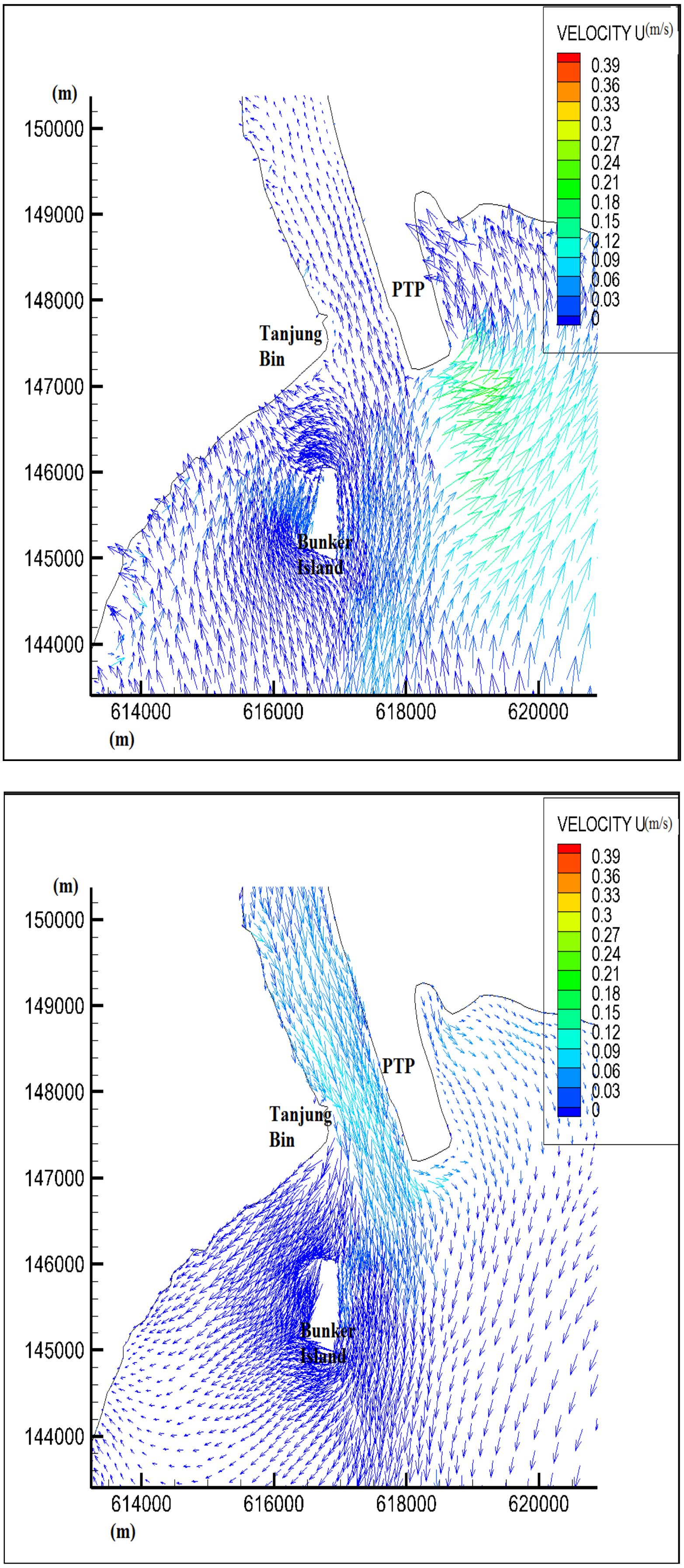

Figure 7. Current vector diagram on flood tide (top) and ebb tide (bottom) during spring tide.

4.2 Simulation of the transport of oil slick on water surface

In the simulation presented in Figure 8, a hypothetical heavy fuel was considered to occur in two different locations with an initial volume of 6 m^3 and the water surface temperature is 303K. The initial release of instantaneous spill was during flood tide. The simulation was carried out between 12th and 15th October 2015 during neap tide condition. A comparison of movement of oil slick on the water surface was modelled within the period of 36 hours in two different initial spill locations, (Figure 8a) estuary of Pulai River (approximately at 1^{o}19'39.29"N, 103^{o}33'23.95"E) and (Figure 8b) entrance of navigation channel (approximately at 1^{o}15'47.95"N, 103^{o}32'21.39"E). The oil has a density of 972 kg/m^3 and kinematic viscosity at 17.22x10^{-6} m^2/s. The black dots shown in the figure represents the oil particles in the water column.

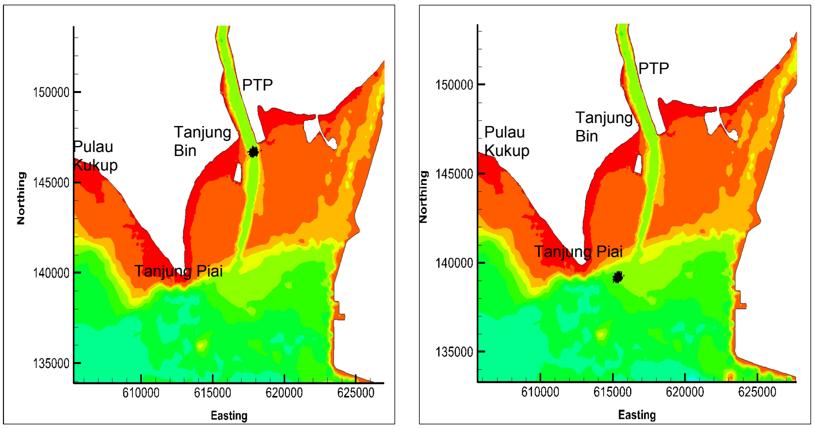

Figure 8. Predicted initial location of spill (a) Estuary of Pulai River (first case) and(b) Entrance of navigation channel (second case).

Based on the 2D simulation of the spill for a period of 36 hours, the transportation and weathering process of the oil over time was obtained. The spill trajectory for the hypothetical initial spill at the estuary of Pulai River was printed at the 6th, 12th, 24th and 36th hour to determine the spreading of oil particles on the water surface as shown in Figure 9.

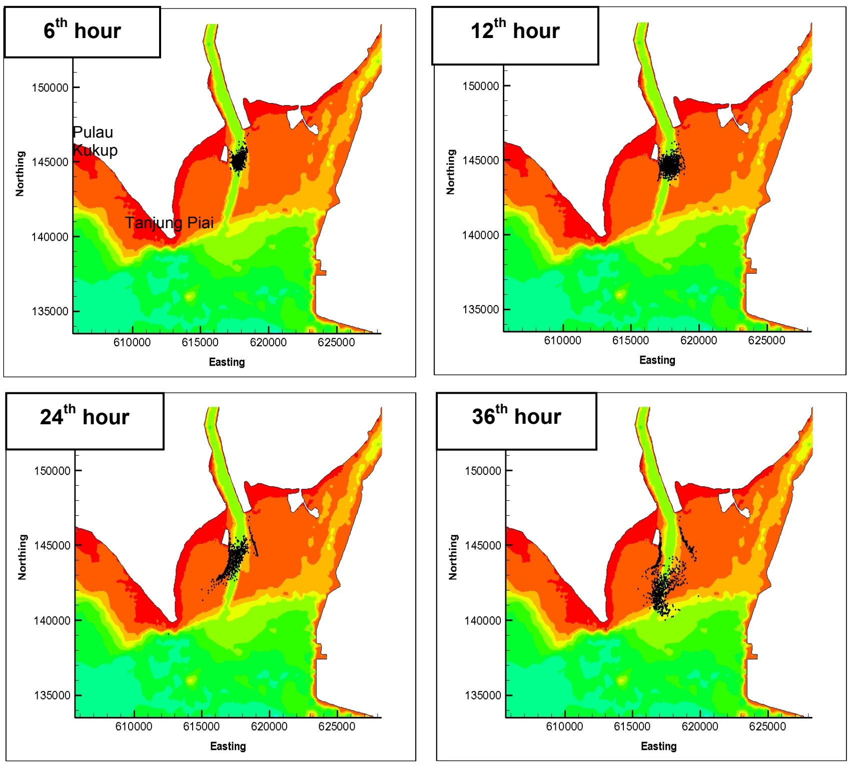

Figure 9. Oil Spillage discharged from the mouth of Pulai River.

During the 6th hour after the spill, the initial spill discharge from the estuary of Pulai River moves away from the channel and continues to deposit along the sides of the channel of the bunker island and the river mouth. The oil eventually spreads out after the 12th hour and the remaining volume continues to flow with the current direction and will eventually move towards Tanjung Piai shoreline if the spill is left unattended within the period of 36 hours.

The spill movement for the initial oil discharge at the entrance of the navigation channel is shown in Figure 10. After the 6th hour, the movement of oil moves and spread westwards until it reaches and deposits at the shoreline of Tanjung Piai. Even after the 24th hour, its movement continues to be carried by tidal currents and there is high possibility that it reaches at leave traces at Pulau Kukup as can be seen at the 36th hour in Figure 10. According to Vethamony et al. (2007), viscosity of oil plays an important role in spreading immediately after spillage. If the oil is less viscous, the spreading of oil would spread and cover a larger area.

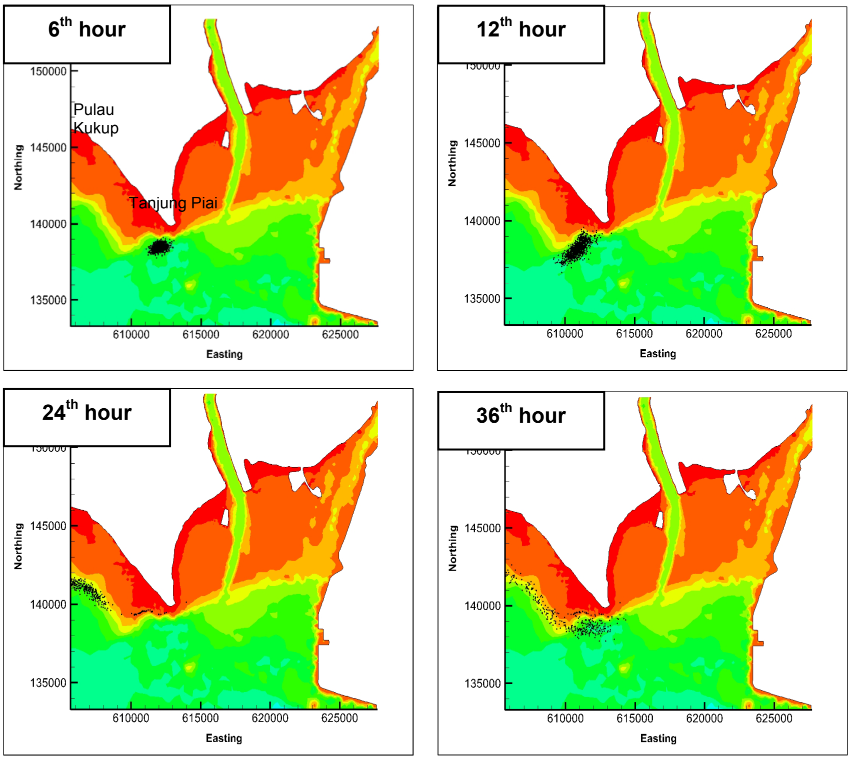

Figure 10. Oil Spillage discharge from the entrance of the navigation channel.

Figure 11 shows the percentage of oil mass remaining in the area over a 6 hour period within 36 hours of spill at both locations. At both locations of the spill, it can be seen that the percentage of mass of moving oil in the domain decreases over time within the period of 36 hour, the percentage of remaining oil that has been discharged from river mouth is 55.17% whereas the percentage of remaining oil discharged from the entrance of the navigation channel is 82.19%. There is less percentage of moving oil remaining in the domain in the first scenario as the oil experienced ebb tide flushing out of the river and due to a smaller channel width, some oil in the domain could be deposited along the shoreline or experience evaporation and dissolution process.

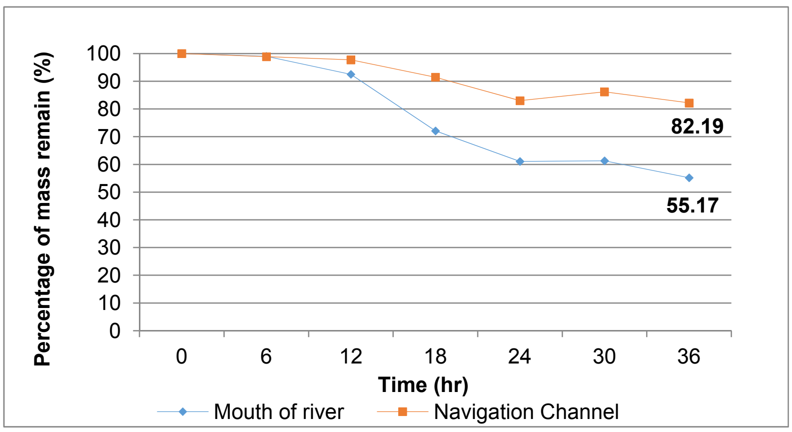

Figure 11. Percentage of mass of oil remaining in the domain.

Figure 12 shows the percentage of oil stranded in the domain in the period of 36 hours. The figure shows that the oil stranded when the spill occurs at the estuary of Pulai River over time (39.51%) is more than that when the spill occurs at the navigation channel (39.51%). According to Goeury et al. (2014), the oil will be stranded along the coastline if the slick thickness is greater than the water level under the oil slick or when the size of bottom roughness is greater than the water level. This shows that the reduction in remaining mass (Figure 11) is due to oil deposition. The slight fluctuation of percentage of stranded oil during 18 to 30 hour is due to the oil refloating process, whereby an oil particle previously deposited on the shore can be picked up again as a result of hydrodynamic variations following the verification of phenomenon when the water level under the oil slick is greater than the slick thickness or when the water level is greater than the size of bottom roughness.

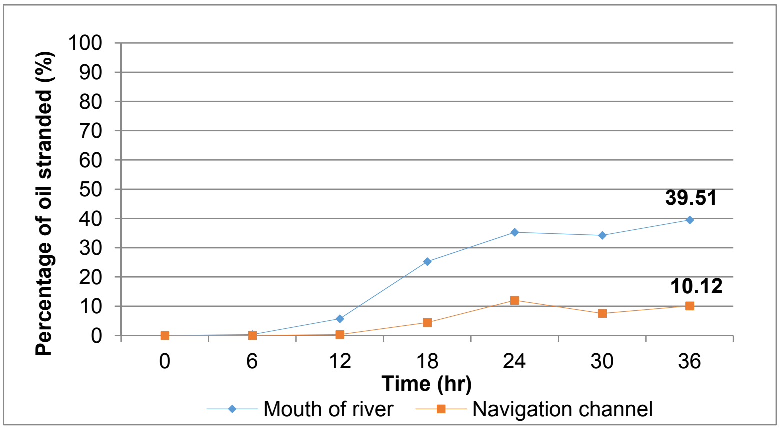

Figure 12. Percentage of oil stranded in the domain.

In the weathering process of oil in a water column, evaporation also plays an important role in the early stages of a spill as this is the process whereby the type of spilled oil and its components are a crucial factor (Inan and Balas, 2010). If a spillage occurs, light crudes or refined products can lose up to 75% of their volume in a few days (Goeury et al., 2012). Light oils have comparatively low viscosity and dispersion thus occurs at a higher rate (Janeiro et al, 2008). Higher dispersion increases surface area of slick and furthermore increases evaporation rate as the oil spreads (Christiansen, 2003). However, since the viscosity of heavy crude oil is higher and the boiling point of each hydrocarbon element is higher, thus the evaporated rate is slower in a few days. Based on Figure 13, generally the percentage of evaporated oil on the water surface in both locations is 5.08% in the first spill scenario and 6.18% in the second spill scenario which is less than ten percent after the 36^{th} hour of instantaneous spill. This shows that after a period of 36 hours, more than 90 percent of the hypothetical spill of $6m^3$ remains in the water column within the domain.

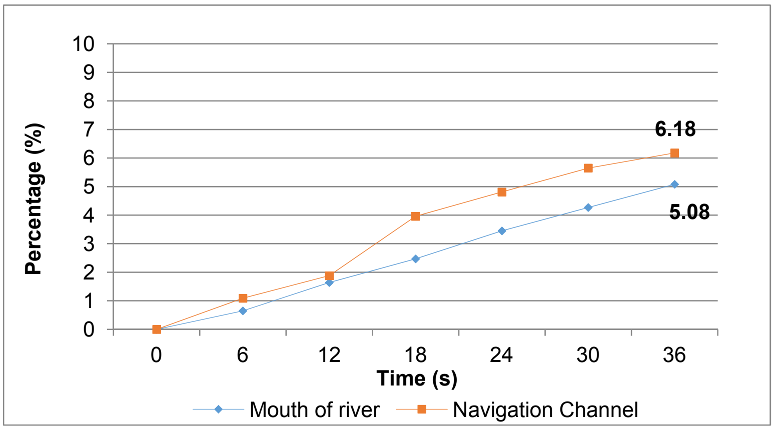

Figure 13. Percentage of oil evaporated in the domain.

5 CONCLUSIONS

In this study, the oil slick model has been coupled with the Telemac2D hydrodynamic model to simulate oil slick movement in coastal waters of Johor estuary under the effects of tidal and current conditions. The model predicts the movement of an oil slick and the fate processes of oil in the water column. Validation of the numerical model was carried out by comparing numerical tidal levels and field data. Two hypothetical scenarios was applied to the Johor Estuary, first with spill occurring at the estuary of Pulai River and the second scenario whereby the spill occur at the entrance of navigation channel. The results obtained show that any oil spill accidents that occur in both scenarios could be a considerable threat to the places nearby such as the reserved mangrove habitat at Kukup and also the Tanjung Bin Power Station and a quick response to contain the oil spill incident will be required. In general, any spill that occurs in the Johor waters will most likely spread towards Tanjung Piai and be stranded along coastal shore. For both situations of spill occurrence, less than ten percent of the oil evaporated within a period of 36 hours. As this study is a hypothetical case study, it could be further refined to include wind and waves factors for real spill scenarios.

ACKNOWLEDGEMENTS

The authors would like to acknowledge the support of Fundamental Research Grant Scheme (reference number: 4F607) under the Ministry of Higher Education Malaysia. The authors wish to thank Johor Port Authority and Port of Tanjung Pelepas Malaysia for the cooperation in environmental data collection.

REFERENCES

Abd Wahab, A.K., Ishak, D.S.M & Jamal, M.H. (2016). Coastal Vulnerability Index at a RAMSAR Site: a Case Study of Kukup Mangrove Island. *Engineering Challenges for Sustainable Future, Proceedings of 3rd International Conference on Civil, Offshore and Environmental Engineering (ICCOEE 2016)*, Taylor and Francis Group, London, ISBN 978-1-138-02978-1, 9-13.

Aghajanloo, K., Pirooz, M.D. & Namin, M.M. (2012). Numerical Simulation of Oil Spill Behavior in the Persian Gulf. *International Journal of Environmental Research*, 7(1), 81-96.

Awang, N.A., Jusoh, W.H.W. & Hamid, M.R.A. (2014). Coastal Erosion at Tanjong Piai, Johor, Malaysia. *Journal of Coastal Research*, 71(sp1), 122-130.

Chao, X., Shankar, N.J. & Cheong, H.F. (2001). Two-and Three-Dimensional Oil Spill Model for Coastal Waters. *Ocean Engineering*, 28(12), 1557-1573.

Delgado, L., Kumzerova, E., Martynov, M., Mirny, K., & Shepelev, P. (2005). Dynamic Simulation of Marine Oil Spills and Response Operations. *WIT Transactions on the Built Environment*, 78, 1-11.

Christiansen, B.M. (2003). Danish Meteorological Institute Technical Report, *ISSN 0906-897*, 14-17

Goeury, C., Hervouet, J. M., Benoit, M., Baudin-Bizien, I. & Fangeat, D. (2012). Numerical Modeling of Oil Spill Drifts for Management of Risks in Continental Waters. *WIT Transactions on Ecology and the Environment*, 164, 275-286.

Goeury, C., Hervouet, J.M., Baudin-Bizien, I. & Thouvenel, F. (2014). A Lagriangian/Eulerian Oil Spill Model for Continential Waters. *Journal of Hydraulic Research*, 52(1), 36-48.

Inan, A. & Balas, L.A.L.E. (2010). An Application of 2D Oil Spill Model to Mersin Coast. *WSEAS Transactions on Environment and Development*, 6(5), 345-354.

Issa, R., Rouge, D., Benoit, M., Violeau, D. & Joly, A. (2010). Modelling Algae Transport in Coastal Areas with a Shallow Water Equation Model Including Wave Effects. *Journal of Hydro-environment Research*, 3(4), 215-223.

Janeiro, J., Fernandes, E., Martins, F. & Fernandes, R. (2008). Wind and Freshwater Influence over Hydrocarbon Dispersal on Patos Lagoon, Brazil. *Marine Pollution Bulletin*, 56(4), 650-665.

Vethamony, P., Sudheesh, K., Babu, M.T., Jayakumar, S., Manimurali, R., Saran, A.K. & Srivastava, M. (2007). Trajectory of an Oil Spill off Goa, Eastern Arabian Sea: Field Observations and Simulations. *Environmental Pollution*, 148(2), 438-444.

Wang, S.D., Shen, Y.M. & Zheng, Y.H. (2005). Two-Dimensional Numerical Simulation for Transport and Fate of Oil Spills in Seas. *Ocean Engineering*, 32(13), 1556-1571.

Proceedings of the 37th IAHR World Congress
August 13 – 18, 2017, Kuala Lumpur, Malaysia

NUMERICAL SIMULATION OF SEAWATER EXCHANGE AND PARTICLE TRANSPORT IN KANMON STRAIT

ANDHITA TRIWAHYUNI(1) & KOJI ASAI(2)

(1) Doctoral student of System Design and Environmental Engineering, Yamaguchi University, Japan,
dhit4bimanyu@gmail.com
(2) Division of Civil and Environmental Engineering, Graduate School of Science and Technology for Innovation, Yamaguchi University
kido@yamaguchi-u.ac.jp

ABSTRACT

The Kanmon strait is a water body that separates two of Japan's four main islands, the south-western edge of Honshu Island and the north of Kyushu Island. It connects the Hibiki Nada in the Sea of Japan and the Suo Nada in the Seto Inland Sea. This strait is important for international shipping, and one of the most difficult strait for ship navigation. A numerical simulation of Kanmon Strait is developed by using Finite Volume Coastal Ocean Model (FVCOM) in order to understand the seawater exchange influence by M2 tidal component. By identifying the surface water exchange from the numerical simulation result, tidal current shows that the current tends to flow eastward during ebb tidal condition and westward during flood. The maximum of tidal current velocity can reach 2.92m/s during ebb tide and 3.07m/s during flood tide. A residual current pattern of Kanmon strait shows there are clockwise water circulation at the center of the strait and anticlockwise on both the strait mouths with a maximum velocities about 0.51m/s. The residual current pattern can be assumed to be occurred by the influence of coastal geometry shape and bathymetry. The 30 days simulation of Lagrangian particle distributions of Kanmon Strait shows that particles released on the eastern side of the strait tend to move westward more than the western side particles move eastward. In general, the numerical simulation result influenced by only M2 tidal component showed that surface seawater exchanges in Kanmon Strait are dominated by the westward movement. This is shown by higher westward current velocity during flood than the eastward current during ebb. Residual current is dominated by the southwest direction current, and also by the Lagrangian particle distribution where the percentages of particles moving to the Hibiki Nada are larger than to the Suo Nada.

Keywords: Kanmon strait; FVCOM; tidal current; particle tracking method; water exchange.

1 INTRODUCTION

The Kanmon strait is a water body that separates the two of Japan's four main islands, the south-western edge of Honshu Island (Shimonoseki City, Yamaguchi prefecture) and the north of Kyushu Island (Moji City, Fukuoka prefecture). It connects the Hibiki Nada in the Sea of Japan and the Suo Nada in the Seto Inland Sea (Figure 1). With a length of about 50km and width of 500~2,200m, the strait is well-known as important international shipping traffic route (to China and Korea). It is also known as one of the most difficult straits for ship navigation with more than 700 vessels passing everyday and the maximum tidal current speed is almost 10 knots (5.1 m/s) at the narrowest point (Nakano and Odamaki, 1990).

Research about Kanmon strait currents had been conducted in the past years. It becomes one of Japan Coast Guard concern due to its important function in safety navigation. The overall feature of Kanmon strait current structures was first understood by the measurement of tidal current carried out by using drifting floats tracked by many small boats (Fukunishi, 1948a; 1948b). Later, filed observation was limited due to the crowded shipping traffic and disastrous hydrodynamic forces acting on bottom-mounted or moored current meters. Elzeir et al. (2000) used a two-dimensional finite element depth-averaged Navier-Stokes primitive-equation model to simulate flow in Kanmon strait. They concluded that this strait has typical narrow water bodies connecting two open seas. It reflects most of the energy of any wave propagating from one open sea and allows very small part of the energy to be transmitted through the narrow channel. Therefore, a steep water surface gradient is generated inside the strait producing high velocities. Matsuura et al. (2002) created a new forecast system based on two-dimensional numerical simulation model with consideration of the meteorological effects to improve the predictive method of tidal current in the Kanmon strait. Yamaguchi et al. (2005) made a continuous mapping of a tidal current structure at the narrowest channel Hayatomono-seto from eight Coastal Acoustic Tomography (CAT) systems distributed on both sides of the straits which result was well compared to the ADCP data.

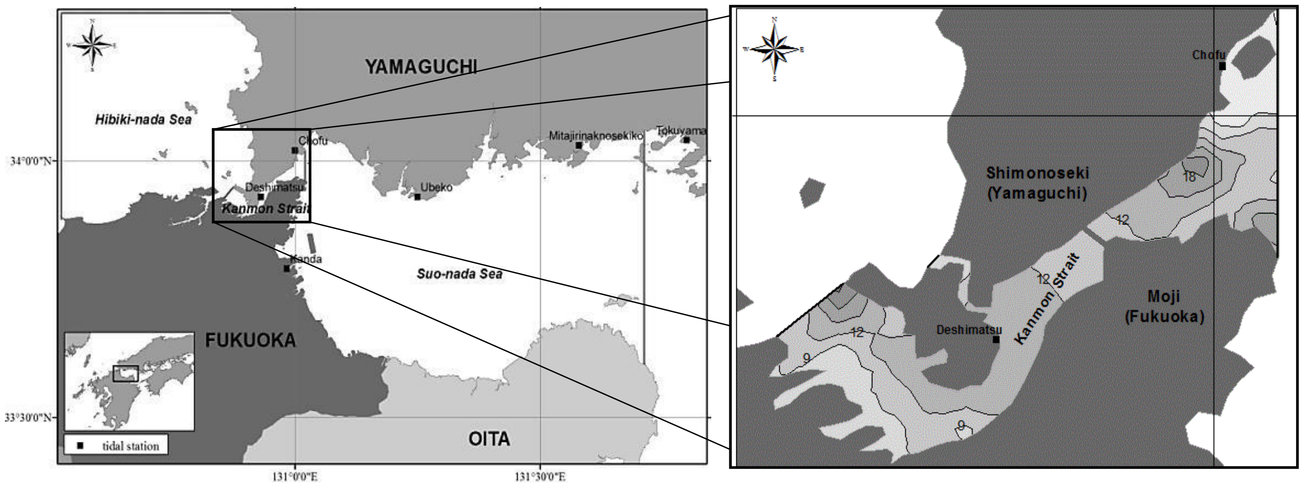

Figure 1. The location (left) and bathymetry of Kanmon Strait (right).

Tidal has an important role in generating currents that lead to the seawater exchange. Tide-induced residual current can be described as a periodic tidal flow generated by a transfer of vorticity from the tidal oscillating velocity field to the mean (residual) field whose magnitude is typically much smaller (Zimmerman, 1981; Sinha and Mitra, 1988). It had a non-linear interaction with the oscillation tidal, and the non-linearity is generated by the flow of water in a shallow region with irregular bottom topography, coastal geometry, and the bottom friction. They were important because of persistent features, link to the local bottom or coastal topography and fluctuating only with the strength of the semi-diurnal tides over the regular spring-neap cycle. They also can contribute significantly to the overall long-term of distribution and transport of water properties (Sinha and Mitra, 1988).

In this study, a numerical simulation model was developed by Finite Volume Coastal Ocean Model (FVCOM) which is a prognostic, unstructured grid, finite-volume, free-surface, three-dimensional (3-D) primitive equations ocean model developed originally by Chen et al. (2003). Based on the tidal components of stations around Hibiki Nada-Kanmon Strait-Suo Nada, the typical of tides type in this area is mixed and is mainly semi-diurnal (Table 1), which M2 is the dominant tidal component. The objective of this study is to identify the tidal current flow pattern, residual current, and Lagrangian particle transport in order to understand the seawater exchange of Kanmon Strait.

Table 1. The amplitude ratio of tidal station around Kanmon strait.

Tidal Station	Ratio of(O1+K1)/(M2+S2)	Tidal type
Saeki	0.61	Mixed tide, mainly semi-diurnal
Uwajima	0.53	Mixed tide, mainly semi-diurnal
Matsuyama	0.38	Mixed tide, mainly semi-diurnal
Kure	0.37	Mixed tide, mainly semi-diurnal
Hagi	0.84	Mixed tide, mainly semi-diurnal
Karatsu	0.35	Mixed tide, mainly semi-diurnal

2 NUMERICAL SIMULATION

2.1 Model setup

Numerical simulation in this study was conducted using Finite Volume Coastal Ocean Model (FVCOM). A simulation domain was built by developing an unstructured triangular grid mesh (Figure 2) using the Japan coastline data from Environmental Systems Research Institute (ESRI) Japan. It was bounded by three open boundary lines of Saeki-Uwajima(a), Matsuyama-Kure(b), and Hagi-Karatsu(c). A 500m gridded bathymetric data set from Japan Oceanographic Data Centre (JODC) was used and re-gridded to match the triangular grid. The model had a total of 7209 nodes and 12957 elements. In the vertical direction, the water column was divided into 11 equal sigma levels (σ =0 at the sea surface and -1 at the sea bottom).

The numerical simulation was forced by the sea level oscillation along the open boundaries (a, b, and c in Figure 2). The tide in the simulation area was dominated by mixed but mainly semi-diurnal type. In this study, only lunar semi-diurnal (M2) tide component obtained from Japan Oceanographic Data Center (JODC) was used as forcing. Uniform temperature and salinity were used as initial input and set uniformly for the whole simulation domain. The simulation was run for 35 days. The hourly results of the last 30 days were used to analyze the sea water exchanged of Kanmon Strait. The tidal residual current was identified due to its fundamental role in transporting various materials. Lagrangian particle on surface water was released at the beginning of the last 30 days in order to identify the surface water exchange influenced by the tidal forcing input to the simulation.

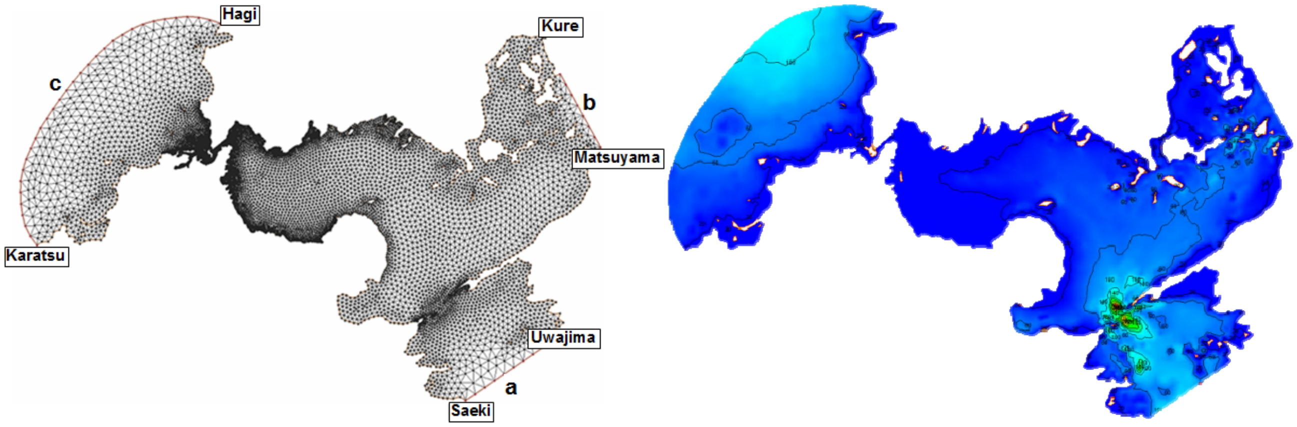

Figure 2. Unstructured triangular mesh grid (left) and bathymetry (right) of simulation domain.

2.2 Tidal simulation and verification

Root Mean Square Error (RMSE) was used to verify the simulation performance by measuring the difference between tidal height predicted by simulation and the tidal observation on station around Kanmon strait.

$$RMSE = \sqrt{\frac{\sum_{i=1}^{n}(X_{obs,i} - X_{sim,i})^2}{n}} \qquad [1]$$

where X_{obs} is observed values and X_{sim} is simulation values at time/place i.

Verification was made to the nearest tidal stations around Kanmon Strait, which are Chofu and Deshimatsu. The RMSE of each station is 0.0590m and 0.0660m. These results indicate good simulation performances represented by tidal height. Figure 3 shows the comparison between the simulation and the observation data in Chofu and Deshimatsu. The amplitude and phase difference of tidal stations around Kanmon Strait are available at Table 2. The observed and numerical simulation results have a good agreement with both stations where r^2 in Chofu shows 0.9944 and 0.9919 in Deshimatsu.

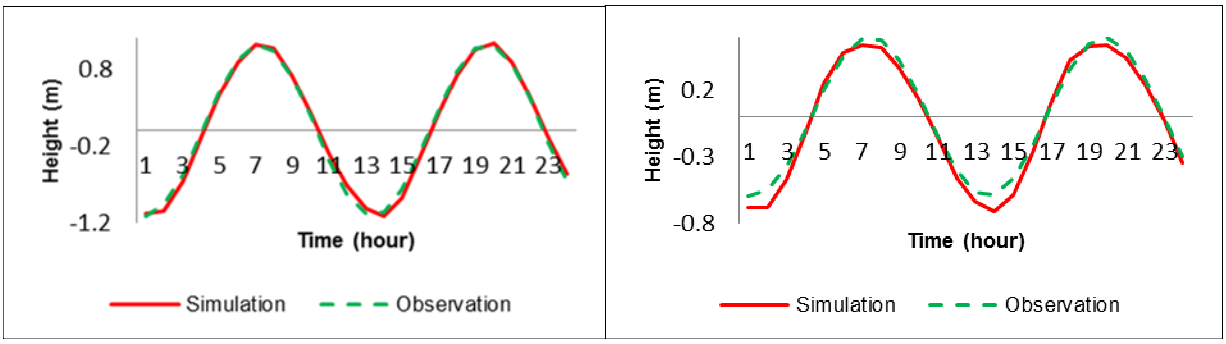

Figure 3. The comparison of water level height between observation and simulation (left: Chofu, right: Deshimatsu).

Table 2. Comparison of simulation and observation of M2 tidal elevation at tidal stations in the model domain.

Station	Amplitude-H			Phase-θ		
	Simulation	Observation	ΔH	Simulation	Observation	Δθ
Kanda	1.1128	1.0863	0.0265	150.2921	152.3131	-2.021
Deshimatsu	0.6431	0.5986	0.0445	146.0783	144.6651	1.4132
Chofu	1.1164	1.1129	0.0035	147.6504	151.0277	-3.3773
Ubeko	1.0813	1.0695	0.0118	153.4114	155.1448	-1.7334
Mitajirinakosekiko	0.9209	0.9233	-0.0024	158.0574	158.7232	-0.6658
Tokuyama	0.898	0.9022	-0.0042	158.6578	158.5701	0.0877

3 RESULTS AND DISCUSSIONS

3.1 Current patterns

The numerical simulation of surface current pattern was shown in Figure 4. In agreement with Elzeir et al. (2000), Kanmon Strait had the characteristic of narrow water bodies which has higher velocity compared to its surrounding. Induced only by the M2, the numerical simulation shows that the current reaches its strongest eastward direction during ebb water level position and oppositely it had the strongest westward current direction during flood. In this simulation, the eastward flow during ebb had the average velocity about 0.79m/s and maximum 2.92m/s. Meanwhile, during the flood-tide, the water tends to flow to the west with average velocity about 0.86m/s and maximum 3.07m/s.

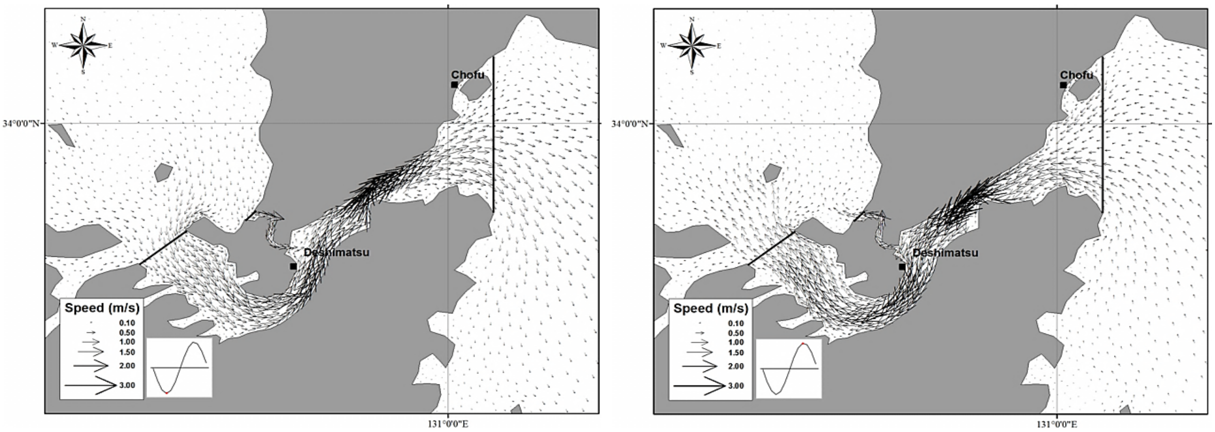

Figure 4. Tidal surface current patterns of Kanmon Strait during ebb (left) and flood (right) condition.

In order to verify the Kanmon Strait current pattern, the tidal current chart at Hayatomo-seto (Figure 5) which is the narrowest part of the strait was used. The verification was done by converting the current velocity of numerical simulation result units (in meter per second) to the same current velocity units in the tidal chart (in knots). The numerical simulation of tidal current induced by M2 tidal component (Figure 6) in Hayatomo-seto shows a good agreement on direction when compared to the tidal current chart. The peak of eastward currents appears during the ebb tidal position and oppositely it happens on flood tidal position in Deshimatsu tidal station. In general, the numerical simulation of tidal currents in Hayatomo-seto can represent well the current velocity condition. It can be seen by the similar increasing velocity current pattern when they move toward the Hayatomo-seto whether in eastward or westward current. Figure 5 and 6 also show us that westward current tend to be larger than the east going.

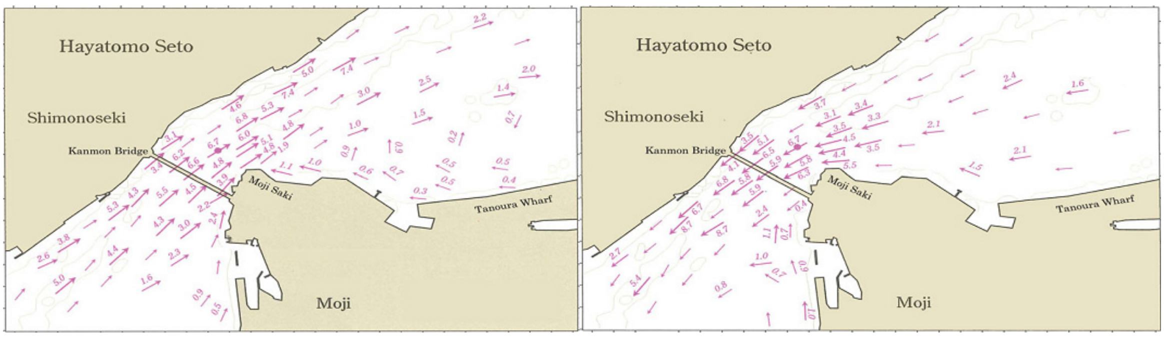

Figure 5. Tidal current charts of Hayatomo-seto at the peak of eastward currents (left), and westward currents (right). (Source: Tidal Current Chart in Kanmon Kaikyo, issued by Japan Coast Guard in February 2006).

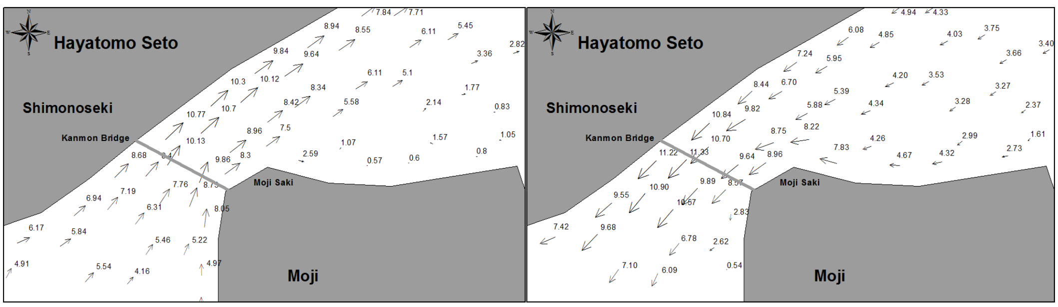

Figure 6. Tidal current of numerical simulation at ebb tidal position (left) and flood tidal position (right).

3.2 Tide-induced residual current

The residual current calculation was also made in this study. Figure 7 shows the three major residual circulations in the surface water of Kanmon Strait. They were anticlockwise current at the center of the strait and clockwise circulations at both of the strait mouths. It had averaged current velocity about 0.15m/s. The circular pattern of residual current in Kanmon Strait can be assumed to be occurred by the influenced of coastal geometry profile and bathymetry. At the narrowest part of the strait (Hayatomo-seto), the clockwise and anticlockwise currents meet and create a large current velocity with a maximum about 0.51m/s toward Shimonoseki. The frequency distribution of Kanmon Strait residual currently shows that the most of the current was about 19.47% flows to the southwest, and the fewest was about 8.72% which flows to the southeast.

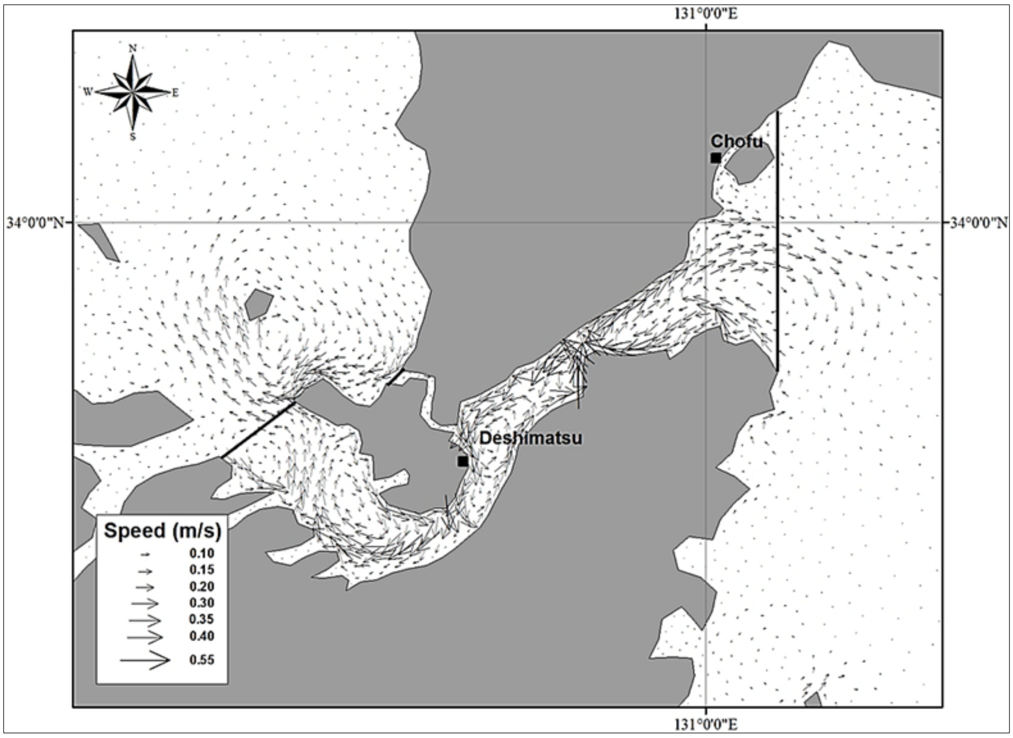

Figure 7. Residual current in Kanmon Strait.

3.3 Particle tracking

Surface water Lagrangian particle transportation was made to identify the surface exchange water that passes through Kanmon Strait. In this study area, the particle was set in 5 domain areas (Figure 8, left) where in total, they are 12759 particles released. They were released and tracked for 30 simulation days (Figure 8, right).

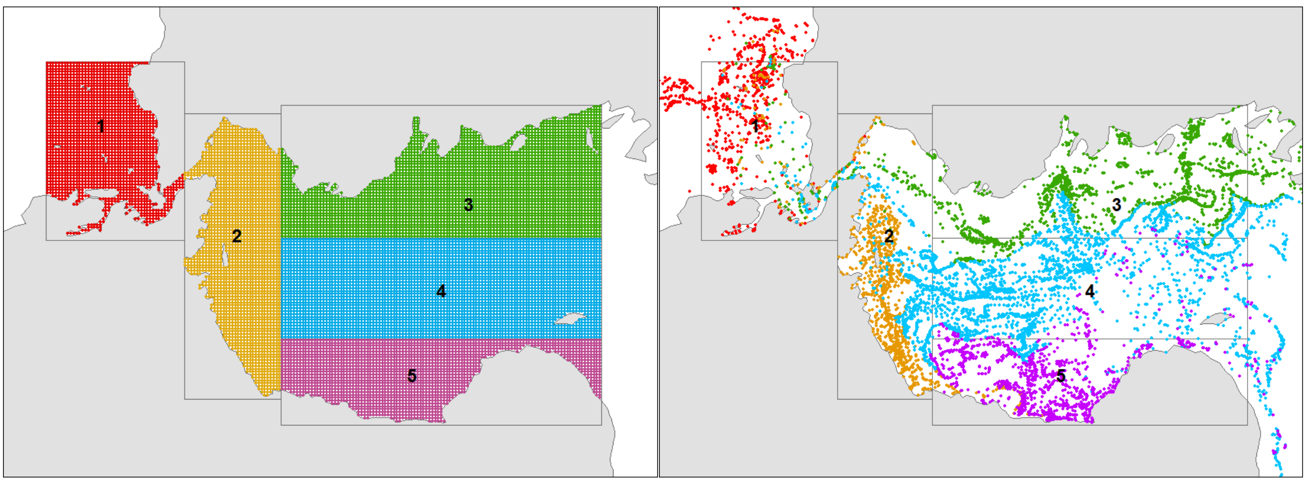

Figure 8. Particle tracking 30-day position before they were released (left), and at days 30 (right).

This study shows that the opportunity of particles to move from Hibiki Nada to Suo Nada is smaller than vice versa. Table 3 shows the portion of particles which remains in their initial area or moves to the other areas. The particles from area 1 were only able to move for about 1.83% inside Suo Nada to area 2 and they cannot be found in the other areas, while the particles from almost all areas inside Suo Nada (22.01% from 2, 6.58% from 3, and 2.90% from 4) are able to move to area 1. This result also shows that 90.12% particles from area 5 tend to be kept inside this area or moved to east. This particle distribution shows that at the surface water level, the water exchange from Suo Nada to Hibiki Nada through the Kanmon Strait tends to be more dominant.

Table 3. The distribution of particle movement.

Area From/To	**1**	**2**	**3**	**4**	**5**	**Out**
1	80.74%	1.83%				17.42%
2	22.01%	72.54%			5.02%	0.43%
3	6.58%	6.24%	73.43%	7.62%		6.12%
4	2.90%	15.29%	11.88%	54.85%	5.94%	9.14%
5		0.27%	0.64%	6.32%	90.12%	2.66%

4 CONCLUSIONS

A numerical simulation of Kanmon Strait surface water current pattern and Lagrangian particle tracking is conducted by only considering M2 tidal component as forcing factor. Based on the verification of tidal height, the numerical simulation can represent the tidal very well which is shown by the RMSE and Coefficient determination value. The numerical simulation also shows a similar current direction pattern, especially in the Hayatomo-seto area.

The numerical simulation can represent the Kanmon Strait seawater exchange well. The surface seawater exchange in Kanmon Strait is dominated by the westward movement. This is shown by higher westward current velocity during flood than the eastward current during ebb, and residual current that is dominated by the southwest direction current. It is also clarified by the Lagrangian particle distribution where the numbers of particle move to the Hibiki Nada are larger than to the Suo Nada.

Overall, this study has develop a general understanding to the seawater exchange of Kanmon Strait by using the FVCOM to analyze the current flow pattern, residual current, and Lagrangian particle transport. However, lack of forcing input that only consider M2 tidal component and the availability of observation data had limit the verification of current velocity result. Therefore, to improve the numerical simulation result and obtain more understanding about these water areas, an analysis of larger areas including Hibiki and Suo Nada will be conduct by using more forcing factors such as other tidal components and meteorological data.

REFERENCES

Chen, C.S., Liu, H.D. & Beardsley, R.C. (2003). An Unstructured Grid, Finite Volume, Three-Dimensional, Primitive Equations Ocean Model: Application to Coastal Ocean and Estuaries. *Journal of atmospheric and oceanic technology*, 20(1), 159-186.

Elzeir, M., Hibino, T. & Nakayama, K. (2000). Simulation of Kanmon Strait; A Channel Between Two Seas. *27th International Conference on Coastal Engineering*, ICCE Coastal Engineering, 3861-3860.

Fukunishi, M. (1948a). The Tidal Current in Kanmon Strait (I). *Journal of the Japan Society of Civil Engineers*, 33(2), 10–13. (in Japanese)

Fukunishi, M. (1948b). The Tidal Current in Kanmon Strait (II). *Journal of the Japan Society of Civil Engineers*, 33(2), 16–19. (in Japanese)

Matsuura, N., Sasaki, T., Sato, S. & Horii, R. (2002). A New Tidal Current Forecasting in the Kanmon Strait. *Journal of the Japan Society for Marine Surveys and Technology*, 14(1), 11-17.

Nakano, S. & Odamaki, M. (1990). *Tide and Tidal Current Around Japan*. In Coastal Oceanography of Japanese Islands. Supplementary Volume, ed. By Coastal Oceanography Research Committee (Tokai University Publish), 143-164. (In Japanese)

Sinha, P.C. & Mitra, A.K. (1988). Tidally Induced Residual Circulation. *Computers & Mathematics with Applications*, 16(1-2), 153-167.

Yamaguchi, K., Lin, J., Kaneko, A., Yamamoto, T., Gohda, N., Nguyen, H.Q. & Zheng, H. (2005). A Continuous Mapping of Tidal Current Structures in the Kanmon Strait. *Journal of Oceanography*, 61, 283-294.

Zimmerman, J.T.F. (1981). Dynamics, Diffusion and Geomorphological Significance of Tidal Residual Eddies. *Nature*, 290, 549-555.

TIDAL BORE GENERATION AT THE EASTURIES OF THE EAST COAST OF SUMATRA

ALAMSYAH KURNIAWAN(1), ULUNG JANTAMA WISHA(2), SEMEIDI HUSRIN(3) & ENTIN A. KARJADI(4)

(1,4) Ocean Engineering Program, Institut Teknologi Bandung (ITB), Bandung, Indonesia,
alamsyah@ocean.itb.ac.id; entinkarjadi@gmail.com
(2) Research Institute for Coastal Resources and Vulnerability, Ministry of Marine Affairs and Fisheries, Padang, Indonesia,
ulungjantama@gmail.com
(3) Research & Development Centre for Coastal and Marine Resources, Ministry of Marine Affairs and Fisheries, Jakarta, Indonesia,
semeidi@gmail.com

ABSTRACT

Tidal bore travels up from estuary to a river against the direction of the river's flow. This phenomenon is a fascinating event as in Kampar River, Indonesia. However, according to the locals, the magnitude of the tidal bore of Kampar known as "Bono" has been decreasing significantly, which may be due to the changes in the physical and hydrodynamic conditions at the estuaries and the river. A better understanding of these processes may help in conservation and restoration of the tidal bore phenomenon. Present work introduces and analyses the physical processes of 4 (four) rivers (i.e. Kampar, Rokan, Indragiri and Siak) along the eastern side of Sumatra Island. Tidal bore generation is analyzed using hydrodynamic models in the estuaries and is validated by field measurement of tides in the river mouth. The model covers Malacca Strait in which the boundaries lies at Andaman Sea, South China Sea and Java Sea. Temporal distributions and comparisons between simulated and observed tidal results suggested that tidal conditions of the 4 (four) estuaries can be analyzed based on the model output. Detailed behavior of the tidal at each estuary is then analyzed qualitatively based on the measured tidal bore upstream taking into consideration the river morphology. A better understanding of these processes may contribute to better management practices in tidal bore affected rivers and estuaries, including Bono of the Kampar river in Indonesia.

Keywords: Tidal bore; estuaries; hydrodynamic models; bono; kampar river Indonesia.

1 INTRODUCTION

The wonderful sight of a tidal bore surging upstream can be seen in many specific estuaries around the world. The best historically documented tidal bores are probably those of the Seine river in France and Qiantang river in China (Chanson, 2003). However, tidal bores are vulnerable to the nature and human activities. According to Lynch (1982), a powerful bore known as the "Burro", which was as much as 4 m high, once regularly went up the Colorado River. Over the past 15 years, however, agricultural water control and silting have changed the geometry of the river mouth. As a result, the bore has been greatly reduced and is usually little more than a ripple lost in the river's other waves. Numerous studies have been carried out to learn this phenomenon (Chanson, 2011). Detail definition and basic theory of tidal bores can be found in Chanson (2010; 2011).

In line with those findings, according to the locals, the magnitude of the tidal bore of Kampar, Indonesia, known as "Bono" has been decreasing significantly which may be due to the changes in the physical and hydrodynamic conditions at the estuaries and the river. Present work introduces and analyses 4 (four) rivers from north to south (i.e. Rokan, Siak, Kampar, and Indragiri) along the eastern side of Sumatra Island, respectively. Their detail locations can be found in Table 1 and Figure 1.

Tidal bore generation is analyzed using hydrodynamic models in the estuaries and is validated by field measurement of tides in the river mouth. The model covers Malacca Strait in which the boundaries lies at Andaman Sea, South China Sea and Java Sea. Temporal distributions and comparisons between simulated and observed tidal results suggest that tidal conditions of the 4 (four) estuaries can be analyzed based on the model output. Detailed behavior of the tidal at each estuary is then analyzed qualitatively based on the spatial distribution of the tidal constituents. A better understanding of these processes may contribute to better management practices in tidal bore affected rivers and estuaries, including Bono of Kampar river in Indonesia.

The aim of the numerical model used in the present work is to analyze and investigate the tidal bore generation at the estuaries. As the present model is not able to simulate the tidal propagation, the present model results can be used as an input data of the subsequent propagation numerical model from estuaries into the river upstream.

Table 1. Estuaries locations.

RIVER	LONGITUDE	LATITUDE
ROKAN	100.771333	2.103213
SIAK	102.168411	1.230658
KAMPAR	103.267086	0.527138
INDRAGIRI	103.249645	-0.297644

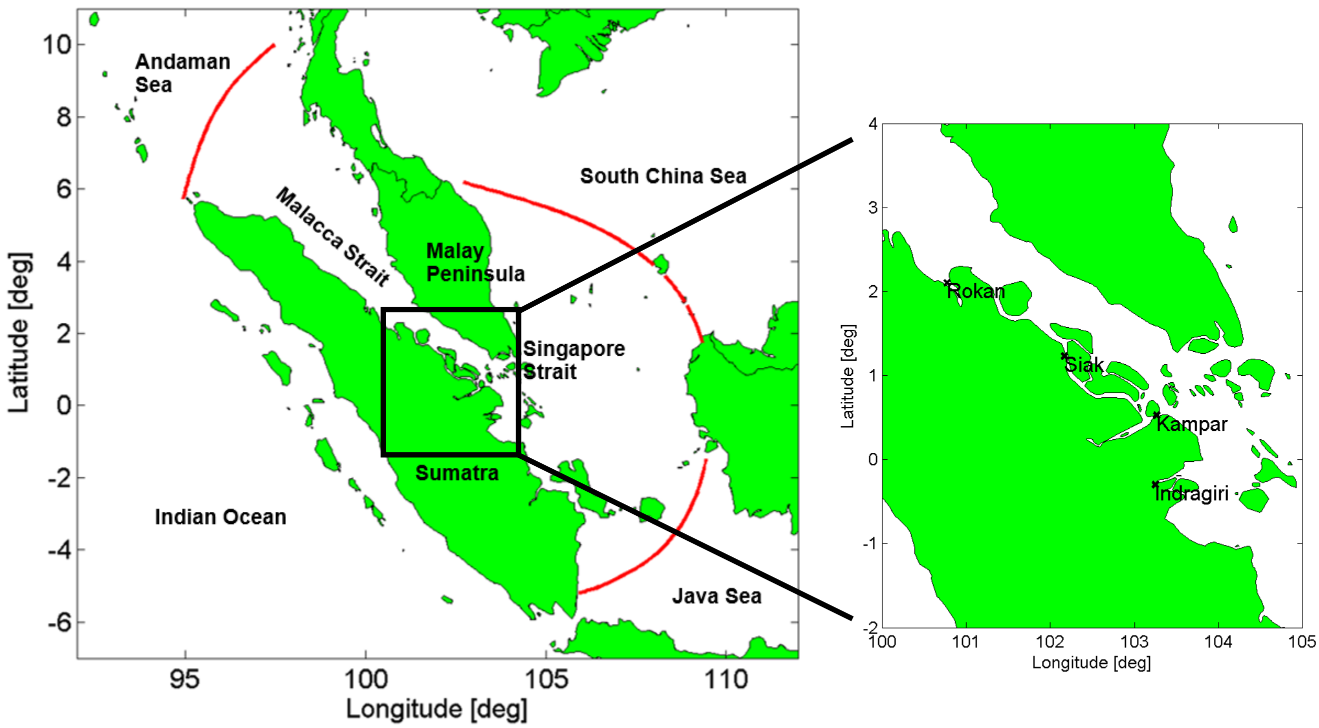

Figure 1. Area of interest showing the numerical model open boundary locations (red lines) and the location of the 4 (four) estuaries. Water level observation is carried out at Kampar.

2 METHODOLOGY

Present work analyzes tidal bore generation at estuaries along the east coast of Sumatra using numerical modelling, spatial distribution of tidal components, quantitative and qualitative assessments.

2.1 Numerical model

The numerical model in this study solves the 2D depth averaged shallow water flow equations (Deltares, 2011). For embedded sub-domains covering coastal areas and straits with complex topographic features in the Malacca Strait, a fine resolution tidal model was used (Figure 2). The tidal model uses a boundary-fitted orthogonal spherico-curvilinear grid which reduces potential modelling errors from representing the coastal geometry, especially when compared to a rectangular grid. The model domain covers the region, stretching from northern Sumatra to the eastern coast of Borneo. The total number of grid cells in the model is approximately 38,500 and the grid cells vary smoothly in size from approximately 20-40 km^2 at the open sea boundaries to approximately 150-200 m^2 in the interior waters. The model has open water boundaries across the Andaman Sea, Java Sea and the South China Sea. Along these open boundaries, best estimates of tidal constituents were prescribed, which are expanded during computations to provide tidal water level forcing of the model. The eight main tidal constituents Q_1, O_1, P_1, K_1, N_2, M_2, S_2 and K_2 were prescribed (phases related to GMT+8) at the three open sea boundaries, while tide generating forces were included in the interior domain. The bathymetry in the model domain ranges from a maximum depth of about 2000 m in the Andaman Sea to approximately 40-50 m depth in the Singapore Strait. A Manning friction coefficient of 0.022 m$^{-1/3}$s had been applied for bed friction. A detailed description of the model including tidal sensitivity analysis i.e. root mean square error (RMSE) and coefficient correlation (r) and improved tidal representation can be found in Kurniawan (2014).

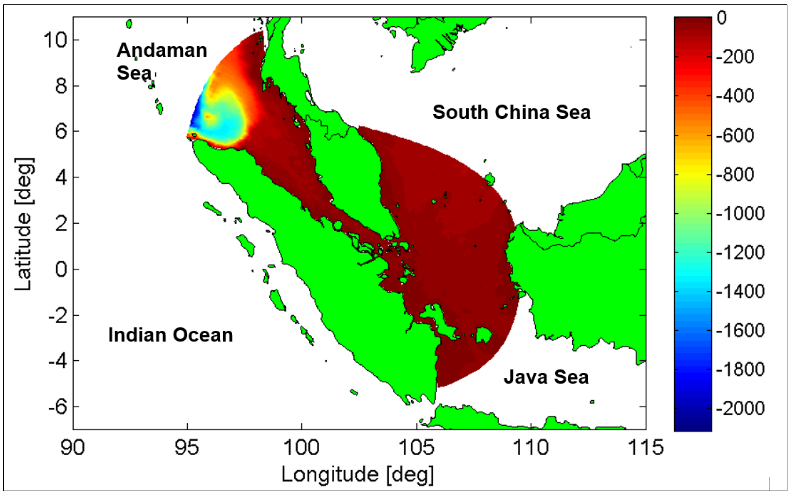

Figure 2. Tidal model domain computation showing its extent and bed level.

2.2 Tidal constituent

The east coast of Sumatra is the Malacca Strait which is dominated by the largest constituent, principal lunar and solar semi-diurnal, also known as the M_2 and S_2 tidal constituent (Wyrtki, 1961; Zu et al., 2008; Kurniawan et al., 2011; 2017). Therefore, present work focuses on these first two largest tidal constituents shown in Table 2.

For large scale tidal flow models, the numerical model is equipped with a facility to perform online Fourier analysis on computational results (Deltares, 2011). This enables the generation of computed co-tidal maps which can be quantitatively and qualitatively analyzed.

Table 2. Tidal Constituents.

	Angular Frequency (Degree/Hour)	Type
M_2	28.9841042	Semi-Diurnal
S_2	30.0000000	Semi-Diurnal

3 RESULTS AND DISCUSSIONS

3.1 Model validation

The 2D depth averaged model developed in the present study was run for 1 month (24 April – 23 May 2016), covering 2 (two) spring and 2 (two) neap periods with a 0.5 min time step. The model results were compared with measured water levels as depicted in Figure 3 for spring-neap variations. The observed tidal range varied from 2 m during neap tide to 3.5 m during spring tide. The water surface fluctuations obtained from the model were in good agreement with the field data though some minor discrepancies exist: the observed high waters were slightly lower than the predicted high waters; however, according to RMSE and 'r' values, these differences are within 10%. It can be concluded that the numerical model deems valid and can be used for quantitative and qualitative assessment of tidal bore generation at 4 (four) estuaries.

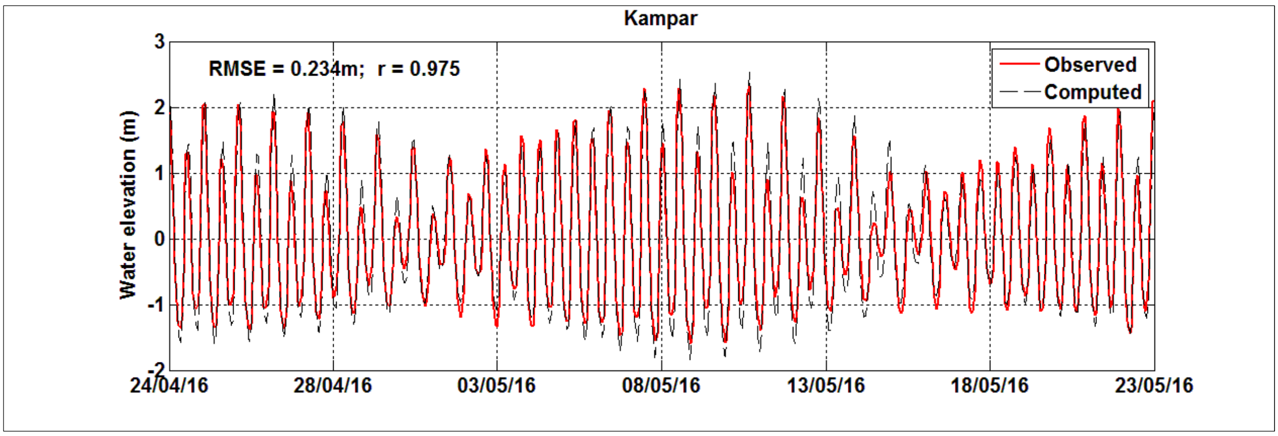

Figure 3. Temporal distribution of water level showing comparison between observed and computed at Kampar. Root Mean Square Error (RMSE) and coefficient correlation (r) are based on Kurniawan (2014).

3.2 Qualitative Assessment

A tidal bore may form with large tidal ranges (more than 4 to 9 m) in a flat converging channel (Donnelly and Chanson, 2005). Based on this finding, as can be seen in Figure 1, all the 4 (four) estuaries have a flat converging channel, which may generate tidal bores. Furthermore, as can be seen in Figure 4, Rokan and Kampar have a tidal range up to 5 m, whereas Siak and Indragiri had a much less tidal range which was up to 2 m. Nevertheless, the water level elevation may increase as the water propagates in to the river.

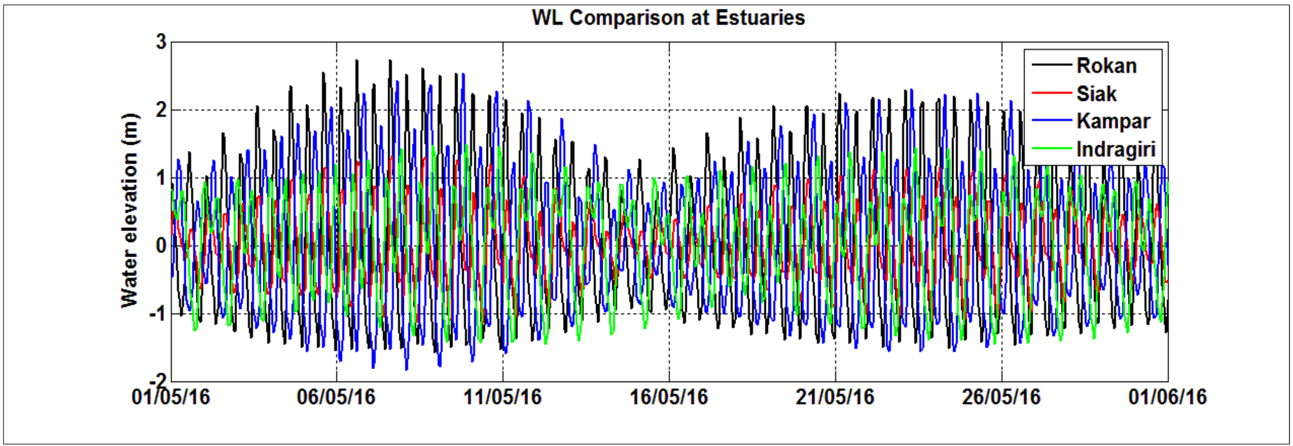

Figure 4. Temporal distribution of water level showing at 4 (four) different estuaries i.e. Rokan, Siak, Kampar and Indragiri.

A temporal distribution of the water level elevation may be insufficient in giving information on tidal range over a long period, therefore, the analysis of the tidal constituents is then carried out to give more information on the water level elevation. Figure 3 and 4 show spatial distribution of semi-diurnal tidal constituent in the model domain and more detail at the 4 (four) estuaries. As can be seen, semi-diurnal tidal constituents were dominant in the Malacca Strait from Andaman Sea in to the Singapore Strait. The results support the basic and general properties of the waters and circulations in the Malacca Strait which were provided by previous studies (Wyrtki, 1961; Zu et al., 2008; Kurniawan et al., 2011; 2017).

Focusing on more detail at 4 (four) estuaries, as can be seen in Figure 5, M2 tidal constituent had larger values at Rokan and Kampar (around 1.4-1.8) compared to Siak and Indragiri (around 0.2-0.6). In addition, Figure 6 shows consistent trend of S2 tidal constituent which had larger values at Rokan and Kampar (around 0.6-0.75) compared to Siak and Indragiri (around 0.075-0.225). The results indicate that the tidal range was larger at Rokan and Kampar compared to Siak and Indragiri. According to the locals, tidal bore only occurs at these 2 locations, i.e. Rokan and Kampar as shown in Figure 7. In addition, as shown in Figure 8, tidal bore elevation, current speed and direction measurement carried out at the Kampar upstream (noted as ADCP in Figure 8) supports the indication that 4-m tidal range at the estuary may form a tidal bore. This was consistent and supports the findings of the present work.

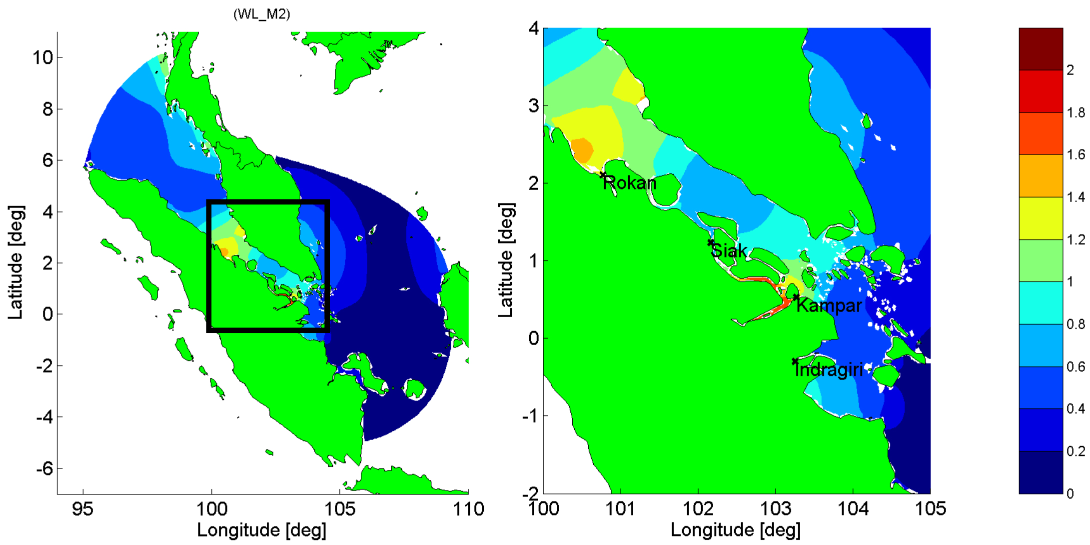

Figure 5. Spatial distribution of magnitude of M_2 tidal constituent showing in the model domain (left) and more detail at 4 (four) estuaries (right).

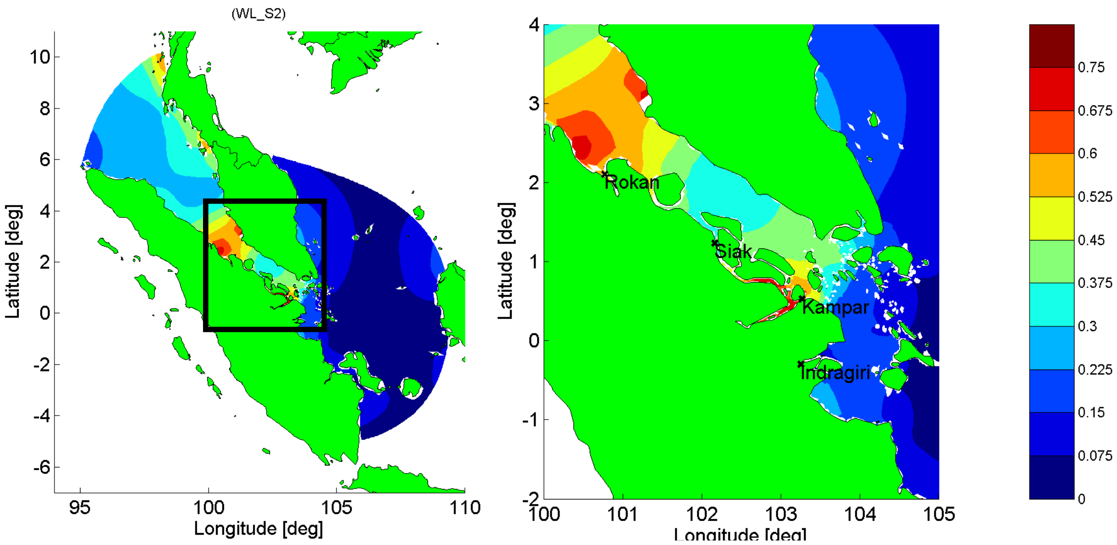

Figure 6. Spatial distribution of magnitude of S_2 tidal constituent showing in the model domain (left) and more detail at 4 (four) estuaries (right).

Figure 7. Photograph of tidal bores propagation (courtesy of Research Institute for Coastal Resources and Vulnerability, Ministry of Marine Affairs and Fisheries, Padang, Indonesia) showing at Rokan (left) and Kampar (right).

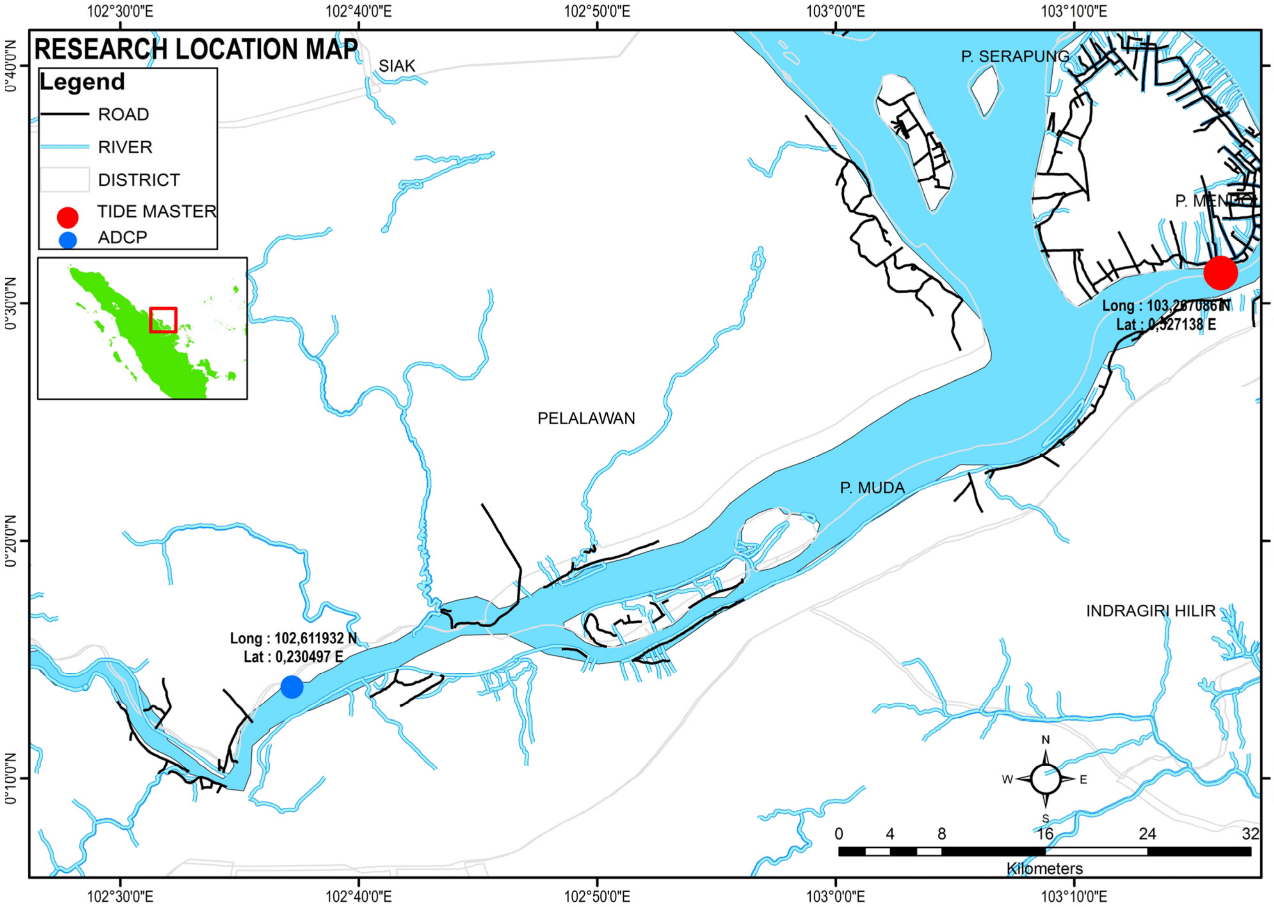

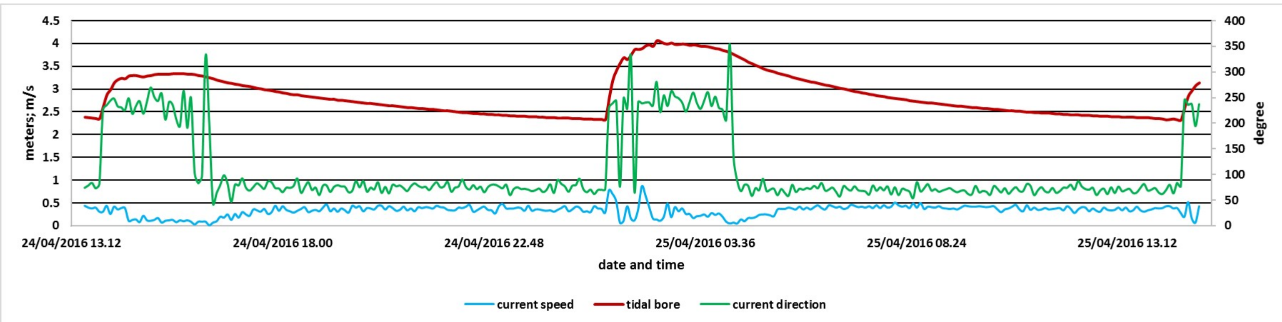

Figure 8. Tidal bores elevation, current speed and direction measurement at showing the location (top) and its processed data (bottom).

4 CONCLUSIONS

The results in this paper illustrate that the tidal bore generation of the east coast Sumatra can be effectively analyzed by using combination of numerical modelling and qualitative assessment. The results support the indication that a tidal bore may form with large tidal ranges (more than 4 to 9 m) in a flat converging channel. In the east coast of Sumatra, the study suggests that a tidal bore can be formed with up to 4-m tidal range in the estuary with a flat converging channel. In addition, tidal bores at Rokan and Kampar may be due to the large magnitude of semi-diurnal tidal constituents. It should be noted that no calibration has been carried out in the present work, therefore, it is recommended to carry out the calibration by e.g. using local bathymetry at the area of interest as well as analysis on the river morphology. In addition, as future work, different techniques and methods of the numerical modelling are recommended to simulate tidal propagation from the estuaries to the river upstream.

ACKNOWLEDGEMENTS

The authors gratefully acknowledge the support and contributions of Research Institute for Coastal Resources and Vulnerability, Ministry of Marine Affairs and Fisheries in Padang, Indonesia, Ocean Engineering Program, Institut Teknologi Bandung and Deltares' open source software for the numerical modelling.

REFERENCES

Chanson, H. (2003). Mixing and Dispersion in Tidal Bores: A Review. In *Proceedings of International Conference on Estuaries & Coasts ICEC-2003,* 8-11.

Chanson, H. (2010). Undular Tidal Bores: Basic Theory and Free-Surface Characteristics. *Journal of Hydraulic Engineering*, 136(11), 940-944

Chanson, H. (2011). Current Knowledge in Tidal Bores and their Environmental, Ecological and Cultural Impacts. *Environmental Fluid Mechanics*, 11(1), 77-98.

Deltares. (2011). *Delft3D-FLOW - Simulation of Multi-dimensional Hydrodynamic Flows and Transport Phenomena, Including Sediments*, User Manual. Deltares, the Netherlands.

Donnelly, C. & Chanson, H. (2005). Environmental Impact of Undular Tidal Bores in Tropical Rivers. *Environmental Fluid Mechanics*, 5(5), 481-494.

Kurniawan, A. (2014). Improved Tidal and Non-Tidal Representation of Numerical Models through Data Model Integration, *PhD Thesis*. National University of Singapore, Singapore.

Kurniawan, A., Ooi, S.K., Hummel, S. & Gerritsen, H. (2011). Sensitivity Analysis of the Tidal Representation in Singapore Regional Waters in a Data Assimilation Environment. *Ocean Dynamics*, 61, 1121–1136.

Kurniawan, A., Tay, S.H.X., Ooi, S.K. & Babovic, V. (2017). Determining Tidal Mixing Zone Using Data Driven Model in Malacca Strait. *IAHR World Congress 2017*, 13-18 August 2017. Kuala Lumpur, Malaysia.

Lynch, D.K. (1982). Tidal Bores. *Scientific American.* 247, 131-143.

Wyrtki, K. (1961). *Physical Oceanography of the Southeast Asian Water,* NAGA Report. In: Scientific Result of Marine Investigation of the South China Sea and Gulf of Thailand 1959e1961, vol. 2. Scripps Institution of Oceanography, La Jolla, California, 195.

Zu, T., Gan, J. & Erofeeva, S.Y. (2008). Numerical Study of the Tide and Tidal Dynamics in the South China Sea. *Deep Sea Research I,* 55, 137-154.

CHANGING SALINITY INTRUSION DUE TO ESTUARINE WATERWAY DEEPENING -ANALYSIS BASED ON ARTIFICIAL NEURAL NETWORKS-

CORDULA BERKENBRINK[1] & HANZ D. NIEMEYER[2]

[1,2] Coastal Research Station of the Lower Saxonian Water Management, Coastal Defence and Nature Conservation Agency, Norderney, Germany,
cordula.berkenbrink@nlwkn-ny.niedersachsen.de

ABSTRACT

The deepening of estuarine waterways primarily effects changes of tidal water levels and secondly those of tidal volumes and salt intrusion. These effects are subjected to Environmental Impact Assessments which are often checked by monitoring for the purpose of preservation of evidence. After the deepening of the waterway in the Outer Weser estuary, certain measurements are carried out among others aimed at detecting potential changes of salinity intrusion. Though the data indicated alterations of salt intrusion into the Weser estuary as a reliable quantification of the changes by conventional procedures when nonlinear regression analysis failed. However, tests with the Artificial Neural Networks (ANN) provided reliable results for each data set gained before and after the waterway deepening. Nevertheless, the application of the ANN that supplied data before deepening of the waterway proved to be a mismatch with the data gained after deepening. These differences provide a reliable measure for the increased salt intrusion into the Weser estuary due to deepening of the Waterway. The method is transferrable to other estuaries in order to determine changing salt intrusion resulting from waterway deepening or other measures.

Keywords: Tide; salinity; artificial neural network (ANN); estuary; waterway deepening.

1 INTRODUCTION

Major harbours are often located at tidal estuaries where as well large natural water depths as traffic connections to the inlands are available, in particular for inland navigation. In order to ensure the accessibility of such harbours for growing container vessels and their corresponding dimensions, depth and sometimes width of the estuarine waterways have been and will be extended several times leading to changes in hydro- and morphodynamics. One of these effects is an increasing salt intrusion in the estuaries affecting both the zones of estuarine habitats and the use of estuaries which procure water or that of connected channels for local farms to be used for animals or crop.

According to planning laws, effects of important infrastructure measures have to be evaluated by an Environmental Impact Assessment (EIA) body. If its results are overall reliable and not beyond any doubt as to a sufficiently credible judgement, planning approval authorities have the option to establish safeguarding procedures as a basis for the ensuing determination project impacts on the environment.

This option was applied by the planning approval authority for the deepening of the waterway in the Outer Weser estuary in 1997. In particular, for hydro- and morphodynamics a detailed measuring programme and corresponding data analysis were included in the decision regarding the official planning approval. Part of the programme was among others measurements of conductivity and temperature at a number of measuring stations in the Weser estuary (Figure 1). This is in order to provide a basis for the later detection of any potential increase of salt intrusion into the estuary.

The first data analysis consisting of a comparison of weighted averages was carried out by the project operator of Federal Waterway Authority Bremerhaven. It provided no indications for a significant change of salt intrusion into the Weser estuary (WSA Bremerhaven, 2010). With respect to essential interests of the Federal State of Lower Saxony a reassessment of the preservation of evidence data sets was carried out by its Coastal Research Station using nonlinear regression analyses as a first approach. Though its results highlighted significant changes of salt intrusion into the estuary after the waterway deepening there was no way to quantify these changes with sufficient accuracy for the whole range of values. In particular, the evaluated adaption functions mismatched the very low and very high values of salinity. In order to overcome these crucial deficits the data were again analysed by applying artificial neural networks (ANN). A suitable set-up by ANN provided a reliable analysis of the increasing salt intrusion into the Lower Weser estuary due to the waterway deepening in the Outer Weser estuary.

2 INVESTIGATION AREA AND DATA SETS

The area of investigation stretches along the Outer Weser estuary between the North Sea and Bremerhaven where the channel deepening took place at the Lower Weser estuary up to the tidal barrier in

  / ISSN 1562-6865 (Online) - ISSN 1063-7710 (Print)

Bremen-Hemelingen (Figure 1). Major ports located at the Weser estuary are Bremerhaven, Nordenham, Brake and Bremen. Since 1887 the Lower Weser estuary has experienced a number of subsequent enlargements of the waterway between Bremerhaven and Bremen (Niemeyer et al., 1996) leading to significant changes of mean tidal peaks and range, mean water level and storm surge set-up (Niemeyer, 2015). Those regular human interferences reshaped the habitats of the Lower Weser estuary enormously (Elsebach et al., 2008). The navigation channel in the Outer Weser estuary was successfully set up by Plate (1926) enabling later adaptations of its navigation channel for larger vessels resulting in economic efforts (Niemeyer et al., 1996; 2009).

The area of interest in particular was the measuring stations of Bremerhaven, Nordenham, Strohauser Plate and Brake which is at the downstream part of the Lower Weser estuary (Figure 1. The effects on hydrodynamics and salinity in the Outer Weser estuary itself was expected to be very limited due to knowledge from previous extensions of its navigation channel. Boundary conditions like tidal water levels and salinity for the German Bight were measured at the station LT Alte Weser (Figure 1). Additionally, the gauge Intschede upstream of the tidal barrier was taken into account where the inland fresh water discharge is determined (Figure 1). Furthermore, the effect of the salt content of fresh water due to industrial wastewater from potassium exploitation was considered by use of data gained near the tidal barrier at Bremen-Hemelingen.

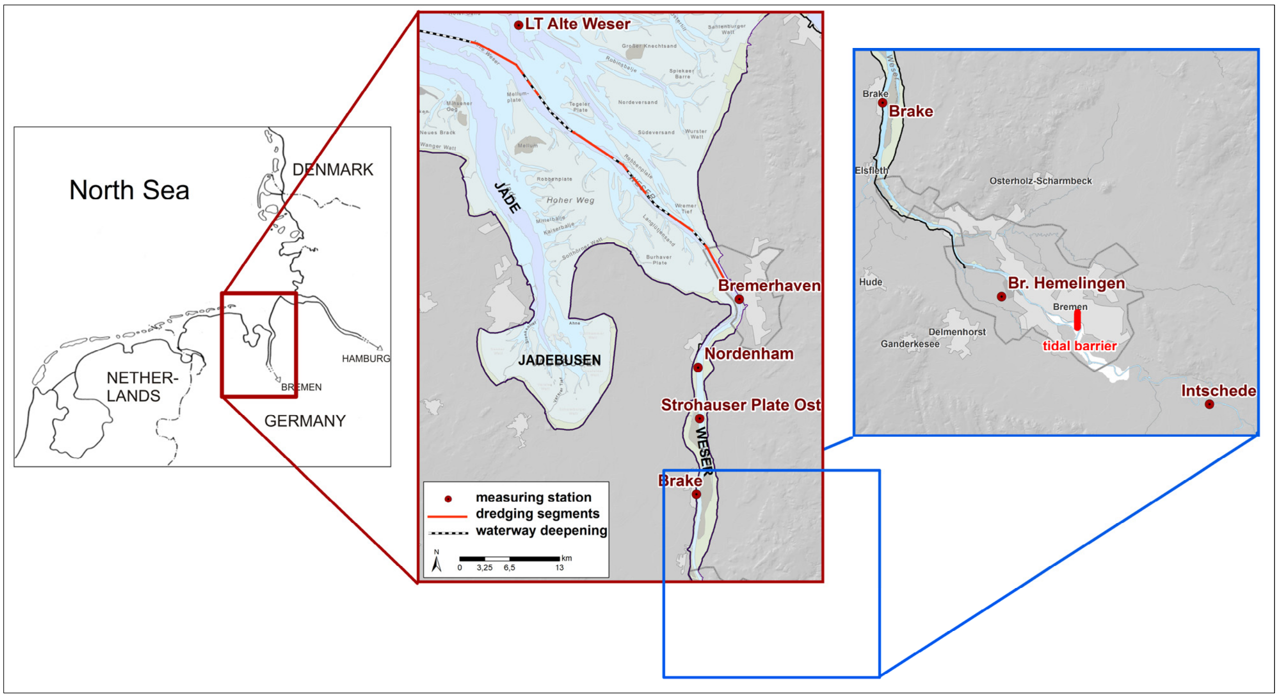

Figure 1. Weser estuary with measuring stations.

The analysis of potential changes of salinity in the estuary could be based on two datasets for salinity for each measuring location (Figure 1) in the estuary (WSA Bremerhaven, 2010). The first dataset contains time series from 1997 to 1998 before the deepening of the Outer Weser estuary had been executed. The second data set starts in 2006 after the major dredging in 1999 and therefore contains time series with the potential impact of the waterway deepening.

3 METHODOLOGY

ANN consists of computational models being inspired by the cognitive processes of brains aiming at a simplified architecture of their central nervous system. They can learn and generalize from experiences, and they can abstract essential information from data. An artificial neural network is made of various single units - the neurons- which contain simple transfer functions. The neurons could be connected to each other by using weights and bias factors in several ways dependent on the interrogation. ANN had been applied successfully to solve distinct problems in coastal hydrodynamics (Herman, 2010).

For the quantification of potential changes of salinity in an estuary a multilayer perceptron was chosen (Berkenbrink and Niemeyer, 2011) in which every neuron of each layer was fully connected to each neuron of the following one (Figure 2). The neurons in the input-layer get all the information about the process governing boundary conditions due to having been evaluated as relevant beforehand. The neurons in the output-layer represent the results. Between these layers were the hidden-layers where input data were processed with the aim to produce results.The neurons of the hidden layer changed the magnitude of their transfer function and their addiction to each other by using weights and bias factors during the learning process until the output-layer gets results with a sufficient quality. The Neural Network Toolbox™ was used as a module of Matlab utilities in which lots of network architectures and training routines were implemented (Demuth et al., 2015).

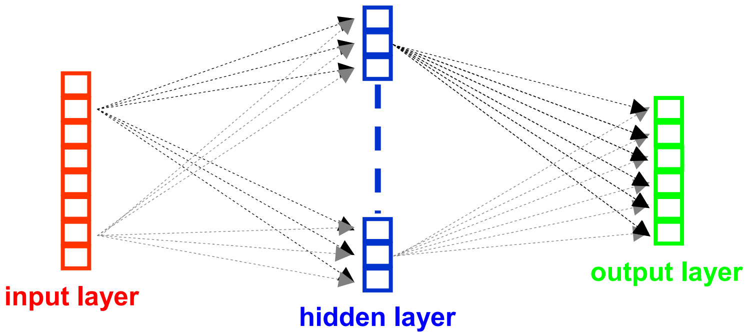

Figure 2. Schematized set-up of the chosen artificial neural network.

In order to successfully achieve this, a supervised learning process was chosen: the results in the output-layer were constantly compared to the measured data that represent the target. The neurons in the hidden-layer and the connections between them were changed until the output-layer sufficiently fits the measured data. After finishing this process, the values for the transfer function, the weight and the bias of each neuron and its connection were fixed. Then ANN was generally applicable for distinct data sets of the same measuring station for the reproduced physical processes.

To ensure a general applicability of the ANN the data set used for training was split into three parts:

1. 70 % of the data were used for the training in order to optimize the transfer functions of the neurons and the connections to each other with the aim to reach the measurements precisely.
2. 15 % of the data were used for validation. This parallel procedure was carried out to ensure that the memorizing of data by ANN was avoided.
3. The remaining 15% of the data were used for independent testing of the established ANN.

During the training the mean-square-error between output and measured data was calculated for each training approach. The same procedure was carried out parallelly for the validation of data set. While the mean-squared-error for training data sets gets continuously smaller after each epoch, it also decreases for the validation-data-set until a certain epoch when the optimal stage of the process was achieved. It increases again beyond that tipping point which indicates the start of the memorizing-process of the ANN. Therefore, the results of the training-process at this stage were fixed and used for the respective application of the ANN (Figure 3).

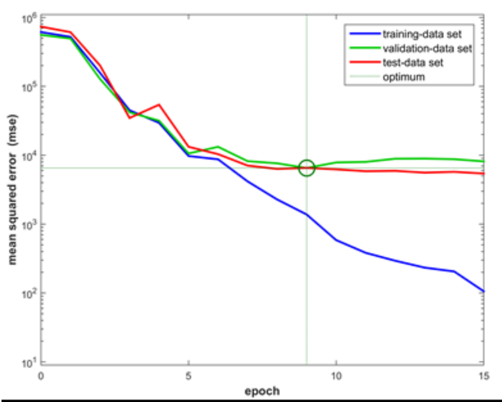

Figure 3. Training-process of the ANN.

The quality of the ANN was documented here by scatter diagrams and regression (Figure 4). The scatter around the 45°-reference line for absolute conformity indicates the achieved accuracy of the approximated data in respect to the measured ones. The linear regression for the approximated data provides a comparison for functional similarity and describes the error with regards to the order of magnitude of the values. Furthermore, the correlation coefficient was generally comparable to statistical quality parameter. The approximated salinity values in the Weser estuary match with corresponding measured data for both training and validation of the ANN. The small scattering around the reference line and the small deviations of the trend of the regression function from 1 and that of its constant from 0 highlight the high accuracy of the results gained by the applied ANN (Figure 4). Another remarkable result was that independently from the amount of

  / ISSN 1562-6865 (Online) - ISSN 1063-7710 (Print)

data the trend of the regression for training, test and overall application was the same and changed only for the test by less than 2 %.

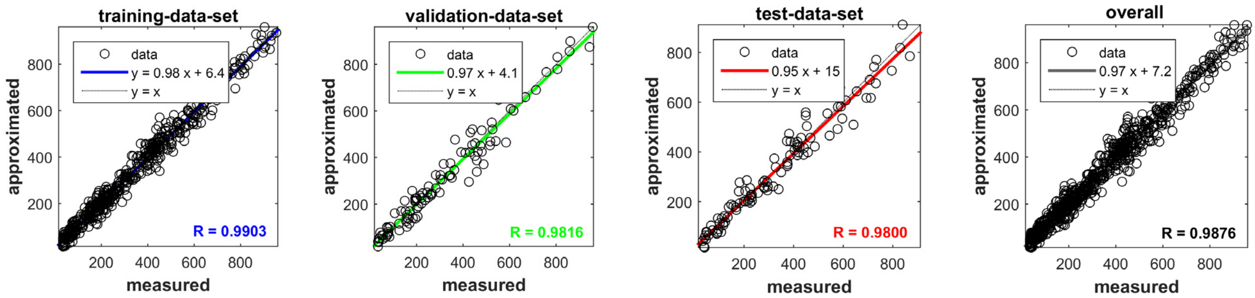

Figure 4. Results of a trained ANN [0.01 ‰] (data set from measuring station Nordenham).

Due to the tests for training and validation the suitability of the ANN has been proven for other data sets from the same estuarine location under similar conditions by using fixed values of the neurons, weights and bias for their connections gained from the training of the ANN. The determination of salinity values in the Lower Weser estuary was also based on the same input parameters being used for training and validation as boundary conditions. Salinity at fixed distinct time steps, tidal range and tidal high water level in the estuarine mouth and the freshwater discharge at Intschede (Figure 1) were the boundary conditions. These priority chosen parameters for the input-layer of the ANN represent the most important governing boundary conditions for the salinity in the estuary beside those characteristics of estuarine morphology. This provides input factors for the establishment of an ANN to be being suitable for the successful reproduction of local salinity values in the Lower Weser estuary. Seasonal effects such as storm surges or dry summers were implicitly included if covered by the data sets. Only the estuarine bathymetry was not considered in the set-up of the ANN. Therefore, morphological changes in the estuary could create significant changes of estuarine salinity values being reproduced by the same ANN for distinct periods.

Additionally potential effects of the salt content of fresh water due to industrial wastewater from potassium exploitation was considered by using measured data near the tidal barrier in Bremen-Hemelingen (Figure 1). Its effects were ignored for the preservation of evidence procedure (WSA Bremerhaven, 2010) and its follow-up checks on the reliability of its results by the Coastal Research Station (Berkenbrink and Niemeyer, 2011). In this follow-up study these effects will be considered in order to optimize the procedure to gain a deeper insight into the processes on the one hand and for improving the procedure itself in respect of potential future preservation of evidence procedures on the other hand.

4 APPLICATION AND SUITABILITY TESTS

4.1 Procedure for quantifying changing salinity intrusion

The suitability of ANN for the reproduction salinity in an estuary by dominant boundary conditions had been proven by training, test, validation and application (Figure 4). On this basis, a follow-up procedure has been developed in order to quantify potential changes after waterway deepening. The ANN for the data set before deepening (Figure 5a) was applied afterwards which will be used for calculating the salinity values after the waterway deepening and then compared with the measured data being available for the years from 2006-2008. The corresponding scatter plot highlights that the approximated salinity values underestimate the salinity values measured after the deepening where the higher absolute values are (Figure 5b). This indicates a significant change in the salt intrusion into the Weser estuary since the measurements in 1998. Obviously, the deepening of the waterway had significantly changed the process of salt intrusion into the estuary. This is a physically absolutely plausible result for which no analysis by ANN is indispensably necessary, but it makes a reliable quantification possible.

The alterations caused by the deepening are neither constant nor linear. Up to a value of about 3 % the salinity remains nearly the same as before, though scattering increases gets stronger around the reference line (Figure 5b). Above that threshold, measured values were underestimated by the ANN which indicates an increase of the salinity after the deepening of the waterway which was represented by a nonlinear regression. The difference between both regressions lines of the calculations with the data set from 1998 and the data set from 2006-2008 manifests itself in the measurement for the increase in salinity caused by the waterway deepening (Figure 5c). For salinities higher than 8 % the increase due to the deepening ranges between values of 3 to 6 %. This result raises the question if the ecological effects of salinity alterations due to waterway deepening were sufficiently described by mean values alone.

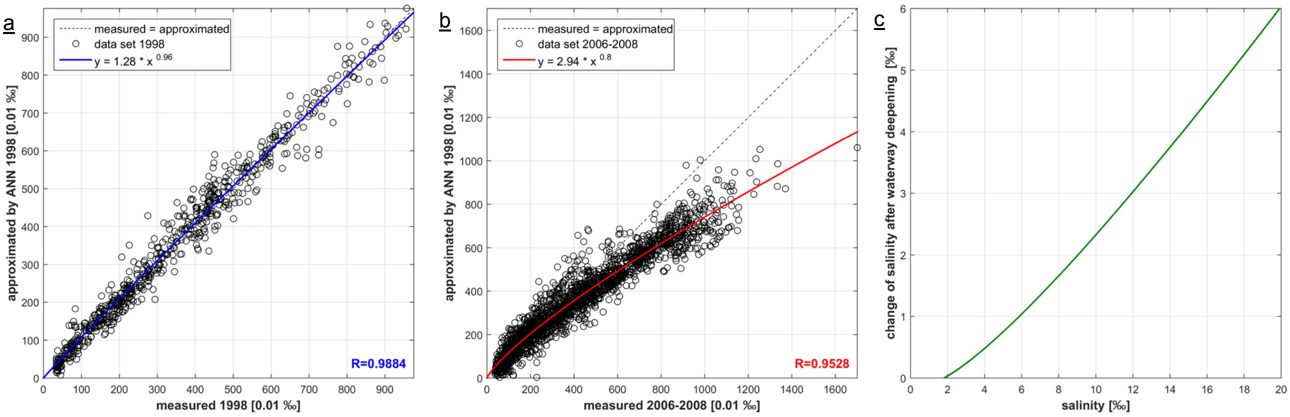

Figure 5. Quantification of changed salinity intrusion due to waterway deepening at the measuring station Nordenham (Figure 1); a: scatter plot for measured and ANN-approximated data from 1998 before deepening of the waterway: b: scatter plot for measured and ANN- approximated data from 2006-2008 after deepening of the waterway; c: change of salinity after waterway deepening (difference between regression in (a) and (b)).

4.2 Plausibility test by backward application

A test for the suitability of the quantification of estuarine salinity due to changes by ANN can be seen in the application of the above described procedure by looking backward from the situation after waterway deepening to the prior situation. In a first step, an ANN was established for a data set measured after the waterway deepening (Figure 6a) proving that the reproduction of these data by an ANN was not only possible for those measured before the waterway deepening. The backward application of this ANN for the data gained before the deepening is shown in Figure 6b. The results highlighted that the data were significantly overestimated by the ANN thus confirming the results of the forward application of an ANN. A major difference to the forward application was a less pronounced nonlinearity occurring for the vice versa application (Figure 5b). In total, these tests generally confirm the same trend for the effect of waterway deepening on salinity intrusion into the inner estuary: a growing increase corresponding with the absolute values of salinity.

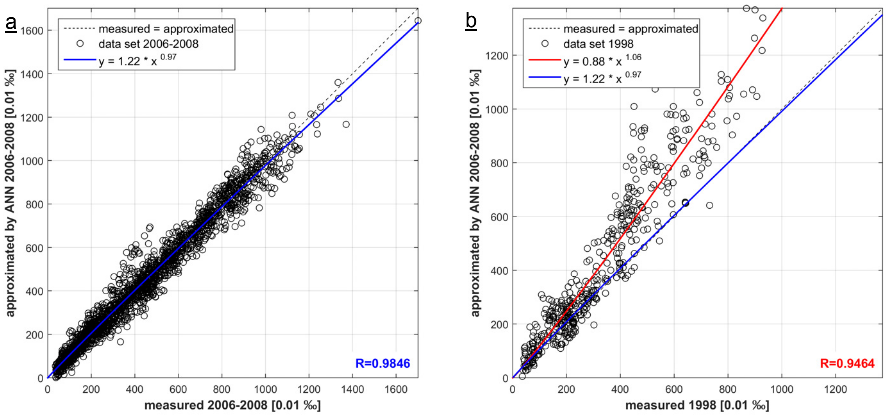

Figure 6. Plausibility test by backward application (measuring station Nordenham); a: scatter plot for measured and ANN-approximated data from 2006-2008 after the deepening of the waterway: b: scatter plot for measured and ANN-approximated data from 1998 before deepening of the waterway.

4.3 Sensitivity concerning missing of rare seasonal events

During measuring campaigns the temporary malfunction of devices was as usual. The resulting loss of information has to be checked in respect of the consequences for data analysis. This occurs more frequently when rare seasonal events like e.g. storm surges, high offshore salinity values or very low fresh water discharges have been missed. Therefore, such effects must considered with respect to the reliability of the ANN analysis of changing salt intrusion due to waterway deepening.

In this case, the results of the developed ANN were obviously insensitive to changes in the amount of the used data sets. At least if a certain -here unknown- threshold was exceeded: for a range between 15 and 100 % of the available data, the structure of the ANN would be quite similar (Figure 4). Since furthermore no changes occur as to low salinity values, any neglection of such events would have no effects on the results gained by the developed ANN.

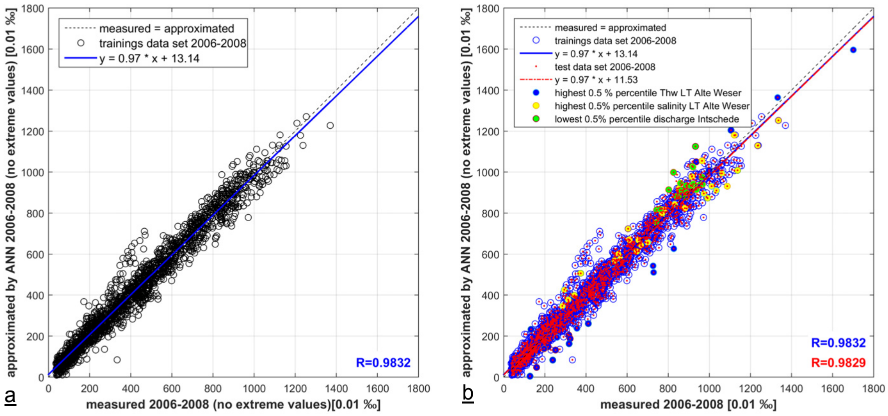

Figure 7. Plausibility test for the station Nordenham by establishing an ANN without rare seasonal events (a) and its application on a data set including these events which are favourable for high salinity values (b) in the inner estuary.

Therefore, the non-occurrence of seasonal effects leading to high values of salinity like e.g. high offshore salinity values, very high offshore tidal water levels or very low fresh water discharges could have an impact on the structure of the ANN. Accordingly such events were identified for the data sets and are exemplary for the station Nordenham parallel to the established ANN. A second one was created on the basis of a data set excluding all data in combination with the following boundary conditions in the input layer of the ANN as being effective on heightening the salinity values in the inner estuary. All tidal high water levels and salinity values above the 99.5-percentile threshold and all fresh water discharges below the 0.5-percentile threshold were taken into consideration. The results apply for this reduced data set very appropriately with a certain scatter due to overestimation in the range of 5 to 7 % (Figure 7a). The same ANN was afterwards applied to the total data set including also those indicating rare seasonal events (Figure 7b). A typical effect of a rare seasonal effect is the increase of the maximum value from approximately 13 to 16 %. Above all, the additional higher values were caused by higher tidal peaks and salinity values at the estuarine mouth whereas lower discharge volumes were at least for this data set less effective. In total the comparison highlights that neither the scatter nor the trend had been changed by the consideration of events being favourable for higher salinity values. Lack of such data is obviously unimportant for the quality of an ANN application.

4.4 Plausibility test for distinct data sets for similar estuarine topographies

Basic assumption for the presented method is that an ANN with an input-layer considering all dominant boundary conditions for salinity values in the inner estuary beside estuarine morphology is representative for all data sets measured in periods without significant changes of estuarine morphology. Though during all measurement periods changes in estuarine morphology, their impact on salinity values was expected to be much less effective than that of a discontinuous substantial impact of estuarine morphology within a short period of a waterway deepening.

In order to check this assumption an ANN for the data set of 2006/2007 of the measuring station Nordenham had been practised, validated and tested (Figure 8a). The statistical quality of the approximation was very good; the scatter of data around the regression was small.

This ANN has been applied for the data set of 2008. Thus, the natural changes of estuarine morphology for a period of two years were considered including maintenance of dredging. The effects of the ANN application on this data were of lower statistical quality but still satisfactory (Figure 8b). Trend factors of the regression were the same for both applications, only the constants differ insignificantly (Figure 8). The increased scatter could be explained by the non-inclusion in the set-up of natural changes of estuarine topography and maintenance dredging.

The plausibility test for similar estuarine topographies highlighted that a major assumption of the study set-up was on the one hand valid. The non-consideration of boundary conditions for estuarine morphology in the input layer of the ANN allows quantifying its impacts by applying an ANN before and after a substantial change of the estuarine topography. On the other hand, the scatters of data for secondary applications in this study were also at least partly explainable by natural changes of estuarine topography in the meantime.

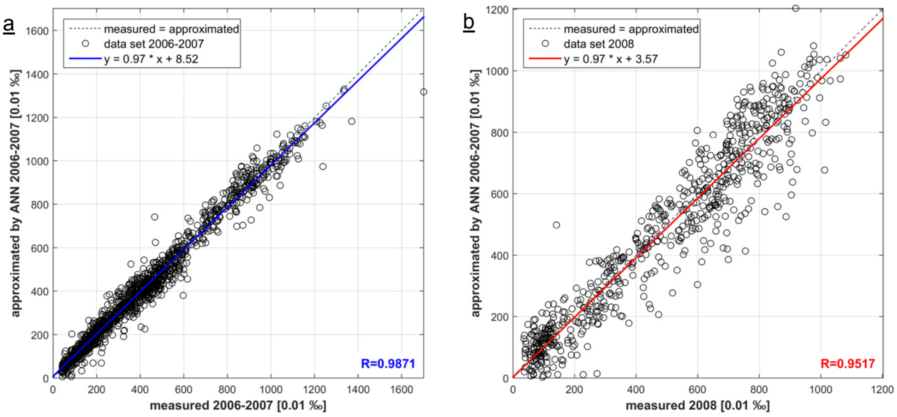

Figure 8. Plausibility test for the station Nordenham for similar estuarine topography. Left: a) establishing of an ANN for a data set covering 2006/2007; right: b) later application of that KNN to a data set covering 2008.

4.5 Effect of fresh water salinity content

The fresh water of the Weser River had salt content due industrial waste water from potassium exploitation which had not been considered up to now in studies on changes of salt intrusion into the Lower Weser estuary due to waterway deepening in the outer part. Necessary measures were taken in order to quantify these effects and thus providing a basis for a decision if their consideration was necessary or negligible for achieving appropriate results for the investigated issue. A reliable study was possible to be undertaken since the whole investigation period data have been measured near the tidal barrier of the Weser estuary in Hemelingen (Figure 1). Therefore, the effect of the fresh water salt content on the analysis of changes of salt intrusion due to waterway deepening will be checked for the data sets from the measuring stations Bremerhaven and Strohauser Plate-Ost (Figure 1). Bremerhaven is located at the upstream end of the Lower Weser estuary and had the highest natural salinity values of all four stations being investigated here. Therefore, it was expected that effects of fresh water salt content on the results of the analysis will be less than anywhere else in the Lower Weser estuary. If these effects were significant, the incorporation of the fresh water salt content for the analysis was inevitable. Furthermore, the data set of the measuring station Strohauser Plate-Ost will be tested for the effect of the fresh water salt content on the analysis of the waterway deepening effects on parts of the Lower Weser estuary where the salinity values were remarkably smaller than at the estuarine mouth.

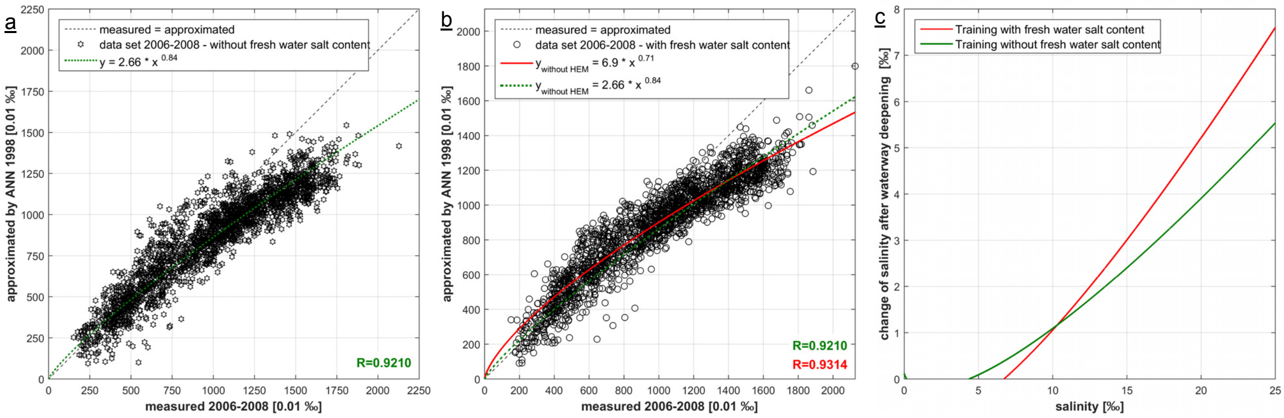

Figure 9. Effect of fresh water salt content on salinity changes in the Weser estuary at the measuring station Bremerhaven; a: scatter plot for measured and ANN-approximated data from 2006-2008 after deepening of the waterway without consideration of fresh water salt content; b: scatter plot for measured and ANN-approximated data from 2006-2008 after deepening of the waterway with consideration of fresh water salt content; c): resulting changes of salinity due to waterway deepening with and without consideration of fresh water salt content.

The application of the ANN on the data set of the measuring station Bremerhaven (Figure 1) in the initial set-up was trained, validated and tested for the data set of 1998 before waterway deepening on the data set of 2006-2008, after the deepening also applies for the measuring station Bremerhaven (Figure 1). The mismatch (Figure 9a where the overwhelming majority of data are more underestimated by the ANN, the higher the absolute values were. If the salinity content in the fresh water were additionally incorporated into the hidden layer of the ANN based on the situation before the waterway deepening, it underestimates the data

  / ISSN 1562-6865 (Online) - ISSN 1063-7710 (Print)

set after the waterway deepening significantly more than for the set-up without considering the salt content of the fresh water discharge (Figure 9b). Moreover, the scatter of the data was remarkably reduced.

The effects of considering the fresh water salt content on the resulting changes of salinity intrusion due to waterway deepening were distinctive (Figure 9c): in the range between approximately 4 to 10 % salinity. The resulting changes between 0 to 1 % were smaller by neglecting the salinity influx from upstream (Figure 9a + b). Both the majority of measured events and the larger resulting changes due to waterway deepening were more pronounced above the threshold of 7% (Figure 9). The differences between the resulting changes of salinity intrusion into the Lower Weser increased above that threshold. More and higher the absolute salinity values rises after both considering and neglecting the fresh water salt content in the input layer of the ANN.

The same procedure carried out here for the data set of the measuring station Bremerhaven was carried out for the data measured at the location Strohauser Plate-Ost (Figure 1). The application of the ANN for the data set from 1998 before the deepening of the waterway were considere on the data measured from 2006-2008 after its execution in 1999 without incorporating the fresh water salt content into the input layer. This delivers similar results as the ones gained for the data of other stations (Figure 5b + 9a). The majority of data measured after completion of the waterway deepening were more significantly underestimated where the larger the absolute salinity values were (Figure 10a). The same applies to the results being achieved with the set-up of the ANN incorporating the fresh water salt content in its input layer (Figure 10b) The underestimation of the data was slightly larger than in the case without considering the fresh water salt content whereas the scatter was similar (Figure 10b).

The resulting changes due to the deepening of the waterway are therefore almost in the same order of magnitude for the whole range of values (Figure 10c), but those for the incorporation of the fresh water salt content are always the larger ones. The resulting changes range from approximately 0 to 6% and were also appllied to all other stations - growing with the absolute values of the local salinity (Figure 10c). The relation of fresh water discharge to local tidal volume was larger at Strohauser Plate-Ost than at Bremerhaven. The impact of the fresh water salt content on the resulting changes was larger in the former than in the latter (Figure 9c + 10c).

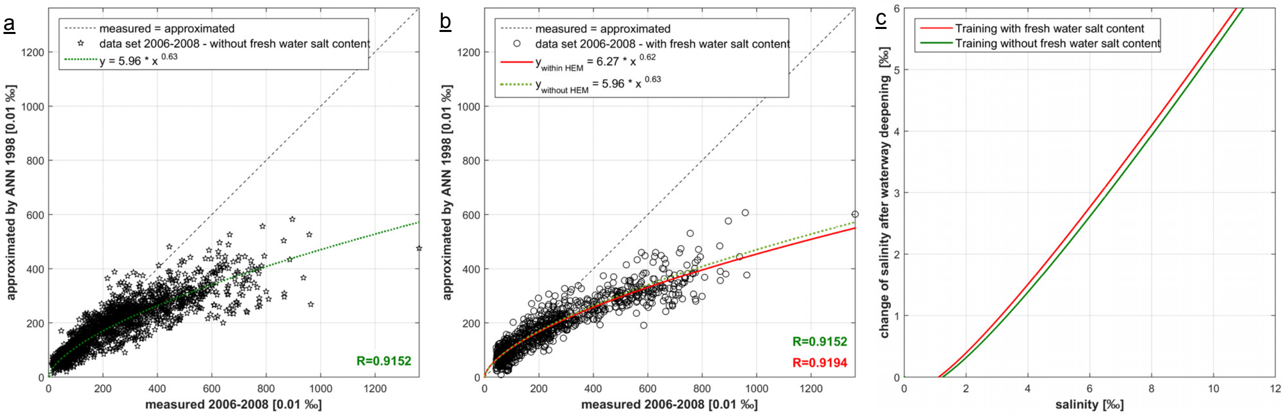

Figure 10. Effect of fresh water salt content on salinity changes in the Lower Weser estuary at measuring station Strohauser Plate-Ost; a: scatter plot for measured and ANN-approximated data from 2006-2008 after deepening of the waterway without consideration of fresh water salt content; b: scatter plot for measured and ANN-approximated data from 2006-2008 after deepening of the waterway with consideration of fresh water salt content; c: resulting changes of salinity due to waterway deepening with and without consideration of fresh water salt content.

Taking the gained results into consideration, the effects of the fresh water salt content on the analysis of the changing salinity intrusion due to the deepening of the waterway are not negligible. This applies on the one hand to the order of magnitude and on the other to the statistical quality of the results. The incorporation of the fresh water salt content was therefore regarded as indispensible for future investigations. The final results presented here were therefore based on an analysis by ANN by including the fresh water salt content in its input layer.

5 RESULTS ON CHANGING SALINITY DUE TO WATERWAY DEEPENING

The transition zone between the Outer and the Lower Weser estuary is the section around Bremerhaven (Figure 1). The data measuring station at this location represents not only the conditions for the upstream end of the Outer Weser but also those for the downstream beginning of the Lower Weser. There was no increase of salinity due to waterway deepening and absolute salinity values below a threshold of approximately 7% was achieved (Figure 11a). Above this they increase up to values of about 6% in the range of absolute values of 15 to 20% (Figure 9b + 11a).

About 20 % of the measured and analysed events remain without changes of local salinity after the execution of the waterway deepening (Figure 11a). Changes of local salinity due to waterway deepening in the ranges between 0 and 1% and between 1 and 2% have a relative frequency in the same order of magnitude (Figure 11a). The changes above the threshold of 2% embrace the remaining approximately at 35 % with a share of more than 25 % in the range of 2 and 4% and nearly 10 % in the range of 4 and 7 %.

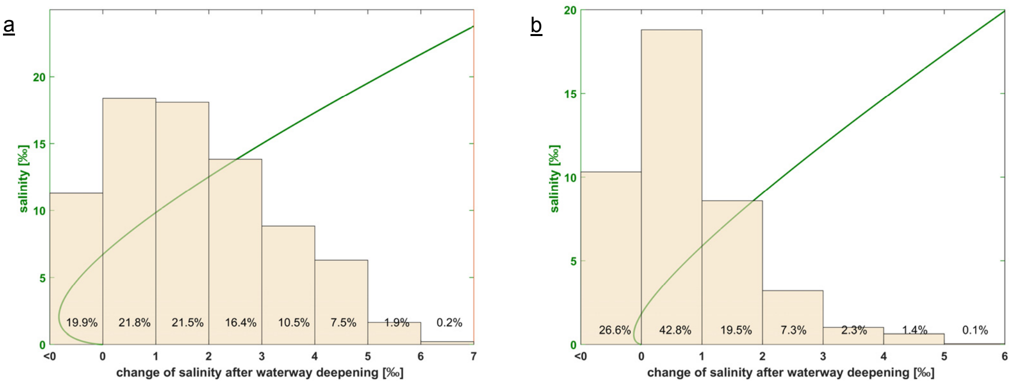

Figure 11. Resulting changes of salinity due to waterway deepening and their relative frequencies. a: results for data from the measuring station Bremerhaven; b: results for data from the measuring station Nordenham.

Upstream of Bremerhaven at the measuring station Nordenham the resulting changes of salinity intrusion already started at a threshold of approximately 2% salinity (Figure 11b). Beyond this the relative changes increase to values of up to 4 to 5% and even in rare seasonal event it increases up to approximately 6%. But the foremost changes of local salinity were significantly smaller. For about a quarter of all events there was no increase of local salinity after the waterway deepening. A change in the range between 0 and 1% has been recorded for slightly more than 40 % of registered events and for about 20 % of them was the range between 1 to 2%. Slightly more than 10 % of the considered events manifest changes in the range between 2 to 6% whereas most ranges between 2 to 3%.

Though the changes at Bremerhaven were significant and are even above a threshold of 2%, a remarkable relative frequency of the resulting changes at the measuring station Nordenham were considerably smaller and show a higher degree of decreasing relative frequencies than registered at Bremerhaven (Figure 11). Thus, the spatial pattern was in tune with the observed local connection between changes due to waterway deepening and absolute salinity values: the higher the latter the more pronounced the resulting changes of salinity caused by the execution of the waterway deepening.

In the central part of the Lower Weser estuary the measuring station Strohauser Plate-Ost (Figure 1) is representative of the estuarine section where the influx of salinity from the North Sea decreases significantly but was still considerable. The resulting changes due to waterway deepening occur above a threshold of approximately less than 1% (Figure 12a) and increase to values of about 6% salinity.

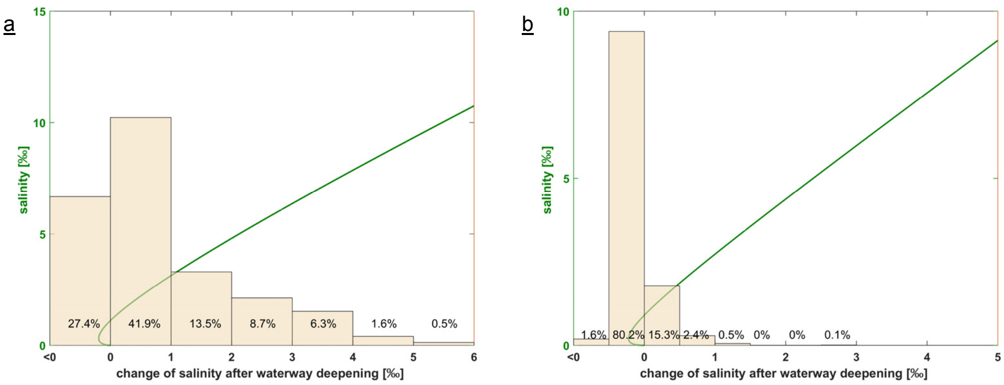

Figure 12. Resulting changes of salinity due to waterway deepening and their relative frequencies. a: results for data from measuring station Strohauser Plate-Ost; right: b: results for data from measuring station Brake.

More than a quarter of all measured and analysed events had no increase of local salinity due to estuarine waterway deepening (Figure 12a). A large amount of events with a relative frequency of more than 40% has resulting changes between 0 to 1%. Higher resulting changes due to waterway deepening can be found in the ranges between 1 to 4%, whereas higher values of resulting local salinity changes due to waterway deepening only show small relative frequencies.

The measuring station Brake in the middle of the Lower Weser estuary is approximately located halfway between Bremerhaven and the tidal barrier in Hemelingen. The changes of local salinity due to waterway deepening were much smaller than at the measuring station Strohauser Plate-Ost and also less frequent. More than 80 % do not increase and the changes above a threshold of 1% occur for less than 1% of events (Figure 12b). The effect of waterway deepening on salinity at this location is therefore negligible.

Independent of the order of magnitude and relative frequency of salinity changes at the distinctly considered measuring stations, the results gained here stress on the one hand that the usual practice in EIA procedures to forecast expected changes by mean values alone is insufficient if the variation of changes remains disregarded. On the other hand, it will be necessary for future EIA to provide sufficient knowledge concerning the effect of variable changes of local salinity on animals and plants.

6 SUMMARY AND CONCLUSIONS

The application of Artificial Neural Networks (ANN) to the analysis of changing salt intrusion into an estuary has provided the following results: ANN is a suitable tool for the approximation of local salinity values in an estuary. Crucial for a reliable approximation is an appropriate evaluation of governing boundary conditions for the input layer of the ANN. The application of an ANN of being trained, validated and tested for a data set on another one with a change in the set-up of the ANN under different boundary conditions allows quantifying the effects of this change on local salinity values as carried out here.

Furthermore, an appropriate procedure has been developed to transfer the results of the ANN analysis to quantified changes of local salinity in respect of the waterway deepening. Plausibility tests have been carried out proving the reverse applicability of the method, its insensitivity to the missing of rare seasonal events and the reproduction of homogenous results for similar estuarine topographies. Finally, the effects of fresh water salt content on the changes of local salinity have been analyzed and the results for an extension of the hidden layer of the finally applied ANN are considered.

An important result of the investigations described at hand is that the changes of local salinity due to waterway deepening vary significantly by increasing of the absolute values. It is evident that a representation by mean values is insufficient. Therefore, it is recommendable to change current practice of Environmental Impact Assessment (EIA) to forecast such mean values. It will be necessary for an appropriate EIA to provide forecasts with locally and spatially varying changes of salinity values connected to a planned waterway deepening. On the other hand, it is regarded necessary to provide sufficient ecological knowledge for the transfer of these data into effects on animals and plants.

REFERENCES

Berkenbrink, C. & Niemeyer, H.D. (2011). Salzgehaltsänderungen in der Unterweser nach 1998 - Quantifizierung mit künstlichen neuronalen Netzen. NLWKN-Forschungsstelle Küste, *Forschungsbericht 01/11*, Norderney.

Demuth, H., Beale, B. & Hagan, M. (2015). *Neural Network Toolbox™ User's guide*, Revised for Version 8.4 (Release 2015b). MathWorks, Natick.

Elsebach, J, Kaiser, R. & Niemeyer, H.D. (2008). *Spatial Balance of Habitats in the Weser Estuary*, HARBASINS Report.

Herman, A. (2010). *Neural-Network Modeling and Data Analysis Techniques in Coastal Hydrodynamic Studies: A Review*. In: Linda L. Wright: Sea Level Rise, Coastal Engineering, Shorelines and Tides. Nova Science Publishers, 295-318.

Niemeyer, H.D. (2015). Effekte des Klimawandels auf Randbedingungen im Insel- und Küstenschutz - gegenwärtige und zu erwartende Trends-. *Berichte der Forschungsstelle Küste*, Bd. 44, Norderney.

Niemeyer, H.D., Eiben, H. & Rohde, H. (1996). *History and Heritage of German Coastal Engineering*. History and heritage of coastal engineering, 169-213.

Niemeyer, H.D., Ladage, F., Meyer, C. & Stephan, H.-J. (2009). Enhancement of Supratidal Forms on Tidal Flats by Dredged Material. *Proceedings of the 31st Conference of the Coastal Engineeing Hamburg/Germany*. Poster Volume.

Plate, L. (1926). Die Vertiefung der Außenweser durch den Ausbau des Fedderwarder Armes. *Jb. Hafenbautechn. Ges. 1926,* Bd. 9.

WSA Bremerhaven. (2010). Dokumentation und Durchführung der im Planfeststellungsbeschluss für den Ausbau der Bundeswasserstraße Weser von km 65 bis km 130 zur Herstellung einer Mindesttiefe von 14 m unter Seekartennull angeordneten Beweissicherungsauflagen und Bewertung der Ergebnisse – *final report*.

Proceedings of the 37th IAHR World Congress
August 13 – 18, 2017, Kuala Lumpur, Malaysia

TRACKING SEDIMENT TRACER IN AN EULERIAN MODEL

HONGHAI LI[1], TANYA M. BECK[2], TAHIRIH C. LACKEY[3], HANS R. MORITZ[4], KATHARINE GROTH[5], TRAPIER PUCKETTE[6] & JON MARSH[7]

[1, 2, 3] Coastal & Hydraulics Laboratory, USACE/ERDC, Vicksburg, Mississippi, USA,
Honghai.Li@usace.army.mil; Tanya.M.Beck@usace.army.mil; Tahirih.C.Lackey@usace.army.mil
[4, 5] USACE Portland District, Portland, Oregon, USA,
Hans.R.Moritz@usace.army.mil; Katharine.Groth@usace.army.mil
[6] RPS Group Plc, Johns Island, South Carolina, USA,
Trap.Puckette@rpsgroup.com
[7] RPS Group Plc, Helensburgh, UK,
j.marsh@environmentaltracing.com

ABSTRACT

A numerical hydrodynamic, wave, and sediment transport model, the Coastal Modeling System (CMS), was applied to investigate the transport of dredged material placed in the nearshore and offshore areas of an ocean dredged material disposal site (ODMDS) adjacent to the Coos Bay inlet, Oregon. Historical oceanic and atmospheric data in the Coos Bay and the inlet system were assembled, and a field program was carried out to collect waves and hydrodynamic data and to implement a sediment tracer study. The data were used to set up the numerical model and to calibrate and validate model calculations. By evaluating local sediment transport and morphological change and simulating the process of sediment tracer release and movement, the pathways of sediment tracer were determined under combined influence of wave, current, and wind conditions within and around the immediate vicinity of the Coos Bay ODMDS. The calculated results and the measured sediment tracer data indicate that the dredged material placed in the nearshore area of ODMDS tends to backfill the navigation channel under normal conditions. Sediment pathways are primarily controlled by tidal current inside the Coos Bay and at the inlet entrance, and responding to wave and storm conditions in the open coastal area.

Keywords: Sediment tracer; sediment transport; coastal hydrodynamic modeling; waves; coastal inlet.

1 INTRODUCTION

The Coos Bay inlet is located on the southern Oregon coast of the USA, about 150 km north of the Oregon/California state line, which connects Coos Bay to the Pacific Ocean through a regularly maintained navigation channel. The Coos Bay inlet and estuarine system receives freshwater from the Coos watershed and is under the combined influence of large ocean waves in the open coastal area and strong tidal current in the system (Figure 1).

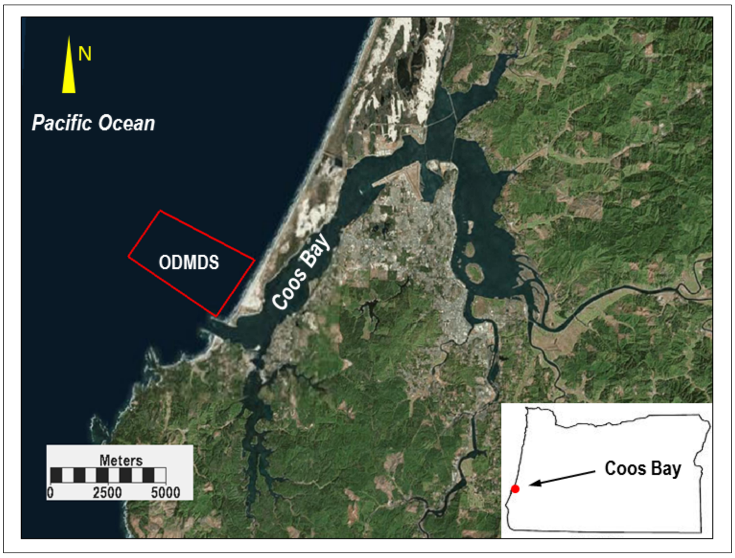

Figure 1. Coos Bay inlet and estuarine system. The red polygon delineates the ocean dredged material disposal site (ODMDS).

Annual maintenance dredging of the Coos Bay navigation channel yields more than half-million cubic yards of sand material. In order to accommodate dredged material and to be more cost-effective, a nearshore ocean dredged material disposal site (ODMDS) was designated north of the Coos Bay inlet in the coastal littoral zone (Figure 1). While the nearshore placed sand material is supplementing the littoral sediment budget to support onshore morphology, the accumulation (mounding) due to dredged material placement within ODMDS is interacting with waves and current, interfering with sediment transport in open coast, inducing channel backfilling, and decreasing channel navigability. A sediment tracer study was conducted and a numerical wave, hydrodynamic, sediment transport model was set up to investigate littoral sediment transport for the Coos Bay inlet and estuarine system as well as to evaluate the effects and the short- and long-term response of nearshore dredged material placement to coastal wave and hydrodynamic environment.

Following the introduction of this paper, the existing data assembly and the field data collection program are described. Section 3 provides information on modeling method. Section 4 presents model simulation results and discussion, and Section 5 summarises the study.

2 DATA

2.1 Existing data assembly

The bathymetry surveys by Oregon State University, the USACE Portland District (NWP), and the Joint Airborne Lidar Bathymetry Technical Center of Expertise (JALBTCX) cover Coos Bay and inlet (Wood and Ruggiero, 2014). Additional bathymetry dataset was obtained from the National Geophysical Data Center (NGDC) Coastal Digital Elevation Models (DEMs), mostly covering open coastal and deeper offshore areas (NOAA, 2016a). The JALBTCX data have complete coverage of the bay area with less than 1 m resolution.

Water surface elevation (WSE) data were downloaded from NOAA tide gage #9432780 at Charleston, Oregon (NOAA, 2016b). The WSEs indicate a mixed, predominately semi-diurnal tidal regime with distinguished spring and neap tidal ranges surrounding the study area. The mean tidal range (mean high water – mean low water) is 1.73 m and the maximum tidal range (mean higher high water - mean lower low water) is 2.32 m.

Wind and wave data were obtained from the National Data Buoy Center (NDBC, 2016) Buoy 46015, located approximately 75 km southwest of Coos Bay. Monthly wind and wave roses from September 2015 to March 2016 were analyzed. During the September time period, wind mostly blew from the north. The October wind rose indicates a wind transition period. Entering the winter period, dominant wind direction was from the south and storm wind speed reached 15 m/s and above. During this fall-winter period, most of the storms occurred in December and January. In September, waves propagated primarily from the northwest sector. From October 2015 to March 2016, 10-20% of waves propagated from the west sector and dominant incident wave directions were the west northwest. The December and January periods had larger monthly mean wave heights of 4.56 m and 3.83 m, respectively. The peak wave height of 6.44 m occurred in late January.

Daily river flow data from September 2015 to March 2016 were obtained from the Coos Watershed Association at four gauging stations, West Fork Millicoma River, East Fork Millicoma River, Marlow Creek, and South Fork Coos River. Flow discharges in September and October were close to zero and started to pick up in November. Peak flows occurred in December 2015.

For a hypoxia study in the Coos Bay estuary, an acoustic Doppler current profiler (ADCP) was deployed in the bay (Sutherland and O'Neill, 2016). The mooring ADCP location has a water depth of 10.3 m near mid-estuary (RM 8.0). The deployment started in late November 2013 and ended in July 2014. Both current and water surface elevation were measured at the location. The velocities were vertically averaged and 30 days' worth of data were extracted for the model calibration.

2.2 Field program

Water surface elevation, current, and wave data were collected by RPS Evans-Hamilton (RPS EH). Figures 2(a) and 2(b) show the locations of the water level gauge in the upper bay and the acoustic wave and current profiler (AWAC) within ODMDS and transects where vessel mounted ADCP data were collected. Water level data were available from 22 September to 22 October, 2015, and current and wave data from 18 September to 21 November, 2015. Instantaneous current measurements in transects were conducted from September 28 through 1 October, 2015.

Sand tracer release and sampling program was designed and implemented by Environmental Tracing Systems (ETS). 600 kg of tracer were released at two sites, DZ-A and DZ-B, within ODMDS, respectively (Figure 2(c)). The tracer at DZ-A was released on 20 September, 2015 and at DZ-B a day earlier. Two rounds of samplings were conducted. The first round was between 20 and 22 November, 2015 and 97 grab samples were taken. The second round was between 12 and 18 March, 2016 and 225 grab samples were taken, including 36 beach samples and 189 offshore surface samples (Figure 2(c)). Total counts of sampling sand grains were converted to weight. The contouring plots in kg/m^2 for Rounds 1 and 2 samplings are shown in Figure 3. Released from DZ-A and DZ-B, the sediment tracer has displayed different distribution patterns.

From Round 1 sampling results (Figures 3(a) and 3(b)), the tracer released from DZ-A tends to move alongshore to the north, but from DZ-B tends to cluster around the inlet entrance. Round 2 sampling results show similar distribution patterns as Round 1 (Figures 3(c) and 3(d)). Although this round of sampling has a larger area coverage, more tracer seems to move out of the sampling domain for the DZ-B release.

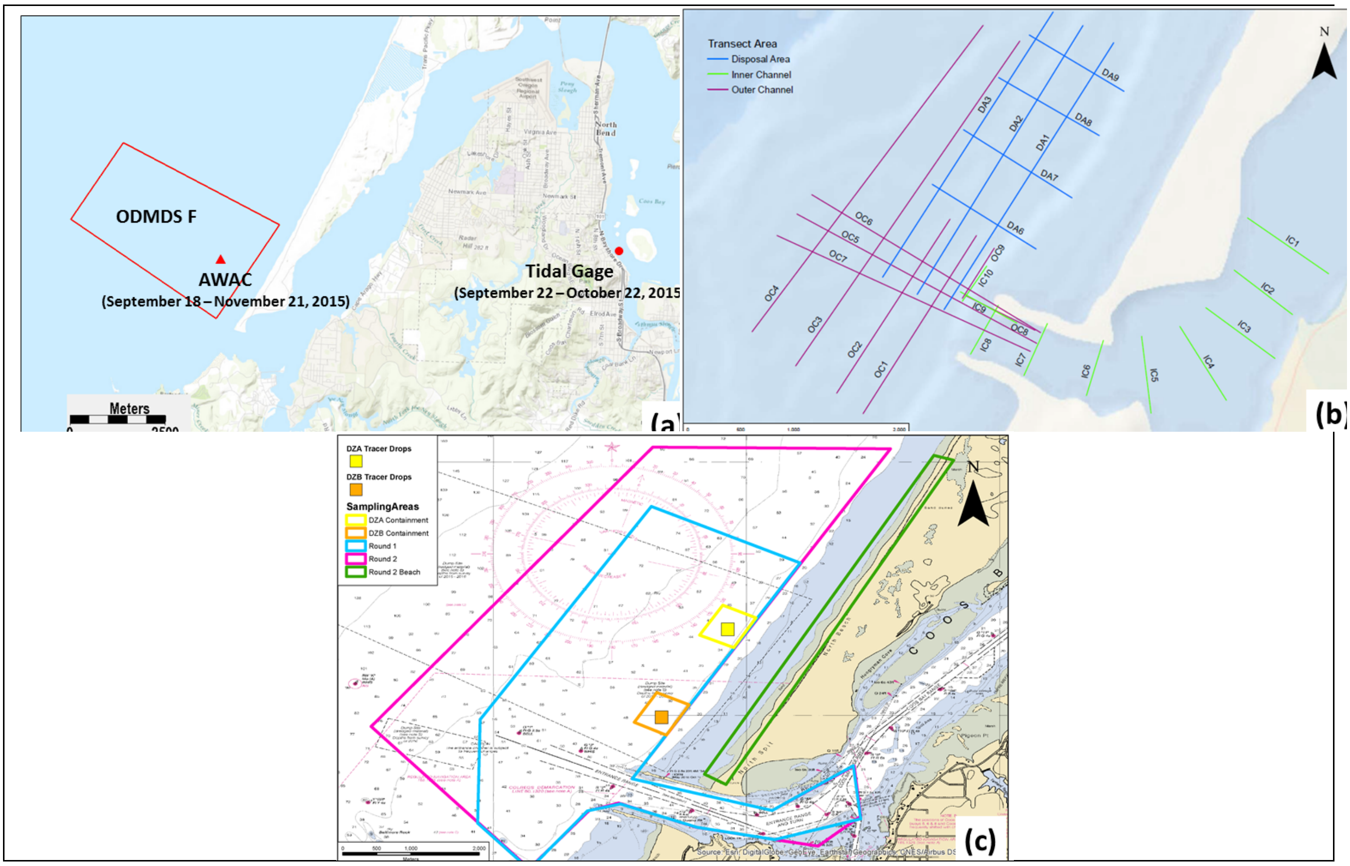

Figure 2. Field data collection. (a) Water surface elevation gauge in Coos Bay and AWAC gauge within ODMDS, (b) Transects where vessel mounted ADCP data were collected, and (c) Two sediment tracer release locations, DZ-A and DZ-B, and sediment tracer sampling coverage during Round 1 sampling (cyan polygon) between 20 and 22 November, 2015 and Round 2 (pink polygon) between 12 and 18 March, 2016.

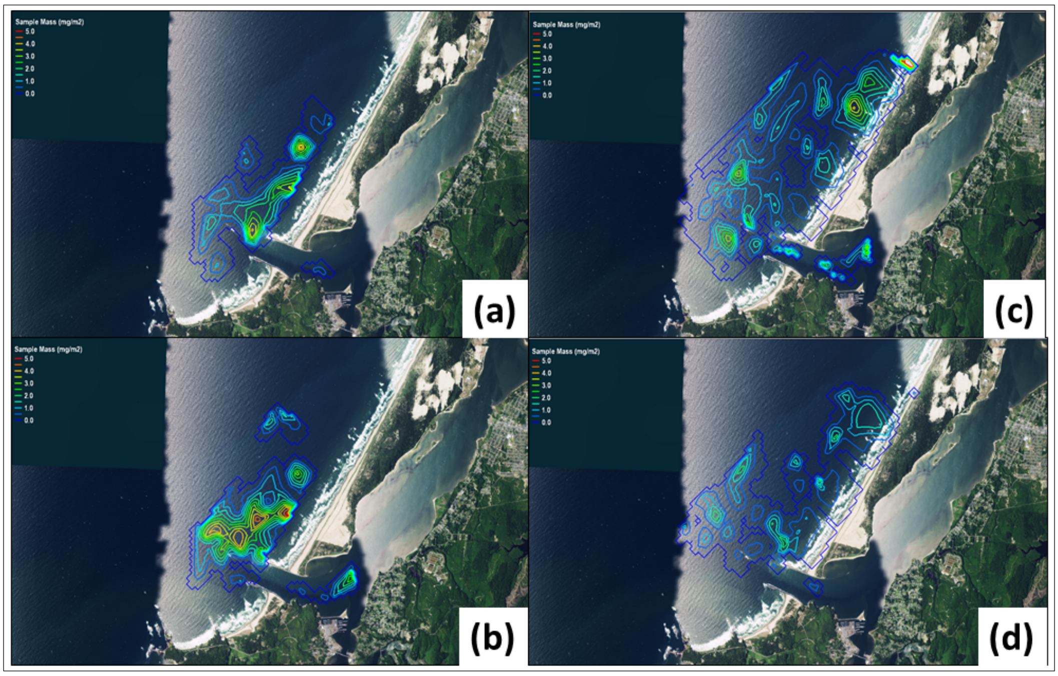

Figure 3. Surface sediment tracer distribution for (a) DZ-A release and (b) DZ-B release from the Round 1 sampling (kg/m^2), and (c) DZ-A release and (d) DZ-B release from the Round 2 sampling (kg/m^2).

  / ISSN 1562-6865 (Online) - ISSN 1063-7710 (Print)

3 METHOD

The Coastal Modeling System (CMS) were selected for the study (Sanchez et al., 2011a; 2011b; Wu et al., 2011; Lin et al., 2008; 2011). The CMS performed wave, hydrodynamic, and sediment transport simulations and the model results were calibrated and validated using the survey data. By performing sediment mapping, sediment transport pathways were investigated under combined wave, hydrodynamic, and atmospheric forcing conditions.

3.1 Coastal modeling system

The CMS is an integrated suite of numerical models for waves, flows, and sediment transport and morphology change in coastal and inlet applications. This modeling system includes representation of relevant nearshore processes for practical applications of navigation channel performance, and sediment management at coastal inlets and adjacent beaches. The CMS consists of a hydrodynamic and sediment transport model (CMS-Flow), and a spectral wave transformation model (CMS-Wave). All pre- and post-processing for these models is performed within the ERDC Surface-water Modeling System (SMS) interface (Aquaveo, 2013).

3.2 Sediment mapping

The CMS includes the calculation of multiple-sized sediment transport, which combines the bed and suspended load transport equations into a single total-load transport equation (Sanchez et al., 2014). The transport due to currents includes the stirring effect of waves, and the wave-related transport includes the contributions due to asymmetric oscillatory wave motion, Stokes drift, surface roller, and undertow. CMS-Flow can simulate any number of sediment size fractions, and considers the interactions between size fractions, bed sorting and layering, and morphology change. The model divides the sediment bed into multiple layers to consider the heterogeneity of bed material size composition along the bed depth. The fraction of each size class is then calculated and stored in each layer using the mixing or active layer concept (Hirano, 1971; Wu, 1991). The sediment in the mixing layer, i.e., the top layer of the bed, directly exchanges or contact with the sediment moving in the water column. By tagging the sediments and bookkeeping the history of bed composition within each layer a multiple-sized sediment transport simulation can present the tracking information of sediment movement.

3.3 CMS simulations

3.3.1 CMS model setup

A telescoping variable-resolution CMS-Flow grid was developed for the Coos Bay estuarine system. The areal extent for the modeling domain is approximately 31 kilometers alongshore and 32 kilometers across shore. The water depth ranges from 1-2 m above the mean sea level at tidal marsh areas in the bay to 16 m at the inlet navigation channel, and further increases to 130 m in the offshore boundary. The cell sizes of the telescoping grid system vary from 20 m around the Coos Bay Inlet and the navigation channel to 320 m in the open ocean (Figure 4). The CMS-Wave grid was generated with varying cell sizes, which covers the same domain and has the similar spatial resolution as the CMS-Flow grid.

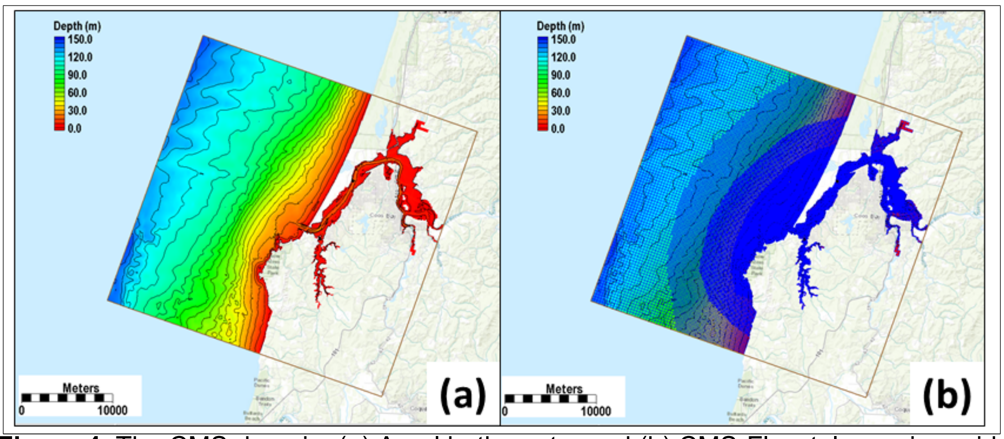

Figure 4. The CMS domain. (a) Areal bathymetry and (b) CMS-Flow telescoping grid.

3.3.2 CMS model forcing

NOAA tide gauge (#9432780) at Charleston provides the tidal forcing for CMS-Flow along open boundaries. Wind speed and direction are available at the Charleston gauge and at the NOAA offshore buoy #46015. The buoy wind data were selected and specified at air-sea interface to well reproduce wind-driven current on the ocean side. Three NDBC buoys, #46015, #46226, and #46050, were measuring directional wave spectra. Through model tests, buoy #46015 was picked to drive CMS-Wave, and large data gaps were filled with the wave spectral data downloaded at buoy #46050.

The inland boundary of the CMS domain was not extended upstream to the four river gauging stations. All the river flows measured at those gauges enter the Coos Bay from the downstream of the South Coos River. The combined river flow is multiplied by a factor of two because Freelin Reasor at the Coos Watershed Association indicated that the measured flows at the four gauges count for 53.84% of the area that drains to Coos Bay (Personal communication, 6 August, 2015).

3.3.3 CMS simulation periods

Simulations were conducted for a summer month (21 June – 20 July 2014, 30 days), and a six-month period (19 October 2015 – 31 March 2016, 165 days). The monthly simulation corresponds to the latest ADCP survey period by Sutherland and O'Neill (2016). The CMS calibration was performed using the measured water surface elevation and current at the bay location (RM 8.0). Accompanying the sediment tracer release by RPS EH is the field program of hydrodynamic and wave data collection and tracer samplings. The results of the six-month simulation validate the CMS hydrodynamic and wave calculations against water surface elevation, current, and wave measurements, and demonstrate the CMS' capability in tracking sediment tracer.

4 RESULTS AND DISCUSSIONS

4.1 CMS calibration and validation

4.1.1 Model calibration

Calibration procedures include examination and adjustment of bottom friction, wall friction, tidal prism, and freshwater inflows. The goodness-of-fit statistics were calculated to quantitatively demonstrate model skill and to determine the level of calibration, which included the calculations of correlation coefficient (R), the Root-Mean-Square Error (RMSE), and the Normalized Root-Mean-Square Error (NRMSE).

The calculated and measured currents at the ADCP station were projected on the principle current direction and the comparison results shown in Figure 5(a) display strong tidal signals. The measured currents range from -1.3 (southward, ebb current) to 0.9 m/s (northward, flood current) in the principle direction. The imbalance in tidal current indicates that the Coos Bay estuary could be ebb-dominated. On the other hand, the river contribution could be another factor. Overall, the calculated currents are in good agreement with the measured currents. The RMSE is 0.157 m/s, the NRMSE 7.43%, and the correlation coefficient R between the model and data is 0.985.

Both the measured and calculated WSEs show that the spring tidal amplitude is close 3.5 m in the area. Visual inspection indicates that the CMS results well reproduce the tidal signals displayed in the WSE survey. The root mean square error (RMSE) is 0.055 m and the NRMSE is 1.56%. The correlation coefficient R between the model and data is 0.998.

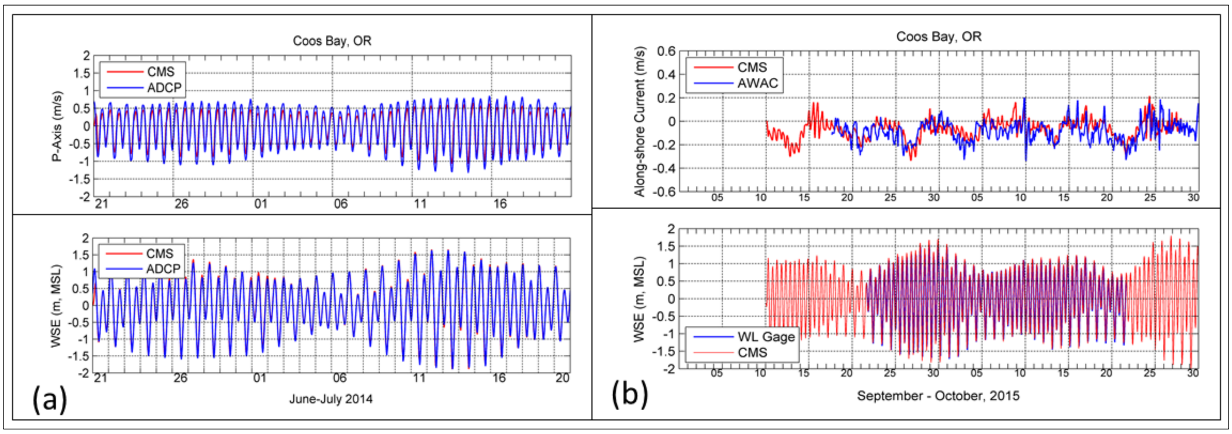

Figure 5. Current and water surface elevation comparisons between the measurements and the CMS calculations (a) at the ADCP station and the tide gauge deployed from 21 June to 20 July 2014, and (b) at the AWAC gauge and the tide gauge in the upper Coos Bay from September to October 2015.

4.1.2 Model validation

The latest WSE, current, and wave data collected by RPS EH were used for CMS validation (Figure 2). Both the calculated and the measured currents were rotated to the coastline direction at AWAC. Figure 5(b) shows the time series of the current speed in longshore direction and WSE comparisons at the tidal gauge inside the Coos Bay (Figure 2). The calculations fairly well reproduced the tidal currents overlapped on top of low frequency wind-driven flows. Major discrepancies between the model and data occurred during a few low frequency events. The RMSE for the current comparison is 0.081 m/s and the NRMSE is 14.98%. The correlation coefficient is 0.538. The goodness-of-fit statistics for WSEs give a correlation coefficient of 0.973. The RMSE and the NRMSE are 0.206 m and 6.19%, respectively.

The calculated wave parameters are well correlated with the measurements at the AWAC gauge. The correlation coefficients are 0.896, 0.811, and 0.840 for wave height, wave period, and wave direction, respectively. The RMSE and the NRMSE for wave height comparison are 0.322 m and 7.35%, for wave period 1.387 sec and 8.05%, and for wave direction 10.0° and 5.56%, respectively. The sensitivity tests on wave transformation show that the calculated wave parameters are closely associated with the wave boundary specifications.

Instantaneous currents were measured by vessel mounted ADCP on transects surrounding the Coos Bay inlet from 28 September through 1 October, 2015 (Figure 2). As a demonstration, Figure 6 shows current comparisons on bay transects on 28 September 2015. The calculated current vectors well match the measured ebb current magnitudes and directions on each transect. Current variations along transects, i.e., strong currents in the center of the navigation channel and weaker currents off the channel, are also well reproduced by the CMS. The current goodness of fit statistics were calculated for U- (east-west) and V-components (north-south) on 10 selected transects close to a peak flood or ebb current period. The overall comparison indicates the close correlation and a good fitting between the model results and the ADCP data.

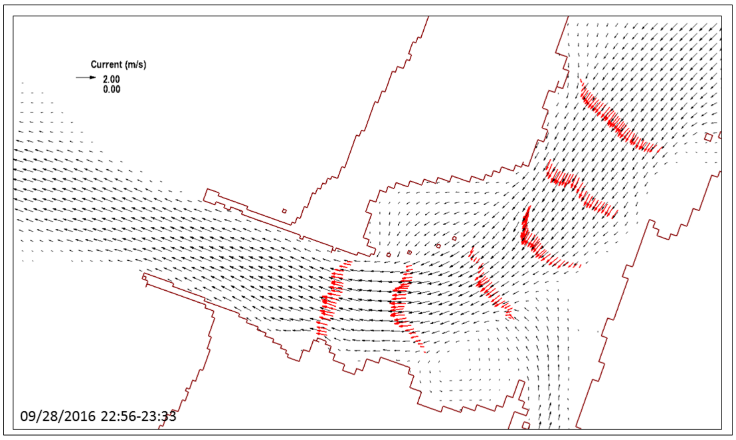

Figure 6. Current comparisons between the boat-mounted ADCP measurements and the CMS calculations in transects on 28 September 2015 between 22:56 and 23:33 GMT.

4.2 CMS sediment mapping

Based on the implementation of the sediment tracer study, the six-month hydrodynamic and wave simulations were conducted. The simulation period includes high-energy, high-flow winter months and the entire duration from sediment tracer release through two rounds of tracer samplings.

4.2.1 Current and sediment transport

The 6-month model simulation results were temporally averaged (Figure 7). The mean current and corresponding sediment transport indicate that the longshore current was dominant in shallow coastal area and there existed a return flow from the nearshore area of ODMDS to the inlet around tip of north jetty. Mean sediment transport pattern well corresponds to the mean current pattern. The sediment in the bay was flushing out along the channel and was carried to the north by the mean longshore current in the open ocean during the 6-month period. The return flow near the jetties moved sediment into the inlet.

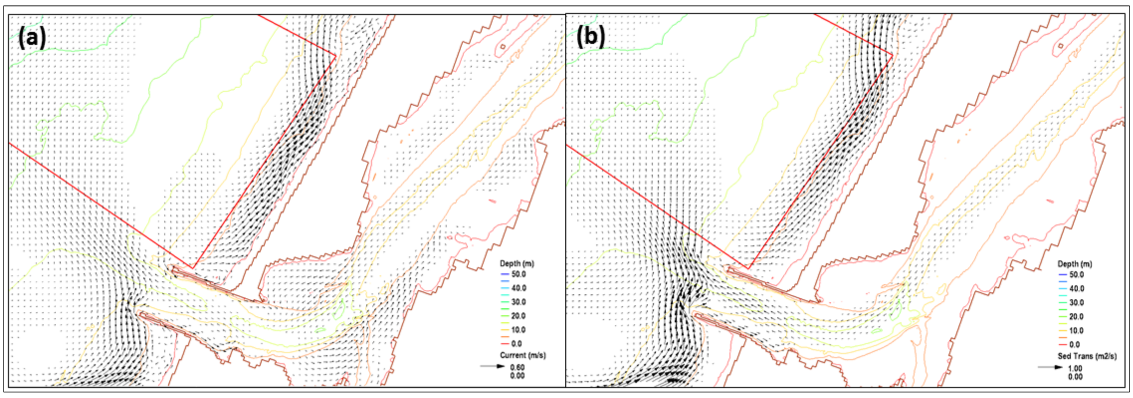

Figure 7. Calculated mean current and sediment transport for the period of September 2015 to March 2016.

Net sediment transport directions were also obtained by examining morphological changes and performing sediment budget analysis, for which the area surrounding the inlet and ODMDS was divided into 9 subareas. Based on net bed volume changes in each subarea, the sediment transport directions can be estimated. The transport directions between 11 September and 23 November 2015 are shown in Figure 8. During this period, it can be seen that the nearshore area of ODMDS and the bay area are losing sediment, and the inlet entrance channel and the ebb shoal are gaining sediment.

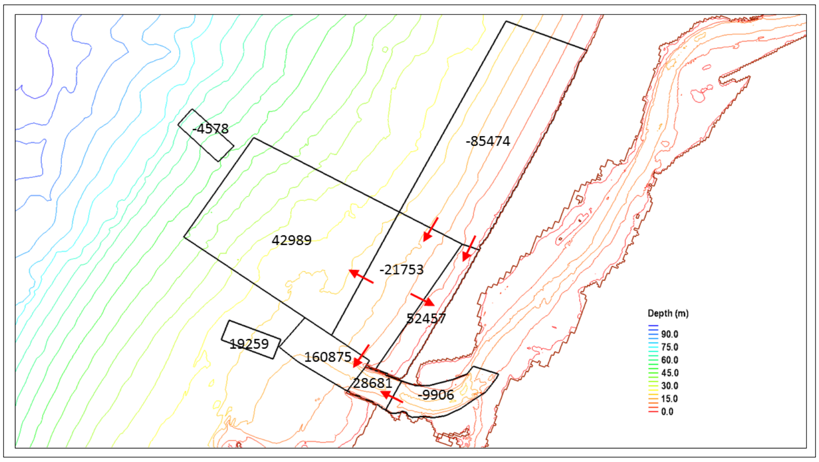

Figure 8. Bed volume changes in 9 divided polygons around the inlet entrance and ODMDS from 11 September to 23 November 2015.

4.2.2 Sediment tracer

For the six month sediment mapping simulations, 600 kg of tracer were specified at DZ-A and DZ-B sites. The grain size of the sediment tracer was 0.32 mm, the same as the native grain size, 5 bed layers were specified, and the tracer was tracked from the beginning of simulations, which was on 20 and 19 September, 2015 for the DZ-A and DZ-B releases, respectively.

Sediment tracer distributions in the top bed layer were retrieved from CMS simulations in every 30 days, starting from day 5. Figure 9 shows the distributions after released at DZ-A and DZ-B, respectively. At the initial stage of the simulation, the sediment tracer released at DZ-A shows more onshore movement while the sediment tracer released at DZ-B displays further offshore spreading. After 3 months of simulations, all the tracer distributions show northward, longshore transport.

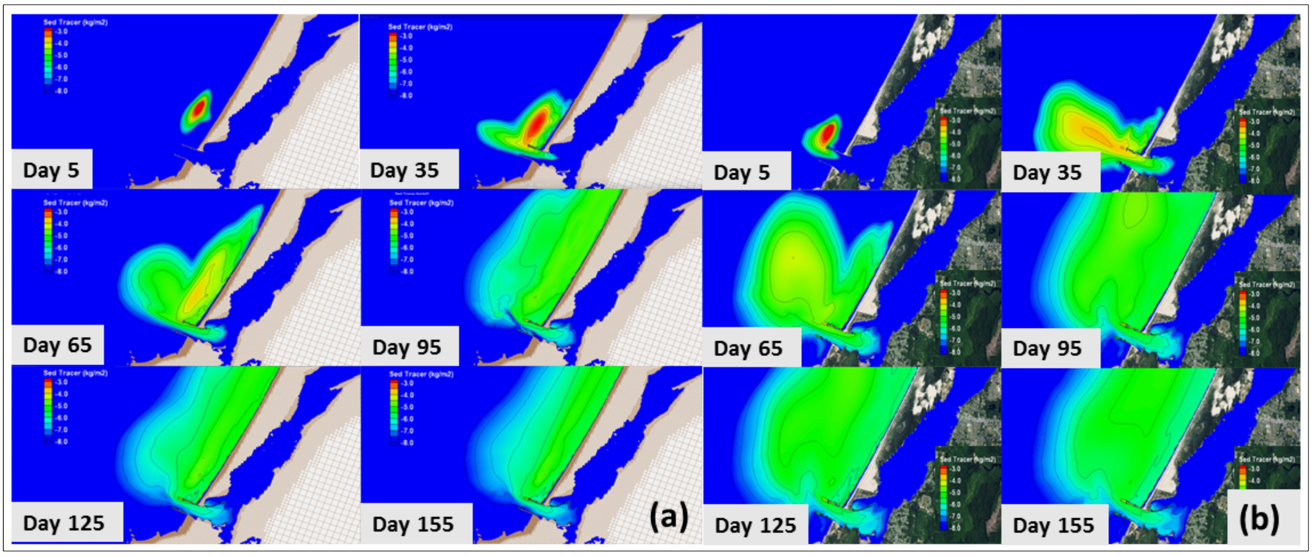

Figure 9. Temporal evolution of sediment tracer concentration for (a) the DZ-A and (b) the DZ-B release in every 30 days from 20 September 2015 through 31 March 2016.

4.3 Transport percentage

Quantitative sediment tracer tracking was also completed by estimating tracer mass within 9 polygons embracing the inlet and ODMDS (Figure 8). Figures 10 (a) and (b) show the tracer mass distributions and the percentages relative to initial released 600 kg of tracer from DZ-A on 23 November, 2015 and 16 March, 2016, respectively, and Figures 10(c) and (d) from DZ-B, respectively. From Figures 10(a) and (b), it can be seen that most of sediment tracer stays adjacent to the DZ-A release site (more than 60%) and a small portion, about 9%, of tracer is moved to the inlet entrance around the north jetty and the inlet ebb shoal after two-month tracer release. Figure 10(b) also displays significant tracer dissipation in the nearshore area of ODMDS almost six months into tracking the tracer movement. In the nearshore polygon of ODMDS, the total tracer mass is reduced to less than 30% of the initial released tracer. The inlet entrance and ebb shoal areas also show tracer dissipation and the tracer mass is reduced to 5%. Since southerly wind had been dominant from December 2015 to March 2016, the sediment tracer was moving alongshore to the north. Sediment tracer mass in the northern most polygon increases from 9% on 23 November, 2015 and to 23% on 16 March, 2016. Only 3% of the sediment tracer released at DZ-A moved to the offshore area of ODMDS and less than 1% to the bay polygon.

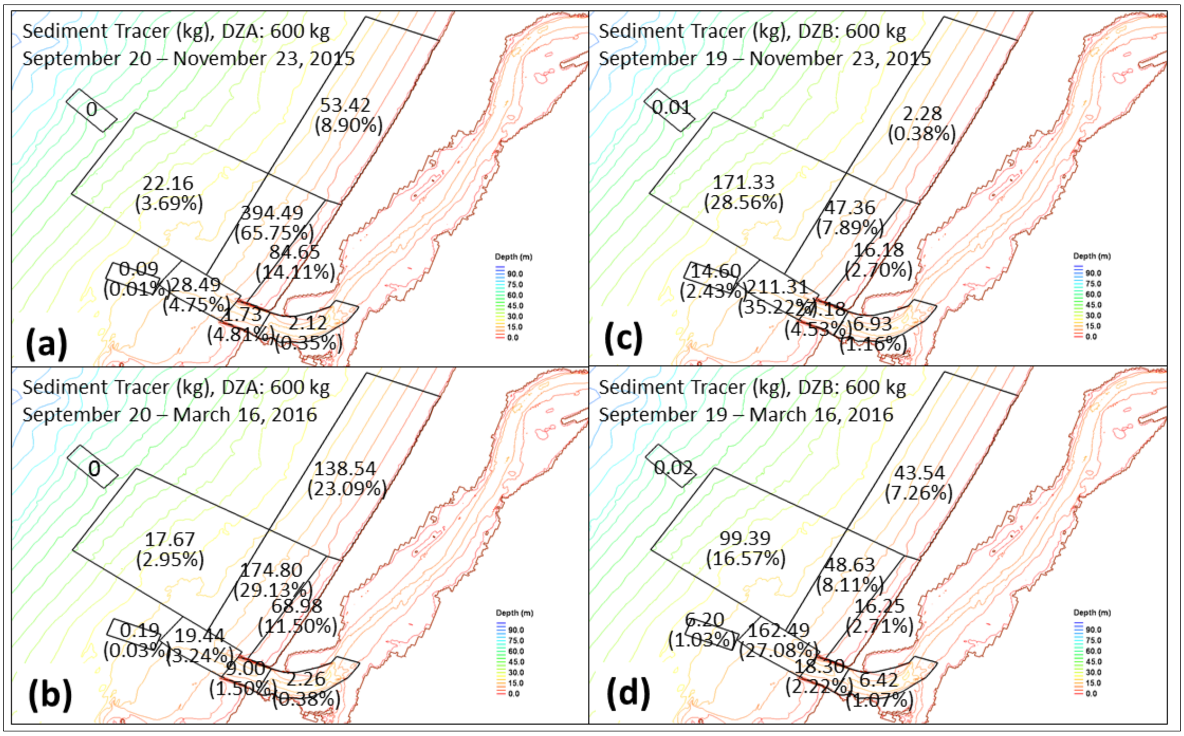

Figure 10. Sediment tracer mass distribution (kg) and percentages relative to initial released 600 kg of tracer from DZ-A on (a) 23 November, 2015 and (b) 16 March 2016, from DZ-B on (c) 23 November, 2015 and (d) 16 March 2016.

The DZ-B site is located closer to the inlet entrance and the sediment tracer release from DZ-B was implemented one day earlier. The difference in tracer release time and location resulted in the difference in sediment tracer distributions as shown in Figure 9. On 23 November, 2015, about 40% of the sediment tracer moved to the inlet entrance and the inlet ebb shoal areas, and less than 10% still stayed near the release location. More tracer is transported to the offshore area and the bay area. Similar tracer dissipation occurred in high tracer concentration areas on 16 March, 2016. The tracer mass is reduced to less than 30% in the inlet entrance and around 16% in the offshore polygon. Sediment tracer was spreading parallel to shoreline towards the north, but not as much sediment tracer moved to the northern in the nearshore polygon area.

An attempt has been made to compare the calculated sediment tracer distribution with that obtained from the field program although the comparison has its limitation related to tracer recovery rate, spatial sampling coverage, and super facial sampling. Figures 11(a) and (b) show the surveyed tracer mass distributions and the percentages relative to total surveyed tracer mass within sampling-covered polygon areas for the DZ-A release on 23 November, 2015 and 16 March, 2016, respectively, and Figures 11(c) and (d) for the DZ-B release, respectively.

Within the polygons fully covered both by Rounds 1 and 2 samplings, the measured tracer distributions show consistency with the calculated results. The sediment tracer released from DZ-A displays high concentration in the nearshore release zone during the Round 1 sampling period and the concentrations in the nearshore and in the inlet ebb shoal polygons show great dissipation from the Round 1 to 2 sampling period. The high tracer concentration in the nearshore northern most polygon indicates the longshore sediment movement to the north. However, the inconsistency between the model results and the measurements is also obvious. For example, the bay polygon shows large tracer variations between the samplings, the channel area has much lower tracer accumulation, and the offshore area always displays high tracer concentration.

From the above analysis and the tracer sampling results, potential sediment tracer pathways are summarized in Figure 12. After released within the nearshore ODMDS, the dominant transport direction of sediment tracer was towards the inlet entrance. Once getting close to the inlet, the tracer was carried away and spread offshore by strong ebb currents. At the late stage of the simulation period, the dominant southerly wind determined the tracer transport direction.

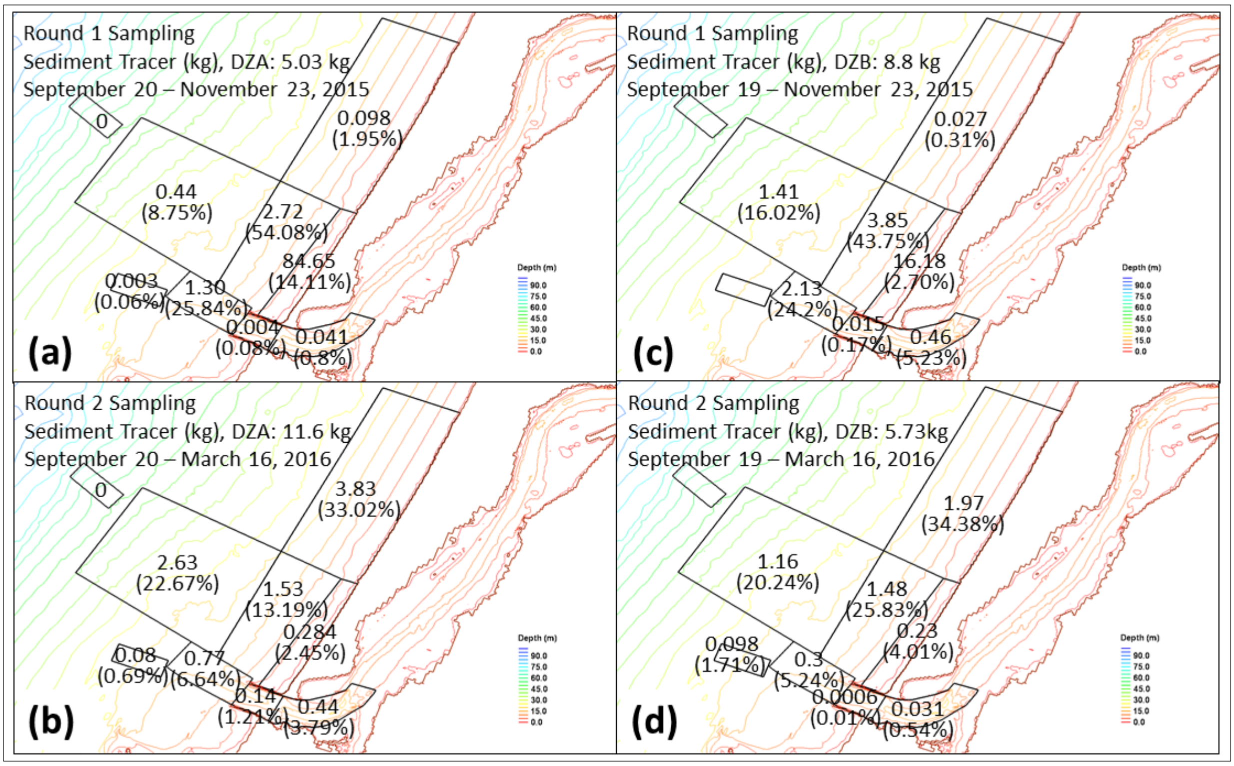

Figure 11. Surveyed tracer mass distribution (kg) and percentages relative to total mass in the Round 1 sampling area for the DZ-A release on (a) 23 November, 2015 and (b) 16 March 2016, for the DZ-B release on (c) 23 November, 2015 and (d) 16 March 2016.

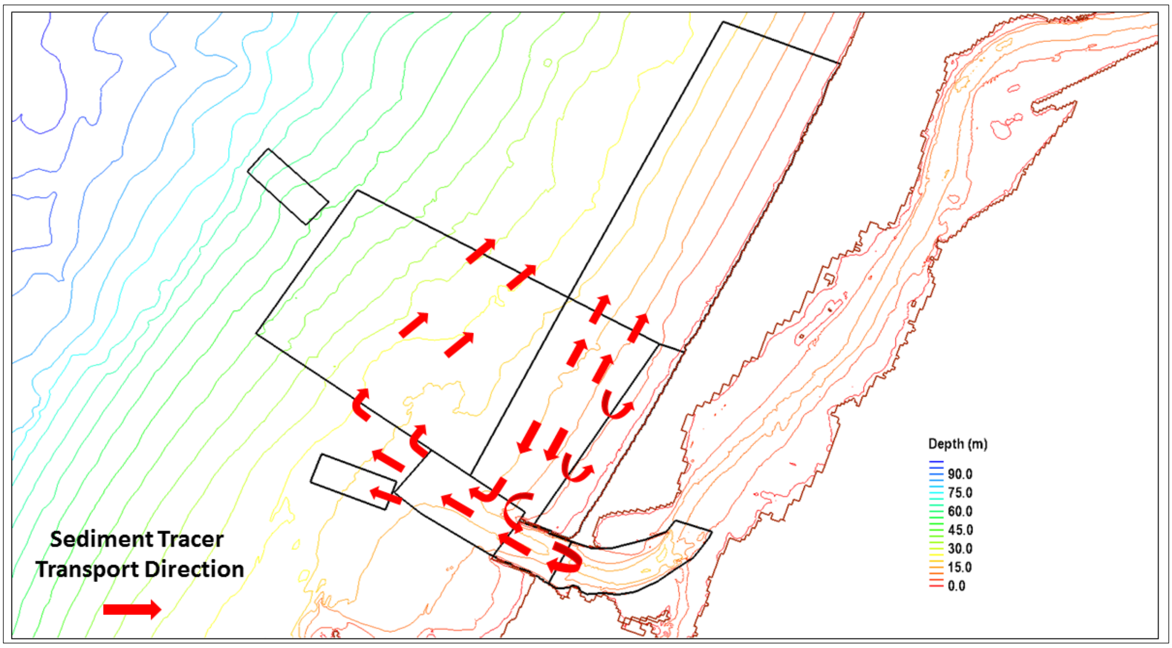

Figure 12. Analyzed sediment tracer pathways around ODMDS and the inlet entrance based on the CMS results and the sediment tracer field program.

5 SUMMARY

With the implementation of a sediment tracer study, a coupled wave, hydrodynamic, sediment transport model (CMS) was set up and model simulations were conducted to investigate sediment tracer movement

  ISSN 1562-6865 (Online) - ISSN 1063-7710 (Print)

after placed in the nearshore zone of an ocean dredged material disposal site (ODMDS F) adjacent to the Coos Bay Inlet, Oregon. For the CMS application in this high-energy coast, the major findings are as follows:

1. The CMS calibration and validation results demonstrate the model's capability in simulating waves, current, water surface elevation, sediment transport, and morphology changes in the coastal estuarine environment.
2. Primary driving forcing in the Coos Bay Inlet system is tide, wind and waves. Tidal current is the dominant flow component in the bay and storm-/wave-driven current is dominant in the open ocean area. River discharges have a significant contribution to temporally averaged current during the high flow period but, generally, play a relatively weaker role in hydrodynamics and sediment transport.
3. Comparisons of the CMS results and the sediment tracer sampling data indicate that the sediment tracer placed within the nearshore ODMDS zone is moving towards the inlet entrance area at the initial stage of the release and is pushed offshore by strong ebb currents once reaching the inlet channel and ebb shoal areas. After three months into the simulation, the sediment tracer starts to spread northward alongshore due to strong dominant southerly wind conditions.
4. The sediment mapping feature in the CMS shows its promising performance in simulating sediment tracer tracking and helping to identify sediment transport pathways.
5. The sediment tracer pathways analyzed and obtained in the study only correspond to the specific forcing conditions during the selected simulation period and the results might vary for different wave, hydrodynamic, atmospheric, and environmental forcing.

ACKNOWLEDGEMENTS

The authors wish to thank the US Army Corps of Engineers Portland District for their support. Permission was granted by the Chief, U. S. Army Corps of Engineers to publish this information.

REFERENCES

Aquaveo. (2013). Surface-water Modeling System (SMS), version 11.1, http://www.aquaveo.com/software/sms-surface-water modeling-system

Hirano, M. (1971). River Bed Degradation with Armoring. *Transactions of the Japan Society of Civil Engineering*, 3(2): 194-195.

Lin, L., Demirbilek, Z. & Mase, H. (2011). Recent Capabilities of CMS-Wave: a Coastal Wave Model for Inlets and Navigation Projects. *Journal of Coastal Research, Special Issue* 59, 7-14.

Lin, L., Demirbilek, Z. & Yamada, F. (2008). *CMS-Wave*: *A Nearshore Spectral Wave Processes Model for Coastal Inlets and Navigation Projects*, Coastal and Hydraulics Laboratory Technical Report ERDC/CHL TR-08-13. Vicksburg, MS: U.S. Army Engineer Research and Development Center.

NOAA. (2016a). NOS Hydrographic Survey Data, National Geophysical Data Center. Office of Coast Survey, National Oceanic and Atmospheric Administration, http://www.ngdc.noaa.gov/mgg/bathymetry/hydro.html, [Accessed 25 October 2016].

NOAA. (2016b). Tides and Currents. National Oceanographic and Atmospheric Administration, http://tidesandcurrents.noaa.gov/, [Accessed 25 October 2016].

NDBC. (2016). National Data Buoy Center, National Oceanographic and Atmospheric Administration, http://ndbc.noaa.gov/, [Accessed 25 October 2016].

Sanchez, A., Wu, W., Beck, T.M., Li, H., Rosati, J.III, Thomas, R., Rosati, J.D., Demirbilek, Z., Brown, M. & Reed, C. (2011a). *Verification and Validation of the Coastal Modeling System,* Report 3: Hydrodynamics, ERDC/CHL Technical Report 11-10, U.S. Army Corps of Engineers Research and Development Center, Coastal and Hydraulics Laboratory, Vicksburg, MS.

Sanchez, A., Wu, W., Beck, T.M., Li, H., Rosati, J.D., Demirbilek, Z. & Brown, M. (2011b). *Verification and Validation of the Coastal Modeling System,* Report 4: Sediment Transport and Morphology Change, ERDC/CHL Technical Report 11-10, U.S. Army Corps of Engineers Research and Development Center, Coastal and Hydraulics Laboratory, Vicksburg, MS.

Sánchez, A., Wu, W., Li, H., Brown, M., Reed, C., Rosati, J.D. & Demirbilek, Z. (2014). *Coastal Modeling System: Mathematical Formulations and Numerical Methods,* ERDC/CHL TR-14-2, U.S. Army Engineer Research and Development Center, Coastal and Hydraulics Laboratory, Vicksburg, MS.

Sutherland, D.A. & O'Neill, M.A. (2016). Hydrographic and Dissolved Oxygen Variability in a Seasonal Pacific Northwest Estuary. Estuarine. *Coastal and Shelf Science*. 172, 47-59.

Wood, J. & Ruggiero, P. (2014). 2014 *Estuarine Bathymetry Data Collection, Analysis, and Archiving at Coos Bay, OR*, CEOAS Technical Report, Oregon State University, Corvallis, OR.

Wu, W. (1991). The Study and Application of 1-D, Horizontal 2-D and Their Nesting Mathematical Models for Sediment Transport. *PhD dissertation*, Wuhan, China: Wuhan University of Hydraulic and Electrical Engineering., Wuhan, China.

Wu, W., Sanchez, A. & Zheng, M. (2011). An Implicit 2-D Shallow Water Flow Model on Unstructured Quadtree Rectangular Mesh. *Journal of Coastal Research Special Issue*. 59, 15-26.

Proceedings of the 37th IAHR World Congress
August 13 – 18, 2017, Kuala Lumpur, Malaysia

UNDERSTANDING THE CHANGING HYDRO-ENVIRONMENT AND ECOSYSTEM-BASED LIVELIHOODS IN COASTAL BANGLADESH

ROBERT J NICHOLLS[(1)], ATTILA N LAZAR[(2)], CRAIG W HUTTON[(3)], HELEN J ADAMS[(4)], MASHFIQUS SALEHIN[(5)], ANISUL HAQUE[(6)], MUNSUR RAHMAN[(7)] & DEREK CLARKE[(8)]

[(1, 2, 3, 8)] University of Southampton, Southampton, United Kingdom,
r.j.nicholls@soton.ac.uk; a.lazar@soton.ac.uk; cwh@geodata.soton.ac.uk; dc@soton.ac.uk
[(4)] King's College London, London, United Kingdom,
helen.j.adams@kcl.ac.uk
[(5, 6, 7)] Bangladesh University of Engineering & Technology, Dhaka, Bangladesh,
mashfiqussalehin@iwfm.buet.ac.bd; anisul@iwfm.buet.ac.bd; mmrahman@iwfm.buet.ac.bd

ABSTRACT

Low and mid latitude deltas provide diverse ecosystem services and benefits for their populations. At the same time, deltas are also recognized as one of the most vulnerable coastal environments, with a range of drivers operating at multiple scales, from global climate change and sea-level rise to deltaic-scale subsidence and land cover changes, such as rice to aquaculture. These drivers threaten deltas and their ecosystem services, which often provide livelihoods for the poorest communities in these regions. The imperative to maintain ecosystem services presents a development challenge: how to develop deltaic areas in ways that are sustainable, and benefit all residents. This paper considers an integrated framework to analyze changing ecosystem services in deltas and the implications for human well-being. The focus is on the provisioning ecosystem services of agriculture, fisheries, wetlands and freshwater that directly support livelihoods. A systemic perspective is adopted to represent the principal biophysical and socio-ecological components and their interaction. A range of methods are integrated within a quantitative framework, including biophysical and socio-economic modelling and include analyses of governance through scenario development. The approach is highly iterative, with learning both within the project team and with stakeholders. The application of the methodological framework is illustrated using coastal Bangladesh, although the approach is generic and could be widely applied.

Keywords: Deltas; integrated assessment; delta planning; livelihoods; biophysical change.

1 INTRODUCTION

Collectively, low to mid latitudes deltas represent some of the most densely populated areas in the world with 500 million people living on one per cent of the planet's land area (Ericson et al., 2006). Deltas are also complex systems which are subject to multiple stresses (Sebesvari et al., 2016). This is especially true for the coastal zone of Bangladesh where there are more than a thousand people per square kilometer. Livelihoods, food security and poverty in Bangladesh are strongly dependent on natural resources affected by several factors including climate variability and change, upstream river flow modifications, fishery exploitation in the Bay of Bengal, and engineering interventions such as polders. Limits on freshwater availability, saline water intrusion and extreme events and natural hazards (*e.g.* river floods, cyclones and storm surges) have a negative impact on water availability and crop irrigation potential. This severely affects land use and livelihood opportunities for the coastal population. Hydro-environmental changes can be especially detrimental for the well-being of the poorest households that are highly dependent on natural resources and ecosystem services.

The ESPA Deltas project has analyzed the bio-physical environment and the livelihoods of the people in coastal Bangladesh from a systemic perspective (Lázár et al., 2015a; Nicholls et al., 2016). This considered both the individual system components and how they are coupled and interact. This is a highly multi-disciplinary problem and involved a large team of experts working together in a collaborative manner. The approach was participatory and involved a range of stakeholders within Bangladesh, including national planners. The project developed, integrated and applied a range of models and databases across the knowledge domains of interest. Empirical data collection was also important, especially concerning livelihoods and ecosystem services, as limited observations existed.

Building on this foundation, a new innovative integrated model called the Delta Dynamic Integrated Emulator Model (ΔDIEM) was developed from scratch within the project. It couples all the relevant processes, including linking ecosystem service production to livelihoods, and has a fast run-time suitable to develop multiple simulations. This allows the long-term analysis of possible changes in the delta by linking scenarios (*i.e.* plausible futures) in physical processes (*e.g.* river flows, nutrients), with productivity (*e.g.* fish, rice), social processes (*e.g.* access, property rights, migration) and governance/management (*e.g.* fisheries, agriculture, water and land use management). This integrated approach is designed to support national policy makers and provide them with science-based evidence concerning the implications of different development trajectories over timescales up to 2050 in detail, and in broader terms up to 2100. This includes the likely robustness of different types of intervention on natural resource conservation and poverty levels. This paper briefly reviews the model framework, presents some of the results on the coupling of changes to the hydro-environment and livelihoods in coastal Bangladesh, and considers the wider implications and how the method could be developed. This approach provides important new information for delta planning by adding a livelihoods dimension to standard civil and hydraulic engineering assessment approaches. It also provides a framework for ongoing incremental development and improvement with the delta management process.

2 STUDY AREA

The Ganges-Brahmaputra-Meghna (GBM) Delta is one of the world's most dynamic and significant deltas. Geologically, it covers most of Bangladesh and parts of West Bengal (India), with a total population exceeding 100 million people (Woodroffe et al., 2006; Ericson et al., 2006). The Ganges and Brahmaputra rivers rise in the Himalayas (collectively with catchments in five countries: China, Nepal, India, Bhutan, and Bangladesh) and ultimately deposit their sediments in the GBM delta and the Bay of Bengal (Wilson and Goodbred, 2015) (Figure 1). The Meghna has a smaller Bangladesh and Indian catchment. The delta is changing rapidly with a growing urban population, including major cities such as Khulna, Chittagong and especially the world cities of Kolkata and Dhaka. At the same time, the delta provides important ecosystem services, especially provision services that sustain this large population (especially intensive rice paddy and fisheries).

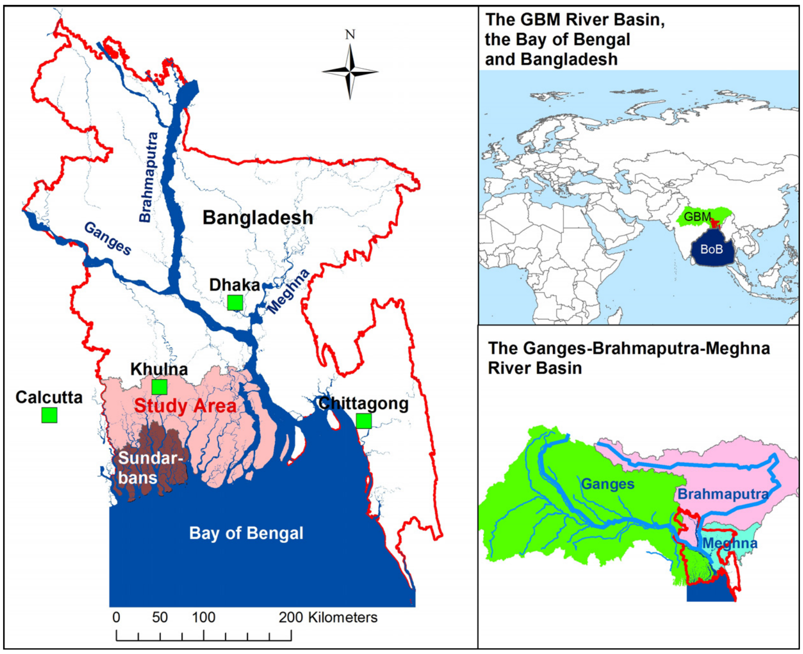

Figure 1. The Study Area, showing the Ganges-Brahmaputra-Meghna (GBM) river basin and the Bay of Bengal (BoB) and the detailed study area – the south-west coastal zone of Bangladesh is shaded including the Sundarbans (in brown).

The national population of Bangladesh in 2013 was 157 million and this is projected to exceed 200 million by 2050 with continued urbanization (UN, 2013). National GDP per capita has risen significantly from US$838 (1996-2000) to US$1087 (2011-2015) (http://data.worldbank.org/indicator/NY.GDP.PCAP.CD). This primarily reflects growth in (1) exports, especially clothing, (2) overseas remittances, and (3) non-farm employment (Hunt, 2015).

The study area is the seaward part of the delta within Bangladesh, south of Khulna and west of the Meghna to the Indian border (Figure 1). This area comprises of one of the world's largest lowlands and it is subject to tidal exchange. Excluding Khulna, Barisal and other regional towns, it is largely rural with extensive agriculture, aquaculture and capture fisheries. These are numerous islands near the Meghna River, isolating many communities. It also includes the Bangladeshi portion of the Sunderbans, the largest mangrove forest in the world. The population of the region is exposed to numerous hazards, including tidal flood, riverine flooding, arsenic in local groundwater supplies, salinity in water supplies and in irrigation water, water logging, with cyclone and associated storm surge being the most damaging hazard. The study area is also highly threatened by sea-level rise (Milliman et al., 1989; Huq et al., 1995; World Bank, 2010) and Bangladesh is considered one of the most vulnerable countries to climate change.

The study area population was about 14 million in 2011, and subject to out-migration. Anecdotally, one key driver of migration is negative environmental stress (salinization, hazards, etc.) that forces people to diversify household livelihoods by sending family members away. (The DECCMA Project is examining such migration in deltas in more detail -- http://www.geodata.soton.ac.uk/deccma/). In the study area, the incidence of poverty is higher than the national average.

The analysis considers three distinct scales: (1) global; (2) regional, including the river basin and Bay of Bengal; and (3) the delta, including the study area (Figures 1). When considering the biophysical processes operating in the study area, they all affect the morphology of the delta plain (Woodroffe et al., 2006). There is a broad regional subsidence (*i.e.* gradual loss of elevation) of two to three millimeters a year, and more localized hotspots with higher subsidence (Brown and Nicholls, 2015). There is both loss and gain of land, with a net gain of land in Bangladesh over the last few decades reflecting the large sediment supply from the rivers (Bammer, 2014; Wilson and Goodbred, 2015). River floods mainly occur during the wet season (monsoon), when a large volume of water is received from the upstream catchments. This results in 20-60 per cent inundation of Bangladesh on an annual basis (Salehin et al., 2007). Cyclones and storm surges regularly make landfall in Bangladesh (> once/year during the 20th Century). Cyclones and storm surges lead to extreme sea levels, high winds, and potentially saltwater flooding, which damage crops and properties, causing immediate catastrophic financial situations for families, and there is only a limited safety net for the poorest. (Alam and Dominey-Howes, 2015). However, improved Disaster Risk Reduction by the growth of flood warnings and cyclone shelters has significantly reduced the death toll during extreme floods and cyclones. For example, while Cyclone 'Sidr' in 2007 caused thousands of deaths and injuries, earlier cyclones of similar magnitude had much higher mortality.

Coastal Bangladesh has a system of polders, where the land is surrounded by embankments with drains to keep out floods to enhance agriculture. The balance between sea water and freshwater is a critical issue in the study area (Clarke et al., 2015; Lázár et al., 2015b). This varies seasonally and salt water pushes far inland during the low river flow period between the annual monsoon rains, and cyclones can also cause saltwater flooding. If the land becomes too saline, traditional agriculture is degraded. If this persists, there are limited options: moving to salt-tolerant crops (which are being continuously developed) or converting to shrimp aquaculture which is usually for export and greatly reduces employment (Islam et al., 2015; Amoako Johnson et al., 2016). Upstream dams and water diversion to irrigation and other uses may enhance salinization. The Sunderbans are an important buffer against cyclones, but will decline with sea-level rise (Payo et al., 2016) and re-threatened by other stresses (*e.g.* pollution). They provide a range of ecosystem goods which are available to the poorest, as well as tourism based around the famous Bengal tiger.

In summary, biophysical processes play an important role in people's lives in the study area.

3 APPROACH

Analyzing the future of ecosystem services and human livelihoods in coastal Bangladesh is a complex multi-disciplinary problem. The core issue when integrating the social, physical and ecological dynamics of deltas is the identification and measurement of the mechanisms by which the system components interact to produce human wellbeing. That is to ask: (1) Which physical and biological processes affect life, livelihoods, health and mobility; and (2) Are these relationships stable and hence predictable over time?

To explore these questions, we build on the key insights from the science of ecosystem services. In deltas, ecosystem services include the processes that bring freshwater, sediments, productive and biologically diverse wetlands and fisheries, and productive land for agriculture. In general, a host of (1) supporting, (2) provisioning, (3) regulating and (4) cultural ecosystem services can be identified (Millennium Ecosystem Assessment, 2005) – here the major focus is on the provisioning ecosystem services, although other types of service are considered where possible, such as the buffering of storms provided by mangroves (a regulating service).

The methodology that we follow to achieve this goal is summarized in Figure 2. Governance analysis and stakeholder engagement run throughout the project and is essential due to its participatory nature. From the literature, our understanding of deltas in this broad interdisciplinary context is limited and an initial conceptual analysis is essential to develop more detailed questions. For example, the relationship between ecosystem services and livelihoods; and the characteristics of the wider socio-ecological system needs to be considered in detail. To do this, we analyzed the population census and implement an innovative household survey which collects empirical data on ecosystem services and livelihoods (Adams et al., 2016). In parallel there is a major effort to analysis a range of biophysical processes in a consistent framework (Figure 3). To apply these results in policy analysis full integration is required. To this end we developed a range of exogenous and endogenous scenarios, including extensive stakeholder participation (Allan and Barbour, 2015). We also developed an integration framework and applied this to develop the Delta Dynamic Integrated Emulator Model (ΔDIEM) that couples a range of biophysical processes and a unique household livelihood module based on the household survey results.

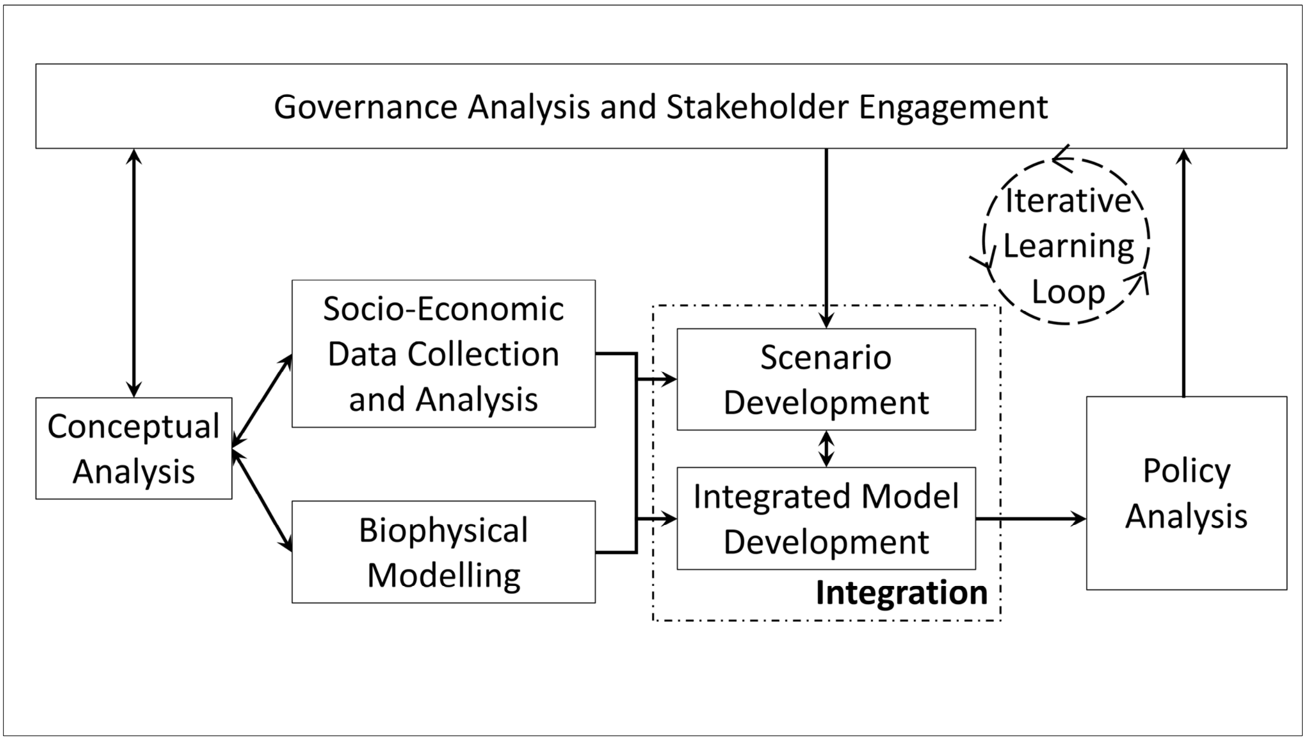

Figure 2. The main tasks and flow of information in the integration methodology – note the explicit Iterative Learning Loop.

4 THE DELTA DYNAMIC INTEGRATED EMULATOR MODEL (ΔDIEM)

Integration within the ESPA Deltas project faced multiple challenges: (1) multiple scientific disciplines; (2) multiple scales of analysis; (3) varying analytical methods; and (4) different computational power and run time requirements (Lázár et al., 2015a; Nicholls et al., 2016). For example, the Delft-3D hydrodynamic model used to simulate flooding takes 2 days to simulate one year for one scenario, whereas the INCA catchment model is much faster, simulating nine scenarios over 100 years within an hour. Thus, the first step of integration is to build on the earlier components and develop a conceptual diagram of the coupled biophysical-human system (Figure 3). This includes issues raised by the stakeholders and identifies the required processes and model elements. At the same time, the spatial and temporal scales of the biophysical models and all analytical methods are mapped, including the schematics of the integrative model. The integration aims to develop a rapid assessment framework which can simulate many future cases, and hence explore policy choices. This was based on a new meta-model that fully couples the required system elements and harmonizes across the spatial and temporal scales. The current version of the model considers the upstream river basin and the Bay of Bengal as boundary conditions (although these can be replaced by dynamic counterparts, if required), because the focus of the analysis is on the Bangladesh coastal zone as defined in Figure 1 and on the environment – human interaction. Thus, the boundary conditions are currently represented by look-up tables of scenarios (climate, upstream hydrology and water quality, Bay of Bengal sea elevation and fisheries), whereas the coastal system has fully coupled representation.

In ΔDIEM the hydrodynamics of the coastal zone was captured by the three-dimensional Delft-3D, FVCOM and Modflow-SEAWAT models for three time-slices, and sophisticated emulators (Hotelling, 1936; Clark, 1975; Challenor, 2012) were created to represent these (surface and groundwater) hydrological and water quality processes within ΔDIEM. Emulation of these complex model results was essential to reduce the computational time and to interpolate the available simulations. A novel, regional soil salinity component of ΔDIEM was also developed that fully couples the climatic, hydrological and land management drivers of soil salinity change and links these with a process-based agriculture model (*i.e.* the improved CROPWAT model; Lázár et al., 2015b). Thus, climate change, flooding, salinization, and land management have a direct impact on crop productivity in the simulations. All these biophysical calculations are done at the union (Parishad) level (which is the smallest planning unit in Bangladesh) and at a daily time step. (Note that there are 653 unions in our study area). Annual fish catches estimated by a coastal fisheries model (Fernandes et al., 2015) is downscaled to the Union scale and a monthly time step by utilizing a new fish market survey conducted within the project. Other livelihoods (*e.g.*, small business, small-scale manufacturing, salaried employment, etc.) are less important in rural Bangladesh, and were not studied in detail. Thus, in ΔDIEM, they are represented with observation-based look-up tables.

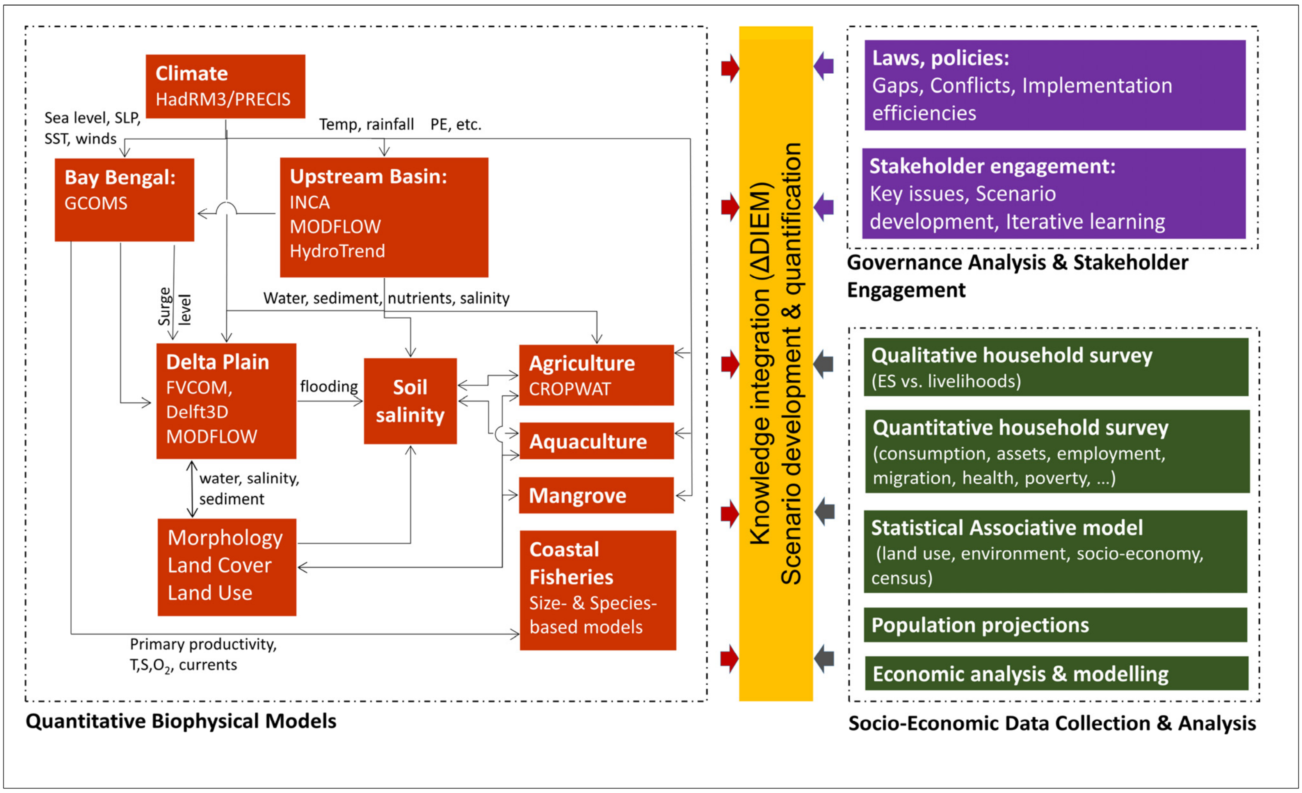

Figure 3. A conceptual diagram showing the flow of information to knowledge integration, which is encapsulated in ΔDIEM.

One of the most novel aspects of the approach is the explicit inclusion of poverty and health in ΔDIEM, rather than as an external piece of analysis. These issues are integrated in two distinct ways, both building strongly on the biophysical simulations of ΔDIEM. The first method uses a spatial statistical asset-poverty model (union-based, annual time step) to directly estimate asset poverty (Amoako Johnson et al., 2016). This is based on biophysical state indicators and some socio-economic scenarios of employment rate, access to education and travel time to cities/markets. The second method approximates household livelihoods, poverty and health from the household survey using an agent-based-type household economy model. Within this process-based calculation, the simulation follows the virtual lives of 37 household archetypes (union-based, monthly time step). These archetypes are identified and parametrized using the household survey. Calculations in the household component are driven not only by the biophysical changes, but also by the demographic, land cover and economic scenarios. Incomes and remittances are matched with direct livelihood costs, affordable household expenditure and farm laboring opportunities. The outputs of the calculation are household welfare and food intake. A range of governance interventions can be tested with this model framework such as: land use restrictions, subsidies, income taxes, market price policies, new crop varieties, embankment projects, infrastructure development, etc. Such a detailed household economy model also produces regional economic indicators (*e.g.* GDP/capita, GINI coefficient), food security indicators (*e.g.* rice production, hunger periods) and the globally used \$1.9/day headcount poverty indicator. These two contrasting methods, the statistical associative model and the household survey model, allow preliminary consideration of uncertainty in the simulations, robustness of governance interventions and identify further research areas.

5 DISCUSSIONS/CONCLUSIONS

Our analysis started with broad qualitative assessment of the system of interest. It progressed with a range of socio-economic analysis and surveys and biophysical modelling. These were developed with integration in mind and also informed scenario development. Stakeholders were consulted throughout this process including within the scenario development. This has culminated in the ΔDIEM model, which offers a practical assessment tool for scientific and policy assessment designed with and for stakeholders in a complex socio-environmental context. The ΔDIEM model has been demonstrated effective and is now beginning to be used in analysis of the development choices for coastal Bangladesh.

In terms of the question concerning the physical and biological processes which affect life, livelihoods, health and mobility, important insights have emerged as outlined below, and will continue to emerge from this analysis. In terms of the stability of the relationships and hence predictability over time for biophysical process our assumption that they are unchanging is reasonable and normal. For socio-economic issues, this is much more challenging and we have had to review the literature and make assumptions about this stability. These assumptions are explicit and will be investigated into the future both in Bangladesh and using appropriate analogues elsewhere. However, we recognize that the timeframes at which the socio-economic results are useful is much shorter than for the biophysical results.

This research has already developed a number of important outputs and conclusions. For example, Adams et al. (2016) demonstrate a novel household survey approach based on socio-ecological zones which provides important new data on ecosystem services. Amoako-Johnson et al. (2016) demonstrate that there are a series of spatially-variable drivers of poverty in the study area, including salinization, water logging, wetland/mudflats, employment, education and access to roads, amongst others. These spatially variable issues need to be considered in poverty alleviation programs. Biophysically, wet season river flows are likely to increase and dry season flows may diminish, but the uncertainty of future catchment management introduces a huge uncertainty (Whitehead et al., 2015). Fisheries seem likely to decline, but better management can maintain current catches if this is implemented (Fernandes et al., 2015). Furthermore, these analyses have all informed the development of ΔDIEM and validated the framework we developed and applied as a useful approach to address and manage complex environmental and development problems. This hybrid integrated framework has allowed a move away from an ad hoc, external expert or purely indicator-based approach and provided an opportunity to explore the interactions between domains of knowledge as diverse as oceanography and perception-based assessments of wellbeing. In this approach, while the analysis is complex, the assumptions are explicit and have been debated, challenged and changed as our knowledge grows and the detailed questions being posed evolve with this understanding. Hence, it provides an explicit framework analyzing the problem and by providing clear spatially explicit output it forces the user to identify, consider and explore the limits to knowledge.

ΔDIEM depends upon systems analysis and simulation modelling. Given the difficulty of predicting change in all of the systems considered here, such simulation modelling could be regarded as being almost naïve. We recognize the limits to what we represent in our models, but we aimed to represent all the relevant processes and their interactions. Developing and linking models was a key process within the project team that facilitated development of our conceptual ideas, promoted detailed discussion between different discipline experts, as well as providing the ΔDIEM software. As we gain experience we will be able to continue to explore the complexities, interdependencies and uncertainties of our study area. This includes considering a wide range of possible strategies for development within the context of a variety of possible futures that might exist. As such, it allows an exploration of uncertainty.

Possible improvements are also readily apparent from this approach. At the most basic, it indicates that the provision of better basic data such as bathymetry and elevation or surface water salinity in the short- and long-term would represent a significant improvement. The household survey might be repeated to explore how these factors and relationships change over a number of years, addressing the issue of the stability of relationships/predictability over time. Moreover, the ΔDIEM framework is flexible and can be adapted to analyze additional issues and it is currently being applied to examine water security issues in the REACH Project (http://reachwater.org.uk/). Therefore, while we have primarily focused on provisioning ecosystem services in a deltaic environment, models used could readily be extended to analyze regulating ecosystem services (Hossain et al., 2016).

Building these types of co-produced analytical tools represents a significant amount of effort and resource, but we would argue that the new insights, capacity building, scientific and policy applications and understanding generated justify this approach. The model framework structures thinking about knowledge and understanding of the relevant processes, information and data. Indeed, the level of integration accomplished in this research is novel and unusual and possibly unique in its strong quantitative coupling of biophysical changes to household livelihoods related to provisioning ecosystem services. This research has already provided important insights about the socio-ecological processes operating in the study area and in the wider region, as already discussed. Many of these insights could have emerged from more traditional sectoral approaches, but the integration is providing further uniquely synergistic insights which are still being developed, building on the new knowledge emerging from the interaction of more traditional knowledge spaces. Furthermore, we have been engaging with national policy processes including the Bangladesh Delta Plan 2100 (http://www.bangladeshdeltaplan2100.org/). This is providing a practical test of the real-world application of this approach in a policy context.

Looking to the future, these methods could be applied more widely in other deltaic areas, as many issues are common. Cross-fertilization with other research efforts in deltas such as the management efforts in the Netherlands and habitat restoration in the Mississippi delta may also be beneficial. In project appraisal terms the methods discussed here complement existing appraisal methods and provide many new indicators that could inform development planning, including distributional effects. In principle, the methods described here are generic and could be applied in other coastal and non-coastal contexts where strong socio-ecological coupling exists. For example, the spatial domain covered in Bangladesh could be expanded in various ways and a national application based on this approach has been discussed. In the near term, further development and piloting of the methods in coastal Bangladesh is planned.

ACKNOWLEDGEMENTS

The research in this paper was funded by the Ecosystem Services for Poverty Alleviation (ESPA) programme (project number NE-J002755-1). The ESPA programme was funded by the UK Department for International Development (DFID), the Economic and Social Research Council (ESRC) and the Natural Environment Research Council (NERC). All our collaborators in the ESPA Deltas project (http://www.espadelta.net/) are thanked for their input.

REFERENCES

Adams, H., Adger, W.N., Ahmad, S., Ahmed, A., Begum, D., Lázár, A.N., Matthews, Z., Rahman, M.M. & Streatfield, P.K. (2016). Spatial and Temporal Dynamics of Multidimensional Well-Being, Livelihoods and Ecosystem Services in Coastal Bangladesh. *Scientific Data 3*, Article number: 160094, doi:10.1038/sdata.2016.94.

Alam, E. & Dominey-Howes, D. (2015). A New Catalogue of Tropical Cyclones of the Northern Bay of Bengal and the Distribution and Effects of Selected Landfalling Events in Bangladesh. *International Journal of Climatology*, 35(6), 801-835.

Allan, A. & Barbour, E. (2015). Integrating Science, Modelling and Stakeholders through Qualitative and Quantitative Scenarios. *ESPA Deltas Working Paper No. 5*. http://www.espadelta.net/resources/docs/working_papers/scenarios_working_paper_v8.pdf.

Bammer, H. (2014). Bangladesh's Dynamic Coastal Regions and Sea-Level Rise. *Climate Risk Management*, 1, 51–62.

Brown, S. & Nicholls, R.J. (2015). Subsidence and Human Influences in Mega Deltas: The Case of the Ganges–Brahmaputra–Meghna. *Science of The Total Environment*, 527, 362–374.

Challenor, P. (2012). Using Emulators to Estimate Uncertainty in Complex Models. In: Dienstfrey, A.M. & Boisvert, R.F. (eds.) *Uncertainty Quantification in Scientific Computing,* Volume 377 of the series IFIP Advances in Information and Communication Technology, Springer, 151-164.

Clark, D. (1975). Understanding Canonical Correlation Analysis, Concepts and Techniques in Modern Geography, No.3, *Geo Abstracts Ltd*, Norwich, UK.

Clarke, D., Williams, S., Jahiruddin, M., Parks, K. & Salehin, M. (2015). Projections of On-Farm Salinity in Coastal Bangladesh. *Environmental Science: Processes & Impacts,* 17(6), 1127-1136, DOI: 10.1039/C4EM00682H.

Ericson, J.P., Vorosmarty, C.J., Dingman, S.L., Ward, L.G. & Meybeck, M. (2006). Effective Sea-Level Rise and Deltas: Causes of Change and Human Dimension Implications. *Glob. Planet. Change,* 50(1), 63-82.

Fernandes, J.A., Kay, S., Hossain, M.A., Ahmed, M., Cheung, W.W., Lázár, A.N. & Barange, M. (2015). Projecting Marine Fish Production and Catch Potential in Bangladesh in the 21st Century under Long-Term Environmental Change and Management Scenarios. *ICES Journal of Marine Science,* 73(5), 1357-1369, doi: 10.1093/icesjms/fsv217.

Hossain, M.S., Dearing, J.A., Rahman, M.M. & Salehin, M. (2016). Recent Changes in Ecosystem Services and Human Well-Being in the Bangladesh Coastal Zone. *Regional Environmental Change,* 16(2), 429-443.

Hotelling, H. (1936). Relations between Two Sets of Variates. *Biometrika,* 28(3/4), 312–377.

Hunt, A. (2015). ESPA Deltas: Economic Policy Dimensions. Identification of Existing and Implied Economic Dimensions in the Scenarios, and Their Levels. *Unpublished project report*, Bath University.

Huq, S., Ali, S.I. & Rahman, A.A. (1995). Sea-Level Rise and Bangladesh: A Preliminary Analysis. *Journal of Coastal Research*, Special issue no 14, 44–53.

Islam, G.M.T., Islam, A.K.M.S., Shopan, A.A., Rahman, M.R., Lázár, A.N. & Mukhopadhyay, A. (2015). Implications of Agricultural Land Use Change to Ecosystem Services in the Ganges Delta. *Journal of Environmental Management*, 161, 443–452.

Johnson, F.A., Hutton, C.W., Hornby, D., Lázár, A. & Mukhopadhyay, A. (2016). Is Shrimp Farming a Successful Adaptation to Salinity Intrusion? A Geospatial Associative Analysis of Poverty in the Populous Ganges–Brahmaputra–Meghna Delta of Bangladesh. *Sustainability Science,* 11(3), 423-439, DOI 10.1007/s11625-016-0356-6.

Lázár, A.N., Nicholls, R.J., Hutton, C., Adams, H., Payo, A., Salehin, M., Haque, A., Clarke, D., Bricheno, L., Fernandes, J.A., Barbour, E., Allan, A., Begum, D. & Szabo, S. (2015a). The Hydro-Environment and Livelihoods in Coastal Bangladesh. *E-Proceedings of the 36th IAHR World Congress*, The Hague, The Netherlands, 4.

Lázár, A.N., Clarke, D., Adams, H., Akanda, A.R., Szabo, S., Nicholls, R.J., Matthews, Z., Begum, D., Saleh, A.F.M, Abedin, M.A., Payo, A., Streatfield, P.K., Hutton, C., Mondal, M.S. & Moslehuddin, A.Z.M. (2015b). Agricultural Livelihoods in Coastal Bangladesh under Climate and Environmental Change - A Model Framework. *Environmental Science: Processes & Impacts,* 17(6), 1018-1031.

Millennium Ecosystem Assessment (2005). *Ecosystems and Human Well-being: Synthesis*. Island Press, Washington, DC.

Milliman, J.D., Broadus, J.M. & Gable, F. (1989). Environmental and Economic Implications of Rising Sea Level and Subsiding Deltas: The Nile and Bengal Examples. *Ambio,* 18(6), 340–345.

Nicholls, R.J., Hutton, C.W., Lázár, A.N., Allan, A., Adger, W.N., Adams, H., Wolf, J., Rahman, M. & Salehin, M. (2016). Integrated Assessment of Social and Environmental Sustainability Dynamics in the Ganges-Brahmaputra-Meghna Delta, Bangladesh. *Estuarine, Coastal and Shelf Science*, 183, 370-381, doi:10.1016/j.ecss.2016.08.017.

Payo Garcia, A., Mukhopadhyay, A., Hazra, S., Ghosh, T., Ghosh, S., Brown, S., Nicholls, R., Bricheno, L., Wolf, J., Kay, S., Lázár, A. & Haque, A. (2016). Projected Changes in Area of the Sundarban Mangrove Forest in Bangladesh due to SLR by 2100. *Climatic Change*, 139(2), 279-291.

Salehin, M., Haque, A., Rahman, M.R., Khan, M.S.A. & Bala, S.K. (2007). Hydrological Aspects of 2004 Floods in Bangladesh. *Journal of Hydrology and Meteorology*, 4(1), 33-44.

Sebesvari, Z., Sebesyari, Z.F.G., Harrison, I., Brondizio, E., Bucx, T., Dearing, J., Ganguly, D., Ghosh, T., Goodbred, S.L., Hagenlocher, M., Hajra, R., Kuenzer, C., Mansur, A., Matthews, Z., Nicholls, R.J., Nielsen, K., Overeem, I., Purvaja, R., Rahman, M., Ramesh, R., Renaud, F., Robin, R., Subba, R.B., Singh, G., Szabo, S., Tessler, Z.D., van de Guchte, C., Vogt, J. & Wilson, C.A. (2016). *Imperatives for Sustainable Delta Futures.* Global Sustainable Development Report (GSDR) 2016 Science Brief. Available from: https://sustainabledevelopment.un.org/content/documents/972032_Sebesvari_Imperatives%20for%20sustainable%20delta%20futures.pdf. [Accessed: 03.04.2016]

United Nations (2013). *World Population Prospects, the 2012 Revision.* Department of Economic and Social Affairs, Population Division, New York.

Whitehead, P.G., Barbour, E., Futter, M.N., Sarkar, S., Rodda, H., Caesar, J., Butterfield, D., Jin, L., Sinha, R., Nicholls, R. & Salehin, M. (2015). Impacts of Climate Change and Socio-Economic Scenarios on Flow and Water Quality of the Ganges, Brahmaputra and Meghna (GBM) River Systems: Low Flow and Flood Statistics. *Environmental Science: Processes & Impacts,* 17(6), 1057-1069.

Wilson, C.A. & Goodbred, S.L. (2015). Construction and Maintenance of the Ganges-Brahmaputra-Meghna Delta: Linking Process, Morphology, and Stratigraphy. *Annual Review of Marine Science*, 7, 67-88.

Woodroffe, C.D., Nicholls, R.J., Saito, Y., Chen, Z. & Goodbred, S.L. (2006). *Landscape Variability and the Response of Asian Megadeltas to Environmental Change*. In: Harvey, N. (ed.), Global Change and Integrated Coastal Management, Chapter C10, 277–314.

World Bank (2010). *Economics of Adaptation to Climate Change (EACC) Report, Bangladesh, 2010*. http://climatechange.worldbank.org/sites/default/files/documents/EACC_Bangladesh.pdf.